

Satoru Kaneko · Paolo Mele  
Tamio Endo · Tetsuo Tsuchiya  
Katsuhisa Tanaka · Masahiro Yoshimura  
David Hui *Editors*

Carbon-related  
Materials — in  
Recognition of Nobel  
Lectures by Prof. Akira  
Suzuki in ICCE

Carbon-related Materials—  
in Recognition of Nobel Lectures by Prof. Akira Suzuki  
in ICCE

Satoru Kaneko • Paolo Mele • Tamio Endo  
Tetsuo Tsuchiya • Katsuhisa Tanaka  
Masahiro Yoshimura • David Hui  
Editors

**Carbon-related Materials—**  
in Recognition of Nobel Lectures  
by Prof. Akira Suzuki in ICCE

 Springer

*Editors*

Satoru Kaneko  
Kanagawa Institute of Industrial Science  
and Technology, KISTEC  
Ebina, Kanagawa, Japan

Tamio Endo  
Sagamihara Surface Treatment Laboratory  
Sagamihara, Japan

Katsuhisa Tanaka  
Department of Material Chemistry  
Kyoto University  
Kyoto, Kyoto, Japan

David Hui  
Department of Mechanical Engineering  
University of New Orleans  
New Orleans, LA, USA

Paolo Mele  
Muroran Institute of Technology  
Muroran, Japan

Tetsuo Tsuchiya  
Advanced Coating Technology Research  
Center  
National Institute of Advanced Industrial  
Science and Technology (AIST)  
Tsukuba, Ibaraki, Japan

Masahiro Yoshimura  
Promotion Centre for Global Materials  
Research (PCGMR)  
Department of Material Science and  
Engineering National Cheng Kung  
University  
Tainan, Taiwan

Professor Emeritus  
Tokyo Institute of Technology  
Tokyo, Japan

ISBN 978-3-319-61650-6

ISBN 978-3-319-61651-3 (eBook)

DOI 10.1007/978-3-319-61651-3

Library of Congress Control Number: 2017949484

© Springer International Publishing AG 2017

This work is subject to copyright. All rights are reserved by the Publisher, whether the whole or part of the material is concerned, specifically the rights of translation, reprinting, reuse of illustrations, recitation, broadcasting, reproduction on microfilms or in any other physical way, and transmission or information storage and retrieval, electronic adaptation, computer software, or by similar or dissimilar methodology now known or hereafter developed.

The use of general descriptive names, registered names, trademarks, service marks, etc. in this publication does not imply, even in the absence of a specific statement, that such names are exempt from the relevant protective laws and regulations and therefore free for general use.

The publisher, the authors and the editors are safe to assume that the advice and information in this book are believed to be true and accurate at the date of publication. Neither the publisher nor the authors or the editors give a warranty, express or implied, with respect to the material contained herein or for any errors or omissions that may have been made. The publisher remains neutral with regard to jurisdictional claims in published maps and institutional affiliations.

Printed on acid-free paper

This Springer imprint is published by Springer Nature

The registered company is Springer International Publishing AG

The registered company address is: Gewerbestrasse 11, 6330 Cham, Switzerland

# Preface

I am not a specialist in studies on carbon-related materials. I attended the International Conference on Composites/Nano Engineering (ICCE), 23 July 2015, in Chengdu, China, on the invitation of Professor David Hui, University of New Orleans. I delivered a Nobel Lecture on “Cross-Coupling Reactions of Organoboranes: An Easy Way for Carbon-Carbon Bonding.” There I made many friends, including Professor Tamio Endo, Sagamihara Surface Lab, and he asked me to write the preface for this book.

In 1963 I joined the research group of Professor Herbert C. Brown, who received the Nobel Prize in Chemistry 1997, at Purdue University, Indiana, US, as a postdoctoral associate, fascinated by the interesting new reaction of hydroboration. After a 2-year stay at Purdue, I returned to Hokkaido University, where I began studying organic synthesis using organoboron compounds. We recognized the potential of organoboranes as intermediates in organic synthesis. Our discoveries of haloboration and cross-coupling reactions are fundamental contributions to the organic chemistry of boron and synthetic methodology.

The cross-coupling reaction is widely used for the stereodefined construction of carbon–carbon bonding in multifunctional systems. I have retired from the university, but I am very happy to have a chance to meet many young researchers at international meetings to discuss this chemistry. I hope this book is useful for such young chemists.

Hokkaido University  
Sapporo, Japan

Akira Suzuki

# Introduction

This book is published in recognition of Nobel Lectures delivered by Akira Suzuki (Emeritus Professor of Hokkaido University, Nobel Prize in Chemistry 2010) and the Special Symposia on Carbon-Related Materials in ICCE-23 (2015) and 24 (2016).

The International Conference on Composites/Nano Engineering (ICCE) <<http://www.icce-nano.org/>> was established by David Hui (University of New Orleans) in 1994 in New Orleans (USA). Subsequently, this Conference has been held every year, initially in the US but latterly all over the world. A few tens of participants attended at the beginning, but recently their numbers have increased to 400-600. In this way, ICCE has been greatly developed and extended throughout the world because of the great efforts of David Hui and major committees. This year (2017) we celebrated the silver jubilee of ICCE, ICCE-25 (2017), in Rome.

The Special Symposium “Oxide Nanocomposites and Heterostructures” was founded in New Orleans for ICCE-10 (2003) by Tamio Endo (Mie University, Japan), Kazuhiro Endo (AIST, Japan), and Team Harmonized Oxides (THO) <<http://www.nims.go.jp/nqe/sa/tho/>>. THO is a Japanese non-profit association, set up by T. Endo and K. Endo to organize various international activities. We had only one THO Special Symposium in ICCE-10, but the numbers increased to around 20 in the subsequent 14 years. In the last 4 years THO have organized a few Special Symposia in ICCE such as “Materials Chemistry” and “Materials for Sustainable Energy.” This is also a feature of the progress of ICCE.

In this development of ICCE, we (THO) invited **Prof. Akira Suzuki** to ICCE-23 (2015) in Chengdu (China) to deliver the Nobel Lecture in Organic Chemistry on “**Cross-Coupling Reactions of Organoboranes: An Easy Way for Carbon-Carbon Bonding.**” The lecture was very interesting and instructive, inspiring all the participants. Most of them working in the field of inorganic materials were inspired to make use of C–C bonding approaches in their work on inorganic materials. This strong impact induced us to invite him again in ICCE-24 (2016) in Haikou (China), and he kindly accepted our invitation. He presented the second Nobel Lecture in the same field, and we again spent very valuable time together. These two Nobel Lectures by Prof. Suzuki drove THO to arrange the “**Suzuki Special Symposium on Carbon-Related Materials**” in ICCE-23 (2015) and

ICCE-24 (2016). Many outstanding presentations were given during these two Special Symposia. The symposium organizers (T. Endo, S. Kaneko, P. Mele, K. Tanaka, T. Tsuchiya, M. Yoshimura, and K. Yasui) were pleased by the disclosure of such excellent papers to such a wide scientific community. This is why we invited our distinguished colleagues to share their results, and why we publish this book entitled “Carbon-Related Materials in Recognition of Nobel Lectures by Prof. Akira Suzuki in ICCE.”

Commemorative photographs taken during ICCE-23(2015) in Chengdu, China and ICCE-25 (2016) in Haikou (China) are shown here. Figure 1 shows Prof. Akira Suzuki giving his Nobel Lecture. Figure 2 shows THO organizers, some of the editors of this book, and Prof. Suzuki after his Nobel Lecture. Figure 3 shows a dinner scene during the Conference, with THO organizers, editors of this book, and Ms. Shun Ying Hui (wife of Prof. David Hui, a Manager of ICCE). At every ICCE Conference we have had very enjoyable mealtimes with representative guests. Figure 4 shows a typical scene at the Conference banquet. On every occasion the singing of the traditional Japanese song “Sakura Sakura” took place, led by Japanese delegates but warmly including foreign delegates. We consider these events of singalongs, dinners, and banquets with the participants of ICCE as very important in the acquisition of international friendship and world peace. This is another purpose and policy of the THO team and ICCE Conferences.

We are planning to publish books relating to the best Special Symposia held in ICCE and aspire to the further development of ICCE.

May 1<sup>st</sup>, 2017

Tamio Endo (Sagamihara Surface Lab., Japan/ICCE Co-Technical Chair)  
Satoru Kaneko (Kanagawa Inst. Indus. Sci. Tech. Japan/ICCE Editorial Board)  
Paolo Mele (Muroran Inst. Tech., Japan/ICCE Co-Technical Chair)  
David Hui (University of New Orleans, USA/ICCE Chair)



**Fig. 1** Prof. Akira Suzuki giving his Nobel Lecture at ICCE-24 (2016) in Haikou, Hainan Island, China



**Fig. 2** Team Harmonized Oxides (THO) organizers, some of the editors of this book, and Prof. Suzuki after his Nobel Lecture at ICCE-23 (2015, Chengdu, China)





**Fig. 3** Dinner scene during ICCE-23 (2015, Chengdu, China), with THO organizers, editors of this book, and Ms. Shun Ying Hui (wife of Prof. David Hui, a Manager of ICCE)



**Fig. 4** Singalong during the Conference banquet of ICCE-24, Haikou (2016, China)

# Contents

## Part I Graphene and Nanocarbon Materials

<b>The Synthesis and the Catalytic Properties of Graphene-Based Composite Materials</b> .....	3
Baojiang Jiang and Chaoyang Li	
<b>Optical Characterization of Graphene and Its Derivatives: An Experimentalist's Perspective</b> .....	27
Dinh-Tuan Nguyen, Ya-Ping Hsieh, and Mario Hofmann	
<b>Submerged Liquid Plasma for the Formation of Nanostructured Carbon</b> .....	61
Masahiro Yoshimura and Jaganathan Senthilnathan	
<b>Lab-on-a-Graphene: Functionalized Graphene Transistors and Their Application for Biosensing</b> .....	79
Takao Ono, Yasushi Kanai, Yasuhide Ohno, Kenzo Maehashi, Koichi Inoue, and Kazuhiko Matsumoto	
<b>Production of Single- and Few-Layer Graphene from Graphite</b> .....	91
Shinya Yamanaka, Mai Takase, and Yoshikazu Kuga	
<b>Graphene-Based Coatings for Dental Implant Surface Modification</b> .....	103
Alina Pruna, Daniele Pullini, and Andrada Soanca	

## Part II Carbon Composites and Thin Films

<b>Effect of CNT on the Mechanical Properties of Composite Materials and Structures</b> .....	119
N. Naveh, Y. Seri, Y. Portnoy, D. Levin, and B. Muravin	
<b>Energy Absorption Capability of Hybrid Fibers Reinforced Composite Tubes</b> .....	145
Yuqiu Yang, Yan Ma, Jing Xu, and Hiroyuki Hamada	

<b>Graphene-Rubber Nanocomposites: Preparation, Structure, and Properties</b> .....	175
Jian Wang, Kaiye Zhang, Qiang Bu, Marino Lavorgna, and Hesheng Xia	
<b>Effects of Graphene and Graphite on Properties of Highly Filled Polybenzoxazine Bipolar Plate for Proton Exchange Membrane Fuel Cell: A Comparative Study</b> .....	211
Manunya Okhawilai, Anucha Pengdam, Ratcha Plengudomkit, and Sarawut Rimdusit	
<b>Electrical Properties of Amorphous Carbon Nitride Thin Films for Pressure Sensor Applications</b> .....	261
Masami Aono and Naoyuki Tamura	
<b>Part III Organic Synthesis and Physical Chemistry</b>	
<b>Combination of Cross-Coupling and Metal Carbene Transformations for the Development of New Multicomponent Reactions</b> .....	279
Lisa Moni, Andrea Basso, and Renata Riva	
<b>Synthetic Molecular Springs: Stretched and Contracted Helices with Their Interconversions of Monosubstituted Polyacetylenes Prepared with a Rhodium Complex Catalyst</b> .....	305
Yasuteru Mawatari and Masayoshi Tabata	
<b>The Spin Coupling in the Polyaromatic Hydrocarbons and Carbon-Based Materials</b> .....	327
Marilena Ferbinteanu, Cristina Buta, Ana Maria Toader, and Fanica Cimpoesu	
<b>Electrocatalytic Hydrogen Production Properties of Polyaniline Doped with Metal-Organic Frameworks</b> .....	373
Kabelo E. Ramohlola, Milua Masikini, Siyabonga B. Mdluli, Gobeng R. Monama, Mpitloane J. Hato, Kerileng M. Molapo, Emmanuel I. Iwuoha, and Kwena D. Modibane	
<b>Plasma Bonding of Plastic Films and Applications</b> .....	391
Kenichi Uehara, Lakshmi Reddy, Hiroaki Nishikawa, Satoru Kaneko, Yoshinobu Nakamura, Kazuhiro Endo, Paolo Mele, David Hui, Rieko Sudo, and Tamio Endo	
<b>Part IV Characterization Tools</b>	
<b>Atomic Force Microscopy for Characterizing Nanocomposites</b> .....	421
Yu Liu, Chao Bao, Heng-yong Nie, David Hui, Jun Mei, and Woon-ming Lau	
<b>Editorial Note</b> .....	443
<b>Index</b> .....	445

# Contributors

**Masami Aono** Department of Materials Science and Engineering, National Defense Academy, Yokosuka, Kanagawa, Japan

**Chao Bao** Chengdu Green Energy and Green Manufacturing Technology R&D Center, Chengdu, Sichuan, China

**Andrea Basso** Department of Chemistry and Industrial Chemistry, University of Genova, Genoa, Italy

**Qiang Bu** State Key Lab of Polymer Materials Engineering, Polymer Research Institute, Sichuan University, Chengdu, China

**Cristina Buta** Faculty of Chemistry, Inorganic Chemistry Department, University of Bucharest, Bucharest, Romania

Institute of Physical Chemistry, Bucharest, Romania

**Fanica Cimpoesu** Institute of Physical Chemistry, Bucharest, Romania

**Kazuhiro Endo** Research Laboratory for Integrated Technological Systems, Kanazawa Institute of Technology, Hakusan, Ishikawa, Japan

**Tamio Endo** Sagamihara Surface Treatment Laboratory, Sagamihara, Japan

**Marilena Ferbinteanu** Faculty of Chemistry, Inorganic Chemistry Department, University of Bucharest, Bucharest, Romania

**Hiroyuki Hamada** Kyoto Institute of Technology, Kyoto, Japan

**Mpitloane J. Hato** Department of Chemistry, School of Physical and Mineral Sciences, University of Limpopo (Turfloop), Polokwane, Sovenga, South Africa

**Mario Hofmann** Department of Material Science and Engineering, National Cheng Kung University, Tainan, Taiwan

Department of Physics, National Taiwan University, Taipei, Taiwan

**Ya-Ping Hsieh** Institute of Atomic and Molecular Sciences, Academia Sinica, Taipei, Taiwan

**David Hui** Department of Mechanical Engineering, University of New Orleans, New Orleans, LA, USA

**Koichi Inoue** The Institute of Scientific and Industrial Research, Osaka University, Osaka, Japan

**Emmanuel I. Iwuoha** SensorLab, Chemistry Department, University of the Western Cape, Cape Town, South Africa

**Baojiang Jian** Key Laboratory of Functional Inorganic Material Chemistry, Ministry of Education of the People's Republic of China, Heilongjiang University, Harbin, China

**Yasushi Kanai** The Institute of Scientific and Industrial Research, Osaka University, Osaka, Japan

**Satoru Kaneko** Kanagawa Institute of Industrial Science and Technology, KISTEC, Ebina, Kanagawa, Japan

**Yoshikazu Kuga** Department of Applied Sciences, Muroran Institute of Technology, Muroran, Japan

**Woon-ming Lau** School of Mathematics and Physics, University of Science & Technology Beijing, Beijing, China

**Marino Lavorgna** Institute of Polymers, Composites and Biomaterials, National Research Council, Portici, NA, Italy

**D. Levin** Rafael Advanced Defense Systems, Haifa, Israel

**Chaoyang Li** Center for Nanotechnology, School of Systems Engineering, Kochi University of Technology, Kami City, Kochi, Japan

**Yu Liu** Jiangsu Key Laboratory of Advanced Food Manufacturing Equipment and Technology, Jiangnan University, Wuxi, Jiangsu, China

**Yan Ma** Kyoto Institute of Technology, Kyoto, Japan

**Kenzo Maehashi** The Institute of Scientific and Industrial Research, Osaka University, Osaka, Japan

Institute of Engineering, Tokyo University of Agriculture and Technology, Tokyo, Japan

**Milua Masikini** SensorLab, Chemistry Department, University of the Western Cape, Cape Town, South Africa

**Kazuhiko Matsumoto** The Institute of Scientific and Industrial Research, Osaka University, Osaka, Japan

**Yasuteru Mawatari** Graduate School of Engineering, Muroran Institute of Technology, Muroran, Hokkaido, Japan

Research Center for Environmentally Friendly Materials Engineering (MURORAN MATERIA), Muroran Institute of Technology, Muroran, Hokkaido, Japan

**Siyabonga B. Mdluli** SensorLab, Chemistry Department, University of the Western Cape, Cape Town, South Africa

**Jun Mei** Chengdu Green Energy and Green Manufacturing Technology R&D Center, Chengdu, Sichuan, China

**Paolo Mele** Research Center for Environmentally Friendly Materials Engineering (MURORAN MATERIA) Muroran Institute of Technology, Hokkaido, Japan

**Kwena D. Modibane** Department of Chemistry, School of Physical and Mineral Sciences, University of Limpopo (Turfloop), Polokwane, Sovenga, South Africa

**Kerileng M. Molapo** SensorLab, Chemistry Department, University of the Western Cape, Cape Town, South Africa

**Gobeng R. Monama** Department of Chemistry, School of Physical and Mineral Sciences, University of Limpopo (Turffloop), Polokwane, Sovenga, South Africa

**Lisa Moni** Department of Chemistry and Industrial Chemistry, University of Genova, Genoa, Italy

**B. Muravin** Integrity Diagnostics Ltd., Netanya, Israel

**Yoshinobu Nakamura** The University of Tokyo, Tokyo, Japan

**N. Naveh** Polymers and Plastics Department, Shenkar College of Engineering and Design, Ramat Gan, Israel

**Dinh-Tuan Nguyen** Department of Material Science and Engineering, National Cheng Kung University, Tainan, Taiwan

**Heng-yong Nie** Surface Science Western, Western University, London, ON, Canada

**Hiroaki Nishikawa** Faculty of Biology-Oriented Science and Technology, Kindai University, Kinokawa, Wakayama, Japan

**Yasuhide Ohno** Graduate School of Science and Technology, Tokushima University, Tokushima, Japan

The Institute of Scientific and Industrial Research, Osaka University, Osaka, Japan

**Manunya Okhawilai** Department of Chemical Engineering, Faculty of Engineering, Chulalongkorn University, Bangkok, Thailand

**Takao Ono** The Institute of Scientific and Industrial Research, Osaka University, Osaka, Japan

**Anucha Pengdam** Department of Chemical Engineering, Faculty of Engineering, Chulalongkorn University, Bangkok, Thailand

**Ratcha Plengudomkit** Department of Chemical Engineering, Faculty of Engineering, Chulalongkorn University, Bangkok, Thailand

**Y. Portnoy** Rafael Advanced Defense Systems, Haifa, Israel

**Alina Pruna** Center for Surface Science and Nanotechnology, University Politehnica of Bucharest, Bucharest, Romania

**Daniele Pullini** Centro Ricerche Fiat, Orbassano, Torino, Italy

**Kabelo E. Ramohlola** Department of Chemistry, School of Physical and Mineral Sciences, University of Limpopo (Turfloop), Polokwane, Sovenga, South Africa

**Lakshmi Reddy** Department of Physics, Sri Venkateswara Degree College, Cuddapah, India

**Sarawut Rimdusit** Department of Chemical Engineering, Faculty of Engineering, Chulalongkorn University, Bangkok, Thailand

**Renata Riva** Department of Chemistry and Industrial Chemistry, University of Genova, Genoa, Italy

**Jaganathan Senthilnathan** Environmental and Water Resources Engineering Division, Department of Civil Engineering, Indian Institute of Technology Madras, Chennai, Tamil Nadu, India

**Y. Seri** Rafael Advanced Defense Systems, Haifa, Israel

**Andrada Soanca** Faculty of Dental Medicine, Iuliu Hatieganu University of Medicine and Pharmacy, Cluj-Napoca, Romania

**Rieko Sudo** Sagamihara Surface Treatment Laboratory, Chuo-ku Sagamihara, Kanagawa, Japan

**Masayoshi Tabata** Center of Environmental Science and Disaster Mitigation for Advanced Research, Muroran Institute of Technology, Muroran, Hokkaido, Japan

Faculty of Science and Technology, Department of Applied Chemistry and Bioscience, Chitose Institute of Science and Technology, Chitose, Hokkaido, Japan

**Mai Takase** Department of Applied Sciences, Muroran Institute of Technology, Muroran, Japan

**Naoyuki Tamura** Department of Materials Science and Engineering, National Defense Academy, Yokosuka, Kanagawa, Japan

**Ana Maria Toader** Institute of Physical Chemistry, Bucharest, Romania

**Kenichi Uehara** Mie University, Tsu, Mie, Japan

**Jian Wang** State Key Lab of Polymer Materials Engineering, Polymer Research Institute, Sichuan University, Chengdu, China

**Hesheng Xia** State Key Lab of Polymer Materials Engineering, Polymer Research Institute, Sichuan University, Chengdu, China

**Jing Xu** Donghua University, Shanghai, China

**Shinya Yamanaka** Department of Applied Sciences, Muroran Institute of Technology, Muroran, Japan

**Yuqiu Yang** Donghua University, Shanghai, China

**Masahiro Yoshimura** Promotion Centre for Global Materials Research (PCGMR), Department of Material Science and Engineering, National Cheng Kung University, Tainan, Taiwan

Tokyo Institute of Technology, Tokyo, Japan

**Kaiye Zhang** State Key Lab of Polymer Materials Engineering, Polymer Research Institute, Sichuan University, Chengdu, China



**Part I**  
**Graphene and Nanocarbon Materials**

# The Synthesis and the Catalytic Properties of Graphene-Based Composite Materials

Baojiang Jiang and Chaoyang Li

## 1 Introduction

Graphene, as an attractive material, catches more and more attention from global scientists. Graphene is one kind of allotrope of carbons with two-dimensional structures and carbon atoms with the p-stacking of graphene holding the lamellar graphite structure strongly in place with an interlayer spacing of 3.34 Å [1, 2]. The comparison of properties of carbon nanotube and graphite is shown in Table 1. The most attractive aspect of graphene might be its electronic properties. Graphene has high mobility of  $10,000 \text{ cm}^2 \text{ V}^{-1} \text{ s}^{-1}$  to  $50,000 \text{ cm}^2 \text{ V}^{-1} \text{ s}^{-1}$  at room temperature with an intrinsic mobility limit of  $4,200,000 \text{ cm}^2 \text{ V}^{-1} \text{ s}^{-1}$  [3]. Despite being one atom thick, graphene is the strongest material ever measured, with a Young's modulus of  $E = 1.0 \text{ TPa}$  and intrinsic strength of  $130 \text{ GPa}$  in its pristine, atomically perfect form [4]. Graphene possesses a very large nonlinear Kerr coefficient of  $10^{-7} \text{ cm}^2 \cdot \text{W}^{-1}$ , almost nine orders of magnitude larger than that of bulk dielectrics [5]. Graphene also possesses the highest specific surface area of all materials with a theoretical value of  $2630 \text{ m}^2 \text{ g}^{-1}$  [6], which makes it an ideal candidate for the processes involving adsorption or surface reactions.

According to the promising properties, graphene can be potentially applied for the lightweight, thin, and flexible display screens. Moreover, graphene-based composites fabricated with inorganic nanostructures, organic crystals, polymers, and metal-organic frameworks (MOFs) [7–9] also can be applied in energy-related areas

---

B. Jiang, Ph.D (✉)

Key Laboratory of Functional Inorganic Material Chemistry, Ministry of Education of the People's Republic of China, Heilongjiang University, Harbin 150080, China  
e-mail: [jiangbaojiang@163.com](mailto:jiangbaojiang@163.com)

C. Li

Center for Nanotechnology, School of Systems Engineering, Kochi University of Technology, 185 Miyanakuchi Tosayamada cho, Kami City, Kochi 782-8502, Japan

**Table 1** The properties of graphene comparing with other form of carbon material

Entry	Young's modulus (TPa)	Intrinsic strength (GPa)	Nonlinear Kerr coefficient ( $\text{cm}^2 \text{W}^{-1}$ )	Specific surface area ( $\text{m}^2 \text{g}^{-1}$ )	Mobility limit ( $\text{cm}^2 \text{V}^{-1} \text{s}^{-1}$ )
Graphene	1.0	130	$10^{-7}$	2630	200,000
Carbon nanotube	1.28	50 ~ 200	$10^{-8}$	400 ~ 1315	100,000
Graphite	$11.5 \pm 0.9$	8 ~ 12	$2.6 \times 10^{-4}$	1 ~ 20	-----

including superior supercapacitors, solar cells, catalytic systems, and chemical sensors.

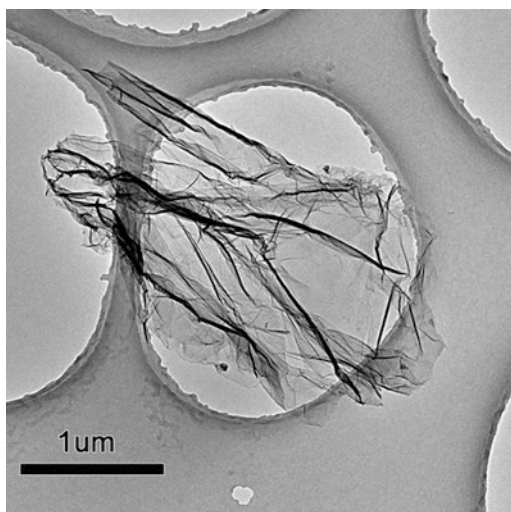
Up to date, the graphene can be obtained by different preparation methods such as micromechanical exfoliation of graphite, chemical vapor deposition (CVD), reduction of graphene oxide (GO), and sonication exfoliation [10, 11]. The single layers of graphene can be generated by exfoliating the graphite using adhesive tape [12]. However, the quantity of graphite from micromechanical cleavage is very limited; therefore, the advanced techniques to obtain large production of graphene are critically needed.

The high-quality graphenes with a well-defined atomic structure are usually prepared by the CVD method [13]. However, the low quantities of graphenes still are a bottleneck for using CVD method to produce large amount of graphenes for wide applications in different industry field. The sonication method has been used for the exfoliation of bulk graphite to the single and multilayer graphene in the presence of polyvinylpyrrolidone (PVP), diazaperopyrenium dications, ionic liquids, etc. [14]. Recent years, the direct exfoliation of graphite has been achieved by surface functionalization of graphene sheets with aromatic carboxylic acids in aqueous solution. However, the ratio of the high-quality single graphene within final products by the sonication technology is worse than that by CVD or chemical reduction of graphene oxide.

In addition, the chemical reduction of GO sheets usually possesses rich oxygen-containing groups, such as carboxylic, hydroxyl, and epoxide functional groups [15, 16]. Figure 1 shows the typical GO structure from Hummer's method [17]. The presence of oxygen functionalities in GO allows interaction with the different precursor cations and provides reactive sites for the nucleation and growth of nanoparticles, which usually results in the rapid growth of various graphene-based composites [18–20]. Unfortunately, production process of GO disrupts the electronic structure of graphene. Although the modified groups can be removed by reduction later, it still remains a large number of defects which will affect the electronic properties of graphene.

Therefore, it is urgently a requirement to develop much efficient methods to produce high-quality and large-yield graphene and graphene-based composites. In this chapter, the novel synthetic methods of graphene and graphene-based composites are discussed, particularly, emphasizing their special fabrication as well as anti-bacterial and catalytic field application.

**Fig. 1** Representative TEM image of GO from Hummer's method. The circular-shaped objects seen on the background of the picture are the carbon-coated copper grids which were used to support sample [17] (Reproduced from *J. Phys. Chem. C*, 2011, 115, 23718–23725)



## 2 Quenching Technology for the Production of High-Quality Graphene

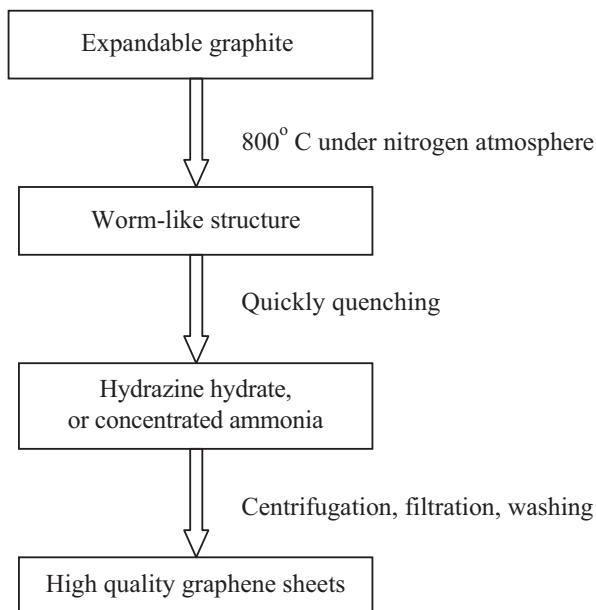
Quenching technology is usually one kind of important techniques as the final fabrication process in steel industry or engineering component, which can make the steel better suited, structurally and physically for the specific applications [21]. However, one of the critical issues is quenching crack because of different quenching stress between the surface and interior of metal, resulting in the deformation and destroys of final products.

However, the quenching technique can be made good use of preparing graphene. Fortunately, we have succeeded to use quenching stress to exfoliate graphite layers for the preparation of high-quality graphene [22]. In this method, the quenching stress can conquer the van der Waals forces between the interlayers of graphite for the formation of graphene sheets. Moreover, the expanded graphite (EG) possesses rich oxygen groups in the interlayer, which is conducive to the rapidly exfoliation. In addition, EG is much less oxidative than Hummer's GO, which contributes to the formation of high-quality graphene sheets. Therefore, we can make full use of the quenching stress to exfoliate expandable graphite for the production of high-quality graphene sheets.

The following process is an experiment to prepare graphene using quenching technique.

The high-quality graphene was prepared from the expandable graphite using quenching technique; the experimental process is shown as Scheme 1 (named as one cycle). During this experiment procedure, the graphene sheets were prepared from inexpensive EG using the quenching method in the pure water, hydrazine hydrate (20%), or concentrated ammonia (28%).

**Scheme 1** The experimental process (one cycle) for preparing high-quality graphene from the expandable graphite



Firstly, EG (0.1 g) was heated to 800 °C in the nitrogen atmosphere, resulting in the formation of wormlike structure. Secondly, the hot samples were quickly quenched to low temperature by the cool quenching media such as pure water, hydrazine hydrate, or concentrated ammonia. After transient quenching, the samples were separated by centrifugation and filtration and washed with large amount of water several times. Finally, the final products were dried at 80 °C for 24 h. The large-scale and high-quality graphene sheets were obtained. The sample obtained from EG using quenching liquid hydrazine hydrate or concentrated ammonia was named as Graphene-1 and Graphene-2, respectively.

The structural property of obtained graphene is characterized by the transmission electron microscope (TEM) measurement (JEM-2100 electron microscope with an acceleration voltage of 200 kV (JEOL, Japan)), as shown in Fig. 2 [23]. TEM images of products including Graphene-1 (using quenching liquid hydrazine hydrate) and Graphene-2 (using quenching liquid concentrated ammonia) show that graphenes from EG are a few micrometers in width and slightly scroll on sheet edges (Fig. 2). Furthermore, we can identify the monolayer or bilayer graphene for Graphene-1 from samples via HRTEM (inset image in Fig. 2a, b) on the folded edges because the folded graphene sheets are located parallel to the electron beam. Inset image of Fig. 2b, d shows that the interlayer separation in the bilayer graphene is 0.34 nm, corresponding to the expected value (0.335 nm) of crystal plane (002) of graphite [22]. The EG has been effectively exfoliated to monolayer or multilayer graphenes.

Atomic force microscopy (AFM) (AFM, Digital Instruments NanoScope IIIa, operating in tapping mode) is also used to investigate the surface property of the obtained graphene. As shown in Fig. 3, the thicknesses of obtained graphenes are

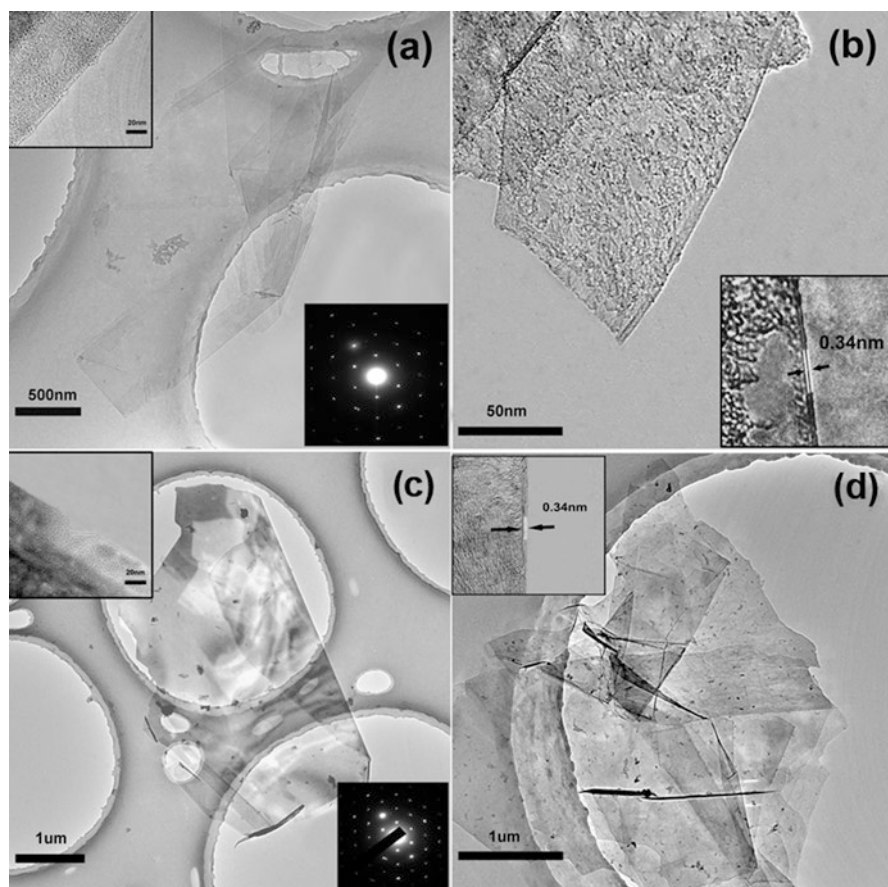


**Fig. 2** TEM images of (a) monolayer Graphene-1 (*inset*: selected HRTEM image and ED pattern). (b) Bilayer Graphene-1 (*inset*: selected HRTEM image). TEM images of (c) monolayer Graphene-2 (*inset*: selected HRTEM image and ED pattern). (d) Tri-layer Graphene-2 (*inset*: selected HRTEM image) (Reproduced from *Chem. Commun.* [22], 2010, 46, 4920–4922)

confirmed by AFM (Fig. 3a, b), which shows thin graphene sheets with the height of 0.476 nm (Graphene-1) and 0.610 nm (Graphene-2), consistent with previous reports of the monolayer graphene [22].

Through five cycles quenching technology treatment, the eventual yield of graphene obtained is about 70 ~ 80 wt % of raw materials. Furthermore, the percentage of monolayer graphene in the final products is about 10 wt %, based on the analysis for a lot of AFM and TEM images. The quenching technology is appropriate for large-scale process. We have succeeded to use quenching stress to simultaneously exfoliate and reduce graphite layers for the preparation of high-quality graphene. In this method, the quenching stress can conquer the van der Waals forces between the interlayers of graphite for the formation of graphene sheets. Moreover, the expanded graphite (EG) possesses rich oxygen groups in the interlayer, which is conducive to

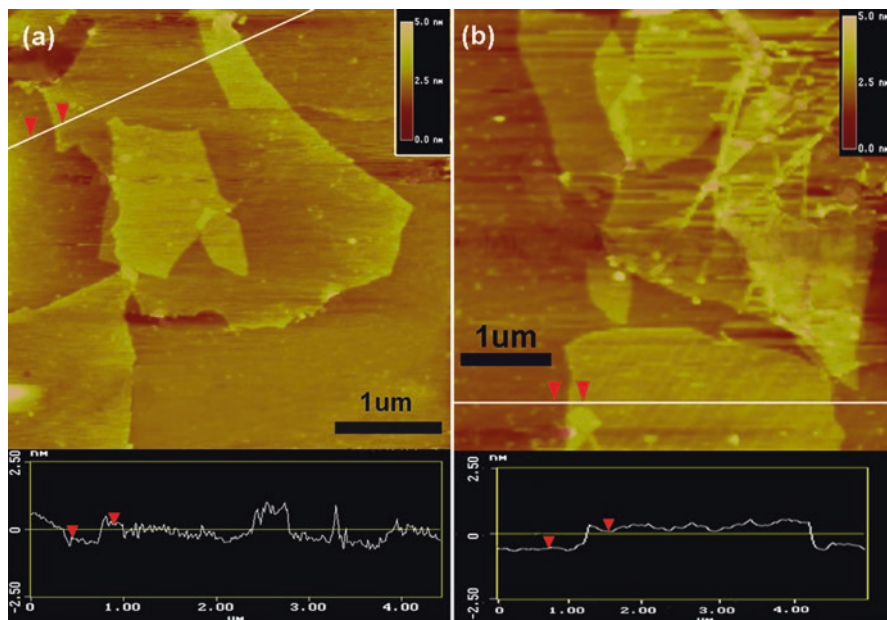


**Fig. 3** AFM images of (a) Graphene-1 and (b) Graphene-2, the corresponding height of sheets are 0.476 nm and 0.610 nm, respectively [22] (Reproduced from *Chem. Commun.*, 2010, 46, 4920–4922)

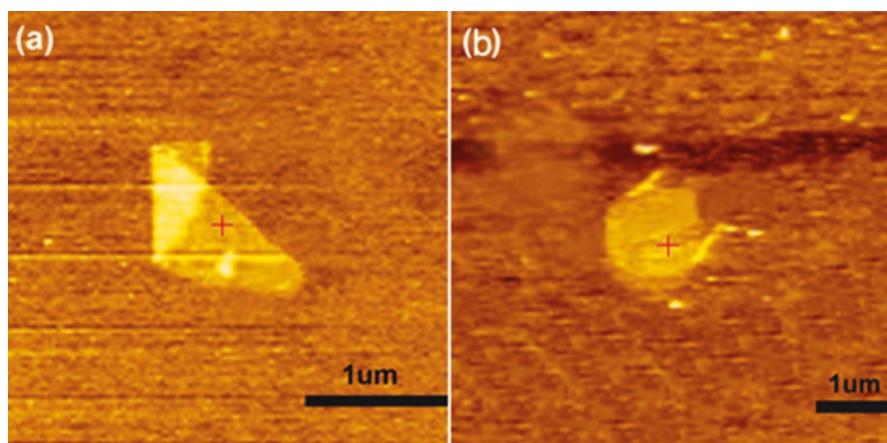


**Fig. 4** AFM images of (a) Graphene-1 and (b) Graphene-2 by conductive AFM at ambient conditions [22] (Reproduced from *Chem. Commun.*, 2010, 46, 4920–4922)

the rapid exfoliation. We can make full use of the quenching stress to exfoliate expandable graphite for the production of high-quality graphene sheets in large scale.

In order to investigate the conductivity of graphenes, the I-V curves are tested by the mean of conductive AFM at the room temperature. The results are shown in Figs. 4 and 5. In Fig. 4, the graphene sheet structure is observed clearly, similar to Fig. 3.

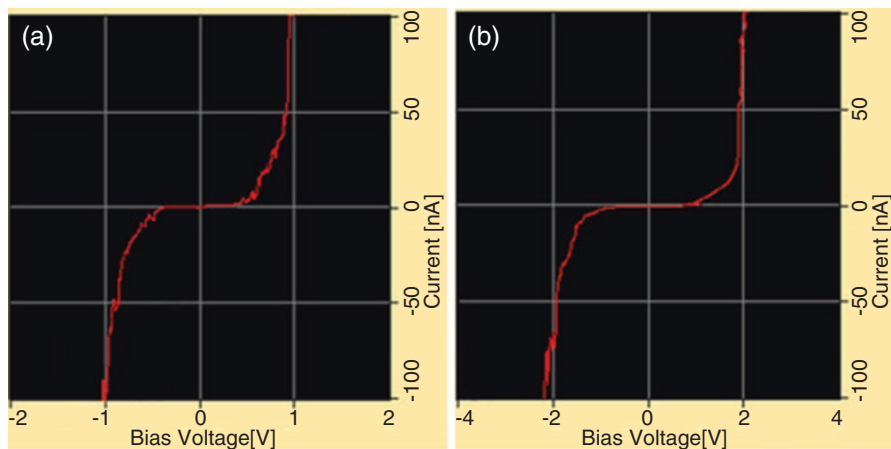


**Fig. 5** The room temperature I-V curves of Graphene-1 (a) and Graphene-2 (b) by conductive AFM under ambient conditions. Bias voltage:  $-2\text{ V} \sim +2\text{ V}$  for Graphene-1 and  $-4\text{ V} \sim +4\text{ V}$  for Graphene-2 [22] (Reproduced from *Chem. Commun.*, 2010, 46, 4920–4922)

In Fig. 5, the high-quality graphene sheet exhibits good conductivity under different bias voltages ( $-2\text{ V} \sim +2\text{ V}$  for Graphene-1 and  $-4\text{ V} \sim +4\text{ V}$  for Graphene-2), which makes the obtained graphene to be the promising candidate for further application in nanoelectronics.

In summary, the high-quality graphenes are prepared by hydrazine hydrate or concentrated ammonia-assisted quenching route. The key point for the experimental process is the strong quenching and the presence of quenching liquid hydrazine hydrate or concentrated ammonia. After many cycles quenching treatment, there are about 70 ~ 80 wt % from the starting material are obtained to produce single- or few-layer graphene sheets with high quality and large scale.

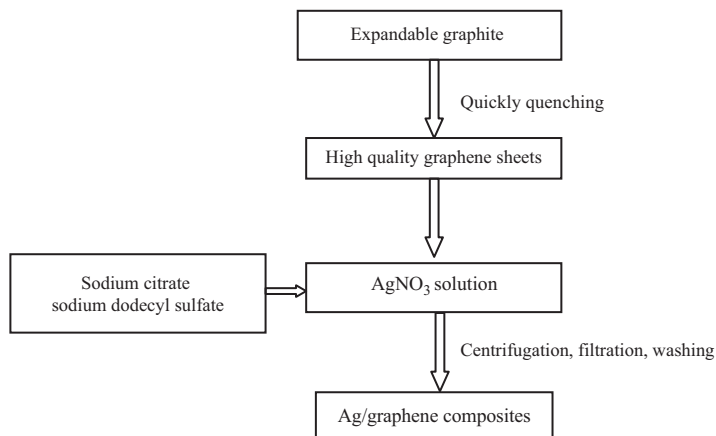
### 3 Synthesis and Antibacterial Application of Ag/Graphene Composite

Many methods have been developed to prepare graphene-based nanocomposites, including non-covalent interaction [23], covalent reaction [24], chemical electroless deposition [25], hydrothermal and solvothermal growth [26], etc.

A great number of inorganic nanostructures have been composited with graphene, for instance, Au [27], Ag [28], oxides like  $\text{TiO}_2$  [29] and ZnO [30], and chalcogenides like CdS [31] and CdSe [32].

Among them, the silver nanoparticles (NPs) are noticed to be able to incorporate into graphene-based composites because of their unique optical, electrical, and thermal properties, being able to apply for biological and chemical sensors and photovoltaics. A common application is the use of silver nanoparticles for antibacterial agents that could release many silver ions to provide protection against bacteria [33]. For this application purpose, the good stability of silver nanoparticle is very important.





**Scheme 2** The experimental process of Ag/graphene composite synthesis for antibacterial agent

Considering as a new allotrope of carbon materials, the graphenes are easily to form composite with silver particles. To date, there are few reports on the Ag/graphene composites for the antibacterial application [34]. Especially, the effect of interaction between Ag and graphene with high electron conductivity probably on antibacterial properties of Ag is still needed to be further investigated.

Herein, we report the synthesis of Ag/graphene composite antibacterial agent through a facile method which is a simple to handle, low-cost, and environmentally friendly process. The high-quality graphene nanosheets are selected from the low-cost expandable graphite (EG) as substrate materials. In this study, the antibacterial property of Ag/graphene composite is evaluated against *E. coli*.

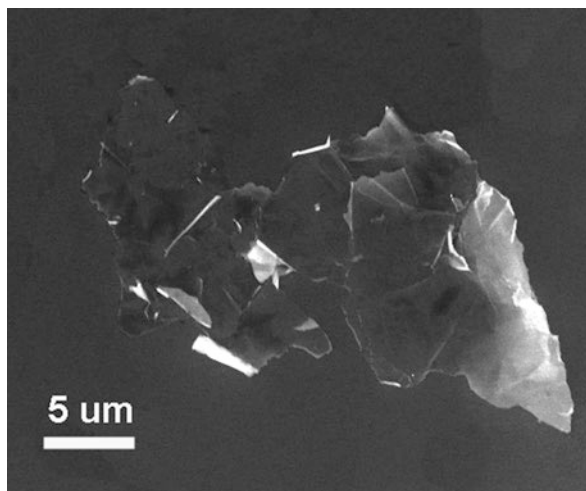
The experimental process for fabricating high-quality graphene from the expandable graphite is shown as Scheme 2. Firstly, the high-quality graphene was prepared from expandable graphite. Silver nanoparticles (NPs) were then supported on the graphene sheets by a facile chemical reduction. During the experimental procedure, 20 mg of graphenes was added into the 200 mL of  $\text{AgNO}_3$  aqueous solution with 36 mg  $\text{AgNO}_3$ . Sequentially, 0.4 g sodium citrate and 0.1442 g sodium dodecyl sulfate (SDS) were added into the above suspension. Following violent stirring for 15 min, the temperature was raised to 80 °C and kept for 150 min. Finally, the solids were obtained after filtrating, centrifuging, and drying at 40 °C for 12 h.

The final products are denoted as the AGC-1 (the graphene is obtained from EG using the hydrazine hydrate-assisted quenching process).

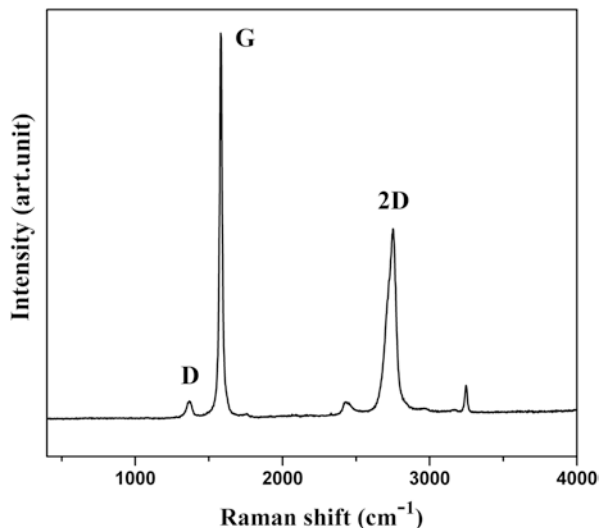
The morphology and quality of substrate material graphene sheet from the expanded graphite could be investigated by the SEM and TEM measurement. For example, we can observe clearly the complete surface morphology of graphene sheet using the SEM measurement, as shown in Fig. 6 [35]. The thin sheet has a typical graphene structure with serial micron in dimension.

Figure 7 is the Raman spectra from graphenes obtained from EG indicating few structural defects in the graphene sheet. In Fig. 7, it is observed that the peaks include a D-band ( $1372\text{ cm}^{-1}$ ), a G-band ( $1580\text{ cm}^{-1}$ ), and a 2D-band ( $2751\text{ cm}^{-1}$ ). The

**Fig. 6** SEM image of high-quality multilayer graphenes as substrate material for AGC-1 [35] (Reproduced from *J Mater Sci*, 2013, 48, 1980–1985)



**Fig. 7** Raman spectra of high-quality multilayer graphenes [35] (Reproduced from *J Mater Sci*, 2013, 48, 1980–1985)



D-band is associated with disorder-induced scattering resulting from imperfections or loss of hexagonal symmetry of disordered graphite. But the G-band corresponds to an  $E_{2g}$  mode of graphite and is related to vibration of  $sp^2$ -bonded carbon atoms in a two-dimensional hexagonal lattice [36]. It is noteworthy that the disorder-induced D peak ( $1372\text{ cm}^{-1}$ ) is not clearly observed in the Raman spectra of graphene sheets.

Moreover, the structure and composition of the Ag/graphene composite are also investigated by TEM techniques. Figure 8 shows typical TEM images of the as-prepared product (AGC-1). The low-magnification TEM image (Fig. 8a) shows a crumpled sheet with several micrometers in size, which is covered with Ag NPs.

The results show that the high-quality graphene sheets from EG can be selected as the substrate material for supporting Ag NPs. Moreover, the nanoparticles are

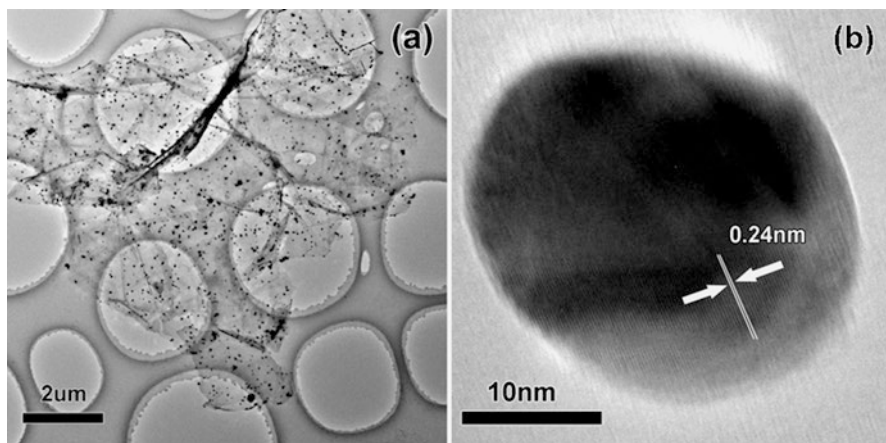


**Fig. 8** (a) Low-magnification TEM image of AGC-1, (b) HRTEM image of the single Ag nanoparticle in composite [35] (Reproduced from *J Mater Sci*, 2013, 48, 1980–1985)

uniform in size, and the average diameter of Ag NPs is about 45 nm. A typical HRTEM image of the Ag nanoparticle is given in Fig. 8b. The lattice fringe spacing is 0.24 nm, indexing the (111) plane of face-centered cubic silver [37].

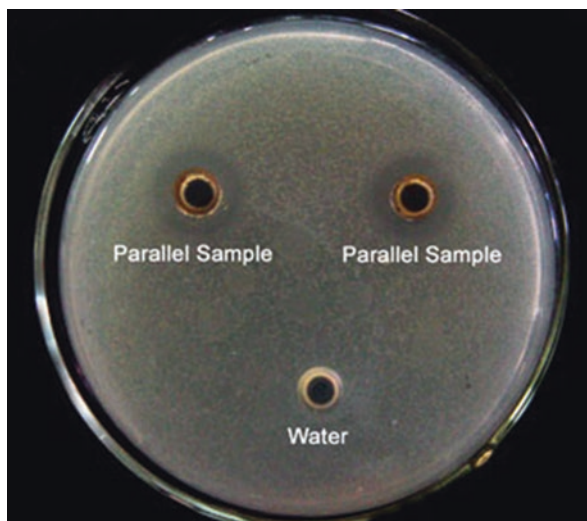
The antibacterial activities of Ag/graphene composites are assessed by determining the presence of inhibition zones against *E. coli*. Antibacterial effects in the form of inhibition zones, evaluated by the disk diffusion assay of the composites, are shown in Fig. 9. The control experiments using pure water possess almost no antibacterial activity, suggesting that the effect of water can be ignored. Figure 9 displays the pictures of inhibition zones for *E. coli* of AGC-1 including two parallel samples. The diameters of the inhibition zones are 18.7 mm and 18.6 mm, respectively. The results indicate that AGC-1 has an excellent inhibitory effect on *E. coli*, which is due to the good dispersibility of Ag NPs and the introduction of high-quality graphene.

In summary, small-size Ag nanoparticles are loaded onto high-quality graphene as antibacterial agent via a simple chemical reduction route. The results demonstrate that the as-prepared Ag/graphene composite exhibited excellent antibacterial activity against *E. coli*. One of the most important features is that the high-quality graphene is selected as the substrate material for Ag particles. The excellent antibacterial activity against *E. coli* of this composite can be attributed to the favorable dispersibility of Ag NPs and the introduction of high-quality graphene.

## 4 Synthesis and Catalytic Application of Nitrogen-Doped Graphene/Pd@PdO

Metal Pd-catalyzed coupling reaction is one of the most important methods for the C-C bond forming in organic chemistry [38]. However, to realize the practical application of Pd catalysts in C-C cross coupling reaction, the synthesis method for

**Fig. 9** Inhibition test for *E. coli* of AGC-1 antibacterial agent with two parallel samples. Pure water is used as the control sample [35] (Reproduced from *J Mater Sci*, 2013, 48, 1980–1985)



small-size Pd particle is still needed to be developed. Especially, Pd clusters, which require that the sizes range from sub-nanometer to about 2 nm, could greatly improve their catalytic properties because of their unique electrical structure, large surface area, and high proportion of surface atoms. However, the surface energy will lead to serious aggregation for Pd clusters, which will decrease the catalytic performance. To avoid these problems, the introduction of support materials can effectively stabilize the Pd clusters to enhance catalytic property.

Recently, many research works suggest that carbon-based support materials can be doped with heteroatoms such as nitrogen and boron to create strong catalyst-carbon support interactions [39]. It is reported that the nitrogen is doped in Vulcan carbon; the nitrogen atoms significantly mediate the Pd adsorption enhancement on its surface based on the density functional theory study [40]. Similarly, graphene can be also used as an ideal support material for growing and anchoring Pd clusters for Suzuki-Miyaura reaction. The nitrogen in graphene also plays a significant role in determining nucleation rate and growth process of Pd clusters. However, it is still difficult to have the direct observation of the spatial relationship between the Pd catalyst and N-doped graphene support; the mechanism for the interaction between the nitrogen and metal Pd particle is still needed to be further investigated.

In this experiment, we firstly use density functional theory (DFT) to calculate the binding energy between nitrogen-doped graphene (NDG) and the Pd@PdO clusters. Then Pd@PdO clusters supported on NDG are prepared for the fabrication of composites, as shown in Fig. 10 [41]. In this synthesis process, the high-quality and smooth graphene sheets are obtained from expanded graphite by quenching method. This smooth support material is beneficial for the uniform distribution of small-size metal clusters. Moreover, the function of the nitrogen element in NDG is not only to stabilize the embedded Pd@PdO clusters and decrease metal Pd@PdO particle size but also to prompt the catalytic activity for Suzuki-Miyaura reaction.

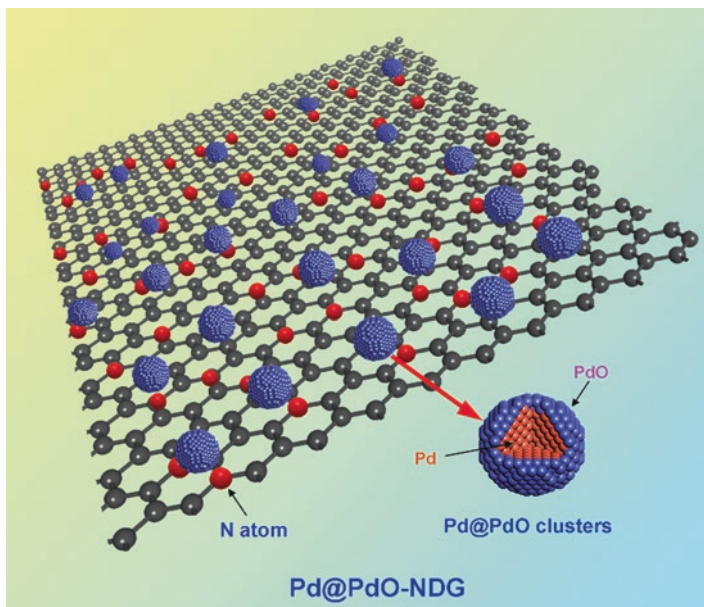
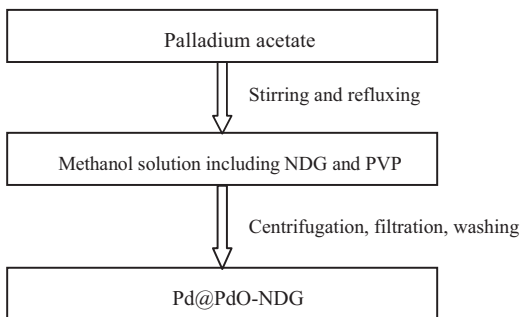


**Fig. 10** Structural image of Pd@PdO clusters on nitrogen-doped graphene [41] (Reproduced from *Nano Res.* 2014, 7(9): 1280–1290)

**Scheme 3** The experimental process of synthesizing Pd@PdO-NDG composite



In this work, the Pd@PdO-NDG was produced by a simple reduction reaction of palladium acetate as follows, as shown in Scheme 3. To produce a homogeneous solution, 150 mL of a methanol solution including 0.05 g of NDG and 2.5 g of PVP was sonicated for 15 min. Then, the solution was transferred to a three-necked flask for the subsequent reflux procedure. Meanwhile, 20 mL of a methanol solution of palladium acetate ( $0.22 \text{ mmol of Pd (C}_2\text{H}_3\text{O}_2)_2$ ) was added into the above solution with continuous stirring and refluxing at  $65^\circ\text{C}$  for 2 h. After the reduction reaction, the black samples (Pd@PdO-NDG) were separated by high-speed centrifugation, washed several times with ethanol and distilled water, and dried at below  $60^\circ\text{C}$ .

The density functional theory (DFT) calculation is applied to evaluate the binding strength between Pd or PdO clusters and NDG. For comparison, the adsorption

energy between Pd or PdO clusters and the intrinsic graphene sheet is also examined. Due to the possible physical adsorptions, it is found that the adsorption energies between Pd or PdO clusters and graphene are about  $-2.21$  eV and  $-2.29$  eV, respectively.

However, when the PdO clusters approach NDG, the adsorption energy of the system decreases remarkably to  $-3.61$  eV, suggesting the existence of strong covalent chemical adsorption between them. The similar results are found for the Pd-NDG system.

Figure 11a, b shows the density of states (DOSs) for Pd@PdO-NDG and Pd@PdO-graphene systems, respectively. The black line in Fig. 11a represents the total density of states (TDOSs) of each element before contact of the Pd@PdO clusters with NDG, while the red line indicates the TDOSs of each element after contact with NDG. The calculated results indicate that the TDOSs of Pd elements, which are mainly composed of Pd 4d states, shifted to a lower energy position. Moreover, the TDOSs for C atoms and N atoms are also changed significantly.

In contrast, the relevant TDOS of each element remains almost unchanged when Pd@PdO clusters are adsorbed onto the graphene, as shown in Fig. 11b. Therefore, the interaction between Pd@PdO and NDG is expected to be much stronger than that between Pd@PdO and graphene, and nitrogen element facilitates the surface chemical adsorption of Pd onto the graphene sheets to control the Pd nanoparticle size and dispersion.

Figure 12a, b depicts the electron density differences (EDD) diagrams for Pd@PdO-NDG and Pd@PdO-graphene, respectively. The positive (in blue) or negative (in red) regions indicate where the electron density is enriched or depleted. For the Pd@PdO-NDG (Fig. 12a, the electron density around nitrogen atoms is enhanced, while that around C atoms in N-C bonds is weakened. Meanwhile, the Mulliken population for Pd in isolated Pd@PdO clusters is about 0.46, and the corresponding values for N and C in the isolated NDG are calculated to be  $-0.30$  and 0.12, respectively. After Pd@PdO cluster contacts with NDG, the Mulliken population of the contacting Pd in Pd@PdO cluster changes from 0.46 to 0.86, and those of N and C atoms change to  $-0.27$  and 0.03, which means considerable electron transfer between Pd and NDG occurs.

The electron transfer process possibly implies the formation of a chemical bond between Pd@PdO and NDG in the Pd@PdO-NDG system. However, observing the Pd@PdO on graphene, as shown in Fig. 12b, the Mulliken change of contacting C atoms varies slightly from 0.00 to  $-0.05$ , and the Pd atoms still remain positive as 0.46. Therefore, the dopant nitrogen atoms serve as a mediator to activate nearby carbon atoms, leading to the enhancement of Pd adsorption. The electron affinity of nitrogen contributes to the nucleation and the growth of Pd@PdO clusters resulting in small-sized, well-dispersed, high-stability Pd@PdO clusters on graphene.

Then the morphology and structure of as-prepared composite catalysts are characterized using TEM. The results are shown in Fig. 13. Figure 13a shows that graphene within the composite is an ultrathin sheet with few folds and crinkles, indicating that graphenes obtained from expanded graphite have a more stable and flat structure than that of graphenes from graphite oxide.

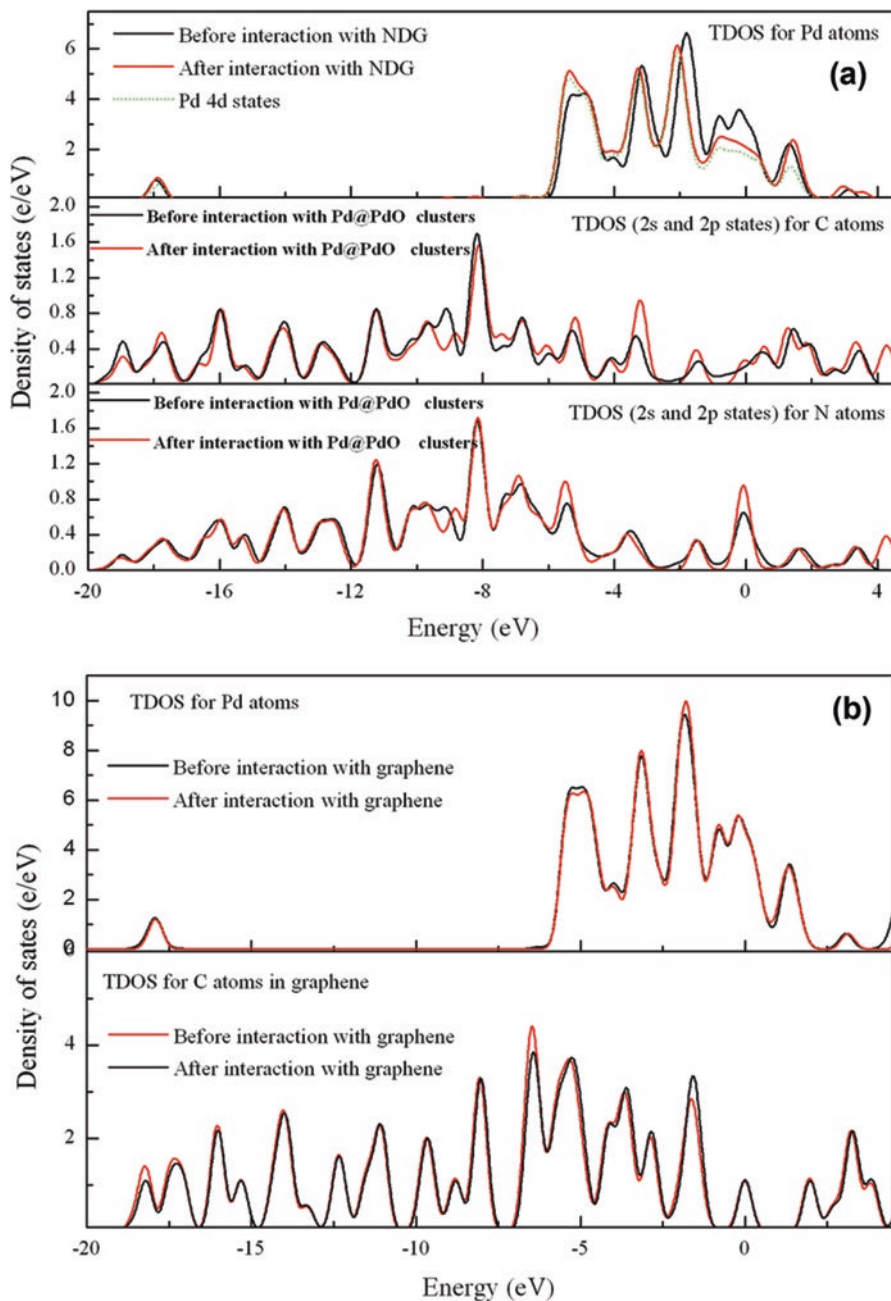


**Fig. 11** Density of states (DOSs) for samples (a) Pd@PdO-NDG and (b) Pd@PdO-graphene [41] (Reproduced from *Nano Res.* 2014, 7(9): 1280–1290)

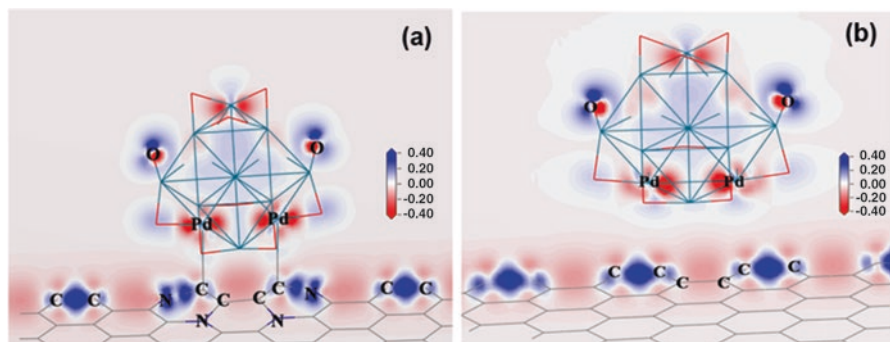


**Fig. 12** Electron-density difference diagrams for (a) Pd@PdO-NDG and (b) Pd@PdO-graphene [41] (Reproduced from *Nano Res.* 2014, 7(9): 1280–1290)

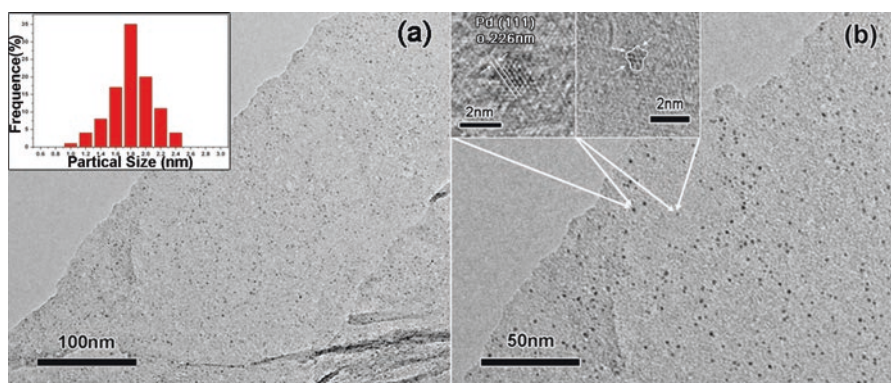
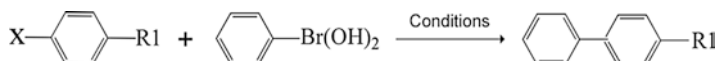


**Fig. 13** TEM images of Pd@PdO-NDG catalyst (a, b), particle size distribution and HRTEM images of Pd@PdO clusters are shown as *insets* in (a) and (b), respectively [41] (Reproduced from *Nano Res.* 2014, 7(9): 1280–1290)

It is interesting to notice that these very small clusters exhibit excellent distribution on the graphene sheets. From the measured particle size distributions, it is clear that the average particle size is about  $1.8 \pm 0.6$  nm. Moreover, the high-resolution TEM (HRTEM) images (Fig. 13b) show an interplanar spacing of particle lattice of 0.226 nm, which has good agreement with the (111) lattice spacing of face-centered cubic Pd [42]. Interestingly, the Pd cluster also exhibits irregular external structure which is possibly due to the part surface oxidation of the Pd clusters forming PdO (Table 2).



The practical application of Pd@PdO-NDG catalysts in C-C cross coupling reaction such as Suzuki-Miyaura reaction is tested using phenylboronic acid and



**Table 2** The Suzuki coupling reactions with the catalyst Pd@PdO-NDG

Entry	R1	X	Reaction time	1st cycle yield <sup>a</sup> (%)	2nd cycle yield <sup>a</sup> (%)	3rd cycle yield <sup>a</sup> (%)	4th cycle yield <sup>a</sup> (%)	5th cycle yield <sup>a</sup> (%)
No.1	NO <sub>2</sub>	Br	60 min	96	94	93	93	92
No.2	CN	Br	60 min	95	94	90	89	85
No.3	OCH <sub>3</sub>	Br	60 min	90	86	84	82	80

Reproduced from *Nano Res.* 2014, 7(9): 1280–1290

<sup>a</sup>*Experiment conditions:* phenylboronic acid (0.75 mmol), K<sub>2</sub>CO<sub>3</sub> (1.25 mmol), different substrate (0.5 mmol), ethanol solution of Pd@PdO-NDG catalyst (4 ml, 5 mg/ml), ethanol (4 ml), 80 °C, 60 min. The yield is determined by high-performance liquid chromatography (HPLC) and <sup>1</sup>H NMR

different substrates in the presence of stabilized Pd@PdO-NDG catalyst. Table 1 gives the reaction conditions and results for the different substrates. As shown in Table 1, both these reactions are successfully performed under these conditions, providing a complete conversion of 100% and high yields of 96% of the corresponding Suzuki reactions products after 1 h at 80 °C, respectively. Among them, No.3 shows a slightly lower yield rate, which is still higher than that of other Pd catalysts for the same period, as given in previous reports, due to the small-size Pd@PdO clusters with high ratio surface atoms.

In summary, the N-doping graphene can modify nucleation and growth of Pd@PdO catalyst, resulting in smaller Pd@PdO particles, uniform dispersion, and enhanced catalyst durability. Furthermore, the Pd@PdO-NDG catalysts exhibit high yields for the C-C cross coupling reaction.

## 5 The Synthesis of (001) Facets TiO<sub>2</sub>/Graphene Composites

TiO<sub>2</sub> has been extensively investigated in the photocatalytic field due to its peculiar chemical and physical behaviors [43]. However, the high charge recombination rate in TiO<sub>2</sub> significantly restricting its photocatalytic application. Recently, researchers find that the introduction of carbon materials can enhance its charge separation rate [44].

Among them, graphene is considered as a good candidate to composite TiO<sub>2</sub> because of excellent electronic property and unique two-dimensional structure of graphene [45]. It has been reported that TiO<sub>2</sub> (P25)-graphene nanocomposite prefers the degradation of methylene blue rather than the bare P25 [46]. The graphene/TiO<sub>2</sub> nanocrystals hybrid structure is also prepared by directly growing TiO<sub>2</sub> nanocrystals on GO sheets [18]. However, the convictive research for the interaction and the electron transfer process within composites is still needed to be improved.

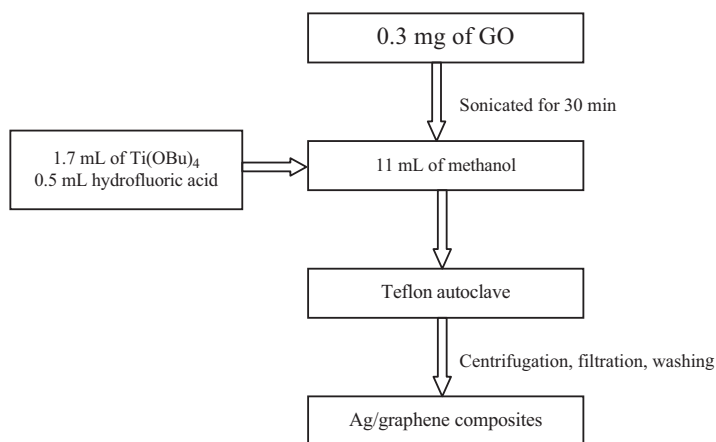
Additionally, photocatalytic efficiency of TiO<sub>2</sub> also depends on the surface atomic structure and the crystallinity. In particular, the highly reactive facets are expected to effectively enhance photocatalytic property [47]. Since the successful synthesis of anatase TiO<sub>2</sub> sheets with exposed {001} facets by Lu and Qiao et al., the research

interest is increased to focus on the exposed highly reactive facets [48]. However, there is few report about the novel  $\text{TiO}_2$ /graphene composites consisting of high-quality graphene and highly reactive anatase  $\text{TiO}_2$  with exposed {001} facets.

In this part, we present a feasible strategy to synthesize the novel anatase  $\text{TiO}_2$ /graphene composites (TGCS) with exposed  $\text{TiO}_2$  {001} facets by the hydrofluoric acid (HF) and methanol joint-assisted solvothermal reactions. The results reveal that graphene is uniformly covered with a large number of anatase  $\text{TiO}_2$  nanoparticles, exposing the {001} facets. The TGCS exhibit high photocatalytic activity compared with the P25 under UV light, likely due to the effective separation of photoinduced charge and exposure of highly reactive {001} facets. It is expected that these detailed studies on novel  $\text{TiO}_2$ /graphene can help to gain deeper insights into the electron transfer process of  $\text{TiO}_2$  and carbon.

The typical experimental procedure is listed as Scheme 4. 0.3 mg of GO was dissolved in 11 mL of methanol and sonicated for 30 min to produce solution of graphene oxide sheets. 1.7 mL of  $\text{Ti}(\text{O}i\text{Bu})_4$  was added to the above graphene oxide solution. Then, 0.5 mL of hydrofluoric acid (HF) was added into the suspension with low speed (4000 ~ 5000 r/min). Finally, the mixed solution was placed in a dried Teflon autoclave with a capacity of 14 mL and then kept at 180 °C for 24 h. After being cooled to room temperature, the gray powder (TGCS-1) was separated by high-speed (12,000 ~ 13,000 r/min) centrifugation, washed with ethanol and distilled water for several times, and dried at 80 °C. A series of  $\text{TiO}_2$ /graphene composites including TGCS-1, TGCS-2, and TGCS-3 were synthesized by varying the volume of GO.

The TEM measurement is carried out to analyze the morphology and structure of a typical sample, observing that GO has a crumpled layered structure with thin thickness. After solvothermal synthesis for 24 h at 180 °C, graphene is covered with  $\text{TiO}_2$  nanoparticles, as shown in Fig. 14a. Fig. 14b is an enlarged image, showing clearly that  $\text{TiO}_2$  nanoparticles (about 20 ~ 25 nm in diameter) uniformly cover the



**Scheme 4** The experimental process of preparing (001) facets  $\text{TiO}_2$ /graphene composites

surface of graphene without obvious aggregation. These results demonstrate that graphenes inhibit the aggregation of  $\text{TiO}_2$  nanoparticles.

In addition, in the HRTEM image of  $\text{TiO}_2$  nanoparticle, as shown in Fig. 14c, the visible lattice fringes and its corresponding FFT image indicate that the top facets of  $\text{TiO}_2$  nanoparticle exhibit the  $\{001\}$  facet. The HRTEM in Fig. 14d shows that the lattice spacing parallel to the top facets of  $\text{TiO}_2$  is 0.235 nm, corresponding to the  $\{001\}$  planes of anatase  $\text{TiO}_2$  [49], which further confirms the above assignment.

We note that the thickness of the graphene is easily observed at the edge of graphene, as shown in Fig. 14e. Therefore, HF plays a key role in the formation of the

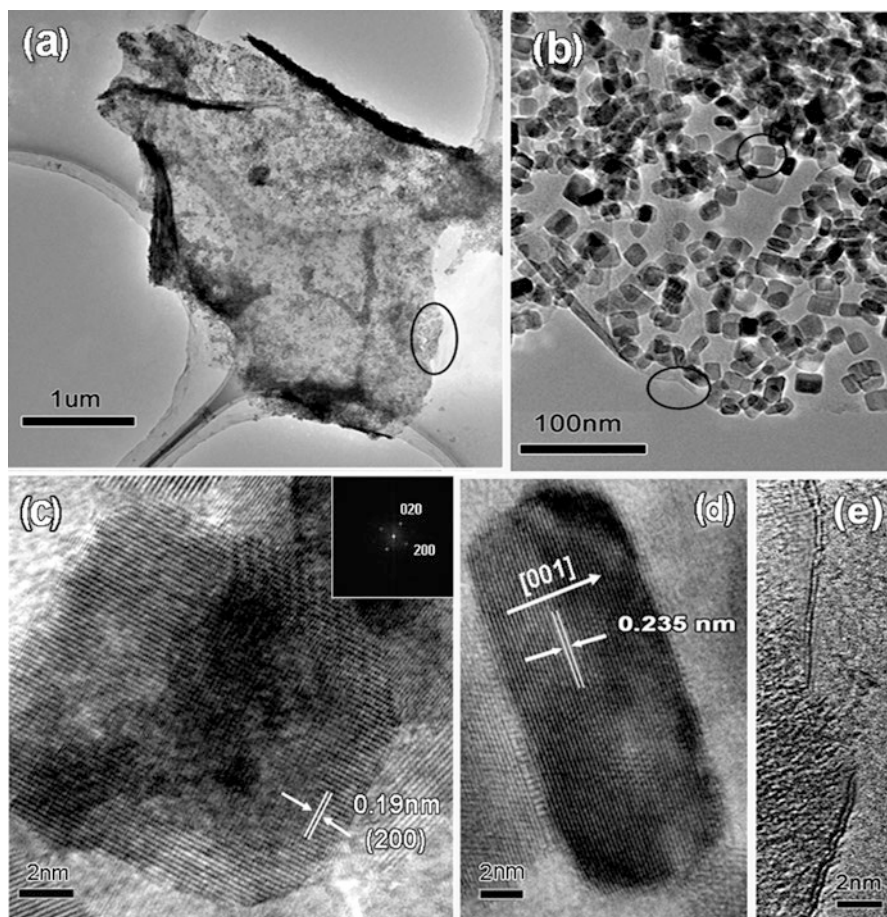


**Fig. 14** (a) TEM images of the TGCS-1, showing the thin graphene sheet and uniform distribution of highly reactive  $\text{TiO}_2$ . (b) Part of enlarged TEM images of TGCS-1 corresponding to the black circle part in (a). HRTEM images of  $\text{TiO}_2$  (inset: the corresponding FFT image). (c) HRTEM image taken from the side face of  $\text{TiO}_2$  nanoparticle, (d) from the thin edge of graphene, and (e) in TGCS-1 corresponding to the black circle parts in (b), respectively [17] (Reproduced from *J. Phys. Chem. C*, 2011, 115, 23,718–23,725)

highly reactive  $\text{TiO}_2$  by  $\text{F}^-$  bounding the  $\{001\}$  surface. Finally, the fine graphene/highly reactive  $\text{TiO}_2$  with exposed  $\{001\}$  facets are prepared successfully.

X-ray diffraction (XRD) (Rigaku D/max-III B with  $\text{Cu K}\alpha$ -radiation) is employed for further analyzing the crystalline phase of obtained composites. The XRD pattern from GO,  $\text{TiO}_2$ , and  $\text{TiO}_2$ /graphene composites is shown in Fig. 15. In Fig. 15a, there is only the diffraction peak of GO ( $2\theta = 10^\circ$ ) observed. Notably, the XRD data for the TGCS-1 exhibit clear peaks of anatase  $\text{TiO}_2$  (JCPDS No. 21-1272), which are similar to the diffraction pattern of pure  $\text{TiO}_2$  (Fig. 15b). Furthermore, by observing the diffraction pattern of TGCS-1 in Fig. 15c, the sharp peak of GO is lacking, suggesting that the disruption of the GO layers leads to the formation of graphene.  $\text{TiO}_2$  nanoparticles uniformly grow on the surface of graphene sheets, which not only promotes the segregation of graphene sheets but also enhances the surface area of composites.

In order to investigate the surface composition and the  $\text{TiO}_2$ -graphene interaction in the composites, X-ray photoelectron spectroscopy (XPS) (PHI 5700) measurement is carried out for obtained different samples. The results are shown in Fig. 16. In Fig. 16a, the main C1s peak for GO shows that the presence of abundant C-O, and C (O) O chemical binding states, corresponding to the peak at 287.3 eV. The peaks of C-O and C (O) O of TGCS-1 become visibly weakened.

In Fig. 16b, two peaks of HR- $\text{TiO}_2$  at 458.8 and 464.7 eV are assigned to the Ti ( $2p_{3/2}$ ) and Ti ( $2p_{1/2}$ ) spin-orbital splitting photoelectrons in the  $\text{Ti}^{4+}$  chemical state, respectively [50]. Interestingly, for TGCS-1, Ti2p slightly shifts toward higher binding energy compared to that of the HR- $\text{TiO}_2$ . Normally, this kind of shift is attributed to the presence of strong interactions at the interfaces between Ti and graphene.

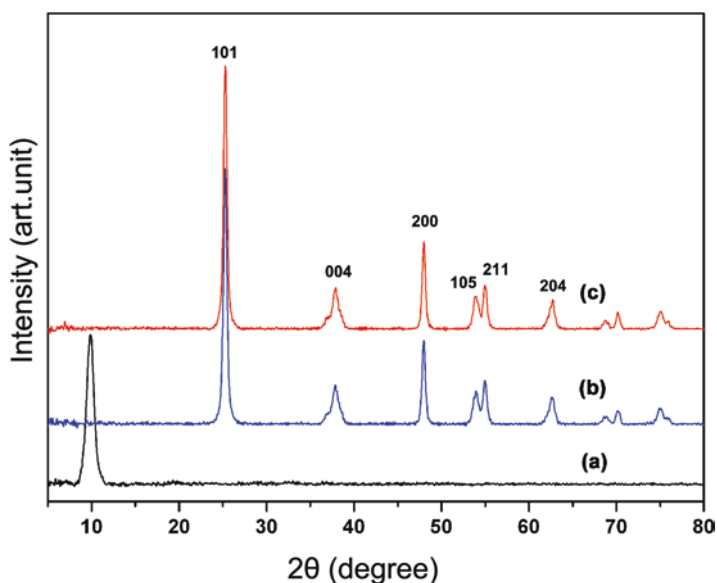


**Fig. 15** X-ray diffraction patterns of (a) GO, (b) highly reactive  $\text{TiO}_2$ , and (c)  $\text{TiO}_2$ /graphene composites (TGCS-1) [17] (Reproduced from *J. Phys. Chem. C*, 2011, 115, 23,718–23,725)

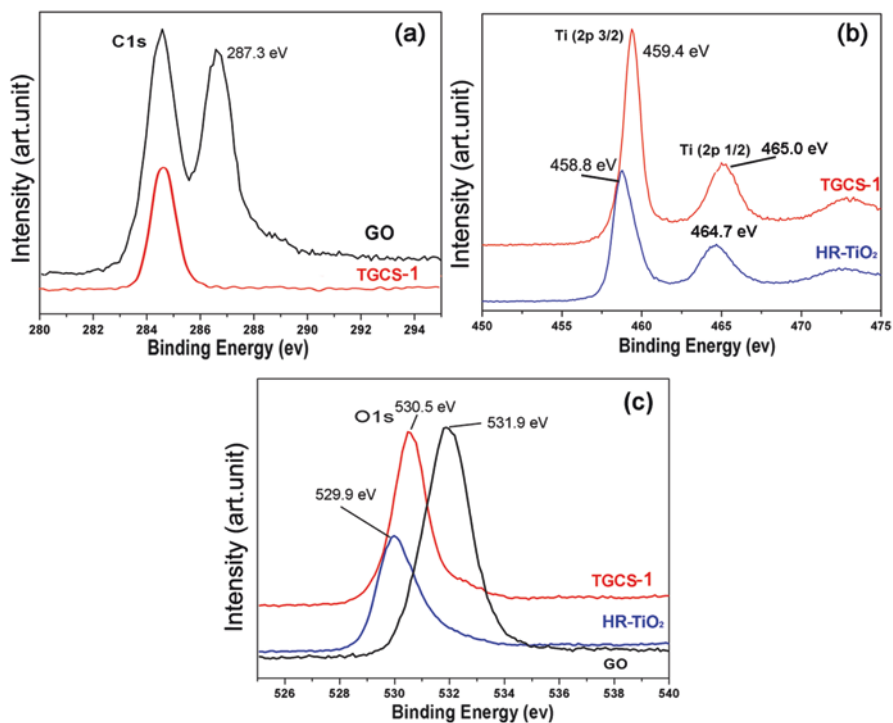


**Fig. 16** XPS spectra of C1s (a), Ti2p (b), and O1s (c) of different samples including GO, HR-TiO<sub>2</sub>, and TGCS-1 [17] (Reproduced from *J. Phys. Chem. C*, 2011, 115, 23,718–23,725)

The intense interaction may result in the formation of an electron transfer channel, which facilitates improvement of photoinduced charge separation rate during the photocatalytic process.

In addition, the O1s XPS spectra exhibit different peak shapes. For GO, the O1s peak at 531.9 eV is related to the significant hydroxyl groups on the surface of GO. The O1s peak at 529.9 eV in HR-TiO<sub>2</sub> is mainly attributed to the oxygen of TiO<sub>2</sub> crystal lattice, agreeing with previous reports [51]. However, the crystal lattice oxygen and hydroxyl oxygen are all present in TGCS-1. These results further confirm the successful incorporation of titania and graphene.

The soft X-ray absorption spectroscopy (soft-XAS) (beamline BL14W1 of the Shanghai Synchrotron Radiation Facility (SSRF), China) is carried out to further investigate the electrical and structural information of surface and interfaces, which has higher probing depth than XPS. Compared with Ti K-edge XAS, the Ti L-edge XAS mainly gives rise to complementary electronic properties of Ti compounds, reflecting the transition from Ti<sub>2p</sub> orbitals into Ti<sub>3d</sub>, 4s orbitals in the conduction band.

The results are shown in Fig. 17; the Ti L-edge XAS spectra in the energy range of 454 ~ 470 eV consist of two sets of peaks (L3 and L2), due to spin-orbit coupling splitting of the initial 2p states into 2p<sub>3/2</sub> and 2p<sub>1/2</sub>. Both of the L3 and L2

features are further split into  $t_2g$  (formed by  $d_{xy}$ ,  $d_{xz}$ ,  $d_{yz}$  orbitals) and  $e_g$  (formed by  $d_{x^2-y^2}$  and  $d_{z^2}$  orbitals) features because of the low symmetry of the Oh ligand field compared to the spherical field. The  $L_3$ - $e_g$  feature splits further into a double-peaked structure centered at 461 eV, which is attributed to the distortions from octahedral symmetry [52].

It is observed that the first two peaks ( $L_3$ - $t_2g$  and  $L_3$ - $e_g$ ) shift to high energy in the presence of graphene (Fig. 17a), which is in accordance with the results from XPS measurements. This kind of shift is normally induced by a change of the metal's chemical state or oxygen vacancies. However, there is no corresponding change in O K edge for TGCS-1 (Fig. 17b). This shows the presence of electron transfer from Ti3d orbitals in the conduction band of  $TiO_2$  to the C2s orbitals (graphene). Additionally, the O K-edge XAS spectra reflect the O2p orbitals coupled with the Ti2p, 3d, 4s, and Ti4p orbitals; the O K edge is almost identical for HR- $TiO_2$  and TGCS-1.

We choose methylene blue (MB) as a representative of organic substances to evaluate photocatalytic activity of the samples. As a reference, the photocatalytic behavior of Degussa P25 is also measured. Prior to photocatalysis, the solution including MB and catalyst is stirred in the dark for 1 h for adsorption equilibrium. In Fig. 18a, under the UV light, the results of photocatalytic evaluation of as-prepared samples and P25 show that TGCS-1 exhibits the highest photocatalytic activity; the average degradation rate of MB is 85.2% within 60 min. In contrast, the photocatalytic activity of Degussa P25 is low with almost 59.2% MB remaining in solution within the same 60 min period. The degradation yield of HR- $TiO_2$  is about 65.5%.

In addition, the photodegradation of MB is monitored for six cycles. The photodegradation rate remains constant during the six consecutive cycles, as shown in Fig. 18b, indicating as-prepared photocatalyst TGCS-1 is stable under UV light irradiation.

In summary, a high-activity  $TiO_2$ /graphene with exposed {001} facets composite photocatalyst is synthesized. The  $TiO_2$ /graphene composites exhibit high photocatalytic activity compared with the P25 under the UV light. The high photocatalytic

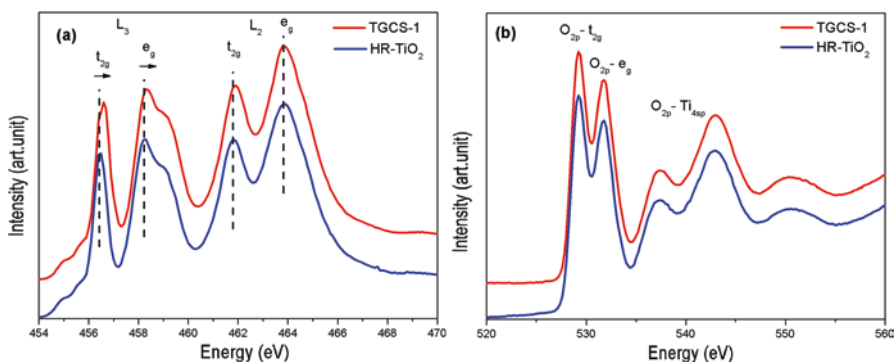


**Fig. 17** (a) Ti L-edge XAS spectra and (b) O K-edge XAS spectra for HR- $TiO_2$  and TGCS-1 [17] (Reproduced from *J. Phys. Chem. C*, 2011, 115, 23,718–23,725)

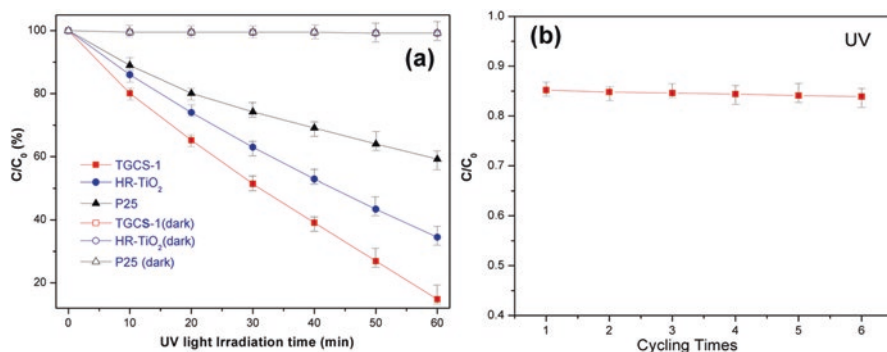


**Fig. 18** (a) Variation of normalized  $C/C_0$  of MB concentration for different times under UV light irradiation ( $C_0$ : the initial MB concentration after adsorption equilibrium). (b) Cycling degradation rate for MB of TGCS-1 under UV irradiation [17] (Reproduced from *J. Phys. Chem. C*, 2011, 115, 23,718–23,725)

activity can be attributed to two crucial factors, the high charge separation rate based on the electron transfer and the effective exposure of highly reactive {001} facets of TiO<sub>2</sub>. This work provides a facile approach to synthesize novel graphene-based photocatalyst and give more direct evidences for the intensified electronic interaction between graphene and TiO<sub>2</sub> nanoparticles.

## References

1. K. Geim, K.S. Novoselov, The rise of graphene. *Nat. Mater.* **6**, 183–191 (2007)
2. X. Li, X. Wang, L. Zhang, S. Lee, H. Dai, Chemically derived, Ultrasmooth graphene nanoribbon semiconductors. *Science* **319**, 1229–1232 (2008)
3. S. Park, R.S. Ruoff, Chemical methods for the production of graphenes. *Nat. Nanotechnol.* **5**, 217–224 (2009)
4. S. Patchkovskii, J.S. Tse, S.N. Yurchenko, L. Zhechkov, T. Heine, G. Seifert, Graphene nanostructures as tunable storage media for molecular hydrogen. *PNAS* **102**, 10439–10444 (2005)
5. E. Hendry, P.J. Hale, J. Moger, A.K. Savchenko, S.A. Mikhailov, Coherent nonlinear optical response of graphene. *Phys. Rev. Lett.* **105**, 212–217 (2010)
6. M. Allen, V.C. Tung, R.B. Kaner, Honeycomb carbon: A review of graphene. *Chem. Rev.* **110**, 132–145 (2010)
7. Q.J. Xiang, Y. JG, M. Jaroniec, Graphene-based semiconductor photocatalysts. *Chem. Soc. Rev.* **41**, 782–796 (2012)
8. L.M. Zhang, S. Diao, Y.F. Nie, K. Yan, N. Liu, B.Y. Dai, Q. Xie, A. Reina, J. Kong, Z.F. Liu, Photocatalytic patterning and modification of graphene. *J. Am. Chem. Soc.* **133**, 2706–2713 (2011)
9. Y.H. Zhang, Z.R. Tang, F. XZ, X. YJ, TiO<sub>2</sub>-graphene nanocomposites for gas-phase photocatalytic degradation of volatile aromatic pollutant: is TiO<sub>2</sub>-graphene truly different from other TiO<sub>2</sub>-carbon composite materials? *ACS Nano* **4**, 7303–7314 (2010)
10. X.S. Li, W.W. Cai, J.H. An, S. Kim, J. Nah, D.X. Yang, R. Piner, A. Velamakanni, I. Jung, E. Tutuc, Large-area synthesis of high-quality and uniform graphene films on copper foils. *Science* **324**, 1312–1314 (2009)

11. M.Y. Han, B. Ozyilmaz, Y.B. Zhang, P. Kim, Energy band-gap engineering of graphene nanoribbons. *Phys. Rev. Lett.* **98**, 206805 (2007)
12. K.S. Novoselov, A.K. Geim, S.V. Morozov, D. Jiang, Y. Zhang, S.V. Dubonos, I.V. Grigorieva, A.A. Firsov, Electric field effect in atomically thin carbon films. *Science* **306**, 666–669 (2004)
13. A. Reina, X. Jia, J. Ho, D. Nezich, H. Son, V. Bulovic, M.S. Dresselhaus, J. Kong, Large area, few-layer graphene films on arbitrary substrates by chemical vapor deposition. *Nano. Lett.* **9**, 30–35 (2008)
14. A. Ciesielski, P. Samorì, Graphene via sonication assisted liquid-phase exfoliation. *Chem. Soc. Rev.* **4**, 381–398 (2014)
15. M. Choucair, J.A. Stride, Gram-scale production of graphene based on solvothermal synthesis and sonication. *Nature Nanotech* **4**, 30–33 (2009)
16. G. Eda, G. Fanchini, M. Chhowalla, Large-area ultrathin films of reduced graphene oxide as a transparent and flexible electronic material. *Nature Nanotech* **3**, 270–274 (2008)
17. B. Jiang, C. Tian, Q. Pan, Z. Jiang, J. Wang, W. Yan, H. Fu, Enhanced photocatalytic activity and electron transfer mechanisms of graphene/TiO<sub>2</sub> with exposed {001} facets. *J. Phys. Chem. C* **115**, 23718–23725 (2011)
18. H. Zhang, X.J. Lv, Y.M. Li, Y. Wang, J.H. Li, P25-graphene composite as a high performance photocatalyst. *ACS Nano* **4**, 380–386 (2010)
19. G. Williams, B. Seger, P.V. Kamat, TiO<sub>2</sub>-graphene nanocomposites. UV-assisted photocatalytic reduction of graphene oxide. *ACS Nano* **2**, 1487–1491 (2008)
20. Y.Y. Liang, H.L. Wang, H.S. Casalongue, Z. Chen, H.J. Dai, TiO<sub>2</sub> nanocrystals grown on graphene as advanced photocatalytic hybrid materials. *Nano Res.* **3**, 701–705 (2010)
21. A.A. Polyakov, Quenching properties of parts having stress concentrators. *Met. Sci. Heat Treat* **37**, 324–325 (1995)
22. B.J. Jiang, C.G. Tian, L. Wang, X. YX, R.H. Wang, Y.Q. Qiao, Y.G. Ma, F. HG, Facile fabrication of high quality graphene from expandable graphite: Simultaneous exfoliation and reduction. *Chem. Commun.* **46**, 4920–4922 (2010)
23. Y.B. Tang, C.S. Lee, Z.H. Chen, G.D. Yuan, Z.H. Kang, S.T. Lee, High-quality graphenes via a facile quenching method for field-effect transistors. *Nano Lett.* **9**, 1374–1377 (2009)
24. X. YX, H. Bai, L. GW, C. Li, G.Q. Shi, Flexible graphene films via the filtration of water-soluble noncovalent functionalized graphene sheets. *J. Am. Chem. Soc.* **130**, 5856–5857 (2008)
25. S. Stankovich, R.D. Piner, S.T. Nguyen, R.S. Ruoff, Synthesis and exfoliation of isocyanate-treated graphene oxide nanoplatelets. *Carbon* **44**, 3342–3347 (2006)
26. Y.M. Li, L.H. Tang, J.H. Li, Preparation and electrochemical performance for methanol oxidation of pt/graphene nanocomposites. *Electrochem. Commun.* **11**, 846–849 (2009)
27. J.F. Shen, M. Shi, B. Yan, H.W. Ma, N. Li, M.X. Ye, One-pot hydrothermal synthesis of ag-reduced graphene oxide composite with ionic liquid. *J. Mater. Chem.* **21**, 7795–7801 (2011)
28. R. Muszynski, B. Seger, P.V. Kamat, Decorating graphene sheets with gold nanoparticles. *J. Phys. Chem. C* **112**, 5263–5266 (2008)
29. J. Liu, S. Fu, B. Yuan, Y. Li, Z. Deng, Toward a universal “adhesive nanosheet” for the assembly of multiple nanoparticles based on a protein-induced reduction/decoration of graphene oxide. *J. Am. Chem. Soc.* **132**, 7279–7281 (2010)
30. J. Liu, H. Bai, Y. Wang, Z. Liu, X. Zhang, D.D. Sun, Self-assembling TiO<sub>2</sub> nanorods on large graphene oxide sheets at a two-phase interface and their anti-recombination in photocatalytic applications. *Adv. Funct. Mater.* **20**, 4175–4181 (2010)
31. Z. Yin, S. Wu, X. Zhou, X. Huang, Q. Zhang, F. Boey, H. Zhang, Electrochemical deposition of zno nanorods on transparent reduced graphene oxide electrodes for hybrid solar cells. *Small* **6**, 307–312 (2010)
32. M. Feng, R.Q. Sun, H.B. Zhan, Y. Chen, Lossless synthesis of graphene nanosheets decorated with tiny cadmium sulfide quantum dots with excellent nonlinear optical properties. *Nanotechnol* **21**, 589–594 (2010)
33. Y.T. Kim, J.H. Han, B.H. Hong, Y.U. Kwon, Electrochemical synthesis of CdSe quantum-dot arrays on a graphene basal plane using mesoporous silica thin-film templates. *Adv. Mater.* **22**, 515–518 (2010)



34. A. Melaiye, Z. Sun, K. Hindi, A. Milsted, D. Ely, D.H. Reneker, C.A. Tessier, W.J. Youngs, Silver(I)-imidazole cyclophane gem-diol complexes encapsulated by electrospun tectophilic nanofibers: Formation of nanosilver particles and antimicrobial activity. *J. Am. Chem. Soc.* **127**, 2285–2291 (2005)
35. B.J. Jiang, C.G. Tian, G. Song, W. Chang, G.F. Wang, W.Q.F. HG, A novel ag/graphene composite: Facile fabrication and enhanced antibacterial properties. *J. Mater. Sci.* **48**, 1980–1985 (2013)
36. H. Zhang, G. Chen, Potent antibacterial activities of Ag/TiO<sub>2</sub> nanocomposite powders synthesized by a one-pot sol-gel method. *Environ. Sci. Technol.* **43**, 2905–2910 (2009)
37. C.G. Navarro, R.T. Weitz, A.M. Bittner, M. Scolari, A. Mews, M. Burghard, K. Kern, Electronic transport properties of individual chemically reduced graphene oxide sheets. *Nano Lett.* **7**, 3499–3503 (2007)
38. A. Mukhopadhyay, S. Basak, J.K. Das, S.K. Medda, K. Chattopadhyay, G. De, Ag-TiO<sub>2</sub> nanoparticle Codoped SiO<sub>2</sub> films on ZrO<sub>2</sub> barrier-coated glass substrates with antibacterial activity in ambient condition. *ACS Appl. Mater. Interfaces* **2**, 2540–2546 (2010)
39. N. Hoshiya, M. Shimoda, H. Yioshikawa, Y. Yamashita, S. Shuto, M. Arisawa, Sulfur modification of au via treatment with piranha solution provides low-Pd releasing and recyclable Pd material, SAPd. *J. Am. Chem. Soc.* **132**, 7270–7272 (2010)
40. S. Pylypenko, A. Queen, T.S. Olson, A. Dameron, K. O’Neill, K.C. Neyerlin, B. Pivovar, H.N. Dinh, D.S. Ginley, T. Gennett, Tuning carbon-based fuel cell catalyst support structures via nitrogen functionalization. I. Investigation of structural and compositional modification of highly oriented pyrolytic graphite model catalyst supports as a function of nitrogen implantation dose. *J. Phys. Chem. C* **115**, 13667–13675 (2011)
41. B.J. Jiang, S.Z. Song, G.Q. Wang, W. Chu, H.F. Li, H. Xu, C.G. Tian, F. HG, Nitrogen-doped graphene supported Pd@PdO core-shell clusters for C–C coupling reactions. *Nano Res.* **7**(9), 1280–1290 (2014)
42. S. Pylypenko, A. Borisevich, K.L. More, A.R. Corpuz, T. Holme, A.A. Dameron, T.S. Olson, H.N. Dinh, T. Gennette, R. O’Hayre, Nitrogen: unraveling the secret to stable carbon-supported Pt-alloy electrocatalysts. *Energy Environ. Sci.* **6**, 2957–2965 (2013)
43. X.M. Chen, W. GH, J.M. Chen, X. Chen, Z.X. Xie, X.R. Wang, Synthesis of “clean” and well-dispersive Pd nanoparticles with excellent electrocatalytic property on graphene oxide. *J. Am. Chem. Soc.* **133**, 3693–3695 (2011)
44. G. Riegel, J.R. Bolton, Photocatalytic efficiency variability in TiO<sub>2</sub> particles. *J. R. J. Phys. Chem* **99**, 4215–4224 (1995)
45. O. Carp, C.L. Huisman, A. Reller, Photoinduced reactivity of titanium dioxide. *Sol. State Chem.* **32**, 33–177 (2004)
46. C.N.R. Rao, K. Biswas, K.S. Subrahmanyam, A. Govindaraj, Graphene, the new nanocarbon. *J. Mater. Chem.* **19**, 2457–2469 (2009)
47. X. Gong, A. Selloni, Reactivity of anatase TiO<sub>2</sub> nanoparticles: The role of the minority (001) surface. *J. Phys. Chem. B* **109**, 19560–19562 (2005)
48. H.G. Yang, C.H. Sun, S.Z. Qiao, J. Zou, G. Liu, S.C. Smith, H.M. Cheng, L. GQ, Anatase TiO<sub>2</sub> single crystals with a large percentage of reactive facets. *Nature* **453**, 638–641 (2008)
49. X.G. Han, Q. Kuang, M.S. Jin, Z.X. Xie, L.S. Zheng, Synthesis of Titania nanosheets with a high percentage of exposed (001) facets and related photocatalytic properties. *J. Am. Chem. Soc.* **131**, 3152–3153 (2009)
50. J. Li, S.B. Tang, L. Lu, H.C. Zeng, Preparation of nanocomposites of metals, metal oxides, and carbon nanotubes via self-assembly. *J. Am. Chem. Soc.* **129**, 9401–9409 (2007)
51. H.B. Zhang, X.L. Pan, J. Liu, W.Z. Qian, F. Wei, Y.Y. Huang, X.H. Bao, Enhanced catalytic activity of sub-nanometer titania clusters confined inside double-wall carbon nanotubes. *Chem. Sus. Chem.* **4**, 975–980 (2011)
52. F.M.F. De De Groot, M. Gnoni, J.C. Fuggle, J. Ghljsen, G.A. Sawatzky, H. Peterson, Oxygen 1s X-ray absorption edges of transition metal oxides. *Phys. Rev. B* **40**, 5715–5723 (1989)

# Optical Characterization of Graphene and Its Derivatives: An Experimentalist's Perspective

Dinh-Tuan Nguyen, Ya-Ping Hsieh, and Mario Hofmann

## 1 Introduction

Prof. Suzuki's arguably biggest contribution to scientific progress is a powerful method to assemble carbon atoms into extended and complex molecules. Despite the limited chemical variety, a large range of chemical properties, electronic structure, and reactivity were observed for thus produced molecules [1]. In addition to the myriad of applications, the ability to produce complex organic molecules has answered fundamental questions of the relation between a molecule's geometry and its properties and has advanced fields ranging from biology to chemical engineering.

The inverse problem, i.e. structure determination from a set of measured properties represents an important challenge for the metrology of produced species and the characterization of novel materials. This is especially taxing considering the richness of carbon chemistry as explored by Prof. Suzuki where that the substitution of a single atom can completely transform the properties of a molecule.

To enhance our understanding of the structure-property relation in complex organic molecules, a model system is needed. Ideally, such a model system would only contain carbon atoms and allow the easy addition of other species. The resulting

---

D.-T. Nguyen

Department of Material Science and Engineering, National Cheng Kung University,  
Tainan 70101, Taiwan

Y.-P. Hsieh

Institute of Atomic and Molecular Sciences, Academia Sinica,  
No. 1, Sec. 4, Roosevelt Rd., Taipei 10617, Taiwan

M. Hofmann (✉)

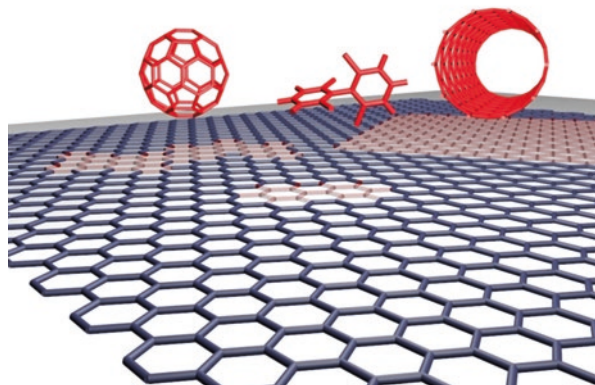
Department of Material Science and Engineering, National Cheng Kung University,  
Tainan 70101, Taiwan

Department of Physics, National Taiwan University,

No.1 Sec.4 Roosevelt Road, Taipei 10617, Taiwan

e-mail: [mario@phys.ntu.edu.tw](mailto:mario@phys.ntu.edu.tw)

**Fig. 1** Depiction of graphene and several materials that can be considered a geometric derivative of graphene



modification of characteristics would then allow inference to a heteroatom's impact on the fundamental behavior of the molecule. Furthermore, an extended molecule would be preferable to neglect effects of edges and corners. Finally, avoiding steric hindrance in the heteroatom addition implies the use of a planar structure.

Fortunately, such a model system exists in the form of graphene. The material consists of an infinite  $sp^2$  network that contains a single atomic layer of carbon atoms. Confining the dimension of graphene in one or two directions would then lead to carbon ribbons or planar carbon molecules. The two-dimensional nature of graphene furthermore permits the formation of carbon nanotubes, fullerenes, or more complex structures by out-of-plane bending (Fig. 1). Furthermore, facile addition of heteroatoms through a large variety of functionalization methods can be achieved [2].

Thus, characterization methods that are applicable to graphene will be suitable for other forms of carbon, and trends that are observed in the modification of graphene can allow extrapolation toward unknown and complex molecules.

In this contribution, we explore the characterization of graphene and its derivatives and highlight the changes that are observed upon modifications of their geometry and chemistry. We will limit ourselves to optical characterization methods since they provide fast, nondestructive, and readily available tools to the research community.

## ***1.1 Outline of This Chapter***

This contribution is trying to set itself apart from the large amount of available literature on the topic of optical characterization of graphene by providing practical guidelines. Many times an experimentalist will try to extract specific information from a sample and needs to decide which experiments to conduct. We will here

provide an overview of techniques available to elucidate certain graphene properties. Intuitive explanations are favored over details in order to facilitate understanding, and the interested reader is referred to in-depth descriptions in the form of review articles, where available.

To accommodate our result-oriented approach, this contribution is organized in the following sequence: First, a short overview of widely available optical techniques will be provided that summarizes the working principle and the requirements for sample preparation. Then, we will illustrate relevant properties of graphene and identify characterization techniques that can elucidate changes of each property.

Finally, examples of complementary experimental characterization approaches will be presented that help distinguishing competing effects.

## 2 Methods

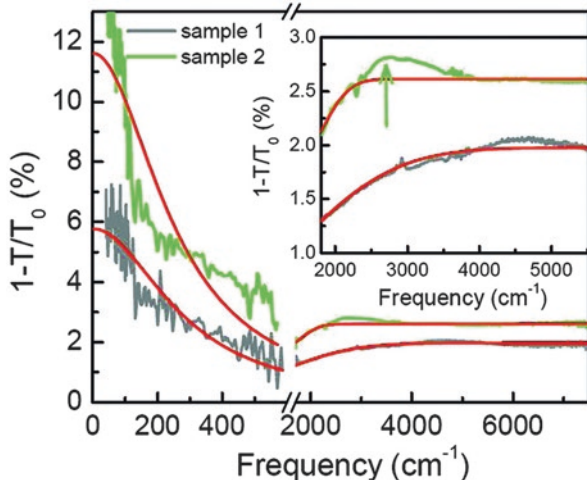
### 2.1 Absorbance Spectroscopy

Optical absorption is among the oldest and arguably simplest characterization methods, but one that can provide important information on structure and electronic properties of materials. Also known as *UV-Vis spectroscopy*, the method in fact encompasses the spectrum in the ultraviolet, visible, and IR regions. Interaction of graphene over this wide excitation energy range is quite diverse. At low energies, the electronic response can follow the electric field, and absorption can be described by classical electrodynamics. At higher energies, graphene photon absorption causes electronic excitation akin to molecular transitions that allow inference to graphene's unique properties.

A modern double-beam UV-Vis spectrometer contains a monochromator transmitting a narrow beam of selectable wavelength from a broadband light source; an optical arrangement separating that beam into two, one of which passes through the sample while the other is used as reference; and two detectors (or one with a chopper) collecting both beams and calculating the absorbance from the intensity of the reference beam ( $I_0$ ) and the signal from sample ( $I$ ). Alternatively, in a single-beam setup,  $I_0$  is acquired by running a background scan prior to sample measurement.

Absorption spectroscopy is most conveniently carried out with liquid samples, as in liquid medium the effects of diffraction, reflection, as well as bulk scattering are minimal. Solid materials can be characterized by being suspended or dissolved in solvents and placed in a transparent cuvette. Note that solvents absorb light at different degrees, which leads to a limit of operating wavelength range called cutoff wavelength (for instance, 240 nm for ethanol). Also, appropriate concentration is a crucial practical factor in obtaining a good-quality spectrum: too low concentration risks signal not being detected by the photodetector, but too high concentration may lead to saturated spectra with peaks buried in the background.

**Fig. 2** Absorbance spectrum of epitaxial graphene in the infrared region and calculated results (red curves) [7]. Green arrow (inset) shows the absorption peak characteristic of AB-stacking bilayer graphene in the mid-IR region (Reproduced with permission from [7])



Much effort has been made to study graphene's optical conductivity in part to realize its application in optoelectronics. It was theoretically calculated [3] and later experimentally verified [4] that monolayer graphene has a constant value of absorbance of around 2.3% which is strikingly large considering its thickness. Moreover, this value is mostly independent of wavelength and solely defined by its fine structure constant and is a direct consequence of graphene's 2D nature and gapless electronic structure. Significant deviations from that universal value occur in two regions (Fig. 2). In the UV range, where a prominent peak is observed at around 4.6 eV due to an excitonic resonance [5], and the far IR range, where the scattering of free carriers dominates. For multilayer graphene, the experimental result still adheres well to predictions due to weak van der Waals interactions between layers. This, in combination with the fact that graphene reflects very little (0.1% incident light for monolayer, around 2% for ten layers), paves the way for the use of absorption measurement as a reliable method to determine the thickness and the number of layer [6].

Moreover, structural modification, either by electrostatic [8] or by chemical interactions [9], can result in band formation and band shift in absorption spectra. Absorption spectrometry therefore has been used to monitor graphene hydrogenation/dehydrogenation [10] and especially graphene oxidation/reduction. The absorption spectrum of fully oxidized graphene in visible range is dominated by a peak at around 230 nm which corresponds to  $\pi \rightarrow \pi^*$  transition of C-C aromatic bonds and a less visible shoulder at about 300 nm assigned to  $n \rightarrow \pi^*$  transitions of C=O bonds. From the absorption intensity, one can evaluate the level of dispersion of graphene oxide in different solvents [11]. The reduction of graphene oxide will leave a characteristic red shift (atom rearrangement) and gradual decay of these features and an overall increase in absorption intensity across the spectral range [12, 13].

## 2.2 Infrared Spectroscopy

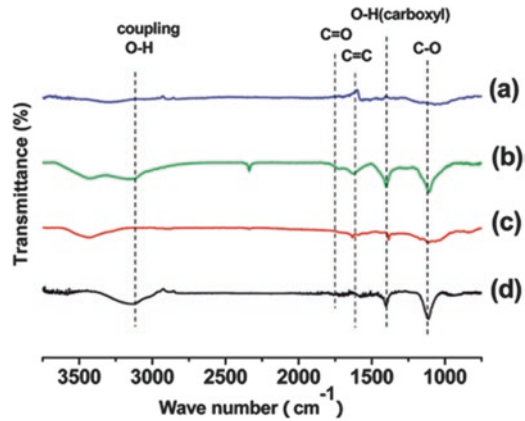
Similar to optical absorption, infrared spectroscopy explores the material structure through the light absorption at certain wavelengths, in this case limited to the IR region. When investigating this region at high-frequency resolution, peaks occur in the absorbance. These are not caused by electronic transitions as described in absorbance spectroscopy but occur when there is resonance between incident radiation and molecular vibration which causes a change in dipole moment. Graphene and its derivatives are largely IR-inactive [14] due to their symmetric  $sp^2$  bonds, but the method is sensitive to the presence of functional groups (especially oxygen) in the lattice.

Early infrared spectrometers used a dispersive element to scan sequentially over the wavelength range, which was very time-consuming and limited in resolution. This setup has been superseded in the last two decades by a much more robust Fourier transform IR (FTIR). In FTIR, a broadband light source is modulated by a Michelson interferometer with a moving mirror generating an IR excitation in the form of an interferogram. The interferogram is then deconstructed by fast Fourier transform into relevant transmittance information (hence its name).

Since the IR signal is weak, appropriate sample preparation is generally needed to ensure high-quality spectra. Because bulk absorption will result in saturated spectra, it is desirable for the sample to be made into a homogenous thin film and contained in a cell made of some IR transparent material (most often KBr, albeit NaCl,  $CaF_2$ , ZnSe, and diamond are also used). Crystalline samples are first ground into fine particles with diameters well below IR wavelengths to minimize light scattering. Then the powder is mixed with a heavy oil (Nujol) or dried KBr and pressed at high pressure into a paste or pellet. Nujol has its own absorption spectra which may interfere with a sample's spectrum, a disadvantage KBr does not have. The latter is highly hygroscopic, though, and humidity will introduce  $-OH$  group, a very strong IR absorber. One of the absorption bands of  $-OH$  lies at  $1630\text{ cm}^{-1}$  [15] which is close to that of  $C=C$  bond, which complicates the interpretation of carbon (and organic) samples. Such difficulties can be avoided by using attenuated total reflection (ATR-FTIR) which exploits the evanescent wave near the interface of a sample with an IR sensing element upon which incident IR light is reflected. The signal only probes the sample surface, and therefore little to no sample preparation is necessary.

FTIR has been used to determine functional groups on carbon materials, such as carbon *black*, for more than three decades [17]. For graphene, as mentioned earlier, this technique is particularly sensitive in detecting oxygen-containing groups. As shown in Fig. 3, characteristic IR spectrum of graphene oxide contains absorption bands at  $1720\text{ cm}^{-1}$  (related to  $C=O$  stretching vibrations),  $1230\text{ cm}^{-1}$  ( $C-OH$  stretching), and  $1070\text{ cm}^{-1}$  ( $C-O$  stretching), in addition to a band around  $1620\text{ cm}^{-1}$  attributed to  $C=C$  stretching of the carbon lattice [18]. The reduction of graphene oxide, for example, would be manifested in FTIR by the decrease in intensity of all those bands except the  $C=C$  stretching, along with a blueshift in  $-OH$  stretching band [19]. Information obtained from FTIR can help evaluate the quality of reduced graphene oxide [16], the types, and even the orientation of various chemical groups and elements like OH, COOH [20],  $C-O-C$  [21], F [22], S [23], and H [24].

**Fig. 3** FTIR transmittance spectra of pristine graphite (a), exfoliated graphene oxide (b), electrochemically reduced graphene oxide, (c) and chemically reduced graphene oxide (Reproduced with permission from [16])



### 2.3 Raman Spectroscopy

Raman spectroscopy is a measurement technique that analyzes the energy loss of the incident light. This approach is different from absorption techniques that characterize the loss in intensity. Energy loss occurs through interaction of incident photons with lattice vibrations or phonons in the sample. Phonons can be thought of as a harmonic oscillation of carbon atoms that exhibits a characteristic resonance frequency which depends on the coupling strength to other atoms in the crystal. While graphene and its derivatives manifest many possible vibration types, only certain “phonon modes” can couple with a photon. These “Raman-active” modes are characterized by a change in the crystal’s response to an electric field upon atomic displacement around the equilibrium position.

Graphene exhibits several such Raman-active modes that are identified by their symmetry according to group theory notation (Fig. 4). A1g represents a breathing-like radial displacement of all carbon atoms within one hexagon and is termed the D-band by spectroscopists [25].

An E2g-type out-of-phase transverse displacement of neighboring carbon atoms along the zigzag direction produces phonons with a higher energy, termed optical phonon, which creates the G-band [26]. Weaker Raman features include the D’-band which originates from a similar symmetry as the G-band but exhibits a longitudinal displacement of neighboring carbon atoms [27].

Each phonon will cause reemission of the incident light with a distinct energy loss that is centered at its resonance frequency. Thus, the intensity distribution of the scattered outgoing light represents a measure of the concentration and availability of phonons and their resonance frequency. Traditionally, the unit of energy loss in such Raman spectra is in wavenumbers ( $\text{cm}^{-1}$ ) which represents the reciprocal wavelength and can be related to energy loss by

$$\Delta E = hc \left( \frac{1}{\lambda_{\text{incident}}} - \frac{1}{\lambda_{\text{scattered}}} \right)$$

where  $h$  is the Planck constant and  $c$  is the speed of light.

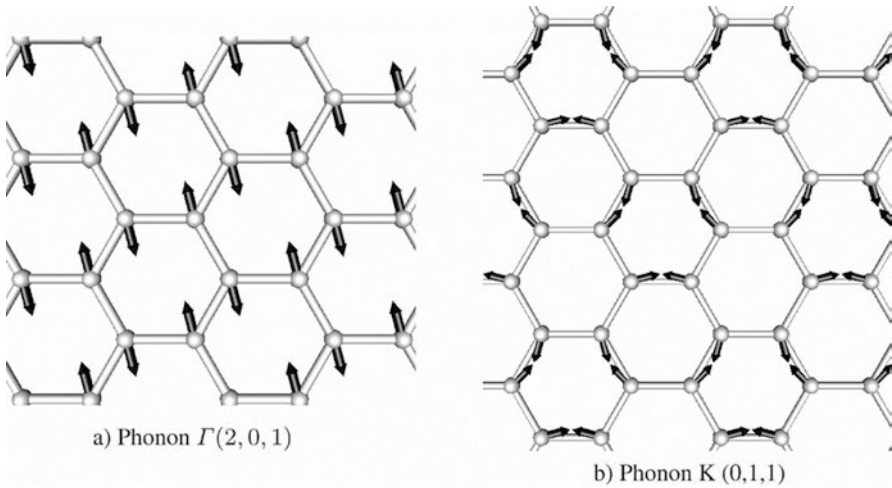


**Fig. 4** Representation of symmetry of (a) G-band and (b) D-band phonon modes (Reproduced with permission from [25])

**Fig. 5** Representative Raman spectra of pristine graphene (*top*) and defected graphene (*bottom*) (Reproduced with permission from [28])

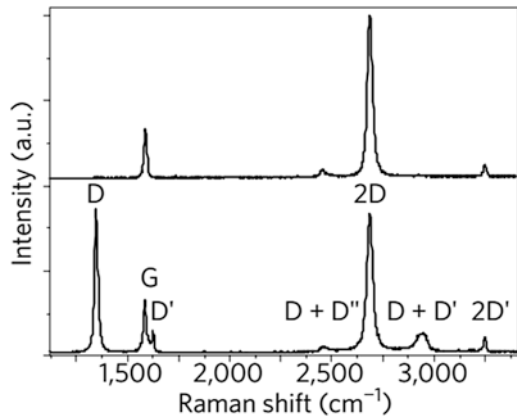


Figure 5 shows a representative Raman spectrum that exhibits distinctive energy losses to the described D-band, G-band, and G'-band phonons at  $1350 \text{ cm}^{-1}$ ,  $1600 \text{ cm}^{-1}$ , and  $1620 \text{ cm}^{-1}$ , respectively. Additionally, second-order Raman features can be observed where simultaneous loss to two phonons occurs. The most prominent of these modes is the 2D-band around  $2700 \text{ cm}^{-1}$  which creates two D-band phonons.

In this description, we have only considered the creation of phonons by incident light which is termed the Stokes condition. Phonon annihilation, on the other hand, would impart additional energy to the outgoing light, and a negative value for the energy loss would occur. This “anti-Stokes condition” follows the same principle as Stokes scattering and can be treated equivalently. It has to be noted, however, that many Raman measurement systems will only allow access to the Stokes portion of the spectrum to reduce the setup’s complexity.



Lasers are used as light sources due to their frequency stability and high spectral power, and several approaches exist to introduce them. For high-resolution measurements, the incident light will be tightly focused through a microscope objective whose resolution can be further enhanced through confocal illumination methods. To collect the outgoing light, a second objective can be employed in a transmission arrangement which requires transparent samples. Alternatively, the outgoing light can be collected with the same objective which, means the incident and outgoing light is sharing the same beam path. To separate them, a half-reflective mirror can be employed which reduces the intensity of the signal. If resolution is not a concern, fiber and free-space coupling in either reflection or transmission geometry can be employed which affords very compact and robust devices for mobile use. [28].

Due to the inherently weak interaction, the Raman signal is approximately  $10^9$  times weaker than the incident light, and high-quality filters and detectors have to be employed to overcome noise limits from sources and electronics.

Despite these challenges, Raman spectroscopy is a commonly used metrology tool due to its ability to characterize graphene in a variety of environments including in liquids and powders.

The detection efficiency can be significantly enhanced by proper sample preparation. The Raman intensity scales with the fourth power of the incident electric field, and several schemes exist to enhance it. First, improvements in Raman intensity can be achieved by tightly focusing the light. Second, suitable substrates can be employed that enhance the reflected light intensity by producing standing waves and positioning the sample at a maximum of this standing wave. Such an enhancement can be achieved in Si samples when an oxide of suitable thickness, such as 90 nm or 300 nm, is deposited. In contrast, conductive substrates will decrease the Raman intensity because they produce nodes in electrical field close to the surface. Lastly, electric field enhancement can be accomplished by producing standing waves or plasmons in the vicinity of the sample. This process is called “surface-enhanced Raman scattering” and can be introduced through suitable nanoparticles or sharp features, such as tips or gratings [29].

## 2.4 Rayleigh Imaging

When light interacts with the carbon lattice, most of the resulting scattering events are of elastic nature (Rayleigh scattering). Though the elastically scattered signal carries less information on a material’s structure compared to Raman scattering, its intensity is several orders higher than the latter and therefore more favorable for imaging applications.

To do this, however, one has to find ways to minimize the background effect of substrate scattering. A common setup to enhance the contrast and spatial resolution is confocal microscopy in which the scattered light from an observed spot is spatially filtered by a pinhole in the beam path, but even then the substrate’s signal can still be stronger than sample’s. This can be solved by suspending graphene to

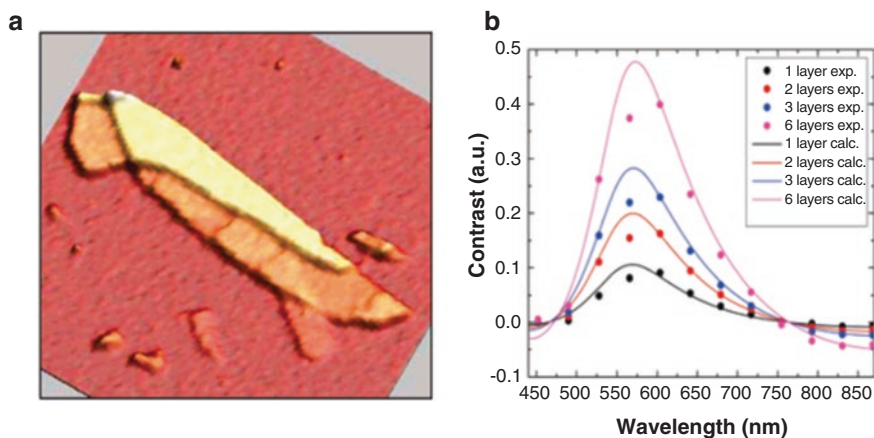


**Fig. 6** A monochromatic confocal Rayleigh mapping of graphene (a) and contrast value as a function of number of layer (b) (Reproduced with permission from [31])

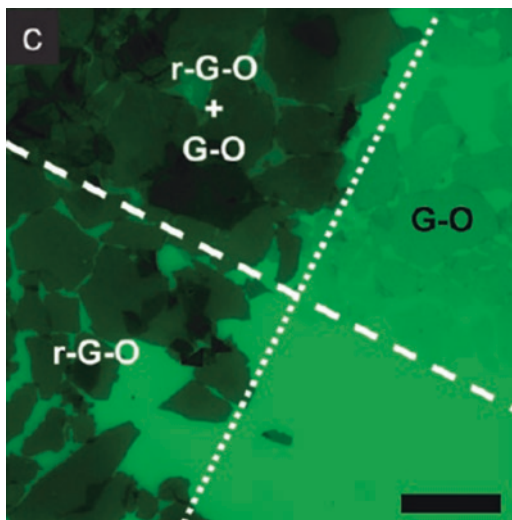
separate it from substrate, which has been realized before on carbon nanotubes, but such delicate and expensive process is often impractical [30]. Alternatively, an interferometric configuration can be employed to exploit the background signal as a reference and to increase the signal-to-noise ratio. Here the contrast is defined as  $\delta = (I_{Si} - I) / I_{Si}$  and depends on the thickness and refractive index of the oxide layer playing the role of a spacer between Si substrate and graphene. The light source can be monochromatic like in the case of Raman spectroscopy or broadband, thanks to the recent availability of supercontinuum light sources.

Rayleigh imaging has been demonstrated [31] to quickly map graphene on a substrate and provide guidance for the optimization of the spacer thickness used to distinguish graphene layers. To make the evaluation quantitative, a contrast spectrum can be obtained much in the same way as absorbance spectroscopy (Fig. 6). From the result, one can estimate the number of layers by comparing it with standard data either directly [32] or through transforming to total color difference values [33].

## 2.5 Photoluminescence

Similar to Raman spectroscopy, photoluminescence measurements rely on the inelastic scattering of incident light. Differently from Raman scattering, however, this process is not instantaneous, and there is a characteristic delay between illumination of a sample with a light source and reemission of light from the sample. The emission energy is determined by the electronic structure (most commonly the HOMO-LUMO gap) of the sample rather than the energy of the excitation source which allows distinction from Raman effects. Furthermore, photoluminescence is usually significantly stronger than Raman which relaxes requirements on the

**Fig. 7** Optical micrograph showing the suppression of fluorescence from defected graphene oxide (GO) and higher-quality graphene oxide (rGO) (Reproduced with permission from [34])



measurement setup. Common measurement setups will have similar layouts as for Raman measurements but allow investigation over a larger range of energy losses. Photoluminescence measurements can be conducted on solid substrates and in liquids, which makes it suitable for many different material types.

Graphene's high electron mobility and semimetallic nature usually impede photoluminescence measurements since photoexcited carriers would relax and recombine before emission takes place. This behavior is exploited in photoluminescence quenching microscopy where the presence of graphene is inferred from the suppression of photoluminescence from neighboring fluorophores (Fig. 7) [34].

Conversely, occurrence of photoluminescence from graphene suggests changes to its electronic structure, and chemical conversion of graphene can be traced by photoluminescence measurements as described later on.

## 2.6 Ultrafast Optics

The characteristic time scales for optical processes reveal important aspects of photoexcitation and carrier relaxation processes. Many of the time-resolved spectroscopy techniques rely on a pump-probe scheme that uses two laser pulses. First, a pulse from a high-intensity laser excites photocarriers or phonons, and then a weaker pulse from a second laser is used to characterize optical properties such as absorption, Raman scattering, or reflection. A variable delay between these two pulses can be used to map out the material's response on the sub-ps time scale. Slower responses can be directly characterized by employing fast detectors.

Ultrafast characterization of liquids, powders, and gasified carbon molecules has been reported [35, 36].

## 3 Properties

### 3.1 Thermal Properties

The combination of strong intralayer  $sp^2$  bonds and weak interlayer bonds dictates not only the electrical properties of graphene and related materials but their thermal properties as well. Graphene is predicted to have phenomenal thermal conductivity and heat capacity, giving rise to potential applications such as heat spreaders in nanoelectronics [37]. It is challenging, however, to measure precisely these properties for microscopic objects where defects, boundaries, and substrate interaction can greatly influence the phonon dispersion. Optical techniques have been an enabling tool for nanoscale measurements of thermal properties in graphene.

#### 3.1.1 Raman Spectroscopy

A higher temperature will give rise to a changed average distance between neighboring carbon atoms due to anharmonic terms in the bonding potential. This effect will cause strain in the graphene lattice and can thus be analyzed by Raman spectroscopy as explained later on. The peak position of the G-band was found to blue-shift with increasing temperatures according to [38]:

$$\Delta\text{Pos}(G) = -4.23 \times 10^{-4} T - 3.03 \times 10^{-5} T^2 + 1.15 \times 10^{-8} T^3$$

A more general approach to determining the temperature of a sample by Raman spectroscopy is to analyze the Stokes and anti-Stokes portion of the Raman spectrum. Since the anti-Stokes Raman requires a phonon for the scattering process to occur, its chance of occurring depends on the amount of present phonons which changes with temperature. Therefore, the ratio of Stokes/anti-Stokes band intensity can be correlated with the temperature according to:

$$\frac{I_{AS}}{I_S} = \frac{(\nu_l + \nu_v)^4}{(\nu_l - \nu_v)^4} e^{\left(\frac{h\nu_v}{kT}\right)}$$

where  $\nu_l$  is the laser frequency (in  $\text{cm}^{-1}$ ) and  $\nu_v$  is the phonon mode frequency.

Raman spectroscopy proves itself a valuable tool to infer graphene's thermal conductivity. Researchers have advanced an optothermal technique [39] where the strong temperature dependence of G-peak in Raman spectra is used to calculate thermal conductivity. During measurement, a graphene sample of length  $L$  and width  $W$  is suspended between two heat sinks, and the shifted position of G-peak  $\delta\omega$  is monitored with power variation  $\delta P$ . The thermal conductivity is then determined as:

$$K = \chi_G (L / 2hW) (\delta\omega / \delta P)^{-1}$$

where  $\chi_G = -1.6 \times 10^{-2} \text{cm}^{-1}/K$  is the linear temperature coefficient of the G-band shift.

It is noted, however, that many theoretical aspects are not well understood yet, and various experimental factors (sample preparation, laser heating setup) can affect the measurement result. The G-band position is also subject to strain and doping as well, and the interplay between these parameters cannot be neglected (e.g., it is argued that introducing strain can cause irregular change in thermal conductivity) [40].

### 3.2 Doping

The charge transfer between graphene and its surrounding is a powerful indicator of adsorbates, reactions, charge accumulation, etc. Graphene can act as a charge donor or acceptor which is termed p-doping and n-doping, respectively.

Raman spectroscopy is a useful technique for the characterization of such transfer processes. Intuitively, it is understandable that addition of positive or negative charges will affect the bonding strength of carbon atoms in the lattice and result in a stiffening of the bonds. The resulting blueshift in the resonance frequency can be seen for the G-band of graphene (Fig. 8). The dissimilar trend of the 2D-band position, however, shows the limit of this simple explanation, and more complex interactions between electronic and phononic processes have to be taken into account [41].

In the linear regime of low doping concentrations, the shift can be used to extract the carrier density using the formula [42]:

$$\Delta\text{Pos}(G) = -0.274n^2 + 14.25n$$

Time-dependent perturbation theory at zero temperature was used to arrive at [43]:

$$\hbar\Delta\omega_G = 4.39 \times 10^{-3} |E_F|,$$

where  $E_F = \hbar v_{\text{Fermi}} \sqrt{\pi n}$ .

Importantly, the 2D-band position follows a similar trend with doping for small dopant concentrations, and the two peak shifts are related by [44]:

$$\frac{\Delta\omega_{2D}}{\Delta\omega_G} \sim 0.7$$

The coupling between electronic and phononic states can also be seen when analyzing the intensity of the Raman features. At high doping, all Raman features decrease in intensity, but the decrease with carrier concentration depends on the difference between carrier energy distribution (Fermi energy  $E_F$ ) and the phonon energy due to Pauli blocking [45].

Therefore, each Raman peak has a distinct intensity variation with doping which depends on its energy, the laser excitation energy, and details of sample stacking and strain. Therefore, intensity ratios, such as the commonly employed 2D/G intensity ratio, should only be compared between similar samples [46].

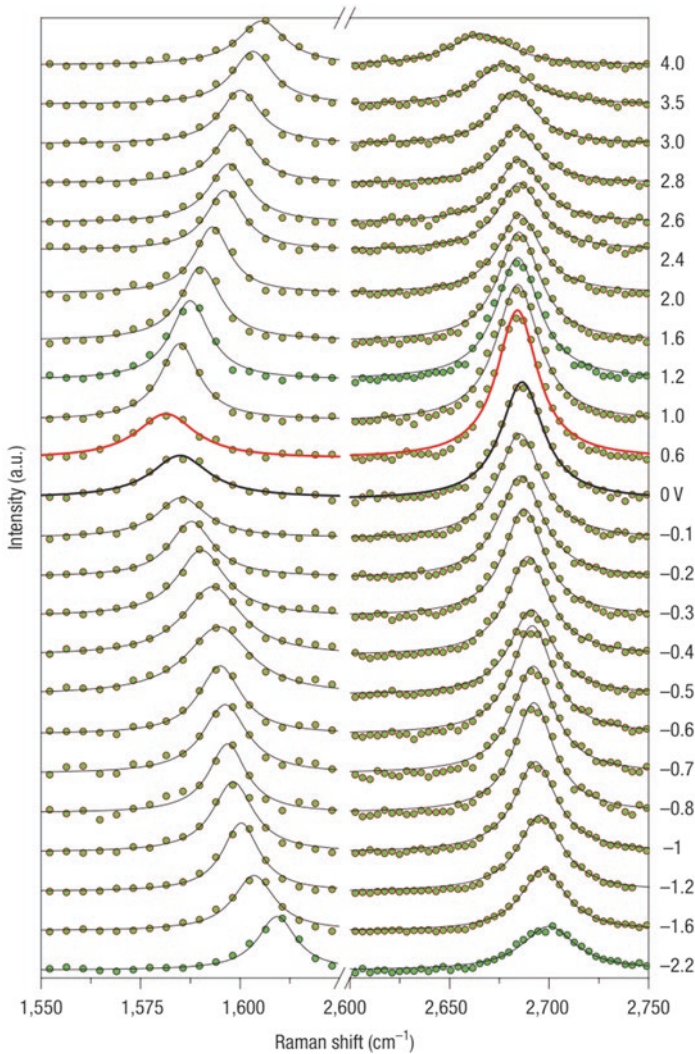


**Fig. 8** Impact of doping on the Raman G- and 2D-band [41]. Regions of G-band (*left*) and 2D-band (*right*) are measured across the top gating voltage range -2.2 Volts to 4 Volts, with *red line* undoped condition where the Fermi level intersects the representing the Dirac point (Reproduced with permission from [41])

### 3.2.1 Absorbance Spectroscopy

An alternative to Raman for extracting the carrier properties of graphene by optical methods is the use of absorbance techniques [47]. Infrared spectroscopy is dominated by two processes. In the far-infrared region ( $<500 \text{ cm}^{-1}$ ), absorption is mainly due to free carriers. The absorption of a material at low (angular) frequencies is then determined by the Drude conductivity of graphene according to:

$$A(\omega) = \frac{4\pi}{c} \operatorname{Re} \left( \frac{\sigma_0}{1 + i\omega\tau} \right)$$

where  $\sigma_0$  is the DC conductivity of graphene and  $\tau$  is the electron scattering time [47]. From these two parameters, the Drude weight  $D$  can be determined  $D = \frac{\pi\sigma_0}{\tau}$  which yields the carrier concentration of graphene  $n$  via the relation  $D = e^2 v_f \sqrt{\pi n}$ , where  $v_f$  is the Fermi velocity ( $1.09 \times 10^6$  m/s).

At higher photon energies ( $>0.1$  eV), the absorption is controlled by interband transitions of electrons. The efficiency of this process is determined by the availability of states and can be affected by Pauli blocking of states due to doping. In this situation, the absorptivity takes the form [47]:

$$A(\omega) = \frac{\pi^2 e^2}{hc} \left[ \tanh \left( \frac{\hbar\omega + 2E_F}{4k_B T} \right) + \tanh \left( \frac{\hbar\omega - 2E_F}{4k_B T} \right) \right]$$

where  $E_F$  is the Fermi energy that yields the doping concentration  $n = E_F^2 / \pi \hbar^2 v_f^2$ .

### 3.2.2 Fast Optics

Another way to probe the carrier concentration of graphene is by characterizing the transient response of electrons to a short pulse (Fig. 9). After excitation, the occupation of the HOMO is smaller than before, while the LUMO occupation is lower

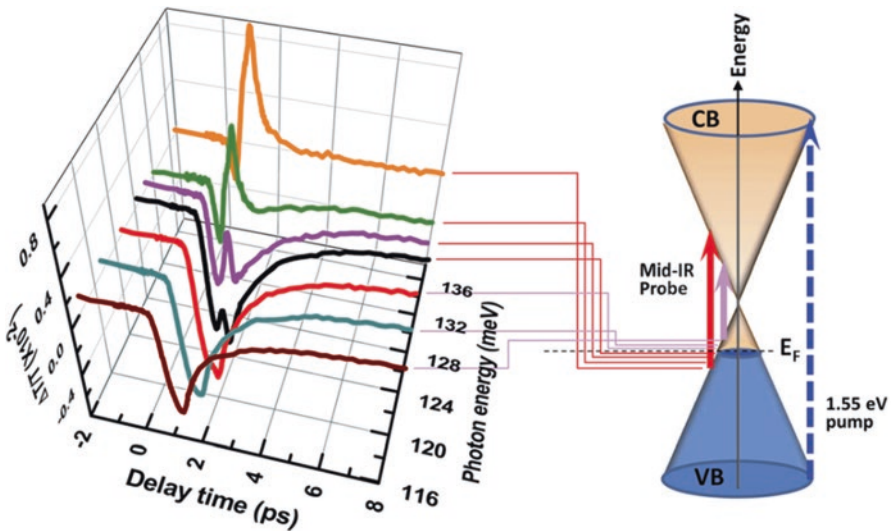


**Fig. 9** Time response of transmittance for varying photon energies (Reproduced with permission from [48])

which gives rise to peaks with different signs in the transient spectra. The energy difference between the peaks and the zero-crossing represents the Fermi-level shift relative to the Dirac point and can be used to extract the carrier concentration [48].

Additionally, the time required for photoexcited electrons to decay depends on the efficiency of coupling with phonons. Close to the Fermi level, this effect is smallest and longer decay times are observed. As the probe's excitation energy is increasing beyond the Fermi-level shift, the coupling strength is becoming larger and the decay time shortens. Thus, the decay time's energy dependence can be employed to estimate graphene's carrier occupation [48].

### 3.3 Strain

The displacement of individual atoms from their equilibrium bond position is an important parameter to evaluate the stability of molecules and crystals. Surprisingly, despite these variations only being in the sub-angstrom range, optical techniques can be employed to analyze even minute changes.

The resonance frequency of phonons as probed by Raman spectroscopy was found to sensitively depend on the strain within a bond, and all Raman features exhibit characteristic shifts in their peak position. The shifts of D-band, G-band, and 2D-band for 1% strain are listed in Table 1 [49, 50].

In the case of uniaxial strain, the G-band splits into two components ( $G^+$  and  $G^-$ ) whose relative ratio depends on the angle of the laser polarization and the strain axis with respect to the lattice [51]. This ability allows inference to the orientation of the graphene lattice from optical measurements.

The reader is reminded that other factors can affect the position of the Raman features as well, such as temperature and doping.

#### 3.3.1 Infrared Spectroscopy

Infrared spectroscopy is expected to be sensitive to bond deformation, and experimental results on graphene oxide paper indeed show a clear trend of infrared-active phonon mode position with applied strain [52]. Figure 10 shows a negative shift in IR features assigned to C=C and C=O bonds, which maintains linearity up to 1% strain. Challenges in this approach include the low spatial resolution of FTIR and the small peak shift ( $\sim 2 \text{ cm}^{-1}$  per 1% strain) compared to Raman spectroscopy.

**Table 1** Overview of Raman shift upon strain in uniaxial and biaxial direction

	G-band	2D-band	D-band
Uniaxial	$-36 \text{ cm}^{-1}/\%$ strain for $G^-$	$-100 \text{ cm}^{-1}/\%$ strain	$-50 \text{ cm}^{-1}/\%$ strain
	$-18 \text{ cm}^{-1}/\%$ strain for $G^+$		
Biaxial	$-63 \text{ cm}^{-1}/\%$ strain	$-200 \text{ cm}^{-1}/\%$ strain	$-100 \text{ cm}^{-1}/\%$ strain



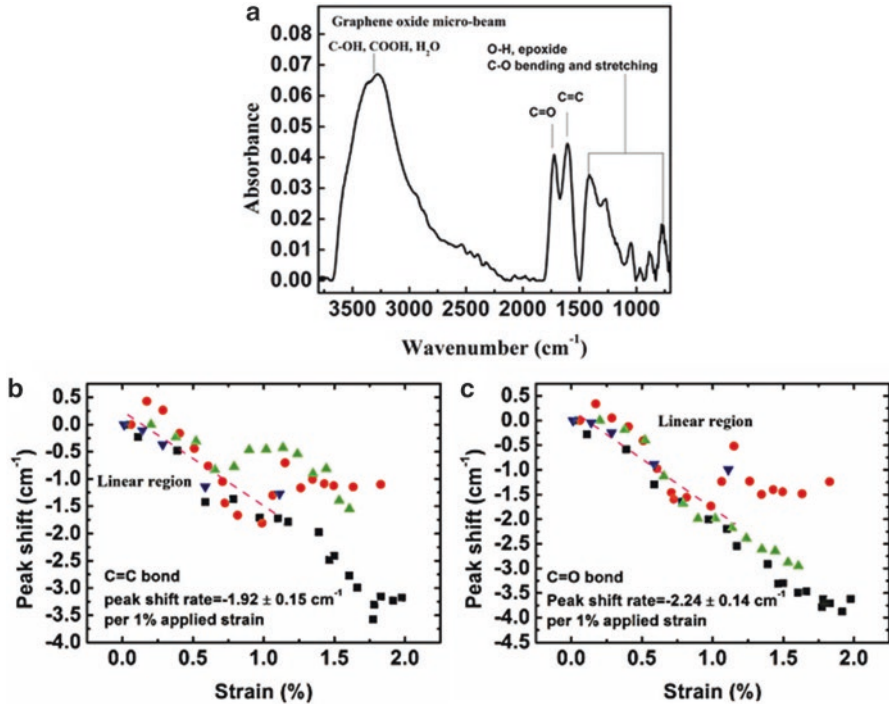


Fig. 10 FTIR spectra of unstrained of graphene oxide (a) and peak positions for different amounts of applied strain for C=C (b) and C=O (c) bonds (Reproduced with permission from [52])

### 3.4 Thickness and Stacking

Due to different preparation methods and different design purposes, researchers often encounter graphene samples with different thickness and even flakes of various numbers of layers in the same sample. Van-der-Waals interaction between layers, though weak, leads to deviations from the ideal model of graphene as an atomic-thin, two-dimensional crystal and with the number of layers ( $n$ ) increasing the material properties approaches those of bulk graphite. It is evaluated that only the materials constituted of less than ten layers [53] retain some properties from monolayer graphene and have been qualified as “few-layer graphene.” Thus, it is important to determine the thickness of prepared graphene.

While the thickness of graphene can be observed through electron and scanning probe microscopy techniques, they are usually slow and potentially damaging to the sample. Similar information can be conveniently obtained by nondestructive optical methods. The decrease of optical transmittance is a powerful indicator of a thickness increase. It is found that [6] at 550 nm wavelength, the transmittance is mostly

independent of stacking order and correlated with the number of layer by a relatively simple equation:

$$T(\omega) = (1 + f(\omega)\pi\alpha \times n / 2)^{-2}$$

where  $\alpha$  is the fine structure constant and  $f(\omega)$  is a correction coefficient, which can be used to determine the thickness up to tens of layers.

Optical microscopy can determine the thickness as well, by exploiting the contrast difference in Rayleigh scattering image [31] or fluorescent quenching image [54] (Fig. 11). Compared with spectroscopy methods, these techniques are more versatile in evaluating sample in larger scale (up to cm size), but not without flaws. Contrast in fluorescence was found to saturate for samples with  $n \geq 3$ , while reflectance is strongly influenced by background, and therefore Rayleigh imaging can be realized only with appropriate substrate of precise thickness (300 nm SiO<sub>2</sub> layer, with anti-reflectance coating). Recently, interference reflection microscopy – a derivative of fluorescence microscopy – proved able to image graphene layers with outstanding contrast [55] even on transparent substrates typically challenging for the other techniques.

The perpendicular arrangement of graphene layers forms weakly bonded van der Van-der-Waals solids that are akin to pi-stacking in organic chemistry. This stacking will change the electronic structure and limit interaction of inner-lying layers with the environment. Furthermore, the effect of the stack size in the transition between graphenic and graphitic properties enhances our understanding of nanoscale confinement effects.

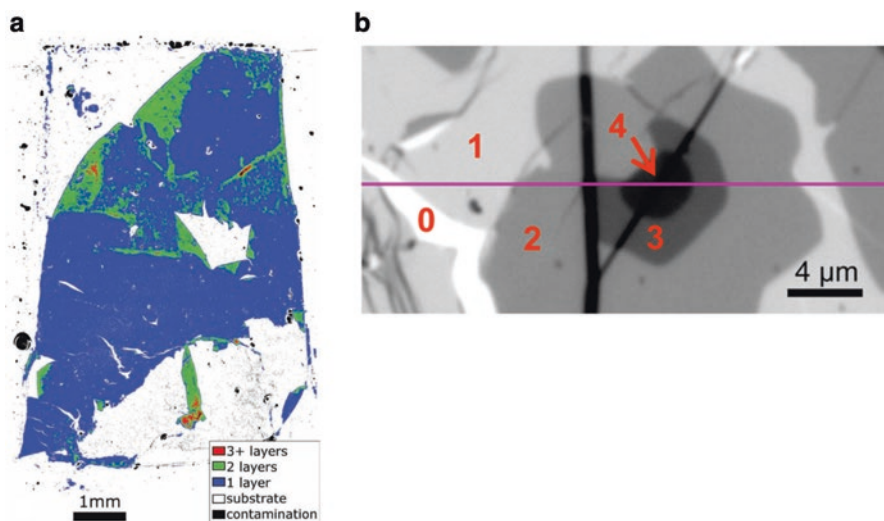


**Fig. 11** Layer identification by fluorescence quenching microscopy (*left*) [54] and interference reflection microscopy (*right*) (Reproduced with permission from [55])

Both the phononic and electronic interaction of stacked graphene layers are sensitive to the number and alignment of adjacent layers that can be detected by optical means.

Since Raman spectroscopy allows characterization of both interactions, it is expected that Raman will be a powerful method to analyze stacks.

As will be discussed later on, graphene's 2D-band is enhanced by resonance effects. This process will selectively enhance phonons with energy and momentum values that can match graphene's band structure. Thus, small changes in graphene's band structure will result in the selection of different phonons. For single-layer graphene, only one phonon can satisfy the scattering conditions, and the 2D-band only consists of one peak. As the graphene stack becomes thicker, more electronic states occur and more phonons can contribute to the scattering. Thus, the 2D-band is composed of more peaks, and deconvolution will allow inference to the thickness [56]. We have to note, however, that changes in graphene's defectiveness will also affect the 2D peak width (as discussed later on), and care has to be taken to account for such modifications, e.g., by comparing stacks of graphene of similar defectiveness.

The interaction of more graphene layers in a stack will produce new bonds and thus new phonons that create additional bands in the Raman spectrum.

The shear mode (or C mode) has very weak bond strengths and thus occurs at low energies (around  $40 \text{ cm}^{-1}$ ) that are not easily accessible by Raman setups. However, its position change with the number of layers is a good indicator of the graphene stack size for a wide range of layer numbers  $N$ :

$$\text{Pos}(C)_N = \sqrt{\frac{2\alpha}{\mu}} \sqrt{1 + \cos\left(\frac{\pi}{N}\right)}$$

where  $\alpha = 12.8 \times 10^{18} N \text{ m}^{-3}$  is the interlayer coupling and  $\mu = 7.6 \times 10^{-7} \text{ kg m}^{-2}$  is the graphene mass per unit area [28].

Additionally, weak higher energy bands between  $1650$  and  $2300 \text{ cm}^{-1}$ , called "combination modes," show interaction between adjacent layers. These bands include the M band around  $1750 \text{ cm}^{-1}$  which only occurs for strongly coupled layers and is activated by scattering with two out-of-plane optical phonons [57]. Other phonon modes represent combinations between in-plane and out-of-plane modes, and their intensity reveals information on the coupling between atoms in neighboring layers [58] (Fig. 12).

When adjacent graphene layers do not perfectly align with each other, the result is twisted bilayer graphene that forms a Moiré pattern (Fig. 13). The electronic structure of twisted bilayer graphene is more complicated than that of the more well-known AB-stacked graphene, with a Fermi velocity slower than in the latter (and much slower than in single-layer graphene) and an electronic structure depending on the angle  $\theta$  between two layers [59].

The most prominent feature of Raman spectra in twisted bilayer graphene is a G-band enhancement that is dependent on the twist angle  $\theta$  and the laser energy. The G-band intensity will increase with increasing rotation angle until it reaches a peak at a critical angle  $\theta_c$  related to the excitation energy  $E_{\text{laser}}$  by the resonance condition [60]:

**Fig. 12** Representative Raman spectra showing combination modes (top) and their relative strength for different carbon systems, i.e. from bottom to top: Single layer graphene, bilayer graphene, few layer graphene, and highly oriented pyrolytic graphite (Reproduced with permission from [57])

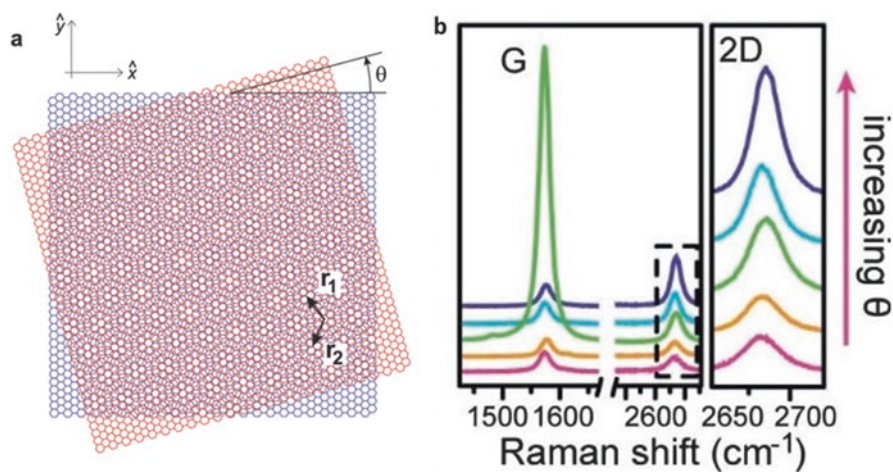
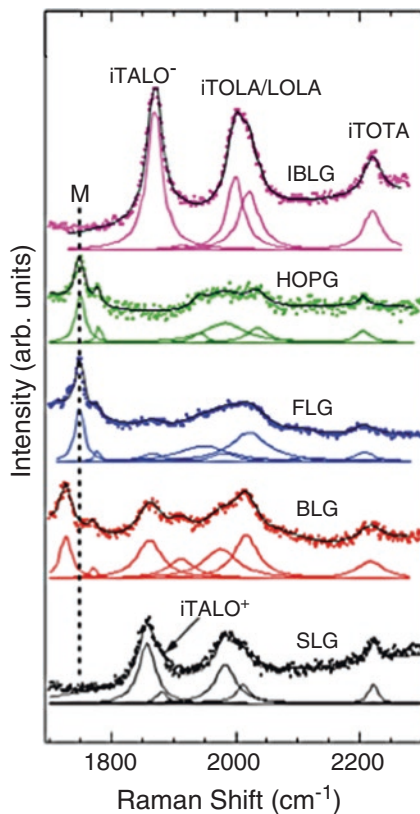


**Fig. 13** (a) Moiré pattern of graphene superlattice (Reproduced with permission from [61]) (b) G- and 2D-Raman features as a function of twisting angle (Reproduced with permission from [62])

$$\theta_c = (\Delta k/k) / (K) = 3aE_{\text{laser}} / \hbar v_f 4\pi$$

where  $a$  is the lattice parameter (2.46 Å) and  $v_f$  is the Fermi velocity of monolayer graphene (10<sup>6</sup>m/s).

Therefore, energy-tunable Raman spectroscopy can be used to determine the rotation angle [62].

The lattice mismatch is also reflected in the complex evolution in the 2D-band intensity, the occurrence of new rotation-induced R- and R'-bands [61], and the splitting of the C mode [63] which, as mentioned above, is often difficult to observe experimentally. Similarly, twisting is predicted to change graphene's optical absorption significantly [64], but aside from the contrast spectra that can be used to locate folded graphene layer, little quantitative work has been carried in this aspect.

When a third layer is added to an AB bilayer graphene, the result can be ABA (Bernal stacking) or ABC (rhombohedral stacking) configurations. The former retains semimetallic characteristics, while the latter resembles a semiconductor with tunable bandgap [65]. There are subtle differences between Raman spectra of the two stacking order, most notably a broader and more asymmetric 2D-band in ABC stacking. By fitting the 2D-band to Lorentzian function for each pixel, it is possible to map the regions with different stacking orders [66]. To rule out the effects of other factors like strain and disorder on the 2D bandwidth, the evaluation can be reinforced by supplementary information from G-band (narrower in ABC) and intermediate frequency modes (1690–2150 cm<sup>-1</sup>) [67]. Differences between the two types of stacking are also observed in infrared optical conductivity [68], but the measurement requires specialized equipment working in low temperature and provides lower resolution.

### 3.5 Defectiveness

Deviations from the perfect sp<sup>2</sup> lattice of graphene are the source of increased reactivity, changes in fundamental properties, and exciting applications. From the here employed simple description, however, they are considered defects, and several techniques exist to identify and quantify them.

Raman spectroscopy of defective graphene shows additional peaks compared to its pristine counterpart. As previously mentioned, the D-band is a Raman active phonon mode of A<sub>1g</sub> symmetry. However, this mode requires an external momentum to be excited. Since light does not have an appreciable momentum, the D-band can only be excited if momentum originates from another source. One such source is a discontinuity in the graphene lattice where some bonds to neighboring carbon atoms are broken. In such a situation, the defect reverses the direction of phonon propagation, and no overall momentum is required to excite the phonon.

Therefore, the D-band will only occur in the presence of defects, and its intensity will change with their concentration. Unfortunately, this dependence is not direct. Instead, the D-band intensity will first increase with defectiveness at low defect concentrations and then decrease with defectiveness at high defect concentrations.

One can understand this behavior by considering the origin of the D-band peak. At low defect concentration, the D-band reflects the concentration of defects because a large population of A1g phonons is available. However, as more and more defects occur, the D-band intensity becomes limited by the number of phonons that originate from the motion of undefected carbon hexagons. Thus, the D-band is an indicator of disorder at low defect concentration but becomes a measure of order for high defect concentrations.

Lucchese et al. [69] have quantitatively described the complete trend of the D-band intensity as normalized by the G-band intensity ( $I_D/I_G$ ), which follows the formula:

$$\frac{I_D}{I_G} = \frac{C_A (r_A^2 - r_S^2)}{r_A^2 - 2r_S^2} \left[ e^{-\frac{\pi r_S^2}{L_D^2}} - e^{-\pi(r_A^2 - r_S^2)/L_D^2} \right] + C_S \left[ 1 - e^{-\frac{\pi r_S^2}{L_D^2}} \right]$$

where  $L_D$  is the average size of a defect cluster. The parameters  $C_A$ ,  $C_S$ ,  $r_A$ , and  $r_S$  were obtained from a fit of experimental data and were found to be  $C_A=4.2$ ,  $C_S=0.87$ ,  $r_A=3\text{nm}$ , and  $r_S=1\text{nm}$ .

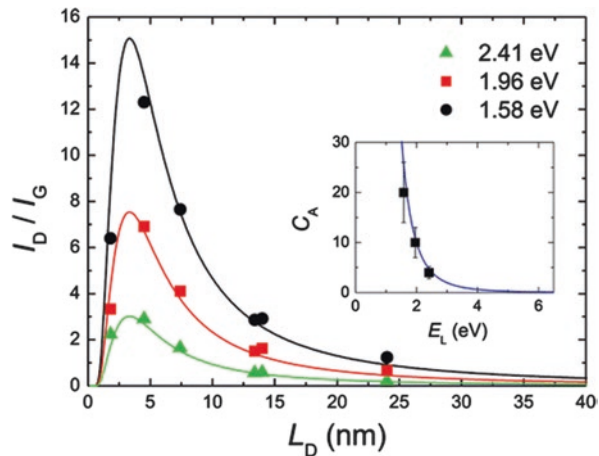
This description was further improved by extracting a quantitative relation between the  $I_D/I_G$  ratio and the defect concentration as a function of laser excitation wavelength  $\lambda_L$  in the region of low defect concentration [70] (see Fig. 14):

$$n_D (\text{cm}^{-2}) = \frac{1.8 \times 10^{22}}{\lambda_L^4} \left( \frac{I_D}{I_G} \right)$$

where  $\lambda_L$  is the wavelength in nm.

At low defect concentrations, an additional Raman band will occur. This feature is termed the D'-band and originates from an out-of-phase longitudinal displacement with small momentum [27]. While the D' intensity increases with defect den-

**Fig. 14** Raman  $I_D/I_G$  ratio for different laser wavelengths as a function of defect cluster size (Reproduced with permission from [70])



sity as well, it requires defects that produce little momentum to satisfy the momentum conservation upon interaction with light. Therefore, it is activated by defects with different properties than the D-band, and the comparison of D'- and D-band intensity allows inference to the types of defects (Fig. 15). It was observed that  $sp^3$ -type defects show a significantly higher  $I_{D'}/I_D$  ratio ( $\sim 13$ ) than vacancies ( $\sim 7$ ) and boundaries ( $\sim 3.5$ ) [71].

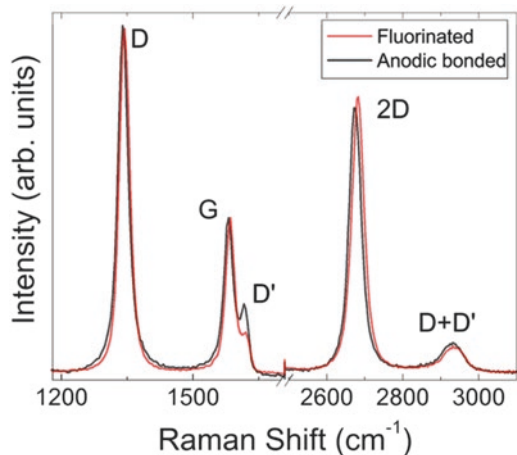
Raman spectroscopy can provide additional information on the type of boundary-type defects due to their relatively long-range order. It was found that armchair edges produce a lower D-band intensity than boundaries formed from zigzag edges [72]. Furthermore, a polarization perpendicular to an edge produces a low D-band intensity than parallel to an edge [72].

One further feature that is normally overlooked in the analysis of graphene's defectiveness is the width of the Raman feature. Intuitively, the increasing heterogeneity in the bonding character around defects can be thought to produce a variability in a bond resonance frequency. This simple explanation does not consider the shortened lifetime of electrons or different coupling strengths of electrons and phonons in the presence of defects, but in general a larger peak width is associated with a higher defectiveness [73].

### 3.5.1 Infrared Spectroscopy

In spite of the rise of other techniques like NMR, mass spectroscopy, and XRD in chemical analysis, FTIR is still favored as a low-cost, versatile tool to elucidate the chemical nature of defects. The identification of functional groups can be conveniently done by looking up the bands of FTIR spectra in well-established correlation tables. If a polarized light source is employed, one can determine the orientation of the functional group and then infer its local distribution [74]. More quantitative

**Fig. 15** Difference in D'-band intensity for two different types of defected graphene (Reproduced with permission from [71])



analysis will require a comprehensive understanding of graphene's IR spectra. As of now, attempts at such model using DFT calculations are still inadequate, generating uncertainty of tens of  $\text{cm}^{-1}$  at best [19].

### 3.5.2 Photoluminescence

As mentioned earlier, pristine graphene does not exhibit photoluminescence due to the fast non-radiative relaxation of photoexcited carriers. Therefore, the occurrence of photoluminescence is a strong indication for increased graphene defectiveness. Several mechanisms for PL emission have been identified [75].

Localized modifications of the graphene basal plane, for example, could result in domains that emit light due to changes in the band structure (Fig. 13). Their emission properties could be further modified through geometric confinement effects. Ab initio simulations suggest a clear trend between apparent bandgap and emissive domain size with 20 aromatic rings exhibiting a bandgap of approximately 2 eV and 100 aromatic rings having 0.5 eV [76].

Alternatively, interaction with chemical groups can produce luminescent centers. These types of defects were reported to produce the strongest emission [77]. Indeed, as demonstrated in Fig. 16, strong quenching of emission has been observed after processing was conducted that aimed at decreasing graphene's defect concentration [78]. Moreover, pH dependence of graphene's fluorescence suggests that these luminescent centers are quasi-molecular in nature [79].

## 3.6 Electronic Structure

### 3.6.1 Raman

Surprisingly, Raman spectroscopy has proven a very useful tool for the identification of the band structure of one of graphene's derivatives – carbon nanotubes [81]. A resonance effect was observed to dramatically increase the Raman intensity when the laser excitation source matches the electronic band structure. This effect was explained by the increased chance of transitioning between two electronic states in the band structure compared to the chance of transitioning to a mixture of states called "virtual" where momentum conservation has to be satisfied for each contributing state. Consequently, Raman scattering mainly originates from nanotubes with suitable band structure that allows access to the Raman response of different constituents of a distribution using different excitation [82].

The same resonance effect can be found in graphene, whose accessible electronic band structure does not span as large of an energy range as in semiconductors that possess large bandgaps.

The 2D-band is a second-order scattering effect where two phonons of equal magnitude and opposite propagation direction have to be created simultaneously to



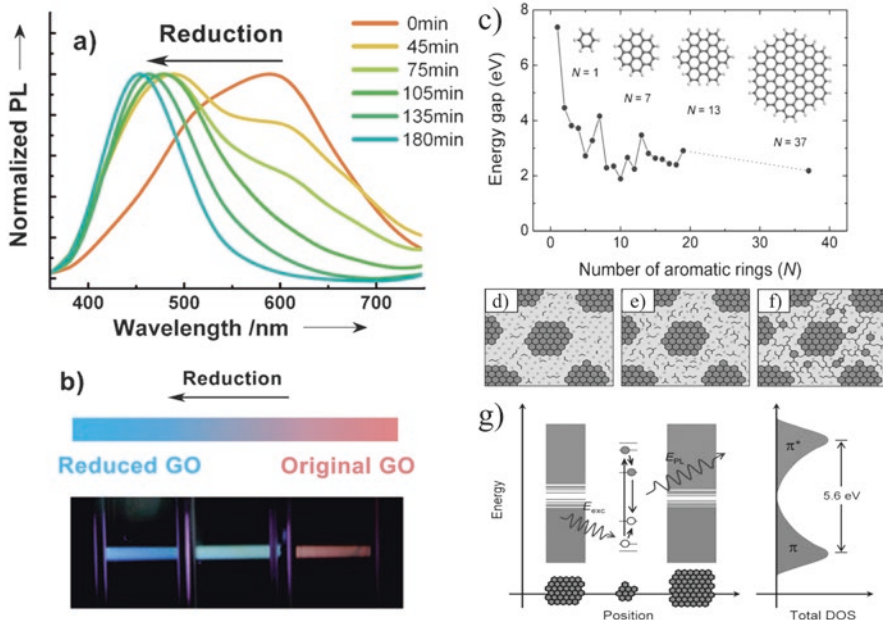


**Fig. 16** (a) Photoluminescence spectra of defected graphene after varying reduction time, (b) photograph of luminescence color for varying graphene oxide reduction. (Reproduced with permission from [80]) and (c) Simulated band gaps for graphenic regions with different dimensions, (d-f) schematic of distribution of defects and (g) corresponding energy diagrams (Reproduced with permission from [76])

satisfy the momentum conservation condition mentioned above. Such a coincidence of steps is commonly very unlikely, and second-order effects are significantly weaker than first-order Raman features. Instead, the 2D-band is usually the largest feature of the graphene Raman spectrum (Fig. 5). This difference is due to a double resonance effect between electronic and phononic interaction. Light excitation will generate electrons in real states that are usually scattered by a phonon to a virtual state. In the case of the 2D-band, however, two A1g phonons connect the initial state to two more real states. This resonance enhancement increases the scattering efficiency so much that even a second-order process is discernable. Consequently, graphene's band structure can be analyzed by the 2D-band intensity and position.

The 2D-band intensity is affected by the availability of electronic states that allow scattering. Therefore, the absence of a 2D-band is an indication of disruptions of graphene's band structure. Such changes can be produced by opening a significant bandgap due to confinement into nano-ribbons or quantum dots [83, 84]. Indeed Raman spectroscopy shows marked variations in their 2D-band intensity, and the polarization dependence can be employed to infer the geometry of the confinement [72].

Unfortunately, the 2D-band intensity is related only to scattering that occur far away from the equilibrium energy levels and is not indicative of more subtle changes to graphene's band structure, such as the opening of mini-gaps or the modification of the bands in multilayer graphene.

Here, the analysis of the position and components of the 2D-band can help. Since resonance can occur between different parts of the band structure, different phonon energies are required to connect those states. Consequently, changes in the phonon energy are an indication of different resonance conditions occurring. One important example of such a process is the change in graphene's thickness and stacking as discussed earlier.

Energy-tunable Raman scattering where the position of Raman features is characterized for different excitation energies can reveal changes to graphene's electronic structure with high sensitivity. For example, hydrogen absorption was found to produce changes in the electronic structure that cause an excitation energy dependent red shift of D- and 2D-bands [85].

Confinement effects for ultra-narrow graphene nanoribbons (<2 nm) not only produce new Raman features associated with the collective displacement of the crystal in a breathing-like pattern but also changes its energy dispersive behavior [86] (Fig. 17). The D-band of such nanoribbons was found to exhibit a different dispersion for low and high excitation energies neither of which agrees with the slope of infinite graphene. This behavior was related to the formation of bandgaps and the relaxation of momentum conservation rules [86].

### 3.6.2 Photoluminescence

Photoluminescence measurements are commonly employed to elucidate the electronic structure of molecules and nanostructures. In the case of graphene, photoluminescence is caused by defects (see above) as well as global modification of the graphene structure. For example, the oxidation of graphene will produce new localized states in its band structure. Due to momentum selection, decay from those states will proceed by emission rather than non-radiative relaxation as is the case for pristine graphene [87]. Theoretical calculations are aiming at quantifying the relation between oxygen concentration and the thus opened energy gap [88].

### 3.6.3 Infrared Spectroscopy

Infrared spectroscopy provides a direct way to identify small changes in the band structure since the excitation energy is low enough to probe even small energy gaps. A common method to identify such changes in graphene's band structure is by detecting deviations from the ideal model. Electrons in ideal graphene behave like massless Dirac fermions, and pristine graphene's IR response can be approximated by the Drude model, with its time constant corresponds to the infrared frequency range. In this range, the Drude conductivity [7] is related to free-carrier scattering rate  $\Gamma$  and Drude weight  $D$ :

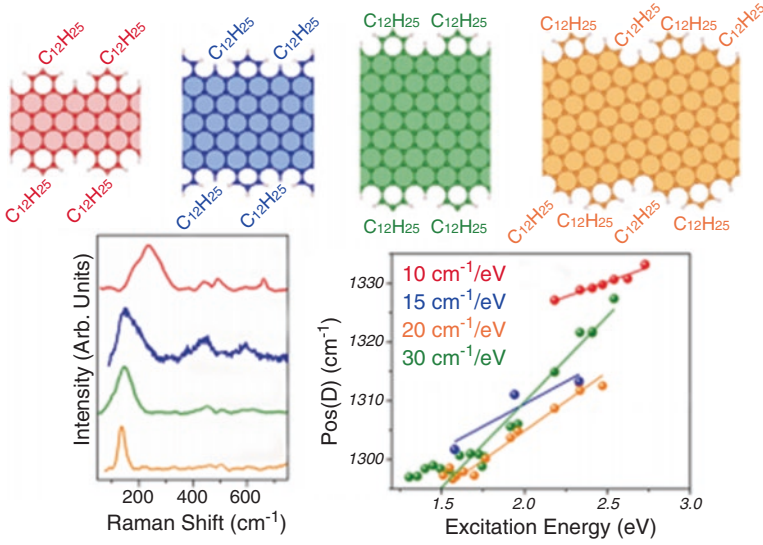


**Fig. 17** Raman spectra of atomically precise nanoribbons with different structures and their energy dispersion (Reproduced with permission from [86])

$$\sigma(\omega) = \frac{iD}{\pi(\omega + i\Gamma)}$$

The sheet conductivity can be calculated from the reduction in transmission:

$$1 - \frac{T}{T_0} = \frac{1}{|1 + Z_0\sigma(\omega)/(1 + n_s)|^2}$$

where  $Z_0 = (\mu_0/\epsilon_0)^{1/2}$  is vacuum impedance and  $n_s$  is the substrate's refractive index.

When analyzing the Drude conductivity of a bilayer graphene sample in a strong perpendicular electric field, characteristic peaks were found (Fig. 18), [89]. These peaks around 0.4 eV and 0.3 eV indicated transition across the bandgap or two states in the conduction band, respectively. A clear dependence on the strength of the applied perpendicular field confirmed the electric field-induced bandgap in bilayer graphene.

### 3.6.4 Ultrafast Optics

For an understanding of carrier relaxation processes that happen in transient time scales, time-resolved spectroscopy is needed. With optical excitation in the infrared range, two distinct decay times are observed in the differential transmission spectra:

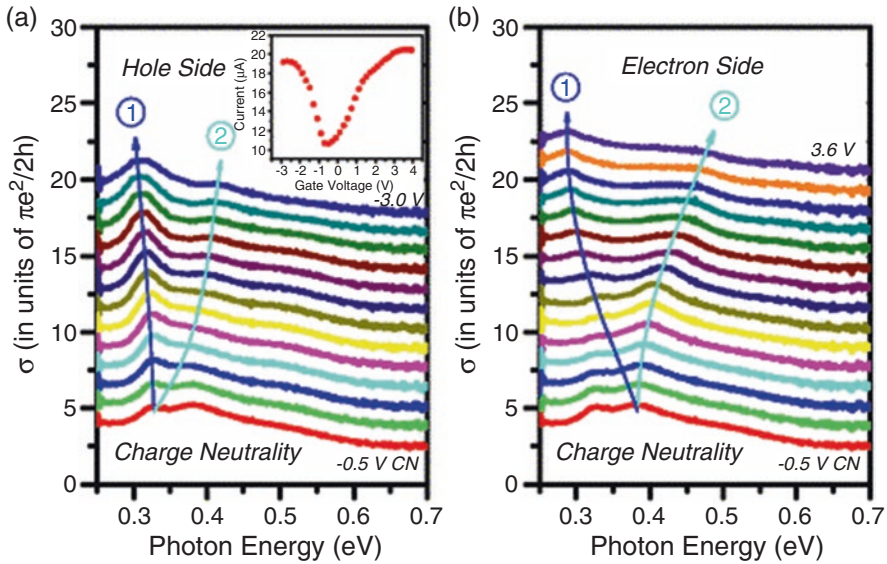


**Fig. 18** Extracted spectral sheet conductivity in bilayer graphene as a function of applied perpendicular field (Reproduced with permission from [89])

the first, at femtosecond scale, is characteristic of carrier thermalization, and the second, at sub-picosecond scale, is caused by carrier cooling, though the measured time constants are varied slightly between studies [90]. Ultrafast infrared spectroscopy has been used to extract Fermi level and other carrier properties in doped layers and deduce the effect of screening by these layers [91].

### 3.7 Distinction of Effects and Combination of Techniques

The presented examples show the power of optical spectroscopy but also reveal shortcomings. Several effects can simultaneously affect an optical process and cannot be distinguished from single measurements.

A common approach to clarifying the origin of changes to one optical process is the combination of several techniques on one sample. Since several techniques can provide complementary information on one property, clearer information on this aspect can be obtained.

For example, a combination of FTIR spectroscopy and Raman  $I_D/I_G$  ratio is routinely used to elucidate the quality of graphene [92]. Furthermore, graphene thickness can be assessed using optical contrast measurements which are relatively quick, while accurate calibration is only carried out on a few samples using Raman spectroscopy [93].

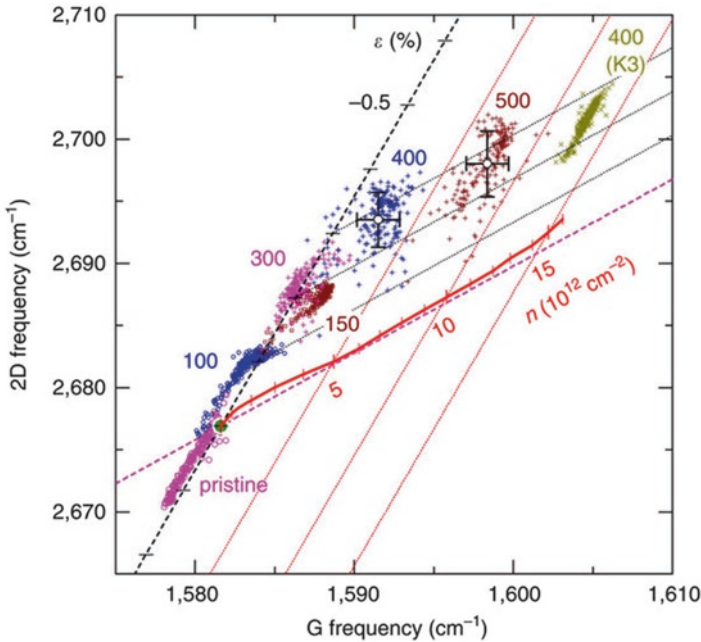


**Fig. 19** Scaling analysis of 2D-band and G-band position for graphene after different heat treatments (Reproduced with permission from [44])

A more sophisticated variant of combining multiple optical techniques is hyperspectral imaging. This approach allows investigation of several optical features at the same location. Combination of UV and visible spectroscopy techniques, for example, revealed the mapping of twist angle and chemical makeup in stacks of bilayer graphene and boron nitride monolayers with high spatial resolution [94].

Alternatively, combination of optical techniques at the same time can reveal subtle changes during processing. Simultaneous analysis of the Raman D/G ratio and the 2D-band position during UV exposure allowed investigation of the charge transfer in graphene due to oxidation while accounting for defect-induced property changes [95].

While the combination of spectroscopic techniques is a powerful approach, suitable experimental setups are not widely available. One elegant approach to extract meaningful data from one measurement is through scaling analysis. Lee et al. [44], for example, could distinguish the effects of temperature-induced strain and doping on graphene Raman spectra (Fig. 19). Since both processes affect the position of the G-band and the 2D-band in a different way, they analyzed the trends in position for a large number of Raman spectra. As explained earlier, the 2D-band position should 2.2 times as much as the G-band position for changes in strain, whereas it should only shift 0.7 times when the doping changes. It was found that the observed change was a mixture of both effects, and an eigenvalue decomposition was used to infer the contribution of strain and doping to each spectrum [96].

## 4 Conclusion

In this contribution, we attempted to give an overview of the wealth of complementary information about graphene that can be revealed by optical spectroscopy techniques. Atomic processes and subtle changes in properties provide clear signatures that allow destruction-free and facile characterization using widely available methods. The relatively simple structure and high quality of graphene makes this material ideally suitable to investigate the complex relation between geometry, electronic properties, and optical characteristics. Many lessons that were learned from graphene can be applied to the characterization of complex molecules. Moreover, compatibility of optical characterization techniques with high reaction temperature and pressures commonly observed in Suzuki reactions enables in situ measurements of bond formation [97]. Obtained Raman spectra show characteristic peaks that originate from similar phonon modes as in graphene, and analysis of their intensity can reveal the mechanism and reaction kinetics of chemical reactions [98].

While these results establish a similarity between complex molecules and graphene, we hope that these research areas can provide new impulses to each other in the future.

## References

1. S. Kotha, K. Lahiri, D. Kashinath, Recent applications of the Suzuki-Miyaura cross-coupling reaction in organic synthesis. *Tetrahedron* **58**, 9633–9695 (2002)
2. V. Georgakilas, M. Otyepka, A.B. Bourlinos, V. Chandra, N. Kim, K.C. Kemp, P. Hobza, R. Zboril, K.S. Kim, Functionalization of graphene: covalent and non-covalent approaches, derivatives and applications. *Chem. Rev.* **112**, 6156–6214 (2012)
3. R.R. Nair, P. Blake, A.N. Grigorenko, K.S. Novoselov, T.J. Booth, T. Stauber, N.M.R. Peres, A.K. Geim, Fine structure constant defines visual transparency of graphene. *Science* **320**, 1308–1308 (2008)
4. J.M. Dawlaty, S. Shivaraman, J. Strait, P. George, M. Chandrashekar, F. Rana, M.G. Spencer, D. Veksler, Y. Chen, Measurement of the optical absorption spectra of epitaxial graphene from terahertz to visible. *Appl. Phys. Lett.* **93**, 131905 (2008)
5. V.G. Kravets, A.N. Grigorenko, R.R. Nair, P. Blake, S. Anissimova, K.S. Novoselov, A.K. Geim, Spectroscopic ellipsometry of graphene and an exciton-shifted van Hove peak in absorption. *Phys. Rev. B* **81**, 155413 (2010)
6. Z. Shou-En, Y. Shengjun, G.C.A.M. Janssen, Optical transmittance of multilayer graphene. *EPL (Europhys Lett.)* **108**, 17007 (2014)
7. H. Yan, F. Xia, W. Zhu, M. Freitag, C. Dimitrakopoulos, A.A. Bol, G. Tulevski, P. Avouris, Infrared spectroscopy of wafer-scale graphene. *ACS Nano* **5**, 9854–9860 (2011)
8. K.F. Mak, F.H. da Jornada, K. He, J. Deslippe, N. Petrone, J. Hone, J. Shan, S.G. Louie, T.F. Heinz, Tuning many-body interactions in graphene: the effects of doping on excitons and carrier lifetimes. *Phys. Rev. Lett.* **112**, 207401 (2014)
9. A. Matković, M. Chhikara, M. Miličević, U. Ralević, B. Vasić, D. Jovanović, M.R. Belić, G. Bratina, R. Gajić, Influence of a gold substrate on the optical properties of graphene. *J. Appl. Phys.* **117**, 015305 (2015)

10. C. Lee, N. Leconte, J. Kim, D. Cho, I.-W. Lyo, E.J. Choi, Optical spectroscopy study on the effect of hydrogen adsorption on graphene. *Carbon* **103**, 109–114 (2016)
11. J.I. Paredes, S. Villar-Rodil, A. Martínez-Alonso, J.M.D. Tascón, Graphene oxide dispersions in organic solvents. *Langmuir* **24**, 10560–10564 (2008)
12. D. Li, M.B. Muller, S. Gilje, R.B. Kaner, G.G. Wallace, Processable aqueous dispersions of graphene nanosheets. *Nat Nano* **3**, 101–105 (2008)
13. J. Zhang, H. Yang, G. Shen, P. Cheng, J. Zhang, S. Guo, Reduction of graphene oxide vial-ascorbic acid. *Chem. Commun.* **46**, 1112–1114 (2010)
14. N. Kurantowicz, E. Sawosz, S. Jaworski, M. Kutwin, B. Strojny, M. Wierzbicki, J. Szeliga, A. Hotowy, L. Lipińska, R. Koziański, J. Jagiełło, A. Chwalibog, Interaction of graphene family materials with *Listeria monocytogenes* and *Salmonella enterica*. *Nanoscale Res. Lett.* **10**, 1–12 (2015)
15. P. Larkin, Chapter 3: Instrumentation and sampling methods, in *Infrared and Raman Spectroscopy*, (Elsevier, Oxford, 2011), pp. 27–54
16. H.-L. Guo, X.-F. Wang, Q.-Y. Qian, F.-B. Wang, X.-H. Xia, A green approach to the synthesis of graphene nanosheets. *ACS Nano* **3**, 2653–2659 (2009)
17. J. O'reilly, R. Mosher, Functional groups in carbon black by FTIR spectroscopy. *Carbon* **21**, 47–51 (1983)
18. C. Hontoria-Lucas, A.J. López-Peinado, J.D.D. López-González, M.L. Rojas-Cervantes, R.M. Martín-Aranda, Study of oxygen-containing groups in a series of graphite oxides: physical and chemical characterization. *Carbon* **33**, 1585–1592 (1995)
19. C. Zhang, D.M. Dabbs, L.-M. Liu, I.A. Aksay, R. Car, A. Selloni, Combined effects of functional groups, lattice defects, and edges in the infrared spectra of graphene oxide. *J. Phys. Chem. C* **119**, 18167–18176 (2015)
20. A. Kaniyoor, T.T. Baby, S. Ramaprabhu, Graphene synthesis via hydrogen induced low temperature exfoliation of graphite oxide. *J. Mater. Chem.* **20**, 8467–8469 (2010)
21. S. Eigler, C. Dotzer, A. Hirsch, M. Enzelberger, P. Müller, Formation and decomposition of CO<sub>2</sub> intercalated graphene oxide. *Chem. Mater.* **24**, 1276–1282 (2012)
22. X. Wang, W. Wang, Y. Liu, M. Ren, H. Xiao, X. Liu, Characterization of conformation and locations of C–F bonds in graphene derivative by polarized ATR-FTIR. *Anal. Chem.* **88**, 3926–3934 (2016)
23. Y. Si, E.T. Samulski, Synthesis of water soluble graphene. *Nano Lett.* **8**, 1679–1682 (2008)
24. S. Konwer, J.P. Gogoi, A. Kalita, S.K. Dolui, Synthesis of expanded graphite filled polyaniline composites and evaluation of their electrical and electrochemical properties. *J. Mater. Sci. Mater. Electron.* **22**, 1154–1161 (2011)
25. I. Milosevic, N. Kepcija, E. Dobardzic, M. Mohr, J. Maultzsch, C. Thomsen, M. Damnjanovic, Symmetry-based analysis of the electron-phonon interaction in graphene. *Physica Status Solidi B-Basic Solid State Phys.* **246**, 2606–2609 (2009)
26. S. Reich, C. Thomsen, Raman spectroscopy of graphite. *Philos. Trans. R. Soc. A Math. Phys. Eng. Sci.* **362**, 2271–2288 (2004)
27. J.F. Rodriguez-Nieva, E.B. Barros, R. Saito, M.S. Dresselhaus, Disorder-induced double resonant Raman process in graphene. *Phys. Rev. B* **90**, 235410 (2014)
28. A.C. Ferrari, D.M. Basko, Raman spectroscopy as a versatile tool for studying the properties of graphene. *Nat. Nanotechnol.* **8**, 235–246 (2013)
29. F. Schedin, E. Lidorikis, A. Lombardo, V.G. Kravets, A.K. Geim, A.N. Grigorenko, K.S. Novoselov, A.C. Ferrari, Surface-enhanced Raman spectroscopy of graphene. *ACS Nano* **4**, 5617–5626 (2010)
30. D.Y. Joh, L.H. Herman, S.-Y. Ju, J. Kinder, M.A. Segal, J.N. Johnson, G.K.L. Chan, J. Park, On-chip Rayleigh imaging and spectroscopy of carbon nanotubes. *Nano Lett.* **11**, 1–7 (2011)
31. C. Casiraghi, A. Hartschuh, E. Lidorikis, H. Qian, H. Harutyunyan, T. Gokus, K. Novoselov, A. Ferrari, Rayleigh imaging of graphene and graphene layers. *Nano Lett.* **7**, 2711–2717 (2007)
32. Z. Ni, H. Wang, J. Kasim, H. Fan, T. Yu, Y. Wu, Y. Feng, Z. Shen, Graphene thickness determination using reflection and contrast spectroscopy. *Nano Lett.* **7**, 2758–2763 (2007)

33. L. Gao, W. Ren, F. Li, H.-M. Cheng, Total color difference for rapid and accurate identification of graphene. *ACS Nano* **2**, 1625–1633 (2008)
34. J. Kim, L.J. Cote, F. Kim, J.X. Huang, Visualizing graphene based sheets by fluorescence quenching microscopy. *J. Am. Chem. Soc.* **132**, 260–267 (2010)
35. J.Z. Shang, L. Ma, J.W. Li, W. Ai, T. Yu, G.G. Gurzadyan, Femtosecond pump-probe spectroscopy of graphene oxide in water. *J. Phys. D-Appl. Phys.* **47**, 173106 (2014)
36. C. Schrieffer, S. Lochbrunner, E. Riedle, D.J. Nesbitt, Ultrasensitive ultraviolet-visible 20 fs absorption spectroscopy of low vapor pressure molecules in the gas phase. *Rev. Sci. Instrum.* **79**, 013107 (2008)
37. D.J. Renteria, L.D. Nika, A.A. Balandin, Graphene thermal properties: applications in thermal management and energy storage. *Appl. Sci.* **4**, 525–547 (2014)
38. N. Rotenberg, L. Kuipers, Mapping nanoscale light fields. *Nat. Photonics* **8**, 919–926 (2014)
39. A.A. Balandin, S. Ghosh, W. Bao, I. Calizo, D. Teweldebrhan, F. Miao, C.N. Lau, Superior thermal conductivity of single-layer graphene. *Nano Lett.* **8**, 902–907 (2008)
40. L. Lindsay, W. Li, J. Carrete, N. Mingo, D.A. Broido, T.L. Reinecke, Phonon thermal transport in strained and unstrained graphene from first principles. *Phys. Rev. B* **89**, 155426 (2014)
41. A. Das, S. Pisana, B. Chakraborty, S. Piscanec, S.K. Saha, U.V. Waghmare, K.S. Novoselov, H.R. Krishnamurthy, A.K. Geim, A.C. Ferrari, A.K. Sood, Monitoring dopants by Raman scattering in an electrochemically top-gated graphene transistor. *Nat. Nanotechnol.* **3**, 210–215 (2008)
42. T.G.A. Verhagen, K. Drogowska, M. Kalbac, J. Vejpravova, Temperature-induced strain and doping in monolayer and bilayer isotopically labeled graphene. *Phys. Rev. B* **92**, 125437 (2015)
43. S. Pisana, M. Lazzeri, C. Casiraghi, K.S. Novoselov, A.K. Geim, A.C. Ferrari, F. Mauri, Breakdown of the adiabatic Born-Oppenheimer approximation in graphene. *Nat. Mater.* **6**, 198–201 (2007)
44. J.E. Lee, G. Ahn, J. Shim, Y.S. Lee, S. Ryu, Optical separation of mechanical strain from charge doping in graphene. *Nat. Commun.* **3**, 1024 (2012)
45. M. Bruna, A.K. Ott, M. Ijas, D. Yoon, U. Sassi, A.C. Ferrari, Doping dependence of the Raman spectrum of defected graphene. *ACS Nano* **8**, 7432–7441 (2014)
46. Y.F. Hao, Y.Y. Wang, L. Wang, Z.H. Ni, Z.Q. Wang, R. Wang, C.K. Koo, Z.X. Shen, J.T.L. Thong, Probing layer number and stacking order of few-layer graphene by Raman spectroscopy. *Small* **6**, 195–200 (2010)
47. K.F. Mak, L. Ju, F. Wang, T.F. Heinz, Optical spectroscopy of graphene: from the far infrared to the ultraviolet. *Solid State Commun.* **152**, 1341–1349 (2012)
48. C.W. Luo, P.S. Tseng, H.J. Chen, K.H. Wu, L.J. Li, Dirac fermion relaxation and energy loss rate near the Fermi surface in monolayer and multilayer graphene. *Nanoscale* **6**, 8575–8578 (2014)
49. E. del Corro, L. Kavan, M. Kalbac, O. Frank, Strain assessment in graphene through the Raman 2D' mode. *J. Phys. Chem. C* **119**, 25651–25656 (2015)
50. N. Ferralis, Probing mechanical properties of graphene with Raman spectroscopy. *J. Mater. Sci.* **45**, 5135–5149 (2010)
51. T.M.G. Mohiuddin, A. Lombardo, R.R. Nair, A. Bonetti, G. Savini, R. Jalil, N. Bonini, D.M. Basko, C. Galiotis, N. Marzari, K.S. Novoselov, A.K. Geim, A.C. Ferrari, Uniaxial strain in graphene by Raman spectroscopy: G peak splitting, Gruneisen parameters, and sample orientation. *Phys. Rev. B* **79** (2009)
52. C.W. Wang, M.D. Frogley, G. Cinque, L.Q. Liu, A.H. Barber, Molecular force transfer mechanisms in graphene oxide paper evaluated using atomic force microscopy and in situ synchrotron micro FT-IR spectroscopy. *Nanoscale* **6**, 14404–14411 (2014)
53. B. Partoens, F.M. Peeters, From graphene to graphite: electronic structure around the K point. *Phys. Rev. B* **74**, 075404 (2006)
54. J.R. Kyle, A. Guvenç, W. Wang, M. Ghazinejad, J. Lin, S. Guo, C.S. Ozkan, M. Ozkan, Centimeter-scale high-resolution metrology of entire CVD-grown graphene sheets. *Small* **7**, 2599–2606 (2011)
55. W. Li, S. Moon, M. Wojcik, K. Xu, Direct optical visualization of graphene and its nanoscale defects on transparent substrates. *Nano Lett.* **16**, 5027–5031 (2016)



56. A.C. Ferrari, Raman spectroscopy of graphene and graphite: disorder, electron-phonon coupling, doping and nonadiabatic effects. *Solid State Commun.* **143**, 47–57 (2007)
57. R. Rao, R. Podila, R. Tsuchikawa, J. Katoch, D. Tishler, A.M. Rao, M. Ishigami, Effects of layer stacking on the combination Raman modes in graphene. *ACS Nano* **5**, 1594–1599 (2011)
58. C. Cong, T. Yu, R. Saito, G.F. Dresselhaus, M.S. Dresselhaus, Second-order overtone and combination Raman modes of graphene layers in the range of 1690–2150  $\text{cm}^{-1}$ . *ACS Nano* **5**, 1600–1605 (2011)
59. J. dos Santos, N.M.R. Peres, A.H. Castro, Graphene bilayer with a twist: electronic structure. *Phys. Rev. Lett.* **99**, 4 (2007)
60. K. Kim, S. Coh, L.Z. Tan, W. Regan, J.M. Yuk, E. Chatterjee, M. Crommie, M.L. Cohen, S.G. Louie, A. Zettl, Raman spectroscopy study of rotated double-layer graphene: misorientation-angle dependence of electronic structure. *Phys. Rev. Lett.* **108**, 246103 (2012)
61. V. Carozo, C.M. Almeida, E.H. Ferreira, L.G. Cançado, C.A. Achete, A. Jorio, Raman signature of graphene superlattices. *Nano Lett.* **11**, 4527–4534 (2011)
62. R.W. Havener, H. Zhuang, L. Brown, R.G. Hennig, J. Park, Angle-resolved Raman imaging of interlayer rotations and interactions in twisted bilayer graphene. *Nano Lett.* **12**, 3162–3167 (2012)
63. J.-B. Wu, X. Zhang, M. Ijäs, W.-P. Han, X.-F. Qiao, X.-L. Li, D.-S. Jiang, A.C. Ferrari, P.-H. Tan, Resonant Raman spectroscopy of twisted multilayer graphene. *Nat. Commun.* **5**, 5309 (2014)
64. C.J. Tabert, E.J. Nicol, Optical conductivity of twisted bilayer graphene. *Phys. Rev. B* **87**, 121402 (2013)
65. A.A. Avetisyan, B. Partoens, F.M. Peeters, Stacking order dependent electric field tuning of the band gap in graphene multilayers. *Phys. Rev. B* **81**, 115432 (2010)
66. C.H. Lui, Z. Li, Z. Chen, P.V. Klimov, L.E. Brus, T.F. Heinz, Imaging stacking order in few-layer graphene. *Nano Lett.* **11**, 164–169 (2011)
67. C. Cong, T. Yu, K. Sato, J. Shang, R. Saito, G.F. Dresselhaus, M.S. Dresselhaus, Raman characterization of ABA-and ABC-stacked trilayer graphene. *ACS Nano* **5**, 8760–8768 (2011)
68. K.F. Mak, J. Shan, T.F. Heinz, Electronic structure of few-layer graphene: experimental demonstration of strong dependence on stacking sequence. *Phys. Rev. Lett.* **104**, 176404 (2010)
69. M.M. Lucchese, F. Stavale, E.H.M. Ferreira, C. Vilani, M.V.O. Moutinho, R.B. Capaz, C.A. Achete, A. Jorio, Quantifying ion-induced defects and Raman relaxation length in graphene. *Carbon* **48**, 1592–1597 (2010)
70. L.G. Cancado, A. Jorio, E.H.M. Ferreira, F. Stavale, C.A. Achete, R.B. Capaz, M.V.O. Moutinho, A. Lombardo, T.S. Kulmala, A.C. Ferrari, Quantifying defects in graphene via Raman spectroscopy at different excitation energies. *Nano Lett.* **11**, 3190–3196 (2011)
71. A. Eckmann, A. Felten, A. Mishchenko, L. Britnell, R. Krupke, K.S. Novoselov, C. Casiraghi, Probing the nature of defects in graphene by Raman spectroscopy. *Nano Lett.* **12**, 3925–3930 (2012)
72. R. Beams, L.G. Cancado, L. Novotny, Raman characterization of defects and dopants in graphene. *J. Phys. Condens. Matter* **27**, 083002 (2015)
73. A.A.K. King, B.R. Davies, N. Noorbehesht, P. Newman, T.L. Church, A.T. Harris, J.M. Razal, A.I. Minett, A new Raman metric for the characterisation of graphene oxide and its derivatives. *Sci. Report.* **6**, 19491 (2016)
74. B. Li, T. He, Z. Wang, Z. Cheng, Y. Liu, T. Chen, W. Lai, X. Wang, X. Liu, Chemical reactivity of C-F bonds attached to graphene with diamines depending on their nature and location. *Phys. Chem. Chem. Phys.* **18**, 17495–17505 (2016)
75. Z. Gan, H. Xu, Y. Hao, Mechanism for excitation-dependent photoluminescence from graphene quantum dots and other graphene oxide derivatives: consensus, debates and challenges. *Nanoscale* **8**, 7794–7807 (2016)
76. G. Eda, Y.Y. Lin, C. Mattevi, H. Yamaguchi, H.A. Chen, I.S. Chen, C.W. Chen, M. Chhowalla, Blue photoluminescence from chemically derived graphene oxide. *Adv. Mater.* **22**, 505–509 (2010)

77. L. Cao, M.J. Meziani, S. Sahu, Y.P. Sun, Photoluminescence properties of graphene versus other carbon nanomaterials. *Acc. Chem. Res.* **46**, 171–180 (2013)
78. S.K. Pal, Versatile photoluminescence from graphene and its derivatives. *Carbon* **88**, 86–112 (2015)
79. C. Galande, A.D. Mohite, A.V. Naumov, W. Gao, L.J. Ci, A. Ajayan, H. Gao, A. Srivastava, R.B. Weisman, P.M. Ajayan, Quasi-molecular fluorescence from graphene oxide. *Sci. Report.* **1** (2011)
80. C.T. Chien, S.S. Li, W.J. Lai, Y.C. Yeh, H.A. Chen, I.S. Chen, L.C. Chen, K.H. Chen, T. Nemoto, S. Isoda, M.W. Chen, T. Fujita, G. Eda, H. Yamaguchi, M. Chhowalla, C.W. Chen, Tunable photoluminescence from graphene oxide. *Angew. Chem.Int. Ed.* **51**, 6662–6666 (2012)
81. M.S. Dresselhaus, A. Jorio, M. Hofmann, G. Dresselhaus, R. Saito, Perspectives on carbon nanotubes and graphene Raman spectroscopy. *Nano Lett.* **10**, 751–758 (2010)
82. J. Maultzsch, H. Telg, S. Reich, C. Thomsen, Radial breathing mode of single-walled carbon nanotubes: optical transition energies and chiral-index assignment. *Phys. Rev. B* **72**, 205438 (2005)
83. S. Kim, D. Hee Shin, C.O. Kim, S. Seok Kang, S. Sin Joo, S.-H. Choi, S. Won Hwang, C. Sone, Size-dependence of Raman scattering from graphene quantum dots: interplay between shape and thickness. *Appl. Phys. Lett.* **102**, 053108 (2013)
84. S. Ryu, J. Maultzsch, M.Y. Han, P. Kim, L.E. Brus, Raman spectroscopy of lithographically patterned graphene nanoribbons. *ACS Nano* **5**, 4123–4130 (2011)
85. Z.Q. Luo, T. Yu, Z.H. Ni, S.H. Lim, H.L. Hu, J.Z. Shang, L. Liu, Z.X. Shen, J.Y. Lin, Electronic structures and structural evolution of hydrogenated graphene probed by Raman spectroscopy. *J. Phys. Chem. C* **115**, 1422–1427 (2011)
86. I.A. Verzhbitskiy, M. De Corato, A. Ruini, E. Molinari, A. Narita, Y. Hu, M.G. Schwab, M. Bruna, D. Yoon, S. Milana, X. Feng, K. Mullen, A.C. Ferrari, C. Casiraghi, D. Prezzi, Raman fingerprints of atomically precise graphene nanoribbons. *Nano Lett.* **16**, 3442–3447 (2016)
87. J.Z. Shang, L. Ma, J.W. Li, W. Ai, T. Yu, G.G. Gurzadyan, The origin of fluorescence from graphene oxide. *Sci. Report.* **2**, 792 (2012)
88. J.A. Yan, M.Y. Chou, Oxidation functional groups on graphene: structural and electronic properties. *Phys. Rev. B* **82** (2010)
89. K.F. Mak, C.H. Lui, J. Shan, T.F. Heinz, Observation of an electric-field-induced band gap in bilayer graphene by infrared spectroscopy. *Phys. Rev. Lett.* **102**, 256405 (2009)
90. R.R. Hartmann, J. Kono, M.E. Portnoi, Terahertz science and technology of carbon nanomaterials. *Nanotechnology* **25**, 322001 (2014)
91. D. Sun, C. Divin, C. Berger, W.A. de Heer, P.N. First, T.B. Norris, Spectroscopic measurement of interlayer screening in multilayer epitaxial graphene. *Phys. Rev. Lett.* **104**, 136802 (2010)
92. G.X. Wang, B. Wang, J. Park, Y. Wang, B. Sun, J. Yao, Highly efficient and large-scale synthesis of graphene by electrolytic exfoliation. *Carbon* **47**, 3242–3246 (2009)
93. D.R. Lenski, M.S. Fuhrer, Raman and optical characterization of multilayer turbostratic graphene grown via chemical vapor deposition. *J. Appl. Phys.* **110**, 013720–013720-4 (2011)
94. R.W. Havener, C.J. Kim, L. Brown, J.W. Kevek, J.D. Sleppy, P.L. McEuen, J. Park, Hyperspectral imaging of structure and composition in atomically thin heterostructures. *Nano Lett.* **13**, 3942–3946 (2013)
95. M. Hofmann, Y.P. Hsieh, K.W. Chang, H.G. Tsai, T.T. Chen, Dopant morphology as the factor limiting graphene conductivity. *Sci. Report.* **5**, 17393 (2015)
96. A. Bosca, J. Pedros, J. Martinez, T. Palacios, F. Calle, Automatic graphene transfer system for improved material quality and efficiency. *Sci. Report.* **6**, 21676 (2016)
97. N.E. Leadbeater, R.J. Smith, Real-time monitoring of microwave-promoted Suzuki coupling reactions using in situ Raman spectroscopy. *Org. Lett.* **8**, 4588–4591 (2006)
98. J.R. Schmink, J.L. Holcomb, N.E. Leadbeater, Use of Raman spectroscopy as an in situ tool to obtain kinetic data for organic transformations. *Chem. Eur. J.* **14**, 9943–9950 (2008)

# Submerged Liquid Plasma for the Formation of Nanostructured Carbon

Masahiro Yoshimura and Jaganathan Senthilnathan

## 1 Introduction

Plasma is one of the main constituents of the universe, though the existence of natural plasma is not so common in the troposphere of the Earth's surface [26]. Plasmas generated from the ionization of neutral gases contain an electron, positive and neutral ions, excited atoms or molecules, radicals, ultraviolet (UV) light, and a strong electric field [14]. Irving Langmuir first introduced the term *plasma* in 1928 [54]. In general, plasma is classified as thermal or non-thermal based on the temperature generated in the system. In thermal plasma, electrons and the ions or heavy particles are in thermal equilibrium (gas molecules are completely ionized;  $T_e \approx T_{ion}$ ) at the same temperature [26]. However, the plasma in these discharges has always been hot or thermal. Non-thermal plasmas can be generated either at low pressures or low power levels, and/or in different kinds of pulsed discharge systems [25, 26]. In non-thermal plasma, electron temperatures are much higher than those of ions or heavy particles, and only a marginal portion of the gas molecules are ionized ( $T_e \gg T_{ion}$ ) [24]. Under such conditions, the electron temperature is much higher than the ion temperature. The temperature in plasma is determined by the average energies of the plasma particles and their relevant degrees of freedom, such as translational, rotational, and vibrational. Furthermore, plasma can exhibit a range of temperatures depending on the nature of the composition and conditions used.

The temperature generated during a plasma process is measured in terms of the electron volt (eV) or Kelvin (K). Cold (non-thermal) plasmas in the gas phase

---

M. Yoshimura (✉)

Promotion Centre for Global Materials Research (PCGMR), Department of Material Science and Engineering, National Cheng Kung University, Tainan, Taiwan

Tokyo Institute of Technology, Tokyo, Japan

e-mail: [yoshimur@mail.ncku.edu.tw](mailto:yoshimur@mail.ncku.edu.tw); [yoshimura@mssl.titech.ac.jp](mailto:yoshimura@mssl.titech.ac.jp)

J. Senthilnathan

Environmental and Water Resources Engineering Division, Department of Civil Engineering, Indian Institute of Technology Madras, Chennai, Tamil Nadu, India

e-mail: [jsn@iitm.ac.in](mailto:jsn@iitm.ac.in)

© Springer International Publishing AG 2017

S. Kaneko et al. (eds.), *Carbon-related Materials in Recognition of Nobel Lectures by Prof. Akira Suzuki in ICCE*, DOI 10.1007/978-3-319-61651-3\_3

require a macroscopic volume to provide enough mean free paths for electron multiplication. Microwave plasma is a type of plasma with high-frequency electromagnetic radiation and capable of exciting electrode-less gas discharges with high plasma density [22, 123]. The application areas are quite different for thermal (more powerful) and non-thermal plasmas (highly selective) [25, 26]. Extensive studies have been carried out on the generation of different forms of cold or non-thermal plasma in liquids by liquid bubbles and/or small vapor channels [14]. Plasma discharges in water have recently become a promising technology for a wide range of applications. Different approaches such as direct current power sources, high-frequency power sources, pulsed high-voltage power supplies, and other methods have been developed to generate micro-plasmas in liquid [63]. The liquid phase micro-plasma can be achieved in two different ways: (1) plasma is formed in the gas phase above the solution surface and (2) plasma is formed inside the aqueous and non-aqueous solution [63].

Discharges of plasma in organic liquids are considered as partial discharges because of the low conductive nature of non-polar solvents when compared to gases or aqueous solutions. Furthermore, denser organic liquid media could create nanoscale transient sparks and streamer corona discharges, which are typically initiated by the rapid application of a high electric field or potential between macroscopic electrodes [106]. Whereas in water, fast-moving electrons accelerated by the applied high electric potential at the electrode interface dissociate or split the water molecule and produce  $\cdot\text{H}$ ,  $\cdot\text{OH}$ , and  $\cdot\text{O}$  radicals, such a dissociation or radical generation is not possible in organic solvents [11, 12, 65]. The short-lived radicals generated in the water by plasma process have higher oxidative potentials.

Radicals generated in plasma processes can be used for various fields of application that include dielectric insulation material synthesis, disinfection, medicine, analytical tools, metal ions reduction, wastewater treatment, hydrogen peroxide generation, liquid analysis, hydrogen production, nanomaterial synthesis, formation of carbon nanomaterials, and tissue ablation [10–12, 15, 17–19, 21, 28, 36, 44, 47, 51, 55, 56, 65, 66, 69, 70, 72, 74, 108, 114]. Furthermore, plasma reactions in liquids have been used for microelectronic applications such as etching, ashing, deposition, oxidation, sputtering, polymerization, and implantation [65]. Radicals generated in the plasma condition used for the different applications are given in Fig. 1.

## 2 Formation of Nanostructured Carbon in Aqueous and Nonaqueous Solutions

The formation of functionalized graphene is complicated by the high temperature and toxic chemicals used in microwave plasma deposition, thermal annealing, chemical vapor deposition, gas plasma or glow discharge plasma deposition, segregation growth, solvothermal synthesis, arc discharge, and thermal exfoliation [97–99, 101]. A comparison of different temperatures involved in the formation of nanostructured carbon by the above techniques with submerged liquid plasma

**Fig. 1** Submerged liquid plasma for various fields of application

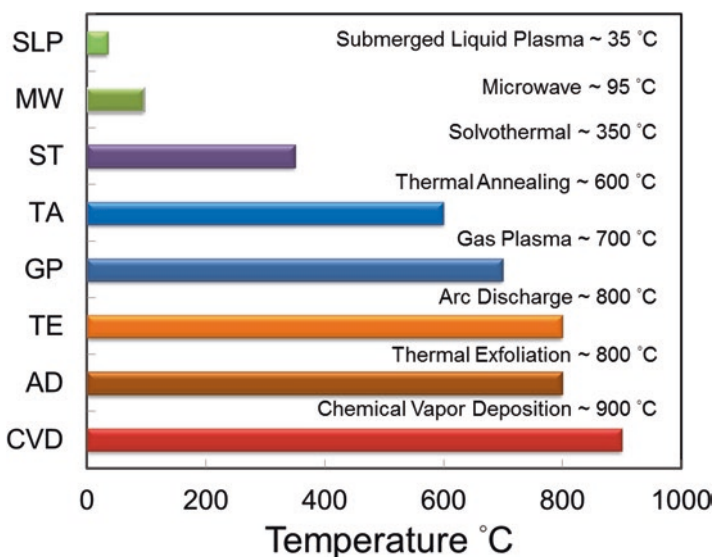
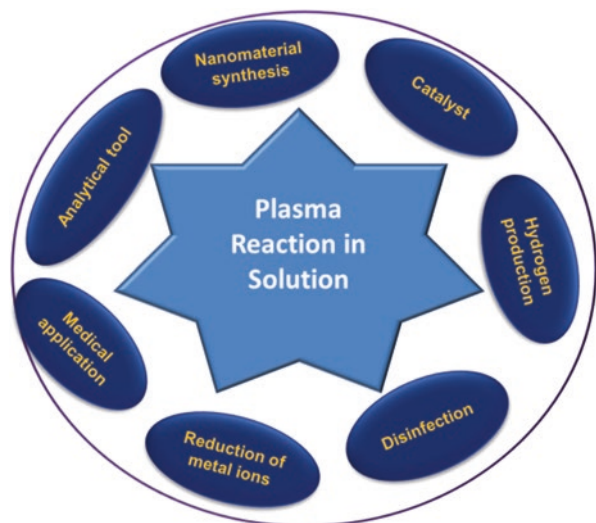


**Fig. 2** Comparison of high-temperature synthesis methods of nitrogen-doped graphene (Reproduced from Senthilnathan et al. [98], with permission from The Royal Society of Chemistry)

processes is shown in Fig. 2. Formation of nanocarbon from gaseous organic precursors in glow discharge processes has been widely studied by various research groups. However, the glow discharge carbonization/polymerizations with gaseous precursor have major shortcomings such as (1) high operation cost, (2) complexity of the process, (3) lesser contact time, which reduces the complete carbonization or polymerization, (4) material loss, and (5) uncertainty and inconsistency in the end

product [97–99, 101, 102]. Different forms of nanocarbon materials have been synthesized using submerged liquid plasma in aqueous and non-aqueous solution with graphite electrode and these are shown in Table 1.

Recently, pulse and arc discharge plasmas in organic and aqueous liquids have earned considerable attention because of their simplicity of use in the formation of nanostructured carbon and hybrids structure [3, 9, 40, 53, 61, 87, 93, 111, 113]. Development of plasmas in liquid has been accepted as a capable suitable technology to synthesize carbon materials due to because of its intrinsic merits, such as simple implementation, low capital cost, and potential for high yield [40, 93–95, 112, 119]. Hsin et al. [32] reported that the low-temperature and solution-phase production of carbon CNTs in water [32]. Sano et al. [95] reported the large-scale formation of carbon nanooxions by applying low discharge currents (30 A) using a graphite electrode submerged in deionized water [95]. In addition, differences in sizes of reactors, electrode materials, and aqueous or organic solvents have also been extensively studied [6–8].

Use of plasma processes for the formation of nanocarbon in aqueous and non-aqueous solutions with different electrodes and electrolytes are listed in Table 1. Microwave plasma discharges in non-aqueous liquids such as *n*-dodecane, benzene, cooking oil, lubricating oil, waste oils, water with trichloroethylene, hexafluoroethylene, and *n*-heptane have been used for the formation of nanocarbon [41, 42, 81–84, 103, 104]. Nomura and Toyota [81] generated microwave plasma in *n*-dodecane by applying ultrasonic (19 kHz) and microwaves (2.5 GHz) for the formation of amorphous/graphitic carbon. In addition, MWCNTs, carbon nanooxions, SWNHs, and carbon nanoparticles have been successfully fabricated by this technology [94, 95, 112, 119]. The decomposition of organic solvents such as toluene, ethanol, and butanol has been used for syntheses of nanostructured carbon. Yoshimura and his research group first reported the formation of diamond-like carbon and the direct patterning of nanocarbon on silica wafer by a submerged liquid plasma process [111, 113]. Direct patterning of diamond-like carbon films on silicon substrate was performed using a thin tungsten anode under high electrical potential in ethanol [111, 113]. The uniqueness of this study was that the carbon film was deposited on the surface of the Si wafer. This method has the potential to enable the production of adhesives with high thermal stability, chemical stability, and sufficient strength to adhere hard particles such as diamond particles onto conductive surfaces (Fig. 3).

## ***2.1 Formation of Unconventional Polymers or Oligomers in Submerged Liquid Plasma Processes***

Gas phase plasma polymerization of various organic compounds, including naphthalene, styrene, benzonitrile, fluorocarbon, acrylonitrile, ethylene, 1,2-dicyanoethylene, and tetracyanoethylene, have been extensively studied by various research groups [31, 38, 39, 78, 86]. Recently, Masaru Hori and his research groups have extensively studied gas plasma for the formation of different

**Table 1** Plasma process for the formation of nanocarbon in aqueous and non-aqueous solution

Sl. No	Plasma	Source	Precursor solution	Nanocarbon	References
1	Pulse plasma	Graphite	Ethanol	Diamond-like carbon	Wang and Yoshimura [111]
2	Pulse plasma	Graphite	Ethanol	Nanocarbon	Watanabe et al. [113]
3	Pulse plasma	Graphene oxide	Acetonitrile	Nitrogen functionalized graphene oxide	Senthilnathan et al. [97–99, 101]
4	Pulse plasma	Graphite	Acetonitrile	Nitrogen polymer	Senthilnathan et al. [102]
5	Arc discharge	Carbon electrode	Water	Carbon nanotube	Biró et al. [9]
6	Arc discharge	Graphite	Toluene	Polycyclic aromatic hydrocarbon	Beck et al. [5]
7	Pulse plasma	Graphite	Acetonitrile	Nanoclay/graphene hybrids	Senthilnathan et al. [97–99, 101]
8	Arc discharge	Graphite	Water	Carbon onion	Sano et al. [95]
9	Arc discharge	Graphite	Water/Liquid nitrogen	Carbon nanotube/carbon onion	Alexandrou et al. [2]
10	Pulse plasma	Graphite	Acetonitrile	Nitrogen functionalized graphene	Senthilnathan et al. [97–99, 101]
11	Arc discharge	Graphite	Water	Carbon onion/fullerene	Sano et al. [94]
12	Arc discharge	Graphite	Toluene	Carbon nanotube	Okada et al. [85]
13	Arc discharge	Graphite	Water	Carbon onion/carbon nanotube	Lange et al. [53]
14	Pulse plasma	Graphene oxide	Acetonitrile	Au/graphene Hybrids	Senthilnathan et al. [97–99, 101]
15	Arc/Laser ablation	Graphite	Liquid N <sub>2</sub> /Water	Graphene/carbon nanotube	Scuderi et al. [96]
16	Electric arc	Graphite	Water	Carbon nanotube	Zhu et al. [126]
17	Pulsed discharge	Graphite	Ethanol/Butanol	Graphene	[29]
19	Pulsed discharge	Graphite	Ethanol	Graphene	[73]
20	Arc discharge	Graphite	Ethanol/alkane/aromatics	Graphene	Muthakam et al. [77]
21	Arc discharge	Graphite	Water	Graphene	[92]

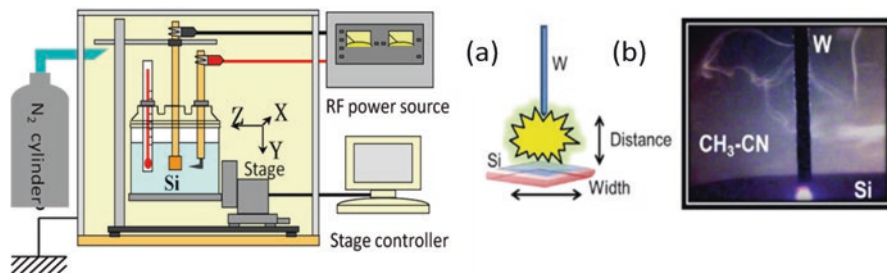


**Fig. 3** (a) Direct patterning of diamond-like carbon on Si wafer. (b) Image of plasma torch generated in acetonitrile solvent (Reproduced from Senthilnathan et al. [102], with permission from the Nature Publishing Group)

nanomaterials, including graphene, carbon nanowalls, and flower-like nanographene, etc. [15, 29, 103, 104]).

Formation of organic polymers from organic compounds in plasma conditions is an emerging soft solution technique at ambient conditions [111, 113]. Formation of unconventional polymer by a submerged liquid plasma process poses great advantages over conventional polymers available on the market. In addition, the properties of polymers produced by plasma conditions differ greatly from those of conventional polymers [102]. An unconventional polymer produced by a plasma process does not contain regular or repeating units and is enriched with radicalized functional groups [122]. Furthermore, submerged liquid plasma provides a number of advantages over other techniques, which includes (1) periodic collection of samples to give clear information about the mechanism and products, (2) reaction at ambient conditions, (3) simple reaction set-up, (4) simple procedure, and (5) lower operating cost. Formation of highly functionalized and non-oriented polymers or oligomers in a soft solution process is one of the most attractive materials for various fields of applications [102, 111]. The reaction of plasma in submerged conditions in an organic solution is not well understood because of the complexity of the role played by the organic compounds and their functional groups [58]. At the interface of plasma and organic solvent, polymerizations are induced by a radical approach rather than an ionic approach [39].

Yoshimura and his research groups developed carbon and polymerized products from different organic solvents [102, 111]. In this study, ethanol was used as the carbon precursor for the formation of conventional polymer in submerged liquid plasma conditions. In addition, it was found that the W needle and Si electrodes distance also plays a significant role in the formation of nanostructured carbons. Hence, W needle and Si electrodes distance was adjusted to get the maximum plasma width (Fig. 3b). When the W needle touched the silicon electrode, there was no plasma observed in the solution. Under plasma conditions, organic solvents such as methanol, ethanol [13, 111, 113], and propanol form less stable radical species and polymerization is not favored in this condition (C—C, C—H, C—O, and O—H) (Fig. 4). However, unsaturated organic solvents or compounds, which have high



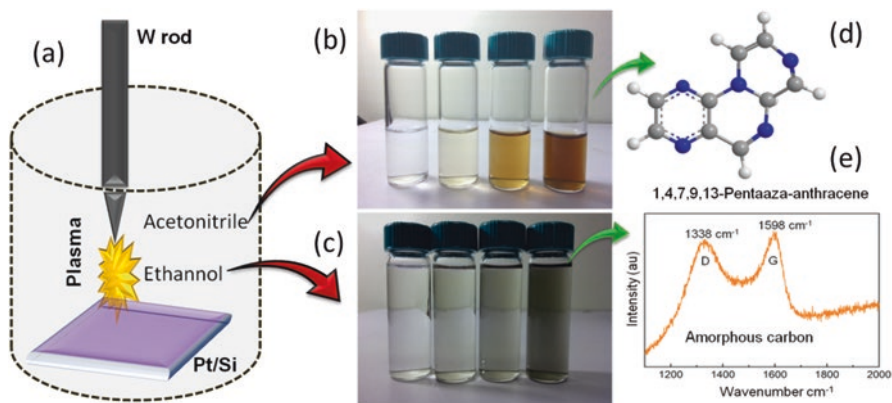


**Fig. 4** (a–c) Formation of nanocarbon and polymeric materials from ethanol and acetonitrile. (d) Structure of nitrogen polymer obtained. (e) Raman spectrum of nanocarbon synthesized from ethanol solvent

bond energy (e.g., C=C, C=N, and C≡N) form stable free radical monomers and initiate polymerization reactions [39, 62, 102, 121]. The nature of the unconventional polymers formed at the end of the plasma reaction purely depends on the nature of plasma formed and the chemical structure and stability of the precursor monomer used [50]. The development of plasma polymers or oligomers in submerged liquid plasma condition can be the potential alternative for the polymers or oligomers currently used for light harvesting, solar cell, and light emitting diode applications.

## 2.2 Formation of Functionalized Graphene in Submerged Liquid Plasma Processes

### 2.2.1 Direct Insertion of Nitrogen Functional Group in $sp^2$ Carbon Domain of Graphene

Formation of graphene/few layer graphene to produce a stable suspension in aqueous or organic solvents is one of the important concerns for the fabrication of various graphene-based devices, such as electrode material, capacitor, hydrogen storage, bipolar plates in fuel cells, and solar cell applications [59, 105]. Large scale synthesis of single or few layers graphene is being constrained by strong van der Waals force of attraction between the layers ( $\pi$ - $\pi$  interactions) and causes an irreversible agglomeration in most of the aqueous and organic solvents [27]. Functionalization of graphene is an important route to increase its stability and dispersibility [115]. GO and r-GO are important functionalized products of graphene. However, high content of  $sp^3$  carbon restricts electron mobility and leads to poor electrical properties [115]. Similarly, chemically modified graphene/organic moieties are more

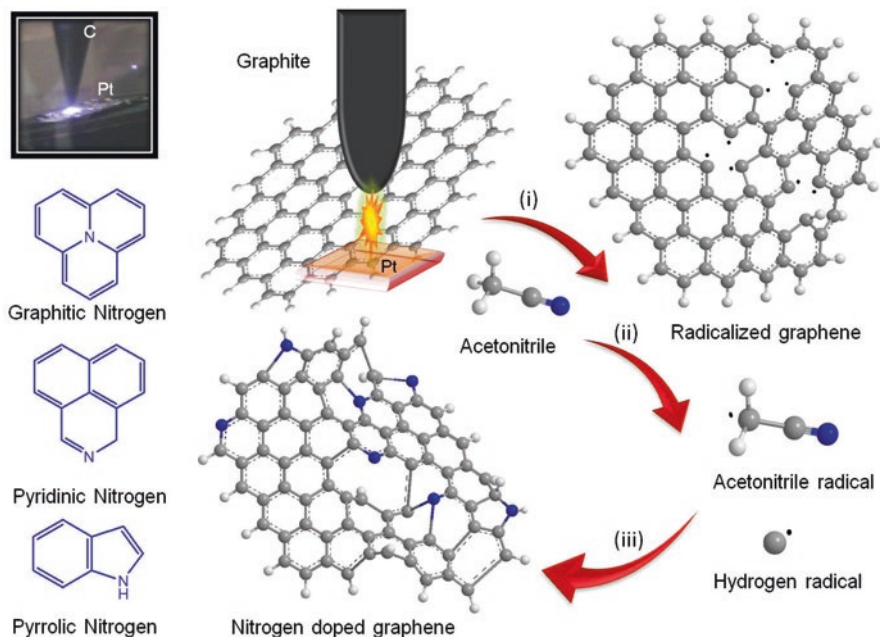


**Fig. 5** Proposed mechanism for the formation of nitrogen-functionalized graphene in submerged liquid plasma process (i) micro plasma discharge facilitates the exfoliation of radicalized graphene layer in the acetonitrile solution (ii) electron generated in micro plasma discharge collision with acetonitrile and forms nascent hydrogen and acetonitrile radicals (iii) formation of nitrogen functionalized graphene (Reproduced from Senthilnathan et al. [98], with permission from The Royal Society of Chemistry)

susceptible to reacting with external impurities and their long-term association with graphene is thus highly questionable. Furthermore, organic polymer/graphene composites have low electrical conductivity and poor cycling stability, limiting their practical applications. The most important aspect of graphene functionalization is to retain its aromaticity and enhance its dispersibility in solvents. To overcome any difficulties, surface functionalization of graphene has been extensively carried out with organic moieties such as pyrrole, porphyrin, polyaniline, conjugative polymers, nafion, and *o*-phenylenediamine [23, 52, 64, 68, 116, 120]. The chemically adsorbed or covalently bonded organic moieties are more susceptible to reacting with external impurities and their long-term stability with graphene is thus highly questionable. Recently, Yoshimura and his research groups have successfully demonstrated the direct insertion of highly dispersive pyridinic and pyrrolic functionalized graphene by a submerged liquid plasma process at ambient conditions [97–99, 101]. A schematic representation of micro-plasma discharge, graphene and acetonitrile radical reaction, and formation of nitrogen-functionalized graphene is given in Fig. 5. The micro-plasma discharge from the graphite electrode forms radicalized graphene sheets, which are instantly exfoliated into the acetonitrile solvent.

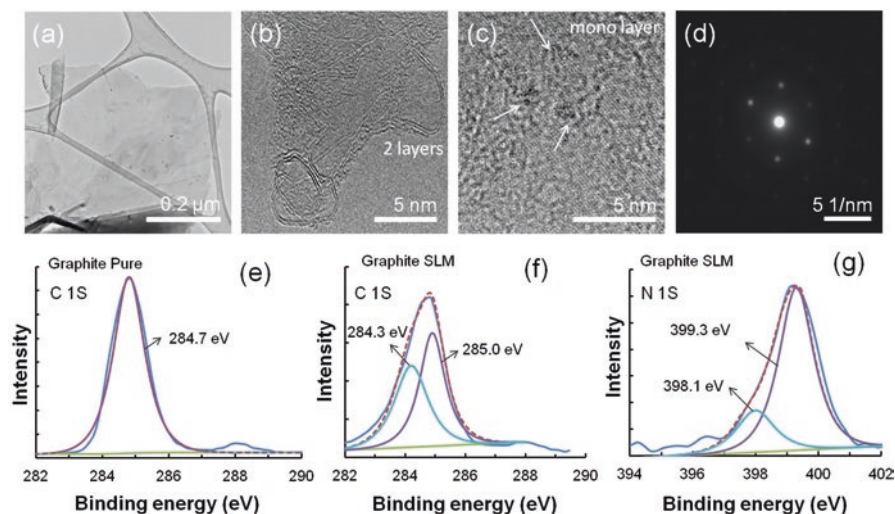


**Fig. 6** (a–c) HR-TEM images of nitrogen functionalized graphene and XPS spectra of (d) SAED pattern of nitrogen functionalized graphene (e) graphite C 1s region, (f) nitrogen functionalized graphene C 1s region, and (g) nitrogen functionalized graphene N 1s region (Reproduced from Senthilnathan et al. [98], with permission from The Royal Society of Chemistry)

Similarly, micro-plasma collides with acetonitrile and initiates hydrogen detachment, which results in highly reactive free radical monomers such as  $\cdot\text{H}$  and  $\cdot\text{CH}_2\text{-CN}$  [37, 43]. Highly reactive nascent  $\cdot\text{H}$  and  $\cdot\text{CH}_2\text{-CN}$  generated in the acetonitrile solvent effectively react with radicalized graphene and partially restore the  $\text{sp}^2$  network by forming pyridinic ( $-\text{N}=\text{CH}-$ ) and pyrrolic ( $-\text{NH}$ ) nitrogen. The pyridinic nitrogen is well inserted into the  $\text{sp}^2$  network and partially restores the aromaticity and conjugation of the graphene layers.

HR-TEM images and XPS spectra of nitrogen-functionalized graphene are given in Fig. 6. Figure 6a–d shows the presence of single to few-layers of nitrogen-functionalized graphene. The defects caused by micro-plasma discharge can be clearly seen in Fig. 6c. The formation of single-layer nitrogen-functionalized graphene in the submerged liquid plasma process is confirmed by selected-area electron diffraction (SAED) as given in Fig. 6d. Similarly, the XPS spectrum of nitrogen-functionalized graphene shows a 4.2% insertion of nitrogen in the graphene domain. The C 1s region of nitrogen-functionalized graphene (Fig. 6f) has two well-resolved binding energy configurations, namely at 284.3 and 285.0 eV, attributed to  $\text{sp}^2$  carbon, and a new peak at 285.0 eV produced by the presence of distorted  $\text{sp}^3$  carbon ( $-\text{CH}_2$  and  $\text{C-N}$ ) present in the nitrogen-functionalized graphene [20, 71]. The N 1s region of nitrogen-functionalized graphene (Fig. 6g) has two broad peaks at 398.1 and 399.3 eV, which can be attributed to the  $-\text{C-NH}$  and  $-\text{C=N}-$  bonds, respectively [20, 45, 71].

### 2.3 *Formation of Nitrogen Functionalized Graphene and Nanometal Hybrid by a Submerged Liquid Plasma Process*

Graphene-based nanometal such as Pt, Au, Ag, Pd, and Ru composites have been extensively used in the areas of electronics, catalysis, sensors, light emitting diodes, solar cells, medicine and catalysts [4, 11, 12, 16, 30, 34, 35, 46, 75, 90, 91]. Among various graphene–metal hybrids, graphene-supported Au hybrids show a greater advantage because of their higher chemical stability, low-cost, and high surface area [33, 118]. Formation of Au-functionalized graphene composite has been achieved by various method of synthesis such as photochemical reduction, sonolytic reduction, microwave-assisted reduction, thermal evaporation, reduction by hydroxylamine,  $\text{NaBH}_4$ , amino terminated ionic liquid, sodium citrate, ascorbic acid, etc. [11, 12, 34, 49, 60, 76, 90, 110, 124]. Eco-friendly and low-temperature synthesis of Au-functionalized graphene composites still remains a challenge [48]. Yoshimura and his research groups have synthesized a nitrogen polymer-stabilized Au nanoparticle (NPs-Au) and NPs-Au-stabilized nitrogen functionalized graphene (NPs-Au-NFG) by a two-step process. First, nitrogen doped graphene and NPs are synthesized by submerged liquid plasma process. Second, the radical-rich nitrogen-doped graphene/NPs reduces tetrachloroauric acid under UV light (254 nm) and forms nitrogen NPs-Au-NFG composites [97–99, 101]. The pyridinic and pyrrolic nitrogen present in the nitrogen-doped graphene effectively binds with nitrogen polymer through  $\pi$ – $\pi$  or  $\sigma$ – $\pi$  interactions. The NPs provide excellent control over the size and shape of the Au nanoparticles by acting as reducing as well as templating agents under UV light (Fig. 7).

The structural morphology of Au-NPs-NFG composite was studied by HR-TEM analysis and is shown in Fig. 8. Figure 8a, b shows that HR-TEM images of NPs and NPs-NFG composite. Figure 8c shows that the particle size of Au present in Au-NPs-NFG is around ~5 nm and evenly distributed on the NPs-NFG surface. The NPs act as a bridge between Au and NFG and effectively controls the size of the Au particles, and hence uniform particle size (~5 nm) was observed throughout the Au-NPs-NFG surface. The HR-TEM image of Au-NPs-NFG shows that the d spacing of Au nanoparticles was 0.24 nm which corresponds to the 111 plane of face centered cubic (Fig. 8f). The selected area electron diffraction pattern (SAED) (Fig. 8f) indicated that the Au nanoparticles present in the Au-NPs-NFG was nanocrystalline in nature. Furthermore, Fig. 8f shows the ring structure of the SAED pattern which has the distinctive nature of polycrystalline gold showing 111, 200, 220, and 311 reflections, corresponding to face centered cubic Au present in Au-NPs-NFG.

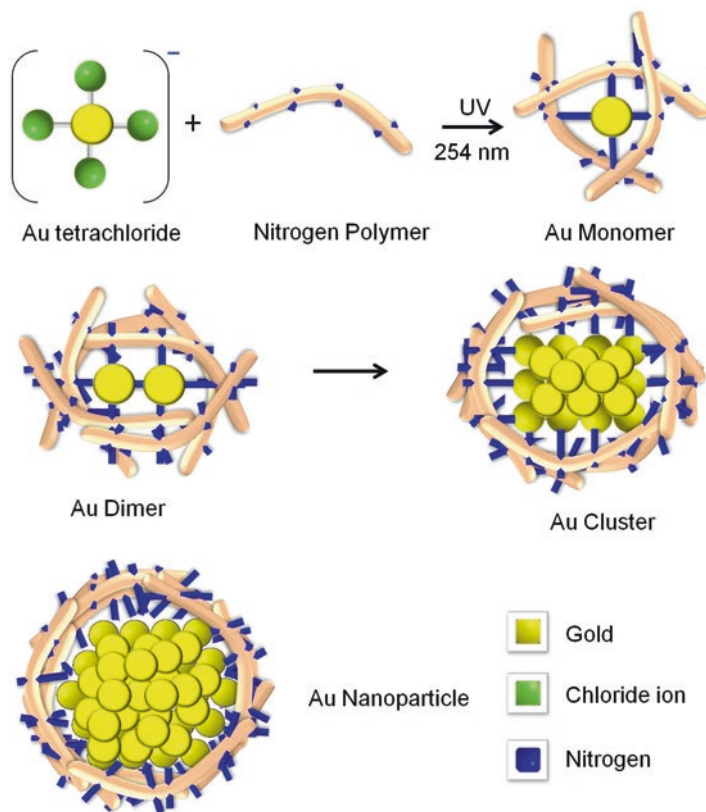


**Fig. 7** Proposed reaction mechanism of reduction of Au<sup>3+</sup> with nitrogen polymers under UV light (Reproduced from Senthilnathan et al. [100] with permission from The Royal Society of Chemistry)

## 2.4 Formation of Nitrogen Functionalized Graphene and Nanoclay Hybrid by Submerged Liquid Plasma Processes

Graphene nanocomposites with different inorganic moieties are one of the most attractive composites and can be used for many different fields of applications, including photovoltaics, supercapacitors, and fuel cells [88, 97–99, 101, 107]. Among the various nanometal composites, silicon has the highest theoretical energy density, and is a non-toxic, cheap, and environmentally friendly material [57]. Furthermore, clay-supported graphene materials can be used for fire resistance [1], hydrogen storage [89], reducing agent (at 300–600 °C) [79, 80], surface energy modification [67], and elastomeric composites [109]. The major drawbacks in the

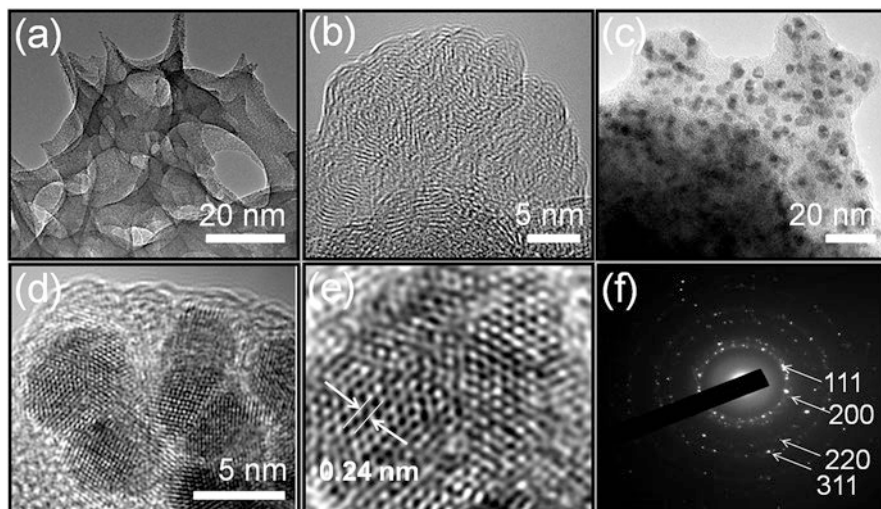


**Fig. 8** (a) HR-TEM image of unconventional NPs. (b) Image of NPs and NFG. (c–e) Images of NPs-Au-NFG nanoparticles. (f) SAED pattern of NPs-Au-NFG nanoparticles (Reproduced from Senthilnathan et al. [100] with permission from The Royal Society of Chemistry)

formation of silicon/clay graphene nanocomposites are (1) getting uniform nano-sized silicon on graphene layers is still challenging, (2) starting with graphene oxide precursor followed by thermal reduction further increases the operation cost, (3) high temperature synthesis leads to the agglomeration of silicon nanoparticles, and (4) graphene/nanoclay composite is highly unstable in aqueous solution because the hydrophilic nature of clay material facilitates the formation of coarse particles [97–99, 101, 117, 125]. Submerged liquid plasma has been used for the direct formation of highly dispersed nanoclay/nitrogen-doped graphene hybrid using hard black (HB) and 4 black (4B) rod pencil in acetonitrile solution at ambient conditions [97–99, 101]. In the plasma experiments, HB (74% carbon; 26% clay) and 4B (84% carbon; 16% clay) pencil rod was used as a point high-voltage electrode and a Pt sheet was used as a planar ground electrode (Fig. 9). A discharge voltage of 3.1 kV was applied between the two electrodes using a pulse generator, with a repetition rate of 10 kHz, a pulse delay of 500  $\mu$ s, and a pulse width of 5 ms. The SEM images of 4B and HB-nanoclay-NFG are given in Fig. 10a, e.

The SEM image shows that 4B-clay-NFG has a uniform sheet-like structure, whereas HB-nanoclay-NFG displays a shiny surface because of the presence of high clay content, which reduces the conductivity of the materials [97–99, 101]. HR-TEM images show the presence of a few layers of graphene embedded with clay particles of size less than 3 nm in both HB (Fig 10b–d) and 4B-nanoclay-NFG (Fig 10f–h). The presence of nanosized clay particles was clearly observed in HR-TEM analysis and proved the formation of nanostructured composite.

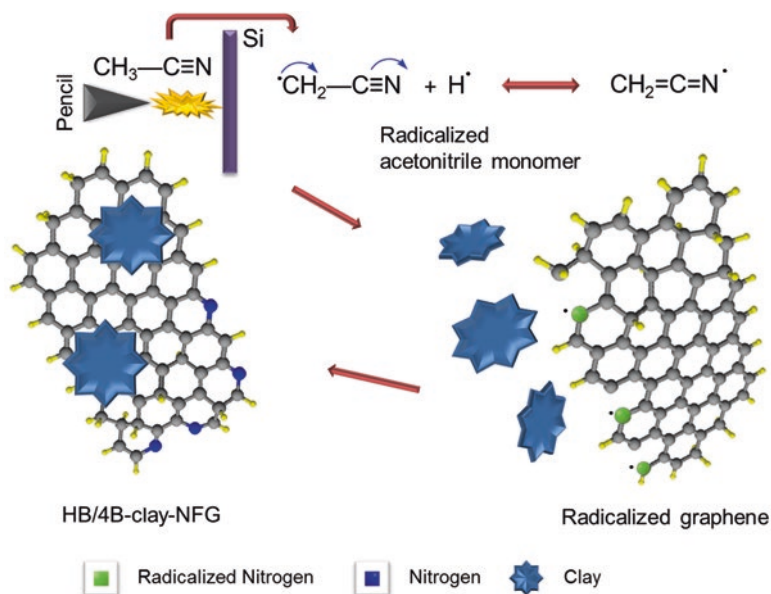


**Fig. 9** Proposed mechanisms for the formation of NFG/nanoclay composite in submerged liquid plasma processes; micro plasma discharge facilitates the exfoliation of radicalized graphene layer in the acetonitrile solution and plasma electron collision with acetonitrile forms nascent hydrogen and acetonitrile radicals. Both radicalized graphene and acetonitrile and nascent hydrogen react to form nanoclay/NFG (Reproduced from Senthilnathan et al. [97] with permission from Elsevier)

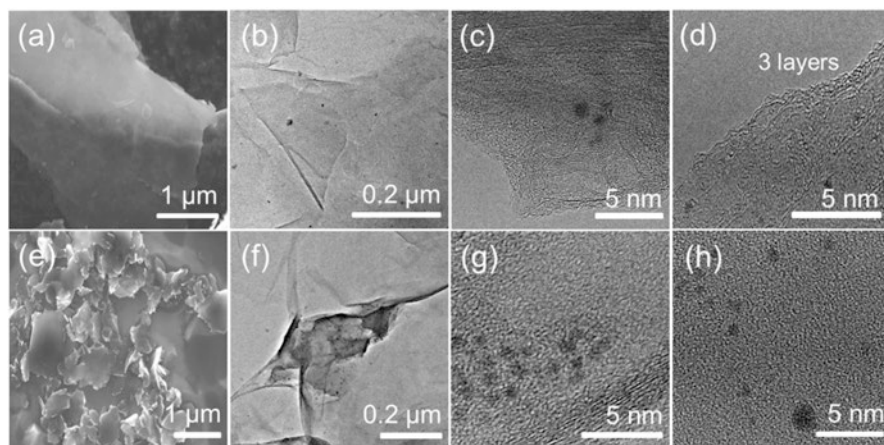


**Fig. 10** SEM and HR-TEM images of clay-NFG from HB and 4B pencils. (a) SEM image of clay-NFG from 4B pencil. (b–d) HR-TEM image of clay-NFG from 4B pencil. (e) SEM image of clay-NFG from HB pencil. (f–h) HR-TEM image of clay-NFG from HB pencil (Reproduced from Senthilnathan et al. [97] with permission from Elsevier)

### 3 Applications of Nanostructured Carbon and Hybrids Synthesized by Submerged Liquid Plasma Processes

Carbon materials have been playing a significant role in the development of alternative clean and sustainable energy technologies. The production of nanostructured carbon materials by submerged liquid plasma processes from organic solvents is one of the most attractive subjects in material science today. The catalytic activity of the Au–NPs–NFG synthesized by a submerged liquid plasma process was used for the selective oxidation of benzyl alcohol to benzaldehyde in both suspended and immobilized forms [97–99, 101]. The Au–ANPs–NFG immobilized on Pyrex glass resulted in 69% conversion of benzyl alcohol to benzaldehyde. In addition, the reuse of immobilized Au–ANPs–NFG led to 69%, 64%, and 61% successive conversions with a reaction time of 330 min. Similarly, the nitrogen-functionalized graphene nanoclay composite displayed distinct redox peaks in a cyclic voltammogram, with high specific capacitances of 40 and 111 F/g, respectively, obtained at a scan rate of 5 mV/s [97–99, 101]. Carbon onion produced by arc discharge showed a very high specific surface area (984.3 m<sup>2</sup>/g), indicating that the material is a promising candidate for gas storage [94]. Nitrogen-functionalized r-GO synthesized by a submerged liquid plasma process shows high cyclic stability with a specific capacitance value of 349 F/g at a scan rate of 10 mV/s [97–99, 101].

### 4 Future Prospects

The submerged liquid plasma technique has emerged as a most powerful tool for the formation of nanostructured carbon/hybrids because of its environmentally friendly approach. Nanostructured carbon synthesized by the submerged liquid plasma process has been applied in various fields of research, including electronics, nanotechnology, mechanics, biotechnology, and biomedicine. Furthermore, the submerged liquid plasma technique for the conversion of organic biomass and organic waste materials into alternative useful products or energy sources opens up new potentials for future research. A considerable amount of research is still required to understand fully the plasma reaction in liquids.

**Acknowledgements** The authors thank Professor Yury Gogotsi (Drexel University) for his encouragement and support. They are also grateful to Prof. Wen-Ta Tsai, Department of Materials Science and Engineering, National Cheng Kung University, Tainan, Taiwan for the discussions and support. The authors gratefully acknowledge the support of Prof. Jiunn-Der Liao, Department of Material Science and Engineering, National Cheng Kung University and Prof. Jih-Jen Wu, Department of Chemical Engineering for help and discussions regarding experiments.



## References

1. A. A'vila, F. Dias, E.C. da-Cruz, D.T.L. Yoshida, M.I. Bracarense, A.Q. Carvalho, M.G. de-Ávila Jr., *J. Mater. Res.* **13**, 143–150 (2010)
2. I. Alexandrou, H. Wang, N. Sano, G.A.J. Amaratunga, *J. Chem. Phys.* **120**(2), 1055–1058 (2004)
3. M.V. Antisari, R. Marazzi, R. Krsmanovic, *Carbon* **41**, 2393–2401 (2003)
4. S.S.J. Aravind, V. Eswaraiyah, S.J. Ramaprabhu, *Mater. Chem.* **21**, 17094–17097 (2011)
5. M.T. Beck, Z. Dinya, S. Keki, L. Papp, *Tetrahedron* **49**, 285–290 (1993)
6. D. Bera, E. Brinley, Kuiry, M.S.C. McCutten, S. Seal, H. Heinrich, B. Kabes, *Rev. Sci. Instrum.* **76**, 033903–033909 (2005)
7. D. Bera, S.C. Kuiry, M. McCutchen, A. Kruize, H. Heinrich, M. Meyyappan, S. Seal, *Chem. Phys. Lett.* **386**, 364–368 (2004)
8. D. Bera, S.C. Kuiry, M. McCutchen, S. Seal, H. Heinrich, G.D. Slane, *J. Appl. Phys.* **96**, 5152–5157 (2004)
9. L.P. Biró, Z.E. Horváth, L. Szalmás, K. Kertész, F. Wéber, G. Juhász, G. Radnóczy, J. Gyulai, *Chem. Phys. Lett.* **372**, 399–402 (2003)
10. J.-L. Brisset, D. Moussa, A. Doubla, E. Hnatiuc, B. Hnatiuc, G. Kamgang-Youbi, J.-M. Herry, M. Naitali, M.-N. Bellon-Fontaine, *Ind. Eng. Chem. Res.* **47**, 5761 (2008)
11. Q. Chen, T. Kaneko, R. Hatakeyama, *Appl. Phys. Express* **5**, 6201 (2012)
12. C.-Y. Chen, C.-Y. Fan, M.-T. Lee, J.-K. Chang, *J. Mater. Chem.* **22**, 7697–7700 (2012)
13. Q. Chen, T. Kitamura, K. Saito, K. Haruta, Y. Yamano, T. Ishikawa, H. Shirai, *Thin Films* **516**, 4435–4440 (2008)
14. Q. Chen, J. Li, Y. Li, *J. Phys. D: App. Phys.* **48**, 42 (2015)
15. H.J. Cho, H. Kondo, K. Ishikawa, M. Sekine, M. Hiramatsu, M. Hori, *Jpn. J. Appl. Phys.* **53**, 040307 (2014)
16. C.M. Cobley, J. Chen, E.C. Cho, L.V. Wang, Y. Xia, *Chem. Soc. Rev.* **40**, 44–56 (2010)
17. T. Cserfalvi, P. Mezei, P. Apai, *J. Phys. D* **26**, 2184 (1993)
18. T. Cserfalvi, P. Mezei, *J. Anal. At. Spectrom.* **9**, 345 (1994)
19. W.C. Davis, R.K. Marcus, *Spectrochim. Acta Part B* **57**, 1473 (2002)
20. A.P. Dementjev, A. de-Graaf, M.C.M. van-de Sanden, K.I. Maslakov, A.V. Naumkin, A.A. Serov, *Diam. Relat. Mater.* **9**, 1904–1907 (2000)
21. D. Dobrynin, G. Fridman, G. Friedman, A. Fridman, *New J. Phys.* **11**, 115020 (2009)
22. D.J. Douglas, J.B. French, *Anal. Chem.* **53**(1), 37–41 (1981)
23. H. Filik, G. Çetintaş, A.A. Avan, S.N. Koç, I. Boz, *Int. J. Electrochem. Sci.* **8**, 5724–5737 (2013)
24. A. Fridman, *Plasma Chemistry* (Cambridge University Press, Cambridge, 2008)
25. G. Fridman, A.D. Brooks, M. Balasubramanian, A. Fridman, A. Gutsol, V.N. Vasilets, H. Ayan, G. Friedman, *Plasma Process. Polym.* **4**, 370–375 (2007)
26. G. Fridman, M. Peddinghaus, H. Ayan, A. Fridman, M. Balasubramanian, A. Gutsol, A. Brooks, G. Friedman, *Plasma Chem. Plasma Process.* **26**, 425 (2006)
27. V. Georgakilas, M. Otyepka, A.B. Bourlinos, V. Chandra, N. Kim, K.C. Kemp, P. Hobza, R. Zboril, K.S. Kim, *Chem. Rev.* **112**, 6156–6214 (2012)
28. S. Glasstone, A.J. Hickling, *Chem. Soc. (Resumed)*, 1772 (1934)
29. T. Hagino, H. Kondo, K. Ishikawa, H. Kano, M. Sekine, M. Hori, *Appl. Phys. Express* **5**(3), 035101 (2012)
30. M. Haruta, *Nature* **437**, 1098–1099 (2005)
31. P.A.F. Herbert, L. O'Neill, J. Jaroszynska-Wolinska, *Chem. Mater.* **21**, 4401–4407 (2009)
32. Y.L. Hsin, K.C. Hwang, F.-R. Chen, J.-J. Kai, *Adv. Mater.* **13**(11), 830–833 (2001)
33. X. Huang, X. Qi, F. Boey, H. Zhang, *Chem. Soc. Rev.* **41**, 666–686 (2012)
34. X. Huang, X. Qi, Y. Huang, S. Li, C. Xue, C.L. Gan, F. Boey, H. Zhang, *ACS Nano* **4**, 6196–6202 (2010)

35. M.D.X. Hughes, Y.-J. Jenkins, P. McMorn, P. Landon, P. Enache, D.I. Carley, A.F. Attard, G.A. Hutchings, G.J. King, F. Stitt, E.H. Johnston, P. Griffin, K. Kiely, C. J. Nature **437**, 1132–1135 (2005)
36. T. Ichiki, T. Koidesawa, Y. Horiike, Plasma Sources Sci. Technol. **12**, S16 (2003)
37. N. Inagaki, *Plasma Surface Modification and Plasma Polymerization* (Technomic Publishing Company, Lancaster, 1996)
38. N. Inagaki, S. Tasaka, Y.J. Yamada, Polym. Sci. Part A. Polym. Chem. **30**(9), 2003–2010 (1999)
39. N. Inagaki, S. Tasaka, Y. Yamada, J. Polym. Sci. Part A Polym. Chem. **30**(9), 2003–2010 (1992)
40. M. Ishigami, J. Cumings, A. Zettl, S. Chen, Chem. Phys. Lett. **319**(5–6), 457 (2000)
41. T. Ishijima, H. Hotta, H. Sugai, Appl. Phys. Lett. **91**, 121501 (2007)
42. T. Ishijima, H. Sugiura, R. Satio, H. Toyada, H. Sugai, Plasma Sources Sci. Technol. **19**, 015010 (2010)
43. M. Jahan, Q. Bao, K.P. Loh, J. Am. Chem. Soc. **134**(6707–6713) (2012)
44. G. Jenkins, A. Manz, J. Micromech. Microeng. **12**, N19 (2002)
45. A. Johanson, S.J. Stafstrom, Chem. Phys. **111**, 3203–3208 (1999)
46. M.R. Jones, K.D. Osberg, R.J. Macfarlane, M.R. Langille, C.A. Mirkin, Chem. Rev. **111**, 3736–3827 (2011)
47. H. Kim, J. Lee, J.H. Kim, M.Y. Cserfalvi, T. Mezei, P. Spectrochim. Acta Part B **55**, 823 (2000)
48. M.J. Kim, Y. Jeong, S. Sohn, S.Y. Lee, Y.J. Kim, K. Lee, Y.H. Kahng, J.-H. Jang, AIP Adv. **3**, 012117 (2013)
49. Y.-K. Kim, H.-K. Na, Y.W. Lee, H. Jang, S.W. Han, D.-H. Min, Chem. Commun. **46**, 3185–3187 (2010)
50. H. Kobayashi, A.T. Bell, M. Shen, Macromolecules **7**(3), 277–283 (1974)
51. M.G. Kong, G. Kroesen, G. Morfill, T. Nosenko, T. Shimizu, J. Van-Dijk, J. Zimmermann, New J. Phys. **11**, 115012 (2009)
52. N.A. Kumar, H.J. Choi, A. Bund, J.B. Baek, Y.T.J. Jeong, Mater. Chem. **22**, 12268–12274 (2012)
53. H. Lange, M. Sioda, A. Huczko, Y.Q. Zhu, H.W. Kroto, D.R.M. Walton, Carbon **41**(8), 1617–1623 (2003)
54. I. Langmuir, Proc. Natl. Acad. Sci. U. S. A. **14**, 627 (1928)
55. M. Laroussi, IEEE Trans. Plasma Sci. **37**, 714 (2009)
56. K.E. Lawrence, G.W. Rice, V.A. Fassel, Anal. Chem. **56**, 289 (1984)
57. J.K. Lee, K.B. Smith, C.M. Hayner, H.H. Kung, Chem. Commun. **46**, 2025–2027 (2010)
58. A.E. Lefohn, N.M. Mackie, E.R. Fisher, Plasmas Polym. **3**(4), 197–209 (1998)
59. D. Li, M.B. Müller, S. Gilje, R.B. Kaner, G.G. Wallace, Nat. Nanotechnol. **3**, 101–105 (2008)
60. F. Li, H. Yang, C. Shan, Q. Zhang, D. Han, A. Ivaskab, L. Niu, J. Mater. Chem. **19**, 4022–4025 (2009)
61. X. Li, H. Zhu, B. Jiang, J. Ding, X. Cailu, D. Wu, Carbon **41**, 1664 (2003)
62. R. Liepins, D. Campbell, C.J. Walker, Polym. Sci. **A1**(6), 3059–3073 (1968)
63. L. Lin, Q. Wang, Plasma Chem. Plasma Process. **35**, 925–962 (2015)
64. Y. Liu, R. Deng, Z. Wang, H. Liu, J. Mater. Chem. **22**, 13619–13624 (2012)
65. B.R. Locke, K.-Y. Shih, Plasma Sources Sci. Technol. **20**, 034006 (2011)
66. B. Locke, M. Sato, P. Sunka, M. Hoffmann, J.-S. Chang, Ind. Eng. Chem. Res. **45**, 882 (2006)
67. J. Longun, G. Walker, J.O. Iroh, Carbon **63**, 9–22 (2013)
68. Y. Lu, F. Zhang, T. Zhang, K. Leng, L. Zhang, X. Yang, Y. Ma, Y. Huang, M. Zhang, Y. Chen, Carbon **63**, 508–516 (2013)
69. M.A. Malik, A. Ghaffar, S.A. Malik, Plasma Sources Sci. Technol. **10**, 82 (2001)
70. M.A. Malik, Plasma Chem. Plasma Process. **30**, 21 (2010)
71. G.P. Mane, S.N. Talapaneni, C. Anand, S. Varghese, H. Iwai, Q. Ji, K. Ariga, T. Mori, A. Vinu, Adv. Funct. Mater. **22**, 3596–3604 (2012)

72. R.K. Marcus, W.C. Davis, *Anal. Chem.* **73**, 2903 (2001)
73. M. Matsushima, M. Noda, T. Yoshida, H. Kato, G. Kalita, T. Kizuki, H. Uchida, M. Umeno, K.J. Wakita, *Appl. Phys.* **113**(11), 114304 (2013)
74. B. Mitra, B. Levey, Y.B. Gianchandani, *IEEE Trans. Plasma Sci.* **36**, 1913 (2008)
75. R. Murray, *Chem. Rev.* **108**, 2688–2720 (2008)
76. R. Muszynski, B. Seger, P.V.J. Kamat, *Phys. Chem. C* **112**, 5263–5266 (2008)
77. P. Muthakarn, N. Sano, T. Charinpanitkul, W. Tanthapanichakoon, T. Kanki, *J. Phys. Chem. B* **110**(37), 18299–18306 (2006)
78. M.G. Neira-Velázquez, L.F. Ramos-deValle, E. Hernández-Hernández, A. Ponce-Pedraza, S.G. Solís-Rosales, S. Sánchez-Valdez, P. Bartolo-Pérez, V.A. González-González, *Plasma Process. Polym.* **8**, 842–849 (2011)
79. C. Nethravathi, J.T. Rajamathi, N. Ravishankar, C. Shivakumara, M. Rajamathi, *Langmuir* **24**, 8240–8244 (2008)
80. C. Nethravathi, B. Viswanath, C. Shivakumara, N. Mahadevaiah, M. Rajamathi, *Carbon* **46**, 1773–1781 (2008)
81. S. Nomura, H. Toyota, *Appl. Phys. Lett.* **83**, 4503 (2003)
82. S. Nomura, H. Toyota, S. Mukasa, H. Yamashita, T. Maehara, *Appl. Phys. Lett.* **8**, 211503 (2006)
83. S. Nomura, H. Toyota, S. Mukasa, H. Yamashita, T. Maehara, A. Kawashima, *J. Appl. Phys.* **106**, 073306 (2009)
84. S. Nomura, H. Toyota, M. Tawara, H. Yamashita, *Appl. Phys. Lett.* **88**, 231502 (2006)
85. T. Okada, T. Kaneko, R. Hatakeyama, *Thin Solid Films* **515**, 4262–4265 (2007)
86. Y.U.M. Qingsong, Y.E. Lizhen, L.U. Jie, C. Fosong, W. Osada, Y. Chinese, *J. Polym. Sci.* **6**(2), 172–177 (1998)
87. J. Qiu, Y. Li, Y. Wang, Z. Zhao, Y. Zhou, Y. Wang, *Fuel* **83**, 615–617 (2004)
88. T. Ramanathan, A.A. Abdala, S. Stankovich, D.A. Dikin, M. Herrera-Alonso, R.D. Piner, D.H. Adamson, H.C. Schniepp, X. Chen, R.S. Ruoff, S.T. Nguyen, I.A. Aksay, R.K. Prud'Homme, L.C. Brinson, *Nat. Nanotechnol.* **3**, 327–331 (2008)
89. C. Ruiz-García, J. Pérez-Carvaja, A. Berenguer-Murcia, M. Darder, P. Aranda, D. Cazorla-Amorós, E. Ruiz-Hitzky, *Phys. Chem. Chem. Phys.* **15**, 18635–18641 (2013)
90. K. Sanjeeva Rao, J. Senthilnathan, J.-M. Ting, M. Yoshimura, *Nanoscale* **6**, 12758–12768 (2014)
91. K. Sanjeeva Rao, J. Senthilnathan, H.-W.W. Cho, J.-J. Yoshimura, M. *Adv. Funct. Mater.* **25**, 298–305 (2015)
92. N. Sano, T. Charinpanitkul, T. Kanki, W.J. Tanthapanichakoon, *Appl. Phys.* **96**(1), 645–649 (2004)
93. N. Sano, M. Naito, M. Chhowalla, T. Kikuchi, S. Matsuda, K. Iimura, *Chem. Phys. Lett.* **378**(1–2), 29–34 (2003)
94. N. Sano, H. Wang, I. Alexandrou, M. Chhowalla, K.B.K. Teo, G.A.J.J. Amaratunga, *Appl. Phys.* **92**(5), 2783–2788 (2002)
95. N. Sano, H. Wang, M. Chhowalla, I. Alexandrou, G.A.J. Amaratunga, *Nature* **414**, 506–507 (2001)
96. V. Scuderi, C. Bongiorno, G. Faraci, S. Scalese, *Carbon* **50**(6), 2365–2369 (2012)
97. J. Senthilnathan, K.S. Rao, W.-H. Lin, J.-D. Liao, M. Yoshimura, *Carbon* **78**, 448–454 (2014)
98. J. Senthilnathan, K.S. Rao, M. Yoshimura, *J. Mater. Chem. A* **2**, 3332–3337 (2014)
99. J. Senthilnathan, Y.-F. Liu, K.S. Rao, M. Yoshimura, *Sci. Reps.*, 4395–4401 (2014)
100. J. Senthilnathan, K.S. Rao, W.-H. Lin, J.-M. Ting, M.J. Yoshimura, *Mater. Chem. A* **3**, 3035–3043 (2015)
101. J. Senthilnathan, C.C. Weng, W.T. Tsai, Y. Gogotsi, M. Yoshimura, *Carbon* **71**, 181–189 (2014)
102. J. Senthilnathan, C.C. Weng, J.-D. Liao, Yoshimura, M. *Sci. Reps.* **3**, 2414–2420 (2013)
103. H. Shimoeda, H. Kondo, K. Ishikawa, M. Hiramatsu, M. Sekine, M. Hori, *Appl. Phys. Express* **7**, 046201 (2014)

104. H. Shimoeda, H. Kondo, K. Ishikawa, M. Hiramatsu, M. Sekine, M. Hori, *Jpn. J. Appl. Phys.* **53**, 040305 (2014)
105. P. Simon, Y. Gogotsi, *Nat. Mater.* **7**, 845–854 (2008)
106. D. Staack, A. Fridman, A. Gutsol, Y. Gogotsi, G. Friedman, *Angew. Chem. Int. Ed.* **47**(42), 8020–8024 (2008)
107. S. Stankovich, D.A. Dikin, G.H.B. Dommett, K.M. Kohlhaas, E.J. Zimney, E.A. Stach, R.D. Piner, S.T. Nguyen, R.S. Ruoff, *Nature* **442**, 282–286 (2006)
108. E. Stoffels, Y. Sakiyama, D.B. Graves, *IEEE Trans. Plasma Sci.* **36**, 1441 (2008)
109. Z. Tang, Q. Wei, T. Lin, B. Guo, D. Jia, *RSC Adv.* **3**, 17057–17064 (2013)
110. K. Vinodgopal, B. Neppolian, I.V. Lightcap, F. Grieser, M. Ashokkumar, P.V.J. Kamat, *Phys. Chem. Lett.* **1**, 1987–1993 (2010)
111. H. Wang, M. Yoshimura, *Chem. Phys. Lett.* **348**, 7–10 (2001)
112. S.D. Wang, M.H. Chang, J.J. Cheng, H.K. Chang, K.M.D. Lan, *Carbon* **43**, 1317–1319 (2005)
113. T. Watanabe, H. Wang, Y. Yamakawa, M. Yoshimura, *Carbon* **44**, 799–823 (2006)
114. C.G. Wilson, Y.B. Gianchandani, *IEEE Trans. Electron Dev.* **49**, 2317 (2002)
115. S.J. Woltornist, A.J. Oyer, J.-M.Y. Carrillo, A.V. Dobrynin, D.H. Adamson, *ACS Nano* **7**(8), 7062–7066 (2013)
116. Q. Wu, Y. Xu, Z. Yao, A. Liu, G. Shi, *ACS Nano* **4**, 1963–1970 (2010)
117. H. Xiang, K. Zhang, G. Ji, J.Y. Lee, C. Zou, X. Chen, J. Wu, *Carbon* **49**, 1787–1796 (2011)
118. X. Xie, J. Long, L. Chen, Y. Wang, Z. Zhang, X. Wang, *RSC Adv.* **2**, 12438–12446 (2012)
119. G. Xing, S. Jia, Z. Shi, *Carbon* **45**(13), 2584–2588 (2007)
120. Y. Xu, Z. Liu, X. Zhang, Y. Wang, J. Tian, Y. Huang, Y. Ma, X. Zhang, Y. Chen, *Adv. Mater.* **21**, 1275–1279 (2009)
121. H. Yasuda, T. Hirotsu, *J. Polym. Sci. Polym. Chem. Ed.* **16**, 743–759 (1978)
122. H. Yasuda, *J. Polym. Sci. Macromol. Rev.* **16**, 199–293 (1981)
123. O. Yukio, *J. Anal. At. Spectrom.* **9**(7), 745 (1994)
124. H.Q. Zhou, C.Y. Qiu, Z. Liu, H.C. Yang, L.J. Hu, J. Liu, H.F. Yang, C.Z. Gu, L.F. Sun, *J. Am. Chem. Soc.* **132**, 944–946 (2010)
125. X. Zhou, Y.X. Yin, L.J. Wan, Y.G. Guo, *Chem. Commun.* **48**, 2198–2200 (2012)
126. H.W. Zhu, X.S. Li, B.X. Jiang, C.L. Zhu, Y.F. Wu, D.H. Chen, *X.H. Chem. Phys. Lett.* **366**(5–6), 664–669 (2002)

# Lab-on-a-Graphene: Functionalized Graphene Transistors and Their Application for Biosensing

Takao Ono, Yasushi Kanai, Yasuhide Ohno, Kenzo Maehashi, Koichi Inoue, and Kazuhiko Matsumoto

## 1 Introduction

Graphene is a two-dimensional material consisting of a hexagonal network of carbon atoms (Fig. 1) and was first isolated in 2004 by simple exfoliation from graphitic carbon using adhesive tape [1]. Research on graphene has progressed rapidly because of graphene's unique electrical and mechanical characteristics and has opened the new research field of two-dimensional materials, such as graphene and transition metal dichalcogenide monolayers [2]. It is noteworthy that several important theoretical studies on graphene and related materials were conducted before their initial isolation [3].

Graphene has the highest theoretical electrical mobility of any known material, at  $2,000,000 \text{ cm}^2/(\text{V s})$  [4]. An experimentally determined mobility of  $230,000 \text{ cm}^2/(\text{V s})$  was reported [5], which is more than 100 times that of silicon, the prototypical semiconductor material. The high electrical mobility of graphene makes it attractive for use in next-generation semiconductors. However, graphene lacks a band gap,

---

T. Ono • Y. Kanai • K. Inoue • K. Matsumoto (✉)  
The Institute of Scientific and Industrial Research, Osaka University,  
8-1 Mihogaoka, Ibaraki-shi, Osaka 567-0047, Japan  
e-mail: [k-matsumoto@sanken.osaka-u.ac.jp](mailto:k-matsumoto@sanken.osaka-u.ac.jp)

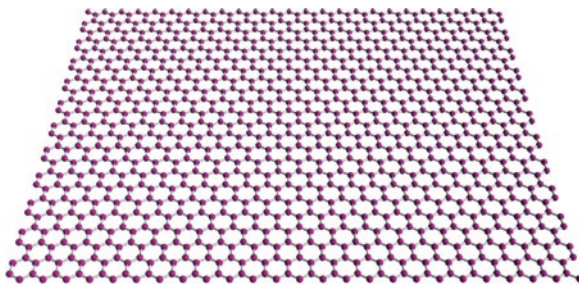
Y. Ohno  
Graduate School of Science and Technology, Tokushima University,  
2-1 Minamijosanjima, Tokushima-shi, Tokushima 770-8506, Japan

The Institute of Scientific and Industrial Research, Osaka University,  
8-1 Mihogaoka, Ibaraki-shi, Osaka 567-0047, Japan

K. Maehashi  
The Institute of Scientific and Industrial Research, Osaka University,  
8-1 Mihogaoka, Ibaraki-shi, Osaka 567-0047, Japan

Institute of Engineering, Tokyo University of Agriculture and Technology,  
2-24-16 Nakacho, Koganei-shi, Tokyo 184-8588, Japan

**Fig. 1** Molecular structure of graphene



and thus graphene transistors cannot realize a high on/off ratio. Although several significant progresses have been made toward opening the band gap such as bilayer graphene [6], graphene nanoribbon [7], and graphene under strain [8], the opened band gap was still insufficient for use in logic circuit. There are a variety of other applications of graphene from transparent electrodes to implant materials [9–11], but there are few cases of practical use and commercialization. Some sort of “killer application” of graphene has been long awaited.

We have investigated biosensing applications of graphene, avoiding the zero-gap issue while fully utilizing the advantages of graphene [12]. Our research uses a graphene field-effect transistor (G-FET) as a sensing platform combined with various device structures and surface functionalization. We named this device “lab-on-a-graphene,” after “lab-on-a-chip,” a general term for microfabricated biochemical sensing platforms. This article reviews the basic principles behind lab-on-a-graphene and recent research results.

## 2 How Does a G-FET Detect Biomolecules?

A schematic of our G-FET platform is shown in Fig. 2a. Graphene sheets were mechanically exfoliated from kish graphite and transferred onto Si substrate with a 290-nm-thick  $\text{SiO}_2$  layer. Graphene sheets were then connected with Au (30 nm)/Ni (10 nm) electrodes as source and drain electrodes through electron-beam lithography, electron-beam deposition, and lift-off processes. Silicone rubber frame was placed on the device chip to store aqueous solution on graphene channel. Ag/AgCl reference electrode was inserted to the solution and applied top-gate voltage to the G-FET through electric double layer between the graphene channel and bulk solution. When the top-gate voltage is applied through a Ag/AgCl reference electrode, the G-FET shows ambipolar characteristics, where the hole current switches to an electron current above the voltage at the minimum current point, called the charge neutrality point or Dirac point. Nucleotides, proteins, and other biomolecules hold surface electrical charges when dissolved in aqueous solution. When these molecules are fixed onto the graphene channel, their surface charges induce carriers of

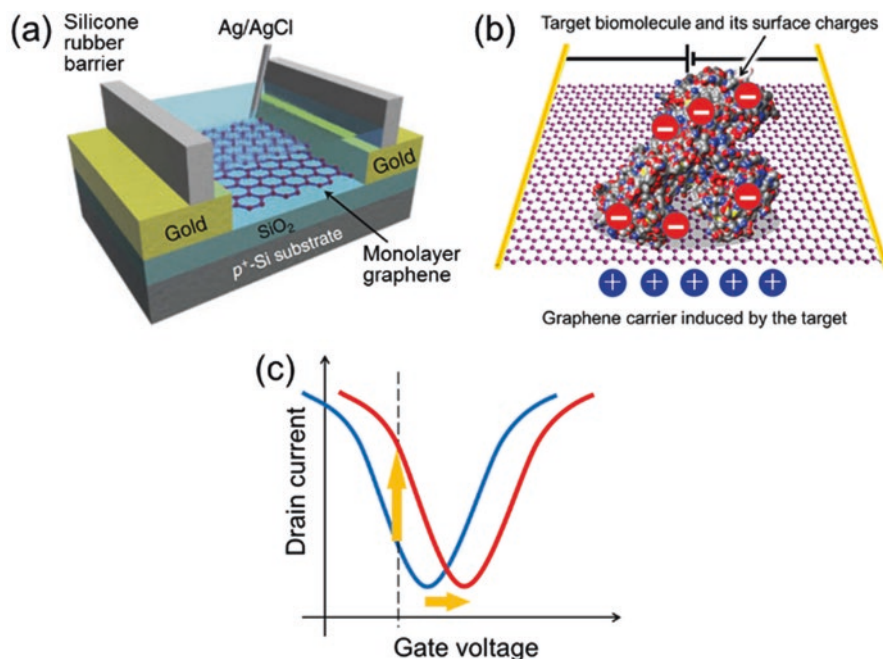


**Fig. 2** Schematics illustrating G-FET biosensing. (a) Schematic of the measurement setup. The sample solution on the graphene channel is surrounded by a silicone rubber barrier (Cited from [19]. Copyright 2011 The Japan Society of Applied Physics). (b) Carriers induced by the surface charges of the attached biomolecules. (c)  $I$ - $V$  characteristics of the G-FET. Following hole induction in the graphene, the  $I$ - $V$  curve shifts horizontally in the positive direction, and the hole current increases at a fixed gate voltage (dotted line)

opposite sign to the graphene channel, i.e., negatively charged molecules induce holes and positively charged ones induce electrons to graphene. It changes Fermi level of the graphene, and the  $I$ - $V$  curve consequently shifts horizontally in the positive or negative direction (Fig. 2b, c). The shift width corresponds to the amount of the attached molecules' charge. Under fixed gate voltage, attachment of the biomolecule is detected as a change in the drain current of the G-FET. The amount of the drain current change is expressed in terms of the product of the horizontal shift width and the slope of the  $I$ - $V$  curve, i.e., transconductance of the G-FET. The transconductance is proportional to the graphene mobility. Therefore, G-FET is the effective transducer for converting attachment of charged biomolecules into large drain current change. This application does not require an on/off ratio for the transistors and takes advantage of graphene's high electrical mobility. Moreover, graphene is a two-dimensional material that is stable when immersed in aqueous solution. Biomolecules can directly attach to the graphene surface and effectively change the transfer characteristics of the G-FET.

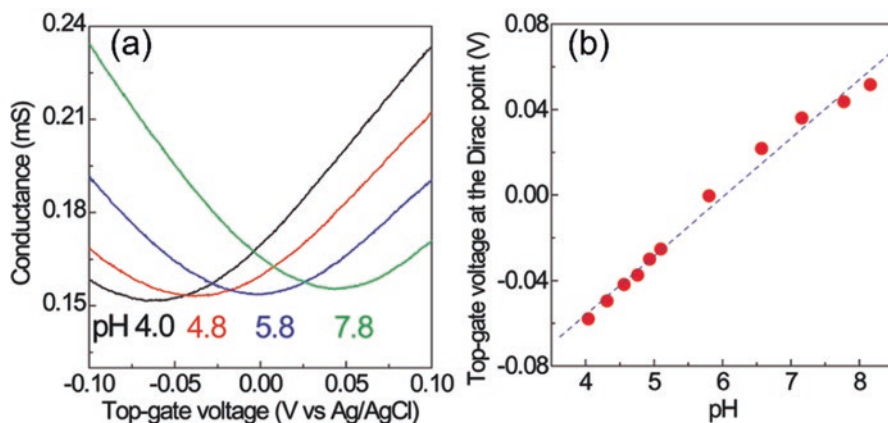


**Fig. 3** pH sensing by G-FET. (a)  $I$ - $V$  characteristics at pH 4.0, 4.8, 5.8, and 7.8. (b) Linear correlation between pH and top-gate voltage at the Dirac point (Reprinted with permission from [13]. Copyright 2009 American Chemical Society)

### 3 Ion Sensing Using a G-FET

An ideal graphene surface has no surface groups, and an aqueous solution maintains the balance between positive and negative charges. Therefore, it seems to be difficult for a G-FET to sense ionic species in the solution. Nevertheless, we succeeded in measuring protons and other ions in the solution. An early study demonstrated that the charge neutrality point shifts in the positive direction as pH increases (the proton concentration decreases), and the hole current increased at the fixed gate voltage (Fig. 3a) [13]. Although the mechanism underlying these measurements remains unclear, we suppose that site-binding model can be expanded to the G-FET sensing [14, 15]. Graphene made by exfoliation and chemical vapor deposition contains crystal defects that form surface groups, such as hydroxyl groups, through oxidization [16, 17]. These oxygen-containing groups exhibit affinity toward positive ions. The attachment of positive ions to the oxidized groups leads to a local charge imbalance, induces negative carriers in the graphene, and shifts the  $I$ - $V$  curve in the negative direction. We demonstrated continuous changes in the hole current between pH 4.0 and pH 8.2 (Fig. 3b).

The above scheme does not impart ion selectivity to the G-FETs. We fabricated a potassium-selective G-FET sensor by spin-coating valinomycin, a potassium ionophore [18]. Valinomycin has a doughnut-shaped structure and effectively and selectively captures potassium ions. Figure 4 shows that the charge neutrality point remained unchanged following the addition of sodium ions but shifted upon the addition of potassium ions.

Proteins have surface charges due to surface groups such as amino and carboxyl groups, and the surface charges vary according to the protein and the pH of the



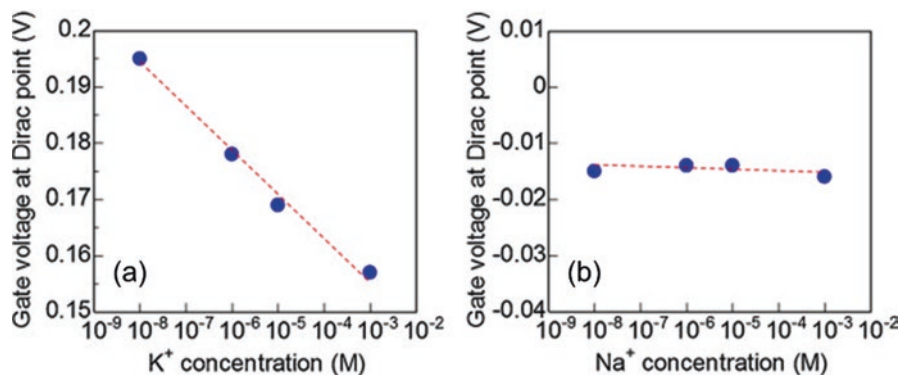
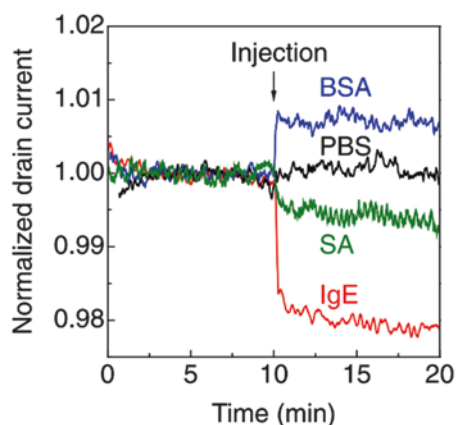


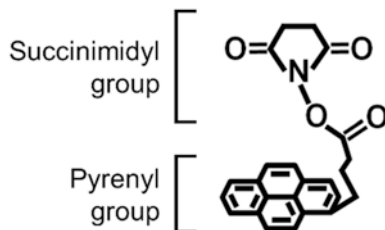
**Fig. 4** Ion-selective response of G-FET. Dirac point of valinomycin-coated G-FET decreased with increasing potassium-ion concentration (a) but was barely affected by changes in sodium concentration (b) (Reprinted from [18], Copyright 2013, with permission from Elsevier)

**Fig. 5** Time course of the normalized drain currents of G-FETs and the effect of introducing various proteins in phosphate-buffered saline (PBS, pH 6.8). Positively charged IgE (30 nM) and SA (100 nM) decreased the hole current, whereas negatively charged BSA (30 nM) increased the current (Cited from [19]. Copyright 2011 The Japan Society of Applied Physics)



environment. Figure 5 shows the changes in drain current induced by the addition of various proteins to the G-FET [19]. Bovine serum albumin (BSA), which was negatively charged under the experimental condition used, was detected as an increase in hole current, whereas streptavidin (SA) and immunoglobulin E (IgE), which were positively charged, were detected as a hole current decrease. Physical adsorption of the proteins induced local imbalances in the charges on the graphene surface. This result shows the considerable promise of the G-FET for detecting biomolecules, but specific biomolecules in a mixture of biomolecules cannot be sensed using this configuration. In the next section, we describe how we achieved selectivity for various biomolecules.

**Fig. 6** Structural formula of PBASE



## 4 Functionalization of G-FET

Practical biosensing requires that the G-FET respond selectively to the target biomolecule. Receptor molecules have specific affinity for their targets and are thus useful for this purpose. Modification of the G-FET with receptor molecules provides the G-FET with biosensor functionality but requires the use of a chemical linker between the graphene and receptor. We chose 1-pyrenebutyric acid *N*-hydroxysuccinimide ester (PBASE, Fig. 6), a pyrene compound that noncovalently binds to hexagonal carbon networks by  $\pi$ -stacking. Various pyrene compounds are commonly used to disperse carbon nanotubes [20]. PBASE also has a succinimidyl group that covalently binds to an amino group on the receptor. Therefore, PBASE immobilizes receptors onto the graphene surface without causing defects in the graphene structure. Experimental results demonstrating selective biosensing using functionalized G-FETs are reviewed below.

### 4.1 DNA Detection Using a Complementary Strand

DNA forms a double helix through the hybridization of complementary base pairs and has a strong negative charge due to its phosphate groups. Therefore, G-FET functionalized with single-strand DNA should function as a biosensor for the complementary DNA sequence. As shown in Fig. 7, modification of graphene with single-strand DNA results in the *I-V* curve shifting in the positive direction due to the negatively charged DNA inducing hole carriers in the graphene. Addition of the complementary DNA sequence further shifts the curve in the same direction, whereas the addition of noncomplementary DNA has little effect. These results show that the G-FET worked as a DNA sensor for the specific sequence [21].

### 4.2 IgE Detection Using a DNA Aptamer

DNA aptamers are small single-strand DNA molecules that specifically bind to a target molecule. DNA aptamers are synthesized by conventional methods, and their specific affinities can be improved by selection from a library of small-DNA

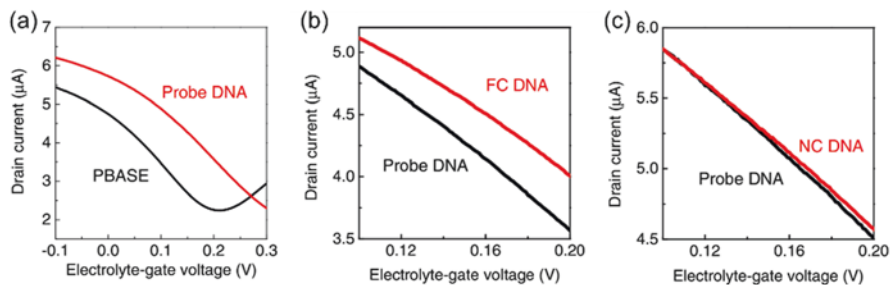


**Fig. 7** The detection of complementary DNA. (a) Transfer characteristics before (PBASE) and after (probe DNA) functionalization with single-strand DNA. (b) Transfer characteristics before (probe DNA) and after (FC DNA) introduction of the complementary DNA strand. (c) Transfer characteristics before (probe DNA) and after (NC DNA) introduction of the noncomplementary (NC) DNA strand (Cited from [21]. Copyright 2013 The Japan Society of Applied Physics)

candidates. It makes production of aptamer easier than that of other receptor molecules such as antibodies. DNA aptamers are therefore attractive for use in biochemical and medical research. In this study, a sensor was constructed by immobilizing an IgE-specific aptamer onto the G-FET via the PBASE linker, followed by surface blocking to prevent nonspecific adsorption. IgE detection is important in allergy testing. Only IgE caused a change in G-FET drain current when the G-FET was sequentially exposed to BSA, SA, and IgE (Fig. 8). The observed hole current decrease is consistent with the binding of positively charged IgE to the graphene surface. A concentration of 290 pM IgE could be detected, demonstrating the high specificity of this aptamer-functionalized G-FET [19, 22].

### 4.3 Heat-Shock Protein Detection Using an Antibody Fragment

Despite the advantages of aptamers, antibodies are preferable for specific detection due to their general versatility and high affinity, but their use for G-FET functionalization is complicated by Debye screening. Debye screening is the neutralization of surface charges on the target biomolecule by ionic species in the surrounding aqueous environment. Complete screening prevents target detection by the G-FET. The thickness of the screening layer is called the Debye length, and it is less than 1 nm under physiological conditions. The Debye length was extended to several nanometers by conducting our experiments in 10 mM salt, which is less than 10% of the physiological concentration of salt. Salt concentrations lower than 10 mM can adversely affect protein activity. Hence, the receptor molecules should be smaller than several nanometers. However, an IgG antibody, the most common isotype, is approximately 10 nm in length, which is significantly larger than the Debye length. We therefore used a Fab antibody fragment, which is the part of the antibody containing the target binding site [23]. Fab-functionalized

**Fig. 8** Selective detection of IgE using aptamer-functionalized G-FET. The G-FET did not respond to the introduction of PBS, BSA, or SA (*inset*). In contrast, the hole current rapidly decreased after the introduction of IgE (Cited from [19]. Copyright 2011 The Japan Society of Applied Physics)

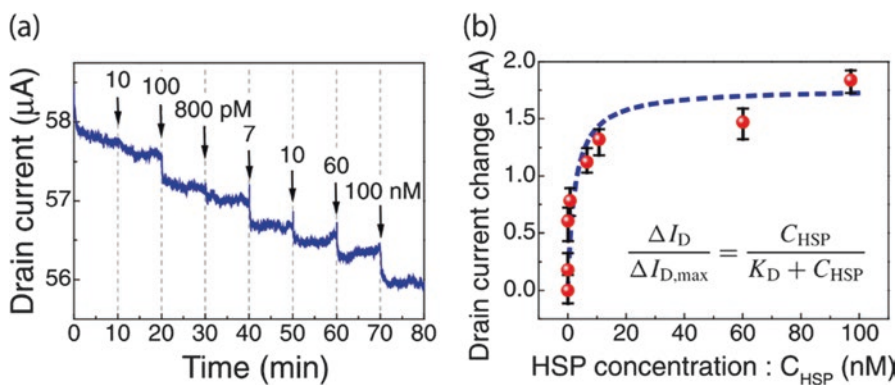
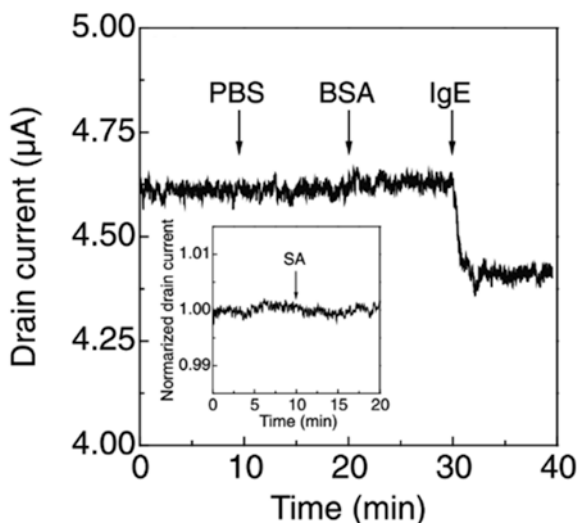


**Fig. 9** HSP detection using Fab-functionalized G-FET. (a) Time course of the drain current upon sequential increases in HSP concentration. (b) Correlation between HSP concentration and the change in drain current. *Inset* shows the Langmuir adsorption isotherm, where  $\Delta I_D$ ,  $\Delta I_{D,\text{max}}$ , and  $K_D$  are the drain current change, the maximum value of  $\Delta I_D$ , and the dissociation constant, respectively.  $K_D$  was estimated as 2.3 nM by fitting the data with the Langmuir adsorption isotherm (*dotted line*) (Cited from [23]. Copyright 2012 The Japan Society of Applied Physics)

G-FET successfully detected its target, heat-shock protein (HSP), at 100 pM HSP (Fig. 9a). Moreover, the correlation between HSP concentration and change in the drain current could be fit well by the Langmuir adsorption isotherm, indicating that Fab binds HSP in a 1:1 ratio and the binding reaction reaches equilibrium as determined by the dissociation constant  $K_D$ .  $K_D$  was estimated by curve fitting to be 2.3 nM (Fig. 9b). These results demonstrate that G-FET can monitor a binding reaction in the equilibrium state. We expect to demonstrate the real-time monitoring of binding kinetics in future work.

## 5 Combination with a Surface-Acoustic Wave Sensor

Wireless operation is important for the practical use of lab-on-a-graphene, since the drain voltage should be applied outside the sample solution to avoid disturbing the measurement. We demonstrated measurements by a G-FET driven by an acoustic current induced by a surface-acoustic wave (SAW) [24].

Single-crystal  $\text{LiTaO}_3$  provided the device substrate to propagate an SH-type SAW. A pair of interdigital transducers (IDTs) was fabricated outside the water reservoir, and a megahertz RF signal was applied. The injected SAW propagated into the G-FET through the solution (Fig. 10a) and induced a current between the source and drain electrodes. This G-FET did not exhibit typical ambipolar transfer characteristics (Fig. 10b, c) because the acoustic current is proportional to the carrier mobility in graphene. Since the SAW moved both holes and electrons in the same direction of propagation, the current direction was reversed at the charge neutrality point of 172 mV where the acoustic current was almost zero. Moreover, the gate voltage at the charge neutrality point was different for G-FETs driven by drain voltage or by SAW because the drain voltage created an extra potential gradient on the graphene. In contrast, the potential gradient created by SAW was small and barely affected the charge neutrality point. SAW transducers were separated from the sample solution and G-FET and provided more precise measurements. We are currently developing this novel device for biosensing.

## 6 Flexible Graphene Sensor

Graphene is a particularly attractive material for the flexible components of wearable sensors, and we reported the fabrication of graphene devices directly on a flexible polymer using a simple new laser irradiation method [25].

Samples were prepared by electron-beam deposition of nickel as a ribbon-shaped thin film on polyethylene naphthalate (PEN) substrates. The middle point of the ribbon was irradiated under vacuum conditions with a focused argon-ion laser. Strong laser irradiation removed the nickel from the surface leaving behind a graphene sheet made from the decomposed PEN surface (Fig. 11a). Two separated nickel ribbons outside the irradiated area were used as the source and drain electrodes. The estimated electric-field-effect mobility of the sample was as low as  $37 \text{ cm}^2/(\text{V s})$ , due to the severe defects in graphene, but ambipolar transfer characteristics of the G-FET were clearly observed when the gate voltage was applied through an ionic liquid and a side-gate electrode (Fig. 11b). Furthermore, a graphene-based strain sensor was demonstrated (Fig. 11c). A concave bend under 0.61% strain resulted in a 35% decrease in the graphene channel resistance, likely due to reduction of the distance between graphene grains. The sensor responded to repeated bending (Fig. 11d), thus showing the promise of flexible graphene devices for applications.

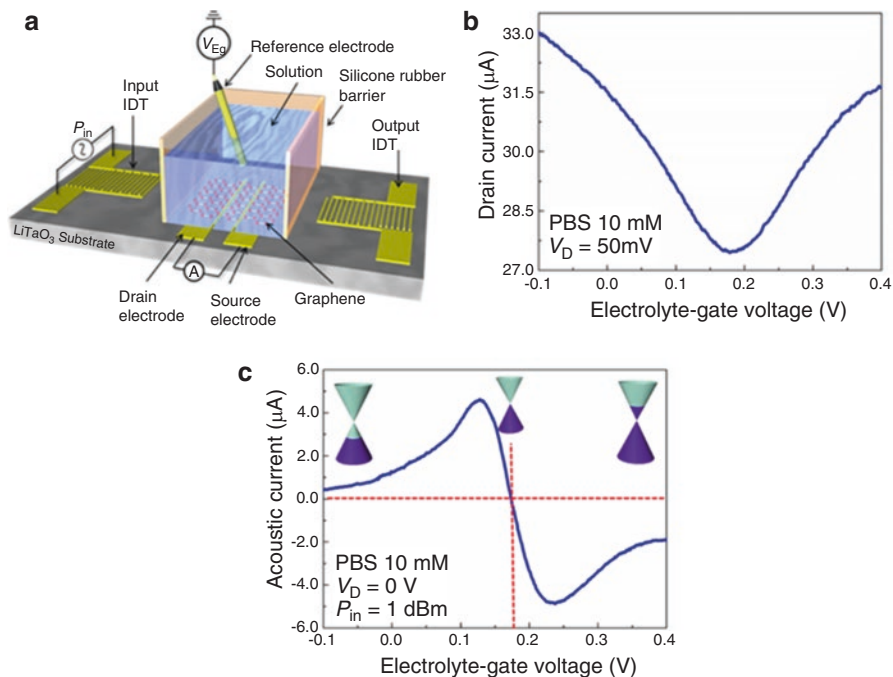


**Fig. 10** (a) Schematic of the SAW-driven G-FET device. (b) The transfer characteristics of G-FET driven by drain voltage. (c) The transfer characteristics of G-FET driven by SAW.  $P_{in}$ : input RF power (Cited from [24]. Copyright 2016 The Japan Society of Applied Physics)

## 7 Conclusion

This article reviewed our research on lab-on-a-graphene and demonstrated attractive applications of graphene. Surface functionalization provides G-FETs that act as highly sensitive biosensors for various biomolecules, such as DNAs and proteins. Also, graphene devices show unique properties when combined with SAW or flexible films. These research results demonstrate the promise of G-FETs for practical use.

## 8 Outlook

For the practical use of G-FETs, several issues still need to be addressed. For example, synthesis for uniform and high-quality graphene is crucial for the conventional application, because exfoliated graphene is randomly transferred on the substrate and the throughput of device fabrication is not sufficient. We are investigating fabrication process of G-FET which uses chemical vapor deposition and achieve the

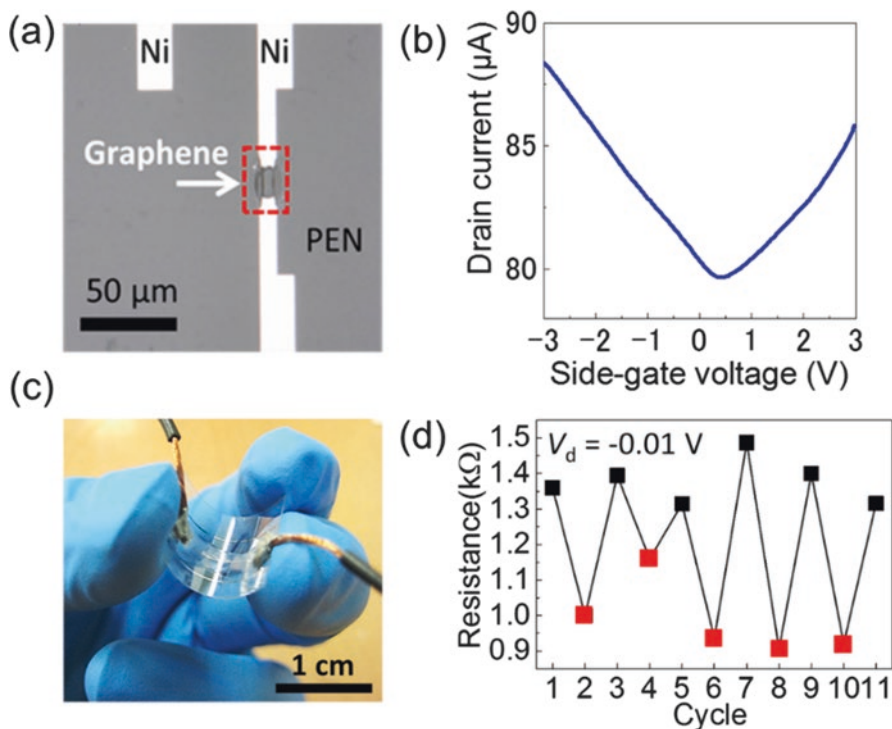


**Fig. 11** (a) Optical microscope image of a channel in a G-FET with a side gate. (b) Transfer characteristics of the G-FET. (c) Photograph of a graphene strain sensor undergoing strain measurement. (d) Repetitive operation of the device under a concave 0.61% strain. Red squares correspond to the bent state

high-performance G-FET comparable to G-FET made by exfoliation method. The other issue is miniaturization of the measurement systems including G-FET device, electrical measurement system, and handling system for biological samples. It is important especially for the clinical use. Microfluidic system is suitable for this purpose. We are now combining our lab-on-a-graphene and the microfluidics.

**Acknowledgements** This research was supported by CREST, JST and Kakenhi, JSPS.

## References

1. K.S. Novoselov et al., *Science* **306**, 666 (2004)
2. A.C. Ferrari et al., *Nanoscale* **7**, 4598 (2015)
3. T. Ando et al., *Rev. Mod. Phys.* **54**, 437 (1982)
4. E.H. Hwang et al., *Phys. Rev. Lett.* **98**, 186806 (2007)
5. K.I. Bolotin et al., *Solid State Commun.* **146**, 351 (2008)

6. Y. Zhang et al., *Nature* **459**, 820 (2009)
7. M.Y. Han et al., *Phys. Rev. Lett.* **98**, 206805 (2007)
8. Z.H. Ni et al., *ACS Nano* **2**, 2301 (2008)
9. S. Bae et al., *Nature Nanotech.* **5**, 574 (2010)
10. M. Kalbacova et al., *Carbon* **48**, 4323 (2010)
11. K.S. Novoselov et al., *Nature* **490**, 192 (2012)
12. K. Matsumoto et al., *J. Phys. D: Appl. Phys.* **47**, 094005 (2014)
13. Y. Ohno et al., *Nano Lett.* **9**, 3318 (2009)
14. D.E. Yates et al., *J. Chem. Soc. Faraday. Trans.* **1**(70), 1807 (1974)
15. Y. Sofue et al., *Jpn. J. Appl. Phys.* **50**, 06GE07 (2011)
16. F. Banhart et al., *ACS Nano* **5**, 26 (2011)
17. P.R. Kidambi et al., *Nano Lett.* **13**, 4769 (2013)
18. K. Maehashi et al., *Sens. Actuators, B* **187**, 45 (2013)
19. Y. Ohno et al., *Jpn. J. Appl. Phys.* **50**, 070120 (2011)
20. T. Fujigaya, N. Nakashima, *Polym. J.* **40**, 577 (2008)
21. Y. Ohno et al., *Jpn. J. Appl. Phys.* **52**, 110107 (2013)
22. Y. Ohno et al., *J. Am. Chem. Soc.* **132**, 18012 (2010)
23. S. Okamoto et al., *Jpn. J. Appl. Phys.* **51**, 06FD08 (2012)
24. S. Okuda et al., *Appl. Phys. Express* **9**, 045104 (2016)
25. Y. Ishibashi et al., *Jpn. J. Appl. Phys.* **56**, 075102 (2017)



# Production of Single- and Few-Layer Graphene from Graphite

Shinya Yamanaka, Mai Takase, and Yoshikazu Kuga

## 1 Electrically Conductive Filler-Polymer Composite

Electrically conductive filler-polymer composites have attracted much interest because of their excellent mechanical and chemical properties. They are promising materials for many applications such as antistatic devices, electromagnetic shielding materials, sensors, and transparent conductive films. The combination of a conductive filler and a nonconductive polymer provides a two-phase system of conductive and nonconductive states. Graphite [1], carbon black [2], tin oxide [3], and titanium black [4] are often used as the conductive filler. When an appropriate amount of graphite particles is mixed with an adhesive resin, heating plywood which provides constant heat by applying a voltage to the conductive bonding layer between wood sheets can be produced [2]. The mass fraction of the conductive graphite plays an essential role in conductivity of the composite resin and its coefficient of variation. A composite resin that included at least ca. 30 mass% of graphite particles yielded a relatively low coefficient of variation for electrical conductivity. Additionally, the composition of the adhesive resin had superior conductivity when the graphite particles were 22.9  $\mu\text{m}$  or less in diameter. Figure 1 shows the influence of graphite particle size on the coefficient of variation (standard deviation divided by the average) of resistance [2]. When the resin contained particles of the largest size of particle (52.5  $\mu\text{m}$  in diameter), the coefficient of variation was high. On the other hand, the coefficient of variation decreased with decrease in the particle size, indicating that the density of particles affected the percolation threshold.

Many researchers have investigated the effects of filler properties (e.g., particle size, shape, and interaction between the filler and polymer) on system transfer from a nonconductive state to a conductive state, called percolation threshold.

---

S. Yamanaka (✉) • M. Takase • Y. Kuga  
Department of Applied Sciences, Muroran Institute of Technology,  
Mizumoto-cho 27-1, Muroran 050-8585, Japan  
e-mail: [syama@mmm.muroran-it.ac.jp](mailto:syama@mmm.muroran-it.ac.jp)

**Fig. 1** Influence of particle size on the coefficient of variation of resistance. The numbers in parenthesis are laser diffraction diameters of the graphite particles. This figure is reproduced from J. Soc. Powder Technol., Japan, **49**, 164 (Copyright (2012), with permission)

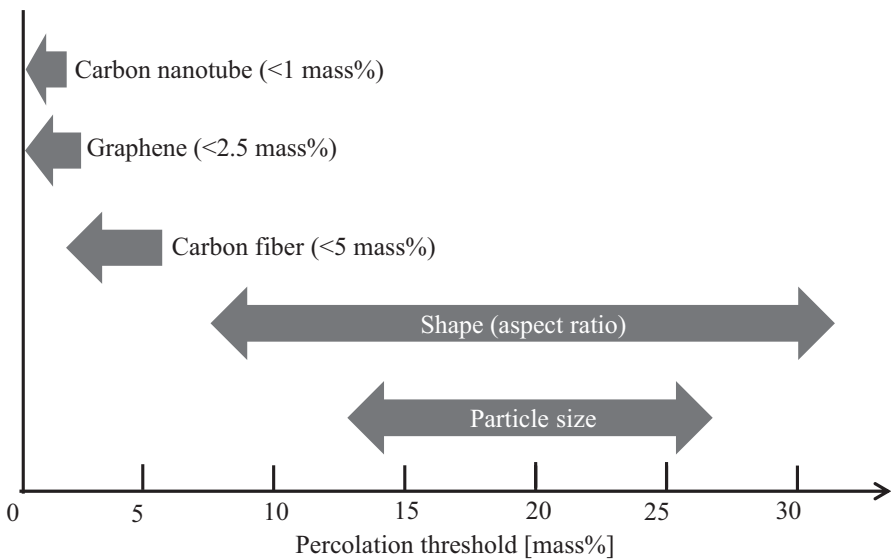
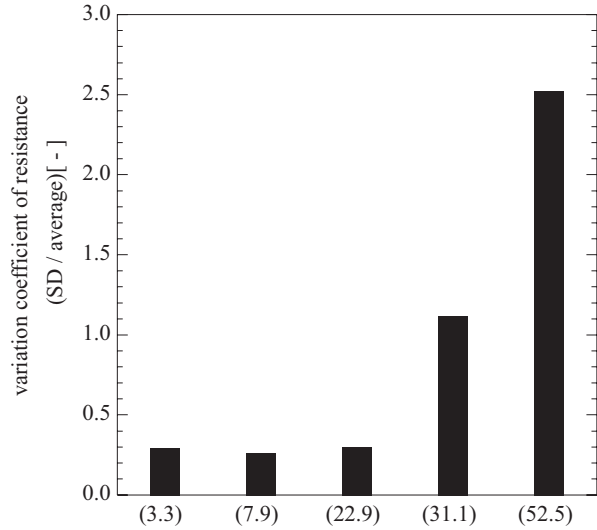


**Fig. 2** Percolation thresholds of several electrically conductive filler-polymer composites. Effects of particle size and shape on the percolation threshold

Figure 2 shows the relationships between filler properties and percolation threshold. According to Fig. 2, we give a brief outline of electrically conductive filler-polymer composites.

Nagata et al. reported the relation between particle size of the filler and percolation threshold [5]. They used graphite particles with particle sizes of 2.1–82.6 μm as the filler and low-density polyethylene as the polymer. The minimum value of

percolation threshold was observed when the polymer was filled with graphite particles of 2.1  $\mu\text{m}$  in size. The threshold value was increased from 13.5 to 25.5 mass% with increase in particle size.

The particle shape [6–12], mainly focusing on the aspect ratio, had a direct impact on percolation behavior. When the aspect ratio was 1 (meaning a spherical particle), the percolation threshold was over 25 mass%, whereas when the ratio was over 10, the threshold was below 10 mass%. The viscosity of the composite polymer was dramatically changed to reflect the dispersion state (network structure) of the filler in a polymeric matrix. The fillers of high aspect ratio were preferred for the reason that electrically conductive filler-polymer composites were obtained with low mass fraction of the filler. From this point of view, carbon nanotubes (CNTs) are most commonly used as the filler because a CNT has high aspect ratio. More than 1000 articles have been published every year over the past decade [13]. The development of a dispersion process for CNTs has been extensively studied [13]. A CNT-polymer composite shows high electrical conductivity ( $10^{-2} \text{ S/cm} = 10^2 \Omega\text{-cm}$ ) when CNTs of 1 mass% or less are added [14–19].

As well as filler particle size and shape, dispersion state in which the filler particles form a network structure in the polymer can be controlled by wettability between filler particles and the polymer [20]. Wu et al. prepared a composite resin composed of vapor-grown carbon fiber (aspect ratio of 50) and polymethyl methacrylate [21]. When high-density polyethylene was added to the composite resin, electrical conductivity was remarkably increased; for instance, with 1–5 mass% inclusion in the composite resin, the percolation threshold was reduced from 8 to 4 phr (per hundred parts of the matrix). Wu et al. proposed that the high-density polyethylene selectively adsorbed on the edge of carbon fiber, and the fiber could form a network structure into the resin.

## 2 Graphite Nanosheets as an Electrical Conductive Filler

As mentioned above, the introduction of particles with a high aspect ratio into the polymer matrix is one of the common approaches to obtain an electrically conductive polymer with the smallest possible amount of filler particles. Vapor-grown carbon fibers, carbon nanotubes, and thin graphite nanosheets have often been used as high-aspect fillers. Recently, significant improvements in the mechanical and electrical properties of polymer composite materials have been achieved with the use of a small amount of carbon fillers [22–24]. Highly crystalline natural graphite shows excellent electrical and lubricant properties, and grinding has often been used to obtain graphite sheets with high crystallinity. Graphite is a fascinating substance because the grinding atmosphere has a great impact on its reduction ratio [25–27]. Ong et al. demonstrated that the reduction ratio of graphite was decreased under an oxygen atmosphere [44]. Kim et al. carried out grinding under reduced pressure in which partial pressure of oxygen and water vapor was suppressed, and they obtained fine graphite particles with maintenance of crystallinity [28]. With these properties

in mind, we have produced fine graphite sheets, which exhibit high electrical conductivity, by grinding natural graphite particles under well-controlled milling atmospheres such as alcoholic vapor [26], nitrogen, hydrogen, oxygen, and vacuum [25]. Both a flaky shape of the graphite sheets and size reduction of the ground products with high crystallinity could be obtained in the milling process.

Intensive research has been carried out to find new methods for preparation of graphite sheets and mono- and few-layer graphene sheets. However, large-scale, economical production of thin graphite sheets with high crystallinity remains challenging. Graphene is a single-atom-thick sheet of carbon with favorable properties, such as the ability to conduct light and electrons, making it potentially suitable for a variety of devices and applications, including electronics, sensors, and photonics. In 2004, Novoselov and coworkers discovered single-layer graphene by peeling graphene from a graphite body [29]. Although their method is not suitable for large-scale production of graphene, their work did spur globally increasing interest in graphene materials. For progress from the laboratory to commercial applications, it is necessary to develop scalable production methods to obtain large quantities of defect-free graphene. Up to now, there have been two main processes for producing thin graphite sheets (including graphene). One is epitaxial growth on the substrate [30] and the other is large-scale exfoliation [31–34]. Liquid phase exfoliation is the most economical owing to low costs of manufacturing equipment and raw materials. Table 1 summarizes the leading exfoliation techniques for the production of single- and few-layer graphene.

Paton et al. showed that high-shear mixing of graphite in suitable stabilizing liquids results in large-scale exfoliation to give dispersions of graphene nanosheets [34]. By fully characterizing the scaling behavior of the graphene production rate, they achieved liquid volumes from hundreds of milliliters up to hundreds of liter and more. Hernandez et al. reported exfoliation of graphite by means of sonication in the organic solvent N-methyl-pyrrolidone [31]. They achieved a yield of mono-layer graphene of up to 1 mass%. In addition, thin graphite nanosheets have been produced by mechanical shearing in a comminuting mill. In this case, a surfactant or a dispersion agent is usually administered to prevent agglomeration and restacking of the delaminated sheets. Knieke et al. reported a scalable production scheme for ultrathin graphite sheets and graphene monolayers [32]. Mono- and multilayer graphene sheets assisted with a surfactant of sodium dodecyl sulfate have been prepared in a stirred-media mill in mild milling conditions, yielding about 2.5 mass% at peeling times of 3 h [32].

**Table 1** Production of single- and few-layer graphene dispersion, liquid phase exfoliation techniques

Technique	Solvent	Sheet conc. (mg/mL)	Processing time (min)	Refs.
High-shear mixer	Water	~0.1	30	[34]
Sonication	N-methyl-pyrrolidone	~0.01	30	[31]
Sonication	Water	~0.05	30	[33]
Ball milling	Water	~25	180	[32]

### 3 Production of Graphite Nanosheets from Graphite Intercalation Compounds

Graphite intercalation compounds (GICs) are well-known complex materials in which guest molecules can be intercalated between the carbon layers. This specific characteristic of the interlayer space is based on the most famous application of a hydrogen storage material [35] and an anode material for a lithium ion battery [36]. The interlayer distances are 0.335 nm for the interlayer separation of intrinsic graphite and 0.88 nm [45] for potassium (K), tetrahydrofuran (THF), and GICs (K-THF-GICs). This expanded interlayer is superior delamination, that is, GICs could be raw material for single- and few-layer graphene. When the intercalate layers are arranged periodically, the stage index,  $n$  ( $n = \text{I, II, III, ...}$ ), is defined as the number of graphene layers between two adjacent intercalate layers, e.g., a stage II GIC has each two adjacent graphene layers sandwiched by two intercalant layers. Shih et al. demonstrated a solution-phase technique for the production of bilayer or trilayer graphene from the stage II or III GICs [37].

We have reported potentially scalable production of highly crystalline graphite sheets by mechanical grinding of graphite intercalation compounds (GICs) without a surfactant [1]. Natural graphite (found in Brazil) with a mean particle size of 19.6  $\mu\text{m}$  was used as a starting material. The feed natural graphite, K, THF, and naphthalene were used for synthesis of GICs. A graphite sheet was used as the starting material for graphite sheet-based phenolic composites. We added 10.0 mass% of graphite sheets to 1.0 g phenolic resin and ground the mixture for 5 min in an agate mortar with a pestle. The resulting composite resin was coated onto a commercial glass slide, dried at 60  $^{\circ}\text{C}$  for 1 h, and heated to 130  $^{\circ}\text{C}$  for 5 min in order to polymerize the resin.

To explain the interlayer stability of the present graphite sheets, it is useful to calculate the van der Waals interaction energy between the graphite sheets [32]. Because electrostatic interactions are negligible in a relatively low dielectric constant medium of THF [38], we calculated the van der Waals interlayer interactions per unit contact area as a function of the thickness of the delaminated sheet. The distances between the two sheets were chosen to be 0.335 nm for the interlayer separation of intrinsic graphite and 0.88 nm [45] for K-THF-GICs. The required delamination energies for the intrinsic graphite interlayer and that for the expanded one are ca.  $15 \times 10^{-3}$  and  $2.2 \times 10^{-3}$   $\text{J/m}^2$ , respectively (Fig. 3, [1]). The calculated results indicated that the required energy for delamination of K-THF-GIC takes more than 85% less energy than that of feed natural graphite. This result clearly indicates that the expanded interlayer is energetically favorable for delamination, i.e., the thickness of the graphite sheets in the milling pot is significantly affected by the stage structure of ternary GICs.

The production of thin graphite sheets is schematically shown in Fig. 4. K-THF-GICs were used as the starting material for thin graphite sheets. Planetary-ball milling was carried out to apply a shear stress that leads to delamination of the thin graphite sheets from GICs. The thickness of the graphite sheets was roughly

**Fig. 3** Interaction energies per unit area between two plates of finite thickness. This figure is reprinted from *Carbon* **50**, 5027–5033, production of thin graphite sheets for a high electrical conductivity film by the mechanical delamination of ternary graphite intercalation compounds (Copyright (2012), with permission from Elsevier)

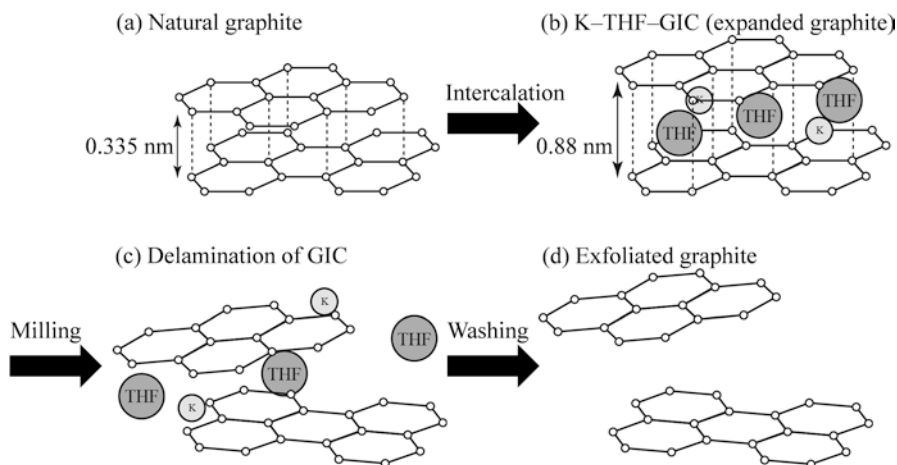
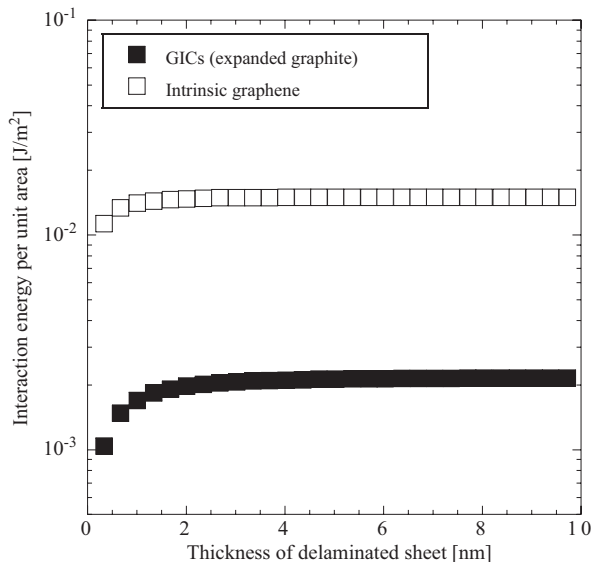


**Fig. 4** Scheme of thin graphite sheet production. This figure is reprinted from *Carbon* **50**, 5027–5033, production of thin graphite sheets for a high electrical conductivity film by the mechanical delamination of ternary graphite intercalation compounds (Copyright (2012), with permission from Elsevier)

controlled by the stage structure of K-THF-GICs. Delamination may occur in the intercalated layer because of the weaker van der Waals interaction between expanded graphene sheets (0.88 nm, [45]) than between intrinsic graphene sheets (0.335 nm) as mentioned above.

We also investigated the influence of multistage GICs on the conductive properties of the composite resin. Figure 5 shows typical SEM micrographs of the feed

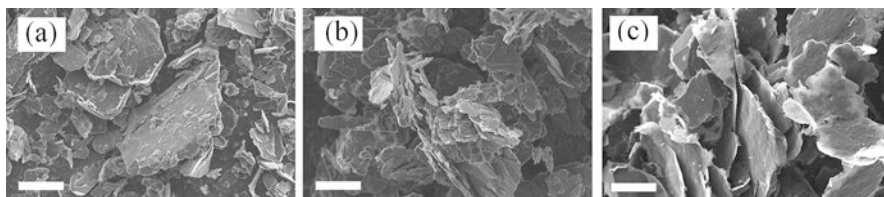
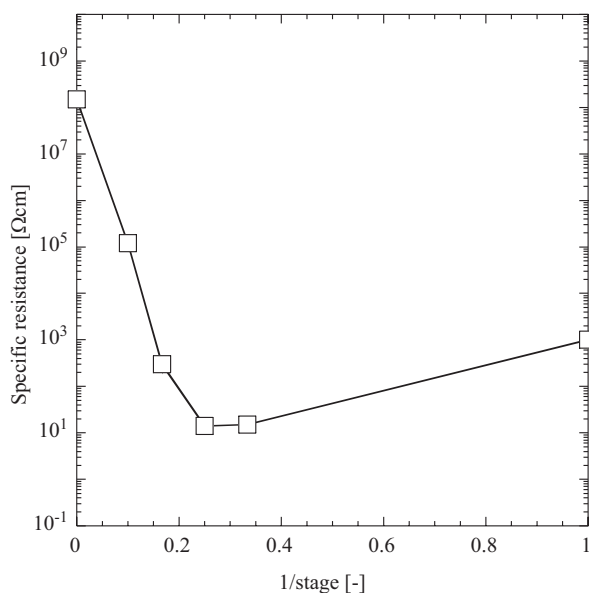


**Fig. 5** SEM images of feed graphite particles and their ground products. (a) Feed natural graphite particles, (b) ground products of the feed graphite into THF, and (c) exfoliated products of grinding stage IV K-THF-GIC. The scale bar is 20  $\mu\text{m}$ . This figure is reproduced from *Carbon* 50, 5027–5033, production of thin graphite sheets for a high electrical conductivity film by the mechanical delamination of ternary graphite intercalation compounds (Copyright (2012), with permission from Elsevier)

**Fig. 6** Structural dependency of estimated specific resistance at 10 mass% of the filled graphite and sheets. This figure is reproduced from *Carbon* 50, 5027–5033, production of thin graphite sheets for a high electrical conductivity film by the mechanical delamination of ternary graphite intercalation compounds (Copyright (2012), with permission from Elsevier)



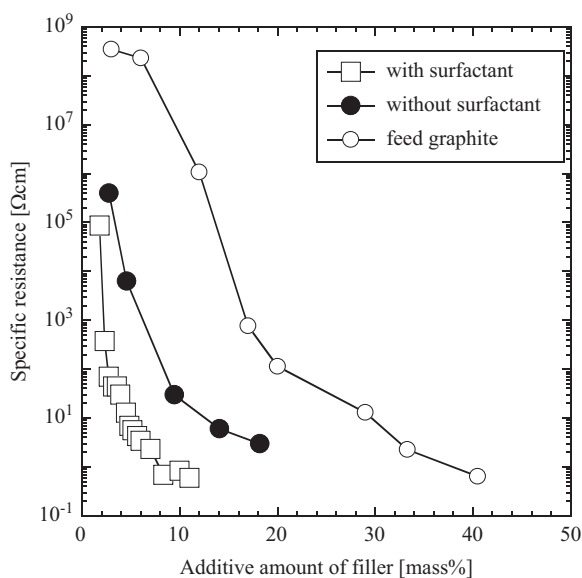
natural graphite particles and several representative pictures of ground products. The initial graphite particles had a thick stacking structure (Fig. 5a). When the feed natural graphite particles were ground into the THF solution, the particles were very similar in thickness as shown in Fig. 5b. On the other hand, as shown in Fig. 5c, the ground product prepared by stage IV K-THF-GIC had some exfoliated graphite interlayers and delamination of the graphite sheets.

The specific resistance of the composite films was measured for several weight fractions of the filling graphite products. Figure 6 shows the influence of stage structures on specific resistance of the films. In Fig. 6, the horizontal axis denotes the inverse of stage structure, representing the composite film using stage  $\infty$  in the same figure. By infinity, we denote the ground products of the feed natural graphite being milled into the THF solvent. Specific resistances were measured when 10 mass% of

the conductive material was added. Note that the specific resistance for the composite film including the feed graphite was  $10^7 \Omega\cdot\text{cm}$ . The composite film made from graphite ground into THF had  $10^2$ – $10^6$  higher resistances than those of the film filled with natural graphite at every weight fraction. It should be noted that there is an optimal stage structure for obtaining a highly conductive film. This is due to the combined effects of the aspect ratio and crystallinity. When the number of percolated graphite sheets was increased, the specific resistance decreased, reaching ca.  $10^1 \Omega\cdot\text{cm}$  for the composite filled with exfoliated products of grinding stage III or IV K–THF–GIC. A slight increase in specific resistance of  $10^3 \Omega\cdot\text{cm}$  was observed for the composite of stage I K–THF–GIC.

Now we discuss the redispersibility of prepared graphite sheets during the collection and film preparation process. Agglomeration or restacking of the peeling sheets reduces the apparent particle number density, which has an enormous impact on the film resistance. A surfactant is needed to prevent agglomeration and restacking of delaminated sheets. Sodium dodecyl sulfate [32, 39], sodium deoxycholate [40, 41], and TritonX [42, 43] have been commonly used as surfactants that adsorb onto the carbon-based particles, resulting in strong repulsive forces. The effect of a surfactant on the dispersibility of the flaky graphite into phenolic resin is shown in Fig. 7. We used TritonX as the surfactant, which was added in the wet grinding process. It should be emphasized that a surfactant is needed to avoid restacking or agglomeration of the peeling sheets during the grinding process. We believe that many comminuting processes using small beads should be applicable to the delamination of expanded layered materials.

**Fig. 7** Specific resistances of composite films including feed graphite particles and graphite sheets obtained by grinding of stage IV K–THF–sGIC with and without a surfactant





## 4 Summary and Future Perspectives

In this chapter, research on several techniques for production of single- and few-layer graphene is summarized. We report our production technique for graphite nanosheets via GICs. Crystalline graphite nanosheets were successfully produced from natural graphite powder. Composite films prepared by mixing phenolic resin and graphite nanosheets showed much higher electrical conductivities than those of films from natural graphite particles. We also found that the stage structure of synthetic graphite intercalation compounds affected film conductivity. There is an optimal stage structure of GICs for obtaining highly conductive films. The composite filled with the exfoliated products of grinding stages III and IV K-THF-GIC displayed the lowest resistance at 10 mass% of the weight fraction. The scheme proposed in this study is scalable production of thin graphite sheets as the starting material for composite resins with high conductivity. In our research, we did not show the dispersion state of graphite sheets in the composite films in detail. The effect of a surfactant on the dispersibility of the graphite sheets into the resin is now investigated.

Both now and in the future, it will be necessary to develop mass production techniques for single- and few-layer of defect-free graphene. The liquid phase exfoliation of graphite into single-layer or few-layer graphene is promising approach because of low costs of manufacturing equipment and raw materials. However, the main drawback of using the liquid exfoliation is that the obtained graphene dispersion is at relatively low concentrations, typically  $<0.1$  mg/mL. Improvements to produce concentrated graphene dispersion will be continued.

## References

1. S. Yamanaka, T. Nishino, T. Fujimoto, Y. Kuga, Production of thin graphite sheets for a high electrical conductivity film by the mechanical delamination of ternary graphite intercalation compounds. *Carbon* **50**, 5027–5033 (2012)
2. Y. Hirabayashi, S. Nakahira, S. Yamanaka, T. Fujimoto, Y. Kuga, Characterization of conductivity of graphite-phenolic resin composite and its application to heating plywood. *J. Soc. Powder Technol. Jpn.* **49**, 164–170 (2012)
3. A. Wakabayashi, Y. Sasakawa, T. Dobashi, T. Yamamoto, Self-assembly of tin oxide nanoparticles: localized percolating network formation in polymer matrix. *Langmuir* **22**, 9260–9263 (2006)
4. K. Ichimura, *Technologies for LCD Color Filters* (CMC, Tokyo, 2010)
5. K. Nagata, H. Iwabuki, H. Nigo, Effect of particle size of graphites on electrical conductivity of graphite/polymer composite. *Compos. Interfaces* **6**, 483–495 (1998)
6. M.H. Al-Saleh, U. Sundararaj, Electromagnetic interference shielding mechanisms of CNT/polymer composites. *Carbon* **47**, 1738–1746 (2009)
7. D.M. Bigg, Mechanical, thermal, and electrical properties of metal fiber-filled polymer composites. *Plym. Eng. Sci.* **19**, 1188–1192 (1979)
8. I.-G. Chen, W.B. Johnson, Alternating-current electrical properties of random metal-insulator composites. *J. Mater. Sci.* **26**, 1565–1576 (1991)

9. T. Katsura, M.R. Kamal, L.A. Utracki, Electrical and thermal properties of polypropylene filled with steel fibers. *Polym. Compos.* **5**, 193–202 (1985)
10. T. Katsura, M.R. Kamal, L.A. Utracki, Some properties of polypropylene filled with metal fibers. *Polym. Compos.* **6**, 282–295 (1985)
11. G.G. Tibbetts, M.L. Lake, K.L. Strong, B.P. Rice, A review of the fabrication and properties of vapor-grown carbon nanofiber/polymer composites. *Compos. Sci. Technol.* **67**, 1709–1718 (2007)
12. Y.S. Wang, M.A. O'Gurkis, T. Lindt, Electrical properties of exfoliated-graphite filled polyethylene composites. *Polym. Compos.* **7**, 349–354 (1986)
13. P.-C. Ma, N.A. Siddiqui, G. Marom, J.-K. Kim, Dispersion and functionalization of carbon nanotubes for polymer-based nanocomposites: a review. *Compos. Part A* **41**, 1345–1367 (2010)
14. W. Bauhofer, J.Z. Kovacs, A review and analysis of electrical percolation in carbon nanotube polymer composites. *Compos. Sci. Technol.* **69**, 1486–1498 (2009)
15. U. Dettlaff-Weghowska, M. Kaempgen, B. Hornbostel, V. Skakalova, J.P. Wang, J.D. Liang, Conducting and transparent SWNT/polymer composites. *Phys. Status Solidi B* **243**, 3440–3444 (2006)
16. B. Hornbostel, P. Potschke, J. Kotz, S. Roth, Single-walled carbon nanotubes/polycarbonate composites: basic electrical and mechanical properties. *Phys. Status Solidi B* **243**, 3445–3451 (2006)
17. A. Mierczynska, M. Mayne-L'Hermite, G. Boiteux, Electrical and mechanical properties of carbon nanotube/ultrahigh-molecular-weight polyethylene composites prepared by a filler pre-localization method. *J. Appl. Polym. Sci.* **105**, 158–168 (2007)
18. J.K.W. Sandler, J.E. Kirk, I.A. Kinloch, M.S.P. Shaffer, A.H. Windle, Ultra-low electrical percolation threshold in carbon-nanotube-epoxy composites. *Polymer* **44**, 5893–5899 (2003)
19. T. Wang, C.H. Lei, A.B. Dalton, C. Creton, Y. Lin, K.A.S. Fernando, Y.P. Sun, M. Manea, J.M. Asua, J.L. Keddie, Waterborne, nanocomposite pressure-sensitive adhesives with high tack energy, optical transparency, and electrical conductivity. *Adv. Mater.* **18**, 2730–2734 (2006)
20. G. Wu, T. Miura, S. Asai, M. Sumita, Carbon black-loading induced phase fluctuations in PVDF/PMMA miscible blends: dynamic percolation measurements. *Polymer* **42**, 3271–3279 (2001)
21. G. Wu, T. Miura, S. Asai, M. Sumita, A self-assembled electric conductive network in short carbon fiber filled poly(methyl methacrylate) composites with selective adsorption of polyethylene. *Macromolecules* **32**, 3534–3536 (1999)
22. M.H. Al-Saleh, U. Sundararaj, A review of vapor grown carbon nanofiber/polymer conductive composites. *Carbon* **47**, 2–22 (2009)
23. G. Chen, D. Wu, W. Weng, C. Wu, Exfoliation of graphite flake and its nanocomposites. *Carbon* **41**, 619–621 (2003)
24. S. Stankovich, D.A. Dikin, G.H.B. Dommett, K.M. Kohlhaas, E.J. Zimney, E.A. Stach, R.D. Piner, S.B.T. Nguyen, R.S. Ruoff, Graphene-based composite materials. *Nature* **442**, 282–286 (2006)
25. Y. Kuga, M. Shirahige, Y. Ohira, K. Ando, Production of finely ground natural graphite particles with high electrical conductivity by controlling the grinding atmosphere. *Carbon* **40**, 695–701 (2002)
26. Y. Kuga, M. Shirahige, T. Fujimoto, Y. Ohira, A. Ueda, Production of natural graphite particles with high electrical conductivity by grinding in alcoholic vapors. *Carbon* **42**, 293–300 (2004)
27. M. Shirahige, J. Iida, T. Fujimoto, Y. Kuga, M. Kawai, J. Katamura, Characteristics and hydrogen desorption property of nanostructured graphite produced by grinding in vacuum atmospheres. *J. Soc. Powder Technol. Jpn.* **42**, 185–191 (2005)
28. B.G. Kim, S.K. Choi, H.S. Chung, J.J. Lee, F. Saito, Grinding characteristics of crystalline graphite in a low-pressure attrition system. *Powder Technol.* **126**, 22–27 (2002)
29. K.S. Novoselov, A.K. Geim, S.V. Morozov, D. Jiang, Y. Zhang, S.V. Dubonos, I.V. Grigorieva, A.A. Firsov, Electric field effect in atomically thin carbon films. *Science* **306**, 666–669 (2004)

30. C. Berger, Z. Song, X. Li, X. Wu, N. Brown, C. Naud, D. Mayou, T. Li, J. Hass, A.N. Marchenkov, E.H. Conrad, P.N. First, W.A. de Heer, Electronic confinement and coherence in patterned epitaxial graphene. *Science* **312**, 1191–1196 (2006)
31. Y. Hernandez, V. Nicolosi, M. Lotya, F.M. Blighe, Z. Sun, S. De, I.T. McGovern, B. Holland, M. Byrne, Y.K. Gun'Ko, J.J. Boland, P. Niraj, G. Duesberg, S. Krishnamurthy, R. Goodhue, J. Hutchison, V. Scardaci, A.C. Ferrari, J.N. Colema, High-yield production of graphene by liquid-phase exfoliation of graphite. *Nat. Nanotechnol.* **3**, 563–568 (2008)
32. C. Knieke, A. Berger, M. Voigt, R.N.K. Taylor, J. Rohrl, W. Peukert, Scalable production of graphene sheets by mechanical delamination. *Carbon* **48**, 3196–3204 (2010)
33. M. Lotya, Y. Hernandez, J.K. Paul, R.J. Smith, V. Nicolosi, L.S. Karlsson, F.M. Blighe, S. De, Z. Wang, I.T. McGovern, G.S. Duesberg, J.N. Coleman, Liquid phase production of graphene by exfoliation of graphite in surfactant/water solutions. *J. Am. Chem. Soc.* **131**, 3611–3620 (2009)
34. K.R. Paton, E. Varrla, C. Backes, R.J. Smith, U. Khan, A. O'Neill, C. Boland, M. Lotya, O.M. Istrate, P. King, T. Higgins, S. Barwich, P. May, P. Puczarski, I. Ahmed, M. Moebius, H. Pettersson, E. Long, J. Coelho, S.E. O'Brien, E.K. McGuire, B.M. Sanchez, G.S. Duesberg, N. McEvoy, T.J. Pennycook, C. Downing, A. Crossley, V. Nicolosi, J.N. Coleman, Scalable production of large quantities of defect-free few-layer graphene by shear exfoliation in liquids. *Nat. Mater.* **13**, 624–630 (2014)
35. A.G. Klechikov, G. Mercier, P. Merino, S. Blanco, C. Merino, A.V. Talyzin, Hydrogen storage in bulk graphene-related materials. *Microporous Mesoporous Mater.* **210**, 46–51 (2015)
36. S.J. An, J. Li, C. Daniel, D. Mohanty, S. Nagpure, D.L. Wood III, The state of understanding of the lithium-ion-battery graphite solid electrolyte interphase (SEI) and its relationship to formation cycling. *Carbon* **105**, 52–76 (2016)
37. C.-J. Shih, A. Vijayaraghavan, R. Krishnan, R. Sharma, J.-H. Han, M.-H. Ham, Z. Jin, S. Lin, G.L.C. Paulus, N.F. Reuel, Q.H. Wang, D. Blankschtein, M.S. Strano, Bi- and trilayer graphene solutions. *Nat. Nanotechnol.* **6**, 439–445 (2011)
38. J.N. Israelachvili, *Intermolecular and Surfaces Forces*, 2nd edn. (Academic, London, 1992)
39. M. Alanyalioglu, J.J. Segura, J. Oro-Sole, N. Casan-Pastor, The synthesis of graphene sheets with controlled thickness and order using surfactant-assisted electrochemical processes. *Carbon* **50**, 142–152 (2012)
40. G.P. Moriarty, J.N. Wheeler, C. Yu, J.C. Grunlan, Increasing the thermoelectric power factor of polymer composites using a semiconducting stabilizer for carbon nanotubes. *Carbon* **50**, 885–895 (2012)
41. H. Xu, H. Abe, M. Naito, Y. Fukumori, H. Ichikawa, S. Endoh, K. Hata, Efficient dispersing and shortening of super-growth carbon nanotubes by ultrasonic treatment with ceramic balls and surfactants. *Adv. Powder Technol.* **21**, 551–555 (2010)
42. N. Erdinç, S. Göktürk, M. Tunçay, A study on the adsorption characteristics of an amphiphilic phenothiazine drug on activated charcoal in the presence of surfactants. *Colloids Surf. B* **75**, 194–203 (2010)
43. M. Majumder, C. Rendall, M. Li, N. Behabtu, J.A. Eukel, R.H. Hauge, H.K. Schmidt, M. Pasquali, Insights into the physics of spray coating of SWNT films. *Chem. Eng. Sci.* **65**, 2000–2008 (2010)
44. T.S. Ong, H. Yang, Effect of atmosphere on the mechanical milling of natural graphite. *Carbon* **38**, 2077–2085 (2000)
45. O. Tanaïke, M. Inagaki, Ternary intercalation compounds of carbon materials having a low graphitization degree with alkali metals. *Carbon* **35**, 831–836 (1997)

# Graphene-Based Coatings for Dental Implant Surface Modification

Alina Pruna, Daniele Pullini, and Andrada Soanca

## 1 Introduction

Considering the increase in the median age of population, the design, development and commercialisation of synthetic materials for bone repair/replacement have attracted significant concerns. In this respect, tissue engineering addresses previously irreparable tissues/organs and has the goal of replacing diseased/damaged tissue with biologic-like substitutes that are able to restore and maintain normal functions. The strategies adopted in tissue engineering involve the cells, signalling molecules, and natural or artificial scaffolds. The scaffolds in regenerative medicine serve for the repopulation and specialisation of stem cells, blood vessels and extra-cellular matrices [1].

The most important criteria under the aspect of designing artificial biomaterial grafts highlights the high degree of compatibility with natural bone tissues, with special attention on the structure, morphology, topography, chemistry, mechanical properties and biological functionalities [2]. Since surface morphology of a scaffold is known to strongly affect the attachment of cells and tissues from the environment after implantation [3], the degree of osteointegration becomes highly dependent on the surface properties of implant materials, indicating the

---

A. Pruna (✉)

Center for Surface Science and Nanotechnology, University Politehnica of Bucharest,  
Bucharest, Romania

e-mail: [ai.pruna@gmail.com](mailto:ai.pruna@gmail.com)

D. Pullini

Centro Ricerche Fiat, Orbassano, Torino, Italy

A. Soanca (✉)

Faculty of Dental Medicine, Iuliu Hatieganu University of Medicine and Pharmacy,  
Cluj-Napoca, Romania

e-mail: [andrapopovici@gmail.com](mailto:andrapopovici@gmail.com)

modification of implant surface as a viable approach for providing with increased surface area for the cellular attachment.

On the other hand, the nanomaterial design, synthesis, characterisation and application faced a tremendous advance as biomaterials in the last decades which led to the discovery of novel materials-based therapies and devices for disease treatments and diagnostics [4]. Carbon-based nanomaterials have been widely explored as implant and device alternatives for various biomedical applications and for stem cell therapies and tissue engineering platforms thanks to their tunable chemistry and excellent mechanical, tribological and corrosion properties [5–7].

Among these, graphene nanomaterials have emerged as promising nanoplat-forms with huge potential for biomedical applications thanks to their excellent physical, chemical and mechanical properties and have been indicated to accelerate the growth, proliferation and differentiation of stem cells [8]. However, due to the short time span since discovery, the reports on the biomedical applications of graphene nanomaterials have appeared only in the last several years. In this chapter, the current state of the art on biomedical applications of graphene for tissue engineering is summarised with focus on graphene application for surface modification of bio-material surface in dental implantology.

## 2 Surface Modification in Dental Implantology

Dental implants first appeared in the early 1930s, but their clinical use is widespread since about 30 years. Because of the high predictability of success, they represent a reliable treatment for replacing missing teeth. The implant surfaces are expected to both enhance the growth of living cells and simultaneously inhibit bacteria. Although the regeneration of periodontium is usually disregarded in a direct insertion of the implant into the alveolar bone in order to achieve osseointegration, the biological properties of bone substitutes are essential for the osteoconductive function [9], because they affect the development of the cellular events towards successful periodontal regeneration. The regenerative potential is thus dependent on genetic determinants, physiological and systemic conditions and local disease state infection or scars.

The gold standard in implant dentistry is titanium (Ti) which has the longest traceable record of predictable clinical performance. The high success rates of Ti implants are mainly attributed to a native oxide layer (3 to 10 nm thick) formed at the surface that is remarkably resistant to corrosion and is biocompatible. Other materials, such as bioactive ceramics showed high potential for bone fixation as they can promote a faster attachment to bone tissue and a mechanically stable interface between implant and bone can be established. Recently full-ceramic implants such as  $ZrO_2$  have been developed with comparable biological responses to Ti [10, 11],  $ZrO_2$  ceramic surface being shown to greatly minimise biocorrosion. However,  $ZrO_2$  is brittle and more expensive than metallic dental implants.

Although the design of dental materials advanced much lately, failures still occur mainly due to biological inertness exhibited by Ti and its alloys which leads to poor cell adhesion, proliferation and poor integration at the tissue/implant interface after implantation [12]. Such materials usually cease to function in the long term because of insufficient biocompatibility, wear, disease or injury.

As the protective oxide layer could fail in the long term and, thus, expose the substrate to accelerated corrosion in oral cavity, the biocompatibility of a dental implant needs to consider its corrosion properties, as well. These properties represent a pertinent clinical issue, since the implant faces a severe corrosion environment not only at implant/bone interface (at the radicular portion of the implant) but also at the gingival/implant one. Moreover, the oral cavity is known to be subjected to wide changes in pH and fluctuation in temperature. Saliva is a complex secretion that regulates the pH in the oral cavity, mostly via bicarbonate and some calcium phosphate buffering [13]. The saliva also has a rinsing effect on teeth, contributes to bacteria clearance and contains antibacterial proteins (e.g. lysozyme, lactoferrin) and components of the immune system (e.g. immunoglobulins). Many factors including age, diseases and medication can affect the quantity (and quality) of saliva. Its flow rate controls the solute concentrations in the oral cavity, and its decrease or absence usually leads to higher food retention or enamel demineralisation due to the acid environment formed when the salivary buffering capacity is lost. Therefore, the corrosion can weaken the restoration and inevitably results in the release of metal ions. In this respect, increasing evidence was found that Ti is released into adjacent tissue [14] and it might even be an allergen [15], despite its high general corrosion resistance. In order to inhibit the corrosion process, protective coatings can be used to isolate the metal from the environment, such as body fluids. Current techniques in bone tissue engineering based on Ti or ceramics can involve also weakness of osteointegration in the long term, inflammation at the implantation site or biomechanical mismatch. There are reports on implant failure highlighting the implant-related infections which can result in higher economic and social associated cost. In order to prevent such infections and improve interactions with the surrounding tissues, antimicrobials could be added to implants in order to reduce bacterial colonisation.

The interaction of implant surface with the proteins can result in a strong immunological response and the induced biochemical reactions may affect negatively the device functionality. These clinical problems determined further research in this field, including interventions on implants characteristics in terms of biocompatibility (physicochemical properties and surface bioactivity) and behaviour of cellular environment involved in osteointegration process.

Advanced new surfaces to control the implant osteointegration and the interactions between biomedical implants and the surrounding biological environment in order to improve their biocompatibility and bioactivity and enhance their corrosion resistance represent the focus of many researches. These designs are aimed to keep intact the bulk mechanical properties while inducing changes in the surface properties – surface composition, structure, morphology, hydrophilicity and roughness since as these affect the protein absorption, cell attachment, protection from

chemical corrosion exerted by body fluids and the reduction of bacterial adhesion hydrophilicity of the surface [16].

One of the most widely used methods for modification of the implant surface properties is represented by the increasing of surface roughness (by techniques including mechanical (grit blasting), chemical (acid or alkaline etch), electrochemical (anodisation) and physical methods (plasma spray)) [17–19] that leads to an increase in the surface area finally resulting in osteoblast differentiation. The possible role of roughened surfaces for the development or at least the maintenance of peri-implantitis [20] has, however, recently raised questions about this approach and suggested the use of different surfaces. Other techniques could be the introduction of specific functional groups in order to increase the wettability, thus, to improve cell attachment *in vitro* or the deposition of biomaterials that can mimic the chemical composition of natural bone on the surface [21].

On the other hand, the surface modification with a coating became a popular approach to enhance the formation of new bone and hinder adverse inflammatory reactions. Moreover, a bioactive coating on the implant surface is generally preferred over possible systemic administration of additional bone healing agents or drugs due to the local effect a coating has on bone healing directly at the implantation site and the significantly decreased amount of the active agent required. Various physical and chemical methods have been applied for biomedical coatings. However, most of them present drawbacks: they cannot coat homogeneously porous surfaces or complicated substrates, are not cost-effective and require high vacuum, high voltages, harmful chemicals or time-consuming transfer steps [22]. In this respect, electrochemical approaches received increased interest for manipulation of the surface chemistry and topography of dental implant as they provide a versatile toolbox of approaches for fabrication of nanostructured coatings [23]. Such approach has some other considerable benefits for fabrication of biological coatings including a low-temperature, fast fabrication process, controlled chemical composition, controlled film thickness, ease of operation, deposition of crystalline and homogeneous and adherent films, and more importantly, it allows the coating of complex geometries such as that of an endosseous dental implant.

### **3 Graphene-Based Coatings for Surface Modification of Dental Implants**

From the graphene family, the graphene oxide (GO) – a graphene-derivative decorated with oxygen functional groups and reduced graphene oxide (rGO) – have received extensive attention for a variety of applications, while the biomedical applicability was triggered specially because of its exotic properties such as biocompatibility, electric conductivity, and transparency, excellent aqueous processability, amphiphilicity and surface functionalisability [24].

The *tunable chemistry* and the *excellent mechanical, tribological* as well as *corrosion properties* of graphene-based materials have indicated their potential applications in implant material. The outstanding surface activity of GO-based nanomaterials, caused by the many functional groups on its surface, can exhibit adsorptive capability to drugs [25], growth factors [26] and other biomolecules via  $\pi$ - $\pi$  stacking or covalent grafting, while the high specific surface area could enable them as platforms for various biological interactions to bring important benefits related to tissue engineering therapy.

The hydrophilic surface of GO materials was indicated to provide a *biocompatible* environment compared to its hydrophobic surface [27, 28]. This is consistent with the case of carbon nanotubes, which are usually functionalised before biomedical applications and show a functionalisation-dependent biological performance [29]. As a partially reduced GO, the biocompatibility of rGO is expected to be lower than GO but higher than pristine graphene. Rapid adsorption of serum protein on rGO materials was indicated to make them a biocompatible and hydrophilic environment for cell adhesion and proliferation [27]. Protein adsorption to implant surfaces is influenced by various factors, including the protein properties, surface properties and the external parameters such as temperature, pH, ionic strength, etc. The biocompatibility of rGO is, therefore, dependent on the oxygen content. Indeed, it has been reported by Liao et al. [30] that *particle size, surface charge* and *oxygen content of graphene* have a high impact on the biological responses of red blood cells, although GO is generally considered to be haemocompatible [31]. It was found that aggregated graphene sheets show the lowest haemolytic activity, i.e. fewest broken cells, while smaller GO size show higher haemolytic activity, which can be attributed to the strong electrostatic interactions between the negatively charged GO surface and positively charged lipids on the outer membrane of red blood cells.

The surface functionalisation approach of a bioactive material in order to achieve a coating presents an important potential for advances in nanomaterial applications due to not only synergistic effects but also to improved biocompatibility and corrosion resistance [32, 33]. Several *in vivo* and *in vitro* studies have suggested that nanomaterial-based coatings may render dental implants more biocompatible while facilitating the formation of new bone and reducing healing time. Currently, coating approaches are being investigated for the application of GO films at the surface of metallic dental implant which would consider the tailoring of the process parameters to ensure the best corrosion barrier properties and biocompatible properties. The promotion of cell behaviour including attachment, growth, proliferation and differentiation exhibited by GO materials can be employed to enhance the local concentration of extracellular matrix by non-covalent binding [34].

The existing strategies of application of carbon-based nanomaterials to tissue engineering and cell differentiation are based on the suspending of nanomaterials into cell culture media or coating nanomaterials for *in vitro* stem cell culture. The second strategy is widely accepted to tailor the stem cell behaviour given that a unique physical framework is provided for stem cells by the nanomaterial-coated substrates. Most of the approaches regarding the use of graphene for coating surfaces are mainly based on chemical vapour deposition (CVD) growth due to superior



anticorrosion properties [35] and further transfer by using a “poly(methyl methacrylate)-mediated” method. For example, a hybrid CVD coating based on graphene and Nb<sub>2</sub>O<sub>5</sub> [36] resulted in improved mechanical properties of substrate (i.e. surface hardness and wear resistance) and protection of the Ti surface from the abrasion process and the release of toxic products of corrosion to the environment, which could cause allergies and metallosis. However, despite some evidences, it has also been demonstrated that CVD-graphene coating cannot be used as a long-term anticorrosion barrier because it is able to promote the metal corrosion [37, 38]. Moreover, the transfer of CVD-graphene on complicated 3D structures, especially screw-shaped dental implants, poses much difficulty; thus, it calls for easier alternatives of coating on the surface of 3D structures with reasonable durability and stability after implantation.

Other more economic approaches proved their potential in surface modification with GO nanomaterials: drop-casted GO coatings were shown to exhibit good biocompatibility and improve the osteoblast cell functions, while effectively killing bacteria [39]; a GO coating obtained by immersion of the substrate in a GO dispersion 5 mg/mL for 12 h resulted not cytotoxic to MC3T3-E1 cells after several days of incubation [40]; the spin-coating of GO onto oxidised Ti and subsequent reduction by exposure to hydrazine resulted in higher pre-osteoblast cell viability and cell attachment with respect to uncoated surface [41].

Modified GO coatings were also demonstrated beneficial: following the confirmation of the drug loading capability of rGO-coated Ti, osteogenic dexamethasone (Dex)-loaded rGO coating resulted in more effective bone regeneration than uncoated surface [27]; good compatibility and corrosion resistance were shown also for GO composites with hydroxyapatite (HAp) [42] which were also found to significantly enhance new bone formation in full-thickness calvarial defects without inflammatory responses [43]. Kang Y.S. et al. had demonstrated the sodium-functionalised GO (NaGO) is an excellent candidate for increasing the life time of Ti implants [44], by exploiting the requirements for elemental Na as an essential macronutrient for regulation of physiological and based on the claims that sodium ion is an essential factor to accelerate in vitro hepatocyte cell proliferation [45]. An aqueous dispersion of NaGO was used to coat the pure Ti plates by heat-controlled spin-coating. The obtained NaGO coating was observed to protect against corrosion by acting as a geometric blocking layer and to exhibit also biocompatibility for cell viability. The immunofluorescence and cell proliferation studies performed on human dermal fibroblast cells showed that NaGO coatings exhibited enhanced cellular viability for in vitro culture than GO and uncoated Ti.

While the above-mentioned techniques require high temperature, high vacuum, high voltages or time-consuming transfer steps and cannot be applied on complicated structures, the electrochemical deposition of GO materials has been demonstrated as highly attractive for coating surfaces and showed benefits with respect to using reducing agents for tailoring the GO surface chemistry [46–48]. During coating of a sample via electrodeposition, many parameters can change the composition and performance of the coating. The in vivo behaviour of a bioactive coating can be greatly affected by its structure. In order to assemble various graphene-based

coatings on metal surfaces, electrophoretic deposition (EPD) can be applied, based on the electrochemical properties of colloidal solutions from which the depositions are done. EPD has many advantages, e.g. high deposition rate, control of deposition parameters affecting the coating thickness, crystallinity, possibility of deposition on complex-shaped substrates and factors that are favourable for the purpose of implant applications with improved, bioactivity, biocompatibility and corrosion resistance [49, 50]. The *toughening property* of graphene on HAp was exploited in an EPD-deposited composite which showed reduced surface cracks, better mechanical resistance and enhanced thermal stability [51]. By modifying the graphene-reinforced HAp coating with antimicrobial Ag, the bioactivity property was evidenced by the formation of the apatite layer in simulated body fluid with enhanced corrosion stability, and the antibacterial activity against *Staphylococcus aureus* and *E. coli* and non-cytotoxicity against healthy peripheral blood mononuclear cells confirmed its high potential for implant surface modification. Other graphene/HAp coating produced by spark plasma sintering showed improved in vitro osteoblast adhesion and apatite mineralisation [52].

It was shown that many complex factors such as *high loads*, complicated surface conditions, *contaminations and quality and continuity of graphene in large scale affect the tribological properties of graphene at macroscale in contrast to those in nano-/microscale*. While graphene-based coatings have shown great lubricity, efforts are still needed to improve the reliability and durability of graphene-based coatings.

An important clinical challenge is represented by the development of implant surfaces with good integration with the surrounding tissues and simultaneous ability to inhibit bacterial colonisation, thus, preventing infection. J. Liu et al. developed surface coatings on NiTi substrates by drop-casting GO-functionalised gelatine (Gel) in order to exploit its cell-binding properties. Their results indicated the cell functions were significantly enhanced on both GO- and GO-Gel-coated NiTi compared with uncoated substrate [53]. The GO-Gel-coated NiTi surface exhibited the best performance for cell adhesion, proliferation and differentiation and resulted in inhibited growth of *E. coli*.

The *adhesion* of the graphene-based coating to the substrate can affect its tribological performance. Therefore, either the graphene coating or the substrate needs to be engineered to enhance the adhesion between them. Introducing bonding/transition layers is an important method that has been adapted in literature. A (3-aminopropyl)triethoxysilane (APTES) bonding layer applied on Ti surfaces [54–56] was shown to exhibit improved tribological properties. Thus, by designing the structure of a graphene-based coating and tuning the chemistry of the coating surface, an improved and reliable performance could be expected from GO.

The following table summarises the approaches employed to obtain the main graphene-based coatings for surface modification in tissue engineering till present. As already mentioned, the materials span a large family of graphene derivatives, from pristine graphene to GO and GO composites, while the most used techniques are solution-based (Table 1).

**Table 1** The main approaches and graphene-based coatings for surface modification in tissue engineering

Approach	Coating material	References
Chemical vapour deposition	Graphene	[36]
	Graphene composites	[37]
		[38]
Drop-casting	GO	[39]
Spin-coating		[40]
Dip-coating		[41]
Electrophoretic deposition	Hydroxyapatite-GO	[42]
Spark plasma sintering		[51]
		[52]
Spin-coating	Functionalised GO	[27]
	Drug-loaded GO	[43]
	Na functionalised GO	[44]
	Gelatine functionalised GO	[53]

## 4 Interaction of Graphene Coatings with Biological Environment

Mesenchymal stem cells (MSCs) are adult stromal multipotent progenitor cells with the ability to differentiate into cells of mesenchymal lineage, including the bone, fat and cartilage [57]. Dental stem cells (SCs) are multipotent MSCs which attracted new interest as the oral cavity proved to be a valuable source of MSCs due to the accessibility, high quality and less ethical concerns [58]. The recent progress in the stem cell-based field has provided interesting opportunities to develop innovative cell-based therapies for regenerative medicine [59]. It is required to use and recruit progenitor cells able to differentiate into specialised cells with a regenerative capacity, followed by the proliferation of these cells and synthesis of the target-specialised connective tissues [60]. The materials selected for dental implants need to be bio-compatible with lost tissue and to allow the recruitment of endogenous stem cells [61]. Despite the intensive progress in human stem cell research till present, only few attempts of use of graphene-based nanomaterials in the stem cell field have been reported. The effect of graphene-based materials on biological systems is still not clear due to their intrinsic properties and the degree of interaction of the tested nanomaterials with the cells during the assay that is challenging to understand due to *the complexity of cellular responses*. Most of the recent in vitro studies indicate that graphene-based nanomaterials (i.e. mainly graphene, GO and carbon nanotubes) promote stem cell adhesion, growth, expansion and differentiation. GO tests on human dental follicle SCs showed high potential for GO use in dental

nanocomposites [62]. A recent study demonstrated that a GO composite film could enhance cell adhesion, proliferation and mesenchymal phenotype expression of human periodontal ligament stem cells (PDLSCs) [63]. The exact reason why GO promotes cell adhesion, proliferation and differentiation still remains unknown. A combination of several factors including *nanoscale structure, mechanical strength, roughness, interactions with proteins through hydrophobic and electrostatic interactions and large dosage of loading capacity* may contribute to the effects of GO on the behaviour of PDLSCs [26, 64].

Although nano-toxic effects of graphene materials on multiple cell types were indicated to significantly hinder their applicability, appropriate surface designs, i.e. surface physical or chemical functionalisations, could minimise them [65, 66]. Some studies on in vitro toxicity have demonstrated the compatibility of graphene nanomaterials with some cells – e.g. it was shown to effectively kill bacteria [28, 67–72]. Graphene was indicated to even inhibit the growth of dental pathogens such as *S. mutans*, *P. gingivalis* and *F. nucleatum* which could be helpful in reducing the abuse of antibiotics in dentistry [41, 42, 53, 73]. There are also multiple conflicting works indicating GO toxicity and damages to the cell membrane leading ultimately to apoptosis [113]. Similar controversy exists regarding the effect of GO on *E.coli* bacteria, being reported as bactericidal and as supporting bacterial growth [74, 75]. For long-term toxicology of graphene in living systems, only one study showed that PEGylated graphene sheets did not cause appreciable toxicity to treated mice over a period of 3 months [26].

As an explanation for these discrepancies, it has generally been suggested that the **surface characteristics** of graphene nanomaterials such as *nanotopography, surface chemistry* and *large adsorption capacity* influence the molecular pathways that control the fate of stem cells [76]. For example, the toxicity of GO was found *dosage-dependent*, as in the case of on A549 human epithelial cells [77], while *content of functional groups* and *surface area* of GO can affect binding with proteins and cell attachment [78]. Interestingly it was also observed that the toxicity occurred mainly at the initial stage and was *not time-dependent*. The toxicity mechanism was believed to be due to the physical damage caused by sharp GO sheets. In their recent article, Horvath et al. [79] reported that GO showed lower toxicity on epithelial cells compared with carbon nanotubes. The mechanism of toxicity in this case, however, was associated with the *reactive oxygen species* generated by the interaction between GO and the cell surface. On the other hand, Akhavan et al. [80] found that a *size-dependency for cytotoxicity* of GO nanoplatelets in the case of mesenchymal stem cells (MSCs).

It should be noted that the available data with regard to the toxicity and biocompatibility of graphene was mainly obtained from works on potential use as drug delivery vehicle. Conversely, when graphene materials are applied as scaffold materials in bone tissue engineering, thus, confined in a specific location, the inflammation or toxic reaction may be different from systemic administration as different graphene materials will have a different toxicological profile.

## 5 Conclusions and Future Perspective

Many potential benefits to patient may stem from using nanotechnology in dentistry. Even though the research regarding biomedical applications of graphene-based nanomaterials is expanding rapidly, relatively little is known about their influence on biological systems or intrinsic toxicity, oral stem cell behaviour, etc. being a relatively new research direction that deserves special attention. Rigorous internationally standardised clinical studies in humans that would aim to assess their nanotoxicology are requested.

The current research in the field of endosseous dental implants focuses at present towards creating a bioactive surface; yet, despite the recent innovative advancements in the design of dental materials, failures still occur, and limitations still exists with respect to potential pathogenic infections, low availability and high costs besides inconclusive evidence for long-term success. Unfortunately, till present there is no general solution to satisfy the requirements for an ideal implant surface. Thus, it is imperative to integrate several coating strategies with complementary strengths to build smarter next-generation biomaterial-based medical implants. Moreover, the controlled modulation of surface topography and alteration to some extent of the surface chemistry, independently of the microscale, could trigger research to new and sophisticated proofs of concepts. Understanding the effect of graphene substrate on graphene–cell interaction is an important issue for considering graphene as a potential candidate for biomedical applications.

**Acknowledgements** Financial support from Romanian National Authority for Scientific Research and Innovation, CNCS – UEFISCDI (project number PN-II-RU-TE-2014-4-0806), is greatly appreciated.

## References

1. F. Chen, Y. Jin, Periodontal tissue engineering and regeneration: current approaches and expanding opportunities. *Tissue Eng. B* **16**, 219 (2010)
2. N. Huebsch, D.J. Mooney, R. Artale, Inspiration and application in the evolution of biomaterials. *Nature* **462**, 426 (2009)
3. D.E. Ingber, *Principles of Tissue Engineering* (Elsevier, Amsterdam, 2000), p. 101
4. F. Watari, N. Takashi, A. Yokoyama, M. Uo, T. Akasaka, Y. Sato, S. Abe, Y. Totsuka, K. Tohji, Material nanosizing effect on living organisms: non-specific, biointeractive, physical size effects. *J.R. Soc Interface* **6**, S371 (2009)
5. Z.J. Han, A.E. Rider, M. Ishaq, S. Kumar, A. Kondyurin, M.M.M. Bilek, I. Levchenko, K.K. Ostrikov, Carbon nanostructures for hard tissue engineering. *RSC Adv.* **3**, 11058 (2013)
6. G.Y. Chen, D.W. Pang, S.M. Hwang, H.Y. Tuan, Y.C. Hu, A graphene-based platform for induced pluripotent stem cells culture and differentiation. *Biomaterials* **33**, 418 (2012)
7. A. Pruna, *Advances in Carbon Nanotube Technology for Corrosion Applications in Handbook of Polymer Nanocomposites*, vol B (Springer, Berlin, 2015), pp. 335–359. doi:10.1007/978-3-642-45229-1\_36

8. T.R. Nayak, H. Andersen, V.S. Makam, C. Khaw, S. Bae, X. Xu, P.L.R. Ee, J.H. Ahn, B.H. Hong, G. Pastorin, B. Özyilmaz, Graphene for controlled and accelerated osteogenic differentiation of human mesenchymal stem cells. *ACS Nano* **5**, 4670 (2011)
9. V. Sollazzo, A. Palmieri, L. Scapoli, M. Martinelli, A. Girardi, F. Alviano, A. Pellati, V. Perrotti, F. Carinci, Bio-Oss® acts on stem cells derived from peripheral blood. *Oman Med J* **25**, 26–31 (2010)
10. M. Gahlert, S. Röbling, M. Wieland, S. Eichhorn, H. Küchenhoff, H. Kniha, A comparison study of the osseointegration of zirconia and titanium dental implants. A biomechanical evaluation in the maxilla of pigs. *Clin. Implant. Dent. Relat. Res.* **12**, 297 (2010)
11. R.A. de Medeiros, A.J. Vechiato-Filho, E.P. Pellizzer, J.V. Quinelli Mazaro, D.M. dos Santos, M. Coelho Goiato, Analysis of the peri-implant soft tissues in contact with zirconia abutments: an evidence-based literature review. *J. Contemp. Dent. Pract.* **14**, 567 (2013)
12. Y.T. Sul, B.S. Kang, C. Johansson, H.S. Um, C.J. Park, T. Albrektsson, The roles of surface chemistry and topography in the strength and rate of osseointegration of titanium implants in bone. *J. Biomed. Mater. Res. Part A* **89**, 942 (2009)
13. A.M. Pedersen, A. Bardow, S.B. Jensen, B. Nauntofte, Saliva and gastrointestinal functions of taste, mastication, swallowing and digestion. *Oral Dis.* **8**, 117 (2002)
14. Y. Mu, T. Kobayashi, M. Sumita, A. Yamamoto, T. Hanawa, Metal ion release from titanium with active oxygen species generated by rat macrophages in vitro. *J. Biomed. Mater. Res.* **49**, 238 (2000)
15. L. Evrard, D. Waroquier, D. Parent, Allergies to dental metals. Titanium: a new allergen. *Rev. Med. Brux.* **31**(1), 44 (2010)
16. Y. Wang, G. Du, H. Liu, D. Liu, S. Qin, N. Wang, C. Hu, X. Tao, J. Jiao, J. Wang, Z.Y. Wang, Nanostructured sheets of Ti-O nanobelts for gas sensing and antibacterial applications. *Adv. Funct. Mater.* **18**, 1131 (2008)
17. D.L. Cochran, R.K. Schenk, A. Lussi, F.L. Higginbottom, D. Buser, Bone response to unloaded and loaded titanium implants with a sandblasted and acid-etched surface: a histometric study in the canine mandible. *J. Biomed. Mater. Res.* **40**(1) (1998)
18. A. Wennerberg, C. Hallgren, C. Johansson, S. Danelli, A histomorphometric evaluation of screw-shaped implants each prepared with two surface roughnesses. *Clin. Oral Implants Res.* **9**, 11 (1998)
19. D. Duraccio, F. Mussano, M.G. Faga, Biomaterials for dental implants: current and future trends. *J. Mater. Sci.* **50**, 4779 (2015)
20. M.A. Atieh, N.H.M. Alsabeeha, C.M. Jr Faggion, W.J. Duncan, The frequency of peri-implant diseases: a systematic review and meta-analysis. *J. Periodontol.* **84**, 1586 (2013)
21. L. Treccani, T. Yvonne Klein, F. Meder, K. Pardun, K. Rezwan, Functionalized ceramics for biomedical, biotechnological and environmental applications. *Acta Biomater.* **9**, 7115 (2013)
22. Y.Y. Shi, M. Li, Q. Liu, Z.J. Jia, X.C. Xu, Y. Cheng, Y.F. Zheng, *J. Mater. Sci. Mater. Med.* **27**, 48 (2016)
23. A. Pruna, D. Pullini, D. Mataix Busquets, *Electrochemical Fabrication of Graphene-Based Nanomaterials in Handbook of Nanoelectrochemistry* (Springer, Cham, 2016), pp. 3–22. doi:10.1007/978-3-319-15207-3\_6-1
24. A.K. Geim, Graphene: status and prospects. *Science* **324**, 1530 (2009)
25. S. Goenka, V. Sant, S. San, Graphene-based nanomaterials for drug delivery and tissue engineering. *J. Control. Release* **173**, 75 (2014)
26. W.G. La, S. Park, H.H. Yoon, G.J. Jeong, T.J. Lee, S.H. Bhang, J.Y. Han, K. Char, B.S. Kim, Delivery of a therapeutic protein for bone regeneration from a substrate coated with graphene oxide. *Small* **9**, 4051 (2013)
27. H.S. Jung, T. Lee, I.K. Kwon, H.S. Kim, S.K. Hahn, C.S. Lee, Surface modification of Multipass caliber-rolled Ti alloy with dexamethasone-loaded graphene for dental applications. *ACS Appl. Mater. Interfaces* **7**, 9598 (2015)
28. W.C. Lee, C.H. Lim, H. Shi, L.A. Tang, Y. Wang, C.T. Lim, K.P. Loh, Origin of enhanced stem cell growth and differentiation on graphene and graphene oxide. *ACS Nano* **5**, 7334 (2011)

29. L. Yang, L. Zhang, T.J. Webster, Carbon nanostructures for orthopaedic medical applications. *Nanomedicine* **6**, 1231 (2011)
30. K.H. Liao, Y.S. Lin, C.W. Macosko, C.L. Haynes, Cytotoxicity of graphene oxide and graphene in human erythrocytes and skin fibroblasts. *ACS Appl. Mater. Interfaces* **3**, 2607 (2011)
31. A.M. Pinto, I.C. Goncalves, F.D. Magalhaes, Graphene-based materials biocompatibility: a review. *Colloids Surf. B: Biointerfaces* **111**, 188 (2013)
32. S. Nagarajan, M. Mohana, P. Sudhagar, V. Raman, T. Tishimura, S. Kim, Y.S. Kang, N. Rajendran, Nanocomposite coatings on biomedical grade stainless steel for improved corrosion resistance and biocompatibility. *ACS Appl. Mater. Interfaces* **4**, 5134 (2012)
33. L. Zhang, T.J. Webster, Nanotechnology and nanomaterials: promises for improved tissue regeneration. *Nano Today* **4**, 66 (2009)
34. H. Chen, M.B. Müller, K.J. Gilmore, G.G. Wallace, D. Li, Mechanically strong, electrically conductive, and biocompatible graphene paper. *Adv. Mater.* **20**, 3557 (2008)
35. A. Krishnamurthy, V. Gadhamshetty, R. Mukherjee, Z. Chen, W. Ren, H.M. Cheng, N. Koratkar, Passivation of microbial corrosion using a graphene coating. *Carbon* **56**, 45 (2013)
36. M. Kalisz, M. Grobelny, M. Mazur, M. Zdrojek, D. Wojcieszak, M. Świniarski, J. Judek, D. Kaczmarek, Comparison of mechanical and corrosion properties of graphene monolayer on Ti–Al–V and nanometric Nb<sub>2</sub>O<sub>5</sub> layer on Ti–Al–V alloy for dental implants applications. *Thin Solid Films* **589**, 356 (2015)
37. M. Schriver, W. Regan, W.J. Gannett, A.M. Zaniwski, M.F. Crommie, A. Zettl, Graphene as a long-term metal oxidation barrier: worse than nothing. *ACS Nano* **7**, 5763 (2013)
38. F. Zhou, Z.T. Li, G.J. Shenoy, L. Li, H.T. Liu, Enhanced room-temperature corrosion of copper in the presence of graphene. *ACS Nano* **7**, 6939 (2013)
39. C. Zhao, S. Pandit, Y. Fu, I. Mijakovic, A. Jesorka, Graphene oxide based coatings on nitinol for biomedical implant applications: effectively promote mammalian cell growth but kill bacteria. *J. Liu RSC Adv.* **6**, 38124 (2016)
40. H. Liu, J. Cheng, F. Chen, F. Hou, D. Bai, P. Xi, Z. Zeng, Biomimetic and cell-mediated mineralization of hydroxyapatite by carrageenan functionalized graphene oxide. *ACS Appl. Mater. Interfaces* **6**, 3132 (2014)
41. H.S. Jung, Y.J. Choi, J. Jeong, Y. Lee, B. Hwang, J. Jang, J.H. Shim, Y.S. Kim, H.S. Choi, S.H. Oh, C.S. Lee, D.W. Cho, S.K. Hahn, Nanoscale graphene coating on commercially pure titanium for accelerated bone regeneration. *RSC Adv.* **6**, 26719 (2016)
42. J.H. Lee, Y.C. Shin, S.M. Lee, O.S. Jin, S.H. Kang, S.W. Hong, C.M. Jeong, J.B. Huh, D.W. Han, Enhanced osteogenesis by reduced graphene oxide/hydroxyapatite nanocomposites. *Sci. Rep.* **5**, 18833 (2015)
43. M. Marimuthu, M. Veerapandian, S. Ramasundaram, S.W. Hong, P. Sudhagar, S. Nagarajan, V. Raman, E. Ito, S. Kim, K. Yun, Y.S. Kang, Sodium functionalized graphene oxide coated titanium plates for improved corrosion resistance and cell viability. *Appl. Surf. Sci.* **293**, 124 (2014)
44. K. Koch, H. Leffert, Increased sodium ion influx is necessary to initiate rat hepatocyte proliferation. *Cell* **18**, 153 (1979)
45. A. Pruna, Q. Shao, M. Kamruzzaman, J.A. Zapien, A. Ruotolo, Enhanced electrochemical performance of ZnO nanorod core/polypyrrole shell arrays by graphene oxide. *Electrochim. Acta* **187**, 517 (2016)
46. A. Pruna, Q. Shao, M. Kamruzzaman, Y.Y. Li, J.A. Zapien, D. Pullini, D. Busquets Mataix, A. Ruotolo, Effect of ZnO core electrodeposition conditions on electrochemical and photocatalytic properties of polypyrrole-graphene oxide shelled nanoarrays. *Appl. Surf. Sci.* **392**, 801 (2017)
47. A. Sahu, W. Choi, G. Tae, A stimuli-sensitive injectable graphene oxide composite hydrogel. *Chem. Commun.* **48**, 5820 (2012)
48. H. Wang, N. Eliaz, L.W. Hobbs, The nanostructure of an electrochemically deposited hydroxyapatite coating. *Mater. Lett.* **65**, 2455 (2011)
49. A.R. Boccaccini, J. Cho, T. Subhani, C. Kaya, F. Kaya, Electrophoretic deposition of carbon nanotube-ceramic nanocomposites. *J. Eur. Ceram. Soc.* **30**(5), 1115 (2010)

50. C. Kaya, I. Singh, A.R. Boccaccini, Multi-walled carbon nanotube-reinforced hydroxyapatite layers on Ti6Al4V medical implants by electrophoretic deposition (EPD). *Adv. Eng. Mater.* **10**, 131 (2008)
51. A. Jankovic, S. Eraković, M. Vukašinović-Sekulić, V. Mišković-Stanković, S.J. Park, K.Y. Rhee, Graphene-based antibacterial composite coatings electrodeposited on titanium for biomedical applications. *Prog. Org. Coat.* **83**, 1 (2015)
52. L. Zhang, W. Liu, C. Yue, T. Zhang, P. Li, Z. Xing, Y. Chen, A tough graphene nanosheet/hydroxyapatite composite with improved in vitro biocompatibility. *Carbon* **61**, 105 (2013)
53. C. Zhao, S. Pandit, Y. Fu, I. Mijakovic, A. Jesorka, J. Liu, Graphene oxide based coatings on nitinol for biomedical implant applications: effectively promote mammalian cell growth but kill bacteria. *RSC Adv.* **6**, 38124 (2016)
54. P.F. Li, Y. Xu, X.-H. Cheng, Chemisorption of thermal reduced graphene oxide nano-layer film on TNTZ surface and its tribological behavior. *Surf. Coat. Technol.* **232**, 331 (2013)
55. P.F. Li, H. Zhou, X.-H. Cheng, Nano/micro tribological behaviors of a self-assembled graphene oxide nanolayer on Ti/titanium alloy substrates. *Appl. Surf. Sci.* **285**, 937 (2013)
56. P.F. Li, H. Zhou, X. Cheng, Investigation of a hydrothermal reduced graphene oxide nano coating on Ti substrate and its nano-tribological behavior. *Surf. Coat. Technol.* **254**, 298 (2014)
57. I.D. Meirelles, N.B. Nardi, Methodology, biology and clinical applications of mesenchymal stem cells. *Front. Biosci.* **14**, 4281 (2009)
58. B.M. Seo, M. Miura, S. Gronthos, P.M. Bartold, S. Batouli, J. Brahim, M. Young, P.G. Robey, C.Y. Wang, S. Shi, Investigation of multipotent postnatal stem cells from human periodontal ligament. *Lancet* **364**, 149 (2004)
59. S. Razzouk, R. Schoor, Mesenchymal stem cells and their challenges for bone regeneration and osseointegration. *J. Periodontol.* **83**, 547 (2012)
60. P.M. Bartold, Y. Xiao, S.P. Lyngstaadas, M.L. Paine, M.L. Snead, Principles and applications of cell delivery systems for periodontal regeneration. *Periodontol.* 2000 **41**, 123 (2006)
61. Z. Yuan, H. Nie, S. Wang, C.H. Lee, A. Li, S.Y. Fu, H. Zhou, L. Chen, J.J. Mao, Biomaterial selection for tooth regeneration. *Tissue Eng. Part B Rev.* **17**, 373 (2011)
62. D. Olteanu, A. Filip, C. Socaci, A.R. Biris, X. Filip, M. Coros, M.C. Rosu, F. Pogacean, C. Alb, I. Baldea, P. Bolfa, S. Pruneanu, Cytotoxicity assessment of graphene-based nanomaterials on human dental follicle stem cells. *Colloids Surf. B: Biointerfaces* **136**, 791 (2015)
63. F.J. Rodríguez-Lozano, D. García-Bernal, S. Aznar-Cervantes, M.A. Ros-Roca, M.C. Algueró, N.M. Atucha, A.A. Lozano-García, J.M. Moraleda, J.L. Cenis, Effects of composite films of silk fibroin and graphene oxide on the proliferation, cell viability and mesenchymal phenotype of periodontal ligament stem cells. *J. Mater. Sci. Mater. Med.* **25**, 2731 (2014)
64. J. Kim, K.S. Choi, Y. Kim, K.T. Lim, H. Seonwoo, Y. Park, D.H. Kim, P.H. Choung, C.S. Cho, S.Y. Kim, Y.H. Choung, J.H. Chung, Bioactive effects of graphene oxide cell culture substratum on structure and function of human adipose-derived stem cells. *J. Biomed. Mater. Res. A* **101**, 3520 (2013)
65. N. Li, Q. Zhang, S. Gao, Three dimensional graphene foam as a biocompatible and conductive scaffold for neural stem cells. *Sci Rep* **3**, 1604 (2013)
66. L. Yan, F. Zhao, S. Li, Low-toxic and safe nanomaterials by surface-chemical design, carbon nanotubes, fullerenes, metallo-fullerenes, and graphenes. *Nano* **3**, 362 (2011)
67. R. Justin, B. Chen, Characterisation and drug release performance of biodegradable chitosan – Graphene oxide nanocomposites. *Carbohydr. Polym.* **103**, 70 (2014)
68. S.H. Ku, C.B. Park, Myoblast differentiation on graphene oxide. *Biomaterials* **34**, 2017 (2013)
69. L. Hui, J.G. Piao, J. Auletta, K. Hu, Y. Zhu, T. Meyer, H. Liu, L. Yang, Availability of the basal planes of graphene oxide determines whether it is antibacterial. *ACS Appl. Mater. Interfaces* **6**, 13183 (2014)
70. S. Agarwal, X. Zhou, F. Ye, Q. He, G.C.K. Chen, J. Soo, F. Boey, H. Zhang, P. Chen, Interfacing live cells with nanocarbon substrates. *Langmuir* **26**, 2244 (2010)
71. T. Lammel, P. Boisseaux, M.L. Fernández-Cruz, J.M. Navas, Internalization and cytotoxicity of graphene oxide and carboxyl graphene nanoplatelets in the human hepatocellular carcinoma cell line Hep G2. *Part. Fibre Toxicol.* **10**, 27 (2013)



72. J. He, X. Zhu, Z. Qi, C. Wang, X. Mao, C. Zhu, Z. He, M. Li, Z. Tang, Killing dental pathogens using antibacterial graphene oxide. *ACS Appl. Mater. Interfaces* **7**, 5605 (2015)
73. O.N. Ruiz, K.A.S. Fernando, B. Wang, N.A. Brown, P.G. Luo, N.D. McNamara, M. Vangsness, Y. Sun, C.E. Bunker, Graphene oxide: a nonspecific enhancer of cellular growth. *ACS Nano* **5**, 8100 (2011)
74. S. Kulshrestha, S. Khan, R. Meena, B.R. Singh, A.U. Khan, A graphene/zinc oxide nano-composite film protects dental implant surfaces against cariogenic *Streptococcus mutans*. *Biofouling* **30**, 1281 (2014)
75. K. Yang, J. Wan, S. Zhang, Y. Zhang, S.T. Lee, Z. Liu, In vivo pharmacokinetics, long-term biodistribution, and toxicology of PEGylated graphene in mice. *ACS Nano* **5**, 516 (2011)
76. E.L.K. Chng, M. Pumera, The toxicity of graphene oxides: dependence on the oxidative methods used. *Chemistry* **19**, 8227 (2013)
77. W. Hu, C. Peng, M. Lv, X. Li, Y. Zhang, N. Chen, C. Fan, Q. Huang, Protein corona-mediated mitigation of cytotoxicity of graphene oxide. *ACS Nano* **5**, 3693–3700 (2011)
78. K.H. Liao et al., Cytotoxicity of graphene oxide and graphene in human erythrocytes and skin fibroblasts. *ACS Appl. Mater. Interfaces* **3**, 2607 (2011)
79. L. Horváth, A. Magrez, M. Burghard, K. Kern, L. Forró, B. Schwaller, Evaluation of the toxicity of graphene derivatives on cells of the lung luminal surface. *Carbon* **64**, 45 (2013)
80. O. Akhavan, E. Ghaderi, A. Akhavan, Size-dependent genotoxicity of graphene nanoplatelets in human stem cells. *Biomaterials* **33**, 8017 (2012)

**Part II**  
**Carbon Composites and Thin Films**

# Effect of CNT on the Mechanical Properties of Composite Materials and Structures

N. Naveh, Y. Seri, Y. Portnoy, D. Levin, and B. Muravin

## 1 Introduction

Enhancement of mechanical properties of composite materials by introduction of carbon nanotubes (CNT) to the matrix has been the focus of many research programs, both academic and industrial, in order to either enhance properties or reduce weight at comparable performance [1, 2]. Fiber-dominated properties such as tensile strength in the fiber direction are hardly improved by addition of fillers. However, matrix-dominated properties such as shear strength and toughness can be largely improved by addition of very low levels of CNT. The interlaminar shear strength (ILSS) of carbon/epoxy composites was increased by up to 50% when 0.25–0.5 wt% multi-walled CNT (MWCNT) was dispersed in the epoxy [3]. Homogenous dispersions are important for achieving high values of ILSS. Chandrasekaran et al. [4] concluded that the manufacturing process may play a critical role in MWCNT distribution. When 5.0 wt% MWCNT and control samples were manufactured using flow flooding chamber (FFC), ILSS was improved by 21%. Bekyarova et al. [5] used functionalized MWCNT and SWCNT for selective deposition on carbon fiber surface by electrophoresis. The introduction of 5.0 wt% of MWCNT in the carbon fiber/epoxy composites resulted in an enhancement of the interlaminar shear strength of 27%. Fan et al. dispersed oxidized 2 wt% MWCNT using acetone and an ultrasonic bath and achieved 33% increase in ILSS [6]. Fang et al. recently reported that deposition of CNT onto carbon fibers by immersion in

---

N. Naveh (✉)

Polymers and Plastics Engineering Department, Shenkar College of Engineering and Design,  
Ramat Gan 5252626, Israel

e-mail: [naumn@shenkar.ac.il](mailto:naumn@shenkar.ac.il)

Y. Seri • Y. Portnoy • D. Levin

Rafael Advanced Defense Systems, P.O.B. 2250, Haifa 3102102, Israel

B. Muravin

Integrity Diagnostics Ltd., Netanya 42100, Israel

an aqueous suspension of CNT and a sizing agent, ultrasonication, and drying at 120 °C led to 67% increase in ILSS of a carbon/epoxy composite [7]. Other techniques have also been reported, showing improvements in ILSS [8–11].

Few efforts have addressed the effect of CNT on the mechanical behavior of a full-scale, large composite part. In particular, we address the potential increase in burst pressure of a composite filament wound pressure vessel by adding CNT or other nanofillers to the epoxy matrix. Improvements in static strength are not expected, since the strength is dictated by the fiber strength and fiber volume fraction for constant composite volume. Applied Nanotech Inc. made a thorough study of the effect of amino- or carboxyl-modified CNT on epoxy nanocomposites and then prepared unidirectional carbon fiber-reinforced composites using 1.5 wt% carboxyl-modified MWCNT [12]. The flexural strength was improved by over 30%. Later, they prepared several pressure vessels with low levels of NH<sub>2</sub>-functionalized CNT in the matrix [13]. The burst pressure of the CNT reinforced tanks was significantly lower compared to baseline values. Furthermore, CNT-modified vessels showed poor endurance to pressure cycles (less than 1000 compared to 15,000 cycles achieved in standard vessels). These results were attributed to increased viscosity which impaired wetting and impregnation of the fibers, in spite of the good dispersion that was shown in SEM micrographs. A higher resin viscosity may have also led to lower fiber volume fraction at higher composite volume (since the fiber content is constant), thus supporting the low burst results. On the other hand, dynamic behavior was improved, and this may be related to the introduction of crack arrest and energy dissipation mechanisms related to the CNT. Similarly, Thunhorst et al. studied type III pressure vessels with Al metal liner and found that 33.5% nanosilica in the epoxy led to an increase of 55% in fatigue resistance (cycles to failure) [14]. 3M claim to have improved the fatigue resistance of LNG type IV (plastic-lined) pressure vessels by introducing 40–50% spherical nanosilica to the thermosetting resin [15].

The following work addresses the manufacturing and static characterization of neat and CNT-modified carbon/epoxy pressure vessels and discusses the effect of CNT on vessel properties, failure mode, strains, and displacements in proof and burst tests.

## 2 Materials

A commercial epoxy/CNT master batch, NC R128-02, was purchased from Nanocyl. This composition comprises a DGEBA epoxy and MWCNT of undisclosed concentration.

Filament wound standard samples and pressure vessels were produced with T800-12 k carbon fiber from Toray, and LY556 DGEBA epoxy resin from Huntsman. Bosses in the vessels were made of PH steel, to which an EPDM shear ply was bonded.

Acoustic emission sensors were bonded to the vessels with a commercial cyanoacrylate adhesive. This allowed appropriate sensitivity and repeatability of installation.

### 3 Experimental

The commercial master batch was diluted to 1/3 of the original CNT concentration with LY556 epoxy to adapt viscosity to the filament winding range. Thorough mixing was accomplished with a three-roll mill (Ross 4 × 8") at 40 Hz rotational speed; two cycles of 5 min were used. By measuring the electrical conductivity of samples [3] and comparing to control samples, we estimate the CNT concentration in the master batch to be 0.8 wt%. The average CNT concentration of the filament winding resin was 0.25 wt%.

NOL rings were wound on a filament winding machine (J. Baer) with water-heated impregnation bath and cured in an air-circulating oven to 160 °C. Mechanical testing was according to ASTM D-2290.

6-mm-thick, 12-mm-wide rings were filament wound and cut into short beams. The specimens were three-point-bent with an appropriate jig according to ASTM D-2344. The sample arc length was 28.4 mm, and the span was set at four times the thickness. Specimens were deflected at 1.0 mm/min. Each set of specimens comprises 30 samples cut from three different rings (10 specimens/ring).

Six pressure vessels, three with CNT in the epoxy and three without, were wound on a computer-controlled filament winding machine (J. Baer, Siemens 840C) with T800-12 k carbon fiber (Toray) at 15 N tension. Cost-effective stainless steel bosses were chosen for this work. EPDM rubber shear plies were bonded to the forward (FWD) and rear (AFT) metal bosses. All pressure vessels were made without dome wafers.

First a hydro proof test was performed to a pressure of 7.4 MPa, by means of a silicone rubber bladder. The pressure was released and immediately raised till burst. The setup included 24 strain gauges, 7 acoustic emission sensors, and several displacement transducers during proof test. Figures 1, 2, 3, and 4 depict the test setup and gauges position. Strain gauges (SG) covered the domes, the transition zone at the edge of the 65° layer (see layup), and the cylinder ("equator" zone at equal distance from the bosses). All strain values reported are tensile strains in the fiber direction. Displacements

**Fig. 1** Strain gauges on the FWD dome

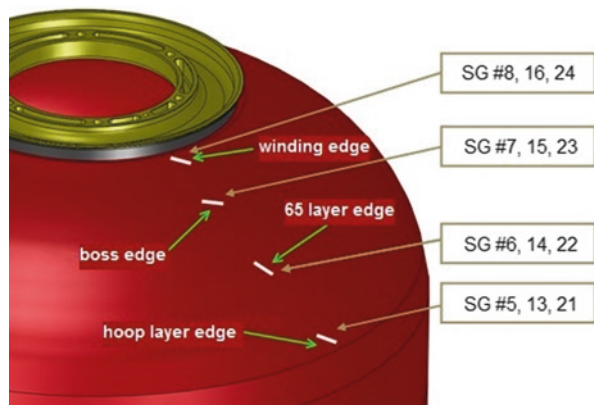


**Fig. 2** Strain gauges on the AFT dome

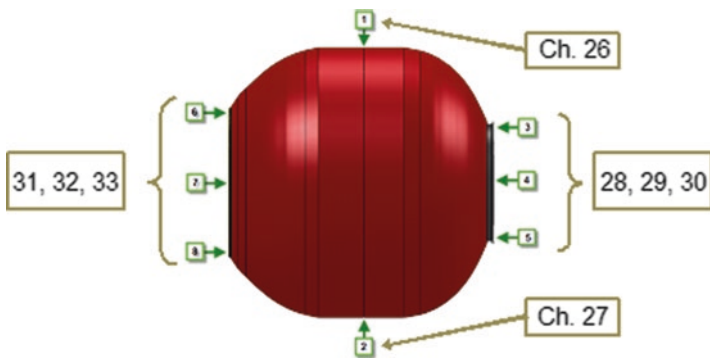
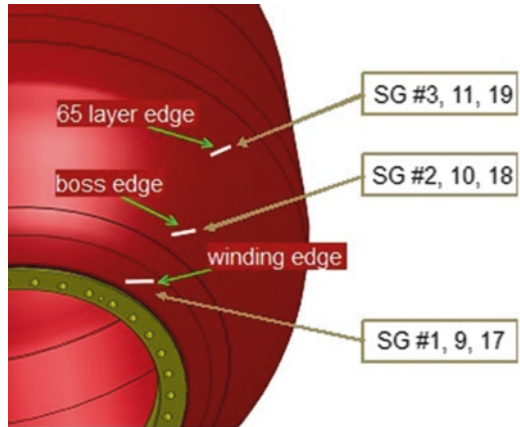
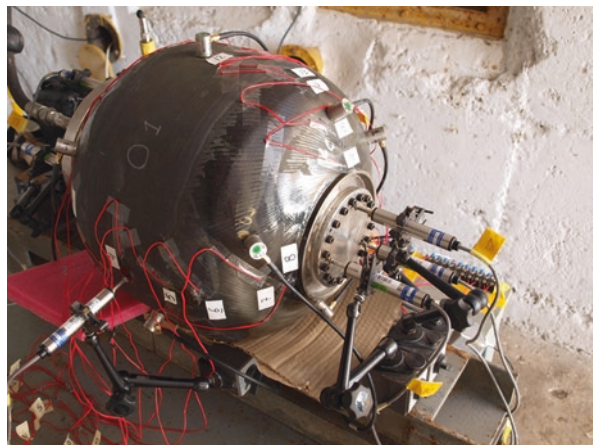


**Fig. 3** Displacement gauges in the proof test

**Fig. 4** Typical setup of a proof test, vessel #1, FWD boss view



of the flanges and at the equator were recorded only during the proof test; gauges in Fig. 3 were removed after the proof test. Two high-speed cameras at 3000 frames/sec were instrumental to locate the burst onset location.

The acoustic emission (AE) hardware and setup comprises 9 AE channels (16 bit, 10 Msamples/sec, 20–400 kHz band width), AE piezo-electric sensors (useful frequency range 50–400 kHz), preamplifiers with 60 dB amplification gain, and 50  $\Omega$  RG 58 coax cables. Signal detection was performed using fixed threshold at all channels. For each detected signal, a corresponding waveform has been recorded.

Sensitivity of the system, velocity of AE wave propagation, and their attenuation characteristics in the vessel were assessed by artificially generating AE waves by breaking 2H pencil leads of 0.5 mm diameter at sensor positions. All sensors maintained required level of sensitivity and can detect AE activity originated in any part of a vessel.

Detection of AE activity was done by application of fixed amplitude threshold, equal for all measurement channels. Flaw suspected activity was selected based on signal's rise time, duration, peak amplitude, and energy values after source-to-sensor distance correction. Frictional and other mechanical noises not related to AE activity were filtered out. 2D time difference of wave arrival locations was performed to evaluate source location whenever was practical. In other cases zone location was performed. Analysis of total number of AE hits per load stage, their energy, amplitude and frequency characteristics, and AE activity vs. location vs. pressure was performed to assess revealed indications.

Acoustic emission parameters (see Terminology Section) of detected and measured signals during the test included time of AE wave arrival, peak amplitude, energy, signal strength, duration, average frequency, RMS (root-mean-square), and ASL (average signal level), a similar parameter to RMS measured in dBAE.

## 4 Results

### 4.1 Process Optimization

Addition of CNT to a carbon/epoxy composite material is not expected to increase the tensile strength or strain to break in the fiber direction. These properties are dominated by the continuous carbon fibers. Nevertheless, a decrease in tensile properties would be detrimental to the pressure vessel performance. Insufficient wetting leading to a weak interface or lower fiber content can result from the higher viscosity of the CNT-modified resin.

As a preliminary work before winding of the pressure vessels with CNT, the effect of bath temperature on the tensile and shear properties of epoxy/CNT samples was learned. Samples with CNT from the diluted MB were prepared at nominal process conditions (50 °C in the resin bath) and at a raised resin bath temperature of 70 °C. The tensile strength of the composite decreased by 9% relative to the neat composite, when prepared at nominal conditions (resin temperature of 50 °C), but

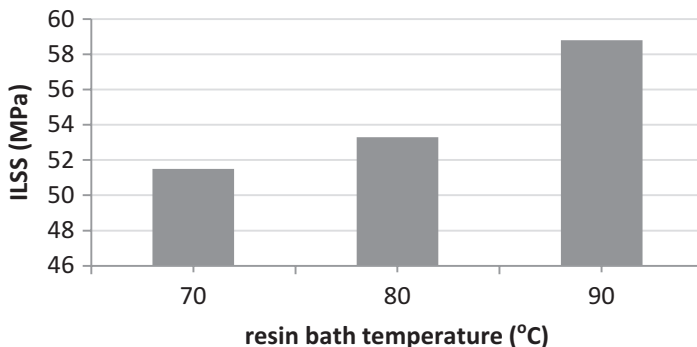


**Fig. 5** Effect of impregnation bath temperature on the ILSS in short beam samples

was unaffected when wound at the higher temperature. This result confirmed the need to increase the resin temperature. Results in Fig. 5 show the ILSS increase when raising the temperature set point, up to 90 °C, reflecting a resin temperature of 70 °C. The bath is water-heated so a higher temperature is neither practical nor safe and would also shorten the gel time of the resin. A typical winding process of a part can last 1–3 days, thus shortening of the gel time is unfavorable.

The temperature of the resin bath in the filament winding machine was adjusted, in order to achieve low viscosity, which in turn allows for good wetting and good impregnation of the carbon bundles.

## 4.2 Finite Element Analysis

One of the purposes of this work was to study the burst mechanism at the domes and see if the CNT-modified vessels behave differently. The geometry of the pressure vessels consists of a very short cylindrical section and two domes with nonsymmetrical flanges. This configuration allows focusing on the domes with ease. The vessels have  $\pm 30^\circ$  angular and hoop layers, and an intermediate  $\pm 65^\circ$  layer is added to strengthen the transition from the domes to the cylindrical part. Fiber layup is [ $\pm 30^\circ$ ,  $90^\circ$ ,  $\pm 30^\circ$ ,  $\pm 65^\circ$ ,  $\pm 30^\circ$ ,  $90^\circ \times 3$ ]. The angular layer winding pattern is polar, a recommended winding pattern for low L/D vessels.

FEA axisymmetric analysis was done with ANSYS on a 7.5° slice. The predicted thicknesses were calculated based on a geodesic winding path model and the known geometry of the mandrel.

The layup predicts burst at the domes. Finite element analysis of the stresses is shown in Figs. 6 and 7. Maximum stresses at the domes are 20% higher than in hoop layers.

A positive contribution of CNT to burst pressure would be explained by the increase in shear strength, in case a mechanism of shear due to bending of the domes and failure by delamination occurs. A negative effect could be caused by impaired interfacial adhesion and poor wetting coupled with lower fiber volume fraction.



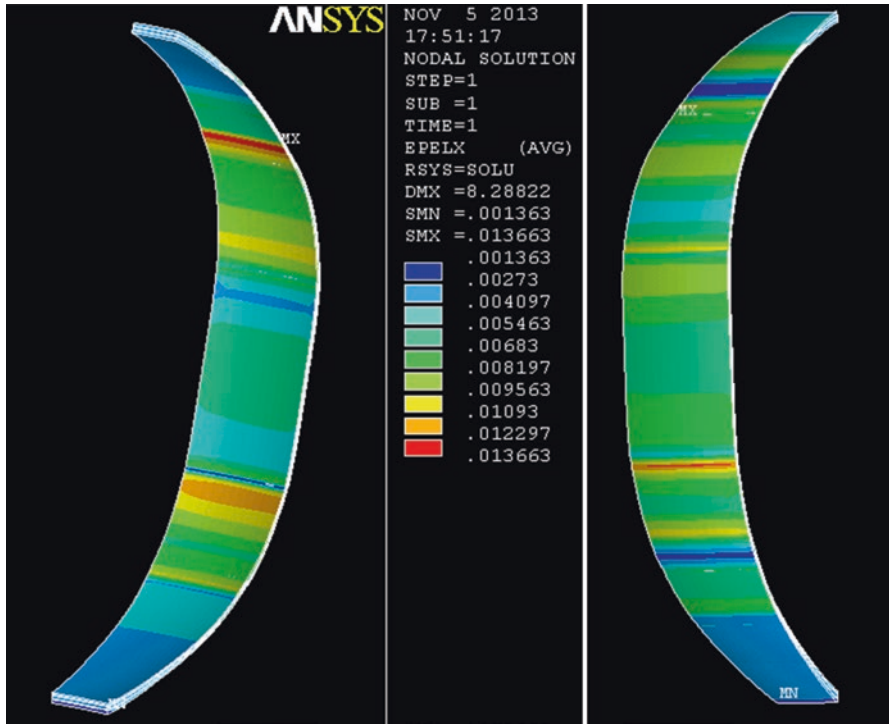


**Fig. 6** Tensile stresses in the fiber direction. Maximum stress (MX) is located in the FWD dome

### 4.3 Pressure Vessel Winding

Pressure vessel winding with a CNT-modified resin is demonstrated in Fig. 8. CNT have shown good dispersion in epoxy, and the spotted pattern on the mandrel is due to poor wetting of the mandrel. After curing, the CNT-modified vessel in Fig. 9 exhibits smooth surface finish, on both outer and inner surfaces, similarly to the neat vessels. The vessels were weighed to estimate the average fiber volume fraction. After deduction of the flanges and shear ply weights, composite weights in Table 1 indicate a decrease in average fiber volume fraction of CNT-modified vessels by ca. 3.5%.

### 4.4 Pressure Vessel Testing

#### 4.4.1 Proof Tests

Strains in a proof test are demonstrated in Figs. 10, 11, and 12. Displacements are shown in Fig. 13. Maximum strains were achieved in the hoop layers, as expected, whereas both domes are balanced, showing similar strains of 7300–7500  $\mu\text{st}$  ( $1000 \mu\text{st} = 0.1\%$ ), either on top of the boss or at the edge of the 65° layer.

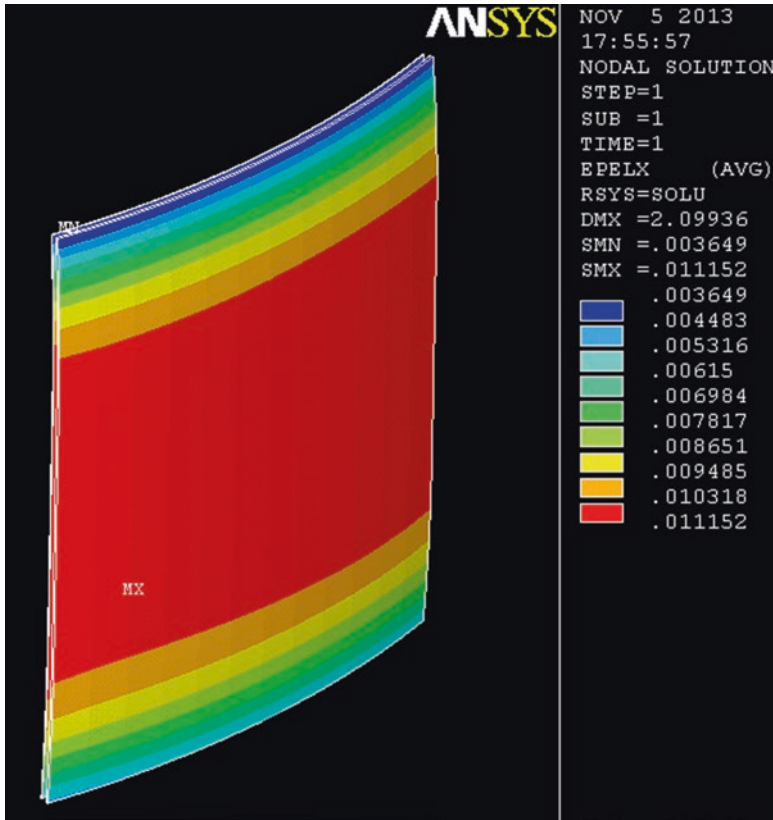


**Fig. 7** Tensile stresses in the hoop layers

**Fig. 8** Winding of the first angular layer

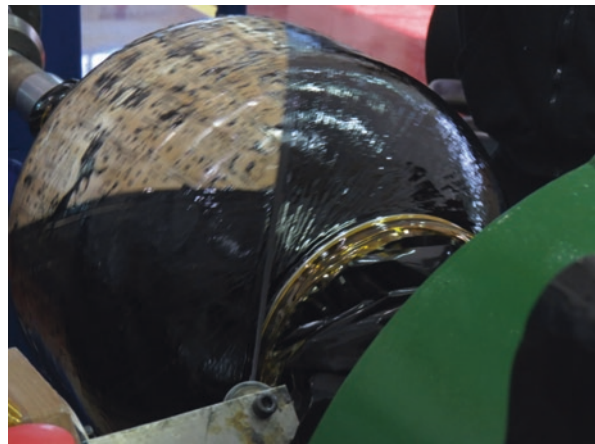


**Fig. 9** Side view of the vessel. Angular and hoop layers are displayed

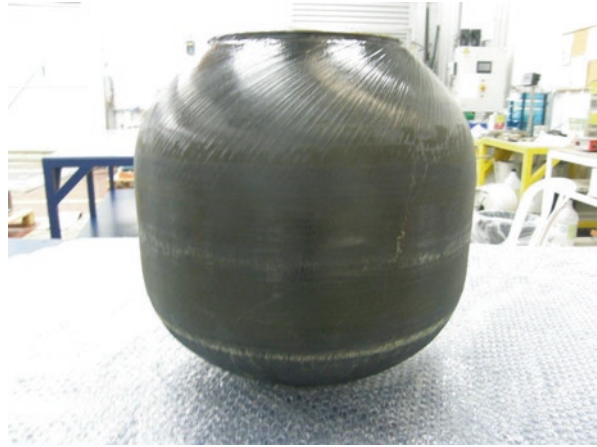


**Table 1** Weights of the pressure vessels and composite material comprising the vessels

Vessel nr.	Contains CNT	Weight (g)	Composite weight, est. (g)
1	NO	4.685	1.18
2	NO	4.670	1.17
5	NO	4.700	1.20
3	YES	4.765	1.26
4	YES	4.745	1.24
6	YES	4.735	1.23
Avg. w/o CNT	NO	4.685	1.18
Avg. with CNT	YES	4.748	1.24

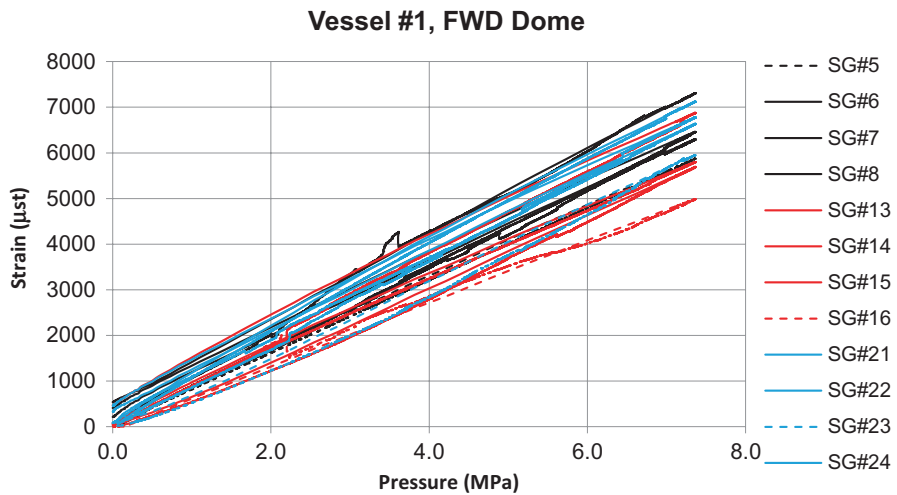


**Fig. 10** Strains in the proof test, vessel #1, strain gauges in the FWD dome

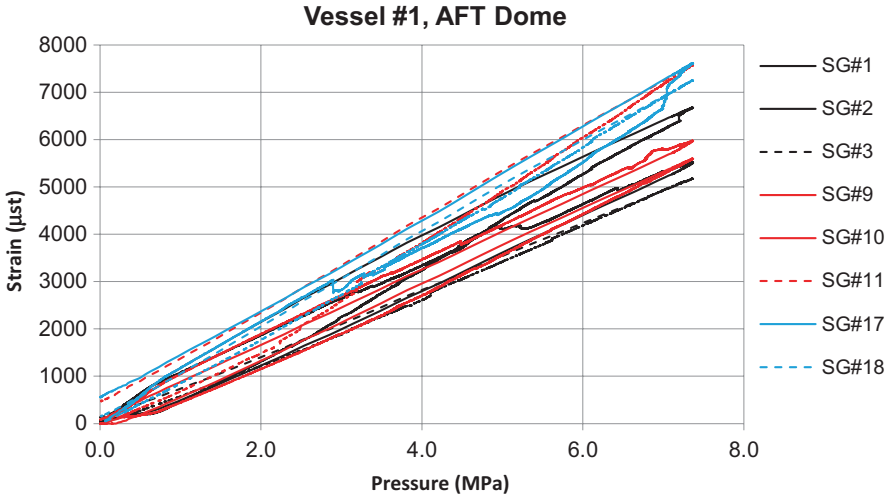


**Fig. 11** Strains in the proof test, vessel #1, strain gauges in the AFT dome

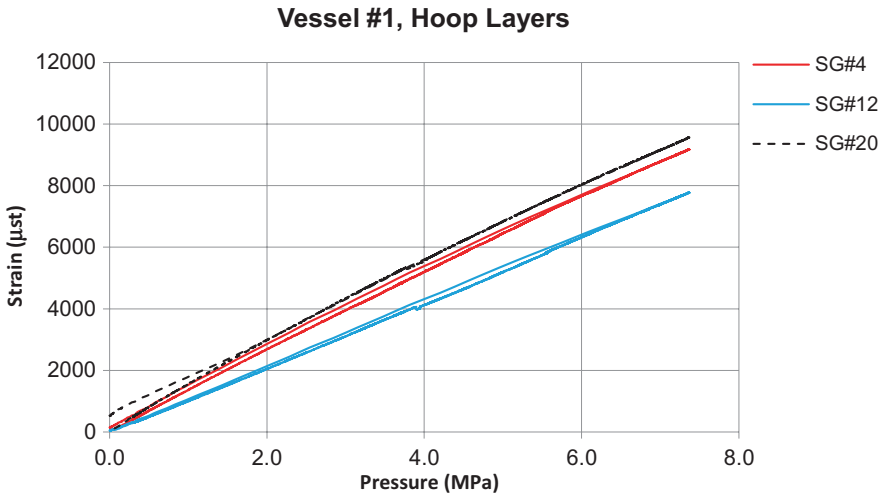


**Fig. 12** Strains in the proof test, vessel #1, strain gauges in hoop direction at the equator

Proof test results of CNT-modified vessels are shown in Figs. 14, 15, 16, and 17. Linear behavior with slight hysteresis is seen in all areas. Sporadic jumps are due to local matrix cracking, and the largest strains are displayed in the hoop layers.

Maximum displacements are viewed in Table 2. Results in the CNT/epoxy vessels are somewhat higher in the FWD dome and lower in the AFT dome. This may result from differences in dome thickness which in turn depend on resin content. Displacements in the cylindrical zone are very similar, and variance among neat vessels is larger than between neat and CNT-modified vessels. There

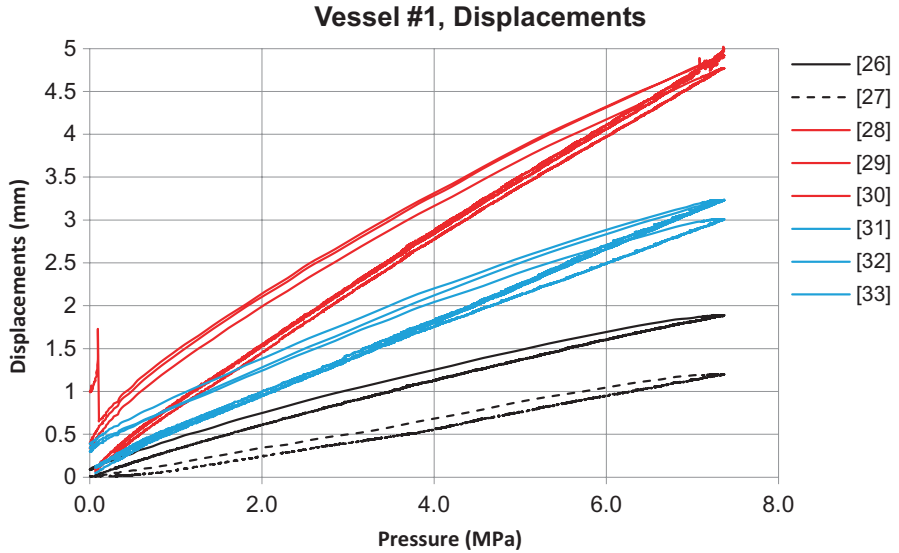


Fig. 13 Displacements in a proof test, vessel #1

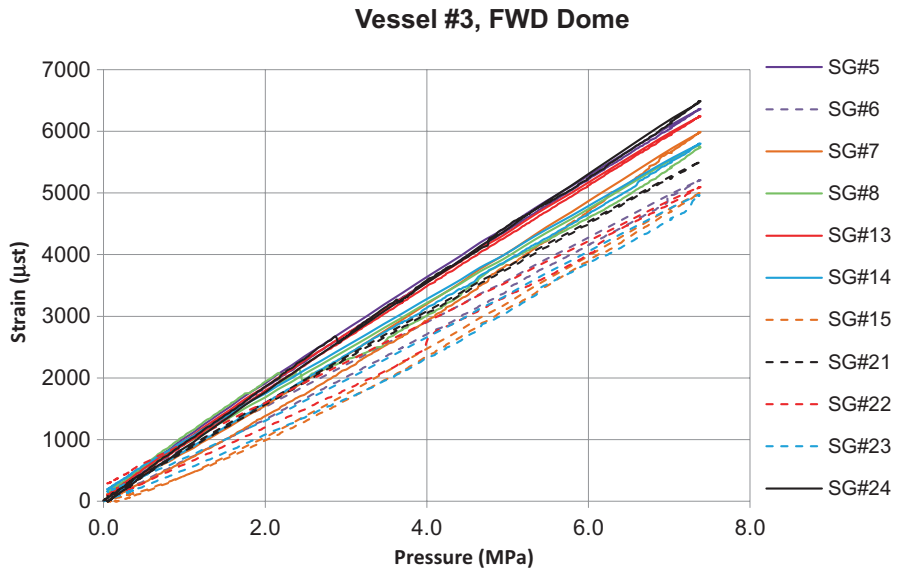


Fig. 14 Strains in the proof test, vessel #3, strain gauges in the FWD dome

is no significant difference among all vessels in terms of elastic compliance to pressure, and we conclude that CNT does not affect the elastic behavior of the pressure vessel.

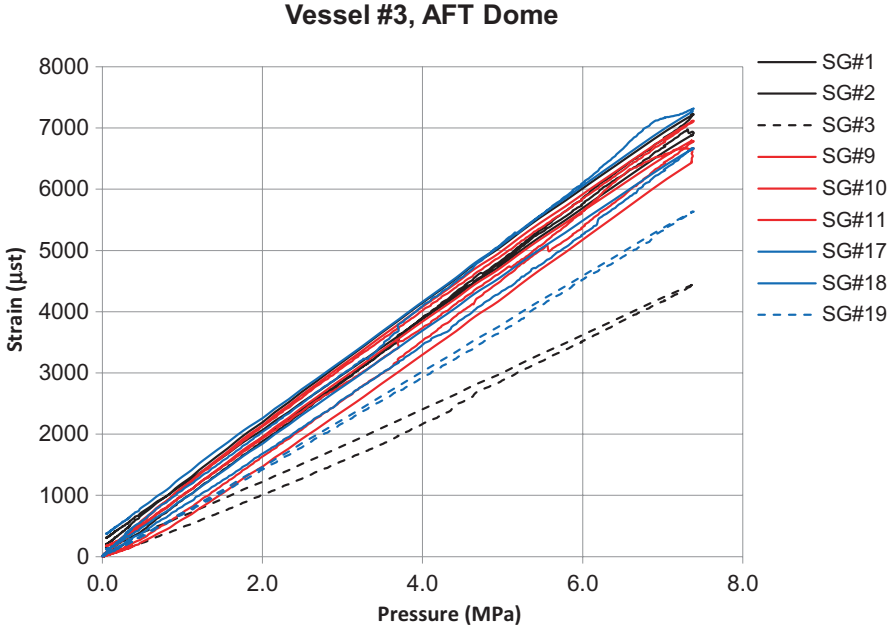


Fig. 15 Strains in the proof test, vessel #3, strain gauges in the AFT dome

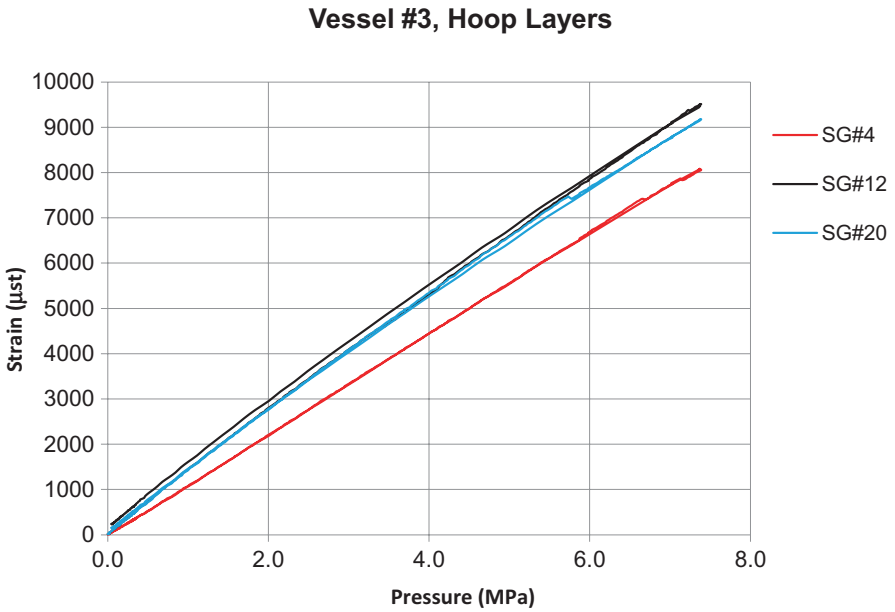


Fig. 16 Strains in the proof test, vessel #3, strain gauges in hoop direction at the equator

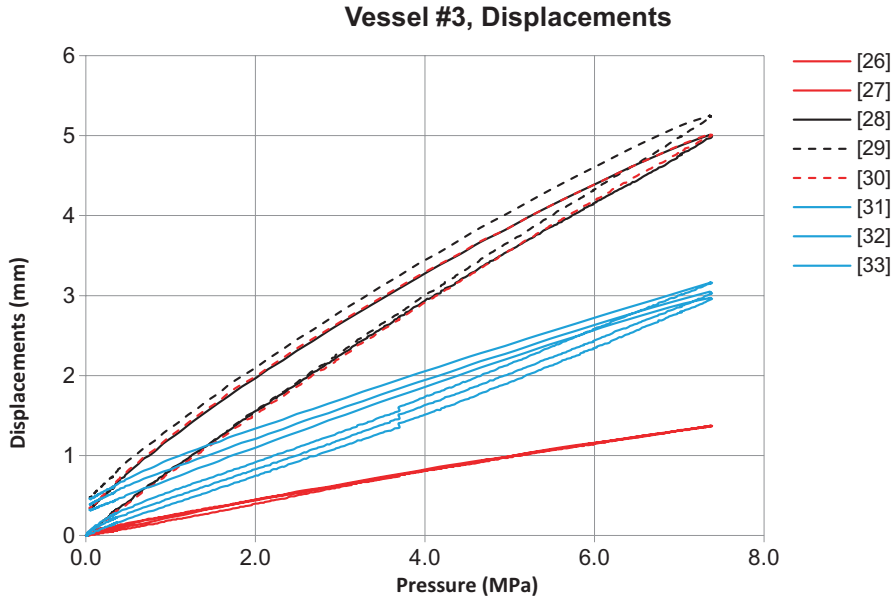


Fig. 17 Displacements in a proof test, vessel #3

Table 2 Comparison of displacements in a proof test in vessels with and without CNT

Displacements (mm)	Displacement gauge #	Vessels w/o NT			Vessels with CNT	
		1	2	5	3	4
FWD Dome	3	4.92	4.22		5.00	5.36
	4	4.77	4.10		5.25	–
	5	5.00	4.40		5.02	4.78
Cylinder	1	1.89	0.92	2.03	1.37	1.28
	2	1.20	2.01	0.89	1.37	1.29
AFT Dome	6	3.23	3.69		3.04	3.35
	7	3.01	4.05		2.97	2.66
	8	3.23	3.82		3.16	2.51

#### 4.4.2 Burst Tests

Burst pressures of the neat vessels were very similar, reaching 13.8 MPa, 12.9 MPa, and 13.5 MPa for vessels #1, #2, and #5 accordingly.

Similar stress-strain linear behaviors and matching burst pressures indicate that the winding process and fiber orientation were robust and well controlled. The low rate of pressurization did not affect linearity, meaning there is no short-term relaxation and the behavior is elastic. Typical strains in the neat vessels are shown in Figs. 18, 19, and 20. All three vessels showed similar behavior, and all bursts originated at the AFT dome, similarly to the neat vessels.

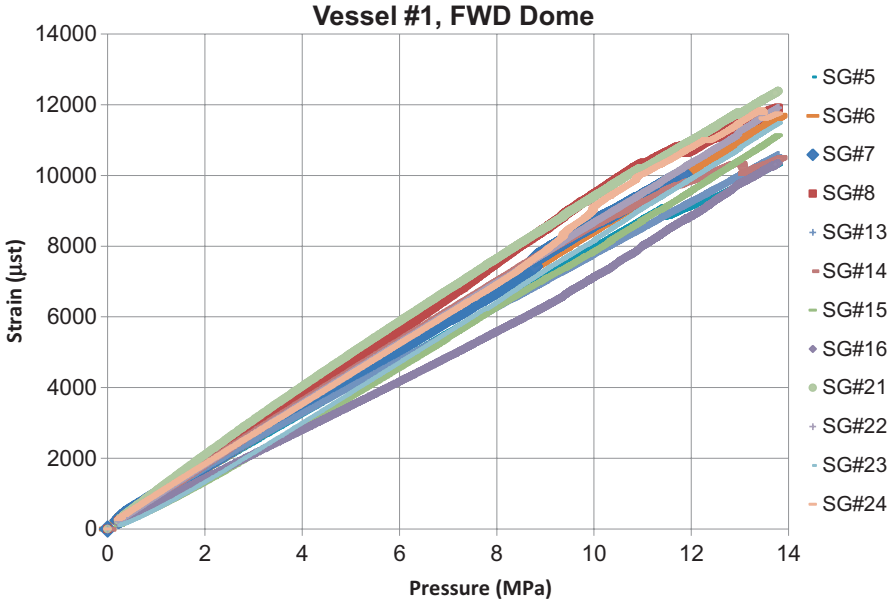


Fig. 18 Tensile strains in the FWD Dome, vessel #1 during burst test

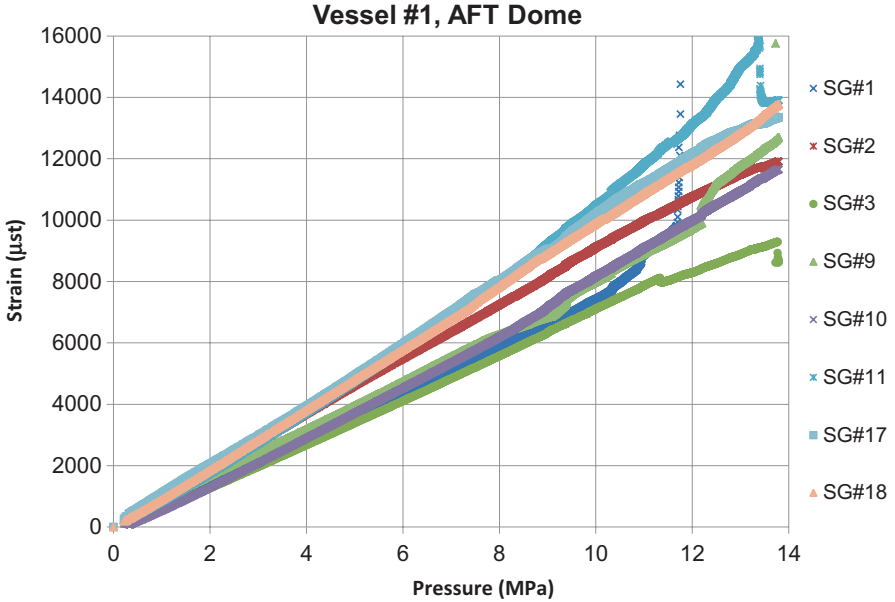


Fig. 19 Tensile strains in the AFT Dome, vessel #1 during burst test



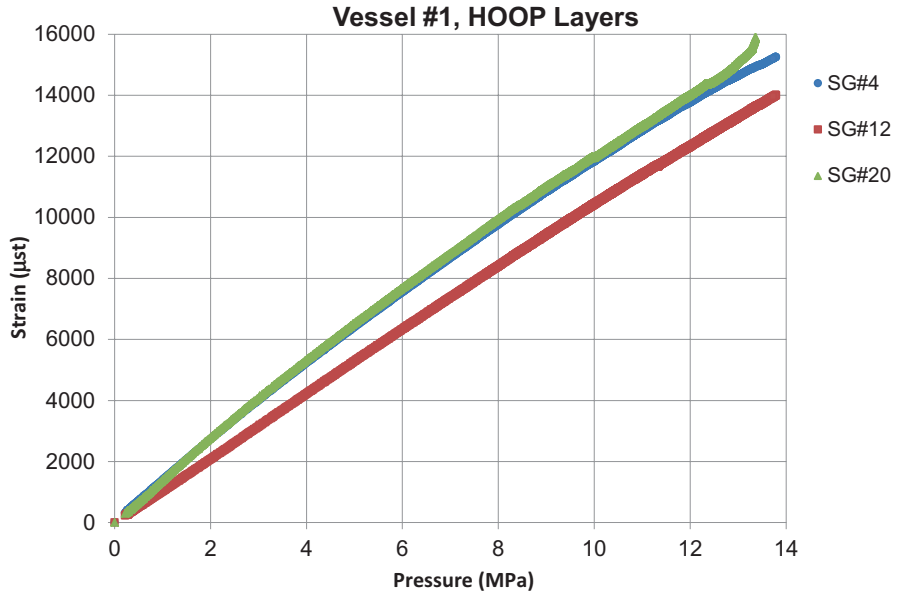


Fig. 20 Tensile strains in the hoop layers, vessel #1 during burst test

Fig. 21 Vessel #1 after burst



Vessel #1 burst originated in the AFT dome, see Fig. 21. This failure mode was followed by extensive damage in the dome and then ripping and breaking of hoop fibers as well as detachment of the boss. A mixed mode cohesive/adhesive failure mechanism can be seen in the boss, between the rubber shear ply and the steel although failure did not begin in this interface.

Vessel #2 burst initiated at the AFT dome, closer to the equator, as shown in Fig. 22. The 30° layer broke in pure tensile mode, followed by ripping of the hoop layers.

Vessel #5 burst is in the AFT dome, and the boss was pulled out from place by the bladder as shown in Fig. 23. This vessel also shows mixed (cohesive/adhesive) failure at the metal/rubber interface. The distinct failure onset location of vessel #2 is explained by small differences in dome thickness which in turn affect fiber volume fraction. Nevertheless, it seems that the domes were well balanced and burst pressures in all three vessels are very close. Figure 24 shows major damage in vessel #5 domes and hoop layers, as expected for a well-balanced vessel.

Effective burst pressures were higher than predicted. This is due to an underestimation of the domes thicknesses. Thicker domes lead to more rigid behavior and higher strength.

**Fig. 22** Vessel #2 after burst



**Fig. 23** Burst of vessel #5. AFT boss is being pulled out by the rubber bladder



**Fig. 24** Vessel #5 after burst

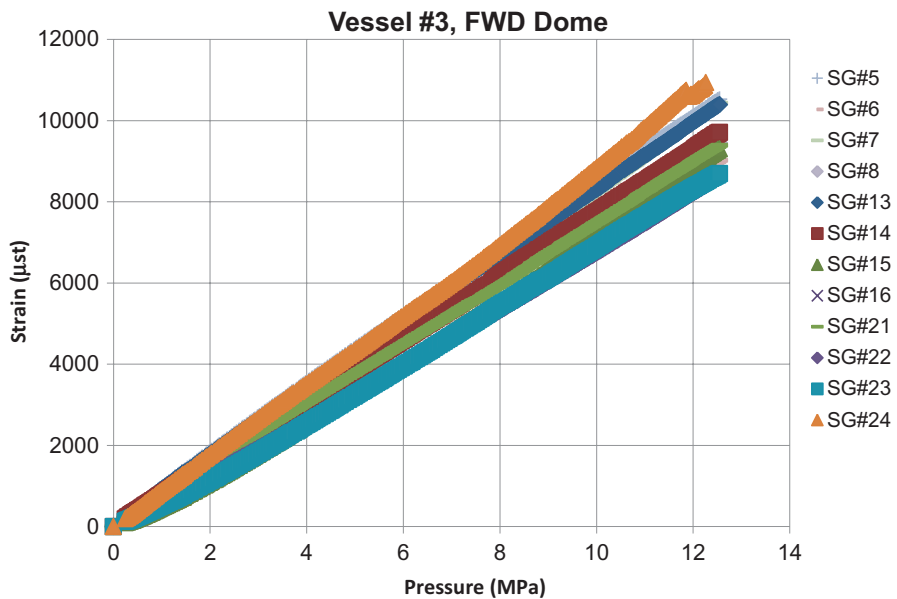


**Fig. 25** Tensile strains in the FWD Dome, vessel #3 during burst test

### 4.4.3 Burst of Pressure Vessels with CNT

Two pressure vessels containing CNT in the epoxy matrix were tested similarly to the neat vessels. They burst at 12.5 MPa and 12.7 MPa in the AFT dome. In view of the homogeneity in pressures and failure mode, the third vessel was not tested.

Tensile strains in the fiber direction are exhibited in Figs. 25, 26, and 27. Maximum tensile strains in Fig. 27 developed in the hoop layers, approaching 15,000 µst which is a typical strain to failure for the materials in use. For instance,

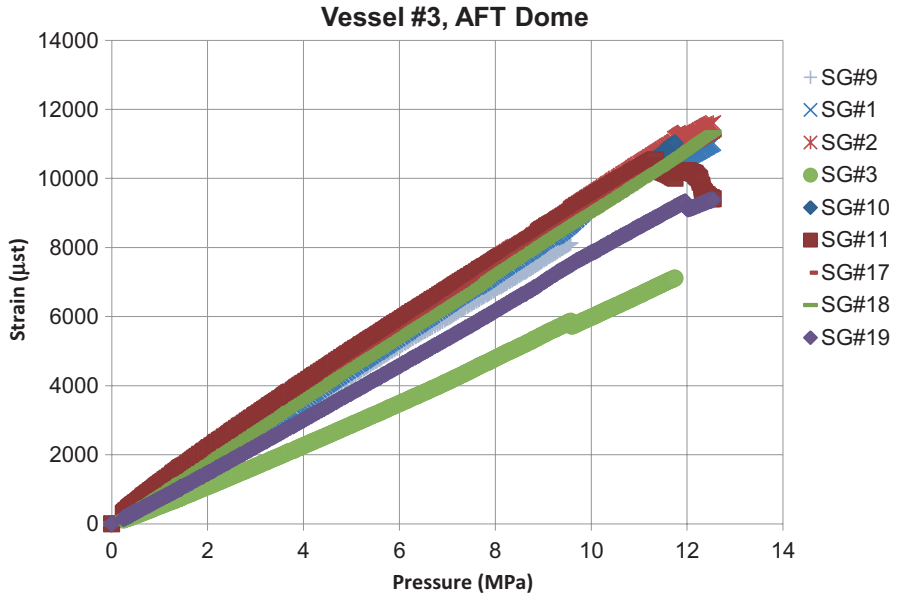


Fig. 26 Tensile strains in the AFT Dome, vessel #3 during burst test

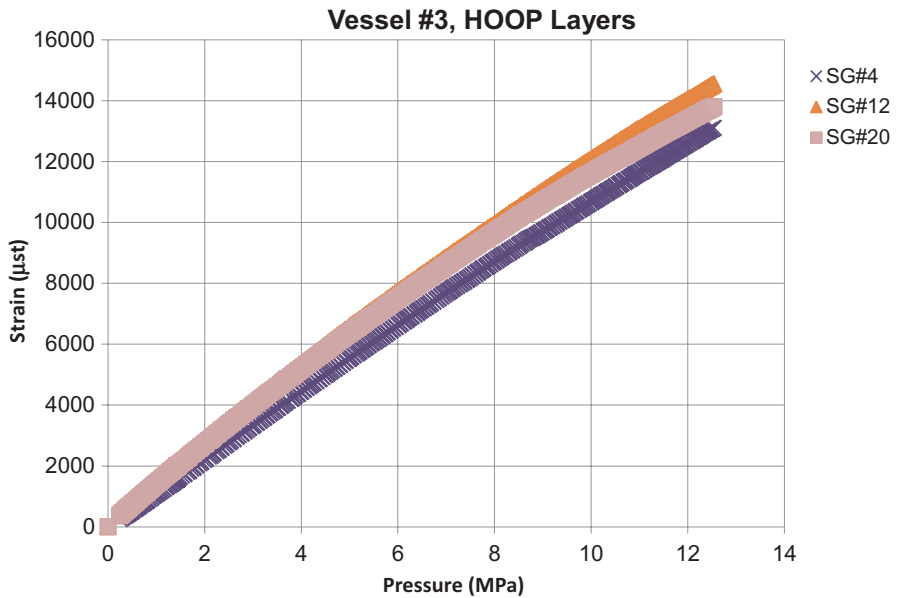


Fig. 27 Tensile strains in the hoop layers, vessel #3 during burst test

standard composite tensile specimens are reported to exhibit a tensile strain to failure of  $16,000 \mu\text{st}$  [16]. The failure characteristics are very similar to the neat vessels in terms of damaged zone, i.e., major damage of the AFT dome first, followed by ripping of the hoop layers and detachment of the boss. Strains in the domes are clearly below  $12,000 \mu\text{st}$ , as opposed to the neat vessels where higher strains were shown. But strains at the cylinder are higher, with a maximum measured value of  $14,500 \mu\text{st}$  in vessel #3, and strains in the AFT dome close to the cylinder, where the vessel failed, were probably in this range.

Based on the classical approach for calculation of composite strength [17], the effect of reduced fiber volume fraction on composite strength is minor, especially given the fact that fiber content (quantity) is constant. Since the effect of lower average fiber content in CNT containing vessels is marginal and the resulting burst pressures are equivalent to those of the neat vessels, we conclude that good impregnation was achieved. Close inspection of the fiber breakage shows no difference among all vessels, thus supporting this conclusion. Figure 28 (vessel #3) and Fig. 29 (vessel #4) depict failure of the CNT-modified vessels.

**Fig. 28** Burst of vessel #3



**Fig. 29** Burst of vessel #4. AFT boss is being pulled out by the rubber bladder



Table 3 summarizes measured burst pressures and maximum tensile strains. Strain values were rounded to the nearest 100  $\mu\text{st}$  (gauges are very precise but variance is several hundred  $\mu\text{st}$ ). Some scatter of measurements is typical and derives from local detachment of the gauge, from resin cracking, and to a lesser degree from misalignment of the SG. For instance, SG #6 in vessel #2 and SG #18 in vessel #4 are clearly low-biased readouts. But the integral result shows that both average and maximum strains in the domes and in the cylinder are very similar in all vessels. This indicates that CNT have neither beneficial nor detrimental effect on the behavior of the pressure vessels.

The mechanism of failure due to interlaminar shear and delamination is not evident in this work. Analysis of the acoustic emissions reveals matrix and fiber localized cracking but no extensive delaminations which would develop during interlaminar shear. Well-balanced domes and cylindrical zone and good control of processing properties seem to support a typical mode of failure by fiber tensile breakage, and the high tensile strains attained in all vessels are indicative of this failure mechanism.

**Table 3** Comparison of burst pressures and maximum strains in vessel with and without CNT

	Vessel #	Vessels w/o CNT			Vessels with CNT	
		1	2	5	3	4
	Burst pressure (MPa)	13.8	12.9	13.5	12.5	12.7
Location	Transducer	Strain ( $\mu\text{st}$ )				
FWD dome	5	10,300	12,700	11,800	10,500	11,100
	6	11,700	5,500	10,100	9,000	8,100
	7	–	–	10,600	10,400	7,100
	8	11,900	9,500	9,400	9,500	9,000
	13	10,600	10,400	10,800	10,400	10,300
	14	10,500	10,900	11,400	9,700	12,500
	15	11,100	9,400	11,900	9,300	11,600
	16	10,300	13,200	11,100	–	12,800
	21	12,400	8,700	11,800	9,400	11,400
	22	11,900	10,400	10,200	8,600	11,400
	23	11,500	8,100	10,000	8,700	10,600
Cylinder	24	11,700	10,600	10,800	12,600	–
	4	15,200	14,800	13,600	13,100	–
	12	14,000	15,200	12,100	14,500	–
AFT dome	20	–	13,800	13,900	13,800	–
	1	–	–	11,100	11,000	–
	2	11,900	11,600	12,100	11,600	10,700
	3	8,600	9,300	11,100	–	10,800
	9	12,700	12,100	10,800	–	11,300
	10	11,700	12,800	–	–	–
	11	13,900	14,100	10,700	9,400	10,700
	17	13,300	10,900	11,800	11,300	–
	18	13,800	11,800	11,300	11,300	6,600
	19	–	12,200	9,100	9,400	9,900

#### 4.5 Acoustic Emission, Failure Modes, and Failure Prediction

Standard short beam samples exhibited higher shear strengths when including CNT in the epoxy resin. In case a mechanism of shear due to bending of the domes and failure by delamination occurs, we would expect the CNT-modified vessels to burst at a higher pressure, compared to the neat vessels. Failure in tensile mode should not be affected by the presence of CNT, and burst pressures should remain unaffected. Nevertheless, other mechanisms developed during testing of the vessels, as evidenced by the acoustic emission recorded during pressurization.

Initiation of significant type II AE activity was detected in all five vessels at a pressure level of around 7 MPa. AE hit rate almost constantly increased during the entire duration of the test. A “felicity ratio” (FR) is calculated as the ratio of pressure level at the start of intensive type II activity during the burst cycle ( $P_{\text{Significant Type II activity}}$ ) to the proof pressure. Lower FR value in Table 4 indicates more significant damage accumulation in a pressure vessel. And since  $P_{\text{Significant Type II activity}}$  is lower than proof pressure, damage accumulation during the proof test was greater in vessels with lower burst pressure. FR correlates well and linearly with burst pressures, as shown in Fig. 30. This prediction is at about 50% of the burst pressure and below proof pressure.

Previous work with filament wound standard samples and various adhesive joints exhibited improved strengths [18]. Fracture surfaces showed that CNT toughened the epoxy resin by crack bridging, thus leading to crack arrest. In this work, acoustic emission was analyzed in terms of signal duration to check for crack length. After high amplitude signals were filtered out, average matrix AE parameters in Table 5 indicate the formation of shorter cracks, along with stronger, more energetic signals of larger amplitude. The shorter duration is in fact indicative of crack arrest, and the higher signal strength and amplitude may be related to additional energy-consuming mechanisms, such as nanofiber pullout and nanofiber breakage.

Bonding of the rubber to the composite resulted in much higher cohesive failure in CNT-modified vessels. Scanning electron micrographs of fracture surfaces, Fig. 31, show the debonding of the rubber from the carbon/epoxy composite material. Apart from the carbon fiber debris that result from the catastrophic failure, a rougher pattern can be observed in the rubber surface for the CNT-modified vessel,

**Table 4** Burst pressures, maximum strains, and AE results in vessels with and without CNT

Vessel #	Vessels w/o CNT			Vessels with CNT	
	1	2	5	3	4
Burst pressure (MPa)	8.13	9.12	5.13	5.12	7.12
Strain (%) @ FWD dome	1.24	27.1	19.1	26.1	28.1
Strain (%) @ cylinder	52.1	52.1	39.1	38.1	–
Strain (%) @ AFT dome	39.1	41.1	21.1	16.1	13.1
$P_{\text{Significant type II activity}}$ (MPa) (% of burst pressure)	7.5 (52%)	6.8 (51%)	7.0 (50%)	6.0 (46%)	6.1 (46%)
FR	0.986	0.893	0.92	0.787	0.800

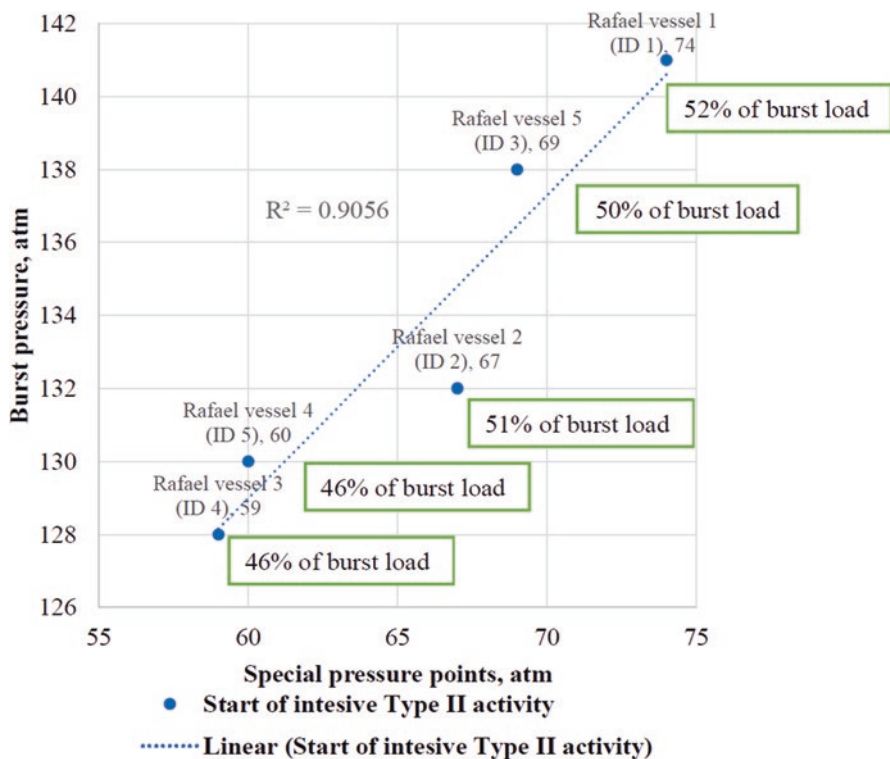


**Fig. 30** Onset of significant type II activity in a burst test

**Table 5** Averaged AE signal characteristics from the composite matrix

Vessel #	Vessels w/o CNT			Vessels with CNT	
	1	2	5	3	4
Avg. duration ( $\mu$ s)	67.9	64.9	62.8	49.2	58.4
Avg. amplitude (dB)	40.0	41.7	41.4	52.2	47.3
Avg. energy (r.u.)	0.91	1.20	1.08	2.96	2.06

along with multiple cracks and mixed mode epoxy/rubber cohesive/adhesive interface. The unmodified vessel exhibits a smoother rubber surface with mostly adhesive failure. This is indicative of the contribution of CNT to epoxy/rubber bonding by physical bridging.

## 5 Conclusions

A series of neat and CNT-modified carbon/epoxy pressure vessels were tested under proof pressure and then burst. The failure mode of the vessels was indistinctive of the CNT presence. Failure onset was at the AFT dome followed by breakage and



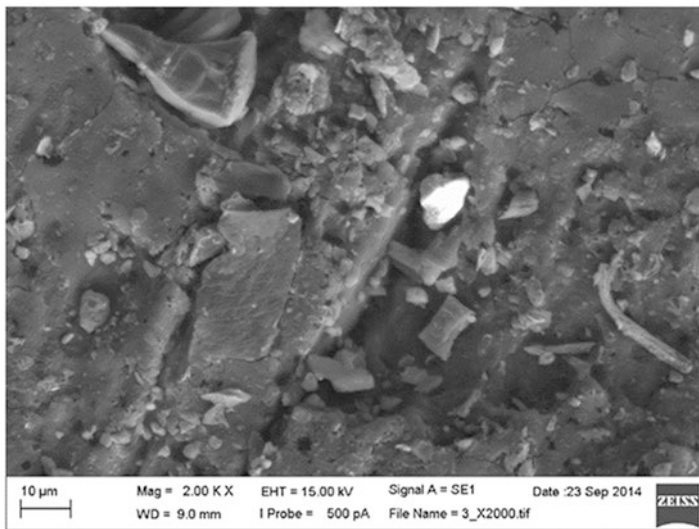
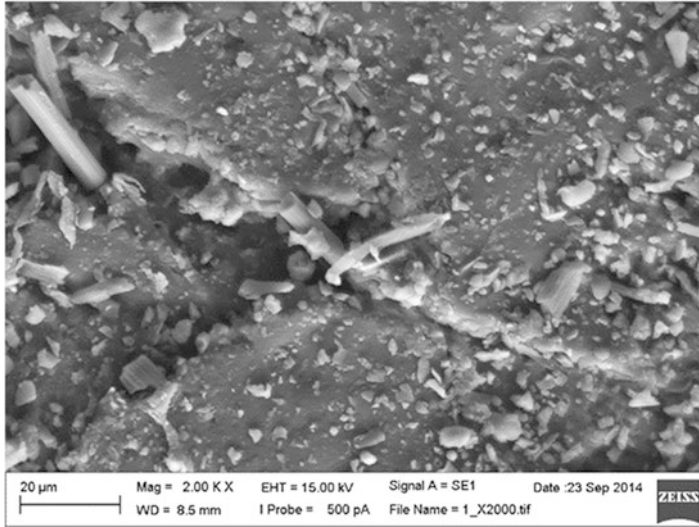


**Fig. 31** SEM of the rubber-carbon/epoxy composite interface after burst: (a) vessel #1; (b) vessel #3

ripping of the hoop layers. This work supports the failure criterion of fiber breakage in tension alone. Very high strains were recorded, at least 15,000  $\mu\text{st}$ , comparable to the strain at break of the carbon/epoxy composite in a standard sample. Interlaminar shear failure and delaminations at the domes were neither observed nor recorded by acoustic emission, despite the lack of wafers or doilies. Therefore the improved ILSS of CNT containing resin was not operative.

Visual inspection after burst indicates an improvement of the boss/composite interface adhesion. Bonding of the rubber to the composite resulted in much higher cohesive failure in CNT-modified vessels. Burst pressures are very even, both with or without CNT. This indicates a good degree of dispersion of the CNT, good fiber impregnation, and good control over winding parameters. Further reduction in the viscosity of the resin may lead to improvements. This could be achieved by further adjustment of process parameters or addition of a diluent to the resin.

A mechanism of crack arrest is shown by the shorter average duration of AE signals. The larger amplitude of matrix-related AE events may be related to mechanisms of energy dissipation such as nanofiber pullout and nanofiber breakage. A felicity ratio based on acoustic emission readouts may help predict burst pressures at pressures lower than the proof pressure, thus allowing some sort of nondestructive structural health monitoring.

The improved ILSS shown in short beam specimens may express in engineering parts where shear stresses are dominant or more significant, for example, wings, ailerons, and other flat surfaces.

**Acknowledgments** This work was partly funded by NES MAGNET Program of the Israel Ministry of Industry and Trade.

## Appendix 1: Terminology

AE parameters used in this study follow ASTM E1316 Terminology for nondestructive examinations [19]:

1. *P significant type II activity* – pressure level at which significant type II activity starts. Lower P significant type II activity indicates lower strength pressure vessels.
2. *FR (felicity ratio)* – ratio of pressure at initiation of significant damage development during the second cycle to the proof test pressure. Lower FR value indicates more significant damage accumulation in pressure vessels.
3. *AE amplitude* – the peak voltage of the largest excursion attained by the signal waveform from an emission event. AE amplitude is normally reported in dBAE – a logarithmic measure of acoustic emission signal amplitude, referenced to 1  $\mu\text{V}$  at the sensor, before amplification. Signal peak amplitude (dBAE) =  $20 \log_{10}(A1/A0)$ , where  $A0 = 1 \mu\text{V}$  at the sensor (before amplification) and  $A1 =$  peak voltage of the measured acoustic emission signal (also before amplification).
4. *Energy and acoustic emission signal* – the energy contained in an acoustic emission signal, which is evaluated as the integral of the volt-squared function over time.
5. *AE signal duration* – the time between AE signal start and AE signal end.
6. *AE signal start* – the beginning of an AE signal as recognized by the system processor, usually defined by an amplitude excursion exceeding threshold.
7. *AE signal end* – the recognized termination of an AE signal, usually defined as the last crossing of the threshold by that signal.

## References

1. J.N. Coleman, U. Khan, Y.K. Gun'ko, Mechanical reinforcement of polymers using carbon nanotubes. *Adv. Mater.* **18–6**, 689–706 (2006)
2. M.F. De Volder, S.H. Tawfick, R.H. Baughman, A.J. Hart, Carbon nanotubes: present and future commercial applications. *Science* **339**(6119), 535–539 (2013)
3. R. Tchoudakov, D. Goldman, N. Belenky, N. Naveh, Y. Portnoy, O. Rozent, M. Narkis, Electrically conductive epoxy/CNT composites containing low CNT contents. In: Proceedings of the 15th European Conference on Composite Materials (ECCM15), Venice, Italy, June 2012
4. V.C.S. Chandrasekaran, S.G. Advani, M.H. Santare, Role of processing on interlaminar shear strength enhancement of epoxy/glass fiber/multi-walled carbon nanotube hybrid composites. *Carbon* **48**, 3692–3699 (2010)
5. E. Bekyarova, E.T. Thostenson, A. Yu, H. Kim, J. Gao, J. Tang, H.T. Hahn, T.W. Chou, M.E. Itkis, R.C. Haddon, Multiscale carbon nanotube-carbon fiber reinforcement for advanced epoxy composites. *Langmuir* **23**, 3970–3974 (2007)
6. Z. Fan, M.H. Santare, S.G. Advani, Interlaminar shear strength of glass fiber reinforced epoxy composites enhanced with multi-walled carbon nanotubes. *Compos. Part A: Appl. Sci. Manuf.* **39**, 540–554 (2008)
7. C. Fang, J. Wang, T. Zhang, Interlaminar improvement of carbon fiber/epoxy composites via depositing mixture of carbon nanotubes and sizing agent. *Appl. Surf. Sci.* **321**, 1–9 (2014)
8. K. Sharma, M. Shukla, Three-phase carbon fiber amine functionalized carbon nanotubes epoxy composite: processing, characterization, and multiscale modeling. *J. Nanomater.* **837492**, 1–11 (2014)
9. J. Li, Z. Wu, C. Huang, L. Li, Multiscale carbon nanotubes-woven glass fiber reinforced cyanate ester/epoxy composites for enhanced mechanical and thermal properties. *Compos. Sci. Technol.* **104**, 81–88 (2014)
10. K.C. Shekar, B.A. Prasad, N.E. Prasad, Interlaminar shear strength of multi-walled carbon nanotube and carbon fiber reinforced, epoxy-matrix hybrid composite. *Procedia Mater. Sci.* **6**, 1336–1343 (2014)
11. J.S. Fenner, I.M. Daniel, Hybrid nanoreinforced carbon/epoxy composites for enhanced damage tolerance and fatigue life. *Compos. Part A: Appl. Sci. Manuf.* **65**, 47–56 (2014)
12. D. Mao, Improving mechanical properties of Nanocomposites using Carbon Nanotubes, SAMPE 2009
13. D. Mao, Ultra Lightweight High Pressure Hydrogen Fuel Tanks Reinforced with Carbon Nanotubes. Applied Nanotech, Inc., Project ST105 Report, Phase II SBIR from US DOE, 2012
14. K.L. Thunhorst, A.M. Hine, P. Sedgwick, M.R. Huehn, R. Mike, D.P. Goetz, The Effect of Nanosilica Concentration on the Enhancement of Epoxy Matrix Resins for Filament-Wound Composite Overwrapped Pressure Vessels. SAMPE 2011, Long Beach, CA, May 2011, pp. 23–26
15. M. Adams, Nanos in the Pressure Vessel, [asme.org](http://asme.org), 2012. See also [www.3M.com/advancedcomposites](http://www.3M.com/advancedcomposites)
16. Torayca T800H Technical Data Sheet No. CFA-007
17. S.W. Tsai, H.T. Hahn, *Introduction to Composite Materials* (Technomic, Westport, 1980)
18. N. Naveh, Y. Portnoy, A. Buchman, “Improvement of Composites and Adhesives with CNT”, NES Consortium Report, Y3, Ministry of Industry and Trade, Israel, 2012
19. ASTM E1316 Standard Terminology for Nondestructive Examinations (2016)

# Energy Absorption Capability of Hybrid Fibers Reinforced Composite Tubes

Yuqiu Yang, Yan Ma, Jing Xu, and Hiroyuki Hamada

## 1 Introduction

Extensive research and development has been carried out in the past few decades to explore an efficient way to improve the safety – especially crashworthiness and crash compatibility – of automobiles [5, 6, 15, 23, 10, 24, 25]. Crashworthiness has attracted significant attention because of its multiple functions, which are to (1) absorb energy, (2) keep the occupant compartments intact, and (3) ensure tolerable deceleration levels for drivers and passengers during a crash [1, 19]. To achieve the above functions, various materials and structures are designed by the automobile industry.

Lightweight carbon fiber-reinforced composites (CFRPs) do not exhibit the ductile failure mechanism found in metals [11–13, 21, 22]. That is to say, unlike metals, which absorb energy through deformation (as shown in Fig. 1a), CFRPs absorb lots of energy through progressive crushing modes by a combination of micro-cracking, splitting, bending, delamination, and friction (as shown in Fig. 1b). It is a well-known fact that one can achieve higher energy absorption, compared to metal alloys, with proper construction and architecture of composite structures.

According to previous studies, the energy absorption capability of composite tubes could be affected by a variety of factors such as raw materials (fiber material [20, 23], resin material [4, 20], and their combination [3, 4]), fiber orientation [14] and lay-up [18], specimen geometry (inside diameter-to-wall thickness ratio [8, 15], collapse trigger mechanism [2, 19], cross-sectional geometry [7]), experimental conditions (strain rate [7, 20], frictional effect [17]), and so on. Most of the static

---

Y. Yang (✉) • J. Xu  
Donghua University, Shanghai, China  
e-mail: amy\_yuqiu\_yang@dhu.edu.cn

Y. Ma • H. Hamada  
Kyoto Institute of Technology, Kyoto, Japan

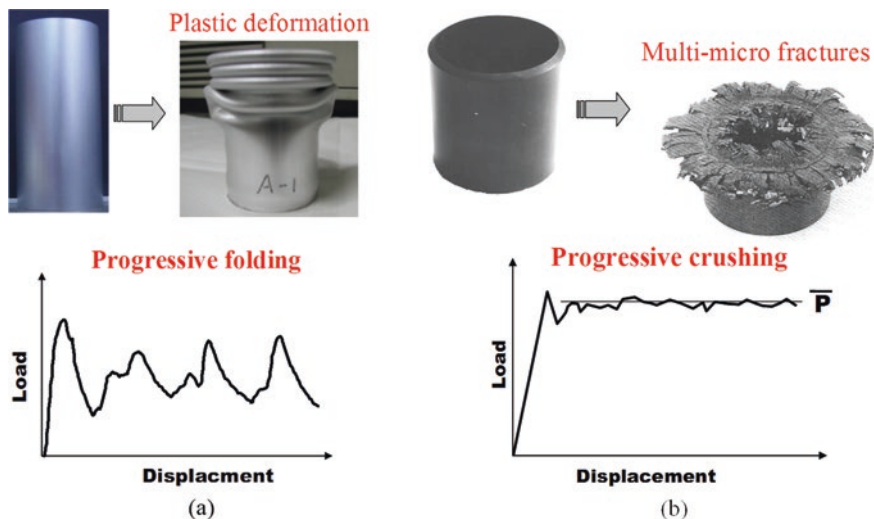


**Fig. 1** Comparison of metal and CFRP tubes (a) Metal tube (b) FRP tube

crushing studies had been carried out to investigate the energy absorption capability and crushing characteristics of composite tubes. With this method, the slow speed of the crushing process helps to effectively capture the crushing behavior of the composite tubes. However, most of the practical conditions are dynamic in nature. Hence, investigations of the crushing process under dynamic condition are necessary.

Fiber-reinforced composites (FRPs) with the above advantages are not being widely used as energy absorption components at present; the most important reasons for this are their high manufacturing cost and their complicated energy absorption mechanism. Yan Ma et al. [10] investigated the static crushing behavior, energy absorption capability, and temperature treatment effect of carbon fiber (CF)/CF-epoxy and CF/aramid fiber (AF)-epoxy composite tubes manufactured by the filament winding method. By optimizing different hybrid methods, ratios, and reasonable geometric shapes of composites, low-cost and high-energy absorption components with specific energy absorption ( $E_s$ ) close to 96 kJ/kg could be manufactured for use on vehicles. However, the investigated aspects were relatively limited, and more practical dynamic methods were not tested. In addition, the effects of temperature on energy absorption components are commonly investigated in the automobile industry because the level of heat release results in a temperature increase when the engine runs. Yan Ma et al. [10] also investigated the temperature treatment effect. However, further investigation needs to be conducted and a more detailed mechanism of temperature treatment effect has to be introduced.

To investigate the energy absorption capability of CF hybrid FRP tubes further, CF, AF, and glass fiber (GF) were chosen as reinforcements and the same epoxy resin was chosen as a matrix to manufacture five new different structures and raw

materials of FRP composite tubes through a highly productive and low-cost winding method. Except for static tests, the effects of material, temperature treatment, and hybrid ratio on the energy absorption capability under dynamic crushing tests were also investigated experimentally.

## 2 Experimental Procedure

### 2.1 Materials and Design

Three kinds of fibers – T700SC-12k carbon fiber provided by Toray, Kevlar 29 provided by Toray, and GF provided by Nittbo – were used as reinforcements in this study. Epoxy resin 308A3801 from Mitsubishi Chemical was chosen as the matrix. The filament winding method was used to manufacture the nine types of specimens. The specifications of the raw materials are shown in Table 1.

Nine types of tubes with different raw materials, fiber orientation, and ratio were designed and manufactured in this study. A 50 mm diameter mandrel was used in this experiment. Each tube consisted of three layers – inner ( $88^\circ$ ), intermediate ( $10^\circ$  or  $17.6^\circ$ ), and outer ( $88^\circ$ ). Two kinds of structures including type A (three layers) and type B (five layers) were investigated as shown in Fig. 2. Specimens were named based on the thickness and material of each layer. For example, G/C2 composite tube consisted of GF( $88^\circ$ )/CF( $17.6^\circ$ )/GF( $88^\circ$ ) layers with thicknesses of 0.15 mm, 2 mm, and 0.5 mm, respectively. A/C1.6' composite tube consisted of AF( $88^\circ$ )/CF( $10^\circ$ )/AF( $88^\circ$ ) layers with thicknesses of 0.15 mm, 1.6 mm, and 0.83 mm, respectively. In particular, A/C1.5-F composite tube consisted of AF( $88^\circ$ )/CF( $10^\circ$ )/AF( $88^\circ$ )/CF( $10^\circ$ )/AF( $88^\circ$ ) fiber layers with thicknesses of 0.15 mm, 0.75 mm, 0.188 mm, 0.75 mm, and 0.188 mm, respectively. Schematic diagrams and the parameters of design of FRPs tubes and fiber volume fractions ( $V_f$ ) measured are shown in Fig. 3 and Table 2, respectively. Thickness measured is about 1 mm thicker than designed thickness, and ratio measured is in line with Table 2.  $V_f$  in Table 2 represents the sum fraction of all hybrid reinforcements. Three replicate specimens were tested in quasi-static test and two used in drop tests in this chapter.

**Table 1** Specification of raw material

Materials	Manufacturers	Type	$E$ (GPa)	$\sigma$ (MPa)	$\rho$ (g/cm <sup>3</sup> )	$\epsilon$ (%)
CF	Toray	T700SC-12k	230	4900	1.8	2.1
AF	Dupont-Toray	Kevlar 29	70.4	2920	1.44	3.6
GF	Nittbo	T-glass	84.3	4650	2.49	2.49
Epoxy	Mitsubishi chemical	308A3801	4	64	–	1.9

$E$  modulus,  $\sigma$  strength,  $\rho$  density,  $\epsilon$  elongation

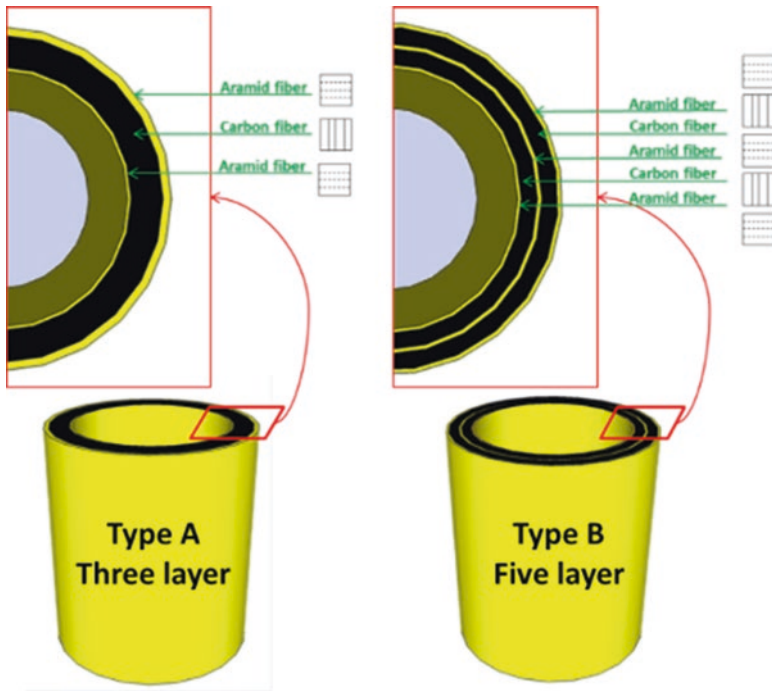


Fig. 2 Schematic diagram of two types of carbon/aramid CFRPs structures (Reproduced with permission from Ref. [10])

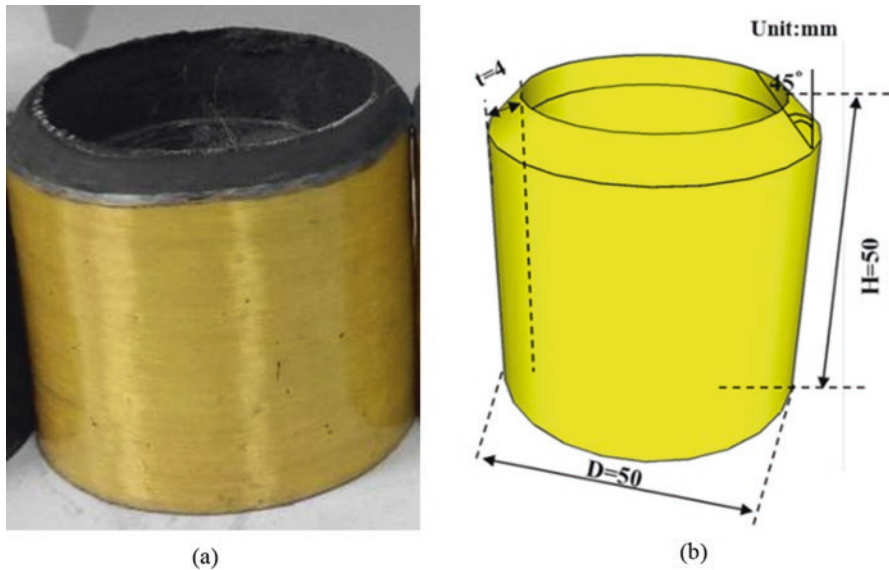


Fig. 3 Realistic appearance (a) and schematic diagram (b) of typical A/C2 specimen (Reproduced with permission from Ref. [24])

## 2.2 Manufacturing and Temperature Treatment

All the specimens were manufactured by the filament winding method. The fabricated specimens were tapered in a 45° chamfer at the compressed head after cutting into approximately 50-mm lengths. This trigger initiated a stable, progressive, high energy crushing rather than a sudden catastrophic type of failure of the FRPs composite tubes. Then specimens were heat treated at 100 °C for 100 h, 200 h, and 400 h, respectively, according to the treatment design for investigating the effect of temperature treatment on crashworthiness, which is shown in Table 3. Specimens treated at 100 °C for 200 h are named TT-type (TT-A/C2 for example). After temperature treatment, specimens did not show any difference in appearance. A representative specimen with marked size ready for compression is shown in Fig. 3.

## 2.3 Compression Tests

### 2.3.1 Quasi-static Tests

All composite tubes were tested in axial compression using a WDW-100KN universal testing machine. Tubes were compressed by 30 mm at a constant cross-head speed of 5 mm/min. The load and crush displacement were recorded by the standard coordinate system ( $x$ - $y$  coordinates). According to the load-displacement curves, crashworthiness characteristics were calculated as follows

Peak load ( $P_{\max}$  or  $P_{\text{Initial}}$  in kN) is the initial peak force (commonly the maximum force) of the curve in the progressive compression. Total energy absorption ( $A_e$  in kJ) is the integral of the load-displacement curve and it is calculated with (1), where  $P$  is the force value at each compression distance. The area under load-displacement curve is equal to  $A_e$ :

$$A_e = \int_{l_{\max}}^0 P(l) dl \quad (1)$$










$P_{\text{mean}}$  (kN) is the mean load, which is calculated as the total absorbed energy per crushed tube length ( $l_{\max}$ , m); see (2):

$$P_{\text{mean}} = \frac{\int_0^{l_{\max}} P(l) dl}{l_{\max}} \quad (2)$$

Specific energy absorption ( $E_s$ , kJ/kg) is the most important parameter to evaluate crashworthiness in vehicles. It is the energy absorbed per unit of crushed specimen mass ( $m_{\text{crush}}$ , kg), calculated in (3):



**Table 2** Parameters of designed CFRPs tubes with measured volume fraction

Type	Parameters	Structure					$V_f$ (%)
		Inner	Middle	Outer			
	Fiber distribution	AF	CF	AF		–	
	Ratio	1.0	10.0	2.5			
	Thickness/ mm	0.15	1.50	0.39			
A/C/A:1/10/2.5	Fiber orientation	88°	17.6°	88°		38.3	
	Fiber distribution	AF	CF	AF			
	Ratio	1.0	11.0	5.5			
	Thickness/ mm	0.15	1.66	0.830			
A/C/A:1/11/5.5	Fiber orientation	88°	10°	88°		–	
	Fiber distribution	AF	CF	AF			
	Ratio	1.0	11.0	5.5			
	Thickness/ mm	0.15	1.66	0.830			
A/C/A:1/11/5.5	Fiber orientation	88°	17.6°	88°		39.6	
	Fiber distribution	AF	CF	AF			
	Ratio	1.0	13.3	3.3			
	Thickness/mm	0.15	2.00	0.50			
A/C/A:1/13.3/3.3	Fiber orientation	88°	17.6°	88°		41.1	
	Fiber distribution	AF	CF	AF			
	Ratio	1.0	14.7	2.0			
	Thickness/ mm	0.15	2.20	0.30			
A/C/A: 11/14.7/2	Fiber orientation	88°	17.6°	88°		–	
	Fiber distribution	CF	CF	CF			
	Ratio	1.0	11.0	5.5			
	Thickness/mm	0.15	1.66	0.83			
C/C/C:1/11/5.5	Fiber orientation	88°	17.6°	88°		43.9	
	Fiber distribution	CF	CF	CF			
	Ratio	1.0	13.3	3.3			
	Thickness/mm	0.15	2.00	0.50			
C/C/C:1/13.3/3.3	Fiber orientation	88°	17.6°	88°		42.9	
	Fiber distribution	GF	CF	GF			
	Ratio	1.0	13.3	3.3			
	Thickness/mm	0.15	2.00	0.50			
C/C/C:1/13.3/3.3	Fiber orientation	88°	17.6°	88°		–	
	Fiber distribution	AF	CF	AF	CF		AF
	Ratio	1.00	5.00	1.25	5.00		1.25
	Thickness/mm	0.150	0.750	0.188	0.750	0.188	
A/C/A/ C/A:1/5/1.25/5/1.25	Fiber orientation	88°	17.6°	88°	17.6°	88°	

Reproduced with permission from Ref. [10, 24]

**Table 3** Treatment design of CFRPs tubes at 100 °C

Type	Structure (Material: thickness (orientation))	Treating time (h)		
A/C1.5	A/C/A:1(88°)/10(17.6°)/2.5(88°)	0	200	400
A/C1.6'	A/C/A:1(88°)/11(10°)/5.5(88°)	0	–	200
A/C1.6	A/C/A:1(88°)/11(17.6°)/5.5(88°)	0	100	200
A/C2	A/C/A:1(88°)/13.3(17.6°)/3.3(88°)	0	100	200
A/C2.2	A/C/A: 11(88°)/14.7(17.6°)/2(88°)	0	–	200
C/C1.6	C/C/C:1(88°)/11(17.6°)/5.5(88°)	0	100	200
C/C2	C/C/C:1(88°)/13.3(17.6°)/3.3(88°)	0	–	200
G/C2	C/C/C:1(88°)/13.3(17.6°)/3.3(88°)	0	–	200
A/C1.5-F	A/C/A/C/A:1(88°)/5(17.6°)/1.25(88°)/5(17.6°)/1.25(88°)	0	200	400

0 in the “Treating time” represent the specimens without heat temperature treatment

$$E_s = \frac{\int_0^{l_{\max}} P(l) dl}{m_{\text{crush}}} \quad (3)$$

Crush efficiency ( $\eta_c$ , %) is a characteristic to evaluate the stability of the crushing process, which is the percentage ratio of  $P_{\text{mean}}$  to  $P_{\text{max}}$ , calculated in (4):

$$\eta_c = \frac{P_{\text{mean}}}{P_{\text{max}}} \quad (4)$$

### 2.3.2 Dynamic Tests

Dynamic tests (or drop tests) were carried out on a free flight drop tower facility LC36-225H6600-III as shown in Fig. 4. A hammer with a weight of 120 kg was mounted at a height of 5 m to achieve the velocity of 10 m/s (Fig. 4a) to ensure the velocity did not decrease intensely during collapse. A high-speed camera Photron SA1.1 (Fig. 4c) was used to record the pictures at the high speed of 400,00 frames per second. Blocks were used to prevent specimens from totally collapsing. Force and displacement were recorded by a computer (Fig. 4d) connected to a force sensor and displacement sensor. Every evaluation index was calculated as shown in the equations above.

## 2.4 Microscopic Observation

Post-crush specimens were cast in resin to retain the crush morphology and were then cut, polished, and finally observed by optical microscope to observe the post-crush cross section and analyze the energy absorption mechanism. The size of the crush zone was too small to be photographed using a camera and too large to be

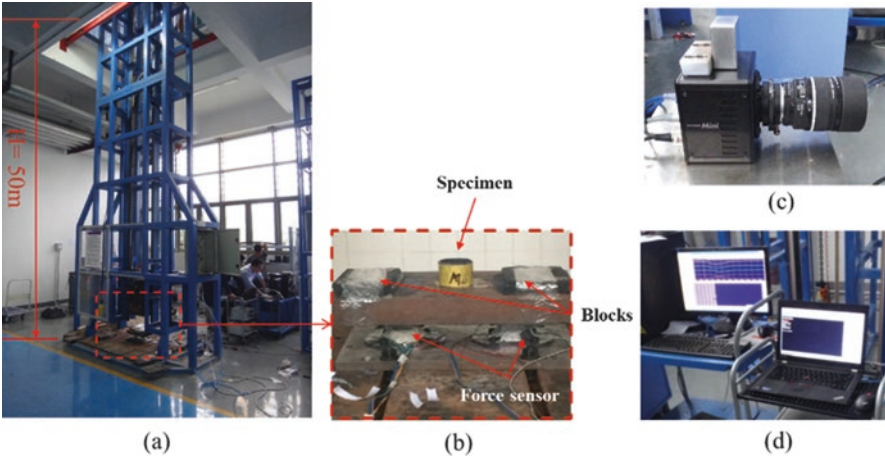


**Fig. 4** Dynamic test system comprising the drop test facility (a), test bench (b), high-speed camera (c), and electronic recorder system (d) (Reproduced with permission from Ref. [24])

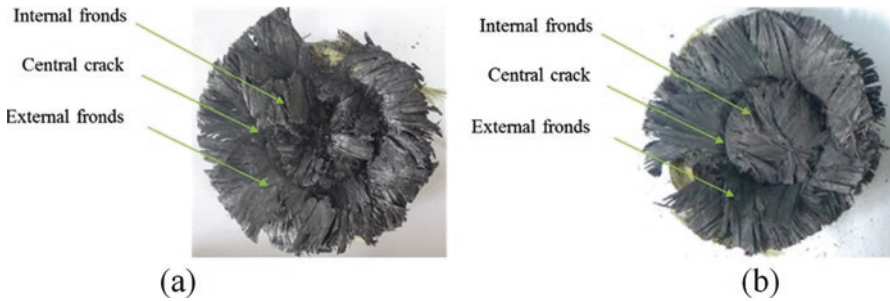


**Fig. 5** Top view of post-crushed tubes after quasi-static test (a) and dynamic test (b) (Reproduced with permission from Ref. [24])

observed using a microscope. This problem could be overcome by using photomontage of the sections from whole frames.

### 3 Results

#### 3.1 Quasi-static and Dynamic Compression Test Results

Representative top views of post-crushed tubes after quasi-static tests and drop tests are shown in Fig. 5a, b respectively. Most of the tubes exhibited typical splaying crushing mode [6]. The axial fibers splayed in a series of fronds to the outside and inside of the tubes, and a crack propagated along the center of the wall of the tube, known as a central crack. A wedge of debris formed at the top side of central crack [10, 24].

Representative load-displacement curves of all the specimens and testing results, including average crushing efficiency ( $\eta_c$ ) and average specific energy absorption ( $E_s$ ), both tested in quasi-static and dynamic tests, are shown in Fig. 6 and Table 4, respectively. According to the displacement-load curves of A/C2.2-Dynamic and G/C2-Dynamic under dynamic tests shown in Fig. 6f, i respectively, the crushing process was found to enter the crushing compaction area at a distance less than 30 mm (about 25 mm). The  $E_s$  of both tubes were calculated from 0 mm to 25 mm [10, 24].

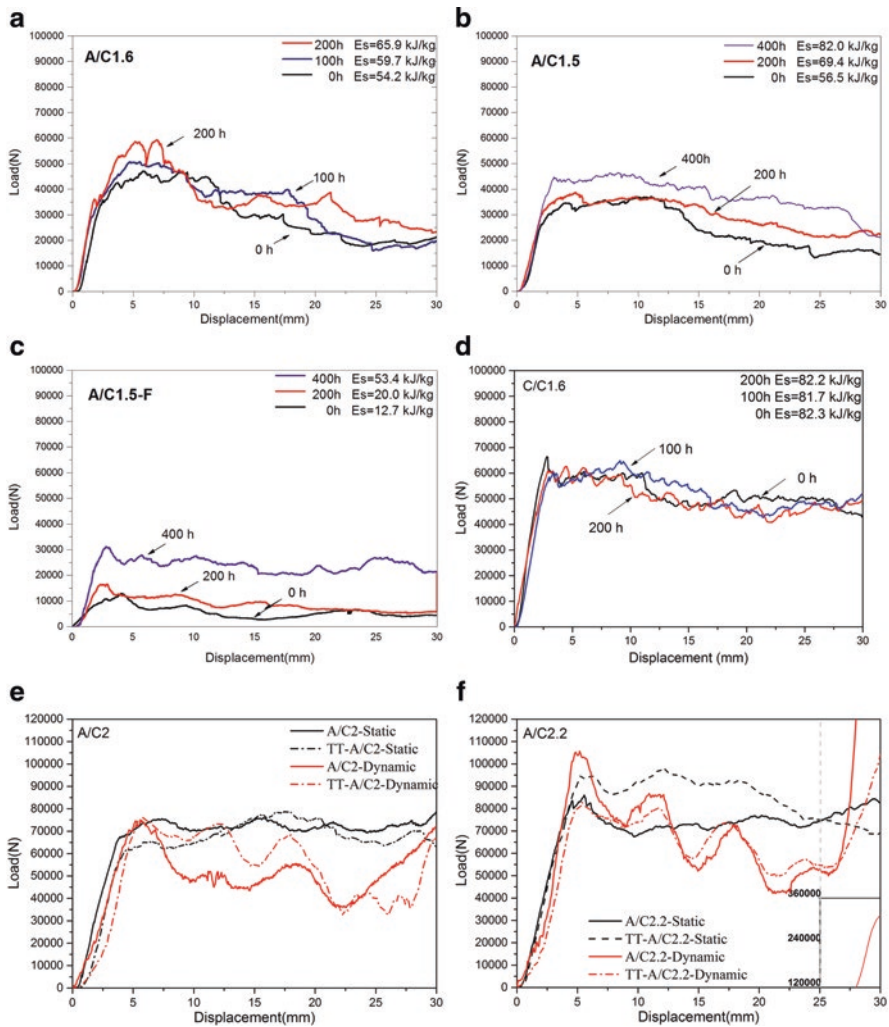


**Fig. 6** Typical load-displacement curves of CFRPs under both quasi-static and dynamic tests (Reproduced with permission from Ref. [10, 24])

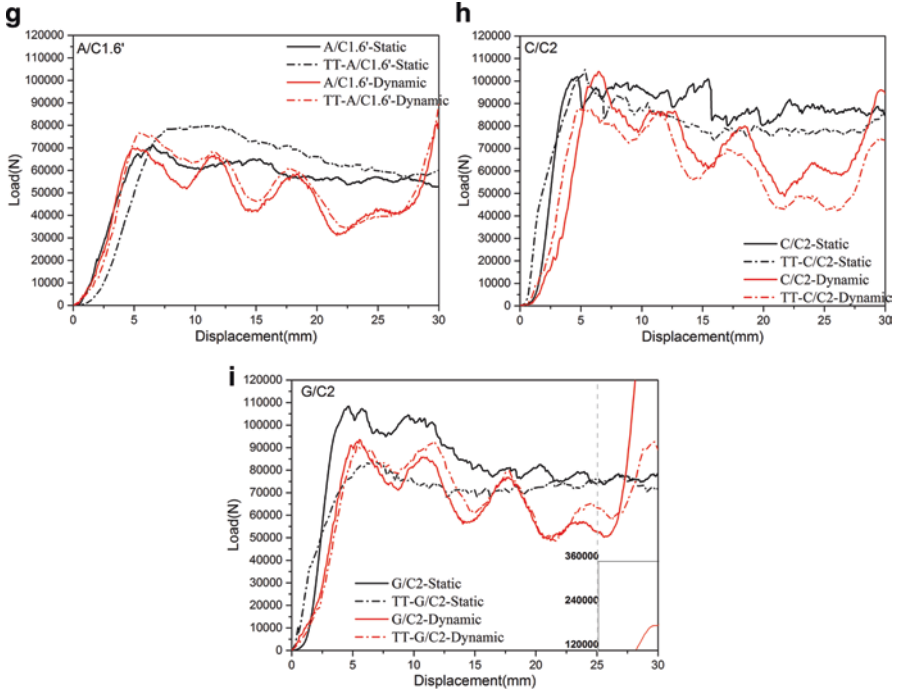


Fig. 6 (continued)

### 3.2 Microscopic Observation

Optical photographs of cross sections through the crush zones of various hybrid FRPs composite tubes with or without temperature treatment are shown in Figs. 10, 11, 12 and 13 and in Figs. 18, 19, 20, 21, 22, 23, 24, 25, 26 and 27. The fracture cross sections are introduced in detail in the following sections.

## 4 Discussion

### 4.1 Effect of Structure on Energy Absorption

Composite tubes A/C1.5 (A88°/C17.6°/A88°:0.15 mm/1.5 mm/0.39 mm) and A/C1.5-F (AF88°/CF10°/AF88°/CF10°/AF88°:0.15 mm/0.75 mm/1.88 mm/0.75 mm/0.188 mm) have the same fiber content and orientation but different structure, as shown in Table 2. From Fig. 7, it is easy to see that a three-layer (A/C1.5) structure exhibited better energy absorption capability than a five-layer (A/C1.5-F) structure of carbon/aramid FRPs, even with same fiber content and orientation. The A/C1.5-F type of tube with five layers has more thin layers than the A/C1.5 type of tube.

**Table 4** Results of quasi-static and drop tests

Type	S/D	$\eta_c$ (%)				$E_s$ (kJ/kg)			
		0	100	200	400	0	100	200	400
A/C1.5	S	35.1 ± 3.2	–	40.64 ± 3.3	48.43 ± 2.3	56.5 ± 4.2	–	69.4 ± 3.5	82.0 ± 5.3
A/C1.6'	S	79.6 ± 8.3	–	74.8 ± 7.0	–	82.8 ± 0.46	–	98.0 ± 1.1	–
	D	68.4 ± 4.6	–	66.0 ± 6.7	–	76.3 ± 2.9	–	82.0 ± 5.0	–
A/C1.6	S	74.2 ± 3.6	44.5 ± 4.2	48.4 ± 3.2	–	54.2 ± 3.0	59.7 ± 2.0	65.9 ± 1.9	–
A/C2	S	89.4 ± 3.3	–	89.1 ± 1.7	–	74.3 ± 0.9	–	83.0 ± 1.7	–
	D	65.8 ± 4.6	–	67.3 ± 5.2	–	63.6 ± 3.7	–	64.5 ± 4.4	–
A/C2.2	S	83.3 ± 6.4	–	80.8 ± 5.6	–	76.1 ± 1.4	–	90.7 ± 1.0	–
	D	59.3 ± 4.2	–	74.5 ± 11.3	–	76.7 ± 3.7	–	72.9 ± 3.7	–
C/C1.6	S	75.9 ± 2.2	77.5 ± 3.1	77.2 ± 1.9	–	82.3 ± 3.2	81.7 ± 3.2	82.2 ± 5.4	–
C/C2	S	82.6 ± 13.4	–	74.2 ± 5.9	–	89.6 ± 2.4	–	90.0 ± 1.4	–
	D	63.0 ± 4.3	–	66.9 ± 4.5	–	74.2 ± 4.4	–	67.2 ± 4.1	–
G/C2	S	79.1 ± 8.2	–	83.5 ± 2.1	–	82.3 ± 1.22	–	77.7 ± 0.9	–
	D	66.9 ± 4.6	–	71.8 ± 10.0	–	68.9 ± 5.2	–	70.9 ± 2.3	–
A/C1.5-F	S	43.5 ± 3.4	–	38.8 ± 3.5	74.0 ± 5.8	12.7 ± 2.0	–	20.0 ± 2.3	53.5 ± 4.5

Reproduced with permission from Ref. [10, 24]

0 represents a specimen without temperature treatment and 100/200/400 represent specimens treated for 100/200/400 h at 100 °C

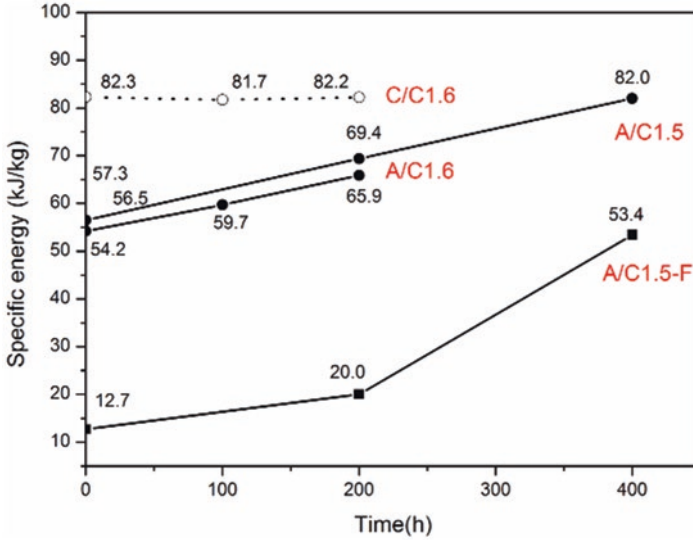


**Fig. 7** Variation of specific energy with treatment time (Reproduced with permission from Ref. [10])

The thinner the layer, the easier the layer buckles according to traditional mechanics of materials. On the other hand, the A/C1.5-F type of tube, with five layers and four carbon-aramid fiber interlayer interfaces, showed poorer mechanical properties. Therefore, the three-layer (A/C1.5) structure with two interfaces only exhibited better energy absorption capability than the five-layer (A/C1.5-F) structure of carbon/aramid FRPs, even with same fiber content and orientation. The interfaces dictate the behavior of these composites [10, 24].

Another effect of structure, including hybrid ratios and fiber orientation of tube walls of carbon fiber, is shown in Fig. 8a, b, respectively.  $V_{CF}$  is the volume content ratio of the intermediate carbon layer.

According to Fig. 8a, it is clear that the  $E_s$  of the CF/AF FRP tube under quasi-static test increased with increased  $V_{CF}$ . The axial fiber layer could effectively carry the axial load, which is closely related to the peak load of the composite tube ( $P_{Peak-0}$ : A/C1.6 = 47.1kN, A/C2 = 70.1kN, A/C2.2 = 83.7kN;  $P_{Peak-TT}$ : A/C1.6 = 59.3kN, A/C2 = 75.1kN, A/C2.2 = 97.2kN). Specimens treated at 100 °C for 200 h are named TT-type (TT-A/C2 for example) throughout the whole text. Outer circumferential fibers could effectively hoop the inner CF layers and constrain the propagation of the central crack, which has an important effect on the crushing efficiency ( $\eta_c-0$ : A/C1.6 = 62.3%, A/C2 = 89.4%, A/C2.2 = 83.3%;  $\eta_c-TT$ : A/C1.6 = 60.1%, A/C2 = 89.1%, A/C2.2 = 80.8%). Either too much or too little hoop fiber can be detrimental for energy absorption. Composite tubes with proper content ratios of hoop fiber to axial fiber (H:A) could largely control the propagation of the crack, even at a lighter weight, compared to other designs [10, 24].

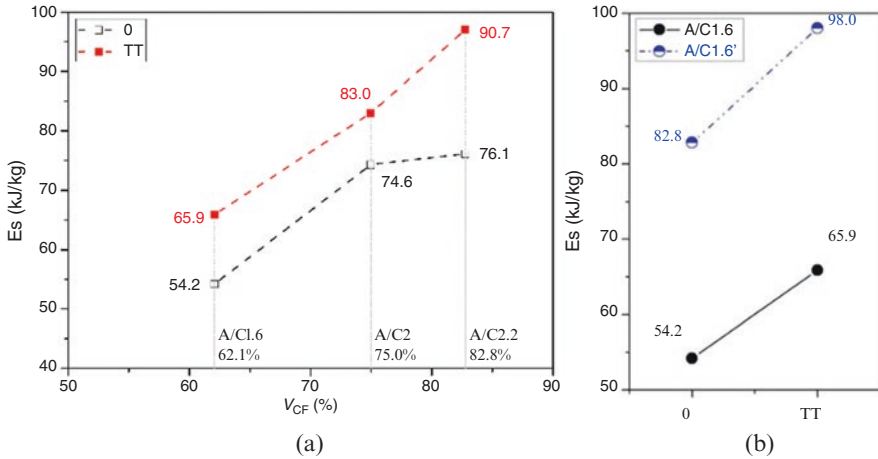


**Fig. 8** The effect of structure on  $E_s$  in a quasi-static test. (a) Hybrid ratio. (b) Fiber orientation (Reproduced with permission from Ref. [24])

According to Fig. 8b, A/C1.6' and A/C1.6 composite tubes have the same material composition and ratio, but different fiber orientation of the inner carbon layer. A/C1.6 composite tube with a 10° inner carbon layer, which is closer to the axial direction, has a higher capability to carry the axial load than A/C1.6' tube with a 17.6° inner CF layer ( $P_{Peak}-0$ : A/C1.6 = 47.1kN, A/C1.6' = 68.7kN;  $P_{Peak}-TT$ : A/C1.6 = 59.3kN, A/C1.6' = 79.4kN). Nevertheless, the outer AFs have enough capability to hoop the inner CF layer ( $\eta_c-0$ : A/C1.6 = 62.3%, A/C1.6' = 79.6%;  $\eta_c-TT$ : A/C1.6 = 60.1%, A/C1.6' = 74.8%) [10, 24].

### 4.2 Effect of Hybrid Material on Energy Absorption

A/C1.6 and C/C1.6 have the same fiber content, orientation, and structure but different raw materials as shown in Table 2. From Fig. 7, it is clear that both are three-layer structures. Carbon/carbon FRPs (C/C1.6) composites showed better performance in terms of energy absorption than carbon/aramid FRPs (A/C1.6) composites without temperature treatment, but carbon/aramid FRPs composites with temperature treatment had a tendency to overpass carbon/carbon FRPs composites. Carbon/carbon FRPs composite C/C1.6 exhibited higher energy absorption than carbon/aramid FRPs composite A/C1.6, having the same fiber content, orientation, and structure but different raw materials. On the one hand, aramid fiber is not suitable for compression; on the other hand, carbon/carbon FRPs composites have better inter-layer properties than carbon/aramid composites [10, 24].

The displacement-load curves of A/C2, C/C2, and G/C2 composite tubes with the same thickness distribution ratio but different raw materials are shown in Fig. 6e, h, i, respectively.  $E_s$  values of every composite tube without temperature treatment



are shown in Fig. 9. It is obvious that C/C2 exhibited higher  $E_s$  than G/C2 and A/C2 composite tubes under both static and dynamic tests. C/C2 composite tubes showed 8.9% and 7.7% higher  $E_s$  values than G/C2 composite tubes, which in turn were 10.7% and 8.3% higher than A/C2 under static and dynamic tests, respectively. Meanwhile, the above-mentioned tubes with the same structure under dynamic tests showed 15–18% decrease in  $E_s$  compared to under static tests [10, 24].

Optical photographs of cross sections through the crush zones of C/C2, A/C2, and G/C2 tubes without temperature treatment under quasi-static tests are shown in Figs. 10a, 12a, and 13a, respectively. For C/C2 tubes, the tube wall is split into internal and external fronds typical of the splaying mode of crushing. A well-defined debris wedge was observed. Below the debris wedge a short crack was observed in the longitudinal direction of the tube wall. Lots of fiber fracture and inter-laminar delamination were observed in both fronds, especially external fronds with small bending curvature. G/C2 tubes showed a similar splaying crushing mode. Compared with C/C2, a relatively longer central crack and larger frond bending curvature could be observed. For A/C2 tubes, only splaying crushing mode could be observed in the top and obvious transversal cracking occurred on the bottom because of the non-ideal constraints of hoop AFs. A high-level axial load could not be sustained because of transversal cracking through the whole tube wall [10, 24].

The mechanical properties of fibers as shown in Table 1 may contribute to the difference between the crushing behavior and the energy absorption capability of CFRP tubes. CF and GF have better mechanical properties as the outside hoop fiber controlled the central crack propagation more effectively. A short central crack led to fronds bending with small curvature; more fibers in fronds could break under

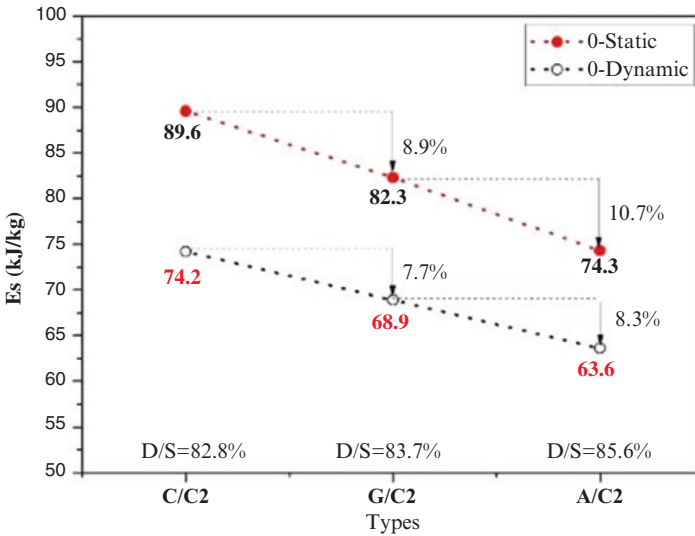
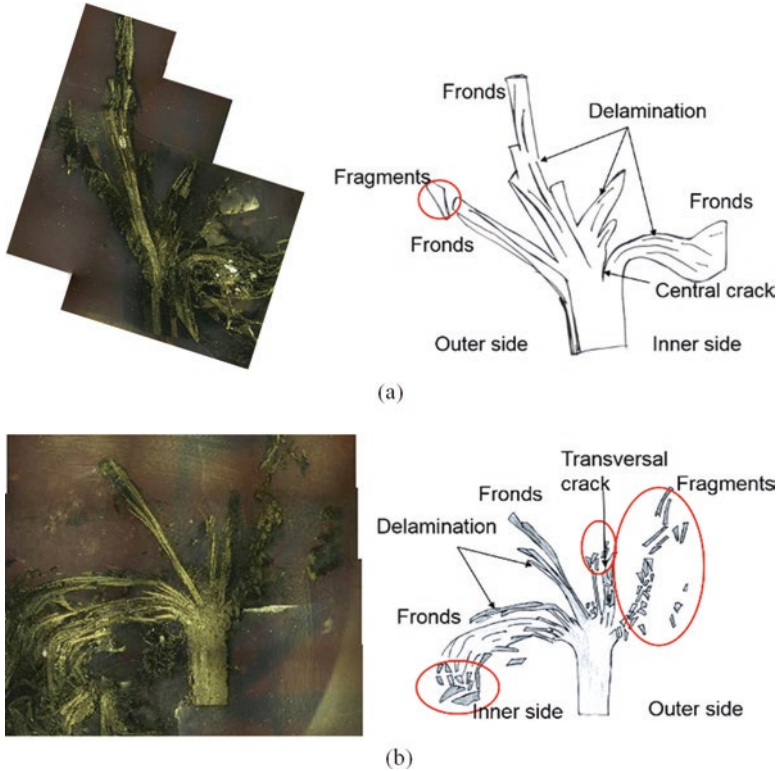


Fig. 9 Variation of  $E_s$  with types of the same thickness distribution ratio but different material (Reproduced with permission from Ref. [24])



**Fig. 10** Representative micro observation (*left*) and schematic diagrams (*right*) of crush zone for post-crushed C/C2-Static (a) and TT-C/C2-Static (b) after quasi-static test (Reproduced with permission from Ref. [24])

higher stresses because they absorb a large amount of energy during the process of compression [10, 24].

### 4.3 Effect of Crushing Speed on Energy Absorption

Results show that every specimen tested in quasi-static tests exhibited progressive and stable crushing. At the initial crushing stage of quasi-static tests, the load rises quickly to a peak value, then drops off slightly and stays relatively constant. It can be seen that the load fluctuates in a quasi-random fashion with serrations of small amplitude. However, about two to five much larger fluctuations in load-displacement curves after the load reaching peak load could be seen in a drop test. Accordingly, lower  $\eta_c$  and  $E_s$  compared to the quasi-static test could be observed as shown in Fig. 14a, b), respectively [10, 24].

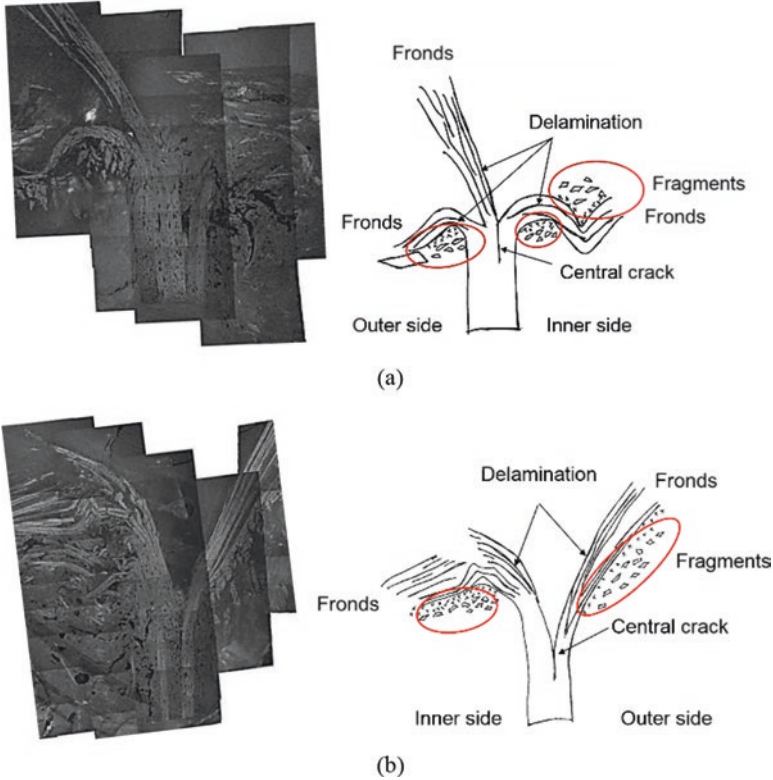


**Fig. 11** Representative micro observation (*left*) and schematic diagrams (*right*) of crush zone for post-crushed C/C2-Dynamic (a) and TT-C/C2-Dynamic (b) after dynamic test (Reproduced with permission from Ref. [24])

According to Hull [6], the serrations are produced by the stick-slip nature of the brittle fracture mechanism in which the stresses required to initiate crack growth are higher than those for propagation. Mamalis et al. [16] attribute the differences in energy absorption under static and dynamic conditions to changes in the crushing mechanisms. In particular, the resin was found to become increasingly brittle under elevated strain rates [9]. Meanwhile, higher fracture toughness of composites makes positive contributions to control the propagation of longitudinal cracks [4, 5], which should be controlled for getting higher energy absorption by making the fronds bend to the inner and outer sides with small curvature [10, 24].

Optical photographs of cross sections through the crush zones of C/C2 with and without temperature treatment under static and dynamic tests are shown in Figs. 12 and 13, respectively. It is clear that composite tubes with large bending curvature under dynamic tests developed longer central cracks than those with small bending curvature under static tests. Moreover, multiple fiber fractures could be observed in the fronds of composite tubes under static tests, which could absorb a great deal of energy [10, 24].

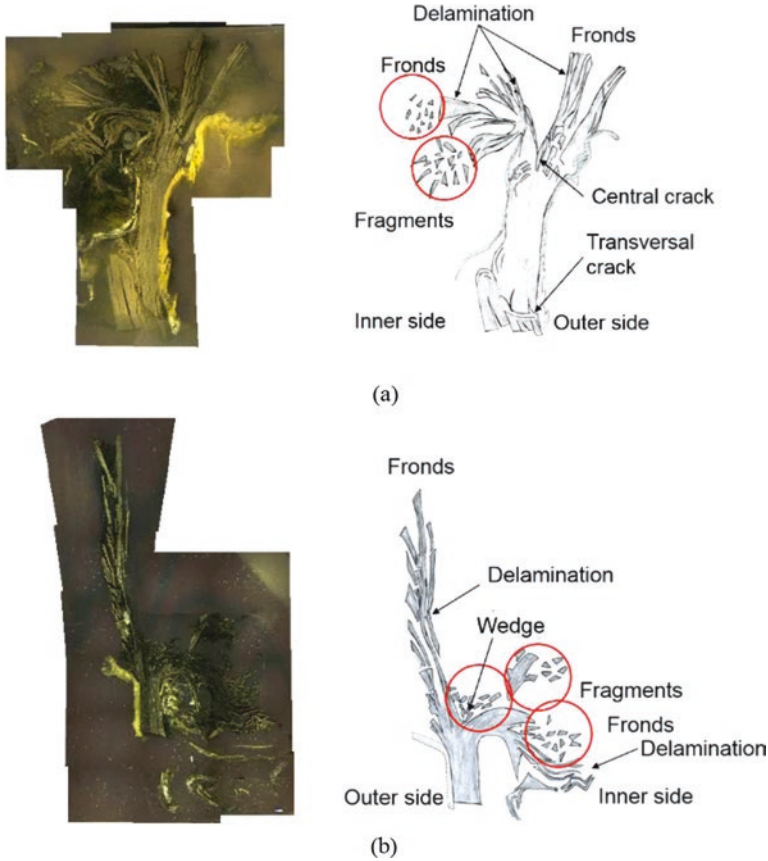


**Fig. 12** Representative micro-observation (*left*) and schematic diagrams (*right*) of crush zone for post-crushed A/C2-Static (a) and TT-A/C2-Static (b) after quasi-static tests (Reproduced with permission from Ref. [24])

#### 4.4 Effect of Temperature Treatment

Polished sections of uncompressed tube walls before and after temperature treatment are shown in Fig. 15. It is apparent that carbon and aramid layers are set apart in untreated specimens but tighten up in treated specimens. The shrinkage of the hoop aramid fiber after temperature treatment is considered to be the main reason for distance change. Shrinkage of the aramid fiber may hoop the inner carbon fibers more effectively. If the distance between layers is large enough, the whole tube wall buckles during the process of compression. A schematic diagram of carbon/aramid FRPs composites crushing mode before and after temperature treatment is shown in Fig. 16. If the distance between layers is not large without treatment, the tube wall splits into internal and external fronds through a blunt radius of curvature typical of splaying mode

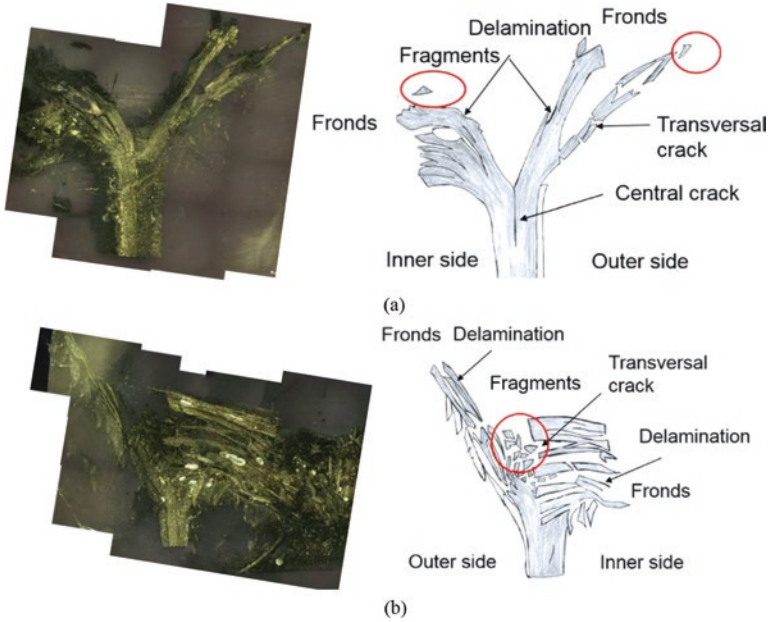


**Fig. 13** Representative micro observation (*left*) and schematic diagrams (*right*) of crush zone for post-crushed G/C2-Static (a) and TT-G/C2-Static (b) after quasi-static test (Reproduced with permission from Ref. [24])

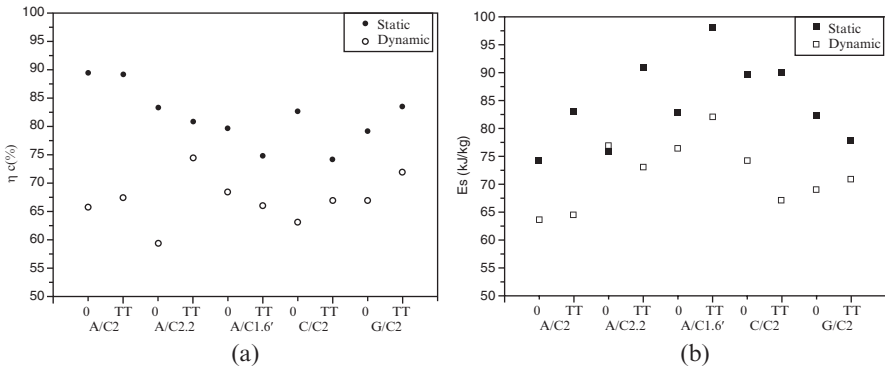


**Fig. 14** Crushing efficiency (a) and specific energy absorption (b) of static and dynamic tests (Reproduced with permission from Ref. [24])

crushing. After treatment, the distance reduction following the shrinkage of the aramid fibers could restrain the propagation of the central crack effectively to make the fronds split into internal and external fronds through a sharp radius of curvature typical of bending mode crushing because of the existence of internal stress [10, 24].

The crushing results including  $\eta_c$  and  $E_s$  are shown in Table 4. The  $E_s$  values of composite tubes with or without temperature treatment are shown in Fig. 16. For

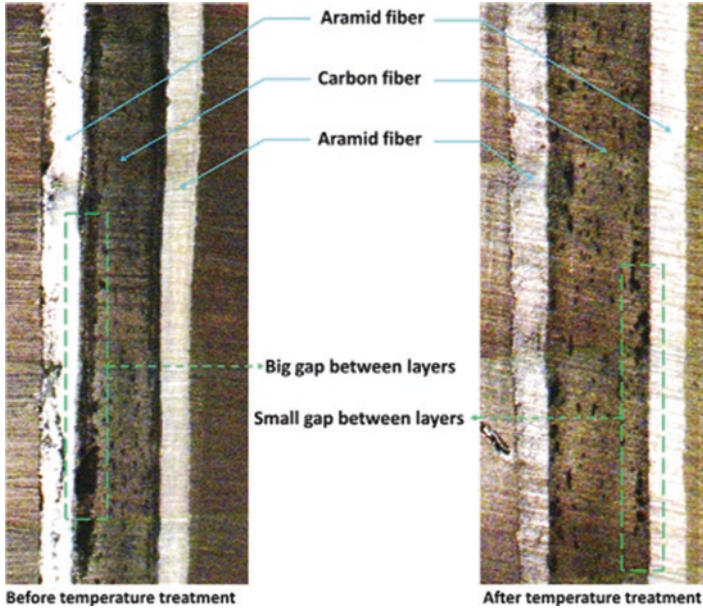


**Fig. 15** Polished section of tube (A/C1.5) wall before and after (100 °C, 200 h) temperature treatment (Reproduced with permission from Ref. [10])

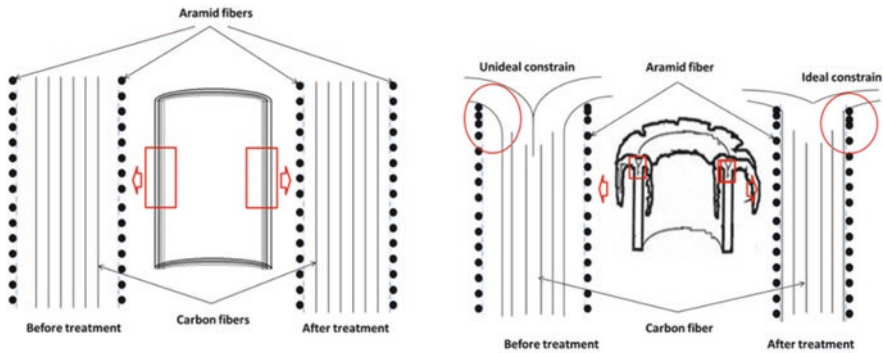


**Fig. 16** Schematic diagram of carbon/aramid FRPs composites crushing mode before and after temperature treatment (Reproduced with permission from Ref. [10])

static tests, the load-displacement curves and  $E_s$  of CF/AF CFRPs (A/C1.6', A/C2, A/C2.2) increased by 18.4%, 11.7%, and 19.2%, after 200 h temperature treatment at 100 °C, respectively. There is no large obvious differences for CF/CF CFRPs (C/C2) and GF/CF GFRPs (G/C2) after temperature treatment when compared to the original results [10, 24].

The  $E_s$  values of composite tubes under dynamic tests are shown in Fig. 17b. Temperature treatment has a negative effect on the  $E_s$  of CF/CF tubes under dynamic

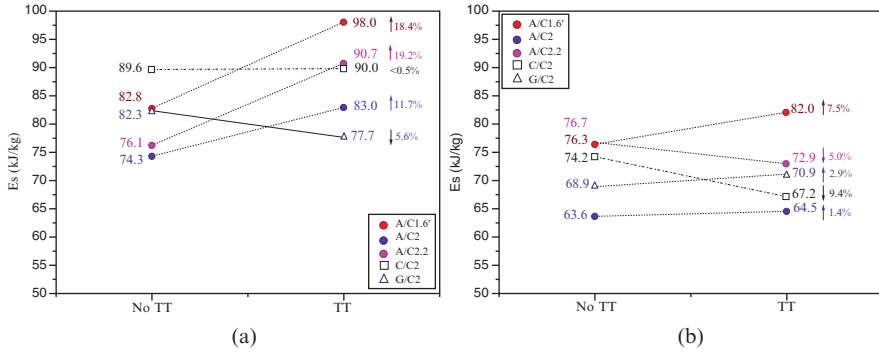


**Fig. 17** Variation of  $E_s$  after temperature treatment. (a) Static tests. (b) Dynamic tests (Reproduced with permission from Ref. [24])

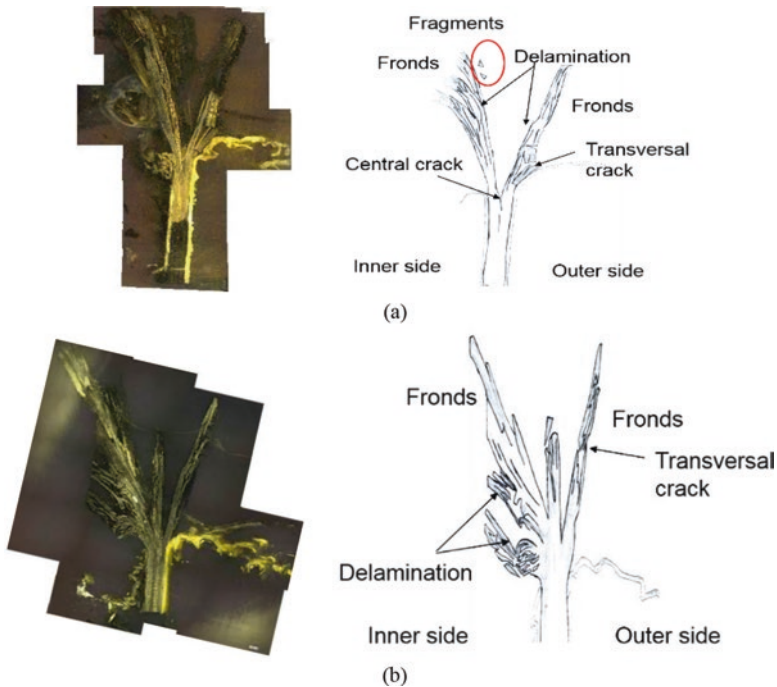


**Fig. 18** Representative micro-observation (left) and schematic diagrams (right) of crush zone for post-crushed A/C1.6'-Static (a) and TT-A/C1.6'-Static (b) after quasi-static test (Reproduced with permission from Ref. [24])

tests, whereas for GF/CF FRP tubes it exhibited a relatively positive effect. At the same time, the  $E_s$  of CF/AF FRP tubes didn't increase proportionally to that in a static test. However, the cause of this behavior is still unclear and further studies are underway [10, 24].

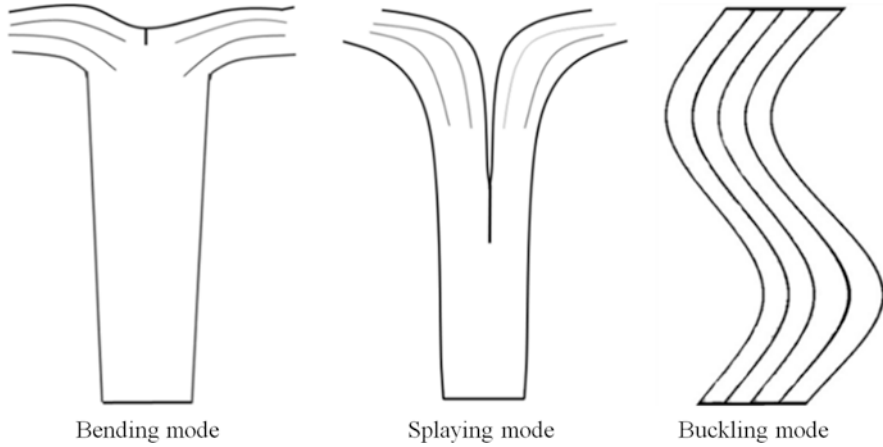


**Fig. 19** Three types of failure modes according to microscope observation of cross section (Reproduced with permission from Ref. [10])

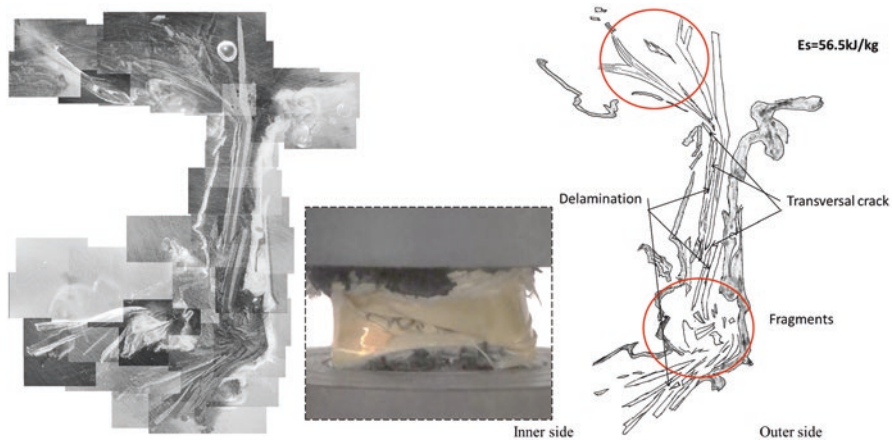


**Fig. 20** Polished section of crush zone of carbon/aramid FRPs composite A/C1.5<sub>0</sub> (Reproduced with permission from Ref. [10])

Optical photographs of cross sections through the crush zones of A/C2 and A/C1.6' tubes with and without temperature treatment under quasi-static tests are shown in Figs. 12 and 18, respectively. For A/C2 composite tube, the crushing mode transformed from bulking crushing mode into splaying crushing mode. For A/C1.6' composite tube, the crushing mode transformed from splaying crushing mode with longer central crack and large bending curvature into splaying crushing mode with shorter central crack and small bending curvature [10, 24].

To investigate the reason for  $E_s$  improvement in CF/AF CFRPs tubes, thermal aging properties for AFs, resin and composite, after temperature treatment were



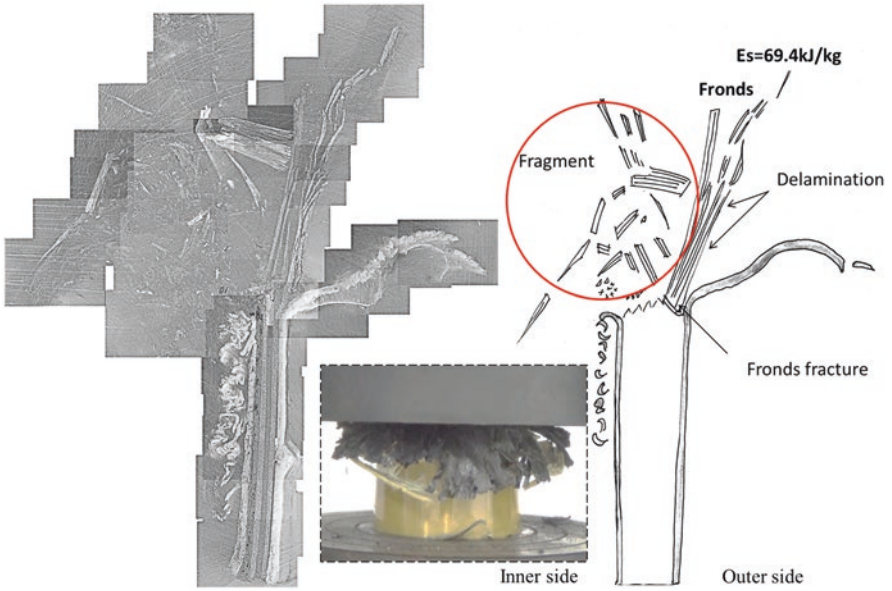


Fig. 21 Polished section of crush zone of carbon/aramid FRPs composite A/C1.5<sub>200</sub> (Reproduced with permission from Ref. [10])

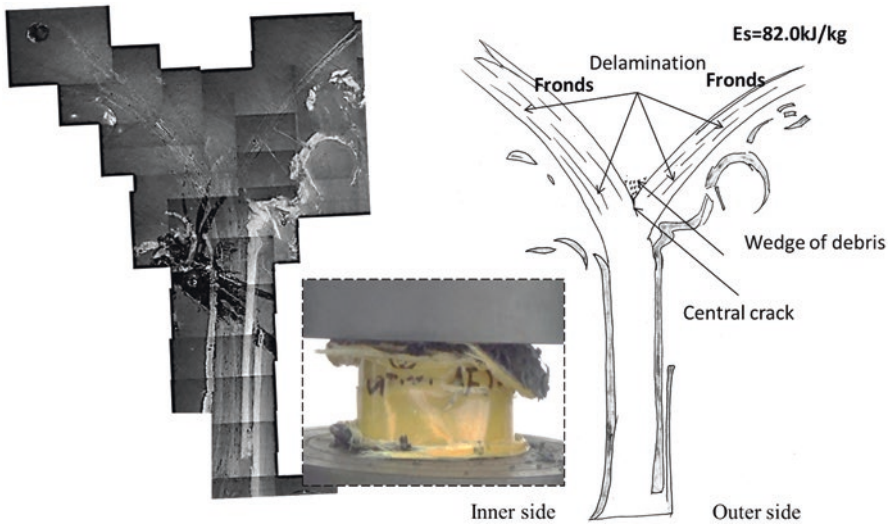


Fig. 22 Polished section of crush zone of carbon/aramid FRPs composite A/C1.5<sub>400</sub> (Reproduced with permission from Ref. [10])

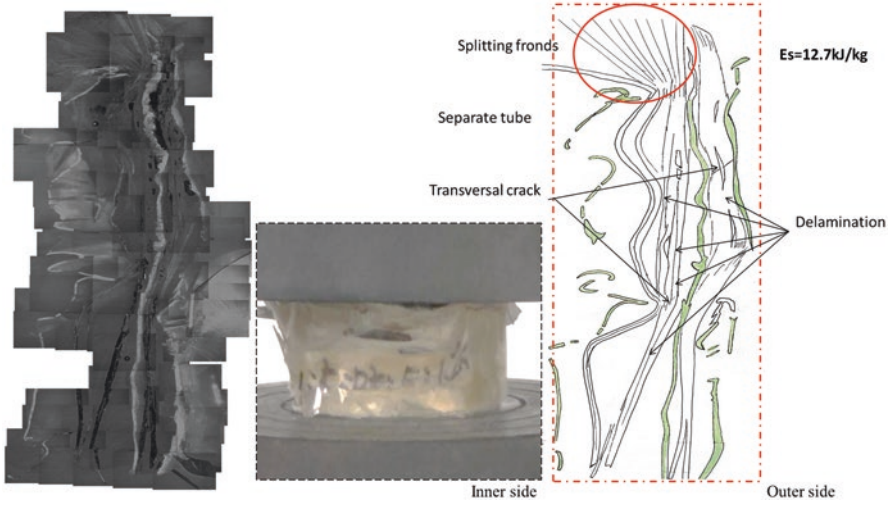


Fig. 23 Polished section of crush zone of carbon/aramid FRPs composite A/C1.5-F<sub>0</sub> (Reproduced with permission from Ref. [10])

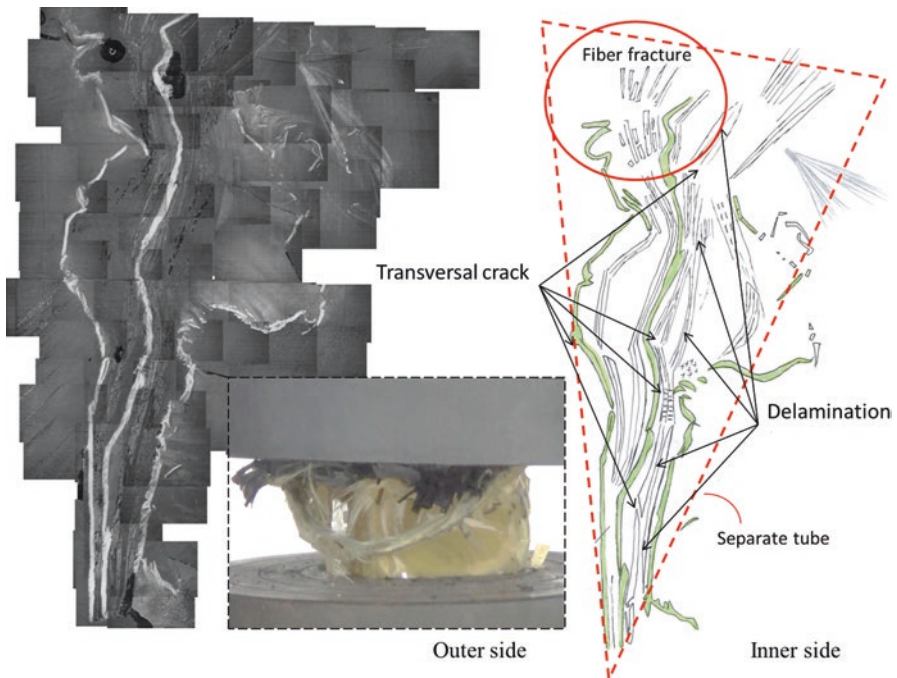


Fig. 24 Polished section of crush zone of carbon/aramid FRPs composite A/C1.5-F<sub>200</sub> (Reproduced with permission from Ref. [10])

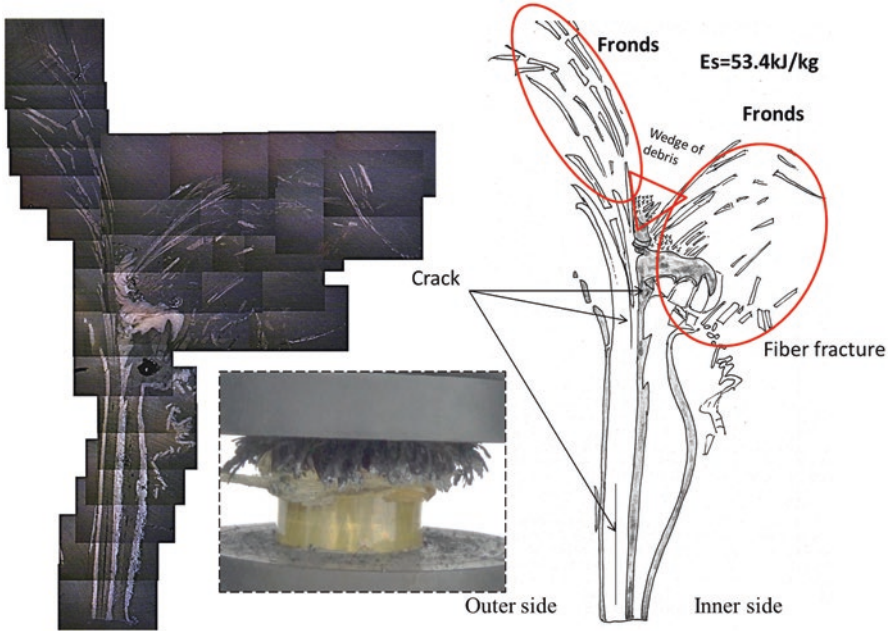


Fig. 25 Polished section of crush zone of carbon/aramid FRPs composite A/C1.5-F<sub>400</sub> (Reproduced with permission from Ref. [10])

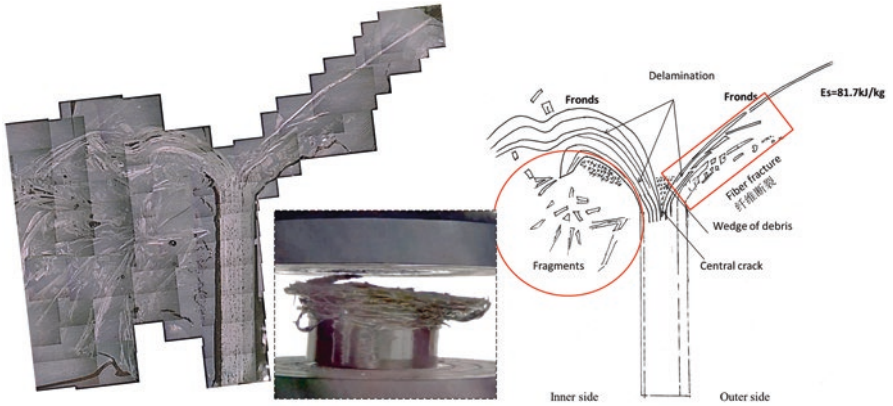
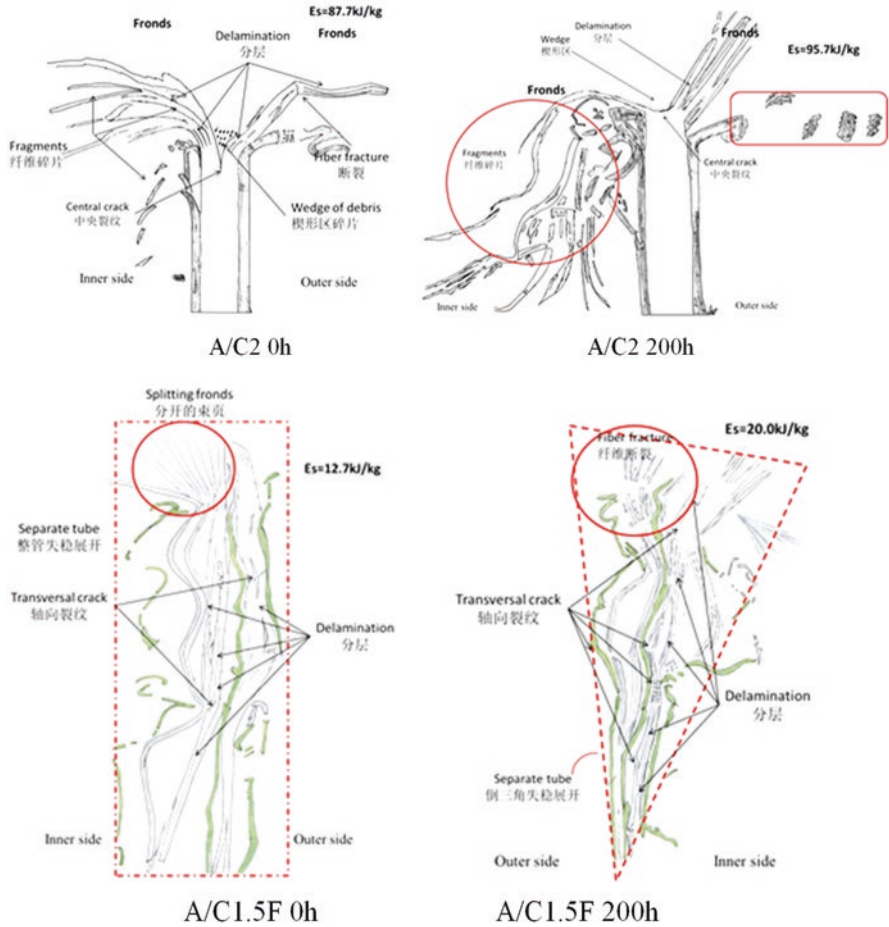


Fig. 26 Polished section of crush zone of carbon/aramid FRPs composite C/C1.6<sub>100</sub> (Reproduced with permission from Ref. [10])



**Fig. 27** The crushing mode variation of high and low specific energy absorption composites (Reproduced with permission from Ref. [10])

examined. Yue et al. [27] showed that Kevlar 29 fibers did not show evident changes in tensile strength but tensile strain decreased at 100, 200, and 300 °C after 2–8 h in vacuum. AFs with an epoxy coating were exposed to a similar vacuum treatment. Yongming [26] showed that thermal aging of the epoxy apparently reduced the strain to break, the flexural strength was slightly affected, and the modulus increased. Thus thermal treatment of the AF composite tubes at 100 °C for 200 h, was expected to affect strength and increase modulus slightly. As a result, the integral tube is more effectively controlled during deformation in compression and tubes under compression show more progressive failure mechanism, leading to higher energy absorption values [10, 24].

## 4.5 Modes of Crushed Specimens

### 4.5.1 Three Crushing Modes

Three types of failure modes – bending mode, splaying mode, and buckling mode – are classified in Fig. 19. In the case of bending mode, a short central crack and bending fronds with small radius of bending curvature can be found in the cross section through the crush zones. Multiple broken fibers in the fronds absorb a large number of energy in the process of compression. For the splaying mode, a long central crack and bending fronds with large radius of bending curvature can be observed in the cross section through the crush zones. Extensive delamination and some broken fibers occurred, thus absorbing some energy during the compression process. With regard to buckling mode, buckle deformation is observed in the whole tube, resulting in significant delamination in both intra-layers and inter-layers. These kinds of tubes absorb limited energy, this depending mainly on deformation of materials [10, 24].

### 4.5.2 Effect of Temperature Treatment on Crushing Mode

Optical photographs of cross sections through the crush zones of carbon/aramid FRPs composite tubes (A/C1.5 and A/C1.5-F) with or without temperature treatment are shown in Figs. 20, 21, 22, 23, 24 and 25. In the case of A/C1.5 tubes without temperature treatment (Fig. 20), the tube wall collapsed and could not bear the axial load. Delamination and transversal cracking was evident through the whole tube wall. After 200 h treatment (Fig. 21), the bottom of the tube wall exhibited firmer behavior, and the whole frond fracture happened in the process of compression. After 400 h treatment (Fig. 22), the tube wall split into internal and external fronds typical of splaying mode crushing. A well-defined debris wedge was observed. Below the debris wedge short cracks were observed in the longitudinal direction of the tube wall. The two fronds both underwent some degree of deformation but were bent through a blunt radius of curvature. Many inter-laminar delaminations were observed in both internal and external fronds. In the case of A/C1.5-F (A88°/C17.6°/A88°/C17.6°/A88°:1/5/1.25/5/1.25) without temperature treatment (Fig. 23), the whole tube wall buckled and a large number of inter-laminations and intra-laminations could be observed. After 200 h temperature treatment (Fig. 24), the whole tube wall buckled and lots of laminations were also observed. After 400 h temperature treatment (Fig. 25), the whole tube wall did not buckle, unlike the former two specimens. The tube wall split into internal and external fronds in which fiber fracture could be observed. It could be inferred that the crushing mode could be changed from buckling mode to splaying mode through temperature treatment according to Figs. 20 and 21 [10, 24].

### 4.5.3 Crushing Mode Variation of High and Low Specific Energy Absorption Composites

Figures 22, 23, 24, 25 and 26 show the crushing modes of high specific energy absorption FRP composites. It is clear that the tube walls split into internal and external fronds although the length of central crack is a little different. At the same time, the bending fronds bend inside with small radii of curvature.

The comparison of crushing mode between high and low energy absorption tubes is shown in Fig. 27. It is obvious that tubes with high energy absorption ability fractured in splaying mode and even in bending mode, whereas the tubes with low energy absorption ability crushed in buckling mode. In the case of splaying mode and bending mode, the obvious difference between them was the radius of curvature of bending fronds, which was related to the length of initial central crack. The shorter the central crack, the smaller the radius of curvature, the result of larger specific energy absorption [10, 24].

## 5 Conclusions

1. Composite tubes under quasi-static tests exhibited higher crushing efficiency ( $\eta_c$ ) and specific energy absorption ( $E_s$ ) than those under dynamic tests.
2. CF/CF composite tubes exhibited higher  $E_s$  than GF/CF and AF/CF composite tubes with the same structure in both static and dynamic tests.
3. The energy absorption capability of aramid/carbon FRPs hybrid tubes could be improved through temperature treatment. This can be attributed to the slightly affected strength and increased modulus of AF composite FRPs as more effective control of tubes during compression could be achieved in this way. However, there is little difference for CF/CF CFRPs after temperature treatment when compared to the original ones. Temperature treatment has a negative effect on the  $E_s$  of CF/CF tubes under dynamic tests, whereas for GF/CF FRP tubes it exhibited a relatively positive effect. At the same time, the  $E_s$  of CF/AF FRP tubes didn't increase proportionally to that in static test.
4. A decrease in fiber angle along the axial direction and a reasonable hybrid ratio between inner carbon and outer aramid layer are helpful in obtaining higher  $E_s$ .
5. A/C1.6 composite tubes after temperature treatment (named "TT-A/C1.6") exhibited the highest  $E_s$  in quasi-static tests (98 kJ/kg on average) and dynamic tests (82 kJ/kg on average), with excellent energy absorption management.
6. FRPs failure modes were divided into three – bending mode, splaying mode, and buckling mode – which ranked from highest to lowest in energy absorption. However, in common, the failure mode of FRPs is not necessarily a single failure mode but a combination of several failure modes, and the failure mode is closely related to the length of the central crack. Under the premise of avoiding buckling deformation, best efforts should be made to control the propagation of the central crack for making the fronds bend to the inner side and outer side with small curving curvature. In this case, more fibers in the bending fronds could break (one of the most important ways to absorb energy).

## References

1. P. Deslauriers, Numerical modeling of composite structures for advanced automotive applications: ProQuest. (2006)
2. R. Eshkoor, S. Oshkovr, A.B. Sulong, R. Zulkifli, A. Ariffin, C. Azhari, Effect of trigger configuration on the crashworthiness characteristics of natural silk epoxy composite tubes. *Compos Part B Eng.* **55**, 5–10 (2013)
3. G.L. Farley, Effect of fiber and matrix maximum strain on the energy absorption of composite materials. *J. Compos. Mater.* **20**(4), 322–334 (1986)
4. H. Hamada, J. Coppola, D. Hull, Z. Maekawa, H. Sato, Comparison of energy absorption of carbon/epoxy and carbon/PEEK composite tubes. *Composites* **23**(4), 245–252 (1992)
5. H. Hamada, S. Ramakrishna, H. Satoh, Crushing mechanism of carbon fibre/PEEK composite tubes. *Composites* **26**(11), 749–755 (1995)
6. D. Hull, A unified approach to progressive crushing of fibre-reinforced composite tubes. *Compos. Sci. Technol.* **40**(4), 377–421 (1991)
7. G.C. Jacob, J.F. Fellers, S. Simunovic, J.M. Starbuck, Energy absorption in polymer composites for automotive crashworthiness. *J. Compos. Mater.* **36**(7), 813–850 (2002)
8. R. Kalhor, S.W. Case, The effect of FRP thickness on energy absorption of metal-FRP square tubes subjected to axial compressive loading. *Compos. Struct.* **130**, 44–50 (2015)
9. J. Ma, Y. Yan, Quasi-static and dynamic experiment investigations on the crashworthiness response of composite tubes. *Polym. Compos.* **34**(7), 1099–1109 (2013)
10. Y. Ma, T. Sugahara, Y. Yang, H. Hamada, A study on the energy absorption properties of carbon/aramid fiber filament winding composite tube. *Compos. Struct.* **123**, 301–311 (2015)
11. Y. Ma, M. Ueda, T. Yokozeki, T. Sugahara, Y. Yang, H. Hamada, A comparative study of the mechanical properties and failure behavior of carbon fiber/epoxy and carbon fiber/polyamide 6 unidirectional composites. *Compos. Struct.* **160**, 89–99 (2017)
12. Y. Ma, Y. Yang, T. Sugahara, H. Hamada, A study on the failure behavior and mechanical properties of unidirectional fiber reinforced thermosetting and thermoplastic composites. *Compos. Part B Eng.* **99**, 162–172 (2016)
13. Y. Ma, Y. Zhang, T. Sugahara, S. Jin, Y. Yang, H. Hamada, Off-axis tensile fatigue assessment based on residual strength for the unidirectional 45 carbon fiber-reinforced composite at room temperature. *Compos. A: Appl. Sci. Manuf.* **90**, 711–723 (2016)
14. E. Mahdi, A. Hamouda, T. Sebaey, The effect of fiber orientation on the energy absorption capability of axially crushed composite tubes. *Mater. Des.* **56**, 923–928 (2014)
15. A. Mamalis, D. Manolakos, M. Ioannidis, D. Papapostolou, Crashworthy characteristics of axially statically compressed thin-walled square CFRP composite tubes: Experimental. *Compos. Struct.* **63**(3), 347–360 (2004)
16. A. Mamalis, Y. Yuan, G. Viegelaan, Collapse of thin-wall composite sections subjected to high speed axial loading. *Int. J. Veh. Des.* **13**(5–6), 564–579 (1992)
17. M. McCarthy, J. Wiggenraad, Numerical investigation of a crash test of a composite helicopter subfloor structure. *Compos. Struct.* **51**(4), 345–359 (2001)
18. M. Mirzaei, M. Shakeri, M. Sadighi, H. Akbarshahi, Experimental and analytical assessment of axial crushing of circular hybrid tubes under quasi-static load. *Compos. Struct.* **94**(6), 1959–1966 (2012)
19. S. Palanivelu, W. Van Paepegem, J. Degrieck, J. Van Ackeren, D. Kakogiannis, D. Van Hemelrijck, et al., Experimental study on the axial crushing behaviour of pultruded composite tubes. *Polym. Test.* **29**(2), 224–234 (2010)
20. C. Priem, R. Othman, P. Rozycki, D. Guillon, Experimental investigation of the crash energy absorption of 2.5 D-braided thermoplastic composite tubes. *Compos. Struct.* **116**, 814–826 (2014)
21. S. Reid, Plastic deformation mechanisms in axially compressed metal tubes used as impact energy absorbers. *Int. J. Mech. Sci.* **35**(12), 1035–1052 (1993)

22. H.-W. Song, Z.-M. Wan, Z.-M. Xie, X.-W. Du, Axial impact behavior and energy absorption efficiency of composite wrapped metal tubes. *Int. J. Impact Eng.* **24**(4), 385–401 (2000)
23. P. Thornton, C. Magee, The interplay of geometric and materials variables in energy absorption. *J. Eng. Mater. Technol.* **99**(2), 114–120 (1977)
24. J. Xu, Y. Ma, Q. Zhang, T. Sugahara, Y. Yang, H. Hamada, Crashworthiness of carbon fiber hybrid composite tubes molded by filament winding. *Compos. Struct.* **139**, 130–140 (2016)
25. Y. Yang, X. Wu, H. Hamada, Application of fibre-reinforced composites beam as energy absorption member in vehicle. *Int. J. Crashworthiness* **18**(2), 103–109 (2013)
26. Y. Yang, G. Xian, H. Li, L. Sui, Thermal aging of an anhydride-cured epoxy resin. *Polym. Degrad. Stab.* **118**, 111–119 (2015)
27. C. Yue, G. Sui, H. Looi, Effects of heat treatment on the mechanical properties of Kevlar-29 fibre. *Compos. Sci. Technol.* **60**(3), 421–427 (2000)



# Graphene-Rubber Nanocomposites: Preparation, Structure, and Properties

Jian Wang, Kaiye Zhang, Qiang Bu, Marino Lavorgna, and Hesheng Xia

## 1 Introduction

Graphene is a two-dimensional atomically thick carbon material with a honeycomb lattice structure, composed of  $sp^2$  hybridized carbon atoms. In 2004, Geim and Novoselov theoretically predicted the existence of a single crystal of graphene and experimentally isolated the graphene sheets by peeling-off graphite using scotch tape and thus won the 2010 Nobel Prize in physics. Graphene possesses ultrahigh mechanical strength, high Young's modulus, structural flexibility, large specific surface area, excellent thermal and electrical conductivity, and optical transmittance, which outperform other ever-reported materials [1–4]. Due to the specific properties, graphene may bring about a new technological revolution in the twenty-first century [5, 6].

Graphene is currently produced by a variety of approaches, such as chemical vapor deposition (CVD), epitaxial growth, micromechanical exfoliation, liquid exfoliation, and oxidation-reduction (i.e., oxidation of graphite to graphene oxide and then reduction to graphene by chemicals or heat). The large-scale production of graphene by using the former three approaches remains a challenge due to their high cost, whereas both the liquid exfoliation and the oxidation-reduction methods exhibit high versatility and industrial scalability, which possibly are the most promising methods for the graphene production. It is noted that the several production approaches allow to obtain graphene with different quality expressed as aspect ratio and amount of defects on the

---

J. Wang • K. Zhang • Q. Bu • H. Xia (✉)

State Key Lab of Polymer Materials Engineering, Polymer Research Institute, Sichuan University, Chengdu 610065, China

e-mail: [waynewj@126.com](mailto:waynewj@126.com); [18354212670@163.com](mailto:18354212670@163.com); [buqiangscu@163.com](mailto:buqiangscu@163.com); [xiahs@scu.edu.cn](mailto:xiahs@scu.edu.cn)

M. Lavorgna (✉)

Institute of Polymers, Composites and Biomaterials, National Research Council, c/o ENEA, P.le E. Fermi, 1, Loc. Granatello, Portici, NA 80055, Italy

e-mail: [mlavorgna@unina.it](mailto:mlavorgna@unina.it)

graphene nanoplatelets. In particular the quality of graphene nanoplatelets is relatively lower due to more defect declines when graphene is produced by oxidation-reduction method. It is widely accepted that graphene produced by liquid exfoliation or by oxidation-reduction methods is suitable to be used as filler for the production of polymer composites. For oxidation-reduction method, except for the low cost and easily scale-up, the most important advantage is its capability to obtain the water-dispersive graphene oxide, which can be easily modified to obtain the range of graphene derivatives compatible with different polymer matrix from nonpolar to polar.

In recent years, there have been growing interests toward elastomeric materials to be used in a multitude of different applications, from automotive to energy sector, from aerospace to the manufacturing of daily goods sector. The conventional rubber material could not meet the ever-increasing demand of applications; thus it is very important to develop innovative multifunctional rubber-based composites. In the last 10 years, graphene/thermal plastic polymer composites were extensively investigated; however, surprisingly, almost no studies involved the preparation and characterization of rubber/graphene composites until 2011, probably due to the dispersion and exfoliation problem of graphene in the cross-linked rubber matrix. Since 2013, the modification of rubber by using graphene nanofillers has become one of the hot topics in the area of graphene, aiming to the automobile or bicycle tire application. Graphene combines the conductivity of carbonaceous materials with the structural characteristics of clay sheets (widely used in the field of elastomeric materials), thus providing new strategies in the development of high-performance multifunctional rubber nanocomposites. Graphene rubber materials can be widely used in tire, high barrier conductive seal, electromagnetic shielding seals, and shock absorber. Graphene, as a prospective filler in rubber materials, possesses many advantages: (1) extraordinary modulus of  $\sim 1$ TPa with flexibility and light weight and thus better mechanical reinforcement effect compared to conventional filler; (2) high electrical and thermal conductivity; (3) gas barrier properties higher than clay; (4) higher specific area, leading more interfacial contact and larger effect on molecular chain, and crystallization such as strain-induced crystallization ability compared with clay and carbon nanotubes; and (5) good heat resistance. (6) For graphene oxide or reduced graphene oxide, there are some polar groups like hydroxyl, carboxyl, and epoxide, which make graphene easily functionalized by grafting small molecules or polymer. Therefore, graphene, as the most powerful 2D materials, may provide a good opportunity for the revolution of traditional rubber technology.

This chapter will review the state of the art on graphene/rubber nanocomposites with specific focus on the preparation approaches, structure and properties, and also the application.

## 2 Preparation of Graphene/Rubber Nanocomposites

In general, three main approaches were adopted for the preparation of graphene-rubber composites, i.e., melt mixing, solution mixing, and latex mixing. In order to produce the valuable composites, or the truly 2D graphene-rubber hybrid, the

methods should solve three important challenges, i.e., the exfoliation and dispersion of graphene nanoplatelets, the construction of well-defined graphene structures (i.e., random dispersion, layered structure, or segregated structure), and the improved interfacial interaction between the 2D graphene and macromolecular chain.

## 2.1 Latex Mixing Method

Graphene (GE)-filled natural rubber (NR) nanocomposites prepared by latex mixing approach have attracted increasing attention [7, 8]. Latex mixing is the most popular and recognized method to make the rubber-graphene nanocomposites. The general process is mixing the aqueous dispersion of graphene or graphene oxide with rubber latex to get a uniform dispersion. Afterward the mixture is subjected to coagulation, drying, and vulcanization to obtain the GE/NR composites. When using the graphene oxide dispersion, the in situ reduction in the latex can be conducted before coagulation to obtain the graphene-rubber nanocomposites. The final properties of GE/NR composites prepared by latex mixing approach depend on the compatibility of graphene or its derivatives with polymer and the graphene morphology in the matrix. The latex mixing has two advantages: (1) the well dispersion of graphene can be realized and (2) the process is relatively easy, low cost, and environment-friendly without using the organic solvent. There are also some disadvantages for latex mixing: (1) due to a low concentration of graphene in aqueous dispersion, too much water will be used for dispersion and washing and (2) the graphene dispersion is highly energy consuming, normally using ultrasound equipment. The machine cost is high when production is in a ton scale.

Zhan et al. firstly prepared GE/NR composites by an ultrasonically assisted latex mixing and in situ reduction (ULMR) method [7]. The innovative method was schematically illustrated as follows: the graphene oxide (GO) prepared from natural flake graphite according to the Hummers' method is well dispersed into water by ultrasonic irradiation due to the presence of oxygen-containing groups in the surface and mixed with NR latex. Then the GO in the latex was in situ reduced by hydrazine hydrate to reduced graphene oxide (rGO) and followed by latex coagulation to get the well-dispersed and exfoliated rGO/NR masterbatch. Through further dilution of the masterbatch with normal NR by a twin-roll mixing process, rGO/NR composites with different GE contents were obtained. This process can make the graphene nanosheets disperse uniformly with a thickness of 1–3 nm. For the GE/NR composites prepared by conventional two-roll milling without using latex mixing, the graphene nanosheets agglomerated in particles with a size ranging from 300 to 800 nm. The results suggested the higher dispersion efficiency of latex mixing compared to the simple two-roll milling of conventional polymeric material. The ULMR method includes two key steps: latex mixing with sonicated GO dispersion and in situ reduction of GO to rGO. Two reasons for using GO dispersion not rGO dispersion in ULMR process are (1) GO aqueous dispersion with single layer graphene nanoplatelets can be obtained by sonication without using the surfactant. (2) The rGO powder is difficult to be dispersed into water down to single layer or few layers

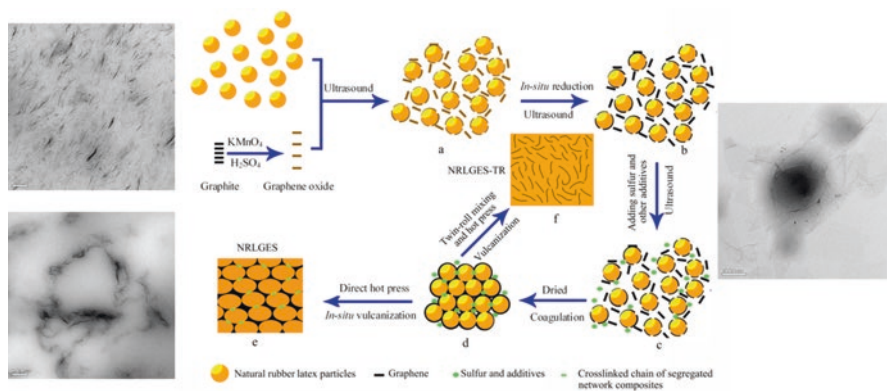


**Fig. 1** The preparation of GE/NR composites with a conductive segregated network of graphene by self-assembly in latex and static hot-press. (a) GO layers were uniformly dispersed in NR latex; (b) graphene nanoplatelets obtained by in situ reduction were self-assembled onto the surface of the NR latex particle; (c) sulfur and other additives were uniformly dispersed in the graphene/NR latex; (d) solid mixture of graphene and NR after latex coagulation and drying; (e) graphene/NR composites with the conductive segregated network; (f) graphene/NR composites with uniform graphene dispersion (Reproduced with permission [8], 2012, Royal Society of Chemistry)

with a layer thickness of less than 10 nm by sonication with the assistance of surfactant, which is also very difficult to be removed by posttreatment. The in situ reduction is another core step to change polar GO to nonpolar rGO, which improves the compatibility with the nonpolar rubber matrix and obtains the good mechanical properties for the rubber composites.

In order to improve the conductivity of rubber materials, Zhan et al. also prepared vulcanized rGO/NR composites with a conductive segregated network by self-assembly in latex, coagulation, and static hot-pressing [8]. The Go and the rGO platelets were self-assembled to form an encapsulated graphene layer on the surface of the latex particles (Fig. 1a, b). Subsequently, the cross-linked agent sulfur and other additives were added into the rGO/NR latex (Fig. 1c) and then the latex was coagulated and filtrated. In the presence of rGO, the NR latex is easily coagulated with the addition of those additives. The filtrated solids fraction was dried and then was directly hot-pressed under static pressure and in situ vulcanized to obtain the cross-linked rGO/NR nanocomposites. During this process, the solid polymer particles create excluded volume and essentially push the graphene nanoplatelets into the interstitial space between them to form the conductive networks (Fig. 1d). Due to the high viscosity of molten rubber particles, the conductive fillers have difficulties to diffuse inside the rubber, and the segregated network structure along the boundary region will be kept when cooling (Fig. 1e). If the coagulated and dried rubber mixture is subjected to twin-roll mixing, the segregated network will be destroyed, and thus the well-dispersed GE/NR composite can be obtained (Fig. 1f).

By using the latex mixing approach, Kim et al. [9] prepared multilayered graphene (MLG)/styrene-butadiene rubber (SBR) composites, which show significant improved thermal stability and electric conductivity. The authors used the surfactant

hexadecyltrimethylammonium bromide (CTAB) to promote the graphene dispersion; however the graphene aggregation is obvious, suggesting the dispersion of thermally reduced graphene in aqueous solution is indeed a big challenge. The mechanical properties of the SBR/GE were not reported; probably the existence of remained CTAB after repeated washing will significantly degrade the mechanical properties. The conductivity of the CTAB-stabilized MLG/SBR composite is not so ideal,  $\sim 8 \times 10^{-6}$  S/cm at a 5 wt% graphene content.

Potts et al. [10] prepared rGO/NR composites using latex mixing with a kinetically stable suspension of rGO in water. The composites were processed by two different routes: (1) two-roll milling with dicumyl peroxide (DCP) as the curing agent; (2) “solution treatment” procedure, the solids (in the form of small pellets) were firstly soaked into a solution of DCP in toluene to swell the rubber and implant DCP into the matrix and then were subject to hot-pressing to form and cure the samples. The two processes were similar as Zhan’s post-processing routes [7, 8]. Very interestingly, the authors independently observed the similar phenomenon reported by Zhan et al.: the processing approach had a tremendous impact on the composite morphology and thus properties. Solution treatment preserved the segregated filler network morphology produced by the co-coagulation procedure, whereas the milling process destroyed this network and generated a homogeneous dispersion of rGO platelets in the NR matrix. The segregated network morphology was shown to be advantageous for conductivity properties and greatly increased the stiffness but also significantly reduced the elongation to break. The milled nanocomposites exhibited enhanced stiffness and strength while maintaining a high elongation to break.

Direct latex mixing using graphene oxide and rubber latex is also used to obtain the GO reinforced rubber nanocomposites. One good example is graphene oxide/butadiene-styrene-vinyl pyridine rubber (VPR) nanocomposites by Tang et al. [11]. Two interactions can be formed through different flocculants during latex coagulation process. The hydrogen bonding interaction is formed between the hydroxyls of GO and nitrogen of VPR by using  $\text{CaCl}_2$  as the flocculant, while the ionic bonding interface, namely, negatively charged groups in GO sheets strongly attached onto the protonated N of the VPR chain, is constructed via electrostatic interaction by using HCl as the flocculant. The mechanical properties and gas permeability of these hybrids with an ionic bonding interface are obviously superior to those of the composites with a hydrogen bonding interface. With the ionic interfacial bonding, inclusion of 3.6 vol% of GO in VPR generates a 21-fold increase in glassy modulus, 7.5-fold increase in rubbery modulus, and 3.5-fold increase in tensile strength. The very fine dispersion of GO and the strong ionic interface in the hybrids are responsible for such unprecedented reinforcing efficiency of GO toward VPR. This work contributes new insights on the preparation of high-performance GO/rubber composites [11].

Yang et al. [12] synthesized high-performance SBR/graphene nanocomposites through latex mixing and post in situ reduction by rhodanine during thermal processing. During the in situ reduction, rhodanine was converted into polyrhodanine via oxidative polymerization initiated by GO, and the rGO was subsequently decorated with polyrhodanine. Because of the substantially improved interfacial adhesion,

combined with the improved dispersion state, the elastomer/rGO composites exhibited significantly improved mechanical properties compared with the elastomer/GO composites. Compared with neat SBR, the modulus of GO is increased by 2.8-fold, while that for rGO is drastically increased by 7.7-fold. This indeed provides a new way to obtain the high-performance elastomer/graphene composites by combining interfacial chemistry and curing chemistry.

Wu et al. prepared graphene/natural rubber and graphene/styrene-butadiene rubber (SBR) composites by latex mixing method, respectively, and investigated the vulcanization mechanism [13]. Schopp et al. [14] prepared SBR composites by using the conventional carbon black and novel carbonaceous fillers (carbon nanotubes and graphene) and compared the different reinforcing effect. Graphene brings about significant improvement in mechanical, electrical, and gas barrier properties of SBR composites, unrivaled by other carbonaceous counterparts. Cui et al. [15] reported the preparation of graphene oxide/SBR composites through an emulsion intercalation method and used the composites in tire applications. Results show that both the storage modulus  $G'$  and Payne effect increase with the increasing amount of graphene, which is due to the cross-link structures originating from the high specific surface area and high aspect ratio of graphene oxide. Liu et al. [16] prepared the graphene/carboxylated nitrile rubber (XNBR) composites by using the sodium hamate-modified graphene oxide. The addition of 1 wt% graphene doubled the fracture energy of the composites, while their modulus remains unchanged. She et al. [17] introduced hydroxyl groups in NR in order to improve the dispersion of graphene oxide. Compared with pristine deoxidized NR, the incorporation of 0.7 phr of GO increases the tensile strength by 87%; in particular, the tensile strength at the strain of 200% increases 8.7-folds. Huang et al. [18] construct sacrificial metal-ligand bonds elastomer/graphene composites. This interface is composed of pyridine- $Zn^{2+}$ -catechol coordination motifs, which is strong enough to ensure uniform graphene dispersion and efficient stress transfer from matrix to fillers. The mechanical properties of the composite are simultaneously and remarkably improved.

## 2.2 Solution Mixing Method

For solution mixing method, rubber material was initially dissolved in solvent and then the graphene or surface-modified graphene was dispersed in the rubber solution, followed by the removal of solvent and vulcanization to get the rubber nanocomposites. This method enables the uniform dispersion of graphene to some degree, and surface modification can further improve the dispersion quality. Compared to the latex mixing approach, there are two disadvantages: (1) the dispersion of graphene down to single layer or a few layers in organic solvent is difficult to realize and (2) the organic solvents need to be recycled which will increase the production cost.

Bai et al. [19] dispersed graphene oxide in dimethyl formamide (DMF) by using an ultrasonically assisted solution mixing. The as-received graphene oxide suspension was added into nitrile-butadiene rubber (NBR), pre-dissolved in tetrahydrofuran, and then the mixture was subjected to ultrasonic dispersion, drying, two-roll milling,

hot-pressing, and vulcanization to obtain the GO/NBR composites. Ozbas et al. [20] investigated the strain-induced crystallization of GE/NR composites prepared by solution mixing method. Lian et al. [21] prepared graphene/butyl rubber (IIR) composites by solution mixing method. Butyl rubber with 10 wt% of graphene exhibits significant increase in mechanical properties, for example, the modulus of GE/IIR increases 16-folds compared with pristine IIR. Sadasivuni et al. [22] prepared maleic anhydride grafted butyl rubber (MA-g-IIR) and produced graphene/MA-g-IIR nanocomposites by solution mixing method. The functional groups on the basal plane of GO allow strong interactions with the carboxyl groups on NBR and lead to a rise in the glass transition temperature. Mensah et al. [23] prepared the reduced graphene oxide/nitrile rubber through solution mixing. By adding 0.1 phr of rGO, the tensile modulus of nitrile rubber at 50%, 100%, and 200% strains increases by 83%, 114%, and 116%, respectively, which is attributed to the uniform dispersion of rGO and improved interfacial interaction between rGO and rubber matrix. Gan et al. [24] developed graphene nanoribbons, originating from unwrapping multiwalled carbon nanotubes (CNTs), and used the graphene nanoribbons as fillers in silicone rubber. The strong oxidants (potassium permanganate, sulfuric acid) allow the decomposition of CNTs to form graphene nanoribbons, which are dispersed in silicon rubber by a facile solution mixing method. Thermal gravimetric analysis revealed that silicone rubber reinforced by graphene nanoribbons exhibits significant improvement of thermal stability. Chen et al. [25] revealed that the use of melt mixing method cannot achieve the uniform dispersion of graphene in silicon rubber. Instead, they used solution mixing method to produce silicone rubber/graphene composites, with graphene content varying from 0 to 2.96%.

### 2.3 Mechanical Mixing

For mechanical mixing method, graphene nanoplatelets were directly mixed with polar or nonpolar rubber matrix either in twin-roll mill or alternatively in a batch mixer (i.e., preblender). The mechanical mixing method has some advantages such as solvent-free, low cost, and simple technical process. However, the challenge in the preparation of graphene-rubber composites through mechanical mixing is the difficulty to obtain a uniform dispersion of graphene nanoplatelets in the rubber matrix.

Yaragalla et al. [26] dispersed the thermal reduced graphene oxide (TRGO) in NR by using a mechanical melt mixing. The modulus of NR filled by 3 phr of TRGO increases by 182%, while the oxygen barrier properties increase by 175% compared with neat rubber. Das et al. [27] prepared SBR nanocomposites containing graphene, expanded graphene (EG), graphene nanoplatelets (GnPs), and multiwalled carbon nanotubes (MWCNTs) by melt mixing and made a comparative study in their electrical and mechanical properties. At a particular filler loading, the MWCNT and the GnP showed the better improving performance. Mahmoud et al. [28] prepared graphene/NBR composites by mechanical mixing and investigated the effect of graphene on the fatigue properties of NBR materials. Al-solamy et al. [29] proposed the microstructure model for the piezoresistive effect of conductive NBR/graphite

nanoplatelets (10 nm thickness) nanocomposites. The rubber was initially mixed with graphene in twin-roll milling and pressed into cylinder with a height of 1 cm and basal area of 1 cm<sup>2</sup>. The result shows that the percolation concentration of the investigated nanocomposites was ~0.5 phr. Of all the composites examined, the sample, in the region of the percolation transition, was found most sensitive to compressive strain. The electrical conductivity was changed by more than five orders of magnitude upon a 60% compression. Araby et al. [30] prepared highly filled graphene/ethylene propylene diene monomer (EPDM) nanocomposites by mechanical mixing with 3.56 nm thick graphene platelets. Most GnPs can be dispersed uniformly in EPDM matrix. A high percolation threshold of electrical conductivity of 18 vol% GnPs was observed. The tensile strength, Young's modulus, and tear strength of EPDM material increased by 404%, 710%, and 270%, respectively, at a GE content of 26.7%. Yaragalla et al. [31] prepare epoxidized natural rubber (ENR) nanocomposites containing the thermally reduced graphene oxide (GR) by conventional mechanical mixing. At a low loadings (2 wt%) of graphene, the barrier and dielectric properties are significantly enhanced. Song et al. [32] prepared the graphene/silicone rubber composites by mechanical mixing using the Flacktek Speed Mixer (Fig. 2) and found the mechanical properties and thermal stability of silicone rubber composites were enhanced.

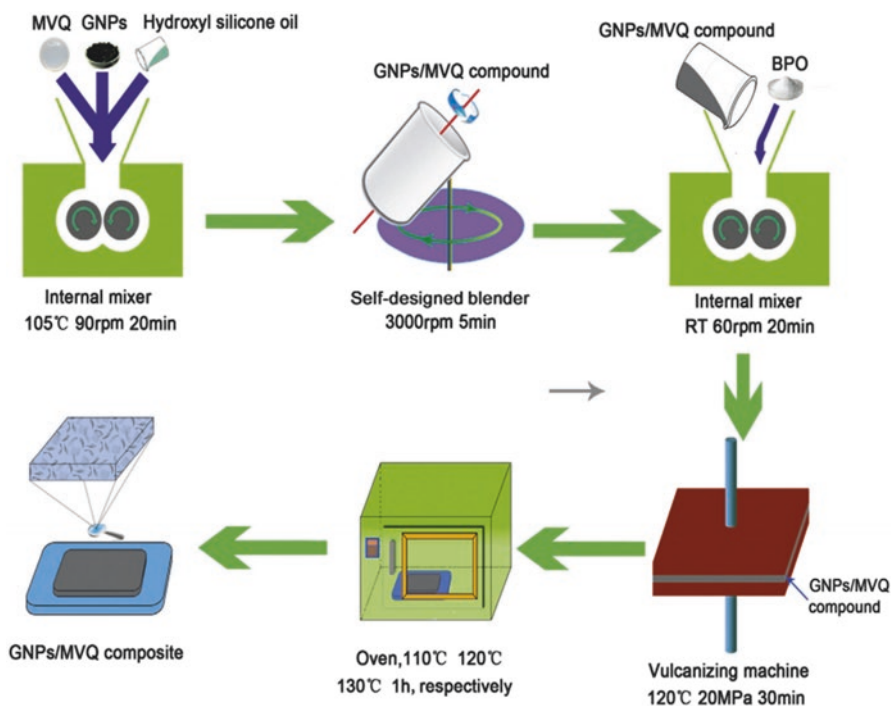


**Fig. 2** Preparation process of the graphene/silicone rubber composites (Reproduced with permission [32], 2015, Elsevier)



For mechanical mixing, the modification is necessary to improve the compatibility between graphene and rubber matrix. Lin et al. [33] studied the static and dynamic mechanical properties of NR filled with zinc oxide-doped graphene (Nano-ZnO-GE) obtained by twin-roll milling. The presence of nano-ZnO on the surface of graphene sheets not only suppresses the aggregation of graphene sheets but also acts as a more efficient cure activator in vulcanization process, with the formation of excellent cross-linked network at a low nano-ZnO-GE content because the GE sheets in nano-ZnO-GE composites act as the physical cross-link points. Compared with NR containing 5 phr of ZnO, Nano-ZnO-GE-modified NR shows remarkably enhanced mechanical properties, due to the inhibitive effect of ZnO on agglomeration of graphene nanoplatelets that promotes the formation of cross-linking network. Suriani et al. [34] used the sodium 1,4-bis(neopentylxy)-3-(neopentylxycarbonyl)-1,4-dioxobutane-2-sulfonate (TC14) to assist the dispersion of GO in the NR. TC14 could adsorb and give triple interactions between the GO and NR. Malas et al. [35] introduced the isocyanate-modified graphene nanosheets and carbon black into butadiene rubber (BR), styrene-butadiene rubber (SBR), and SBR/BR blends by mechanical mixing. Because of the higher basal spacing and exfoliated structure of isocyanate-modified graphene (i-MG) nanosheets than expanded graphite (EG), i-MG sheets were uniformly dispersed in the different rubber matrices in the presence of CB, resulting in an improved storage modulus, lower rolling resistance, and better anti-skid properties compared to the EG-filled rubber vulcanizates. Song et al. [36] prepared SBR-based nanocomposites with 50 phr carbon black and 5 phr natural graphite (NG) or acid-graphite (AG) platelets or modified graphite fabricated by the processes of thermal shock (NGT and AGT), sonication (NGS and AGS), and sonication after thermal shock (NGTS and AGTS). The modulus of the AG composites increased ~32%, and the tensile strength increased ~18% compared with that of control. Using acid-graphite platelets, the fatigue crack growth of composites is decreased, and the thermal and electrical properties of nanocomposites were enhanced. This is because the acid-graphite is uniformly dispersed in SBR due to the functional groups and improved both physical and chemical interactions between graphite and polymer by the coupling agent. Zhang et al. [37] investigated the functional graphene nanoplatelets modified by silane coupling agents and surfactant on the mechanical and thermal properties of silicone rubber composites. The results show that functional graphene nanoplatelets improved the mechanical and thermal stability of silicone rubber. Yin et al. [38] found that polyvinylpyrrolidone (PVP) molecules have strong interaction with GO via hydrogen bond; meanwhile, PVP molecules have a better compatibility with SBR, and as a result, the functional GO enhances the mechanical and thermal conductivity properties significantly. Tang et al. [11] investigated the difficulties in compounding styrene-butadiene rubber (SBR) and reduced graphene oxide and revealed that the optimal compatibility and interfacial interaction occur for GO filler with O/C ratio equal to 0.2, which allows a significant improvement on mechanical properties. Wang et al. [39] represented an improved compatibility between graphene and SBR when graphene oxide was modified by octadecylamine, as a result, greatly improving the properties of the composites.

Lin et al. [40] prepared the SiO<sub>2</sub>/rGO mixture by electrostatic assembly between 3-glycidoxypropyltrimethoxysilane (GPTMS)-modified graphene oxide and 3-aminopropyltriethoxysilane (APES)-modified silica and combined a reduction process with hydrazine hydrate. The SBR composites were fabricated by simple mechanical blending with the SiO<sub>2</sub>/rGO mixture in an open two-roll mill. The SiO<sub>2</sub>/rGO has a higher reinforcing effect for SBR than the individual SiO<sub>2</sub> or rGO due to the better dispersion and stronger interfacial interaction with the rubber matrix. The tensile strength, modulus at 300% strain, and tear strength for SBR/SG30 (SiO<sub>2</sub>/rGO) are dramatically increased by about 1204%, 170%, and 274% as compared with those of neat SBR, respectively. The DMA loss factor ( $\tan\delta$ ) at 0 °C and 60 °C, was adopted as measures of wet grip property and rolling resistance. Compared with SBR/S29.7 (individual SiO<sub>2</sub>), the wet grip property of SBR/SG30 (SiO<sub>2</sub>/rGO) is improved by 10.2%, and the rolling resistance is reduced by 10.3%.

### 3 Performance of Rubber/Graphene Composites

#### 3.1 Mechanical Properties

Mechanical properties of GE/NR nanocomposites could be affected by various factors, such as the dispersion of graphene, the interfacial interaction between rubber and graphene, orientation and network structure of graphene, and cross-link density of composites. Graphene is more effective in improving mechanical properties of rubber composites compared to other carbonaceous fillers. The reasons are:

1. Graphene, as a flexible and ultrathin two-dimensional nanosheet, possesses wrinkle structured topologies [41], which allows the higher absorption and adhesion compared to CNTs and CB.
2. Exceptional mechanical properties: graphene is regarded as the strongest material yet disclosed [4]. Graphene has theoretical Young's modulus of 1.05 TPa [42], while the modulus of CNTs is 450 GPa [41, 43, 44].
3. Graphene has a large specific surface area, ~2600 m<sup>2</sup>/g, leading to the generation of physical cross-linking and entanglements in rubber matrix.
4. Cross-link density increases with increasing GE content, resulting in the enhanced mechanical properties.
5. Graphene facilitates strain-induced crystallization, which plays a key role on mechanical enhancement of NR.
6. Graphene as a 2D filler is more flexible than a 3D material due to the spatial degree of freedom. Graphene can be stretched or bent or compressed in-plane to some degree. Graphene actually forms with ripples/corrugations on a length scale of tens of nanometers. Therefore, if graphene is dispersed in a single layer or very few layer, it is possible to improve the modulus and toughness simultaneously, or improve the modulus without degrading the materials flexibility, and also to exhibit excellent dynamic properties, different from the normal rigid 3D fillers like carbon nanotubes.

Zhan et al. [7] compared the mechanical properties of NR composites with different nanofillers. The tensile strength of NR/GE composites containing 2 wt% GE increased by 47% compared with pristine NR. In contrast, the tensile strength of NR/CB and NR/MWCNT composites was increased by only 6% and 9%, respectively. The stress at 300% strain for NR/(2 wt%) GE composites is two times that of NR/(2 wt%) MWCNT composites and 2.5 times that of NR/(2 wt%) CB composites. Compared to pure NR, the incorporation of 2 wt% GE enhanced the tear strength by 50%. With increasing GE content, the tensile strength of composite increases, while the elongation at break decreases. This is ascribed to the strong interfacial interaction between graphene and rubber matrix which immobilizes the molecule chains [45]. She et al. [17] added epoxy and hydroxyl groups into the NR that enhance the interfacial interaction between GO and rubber. The results showed that compared with those of pure ENR, the composite with 0.7 wt% GO loading shows a 87% increase in tensile strength and a 8.7-fold increase in modulus at 200% elongation after static in situ vulcanization. Yaragalla et al. [26] reported that with 3 phr of reduced graphene oxide in epoxidized nature rubber composites, the modulus of composite increased by 282% with respect to that of pristine materials.

Schopp et al. [14] investigated the effect of graphene layers on the mechanical properties of the composites and confirmed the graphene is the ideal fillers of SBR by comparison. They found that the mechanical properties of SBR/TRGO, SBR/CRGO, and SBR/MLG350 with graphene layers less than 10 were far superior to those containing graphene layers more than 60 (EG40) and conventional carbon fillers such as carbon black and CNTs. The stress at 50% strain for SBR/MLG350 and SBR/TRGO at a filler content of 25 wt% is 8 and 14 times higher than that of pristine SBR, respectively. The chemical reduced system SBR/CRGO shows simultaneously increase in both tensile strength and elongation at break. Mensah et al. [23] revealed the tensile modulus of NBR at strains of 50%, 100%, and 200% increased by 83%, 114%, and 116%, respectively, with the addition of 0.1 phr rGO. The NBR-rGO nanocomposite obtained by solution mixing demonstrated a higher hardness and higher modulus compared to the NBR gum and NBR-GO compounds. Gan et al. [24] found that the elongation at break of silicone rubber containing 0.4 wt% of graphene increased by 64%. With increasing graphene content to 2.0 wt%, the tensile strength and Young's modulus increase by 67% and 93%, respectively. Bai et al. [46] studied the influence of thermal treatment temperature of GO. Compared with neat silicone rubber, the tensile strength for the composites containing the rGO obtained at different treatment temperature 350, 700, and 1050 °C is improved from 0.32 MPa to 0.85, 0.86, and 0.94 MPa, respectively. After aging, the tensile strength of neat silicone rubber is down to 0.17 MPa, while the tensile strength of silicone rubber/GE (GO after thermal treatment under 1050 °C) remained at 0.63 MPa. Luo et al. [47] prepared the graphene/solution-polymerized styrene-butadiene rubber (SSBR) composites using three types of SSBR with different vinyl contents. The composites were investigated through experimental and molecular dynamics (MD) simulation approach. The authors found that as the vinyl content increases in the SSBR matrix, the graphene/SSBR interfacial interaction increases, and as a consequence, the mechanical properties of SSBR/GE were improved.

Lin et al. [33] substituted conventional ZnO by nano-ZnO to prepare nano-ZnO-GE/NR composites. NR composite containing 1.5 phr of nano-ZnO-GE shows a tensile strength of  $\sim 31$  MPa and tear strength of  $\sim 109$  kN/m, respectively, which are increased by 12.7% and 32.3%, respectively, compared to the pristine NR. Graphene showed a higher reinforcing efficiency than CB and CNTs. Yin et al. [38] used the polyvinylpyrrolidone to modify GO and found that after adding 5 phr functional GO, the tensile strength and tear strength are enhanced to 517% and 387%, respectively.

Yan et al. [48] observed two opposite effects of GE on the crack growth resistance of NR: at lower strains, the inclusion of GE accelerates the crack growth; at higher strains, the crack growth is retarded with the addition of GE. Strain-induced crystallization at crack tip has been investigated. The GE/NR composite starts to crystallize near the crack tip at the strain of 30%, while unfilled NR does not. Also GE/NR has a much higher crystallinity and larger crystalline zone than unfilled NR at the same strains, which allows the crack branching and more energy dissipation and prevents the crack growth.

Li et al. [49] found that tensile strength and elongation at break for GE/NR composite increase by about 9% and 3%, respectively, with the addition of 0.07 wt% of GE. Wang et al. [50] revealed a remarkable mechanical enhancement of SBR with the addition of CB and rGO. Wu et al. [51] modified graphene oxide with silane coupling agent, which was used to reinforce the NR. Figure 3 shows that tensile strength and tensile modulus of NR were increased by 100% and 66%, respectively,

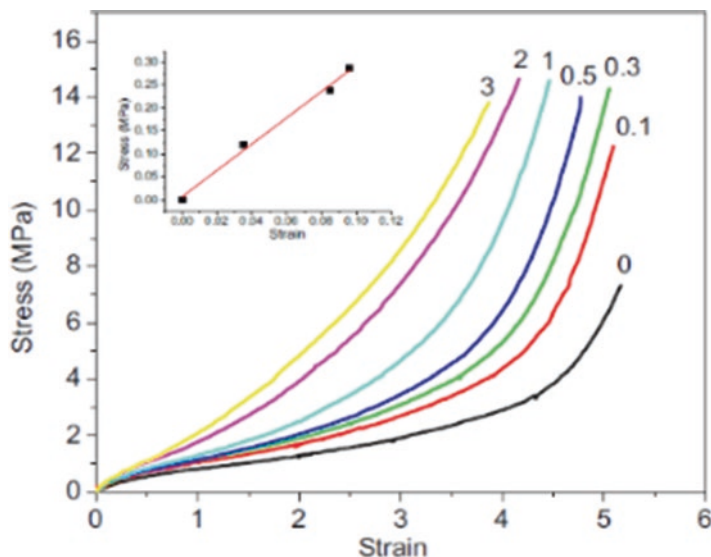


**Fig. 3** Representative stress-strain curves of unfilled NR and graphene/NR nanocomposites. The numbers in the figure indicate the weight fractions of graphene in the nanocomposites. The upper inset shows the linear fitting to the data below 10% strain (Reproduced with permission [51], 2013, Elsevier)

with the incorporation of 0.3 wt% graphene, while the ultimate strain remains unchanged. Sadasivuni et al. [22] reported the Young's modulus of butyl rubber-graphene composite was improved from 0.9 to 1.9 MPa, the tensile strength was enhanced from 0.8 to 2.7 MPa, and the elongation at break was increased from 106 to 220% at a graphene content of 2 wt%. Liu et al. [52] prepared the carboxylated nitrile-butadiene rubber (XNBR)/graphene hybrid nanocomposites (PEI/XNBR/PEI/GO)<sub>30</sub> (30 is referred to the number of deposition cycles) via layer-by-layer (LBL) method and showed that the tensile strength was increased by 192% and elastic modulus was increased by 215%.

There are more reports showing the improved mechanical properties of rubber composites with graphene [27, 53–55].

### 3.2 Electrical Properties

The stretchable conductive rubber is one of the most important materials in the manufacturing of flexible electronic devices [56]. The conductivity of composite depends on the filler content with a power law relationship (see Eq. 1). When filler content reaches the percolation threshold, the composite converts to an electrical conductor. According to the theory of percolation threshold, the conductivity of composite ( $\sigma$ ) is represented as [57, 58]

$$\sigma = \sigma_0 (\varphi - \varphi_c)^s (\varphi > \varphi_c) \quad (1)$$

where  $\varphi$  is the volume fraction of filler,  $\varphi_c$  is percolation threshold value, and  $\sigma_0$  is a constant, determined from the conductivity of filler. Exponent  $s$  represents the correlation between  $\varphi$  and  $\varphi_c$ . Table 1 summarized the threshold values for various GE/NR composites.

Zhan et al. [8] constructed graphene-segregated network in NR matrix, so as to enhance the conductivity as well as to decrease the percolation threshold value. The conductivity for the composite prepared by ultrasonic assisted latex mixing and in situ reduction followed by a static heat press and vulcanization reached  $\sim 0.03$  S/m, due to the construction of conductive network in the polymer matrix, while for GE/NR composite prepared by Haake mixing or by twin-roll milling, it is only  $5.7 \times 10^{-7}$  S/m. The percolation threshold value of GE/NR composite with segregated network is 0.62 vol%, while for the NR composite with well-dispersed graphene, it is 4.62 vol% (Fig. 4). Potts et al. [10] found that the electric conductivity of GE/NR composites prepared by latex mixing was higher than that of composites prepared by mechanical mixing. Araby et al. [59] reported that the percolation threshold of GE/SBR composites prepared by solution mixing is 5.3 vol%, while for the GE/SBR composites prepared by mechanical blending, the percolation threshold is 6.5 vol% [60].

He et al. [61] showed that the percolation threshold for ENR-GE composites depends on the evolution of the GE networks in the composites. At low GE

**Table 1** Electrical percolation threshold of GE/NR nanocomposites

Elastomer	Processing	Electrical percolation threshold
NR [8]	Emulsion blending	0.62 vol%
	Mechanical blending	4.62 vol%
EPDM [30]	Mechanical blending	18 vol%
SBR [62]	Emulsion blending	0.5–1.0 wt%
NR [64]	Mechanical blending	0.1–0.5 wt%
SBR [59]	Solution blending	5.3 vol%
SBR [60]	Mechanical blending	16.5 vol%
NBR [29]	Mechanical blending	0.5 wt%
SR [70]	Solution blending	2 wt%
SR [25]	Solution blending	0.9 vol%
PDMS [71]	Solution blending	3 wt%
SBR [14]	Emulsion blending	0.5 wt%
NBR [28]	Mechanical blending	0.5 wt
PDMS [63]	Solution blending	0.8 wt% (650 m <sup>2</sup> /g graphene)
		1.6 wt% (400 m <sup>2</sup> /g graphene)

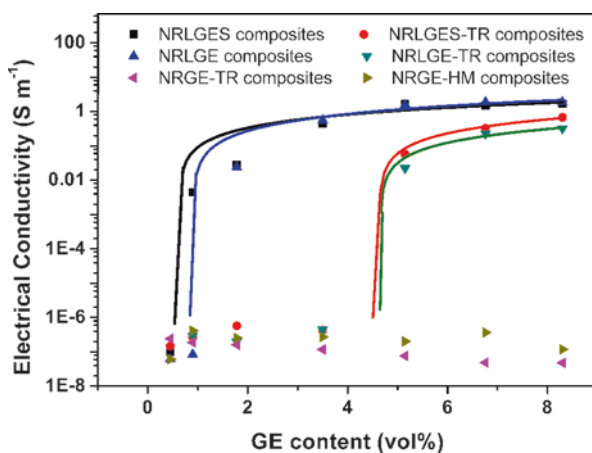


**Fig. 4** The electrical conductivity as a function of the graphene content for graphene/NR composites prepared by the different methods. NRLGES: the cross-linked graphene/NR composites with the segregated network prepared by self-assembly in latex and direct hot-pressing. NRLGES-TR: the cross-linked graphene/NR composites without the segregated network prepared by latex mixing and twin-roll mixing. NRLGE: the uncross-linked graphene/NR composites with the segregated network prepared by self-assembly in latex and direct hot-pressing. NRLGE-TR: the uncross-linked graphene/NR composites without the segregated network prepared by latex mixing and twin-roll mixing. NRGE-TR: the composites prepared by direct twin-roll mixing of graphene powders and rubber. NRGE-HM: the composites prepared by direct Haake mixing of graphene powders and rubber (Reproduced with permission [8], 2012, Royal Society of Chemistry)

concentrations (0.17 vol%), GE existed as individual units, while a “polymer-bridged GE network” was constructed in the composites when GE concentrations exceeded 0.17 vol%. Finally, a “three-dimensional GE network” with percolation conductive paths was formed with a GE concentration of 0.23 vol%, where a remarkable increase in the conductivity of ENR-GE composites was observed.

Graphene has high electrical conductivity, large aspect ratio, and specific area compared to other conductive filler (i.e., CNTs or carbon black powder). Thus to attain the same conductivity, the required concentration of graphene is much lower than that of traditional carbonaceous fillers [14]. Kim et al. [62] evaluated the percolation threshold of graphene/SBR composites ranging from 0.5 to 1.0 wt%. The conductivity of composites increases from  $4.52 \times 10^{-13}$  to  $4.56 \times 10^{-7}$  S/cm as the graphene concentration increases from 0.5 to 5.0 wt%. Ozbas et al. [63] studied the effect of graphene with varied specific surface area on the electrical conductivity of polydimethylsiloxane (PDMS) and showed that PDMS filled by graphene with specific surface area of 650 m<sup>2</sup>/g has a percolation threshold of 0.8 wt%, while for the PDMS containing graphene with a specific area of 400 m<sup>2</sup>/g, the percolation threshold value is 1.6 wt%. The electrical conductivity of graphene/EPDM prepared by mechanical mixing was examined by Araby et al. [30]. They showed that the percolation threshold of graphene/EPDM composite is 18 vol%. After vulcanization, the volume resistivity of graphene/EPDM composite was increased by seven orders of magnitude compared to that of the composite before vulcanization. This result indicates that cross-linking rubber promotes the construction of graphene network.

Hernández et al. [64] prepared GE/NR composites with percolation threshold ranging from 0.1 to 0.5 wt%. The conductivity of composites as a function of frequency of alternate current was also examined. Results showed that conductivity of composite increases with increasing frequency. Wang et al. [50] studied the conductivity of SBR/GE composite as a function of graphene content. The conductivity increases with the increasing concentration of graphene. Specifically, SBR/GE composite converts into conductor with the addition of 7 phr of graphene. For graphene, the ease of dispersion and construction of the three-dimensional conductive network of graphene in polymer matrices are the key points for the preparation of conductive polymer composites (CPCs) and flexible electronic devices. Polyaniline/graphene nanohybrids were prepared by in situ reduction of graphene oxide using aniline as both reducing and stabilizing agents. The as-prepared CPCs with 3D conductive network exhibited a very low percolation threshold (threefold lower than that of the conventional NR/graphene blends), reported by Zhou et al. [65]. Suriani et al. [39] enhanced the dispersion of GO in NR latex by using 1,4-bis(neopentyloxy)-3-(neopentyloxycarbonyl)-1,4-dioxobutane-2-sulfonate (TC14), the tri-chain of the hyper-branched TC14 surfactant that successfully improved the dispersions and the conductivity of the composites.

Researchers further studied the effect of pressure and temperature on the electrical conductivity of GE/NR composites. The piezoresistance of graphene/NBR composites shows strong dependence on the compressive strain when the content of conductive filler reaches the percolation threshold. In detail, the resistance of

graphene/NBR composite reduces by five orders of magnitude at the compressive strain of 60%. On the other side, the resistance increases by two orders of magnitude under the pressure of 6 MPa. Chen et al. [25] and Hou et al. [66] also studied the piezoresistance of graphene/polydimethylsilicone composites and showed that the graphene nanosheets were homogeneously dispersed in the PDMS matrix and an ultralow percolation threshold (0.63 vol%) of the composites was obtained. The octadecylamine-modified graphene oxide (G-ODA)/styrene-butadiene rubber composites with 1.19 vol% content of G-ODA show a remarkable positive piezoresistivity of high sensitivity higher than 400 under the pressure of 1.2 MPa, excellent repeatability, small hysteresis, and long-term durability. The effect of temperature on the conductivity of graphene/NBR was reported by Mahmoud et al. [67]. They showed electrical conductivity increases with increasing temperature. Tian [68] used the combined strategy of encapsulating of graphene oxide nanosheets (GONS) on carboxylated nitrile rubber (XNBR) latex particles and the in situ thermal reduction in GONS at a moderate temperature. The dielectric constant at 100 Hz obviously increased from 23 for pure XNBR to 2211 and 5542 for the composite with 0.5 vol% and 0.75 vol% of TRGO, respectively, and it also had the dielectric loss. Araby et al. [69] prepared a MWCNTs/graphene/EPDM rubber composites in which MWCNTs worked supplementally with GnPs by forming conductive networks, where MWCNTs acted as long nanocables to transport electrons and stress, while GnPs served as interconnection sites between the tubes forming local conductive. As a result, it produced a percolation threshold of electrical conductivity at 2.3 vol% for three-phase composites, 88% lower than that of two-phase composites.

There are more reports on electrical percolation threshold of rubber/graphene nanocomposites as shown in Table 1.

### 3.3 Gas Barrier Properties

Rubber materials have a variety of applications, such as automobile tire, outdoor, and aerospace sealing products. Many rubber products require extremely high standards in terms of gas barrier properties. There are mainly two kinds of high gas barrier rubber materials, one consists of the special rubber such as butyl rubber, chloroprene rubber, and functionalized NR, which intrinsically exhibits high barrier properties, and the other one is the nanofiller-modified rubber or rubber-based composites. Compared to CNTs, two-dimensional graphene filler exhibits much higher efficiency in improving the gas barrier properties of rubber composite due to the tortuous pathways for the gas molecules diffusing through graphene layers in the rubber matrix.

Zhan et al. [8] reported a more significant enhancement in water vapor barrier properties of GE/NR composites than that of the clay-based rubber materials [72, 73]. Interestingly, GE/NR composites with segregated network show higher gas barrier properties than that of NR containing uniformly dispersed graphene. For instance, natural rubber including segregated graphene network has a water transmission rate



(WTR) coefficient of  $1.00 \times 10^{-16}$  g/m.s.Pa at 25 °C at a filler content of 1.78 vol%, while NR with homogeneously dispersed graphene at the same content has a higher WTR coefficient of  $1.31 \times 10^{-16}$  g/m.s.Pa. This was ascribed to the graphene-segregated network which makes the diffusion of water vapor more difficult. Wang et al. [50] found that graphene nanoplatelets dispersed in rubber matrix either in molecular level and orientated along the surface contributes to increase the tortuosity of gas diffusing pathway. In particular the gas transmission rate of SBR composites containing 3 and 7 phr of graphene decreases by ~67% and ~88%, respectively, compared with that of pristine SBR. Yaragalla et al. [26] showed that oxygen transmission rate (OTR) of NR containing 3 phr of graphene decreases by ~75% compared to that of pristine NR.

Sadasivuni et al. [74] showed graphene-filled butyl rubber has a lower OTR value than clay-filled rubber composites. The aspect ratios of graphene and clay determined from experiments are 130 and 108, respectively. The higher aspect ratio of graphene mainly results in the lower OTR value of IIR composites. Moreover, the larger specific area and the uniform dispersion of graphene also contribute to the lower OTR of graphene/IIR composites compared to that of clay/IIR composites. The oxygen barrier properties of SBR modified by varied carbonaceous fillers have been investigated by Schopp et al. [14]. Results show that rubber material filled with TRGO has a lower OTR value than multilayered graphene-filled rubber, while the rubber material filled by CNTs or CB exhibits a higher OTR value compared to the graphene-filled rubber materials. The uniform dispersion and the large lateral dimension of graphene in rubber matrix decrease the area available for the diffusion of gases and meanwhile lead to the increase of the tortuous pathway for gas and thus a consequent improvement of the barrier properties.

Graphene, treated by different methods, differs in improving gas barrier properties of rubber. Wu et al. [51] studied the barrier properties of bis(triethoxysilylpropyl) tetrasulfide functionalized graphene oxide (SGO)/natural rubber composites and showed that gas transmission rate decreases by about 48% compared to that of pristine NR with the only 0.3 wt% graphene content. The remarkable improvement in the gas barrier properties of the composites is attributed to the strong interfacial interaction and the molecular-level dispersion of SGO in the NR matrix. It is noteworthy that for clay/NR composite, the same barrier properties can be reached only at the clay content of 16.7 wt% [5].

Modification of the rubber molecular chain also has an effect on the gas barrier properties of the material. Yaragalla et al. [31] used the thermal reduced graphene oxide to mix with epoxidized natural rubber. The composites with high epoxidation level (50%) showed good impermeability to O<sub>2</sub> gas. At 2 wt% graphene, the oxygen shielding rate is increased by 62% compare to the pure rubber. This is owing to the homogeneous distribution and the platelet-like morphology of the GR layers in the ENR matrix and also due to the hydrogen bonds between ENR and GR layers. Guo et al. [75] prepared the graphene oxide/carboxylated acrylonitrile butadiene rubber (GO/XNBR) nanocomposites with latex mixing method and found that the gas permeability of the nanocomposite is much lower than that of the matrix.

### 3.4 Thermal Properties

Thermal conductive rubber composites have been used in a wide range of applications, including engines, electric generator, and heat exchanger, as prospective alternatives to the metal products. Graphene, with a theoretical thermal conductivity of 5300 W/(m·K) [76–78], is one of best choices to be used as fillers to improve the thermal conductivity of rubber composites. Zhan et al. [7] showed that the thermal conductivity of NR increases by about 12%, i.e., from 0.174 to 0.196 W/(m·K), with the graphene content of 5 wt%. Song et al. [32] revealed that the thermal conductivity of SBR composites at the graphene content of 5 wt% increases by about 20% compared to pristine SBR, whereas, for the conventional CB or graphite-filled SBR at comparable concentration, the thermal conductivity increases by only 2.4% and 10%, respectively. This might be ascribed to the higher specific surface area of graphene which facilitates both more contact possibility and interfacial interaction with rubber matrix. Potts et al. [79] studied the thermal conductivity of GE/NR prepared in different methods and showed that composites produced by latex mixing exhibit higher thermal conductivity than those prepared by mechanical mixing. In detail, GE/NR composites prepared by latex mixing show thermal conductivity of 0.219 W/m·K, while for the composite prepared by mechanical mixing, the thermal conductivity is 0.188 W/m·K, which is improved by ~40% and 20%, respectively, than that of pristine NR. Zhang et al. [37] showed that functional graphene nanoplatelets (GnPs) modified by silane coupling agents and surfactant can improve the thermal conductivity of silicone rubber (SR) significantly. The neat silicone rubber has low thermal conductivity of ~0.171 W/m·K; when the graphene loading is 2 phr, the thermal conductivity for three different kinds of graphene/silicone composites (aminopropyltriethoxysilane) APTES-GnP/SR, (vinyltrimethoxysilane) VTMS VTMS-GnP/SR, and Triton-GnP/SR enhanced by ~46.2%, 54.4%, and 57.3%, respectively.

Thermal stability is a key parameter for rubber material. Rubber material in the thermal oxygen aging process generally contains three kinds of reactions: pendant oxidation and scission, main chain scission, and the formation of new cross-links. The effect of GO and thermal reduced graphene on the thermal stability of silicone rubber is reported by Li et al. [78]. They showed that the decomposition temperature of silicone rubber increase with the increasing concentration of graphene. In particular, the decomposition temperature increased from 356 °C to 417 °C with the addition of 1 wt% of graphene oxide, and the decomposition temperature can further increase up to 489 °C by using TRGO as the filler. Malas et al. [35] showed the decomposition temperature of BR, SBR, and SBR/BR composites increases with the addition of graphene. The uniform dispersion of graphene facilitates heat transfer in the rubber matrix, thus preventing the partial oxidative decomposition of the rubber material. Kim et al. [62] studied the thermal stability of multilayered graphene/SBR composites and revealed the existence of  $\pi$ - $\pi$  interaction between graphene and phenyl groups, resulting in the improved thermal stability. Wang et al. [80] found that the incorporation of GO could increase the thermal stability of

XNBR, because of the strong interaction arising from function oxygen-containing group of GO. They found the addition of 40 phr of CB cannot affect the thermal stability of XNBR, whereas the simultaneous presence of 40 phr of CB and 1 phr graphene raised the decomposition temperature of SBR from 318 to 350 °C. This is because the  $\pi$ - $\pi$  conjugation between graphene and SBR and the large specific surface area of graphene sheet could inhibit the emission of gaseous small molecule, resulting in the improved thermal stability. Nevertheless further increasing the amount of GE does not change the decomposition temperature. On the contrary, Schopp et al. [14] reported the unaltered thermal stability and glass transition temperature (retaining at  $-44$  °C) of SBR with the addition of 25 phr of thermal reduced graphene oxide (TRGO). Also, Zhang et al. [81] found that there is not any difference in the thermal stability of pristine SBR and CB or CB/rGO filled SBR composites. Therefore, the effect of graphene on thermal stability remains uncertain, and further studies are needed to gain in-depth understanding. Araby et al. [59] introduced the graphene platelets (GnPs) of 3 nm in thickness to SBR by solution mixing, and as a result, thermal conductivity for graphene/SBR composite enhanced by 300% at a GnPs content of 24 vol%.

Recently, it is found that the graphene has the capability to quench the free radicals and thus improve the antiaging behavior. Qiu et al. [82] reported that multilayer oxidized graphene has a better the effect of quenching free radicals than single graphene. Liu et al. [83] showed that after  $\gamma$  irradiation, the rGO/NR composites have a better tensile strength compared with blank NR, indicating that the graphene had the effect of quenching free radicals.

### 3.5 Other Property

There are many other properties for the GE/NR composites. Dong et al. produced high-concentration rGO solution using gelatin (Gel) as the stabilizer and subreductant and hydrazine hydrate (HHA) as the main reductant [84]. The Gel-HHA-rGO nanosheets exhibited excellent colloidal disposability and stability in alkaline condition. Then Gel-HHA-rGO-filled natural rubber composites were prepared by water-based solution casting. Well-organized interconnected rGO networks were constructed throughout the NR matrix. The strain-sensing tests revealed that the rGO/NR composites exhibited outstanding strain sensitivity and repeatability, which could be used to detect the cyclic movements of human joints. The results are promising in the rubber industry to guide the fabrication of highly sensitive and stretchable strain sensors for engineering application. They also fabricate electrically conductive NR-rGO hybrid films for solvent-sensing application [85]. The materials can exhibit different stimuli-sensing responses for different organic solvents.

Lin et al. [86] made the binary rubber blend/graphene composites which can be used for strain sensor. The conductive percolation threshold of this material is 0.3 vol%, 12-fold lower than that of the conventional graphene-based composites

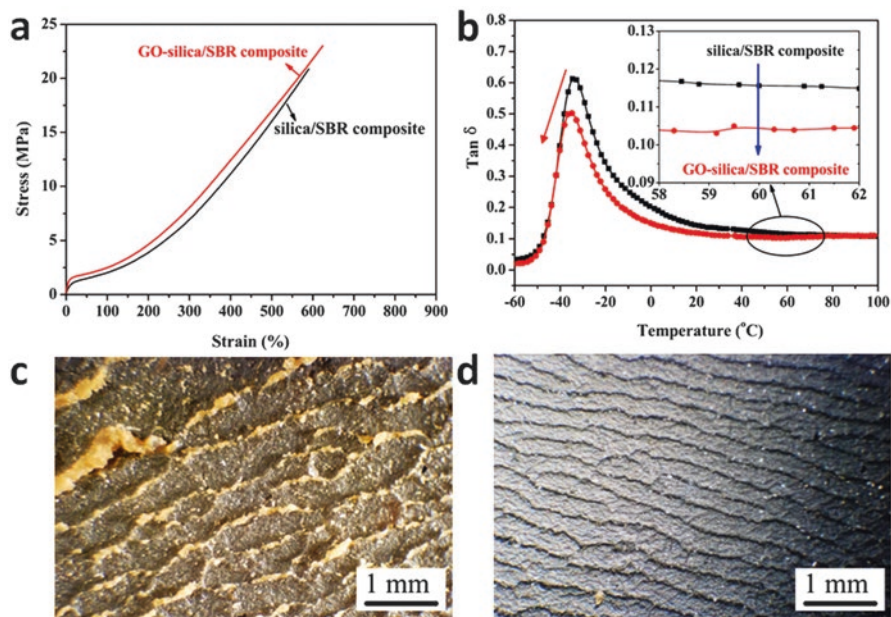


**Fig. 5** Properties of silica/SBR composite and GO-silica/SBR composite at total filler loading of 20.1 vol%. **(a)** Stress-strain curves for silica/SBR composite (0 vol.% GO, 20.1 vol.% silica) and GO-silica/SBR composite (0.6 vol.% GO, 19.5 vol.% silica). **(b)** Mechanical loss factor ( $\tan\delta$ ) as a function of temperature for silica/SBR composite and GO-silica/SBR composite. **(c–d)** Optical images (403 magnification) of Akron abrasion surface of silica/SBR composite **(c)** and GO-silica/SBR composite **(d)** (Reproduced with permission [87], 2013, Nature Publishing Group)

with a homogeneously dispersed morphology (4.0 vol%). Near the percolation threshold, the sensors could be stretched in excess of 100% applied strain with a gauge factor of  $\sim 82.5$  and good reproducibility with  $\sim 300$  cycles.

Mao et al. [87] made the graphene oxide/silica/styrene-butadiene rubber (GO-silica/SBR) composites using SBR latex and a small loading of butadiene-styrene-vinyl pyridine rubber (VPR) latex, followed by latex co-coagulation. The results showed that GO-silica/SBR composite exhibited outstanding wear resistance and low-rolling resistance which make it very competitive for the green tire application and also open up enormous opportunities to prepare high-performance rubber composites for future engineering applications. Figure 5c, d showed that a large amount of debris and deep wear patterns were found on the worn surface of silica/SBR composite (Fig. 5c), indicating a poor wear resistance (Akron wear  $0.27 \text{ cm}^3/1.61 \text{ km}$ ). For GO-silica/SBR composite, the worn surface became smoother and showed much narrower wear patterns (Fig. 5d), indicating an improved wear resistance (Akron wear  $0.19 \text{ cm}^3/1.61 \text{ km}$ ) and low-rolling resistance.

Lin et al. [33] measured the dynamic mechanical properties for the nature rubber composites containing ZnO nanoparticle-doped graphene (Nano-ZnO-GE). The results showed that NR/Nano-ZnO-GE nanocomposites exhibited higher wet grip

property and lower rolling resistance compared with NR. Boland et al. [88] used the liquid-exfoliated graphene to prepare the super conducting rubber composites which have potential application in strain sensors. The strain sensitivity for the composites is reasonably high, with gauge factors of up to 35. Moreover, these sensors can effectively track dynamic strain, working well at vibration frequencies of at least 160 Hz. These GE/NR composites can use as bodily motion sensors, especially in monitoring joint and muscle motion and breathing and pulse.

## 4 Understanding for Graphene Effects as a 2D Filler for Rubber

### 4.1 Reinforcing Mechanism

The mechanical properties are significantly improved even with a low addition of GE which is not achieved for other conventional fillers. It is necessary to gain insight into the reinforcing mechanism of NR/GE nanocomposites. Generally, for rubber the most important factors to affect the mechanical properties are strain-induced crystallization and vulcanization. Strain-induced crystallization plays a key role in the mechanical properties of nature rubber. When stretching to a critical strain, rubber molecular chain starts to crystallize and becomes “self-reinforcing,” and the mechanical properties increase. The mechanical properties of rubber also depend strongly on the cross-link density which relates to the vulcanization process and mechanism.

Ozbas et al. [20] firstly investigated the effects of graphene sheets on the strain-induced crystallization of NR. Through Synchrotron X-ray scattering experiment, they observed that the onset of crystallization occurs at significantly lower strains for graphene-filled NR samples compared with carbon black-filled NR. The unfilled NR exhibits strain-induced crystallization at a strain of  $\sim 2.25$ , while incorporation of 1 wt% graphene shifts the crystallization to a strain of  $\sim 1.25$  (Fig. 6). In contrast, loadings of 16 wt% CB do not significantly shift the critical strain for crystallization. Small angle X-ray scattering shows that graphene is aligned in the stretching direction, whereas carbon black does not show alignment or anisotropy.

Li and Fu et al. [89, 90] investigated the reinforcing mechanism of graphene, graphene oxide, and carbon nanotubes in rubber through experimental synchrotron WAXD and theoretical entanglement bound rubber tube (EBT) model. The influences of GE, GO, and CNTs on the crystallinity of NR during stretching were determined by synchrotron WAXD. It was found that the incorporation of GE produces a faster strain-induced crystallization (SIC) rate and a higher crystallinity compared with GO and CNTs, as shown in Fig. 7. The same change trend in tensile modulus and crystallinity suggests that SIC plays a crucial role in the NR reinforcement.

To gain insight into the reinforcing effect of graphene on NR on the molecular level, the EBT model was used to analyze the microstructure of the rubber network. The EBT model allows a proper separation of cross-links and constraint contribution to the stress-strain behavior and a reliable determination of cross-link densities.

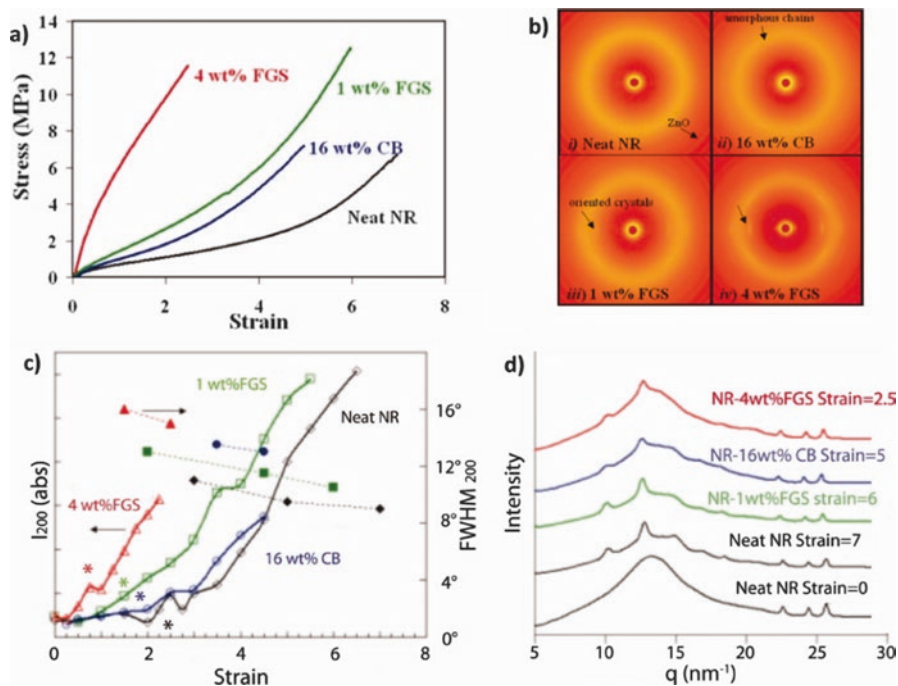


**Fig. 6** Coupled WAXD and tensile tests for neat NR and NR filled with 1 and 4 wt% FGS and 16 wt% CB. **(a)** Engineering stress versus strain. **(b)** 2D WAXD patterns at strain = 2 (air scattering is subtracted as background). Stretch direction is vertical. **(c)** Integrated intensity (open symbols, left axis) and azimuthal breadth (FWHM, filled symbols, right axis) for the NR 200 reflection versus strain. Asterisks represent the onset of crystallization, as detected by a visible 200 arc on the equator. **(d)** 1D WAXD patterns for unstretched neat NR and all samples shortly before failure in the tensile test. Small peaks from 22 to 26 nm<sup>-1</sup> are from ZnO in the base rubber formulations (Reproduced with permission [20], 2012, John Wiley and Sons)

The topological constraint was assumed to act on the entire network chains to restrict them from fluctuating within small length scale by packing effects that result from the inability of the chains to pass through their neighbors. According to the EBT model, it is assumed that a number of entanglements are formed in the transition zones between the tightly adsorbed bound and bulk rubbers far from the filler surface phases, which are believed to dominate the rubber property. The molecular network parameters can be calculated according to the equations as summarized in Table 2. With the addition of the filler, the tube dimension  $d_0$  decreases; also the mean number of Kuhn's statistic chain segments between two successive entanglements ( $n_e$ ), and the average molecular mass of the chain ( $M_c$ ) decrease. The EBT model is schematically represented in Fig. 8 to visualize the effect of the filler on the rubber chain network structure.

To understand the basic physics for graphene-reinforced rubber nanocomposites, especially the interfacial bonding characteristics at the molecular level, Luo et al. [47] investigated the thermodynamics, dynamics, interfacial bonding characteristics, and

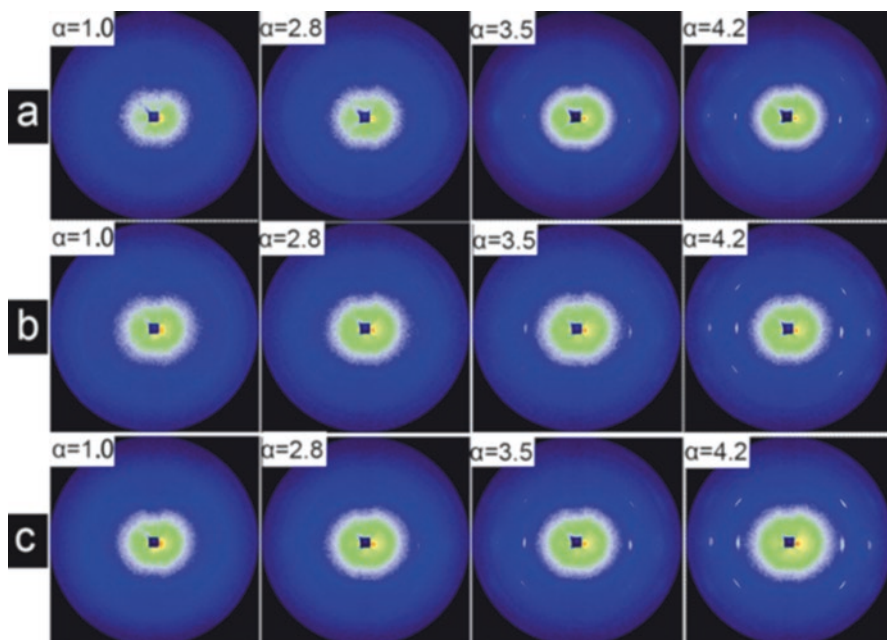


**Fig. 7** Sequential changes of WAXD patterns from **a** NR, **b** 0.7 GO/NR, and **c** 0.7 GE/NR. Corresponding strain ( $\alpha$ ) values are indicated at the left top in each pattern (Reproduced with permission [89], 2013, John Wiley and Sons)

**Table 2** Network molecular parameters of unfilled and filled rubbers

	$G_c^{*a}$ (MPa)	$G_e^{*b}$ (MPa)	$d_o$ (nm)	$n_e$	$M_c$ (g/mol)	$R_c$ (nm)
NR	0.38	0.51	1.54	3.1	4822	7.43
GO/NR	0.37	0.58	1.46	2.8	4340	7.05
GE/NR	0.45	0.61	1.42	2.6	4089	6.84

Reproduced with permission [89], 2013, John Wiley and Sons

$G_c^{*a}$  and  $G_e^{*b}$  can be determined from the slope and y-axis interception of the linear part of the intermediate deformation in the modified Mooney plot  $\sigma^*$  vs  $f(\alpha)$ , respectively

fractional free volume (FFV) of graphene/solution-polymerized styrene-butadiene rubber (SSBR) composites through a combined experimental and molecular dynamics (MD) simulation approach. The surface energies of SSBR and the work of adhesion between SSBR and graphene were calculated. MD simulations of the pullout of the graphene from SSBR matrix were carried out to explore the interfacial bonding characteristics at the molecular level, which show that the interaction energy, pullout energy, and shear stress between graphene and SSBR increase with the increase of the vinyl content in the SSBR molecular structure. The modeling results were in good agreement with the experimental results. The snapshots of the pullout process are shown in Fig. 9.  $\Delta Z$  represents the displacement of graphene during pullout. The graphene sheets were first fully embedded in the SSBR matrix and then gradually

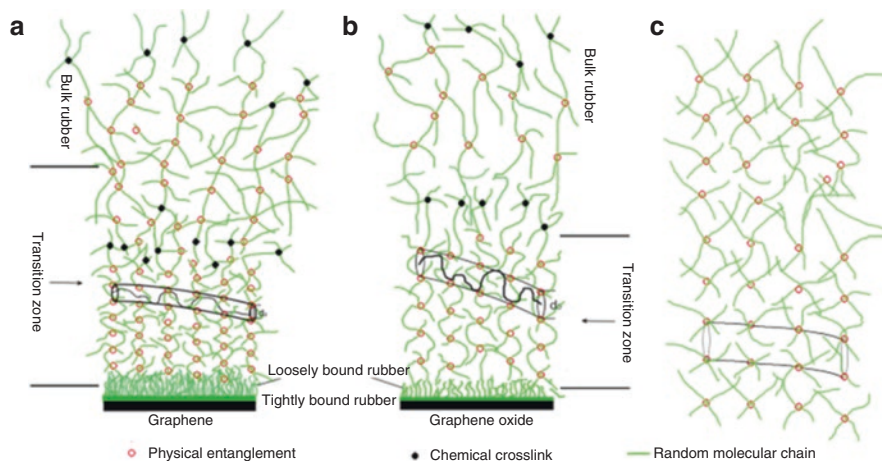


**Fig. 8** Schematic representation of the EBT model, (a) GE/NR, (b) GO/NR, and (c) NR (Reproduced with permission [89], 2013, John Wiley and Sons)

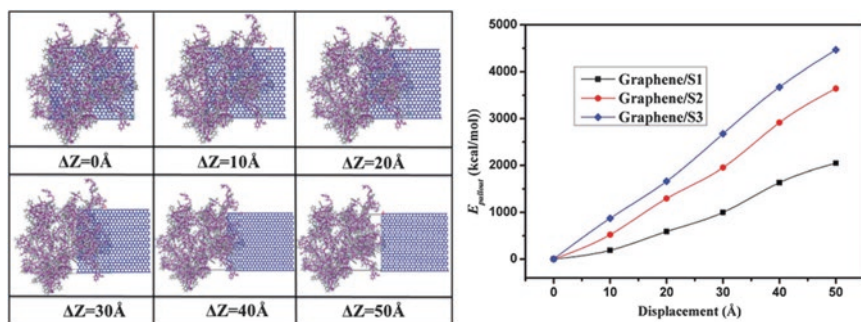


**Fig. 9** (Left) Simulated snapshots of pullout of graphene ( $\Delta Z$  is defined as the displacement of graphene during pullout); (right) pullout energy during pullout (Reproduced with permission [47], 2016, Royal Society of Chemistry)

pulled out in the pullout simulation. The energies related to the graphene/SSBR interface during pullout were calculated.

For in-depth understanding of material behavior, Heinrich [91] exploited the three-dimensional transmission electron microscopy (3D-TEM) to characterize the complex filler morphology of CB/graphene/SSBR rubber matrix in a qualitative way. The 3D tomography can provide a useful method to detect and recognize individual objects, i.e., to distinguish different filler platelets from each other (Fig. 10). It was found that the dispersion/exfoliation of the stacked graphene sheets into individual single sheets was facilitated by the presence of carbon black in the system. The existence of oligo-layer graphene sheets was detected by this 3D-TEM, especially when the rubber matrix exists in a complex morphology arisen from filler-filler networks in all spatial dimensions.



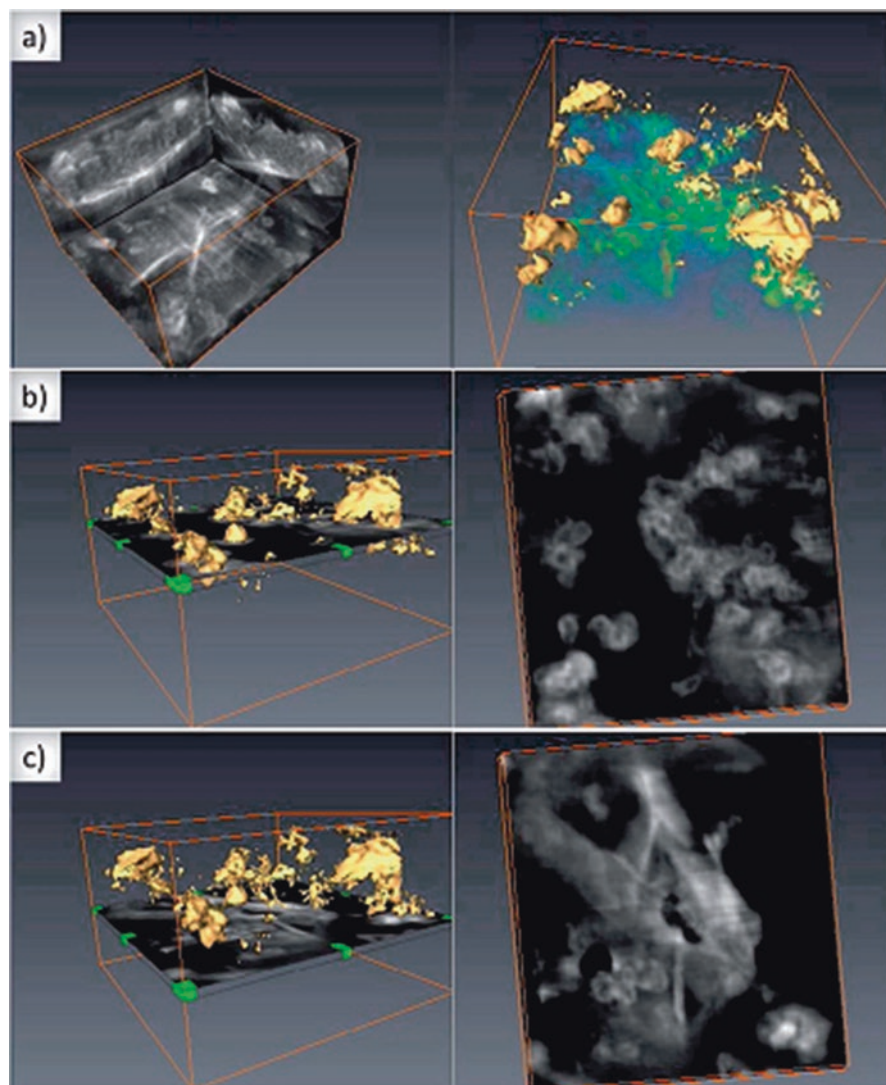


**Fig. 10** (a) Visualization of the 3D reconstruction of SSBR filled with 35 phr CB and 5 phr GnP; yellow and green regions represent CB and GnP, respectively, (b and c) present the resultant volume on the left side and a slice in z-direction on the right side (Reproduced with permission [91], 2014, Royal Society of Chemistry)

Yan et al. [48] observed an interesting phenomenon, i.e., GE has an opposite effect on crack growth resistance of NR, and at lower fatigue strains, the inclusion of GE accelerates the crack growth, whereas at higher strains, the crack growth is retarded. This is attributed to a competition between strain-induced crystallization and cavitation at crack tip. The microfocus hard X-ray diffraction (MF-XRD)

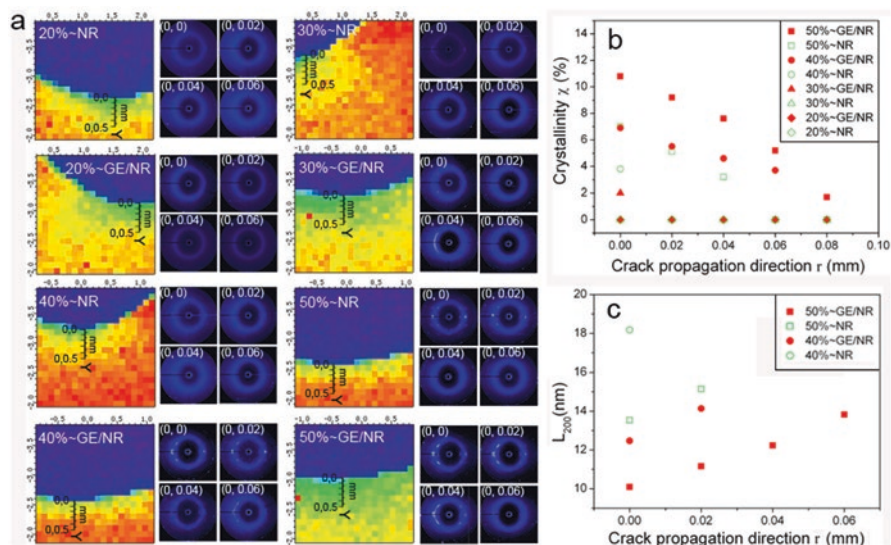


**Fig. 11** (a) Contour maps of the crack tip for blank NR and GE/NR composite at various stretch strains (b) Crystallinity  $\chi$  of NR and GE/NR composite near the crack tip as a function of the distance  $r$  along the crack propagation direction for various stretch strains. (c) Lateral crystallite size ( $L_{200}$ ) versus  $r$  along  $y$ -axis for the samples NR and GE/NR at various stretch strains (Reproduced with permission [48], 2012, John Wiley and Sons)

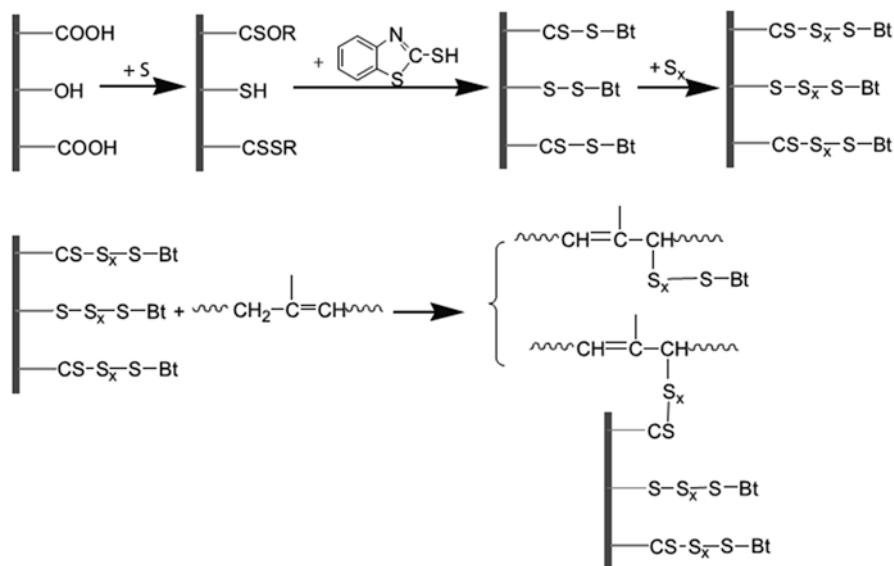
beamline was utilized for the investigation of strain-induced crystallization at the crack tip, and the correlation of strain-induced crystallization at the crack tip and fatigue crack growth resistance was investigated. Figure 11 shows that near the crack tip, the crystallization at different strains is strong and far from the crack tip it becomes weak. At the strain of 50%, the  $r$  values (the distance along the crack propagation direction) at which crystallization disappears for NR and GE/NR are 0.04 and 0.08 mm, respectively, suggesting that GE/NR has a larger crystalline zone around the crack tip, approximately twice than that for NR at the same strain. The MF-XRD experimental data supports the assumption, i.e., GE/NR composite has a higher crystallinity, a larger crystallization zone, and a smaller lateral crystallite size at higher strains, and thus it has a more pronounced effect of preventing the crack growth and initiating the crack bifurcation which allows much more energy dissipation and improves the crack growth resistance compared to unfilled NR. The result provides a new insight into the mechanism of fatigue crack growth that was proposed, which will be useful for the design of the advanced anti-fatigue material.

## 4.2 Vulcanization Mechanism

The mechanical properties of rubbers strongly depend on the cross-link of rubber molecular chain. The effect of filler on the vulcanization is complicated, and some conclusions are not consistent [9, 21, 27, 44]. Zhan et al. observed a reduction of

the vulcanization time of rubber with the addition of graphene [7], and later a lot of work reported the accelerating effect of vulcanization with graphene in rubber [13, 92–94]. Wu et al. investigated the vulcanization kinetics and mechanism of NR and SBR nanocomposites with graphene [13]. They found that on adding graphene, the induction period of the vulcanization process is depressed, whereas the vulcanization rate is enhanced at low graphene loading and then suppressed. Interestingly they found that the observed single exothermal peak by DSC during the vulcanization process for unfilled nature rubber was split into two peaks at higher graphene-filled rubber. This is interpreted in terms of two reaction stages, i.e., chemical reaction controlling stage and diffusion controlling stage. The activation energy of the former stage decreases with increasing graphene loading, while that of the latter stage is higher than the former one and increases with graphene loading. For the mechanism of accelerating effect of graphene, the authors proposed a hypothesis: the graphene takes part in the vulcanization process as shown in Scheme 1. However, the authors didn't provide any evidence about the reaction between graphene and sulfur.

Wu et al. [92] also found that graphene accelerates the vulcanization process of SBR with dicumyl peroxide as the curing agent. With increasing graphene content, the optimum cure time shows a monotonous decrease, and the induction period of the vulcanization process of SBR decreases and then levels off. As a result, the vulcanization rate is decreased in the beginning and improved later. The corresponding activation energy increases slightly at first and then decreases. The cross-linking density of the nanocomposites remarkably increases, owing to the fact that graphene is involved in the vulcanization process.



**Scheme 1** Reaction scheme for CZ-accelerated sulfur vulcanization of GE/NR nanocomposites (Reproduced with permission [13], 2013, Elsevier)

By X-ray photoelectron spectroscopy (XPS), X-ray-induced Auger spectra (XAES), small angle X-ray scattering (SAXS), and solid-state  $^{13}\text{C}$  NMR analysis, Yan and Kaciulis et al. found several evidences that graphene took part in the vulcanization process of NR [93, 94]. XPS results showed that the chemical bond of sulfur is different in pristine NR and rGO/NR composites: two chemical species of sulfur at BE = 161.7, S1, and at 163.8 eV, S2, are identified in pristine NR, whereas only the chemical state of sulfur S2 at 163.8 eV is identified for rGO/NR composites. The first chemical state is attributed to polysulfide or clusters of sulfur, while the second one is characteristic for thiolic C-S bond. For the rGO/NR composites, the polysulfide species disappear with the addition of rGO, and the percentage of S2 atoms assigned to thiolic C-S bond decreases with increasing rGO content. This confirms that the rGO interferes with the pathways of vulcanization reaction. Moreover, there is a greater percentage of S2 atoms assigned to C-S bond in the segregated sample with graphene network, compared to the ones in not-segregated sample. This suggests that mainly in the rGO-segregated network, the sulfur species react with carbon atoms of rGO platelets, resulting preferentially in the formation of monosulfidic C-S species connecting graphene platelets and rubber macromolecules.

Small angle X-ray scattering (SAXS) and nuclear magnetic resonance were also used to investigate the cross-link structure of the graphene-NR composites. A remarkable difference in scattering signals over the  $q$  range of  $0.1\text{--}2.0\text{ nm}^{-1}$  in the SAXS curve was observed between the unfilled NR and graphene/NR. The cross-link sites, where NR macromolecular chains are attached each other through polysulfidic species ( $-\text{C-S}_x\text{-C-}$ ), give rise to a bump in the SAXS curve as shown in Fig. 12a, b. The higher the number of sulfur atoms involved in the cross-linking species, the higher becomes the local increase of electron density, and consequently the higher is the intensity of the scattering peak in the SAXS spectrum. The position of the maximum scattering intensity,  $q_{\text{max}}$ , systematically shifts to higher values as the rGO content increases, while maximum scattering intensity  $I(q_{\text{max}})q_{\text{max}}^2$  exhibits a decreasing trend for the composites both with segregated morphology and not-segregated morphology. The segregated rGO/NR composites have higher  $q_{\text{max}}$  values than those of the not-segregated samples at the same rGO content. That is to say, the segregated rGO morphology affords to decrease the distance,  $d$ , between scattering sulfur centers.

The  $^{13}\text{C}$  NMR peaks centered at 37 and 51 ppm, assigned to A1 cis polysulfidic species, show significant differences among the selected pristine NR, segregated, and not-segregated samples. When rGO is added in the composite, the polysulfidic clusters mainly present in pristine NR split into smaller polysulfidic species with a limited number of sulfur atoms, i.e.,  $-\text{C-S}_x\text{-C-}$  with  $x \leq 8$ . In this case, more sulfide linkages are formed with a consequent increase of the peak intensity related to polysulfidic linkages,  $-\text{C-S-}$  as detected in NMR.

These results indicate that rGO platelets both in the segregated and not-segregated morphology affect the vulcanization process, promoting the formation of sulfur

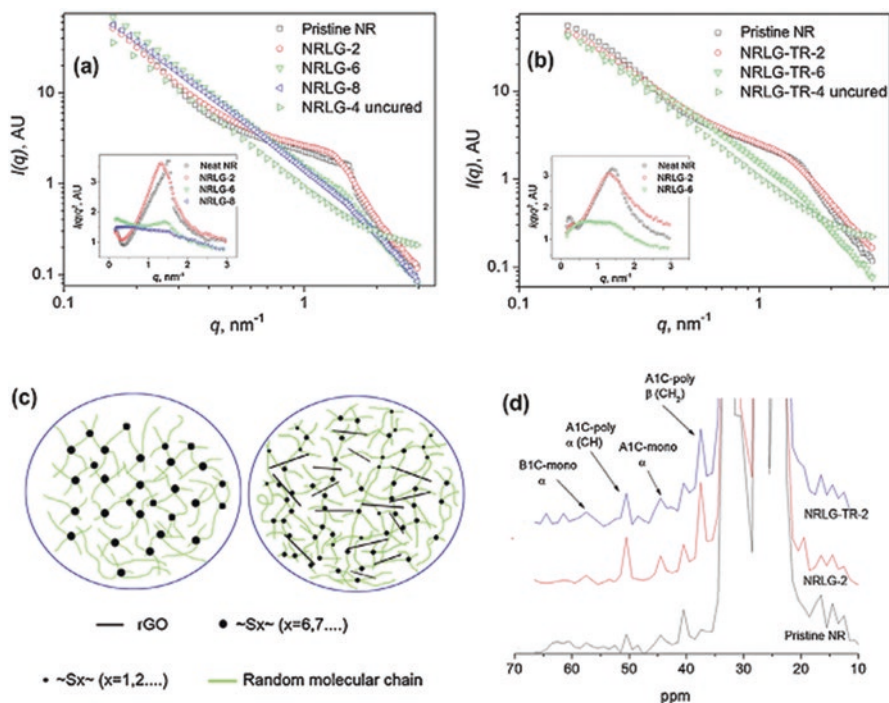


**Fig. 12** Small angle X-ray scattering profiles of the uncurated NR without curatives, rGO/NR composites with segregated morphologies (a) and rGO/NR composites with not-segregated morphologies (b), and the *insets* are the corresponding Lorentz plots of NR-vulcanized composites. (c) Schematic representation of the networks of pristine natural rubber (*left*) and rGO/NR composite with not-segregated morphology (*right*). (d) Selected  $^{13}\text{C}$  NMR spectra of pristine NR and rGO/NR composites (Reproduced with permission [93], 2013, Elsevier)

cross-linking species with a limited number of sulfur atoms in place of polysulfidic clusters with a large number of sulfur atoms.

Kaciulis et al. characterized the diamond-like Auger spectrum of C KVV together with the standard XPS analysis of composite samples prepared by using two methods of vulcanization: roll mixing and hot-pressing [94]. The diamond-like feature is observed only in the spectra excited by X-rays, whereas the Auger spectra excited by electron beam present a graphitic shape. It was found that the shape of Auger line C KVV is different in the reference rubber and the samples with graphene. The values of the D parameter, which is the distance between the most positive maximum and the most negative minimum of the first derivative, are very low in the case of the samples with graphene; they are even lower than the typical value for diamond  $Dx = 13.7$  but are characteristic for graphene. The authors concluded that the thiolic sulfur bonds, which are connecting graphene platelets and rubber macromolecules, were present in the rubber composites.

### 4.3 Barrier Mechanism

Adding graphene into the rubber matrix can greatly increase the barrier properties of graphene due to the construction of graphene network in rubber matrix that bring about an increment of tortuous pathways for the gas molecules diffusing through the rubber matrix, with consequent improvement of the barrier properties.

Scherillo et al. [95] investigated the effect of both the segregated and not-segregated graphene morphology on the gas permeability of NR/rGO nanocomposites. The gas permeability of NR/rGO nanocomposites with graphene-segregated structure was compared with those with homogeneously dispersed graphene in a not-segregated morphology. The significant qualitative and quantitative differences in the dependence of the relative permeability on the volume fraction of filler were found for the two morphologies. Samples with uniformly oriented platelets show a smooth decrease of gas permeability with volume fraction of graphene. To interpret the results, the permeability data for the GE/NR composites with different morphologies were fitted by different models (Fig. 13). For the not-segregated morphology, it was used an expression for the relative permeability provided by the theory developed by Bharadwaj, which accounts for the orientation of impermeable disk platelike particles dispersed in a matrix

$$P_R = P_{nc} / P_m = \frac{1 - \phi}{1 + (L / 2W)(2 / 3)\phi(s + 0.5)}$$

where  $P_{nc}$  and  $P_m$  represent, respectively, the permeability of the nanocomposite and that of the neat matrix,  $\phi$  represents the volumetric fraction of the filler, and

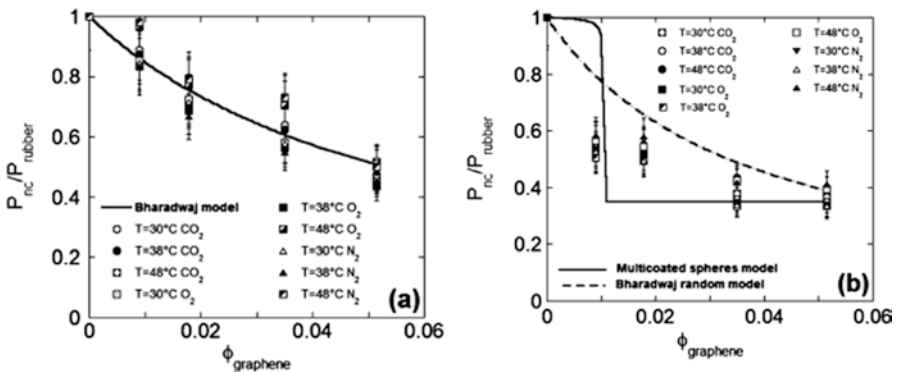


**Fig. 13** (a) Experimental relative permeability of investigated gases for nanocomposite with not-segregated morphology along with fitting by Bharadwaj model. (b) Experimental relative permeability of investigated gases for nanocomposite with segregated morphology and prediction of modified Moosavi model (Reproduced with permission [95], 2014, American Society Chemistry)

$L/W$  represents the aspect ratio of the platelike filler,  $L$  being the main dimension of the particles and  $W$  their thickness. The order parameter,  $s$ , accounts for the orientation of the particles with respect to the normal to the surfaces of the nanocomposite sheet.

The samples characterized by a “segregated” morphology display a steeper decrease of permeability at low graphene concentration, the filler arrangement being more effective in decreasing the overall permeability of the sample due to confinement of graphene on the surface of the rubber latex spheres. For the case of segregated morphology, permeability data were interpreted by a modified model proposed by Moosavi et al. This model was extended to mass transport under the following hypothesis: (i) spheres are coated by a single layer of rGO particles and (ii) simple ideal Fickian constitutive expression for mass flux holds.

He et al. [96] investigated the differences between nanocomposites with a “segregated” structure and those with a “not-segregated” structure for graphene oxide (GO) nanoplatelets filled bromobutyl rubber (BBR) composites. The significant quantitative and qualitative differences in the dependence of oxygen and carbon dioxide permeability were detected comparing the case of such “segregated” nanofiller structure to the case of a rubber where the nanofiller is homogeneously dispersed with a “not-segregated” morphology. It has been found that the segregated morphology enables a significant enhancement of the barrier properties of pristine rubber already at low levels of nanofiller loading. The results of mass transport analysis are confirmed by dielectric measurements that have evidenced how the electrical percolation threshold, in “segregated” samples, is reached at an exceptionally small volume fraction of nanofiller.

## 5 Application of Graphene-Rubber Nanocomposites

For the application of GE/NR materials, the Vorbeck Materials did a pioneering work in developing the graphene/nitrile rubber conductive rubber plates (Vor-flex™ 50). In 2015, Italian company Vittoria developed a graphene-modified mountain bicycle tire in cooperation with Directa Plus. The tire containing graphene exhibits numerous advantages such as the improved abrasion resistance, the decreased rolling resistance of tire, etc. In 2015, Chengdu Trustwell Company, in cooperation with Sichuan University, conducted the pioneering scale-up fabrication of GE/NR masterbatch and graphene-based NR composites with high barrier and high electrical conductive performances. The as-prepared materials have been used in wide range of applications including tire, seals, vibration absorbents, and plastic-rubber composite. In March 2016, Double Star Company in Qingdao developed the graphene tire in cooperation with Chengdu Trustwell Company. In addition, National Institute of Graphene in University of Manchester is developing the next generation of condom based on the rubber/graphene nanocomposites under the support of Bill and Melinda Gates Foundation.

## 6 Summary

The graphene-rubber composites have been extensively investigated recently. Graphene incorporation in the NR has many advantages as follows: (1) the enhancement of the mechanical properties is better than other fillers, (2) excellent electrical conductivity, (3) the gas barrier properties are better than the other additives such as clay, (4) the stronger strain-induced crystallization capability compared with carbon black, clay, and carbon nanotubes, and (5) good thermal conductivity. The dispersion of graphene in the rubber and the formation of the network structure can be controlled by an environment-friendly water-based latex mixing method and post-processing. Therefore, it is no doubt that the graphene is an ideal filler for high-performance and multifunctional rubber.

But there are still some challenges in the research and development of rubber/graphene composites. (1) The defect-free graphene and monolayer-dispersed graphene/NR composites are difficult to prepare in a high efficient way. (2) The precisely control of the highly ordered structure of graphene such as the formation of liquid crystal ordered phase structure of graphene, as well as the uniform, controllable network structure of graphene, is still a challenge. (3) The understanding for the interaction between graphene and rubber in the molecular scale, especially the modeling on the segregated network of graphene. Presently a lot of work reported the approaches to form the segregated network of graphene; however it remains unclear how the segregated network parameters such as the network edge layer thickness; the graphene arrangement such as dispersion, aggregation, or alignment in the network edge; and the stability of the graphene network affect the properties of rubber materials. (4) The realization of reinforcing effect in a highly filled rubber composite system. Most research presently focused on the lowly filled rubber system. However in most cases, for industrial engineering rubber articles such as tire, damper, etc., the carbon black or silica contents are much higher, even more than 50 wt%. In such cases, how small can graphene content realize the reinforcing effect to the greatest extent? The process to prepare a high-quality graphene segregation network will affect the interaction between the graphene and rubber molecular chain. (5) The main problem of graphene-rubber composites in the process of industrialization is the high cost of graphene. However, we believe that with more in-depth theoretical study and technology advance, these problems will eventually be resolved in the future.

## References

1. K.S. Novoselov, A.K. Geim, S.V. Morozov, D. Jiang, Y. Zhang, S.V. Dubonos, I.V. Grigorieva, A.A. Firsov, *Science* **306**(5696), 666–669 (2004)
2. M.D. Stoller, S. Park, Y. Zhu, J. An, R.S. Ruoff, *Nano Lett.* **8**(10), 3498–3502 (2008)
3. R.R. Nair, P. Blake, A.N. Grigorenko, K.S. Novoselov, T.J. Booth, T. Stauber, N.M.R. Peres, A.K. Geim, *Science* **320**(5881), 1308–1308 (2008)
4. C. Lee, X. Wei, J.W. Kysar, J. Hone, *Science* **321**(5887), 385–388 (2008)



5. A.A. Balandin, S. Ghosh, W. Bao, I. Calizo, D. Teweldebrhan, F. Miao, C.N. Lau, *Nano Lett.* **8**(3), 902–907 (2008)
6. X. Huang, X. Qi, F. Boey, H. Zhang, *Chem. Soc. Rev.* **41**(2), 666–686 (2012)
7. Y. Zhan, J. Wu, H. Xia, N. Yan, G. Fei, G. Yuan, *Macromol. Mater. Eng.* **296**(7), 590–602 (2011)
8. Y. Zhan, M. Lavorgna, G. Buonocore, H. Xia, *J. Mater. Chem.* **22**(21), 10464–10468 (2012)
9. J.S. Kim, S. Hong, D.W. Park, S.E. Shim, *Macromol. Res.* **18**(6), 558–565 (2010)
10. J.R. Potts, O. Shankar, L. Du, R.S. Ruoff, *Macromolecules* **45**(15), 6045–6055 (2012)
11. Z. Tang, L. Zhang, W. Feng, B. Guo, F. Liu, D. Jia, *Macromolecules* **47**(24), 8663–8673 (2014)
12. Z. Tang, W. Kuang, P. Weng, Z. Tang, B. Guo, *RSC Adv.* **5**(103), 84398–84405 (2015)
13. J. Wu, W. Xing, G. Huang, H. Li, M. Tang, S. Wu, Y. Liu, *Polymer* **54**(13), 3314–3323 (2013)
14. S. Schopp, R. Thomann, K.-F. Ratzsch, S. Kerling, V. Altstädt, R. Mülhaupt, *Macromol. Mater. Eng.* **299**(3), 319–329 (2014)
15. J. Cui, L. Liu, Y. Mao, S. Wen, L. Zhang, *Rubber Ind.* **62**(8), 453–457 (2015)
16. X. Liu, D. Sun, L. Wang, B. Guo, *Ind. Eng. Chem. Res.* **52**(41), 14592–14600 (2013)
17. X. She, C. He, Z. Peng, L. Kong, *Polymer* **55**(26), 6803–6810 (2014)
18. J. Huang, Z. Tang, Z. Yang, B. Guo, *Macromol. Rapid Commun.* **37**(13), 1040–1045 (2016)
19. X. Bai, C. Wan, Y. Zhang, Y. Zhai, *Carbon* **49**(5), 1608–1613 (2011)
20. B. Ozbas, S. Toki, B.S. Hsiao, B. Chu, R.A. Register, I.A. Aksay, R.K. Prud'homme, D.H. Adamson, *J. Polym. Sci. B Polym. Phys.* **50**(10), 718–723 (2012)
21. H. Lian, S. Li, K. Liu, L. Xu, K. Wang, W. Guo, *Polym. Eng. Sci.* **51**(11), 2254–2260 (2011)
22. K.K. Sadasivuni, A. Saiter, N. Gautier, S. Thomas, Y. Grohens, *Colloid Polym. Sci.* **291**(7), 1729–1740 (2013)
23. B. Mensah, D. Kumar, D.-K. Lim, S.G. Kim, B.-H. Jeong, C. Nah, *J. Appl. Polym. Sci.* **132**(36), 42457–42460 (2015)
24. L. Gan, S. Shang, C.W.M. Yuen, S.-x. Jiang, N.M. Luo, *Compos. Part B* **69**, 237–242 (2015)
25. L. Chen, L. Lu, D. Wu, G. Chen, *Polym. Compos.* **28**(4), 493–498 (2007)
26. S. Yaragalla, M. A.P. N. Kalarikkal, S. Thomas, *Ind. Crop. Prod.* **74**, 792–802 (2015)
27. A. Das, G.R. Kasaliwal, R. Jurk, R. Boldt, D. Fischer, K.W. Stöckelhuber, G. Heinrich, *Compos. Sci. Technol.* **72**(16), 1961–1967 (2012)
28. W.E. Mahmoud, A.A. Al-Ghamdi, F.R. Al-Solamy, *Polym. Adv. Technol.* **23**(2), 161–165 (2012)
29. F.R. Al-solamy, A.A. Al-Ghamdi, W.E. Mahmoud, *Polym. Adv. Technol.* **23**(3), 478–482 (2012)
30. A. Sherif, Z. Izzuddin, M. Qingshi, K. Nobuyuki, M. Andrew, K. Hsu-Chiang, M. Peter, M. Jun, Z. Liqun, *Nanotechnology* **24**(16), 165601 (2013)
31. S. Yaragalla, C.S. Chandran, N. Kalarikkal, R.H.Y. Subban, C.H. Chan, S. Thomas, *Polym. Eng. Sci.* **55**(11), 2439–2447 (2015)
32. Y. Song, J. Yu, L. Yu, F.E. Alam, W. Dai, C. Li, N. Jiang, *Mater. Des.* **88**, 950–957 (2015)
33. Y. Lin, Y. Chen, Z. Zeng, J. Zhu, Y. Wei, F. Li, L. Liu, *Compos. A: Appl. Sci. Manuf.* **70**, 35–44 (2015)
34. A.B. Suriani, M.D. Nurhafizah, A. Mohamed, A.K. Masrom, V. Sahajwalla, R.K. Joshi, *Mater. Des.* **99**, 174–181 (2016)
35. A. Malas, P. Pal, C.K. Das, *Mater. Des.* **55**, 664–673 (2014)
36. S.H. Song, H.K. Jeong, Y.G. Kang, *J. Ind. Eng. Chem.* **16**(6), 1059–1065 (2010)
37. G. Zhang, F. Wang, J. Dai, Z. Huang, *Materials* **9**(2), 92 (2016)
38. B. Yin, J. Wang, H. Jia, J. He, X. Zhang, Z. Xu, *J. Mater. Sci.* **51**(12), 5724–5737 (2016)
39. C. Wang, Z. Liu, S. Wang, Y. Zhang, *J. Appl. Polym. Sci.* **133**(4), 42907 (2016)
40. Y. Lin, S. Liu, J. Peng, L. Liu, *Compos. A: Appl. Sci. Manuf.* **86**, 19–30 (2016)
41. RamanathanT, A.A. Abdala, StankovichS, D.A. Dikin, M. Herrera Alonso, R.D. Piner, D.H. Adamson, H.C. Schniepp, ChenX, R.S. Ruoff, S.T. Nguyen, I.A. Aksay, R.K. Prud'Homme, L.C. Brinson, *Nat. Nano.* **3**(6), 327–331 (2008)
42. F. Liu, P. Ming, J. Li, *Phys. Rev. B* **76**(6), 064120 (2007)
43. M.A. Rafiee, J. Rafiee, Z. Wang, H. Song, Z.-Z. Yu, N. Koratkar, *ACS Nano* **3**(12), 3884–3890 (2009)
44. M.A. Rafiee, J. Rafiee, I. Srivastava, Z. Wang, H. Song, Z.-Z. Yu, N. Koratkar, *Small* **6**(2), 179–183 (2010)
45. X. Zhao, Q. Zhang, D. Chen, P. Lu, *Macromolecules* **43**(5), 2357–2363 (2010)

46. Y. Bai, H. Cai, X. Qiu, X. Fang, J. Zheng, *High. Perform. Polym.* **27**(8), 997–1006 (2015)
47. Y. Luo, R. Wang, S. Zhao, Y. Chen, H. Su, L. Zhang, T.W. Chan, S. Wu, *RSC Adv.* **6**(63), 58077–58087 (2016)
48. N. Yan, H. Xia, Y. Zhan, G. Fei, *Macromol. Mater. Eng.* **298**(1), 38–44 (2013)
49. C. Li, C. Feng, Z. Peng, W. Gong, L. Kong, *Polym. Compos.* **34**(1), 88–95 (2013)
50. W. Xing, M. Tang, J. Wu, G. Huang, H. Li, Z. Lei, X. Fu, H. Li, *Compos. Sci. Technol.* **99**, 67–74 (2014)
51. J. Wu, G. Huang, H. Li, S. Wu, Y. Liu, J. Zheng, *Polymer* **54**(7), 1930–1937 (2013)
52. L. Wang, W. Wang, Y. Fu, J. Wang, Y. Lvov, J. Liu, Y. Lu, L. Zhang, *Compos. Part B* **90**, 457–464 (2016)
53. Y. Lin, K. Liu, Y. Chen, L. Liu, *Polym. Compos.* **36**(10), 1775–1785 (2015)
54. Y. Lin, Y. Chen, Y. Zhang, D. Jia, Y. Luo, L. Liu, *Polym. Adv. Technol.* **26**(5), 423–431 (2015)
55. Y. Lin, Z. Zeng, J. Zhu, S. Chen, X. Yuan, L. Liu, *RSC Adv.* **5**(71), 57771–57780 (2015)
56. T. Sekitani, Y. Noguchi, K. Hata, T. Fukushima, T. Aida, T. Someya, *Science* **321**(5895), 1468–1472 (2008)
57. G. Deutscher, A. Kapitulnik, M. Rappaport, *Ann. Isr. Phys. Soc. (Israel)* **5**, 207–228 (1983)
58. A.S. Edelstein, B.N. Das, R.L. Holtz, N.C. Koon, M. Rubinstein, S.A. Wolf, K.E. Kihlstrom, *J. Appl. Phys.* **61**(8), 3320–3322 (1987)
59. S. Araby, Q. Meng, L. Zhang, H. Kang, P. Majewski, Y. Tang, J. Ma, *Polymer* **55**(1), 201–210 (2014)
60. S. Araby, L. Zhang, H.-C. Kuan, J.-B. Dai, P. Majewski, J. Ma, *Polymer* **54**(14), 3663–3670 (2013)
61. C. He, X. She, Z. Peng, J. Zhong, S. Liao, W. Gong, J. Liao, L. Kong, *Phys. Chem. Chem. Phys.* **17**(18), 12175–12184 (2015)
62. J.S. Kim, J.H. Yun, I. Kim, S.E. Shim, *J. Ind. Eng. Chem.* **17**(2), 325–330 (2011)
63. B. Ozbas, C.D. O’Neill, R.A. Register, I.A. Aksay, R.K. Prud’homme, D.H. Adamson, *J. Polym. Sci. Part B: Polym. Phys.* **50**(13), 910–916 (2012)
64. M. Hernández, M.d.M. Bernal, R. Verdejo, T.A. Ezquerro, M.A. López-Manchado, *Compos. Sci. Technol.* **73**, 40–46 (2012)
65. Z. Zhou, X. Zhang, X. Wu, C. Lu, *Compos. Sci. Technol.* **125**, 1–8 (2016)
66. Y. Hou, D. Wang, X.-M. Zhang, H. Zhao, J.-W. Zha, Z.-M. Dang, *J. Mater. Chem. C* **1**(3), 515–521 (2013)
67. W.E. Mahmoud, A.A. Al-Ghamdi, *Polym. Int.* **61**(1), 51–54 (2012)
68. M. Tian, J. Zhang, L. Zhang, S. Liu, X. Zan, T. Nishi, N. Ning, *J. Colloid Interface Sci.* **430**, 249–256 (2014)
69. S. Araby, N. Saber, X. Ma, N. Kawashima, H. Kang, H. Shen, L. Zhang, J. Xu, P. Majewski, *J. Ma, Mater. Des. (1980–2015)* **65**, 690–699 (2015)
70. H. Hu, L. Zhao, J. Liu, Y. Liu, J. Cheng, J. Luo, Y. Liang, Y. Tao, X. Wang, J. Zhao, *Polymer* **53**(15), 3378–3385 (2012)
71. M. Kujawski, J.D. Pearse, E. Smela, *Carbon* **48**(9), 2409–2417 (2010)
72. J.-T. Kim, T.-S. Oh, D.-H. Lee, *Polym. Int.* **53**(4), 406–411 (2004)
73. Y.-P. Wu, Y.-Q. Wang, H.-F. Zhang, Y.-Z. Wang, D.-S. Yu, L.-Q. Zhang, J. Yang, *Compos. Sci. Technol.* **65**(7–8), 1195–1202 (2005)
74. S. Wu, Z. Tang, B. Guo, L. Zhang, D. Jia, *RSC Adv.* **3**(34), 14549–14559 (2013)
75. H. Kang, K. Zuo, Z. Wang, L. Zhang, L. Liu, B. Guo, *Compos. Sci. Technol.* **92**, 1–8 (2014)
76. S.T. Huxtable, D.G. Cahill, S. Shenogin, L. Xue, R. Ozisik, P. Barone, M. Usrey, M.S. Strano, G. Siddons, M. Shim, P. Keblinski, *Nat. Mater.* **2**(11), 731–734 (2003)
77. T. Kashiwagi, E. Grulke, J. Hilding, K. Groth, R. Harris, K. Butler, J. Shields, S. Kharchenko, J. Douglas, *Polymer* **45**(12), 4227–4239 (2004)
78. W. Ma, J. Li, B. Deng, X. Lin, X. Zhao, *J. Wuhan Univ. Technol.-Mater. Sci. Ed.* **28**(1), 127–131 (2013)
79. J.R. Potts, O. Shankar, S. Murali, L. Du, R.S. Ruoff, *Compos. Sci. Technol.* **74**, 166–172 (2013)

80. J. Wang, H. Jia, Y. Tang, D. Ji, Y. Sun, X. Gong, L. Ding, *J. Mater. Sci.* **48**(4), 1571–1577 (2013)
81. H. Zhang, C. Wang, Y. Zhang, *Journal of Applied Polymer Science* **132**(3), n/a-n/a (2015)
82. Y. Qiu, Z. Wang, A.C.E. Owens, I. Kulaots, Y. Chen, A.B. Kane, R.H. Hurt, *Nanoscale* **6**(20), 11744–11755 (2014)
83. Y. Liu, Y. Lin, D. Zhang, C. Chen, G. Wu, Y. Zhang, L. Weiling, *Chem. J. Chin. Univ.* **37**(7), 1402–1407 (2016)
84. B. Dong, S. Wu, L. Zhang, Y. Wu, *Ind. Eng. Chem. Res.* **55**(17), 4919–4929 (2016)
85. B. Dong, L. Zhang, Y. Wu, *J. Mater. Sci.* **51**(23), 10561–10573 (2016)
86. Y. Lin, S. Liu, S. Chen, Y. Wei, X. Dong, L. Liu, *J. Mater. Chem. C* **4**(26), 6345–6352 (2016)
87. Y. Mao, S. Wen, Y. Chen, F. Zhang, P. Panine, T.W. Chan, L. Zhang, Y. Liang, L. Liu, *Sci. Rep.* **3** (2013)
88. C.S. Boland, U. Khan, C. Backes, A. O'Neill, J. McCauley, S. Duane, R. Shanker, Y. Liu, I. Jurewicz, A.B. Dalton, J.N. Coleman, *ACS Nano* **8**(9), 8819–8830 (2014)
89. F. Li, N. Yan, Y. Zhan, G. Fei, H. Xia, *J. Appl. Polym. Sci.* **129**(4), 2342–2351 (2013)
90. D.H. Fu, Y.H. Zhan, N. Yan, H.S. Xia, *Express Polym. Lett.* **9**(7), 597–607 (2015)
91. A. Das, R. Boldt, R. Jurk, D. Jehnichen, D. Fischer, K.W. Stockelhuber, G. Heinrich, *RSC Adv.* **4**(18), 9300–9307 (2014)
92. M.-z. Tang, W. Xing, J.-r. Wu, G.-s. Huang, H. Li, S.-d. Wu, *Chin. J. Polym. Sci.* **32**(5), 658–666 (2014)
93. N. Yan, G. Buonocore, M. Lavorgna, S. Kaciulis, S.K. Balijepalli, Y. Zhan, H. Xia, L. Ambrosio, *Compos. Sci. Technol.* **102**, 74–81 (2014)
94. S. Kaciulis, A. Mezzi, S.K. Balijepalli, M. Lavorgna, H.S. Xia, *Thin Solid Films* **581**, 80–85 (2015)
95. G. Scherillo, M. Lavorgna, G.G. Buonocore, Y.H. Zhan, H.S. Xia, G. Mensitieri, L. Ambrosio, *ACS Appl. Mater. Interfaces* **6**(4), 2230–2234 (2014)
96. F. He, G. Mensitieri, M. Lavorgna, M.S. de Luna, G. Filippone, H. Xia, R. Esposito, G. Scherillo, *Compos. Part B* **116** (2016). doi:[10.1016/j.compositesb.2016.10.076](https://doi.org/10.1016/j.compositesb.2016.10.076)

# Effects of Graphene and Graphite on Properties of Highly Filled Polybenzoxazine Bipolar Plate for Proton Exchange Membrane Fuel Cell: A Comparative Study

Manunya Okhawilai, Anucha Pengdam, Ratcha Plengudomkit,  
and Sarawut Rimdusit

## 1 Introduction

Fuel cells are the key enabling technologies for the transition to a hydrogen-based economy. Fuel cells are devices for conversion of chemical energy of a fuel to electricity by electrochemistry. Among various types of fuel cells, proton exchange membrane fuel cells (PEMFCs) have gained much attention due to the increasing awareness of environmental factors and high efficiency to energy conversion. Bipolar plate acts an essential key multifunctional component in PEMFC. Its functionality includes separating the individual fuel cells, connecting the cathode side of one cell to anode side of the other one, feeding hydrogen gas on anode side and oxygen gas on cathode side via flow channel, and removing by-products, i.e., heat and water. Consequently, bipolar plate materials should provide high electrical conductivity, high gas impermeability, good mechanical performance, good corrosion resistance, and low cost [1]. Department of Energy (DOE), USA, proposed the targets for bipolar plate applications. Major requirements according to DOE include thermal conductivity  $>10$  W/mK, electrical conductivity  $>100$  S/cm, flexural modulus  $>10$  GPa, flexural strength  $>25$  MPa, and water uptake at 24 h  $<0.3\%$ , etc. [2]. Materials for bipolar plates have been traditionally produced from pure high-density graphite with superior corrosion resistance, chemical stability, and high thermal conductivity. Due to its poor mechanical properties and high manufacturing cost, the use of pure graphite bipolar plate has been limited. Metallic is another choice for bipolar plate production due to their high mechanical strength over pure graphite. They also provide high electrical conductivity, high gas impermeability, low cost, and ease of fabrication [3–5]. However, the main drawbacks of metal plates are their susceptibility to corrosion and dissolution in the fuel cell. Conductive filler-filled

---

M. Okhawilai • A. Pengdam • R. Plengudomkit • S. Rimdusit (✉)  
Department of Chemical Engineering, Faculty of Engineering, Chulalongkorn University,  
Bangkok 10330, Thailand  
e-mail: [sarawut.r@chula.ac.th](mailto:sarawut.r@chula.ac.th)

polymer composite bipolar plates have been intensively investigated due to their lower cost, less weight, higher corrosion resistivity, and ease of manufacturing in comparison with available bipolar plate materials, for example, graphite- and graphene-based bipolar plates.

Recently, polybenzoxazine (PBA) resins which are a novel type of phenolic resins have been widely used as polymer matrix for variety of applications because they provide such many outstanding properties including no requirement of addition curing agent, no by-product formation during polymerization, long shelf life, high thermal stability, excellent mechanical properties, and ability to alloy with various types of resins to provide fine-tuned properties. Particularly, bisphenol A-based benzoxazine monomer exhibits a very low melt viscosity for about  $<1000$  cP at  $120$  °C [6] which facilitates filler wetting and mixing during preparation of molding compound, thus providing its outstanding characteristic as composite with high filler loading such as those reported in highly filled graphite/PBA composite [7], highly filled graphene/PBA composite [8], highly filled graphite/graphene/PBA composite [9], highly filled nanosilica/PBA [10], and highly filled alumina/PBA composite [11]. In this chapter, we have reviewed the development of bipolar plate based on highly filled graphite PBA composite and highly filled graphene-PBA composite as well as the combination of graphite- and graphene-filled PBA composite. The properties of those highly filled composites are intensively compared.

## 2 Fuel Cell Fundamentals

Fuel cells are electrochemical galvanic cell device that converts chemical energy, from typically hydrogen, directly into electrical energy [12]. Fuel cells are expected to play a major role in the economy of this century and for the foreseeable future. It is anticipated that the development and deployment of economical and reliable fuel cells would guide in the sustainable hydrogen age [13]. Nowadays, there are six major types of fuel cells including polymer electrolyte membrane (also called proton exchange membrane) fuel cell (PEMFC), alkaline fuel cell (AFC), phosphoric acid fuel cell (PAFC), direct methanol fuel cell (DMFC), solid oxide fuel cell (SOFC), and molten carbonate fuel cell (MCFC). The first four types of fuel cells operate at low to medium temperature ( $50$ – $220$  °C), and the last two types of fuel cells are high temperature fuel cells ( $600$ – $1000$  °C). Their main features are summarized in Table 1 [13, 14].

The development on fuel cell aimed at achieving high efficiency and durability along with manufacturing costs for the fuel cell stack. An operation of each type of fuel cells is shown in Fig. 1 [14]. AFCs are the oldest type of fuel cell which has long been used in space applications where pure hydrogen and oxygen are needed in order to avoid the production of  $\text{CO}_2$ . AFCs require alkaline solution, for example, potassium hydroxide (KOH) solution as electrolyte. PAFCs use phosphoric acid as electrolyte which provides adequate properties, i.e., high thermal and chemical

**Table 1** Types of fuel cells and their features [13, 14]

Fuel cell	Operating temp. (°C)	Electrolyte (charge carrier)	Power density (mW/cm <sup>2</sup> )	Lifetime (h)	Capital cost (\$/kW)
PEMFC	50–80	Perfluorosulfonic acid (H <sup>+</sup> )	350	>10,000	>200
AFC	60–90	Alkaline polymer, KOH (OH <sup>-</sup> )	100–200	>10,000	>200
PAFC	160–220	H <sub>3</sub> PO <sub>4</sub> , polymer (H <sub>3</sub> PO <sub>4</sub> , H <sup>+</sup> )	200	>40,000	3000
DMFC	50–100	Perfluorosulfonic acid (H <sup>+</sup> )	–	–	–
SOFC	800–1000	Yttria-stabilized zirconia (O <sup>2-</sup> )	240	>40,000	1500
MCFC	600–700	(Li, K, Na) <sub>2</sub> CO <sub>3</sub> (O <sup>2-</sup> )	100	>40,000	1000

stability including low volatility to withstand a higher operating temperature at 200 °C. The use of phosphoric acid as electrolyte overcomes the use of alkaline solution on no formation of carbonate substance from the reaction of impurity CO<sub>2</sub> and alkaline group. The efficiency of DMFC is quite low compared to other fuel cells. DMFCs are well suited for portable power applications in consumer electronic devices where the power requirements are low. A higher energy density alternative is required to fill the gap between energy demand and energy storage capacity in these applications. SOFCs use a thin ceramic membrane as an electrolyte. SOFCs are more applicable where system may run for extended periods without frequent start and stop cycles. MCFCs operate at a high temperature of about 600–700 °C. This type of fuel cell used molten mixture of alkaline metal carbonate as electrolyte and simple catalyst. It is typically used for stationary distributed power generation applications. Apart from hydrogen, MCFCs can also run on hydrocarbons (e.g., natural gas, methane, or alcohol) as fuel. PEMFCs are considered for an application that requires faster start-up times and frequent starts and stops such as automotive applications, material handling equipment, and backup power [14]. The work on PEMFC will be thoroughly described in Sect. 4.

For all these systems, improved fuel processing and cleanup, especially for fuel-flexible operation and operation on biofuels, are needed to improve durability and reduce system costs. Table 2 summarizes the use of these fuel cell types in three main applications [15].

### 3 Proton Exchange Membrane Fuel Cell (PEMFC)

PEMFCs have been known as the most promising alternative source of energy due to their high efficiency and zero emission as well as low weight and volume compared with other fuel cells [16]. PEMFCs use a solid polymer as an electrolyte and porous carbon electrodes containing platinum as catalyst. The requirement on PEMFC operation is only hydrogen and oxygen. They do not require corrosive fluids like other fuel cells. They are typically fueled with pure hydrogen supplied

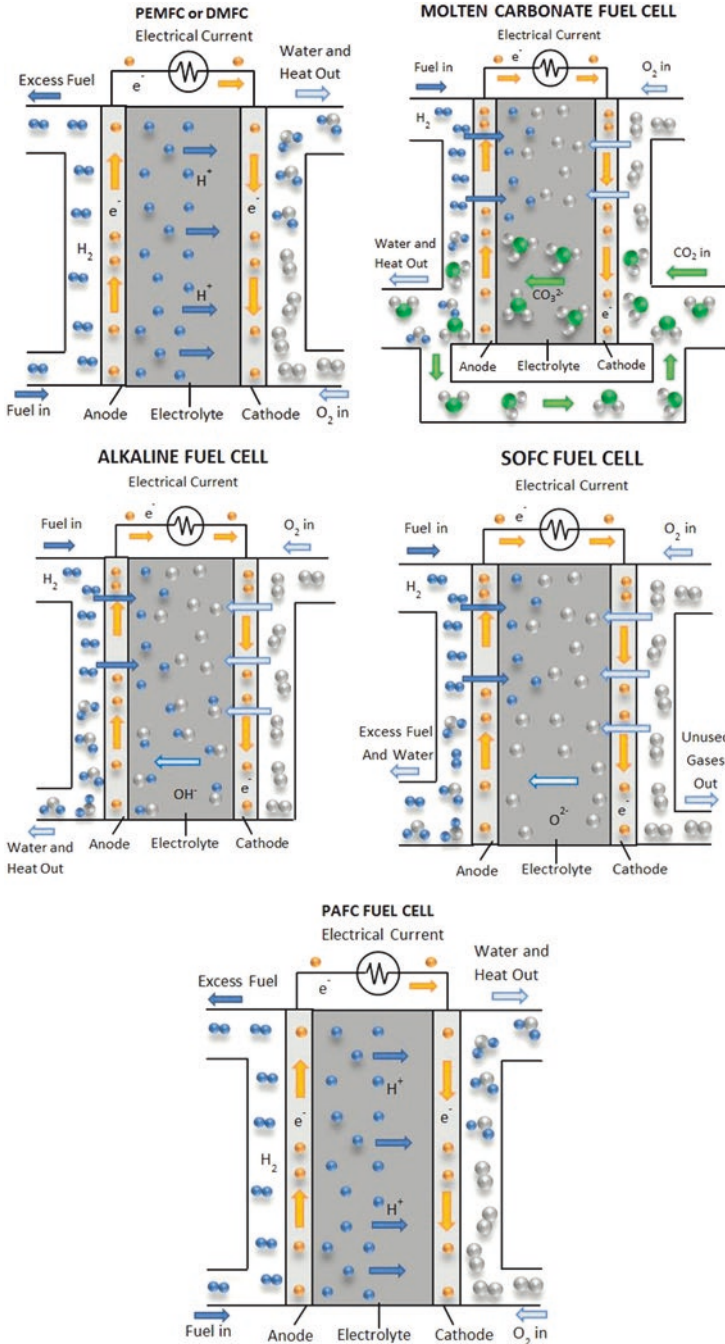


Fig. 1 Operation of each types of fuel cells (Adapted from Ref. [14])

**Table 2** The use of fuel cell in three main applications [15]

Application	Portable	Stationary	Transport
Definition	Units that are built into, or charge up, products that are designed to be moved, including auxiliary power units (APU)	Units that provide electricity (and sometimes heat) but are not designed to be moved	Units that provide propulsive power or range extension to a vehicle
Typical power range	5 W–20 kW	0.5–400 kW	1–100 kW
Typical technology	PEMFC DMFC	MCFC – SOFC PAFC – PEMFC	PEMFC, DMFC
Examples	Non-motive APU (campervans, boats, lighting)	Large stationary combined heat and power (CHP)	
	Military applications (portable soldier-borne power, skid-mounted generators)	Small stationary micro-CHP	Fuel cell electric vehicles (FCEV)
	Portable products (torches, battery chargers),	Uninterruptible power supplies (UPS)	Trucks and buses

from storage tanks or on-board reformers. PEMFCs operate at relatively low temperature around 80 °C which allows them to start quickly (less warm-up time). PEMFCs are used primarily for stationary applications and transportation applications such as passenger vehicles due to their fast start-up time, low sensitivity to orientation, and favorable power-to-weight ratio.

### 3.1 Operation of a PEMFC

Nowadays, hydrogen is the fuel of choice for high performance of fuel cell applications. Hydrogen-powered fuel cells are also the “greenest” fuel cells since their products are only heat and water. One advantage of hydrogen is that it easily undergoes catalyzed reactions under mild conditions [17]. The electrochemical reactions in fuel cells happen simultaneously on both sides of a membrane (the anode and the cathode). The basic PEM fuel cell reactions are shown as follows [13]. Figure 2 shows a schematic of a PEMFC operation to gain a fundamental understanding of the polymer electrolyte membrane fuel cell technology.

At the anode, hydrogen is oxidized to liberate two electrons and two protons, producing the reaction (1) in Table 3. The protons are conducted from the catalyst layer through the proton exchange membrane, and the electrons travel through the external electronic circuit. At the cathode, oxygen permeates to the catalyst sites where it reacts with the protons and electrons when properly hydrated, producing the reaction (2). The overall cell reaction is shown in (3). Consequently, the products of the PEMFC reactions are electricity, water, and heat.



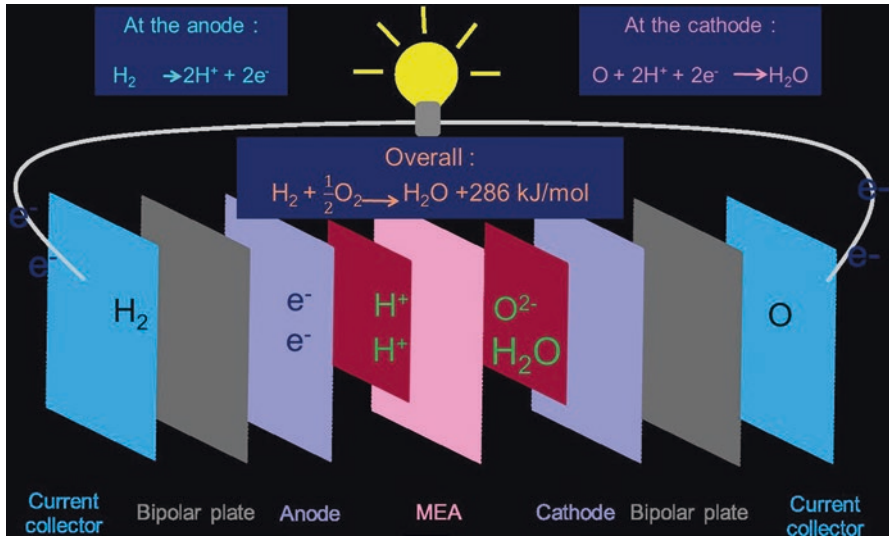


Fig. 2 Diagram of PEMFC

Table 3 Chemical reaction occurred on each side in PEMFC

Reaction	Amount of energy production
1. Anode side $H_2 \rightarrow 2H^+ + 2e^-$	–
2. Cathode side $\frac{1}{2}O_2 + 2H^+ + 2e^- \rightarrow H_2O$	$286 \frac{\text{kJ}}{\text{mol}}$
3. Overall $H_2 + \frac{1}{2}O_2 \rightarrow H_2O$	$286 \frac{\text{kJ}}{\text{mol}}$

### 3.2 PEMFC Components

About 1 V is produced in a single fuel cell. As a consequence, typical fuel cell designs link many individual cells together to form a stack to produce a more useful voltage. A fuel cell stack can be configured with many groups of cells in series and parallel connections to further tailor the voltage, current, and power. The number of individual cells contained within one stack is typically greater than 50 cells and varies significantly with stack design. The basic components of the fuel cell stack include the electrodes and electrolyte with additional components required for electrical connections and/or insulation and the flow of fuel and oxidant. These key components include current collectors and separator plates. The current collectors conduct electrons from the anode to the separator plate. The separator plates provide the electrical series connections between cells and physically separate the oxidant flow of one cell from the fuel flow of the adjacent cell. The channels in the current collectors serve as

the distribution pathways for the fuel and oxidant. Typically, the current collectors and the separator plate are combined into a single unit called a bipolar plate. The basic components of the fuel cell stack are as follows:

### 3.2.1 Membrane Electrode Assembly (MEA)

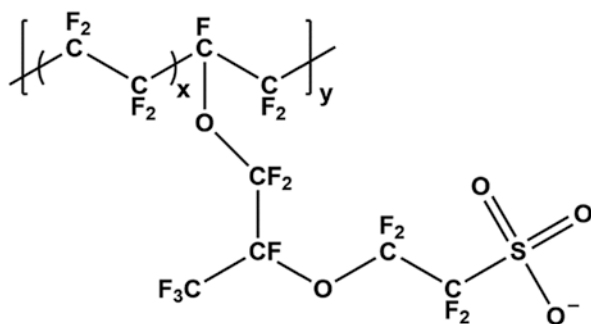
MEA is the heart of a PEMFC. MEA normally consists of three main components, i.e., a membrane, a gas diffusion layer (GDL), and a dispersed catalyst layer.

Polymer electrolyte membrane is the key to the fuel cell technology. It must permit only the necessary ions to pass between the anode and cathode. Other substances passing through the electrolyte would disrupt the chemical reaction. Material for membrane should be durable, robust, and resistant to chemical attack. Sulfonated polymer such as sulfonated tetrafluoroethylene such as Nafion® is the most suitable membrane with operating temperature below 100 °C. Chemical structure of Nafion is shown in Fig. 3. Nafion is highly selective in the removal of water. There are two major advantages of using perfluorosulfonic acid as membrane material for PEMFCs. First, the membranes are relatively strong and stable in both oxidative and reductive environment due to the structure based on polytetrafluoroethylene backbone. Second, the protonic conductivities achieved in a well-humidified perfluorosulfonic acid membrane can be as high as 0.2 S/cm at PEMFC operating temperature. This translates to a cell resistance as low as 0.05  $\Omega$  cm<sup>2</sup> for a 100  $\mu$  thick membrane with voltage loss of only 50 mV at 1 A/cm<sup>2</sup> [18, 19].

Two GDLs further improve the efficiency of the system by allowing direct and uniform mass transfer access of the fuel and oxidant to the catalyst layer and mechanical support to the membrane. In addition to distributing the gases, the anode GDL also conducts the electrons away from the anode. Then the electrons go back to the anode bipolar plate and current collector. The cathode GDL conducts the electrons to the cathode catalyst layer from the cathode bipolar plate and the current collector, ensuring the complete flow of electrons. Typically, porous carbon paper or cloth is the material used for GDLs.

All electrochemical reactions in a fuel cell consist of two separate reactions: an oxidation half reaction at the anode and a reduction half reaction at the cathode.

Fig. 3 Chemical structure of Nafion



Normally, the two half reactions would occur very slowly at the low operating temperature of the PEM fuel cell. Each of the electrodes is impregnated on one side with a catalyst layer that accelerates the reaction of oxygen and hydrogen. It is usually made of platinum powder very thinly coated onto carbon paper or cloth. The catalyst is rough and porous so the maximum surface area of the platinum can be exposed to the hydrogen or oxygen.

### 3.2.2 Electrode

An electric conductor through which an electric current enters or leaves a medium, whether it be an electrolytic solution, solid, molten mass, gas, or vacuum.

### 3.2.3 Anode and Cathode

The anode is the negative side of the fuel cell. It conducts the electrons that are freed from the hydrogen molecules so they can be used in an external circuit. Channels etched into the anode disperse the hydrogen gas over the surface of the catalyst. The cathode, the positive side of the fuel cell, also contains channels in the same manner as anode and distributes the oxygen to the surface of the catalyst. Moreover, it conducts the electrons back from the external circuit to the catalyst, where they can recombine with the hydrogen ions and oxygen to produce water, a by-product. The last and most important component in PEMFCs is bipolar plate (see Sect. 4).

## 4 Bipolar Plate for PEMFCs

Bipolar plates represent one of the most important of the stack with about 80% of total weight and 45% of stack cost [20]. As a consequence, the major targets for all developers are to focus on the bipolar plate cost reduction, decrease the weight, increase the electrical conductivity, and improve corrosion resistance [21]. The bipolar plate performs a variety of functions within the PEMFC including [20, 22]:

- Connecting individual fuel cells in series to form a fuel cell stack of the required voltage
- Collecting and transporting electrons from the anode and cathode
- Providing a flow path for gas transport to distribute the gases over the entire electrode area uniformly
- Separating oxidant and fuel gases and feeding  $H_2$  to the anode and  $O_2$  to the cathode while removing product water and unreacted gases
- Providing thermal conduction to help regulate fuel cell temperature and removing heat from the electrode to the cooling channels
- Providing mechanical strength and rigidity to support the thin membrane and electrodes and clamping forces for the stack assembly

**Table 4** US DOE technical targets for composite bipolar plates as transportation fuel cells [2]

Properties	Units	2010 target	2020 target
Electrical conductivity (bulk)	S/cm	>100	>100
Thermal conductivity	W/mK	>10	–
Flexural strength	MPa	>25	>25
Flexural flexibility	Percent (deflection at midspan)	3–5	3–5
Hydrogen permeation rate	Std. cm <sup>3</sup> /s cm <sup>2</sup> Pa at 80 °C, 3 atm 100% RH	<2 × 10 <sup>-6</sup>	<2 × 10 <sup>-14</sup>
Water absorption	%	<0.3	<0.3
Weight	kg/kW	<0.4	–
Cost	\$/kW	5	3

- Sealing fluids with port seals and MEA seals to avoid fluid leakage

The materials of the bipolar plate must have particular properties because of its responsibilities and the challenging environment in which the fuel cell operates. Properties of material must be considered for achievable design for a fuel cell application, specifically, electrical and thermal conductivity, gas permeability, mechanical strength, corrosion resistance, and low weight. An ideal material should combine the following characteristics that are defined by Department of Energy (DOE) of the USA as seen in Table 4 which are the value requirements to meet DOE target in year 2020 [2].

#### 4.1 Materials for Bipolar Plate

Challenges facing the commercialization of PEMFCs are large-scale manufacturing and material costs, material durability, material reliability, and hydrogen storage and distribution issues [23]. Currently, efforts to improve the PEMFC cost and reliability for the industry, including the automotive industry, are comprised of reducing the cost and weight of the fuel cell stack, the goal being a 50 kW system of \$35/kW and <133 kg in mass [2]. The bipolar plates in the stack require significant improvement, since bipolar plates account for approximately 55% of the PEMFC weight and 37% of the stack manufacturing and material cost [2, 22] as shown in Fig. 4. Accordingly, the development of bipolar plates may present opportunities for cost and weight reductions in PEMFCs.

Bipolar plate characteristic requirements are a challenge for any class of materials. Therefore, many researchers have focused on development of materials and designs and fabrications of bipolar plates for PEMFC applications. Currently, there are three major classes of materials used to produce bipolar plate including metal, nonmetal (as nonporous graphite), and composite as illustrated in Fig. 5 [24].

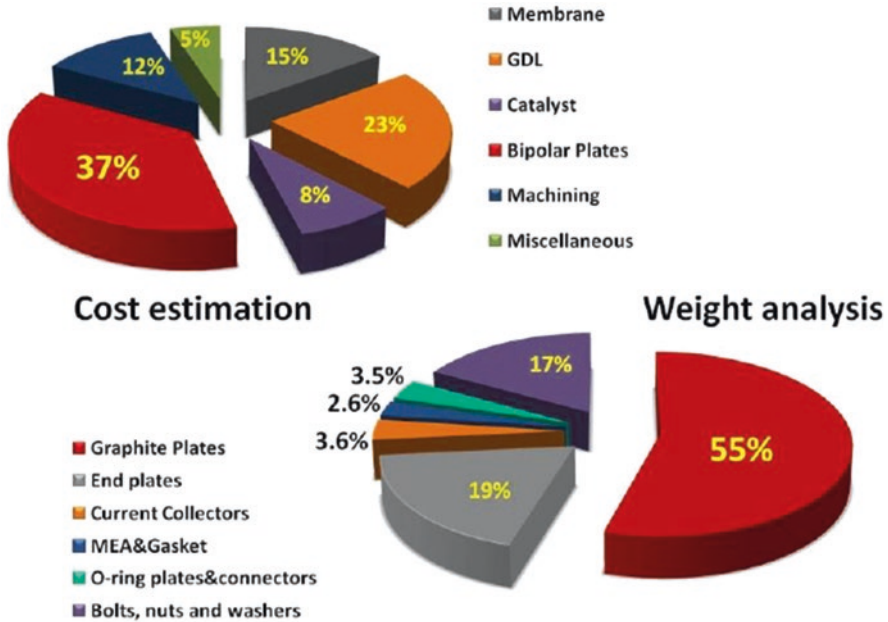


**Fig. 4** Relative cost and weight components from a PEMFC using graphite bipolar plate (Adapted from Ref. [2])

#### 4.1.1 Metallic Bipolar Plates

Metals are potential candidates for bipolar plate material since they have good mechanical stability, electrical and thermal conductivity, and gas impermeability. The most important benefit of metal bipolar plate is that the resultant stack can be smaller and lighter than graphite bipolar plates. However, the main disadvantage of metal plates is their susceptibility to corrosion and dissolution in the fuel cell. A simple metallic bipolar plate is shown in Fig. 6 [25, 26].

Aluminum, titanium, and nickel are considered to be possible alternative materials for bipolar plates in PEMFCs [22, 27] due to their corrosion resistance, low density, low manufacturing cost, and high strength. Certain higher grades of stainless steel have also been shown to be effective. However, their corrosion resistance results from a passive oxide film that reduces surface conductivity or increases contact resistance in which the bipolar plate performance is significantly related to the thickness of the passive layer and surface contact resistance [28]. The increase in thickness and contact resistance of bipolar plate results in more thermal energy to be generated, causing a decrease in output electrical energy.

In addition to the contact resistance issues, metallic plates are also quite heavy. Therefore, plates are made as thin as can be out of these materials, allowing for smaller and lighter fuel cells. In the case of nickel, because it does not form a protective oxide layer, it will undergo corrosion in the harsh fuel cell environment.

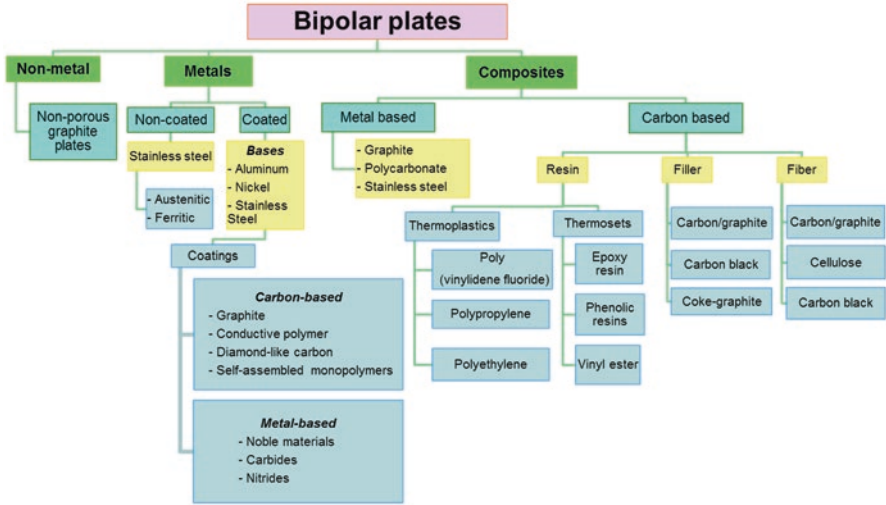


**Fig. 5** Classification of materials for bipolar plates used in PEM fuel cells (Reproduce with permission from Ref. [24])

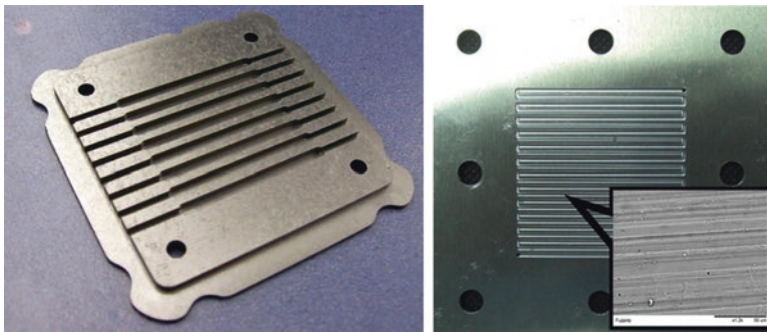


**Fig. 6** Metallic bipolar plate (Reproduced with permission from Refs. [25, 26])

Nickel has to be subjected to surface treatment or alloyed with chromium to make it a feasible choice. Stainless steel alloys are considered to be good candidates for bipolar plate materials because of their low cost and high strength and corrosion resistance. Despite this, the environment within fuel cells still proves a challenge for these materials, and corrosion is still a problem for some types of stainless steel such as low-chromium stainless steel [28].

Besides, metallic bipolar plates with protective coating layers have been developed to improve their corrosion resistance. Coating materials should be conductive and adhere to the base metal. Furthermore, the coefficient of thermal expansion of the base metal and the coating should be as close as possible to eliminate the formation of micropores and micro-cracks in coatings due to unequal expansion. Two types of coatings, carbon-based and metal-based, have been used. Carbon-based

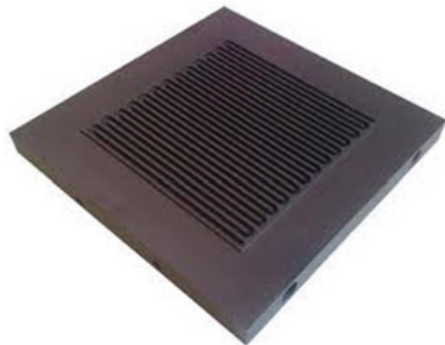
coatings include graphite, conductive polymer, e.g., polyaniline, polypyrrole, and diamond-like carbon. Noble metals, metal nitrides, and metal carbides are some of the metal-based coatings. The early transition metal elements, for example, molybdenum, vanadium, and niobium, which form a thin oxide layer to against corrosion, have also been used [29].

#### 4.1.2 Nonmetal (Nonporous Graphite Bipolar Plates)

Apart from metallic, bipolar plates in the PEMFC have traditionally been made from graphite, one of the most well-established materials for bipolar plate, since graphite has excellent chemical stability to survive the fuel cell environment. Other advantages of graphite are low bulk resistivity, low specific density, and low electrical contact resistance with electrode backing materials which results in high electrochemical power output. However, graphite still provides major shortcomings, i.e., high cost, difficulty of machining, porosity, and brittleness leading several millimeters thick of graphite plates to add to the volume and weight of the stack [20]. An appearance of graphite bipolar plate is shown in Fig. 7 [30].

Commercially, bipolar plates have been created from graphitic carbon impregnated with a resin. This type of bipolar plate is available in the fuel cell market from the likes of POCO Graphite and SGL Carbon. Moreover, flexible graphite is considered as the material of choice for bipolar plates in PEMFC to solve their brittleness. The graphite principally used for the composite is expanded graphite (EG). The flakes can be expanded up to a few hundred times their initial volume [31]. The expansion leads to a separation of the graphite sheets into nanoplatelets with a very high aspect ratio. This layered structure gives higher electrical and thermal conductivity. In comparison to conventional graphite bipolar plates, the bipolar plates produced from EG were found to be thinner [20]. Chao Du and coworkers manufactured a compressed-expanded graphite bipolar plate with a thickness of only 1 mm [32]. Thinner EG plates, for example, the EG/phenol, showed an increase in flexural strength up to 40 MPa [33]. In the current market, flexible graphite bipolar plates are

**Fig. 7** Graphite bipolar plate [30]



manufactured mainly by GRAFCELL from GraphTech (Ohio, USA) for the automotive industry.

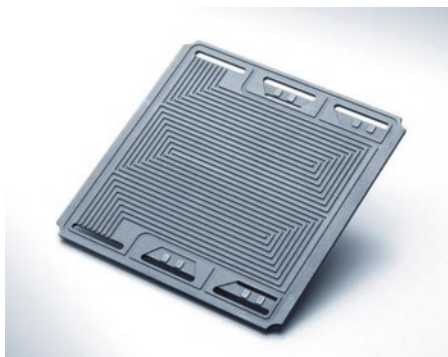
### 4.1.3 Composite Bipolar Plate

The composite as a unique material normally refers to hybrid or mixed materials between dispersed filler or reinforcement in the form of fiber, powder, flake, etc. and the continuous matrix [34]. Polymer composite bipolar plates including thermoplastic and thermosetting composites are beneficial over metallic and traditional graphite materials with regard to corrosion resistance, flexibility, and low weight. In addition, polymer composites may be produced in economical processes, such as compression, transfer, or injection molding processes, depending on the number of units to be manufactured. The main drawback to polymer composite is the lack of electrical conductivity. To enhance the electrical conductivity of the bipolar plates, electrically conductive polymeric materials have been used as bipolar plate materials. Electrically conductive polymeric materials are organic-based materials that permit electron transfer. Bipolar plate made from composite material is shown in Fig. 8 [35].

Composite bipolar plate. Metal-based bipolar plates are made of multiple materials, such as stainless steel, plastic, or porous graphite, so that the benefits of different materials can be harvested in a single bipolar plate.

Carbon-based bipolar plates can be classified as either carbon-carbon or carbon-polymer composites. Carbon-carbon composites are almost entirely made of a carbon matrix reinforced with carbon fibers. The preparation of the composite plate involves an initial slurry-molding process followed by chemical vapor infiltration (CVI). During the former process, carbon fibers and phenolic resin were formed into a plaque by means of a vacuum-molding process. After that, the surface of the plaque is sealed by the CVI technique which deposits carbon near the surface of the material, making the plate impermeable to reactant gases and greatly increasing surface electrical conductivity. Another type of carbon-based bipolar plate is carbon-polymer composite which is extensively reviewed in Sect. 6.

**Fig. 8** Composite bipolar plates [35]





## 5 Carbon-Polymer Composite Bipolar Plate

Polymers are commonly electrical insulators; thus, the conductivity is enhanced by incorporating with conductive filler. There are two types of potential conductive filler to be considered including metallic conductors and the derivatives of carbon. However, the electrical conductivity of metallic is very high, but most of the researchers focus on the use of carbon fillers because of its lower weight. Carbon-polymer composites are created by incorporating a carbonaceous material as a conductive filler into a polymer matrix. The carbonaceous fillers include graphene, graphite, carbon black, carbon fiber, and carbon nanotube. The preference for the polymer binder is governed by the chemical compatibility with the fuel cell environment, mechanical and thermal stability, and processability when loaded with conductive filler. Two different main types of resins are used to fabricate composite plates: thermoplastic and thermosetting.

### 5.1 Carbon Fillers

#### 5.1.1 Graphite

Graphite is one of four forms of crystalline carbon apart from carbon nanotubes, diamonds, and fullerenes. Graphite occurs naturally in metamorphic rocks, such as gneiss, marble, and schist. Graphite exhibits the properties both of a metal such as thermal and electrical conductivity and of a nonmetal such as inertness, high thermal resistance, and lubricity. Typical properties of graphite fillers are presented in Table 5 [36]. In comparison with carbon fillers, electrical conductivity of graphite is rather high. Conductivity is also dependent on crystallographic direction, with a high in-plane conductivity arising from the presence of delocalized electrons. Figure 9 shows metallic appearance of graphite [37].

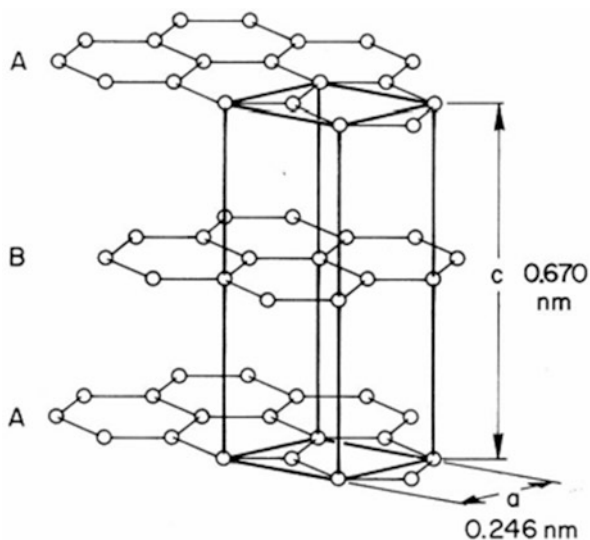
The unique properties of graphite resulting from its distinctive layered structure and chemical inertness make it the material of choice in many applications:

- Good electrical conductivity: the temperature coefficient of electrical resistance of graphite is negative in a certain range of temperature, unlike that of metals. Near absolute zero, graphite has only a few free electrons and acts as an insulator. As temperature rises, electrical conductivity increases.
- Good thermal conductivity.
- Unique mechanical strength: the tensile, compressive, and flexural strength of graphite increases as temperature increases to 2700 K. At 2700 K graphite has about double the strength it has when at room temperature. Above this temperature, its strength falls.
- Low coefficient of thermal expansion.
- High thermal shock resistance: low coefficient for friction.
- High chemical resistance.

**Table 5** Properties of graphite [36]

Properties	Units	Test	Value
<i>Physical properties</i>			
Chemical formula	–	–	C
Density, $\rho$	$\text{g/cm}^3$	ASTM C20	2.25
Color	–	–	Black
Crystal structure	–	–	Hexagonal
Water absorption	%	ASTM C373	0.5–3.0
Hardness	Moh's	–	1.0–1.5
<i>Mechanical properties</i>			
Compressive strength	MPa	ASTM C773	96
Tensile strength	MPa	ACMA Test	4.8
Modulus of elasticity	GPa	ASTM C848	4.8
Flexural strength	MPa	ASTM F417	50
<i>Thermal properties</i>			
Max. use temperature	$^{\circ}\text{C}$	No load cond.	3650
Thermal shock resistance	DT ( $^{\circ}\text{C}$ )	Quenching	200–250
Thermal conductivity	W/mK	ASTM C408	(On plane)
Specific heat, $C_p$	cal/g $^{\circ}\text{C}$	ASTM C351	0.16
<i>Electrical properties</i>			
Electrical resistivity	$\Omega\text{cm}$	ASTM D1829	$7 \times 10^{-3}$

**Fig. 9** The crystal structure of perfect graphite, with the unit cell demarcated in *bold lines*. Also shown are the characteristic lattice parameters at 0 K



- Corrosion resistance: oxidation resistance in air up to 500 °C.
- Low capture cross-section for neutrons.
- Problem-free machining with standard machine tools: graphite can be machined easily. Complicated parts with close tolerances can be machined with precision.
- Reasonable cheap material in comparison to other materials with similar corrosion resistance.
- Graphite does not melt but sublimates at about 3900 K. In air, graphite is resistant to oxidation up to temperatures of about 750 K.
- Graphite displays extremely low creep at room temperature, its flow characteristics being comparable to those of concrete. Creep in graphite is strongly dependent on the grain orientation (creep is defined as plastic flow under constant stress).

Graphite exhibits inert behavior toward most chemicals, and high melting point makes it an ideal material for various applications such as the steel manufacturing process, refractory linings in electric furnaces, containment vessels for carrying molten steel throughout manufacturing plants, and casting ware to create a shaped end product. In addition, graphite is used as a foundry dressing, which assists in separating a cast object from its mold following the cooling of hot metal. The automotive industry uses graphite extensively in the manufacture of brake linings and shoes. Graphite is an effective lubricant over a wide range of temperatures and can be applied in the form of a dry powder or as a colloidal mixture in water or oil. Other uses include electrodes in batteries, brushes for electric motors, and moderators in nuclear reactors [38].

### 5.1.2 Graphene

Graphene is a fascinating material with several advantages. Graphene is the strongest material with Young's modulus of 1 TPa and ultimate strength of 130 GPa. It provides very high electrical conductivity (>6000 S/cm), thermal conductivity (5000 W/mK), surface area (2630 m<sup>2</sup>/g), elasticity, and gas impermeability [39]. Consequently, graphene is very popular for improving mechanical, thermal, electrical, and gas barrier properties of polymer composite in a wide range of applications. Figure 10 [40] shows structure of a single graphene sheet. Table 6 lists properties of graphene. A comparison on properties of various types of carbon filler is summarized in Table 7.

## 5.2 Polymer Matrix

Among various thermosetting resins, phenolics [42–44], epoxies [45–50], and vinyl ester [51–53] are popular choices for carbon-polymer composite bipolar plate due to their low melt viscosity and thereby contain a higher proportion of conductive

**Fig. 10** Idealized structure of a single graphene sheet [40]

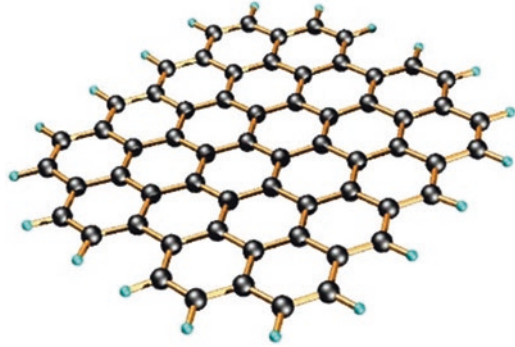


**Table 6** Properties of graphene [39]

Properties	Values
<i>Physical properties</i>	
Chemical formula	C
Color	Black
Crystal structure	Hexagonal
Density ( $\rho$ )	2.2 g/cm <sup>3</sup>
Carbon-carbon bond length	0.142 nm
Thickness	35–1 nm
Extremely high surface area	2630 m <sup>2</sup> /g
High chemical and corrosion resistance	
<i>Electrical property</i>	
Electrical conductivity	>6000 S/cm
<i>Thermal properties</i>	
Thermal conductivity	5000 W/mK in-plane
Low coefficient of thermal expansion	$1 \times 10^{-6} \text{ K}^{-1}$
Young's modulus	
Ultimate strength	1 TPa 130 GPa

fillers. Thermosetting resins are known to have more brittle than thermoplastics. However, thermosetting resins overcome thermoplastic resins by means of their dimensional stability and high thermal stability so as they can operate at high temperature. Another benefit of thermosetting resins is that at temperature higher than glass transition temperature, the viscosity is lower than that of thermoplastics, and thus those can be loaded with higher level of conductive fillers. This leads to an enhancement in electrical conductivity, thermal conductivity, as well as mechanical strength. Thermoplastics including polyvinylidene (PVDF) [41, 54–56],

**Table 7** Properties of important conductive filler for bipolar plate application [41]

Properties	Graphite	Graphene [8, 39]	Carbon fibers	Carbon black	Carbon nanotubes
Density (g/cm <sup>3</sup> )	2–2.25	2.2	1.79–1.99	1.7–1.9	2
Particle size	6–100 $\mu\text{m}$	5–25 $\mu\text{m}$	L: 10–100 $\mu\text{m}$	14–250 nm	L: 10–100 $\mu\text{m}$
			D: 4–10 $\mu\text{m}$		D: few nm
Specific surface area (m <sup>2</sup> /g)	6.5–20	2630	0.27–0.98	7–560	200–250
Aspect ratio	Close to 1	~1000	6–30	Close to 1	1000–50,000
Electrical conductivity (S/cm)	400–1250	>6000	0.03–0.7	2.5–20	10 <sup>-4</sup> –10 <sup>2</sup>

**Table 8** Relative merits of bipolar plate materials from carbon-polymer composite [66]

	Thermoset	Thermoplastic
Advantages	Higher-temperature operation	Injection molding lends itself to manufacturing automation
	Fast cycle time	Fast cycle time
	Flow field introduced during molding	Flow field introduced during molding
	Low contact resistance	Low contact resistance
Disadvantages	Relatively low electrical conductivity	Low electrical conductivity when using standard thermoplastics
		Limited to low-temperature operation
		Injection molding difficult at high loadings
		Generally less chemically stable than thermoset resins
Processing options	Compression molding	Injection molding
	Post-molding CNC milling of blank	Compression molding Post-molding CNC milling of blank

polypropylene [57–60], and polyphenylene sulfide (PPS) [61–65] have been applied to a lesser extent because they are generally less chemically stable than thermosets and must operate at lower temperature to avoid melting. Higher viscosities of thermoplastics are limited with respect to the amount of filler to be added. Consequently, thermoplastic-based composites suffer from lower electronic conductivity than other technologies. The main advantages of using thermoplastic rely on that they can be injection-molded and are therefore more conducive to automated manufacturing. Table 8 shows the comparison merits of bipolar plate made from carbon-filled thermoplastic and thermosetting polymers [66]. Table 9 summarizes the properties of carbon-polymer composites for bipolar plate application [67–69].

**Table 9** Carbon-polymer composites and their essential properties for bipolar plate application

Polymer matrix	Filler	Thermal conductivity	Electrical conductivity (S/cm)	Flexural properties	N <sub>2</sub> permeation rate	Refs.
20–40 % Resole-phenolic resin	50 vol% natural graphite + synthetic graphite		10–120	–	–	[67]
Novolac-phenolic resin	Natural graphite + carbon black + carbon fiber		145–250 (x-y plane)	Modulus 12–14 GPa	–	[67]
			60–75 (z plane)			
Epoxy resin (cured with phenolic resin)	Expanded graphite		180–190 (x y plane)	Strength 40–75 MPa	2 × 10 <sup>-6</sup>	[68]
			Through-plane resistance 15			
35% phenolic resin	65% Natural graphite + MWCT (0–2%)	(xy) 25–50	(xy) 80–178	Modulus 13–15.5 GPa	–	[69]
		(z) 0–12	(z) 10–30			
23% polypropylene + 5% polypropylene-maleic anhydride	65% graphite + 7% carbon black		104.63	Strength 44.28	–	[70]

## 6 Graphite-Filled PBA and Graphene-Filled PBA Composites

PBAs are a newly developed class of thermosetting resins. PBAs are heterocyclic macromolecules, which processed nitrogen and oxygen in their cyclic molecular structure and fuse to another benzene ring. A common type of benzoxazine resin is bisphenol A- and aniline-based benzoxazine which is synthesized from the reaction of bisphenol A, paraformaldehyde, and aniline at 1:4:2 mole ratio at 110 °C without the use of any solvent as disclosed by Ishida in 1996 [71]. This solventless synthesis method is a convenient, cost-competitive, and environmentally friendly method for preparation of various types of benzoxazine monomers. The synthesis path of benzoxazine monomer is shown in Fig. 11. PBA can be prepared through the ring-opening polymerization at oxazine ring of benzoxazine monomer by thermal activation with no further addition of initiator or catalyst [6]. The structural change in benzoxazine monomer to PBA is shown in Fig. 12.

PBAs provide various outstanding characteristics of near-zero volumetric change (near-zero shrinkage) upon thermal curing rendering dimensional stability, no

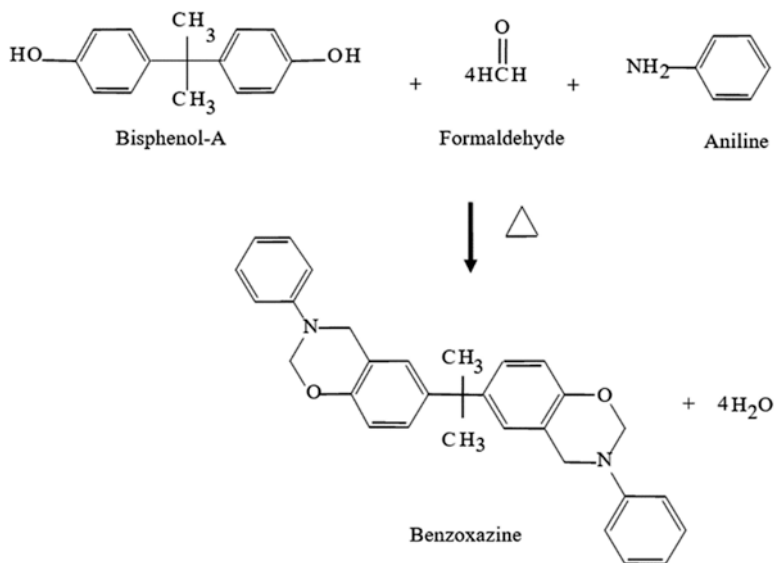


**Fig. 11** Synthesis route of BA-a-type benzoxazine resin

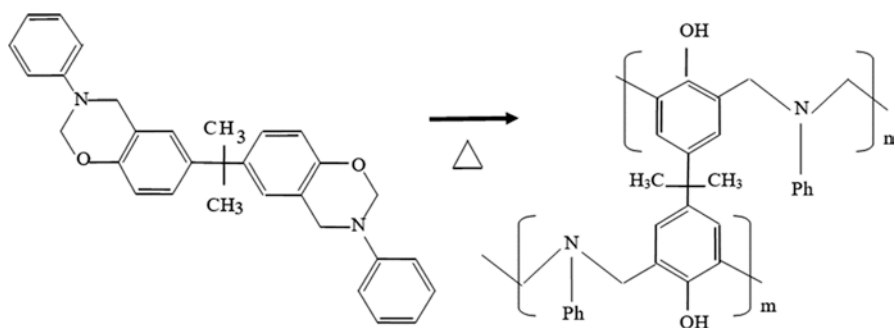


**Fig. 12** Formation of PBA resin network by thermal curing process

by-product released during polymerization leading to no additional removal of volatile by-product. Moreover, PBAs offer a number of attractive properties such as high glass transition temperature, high thermal stability, good mechanical strength and modulus, low water absorption, low dielectric constant, good adhesive properties, and high chemical resistance to burning. The properties of PBA compared to other thermosetting resins are listed in Table 10 [72].

Moreover, BA-a resin shows a very low melt viscosity before curing which is one of those useful properties, rendering the ability of BA-a to easily wet the filler or reinforcement in a compounding process in highly filled system composites. This property is desirable and crucial in various composite applications.

**Table 10** Properties' comparison of major thermosetting resins

Property	Epoxy	Phenolics	Cyanate ester	PBA
Density (g/cc)	1.2–1.25	1.24–1.32	1.1–1.35	1.19
Max use temperature (°C)	180	~200	150–200	130–280
Tensile strength (MPa)	90–120	24–25	70–130	100–125
Elongation (%)	3–4.3	0.3	0.2–0.4	2.3–2.9
Dielectric constant (1 MHz)	3.8–4.5	0.4–10	2.7–3.0	3–3.5
Cure temperature (°C)	RT–180	150–190	180–250	160–220
Cure shrinkage (%)	>3	0.002	~3	~0
TGA onset (°C)	260–340	300–360	400–420	380–400
$T_g$ (°C)	150–220	170	250–270	170–340

Adapted from Ref. [72]

The other advantages of PBA include easy processing ability and lack of volatile formation, all attractive for composite material manufacturing. Furthermore, benzoxazine resin is able to be alloyed with several other polymers or resins. In this literature reported, the mixture of the benzoxazine resin with bisphenol A-type epoxy with the addition of epoxy to the PBA network greatly increases the crosslink density of the thermosetting matrix and strongly influences its mechanical properties [6]. Consequently, PBAs have gained much attention from scientists in the field of polymer research as well as from the industrial researchers.

In this work, graphite powders having an average particle size of 50  $\mu\text{m}$  and a density of 2.2  $\text{g}/\text{cm}^3$  were purchased from Merck Corporation, whereas grade H graphene nanoplatelets having a diameter in the range of 5–25  $\mu\text{m}$ , a thickness of 15 nm, and a surface area of 50–80  $\text{m}^2/\text{g}$  were purchased from XG Sciences, USA. The graphite-filled PBA and graphene-filled PBA compounds at various filler contents were prepared using an internal mixer at about 110 °C. For thermal-cured specimen, the compound was compression-molded by hot pressing at a temperature of 200 °C and a hydraulic pressure of 15 MPa for 3 h. The obtained composites were cut to a desired shape for further characterization.

## 6.1 Highly Filled Graphite/PBA and Graphene/PBA Composites

To qualify the maximum packing of the composite, density measurement is an effective method used to examine the quality of highly filled composite by investigating the presence of void in the composite specimens [73–75]. The density of composite was determined by water displacement method according to ASTM D792 (Method A) and was calculated based on Eq. (1):

$$\rho = \frac{A}{A - B} \times \rho_0 \quad (1)$$



where

$\rho$  = density of the specimen ( $\text{g}/\text{cm}^3$ )

$\rho_o$  = density of the water at the given temperature ( $\text{g}/\text{cm}^3$ )

$A$  = weight of the specimen in air (g)

$B$  = weight of the specimen in liquid (water) (g)

The theoretical density by mass of PBA filled with filler can be calculated according to Eq. (2):

$$\rho_c = \frac{1}{\frac{W_f}{\rho_f} + \frac{(1 - W_f)}{\rho_m}} \quad (2)$$

where

$\rho_c$  = composite density,  $\text{g}/\text{cm}^3$

$\rho_f$  = filler density,  $\text{g}/\text{cm}^3$

$\rho_m$  = matrix density,  $\text{g}/\text{cm}^3$

$\rho_c$  = composite density,  $\text{g}/\text{cm}^3$

$W_f$  = filler weight fraction

$(1 - W_f)$  = matrix weight fraction

The calculation is based on the basis that the densities of the graphite, graphene, and PBA are 2.22, 2.20, and 1.20  $\text{g}/\text{cm}^3$ , respectively. Figure 13 shows the comparison of calculated and actual densities of graphite-filled PBA composites and graphene-filled PBA composites, respectively. From the figure, the theoretical and actual densities of both graphite-filled PBA composites and graphene-filled PBA composites were linearly increased with increasing filler content following the rule of mixture, thus suggesting negligible void or air gap in the composite samples. This is due to the most outstanding property of PBA matrix, that is, its low melt viscosity in which the highly filled void-free composite can easily be obtained. The maximum graphite loading and graphene loading in PBA composites were 80 wt% and 65 wt%, respectively. However, the experimental densities of graphite-filled PBA at higher than 80 wt% (68 vol%) of graphite content and that of graphene-filled PBA composite at higher than 65 wt% (50.1 vol%) of graphene content were found to be slightly lower than that of their theoretical density value. It might be due to the presence of small content of void or air gap in the composite specimen from the incomplete wetting of the resin at such too high amount of the filler loading.

Therefore, the maximum graphite loading and graphene loading in the PBA composites were found to be 80 wt% (68 vol%) and 65 wt% (50 vol%), respectively. Furthermore, the maximum packing density of graphite-filled PBA composite was found to be higher than the maximum loading of graphene-filled PBA composite. It is due to lower surface area of graphite filler compared to graphene filler, thus facilitating the higher filler loading content in the composite.

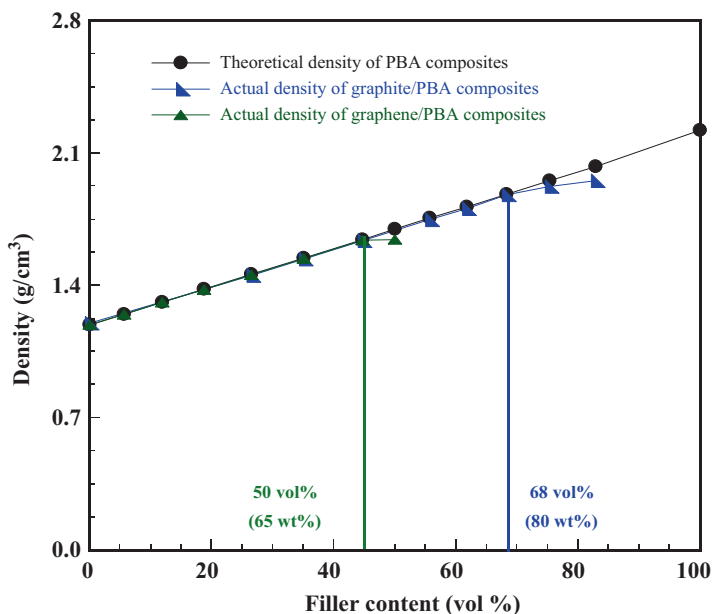


**Fig. 13** Maximum packing density of PBA composites: (●) theoretical density (▲) and actual density of graphite/PBA composites and (▲) graphene/PBA composites at different filler contents (Reproduced with permission from Refs. [7, 8])

## 6.2 Curing Behavior of Graphite/PBA and Graphene/PBA Composites

The curing behavior of graphite-filled PBA composite and graphene-filled PBA composite was investigated by means of onset and maximum peak temperatures of curing thermograms. Figure 14a exhibits the curing exotherms of the neat BA-a and the benzoxazine-graphite molding compounds at various amounts of graphite. A maximum exothermic peak of the benzoxazine and its molding compounds was located at 233 °C, which is the characteristic of oxazine ring opening of benzoxazine monomer [73].

Such exothermic peak reflects the cure characteristic and suggests appropriate thermal curing scheme of the benzoxazine resin. The unchanged exothermic peak position of the benzoxazine molding compounds implied that graphite showed negligible effect on curing reaction of the benzoxazine monomers, e.g., curing retardation. On the other, an incorporation of graphene filler in benzoxazine molding compound showed the shift of curing peak temperature to lower temperature compared to that of the neat benzoxazine as observed from DSC thermogram in Fig. 14b. The characteristic exothermic peaks of 10, 20, 30, 40, 50, and 60 wt% of graphene content in benzoxazine molding compound were 218, 212, 211, 209, 202, and 196 °C, respectively. The results indicated that graphene acts as a catalyst for oxazine ring-opening reaction, thus minimizing the curing condition in terms of

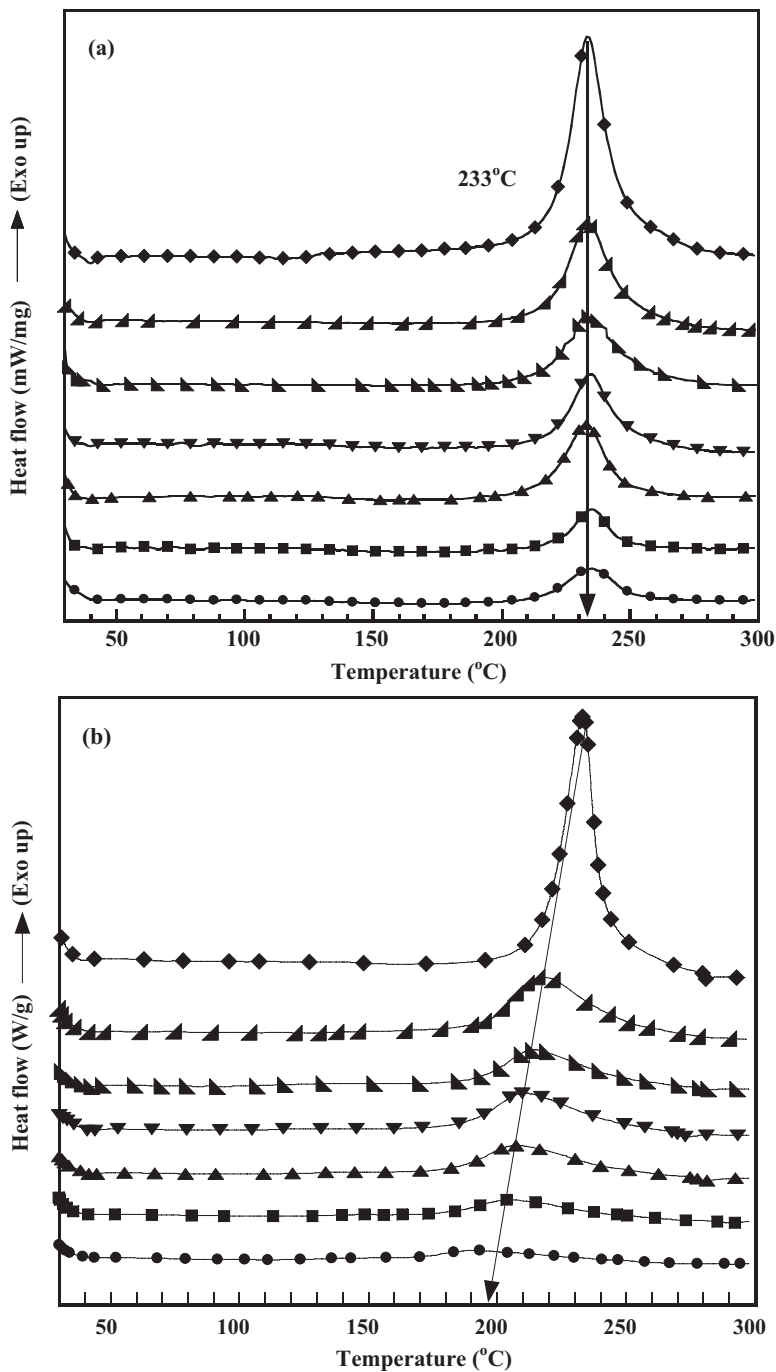


**Fig. 14** DSC thermograms of benzoxazine molding compound: (a) graphite-filled BA-a (◆) neat BA-a (▲) 40 wt%, (▼) 50 wt%, (▲) 60 wt%, (▲) 70 wt%, (■) 75 wt%, (●) 80 wt% (b) graphene-filled BA-a (◆) neat BA-a (▲) 10 wt%, (▼) 20 wt%, (▼) 30 wt%, (▲) 40 wt%, (■) 50 wt%, (●) 60 wt% (Reproduced with permission from Refs. [7, 8])

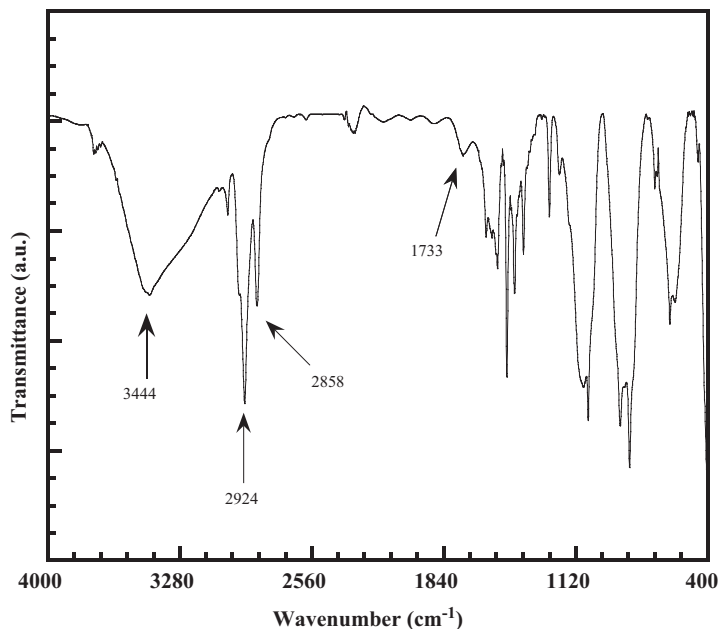


**Fig. 15** FTIR spectra of grade H graphene nanoplatelets from XG Sciences, USA (Reproduced with permission from Ref. [8])

energy consumption to undergo polymerization. The result of the catalytic reaction was also confirmed by FTIR spectra of pure graphene as can be seen in Fig. 15.

As can be seen in Fig. 15, the wave number at 1733 and 1607  $\text{cm}^{-1}$  was observed to be the characteristic peak of C=O stretching and O-H bending in carboxylic group, respectively. Moreover, the strong and broad band at 3444  $\text{cm}^{-1}$  also confirmed the presence of this carboxylic functional group which is normally formed during graphene synthesis [76]. The result indicated that graphene used in this research was graphene oxide. The catalytic effect of carboxylic functional group on ring opening of benzoxazine monomer was also noticed by P. Kasemsiri in the study of cashew nut shell liquid and benzoxazine resin [77]. Curing retardation has been observed in the systems cardanol-benzoxazine resin [78], while curing acceleration was found in epoxy novolac resin-benzoxazine resin [74].

### 6.3 *Dynamic Mechanical Properties of Graphite/PBA and Graphene/PBA Composites*

Since all polymers are viscoelastic in nature, dynamic mechanical analysis method is suitable to evaluate complex transition and relaxation phenomena when polymeric materials are presented.

Figure 16a illustrated the storage modulus ( $E'$ ) of the graphite-filled PBA as a function of temperature with the graphite ranging from 0 to 80 wt%. At room temperature, the  $E'$  of the graphite-filled PBA steadily increased with increasing graphite content which was ranging from 5.2 GPa of the neat PBA to 23 GPa of 80 wt% of graphite loading in PBA composites which accounted to be about 290% stiffness enhancement. Meanwhile,  $E'$  of graphene-filled PBA also enhanced with an incorporation of graphene filler loading which was as high as 25.1 GPa with 60 wt% of graphene loading in the composite as seen in Fig. 16b. The phenomenon was due to the fact that with substantial interfacial interaction between the filler and the matrix, the addition of more rigid particulate of both graphite and graphene into the PBA matrix was able to improve the stiffness of the resulting polymer composites. Meanwhile, the moduli of the graphite-filled PBA and graphene-filled PBA in the rubbery plateau region were also investigated and were found to increase significantly with increasing amount of the filler, again, implying substantial interaction between the filler and the polymer matrix. Furthermore,  $E'$  of the maximum graphene content-filled composite, i.e., 60 wt%, was greater than that of graphite-filled PBA composite at its maximum graphite contents as high as 80 wt%. This phenomenon is likely due to the reinforcing effect of the graphene filler in PBA composites. The presence of oxygen-containing functional groups in graphene has been reported to help improve the modulus of the composites from better interfacial bonding with the matrix [79].

#### 6.4 Glass Transition Temperature of Graphite/PBA and Graphene/PBA Composites

Glass transition temperature ( $T_g$ ) of graphite-filled PBA and graphene-filled PBA composites was determined from the maximum peak temperature of loss modulus curves of the composites as displayed in Fig. 17. As seen in the inset of Fig. 17a, the linear relationship between the  $T_g$  of the composite and the graphite content was clearly observed. The  $T_g$  of the neat PBA was determined to be 174 °C, whereas the  $T_g$  of PBA composite with 80 wt% of graphite was about 194 °C. Furthermore,  $T_g$  of graphene-filled PBA composite showed the same trend as that of graphite composite, i.e.,  $T_g$  of graphene composite also increased with increasing graphene content. An increase of the  $T_g$  with an addition of the graphite is likely due to the good interfacial adhesion between the graphite filler and PBA matrix resulting in a high restriction of the mobility of the polymer chains [7]. In comparison,  $T_g$  values of graphene-filled PBA composite were found to be lower than that of graphite-filled PBA composite, the values of which were observed to be in the range of 176–188 °C with 10–60 wt% of graphene as seen in Fig. 17b.

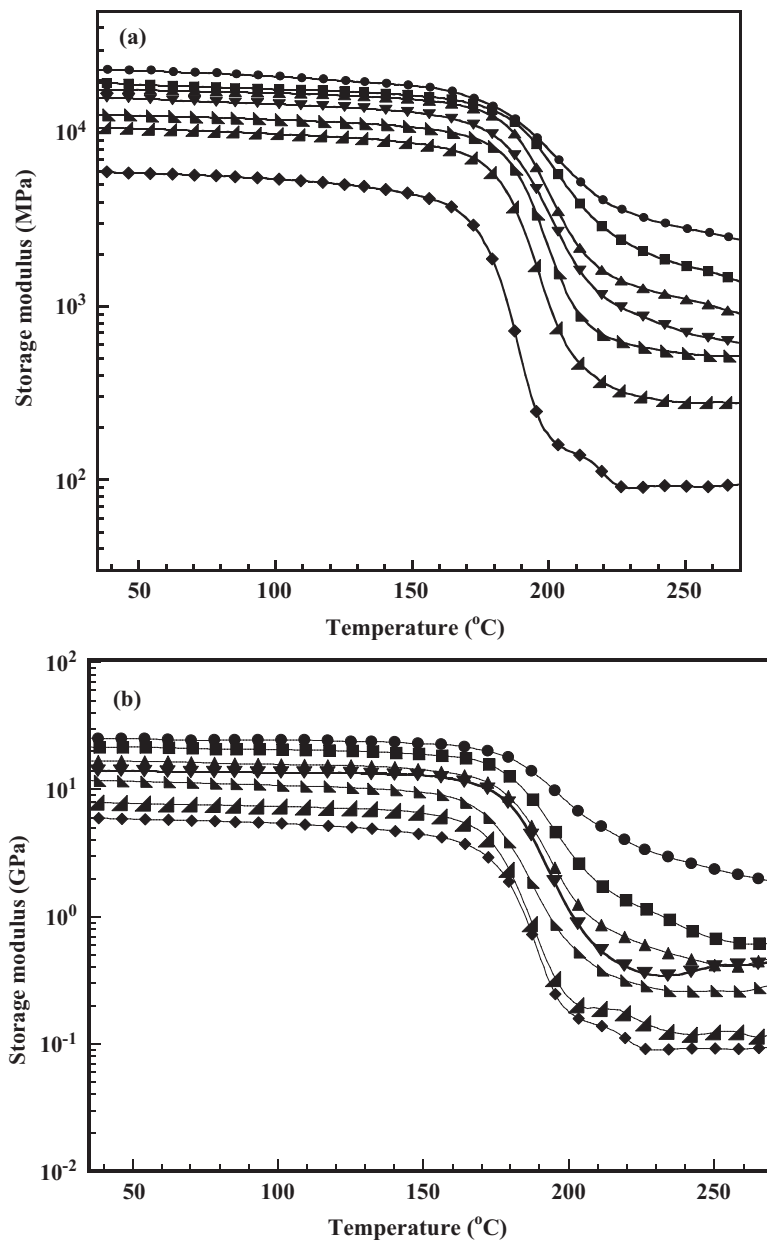


**Fig. 16** DMA thermograms of storage modulus of (a) graphite-filled PBA composites: (◆) neat PBA (▲) 40 wt%, (▴) 50 wt%, (▼) 60 wt%, (▲) 70 wt%, (■) 75 wt%, (●) 80 wt%. (b) Graphene-filled PBA composites: (◆) neat PBA (▲) 10 wt%, (▴) 20 wt%, (▼) 30 wt%, (▲) 40 wt%, (■) 50 wt%, (●) 60 wt% (Reproduced with permission from Refs. [7, 8])

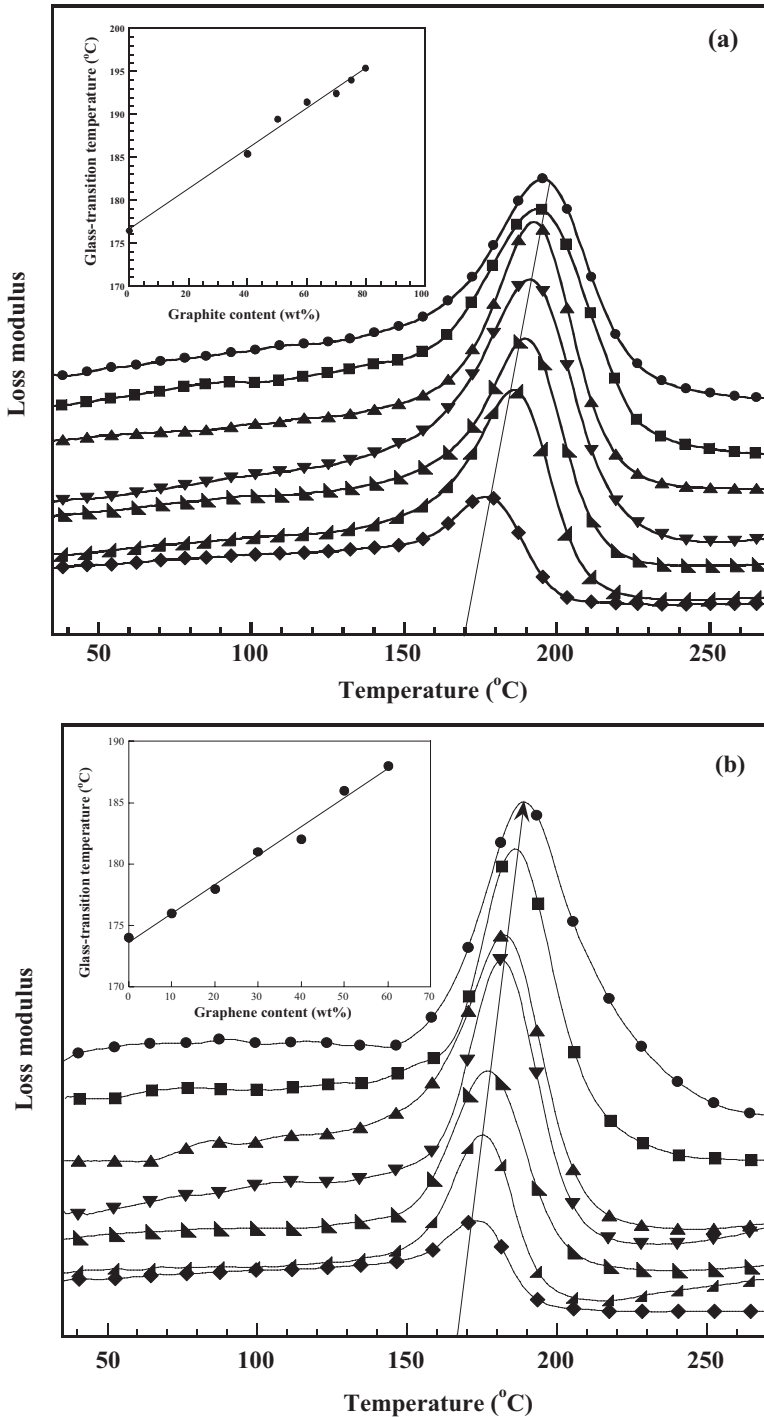


**Fig. 17** DMA thermograms of loss modulus of (a) graphite-filled PBA composites: (◆) neat PBA (▲) 40 wt%, (▴) 50 wt%, (▼) 60 wt%, (▲) 70 wt%, (■) 75 wt%, (●) 80 wt%. (b) Graphene-filled PBA composites: (◆) neat PBA (▲) 10 wt%, (▴) 20 wt%, (▼) 30 wt%, (▲) 40 wt%, (■) 50 wt%, (●) 60 wt% (Reproduced with permission from Refs. [7, 8])

## 6.5 Thermal Stability of Graphite/PBA and Graphene/PBA Composites

Degradation temperature ( $T_d$ ) is one of the key parameters used to determine temperature stability of polymeric materials. Fig. 18a exhibited TGA thermograms of graphite-filled PBA composites at various filler loadings under nitrogen atmosphere.

From the figure, an outstanding high thermal stability of pure graphite was observed with only 0.8% total weight loss of up to 800 °C, whereas PBA matrix possesses a  $T_d$  at its 5% weight loss of 320 °C and the char residue at 800 °C of 25%. With an addition of graphite into PBA matrix, the  $T_d$  at 5% weight loss of composite systematically increased with increasing graphite content. At the maximum graphite content of 80 wt%, the  $T_d$  value was as high as 420 °C which accounted to be 100 °C higher than PBA matrix. This enhancement in  $T_d$  of the highly filler PBA is likely due to the barrier effect of graphite as well as the strong bonding of the benzoxazine resin to the graphite, thus, increasing the  $T_d$  of PBA composite, which minimize the permeability of volatile degradation products out from the material.

The TGA curves of graphene-filled PBA composites with different graphene loadings were also investigated as illustrated in Fig. 18b. As can be seen in Fig. 18b, pure graphene exhibited the  $T_d$  at a 5% weight loss to be about 461 °C. However, around 200–700 °C, the weight loss of pure graphene increased which associated with the removal of oxygen-containing functional groups such as carboxyls, or hydroxyls [80], which were reported to be naturally presented during typical graphene synthesis such as that suggested in the technical data sheet of graphene nanoplatelets – grade H from XG Sciences, USA [76]. Moreover, the presence of these functional groups was also confirmed by FTIR spectra of the pure graphene used in this study as can be seen in Fig. 15. TGA curves of graphene showed a relatively high thermal stability behavior, presenting a total char residue of about 91.4% at 800 °C. This char value of graphene was found to be consistent with that reported by G. Gedler et al. (93%) [80]. Additionally, the  $T_d$  at 5% weight loss of highly filled PBA composites were found to increase with graphene content. Graphene-filled PBA composite with 0–60 wt% of graphene in the composite exhibited  $T_d$  value in the range of 327–353 °C which was 26 °C higher than PBA matrix. This enhancement is attributed to the graphene flakes which acted as a gas barrier and could delay the decomposition of volatile products [81, 82].

## 6.6 Specific Heat Capacity of Graphite/PBA and Graphene/PBA Composites

The ability of a material to store thermal energy can be described in terms of specific heat capacity ( $C_p$ ). In particular,  $C_p$  dictates the amount of energy one must put into the system in order to heat the material to a certain temperature [83]. The effect of temperature on  $C_p$  of composite at different filler loading is shown in Fig. 19.

Within the temperature range of 60–280 °C, the  $C_p$  of graphene-filled PBA composite was found to increase with increasing temperature. The effect of temperature



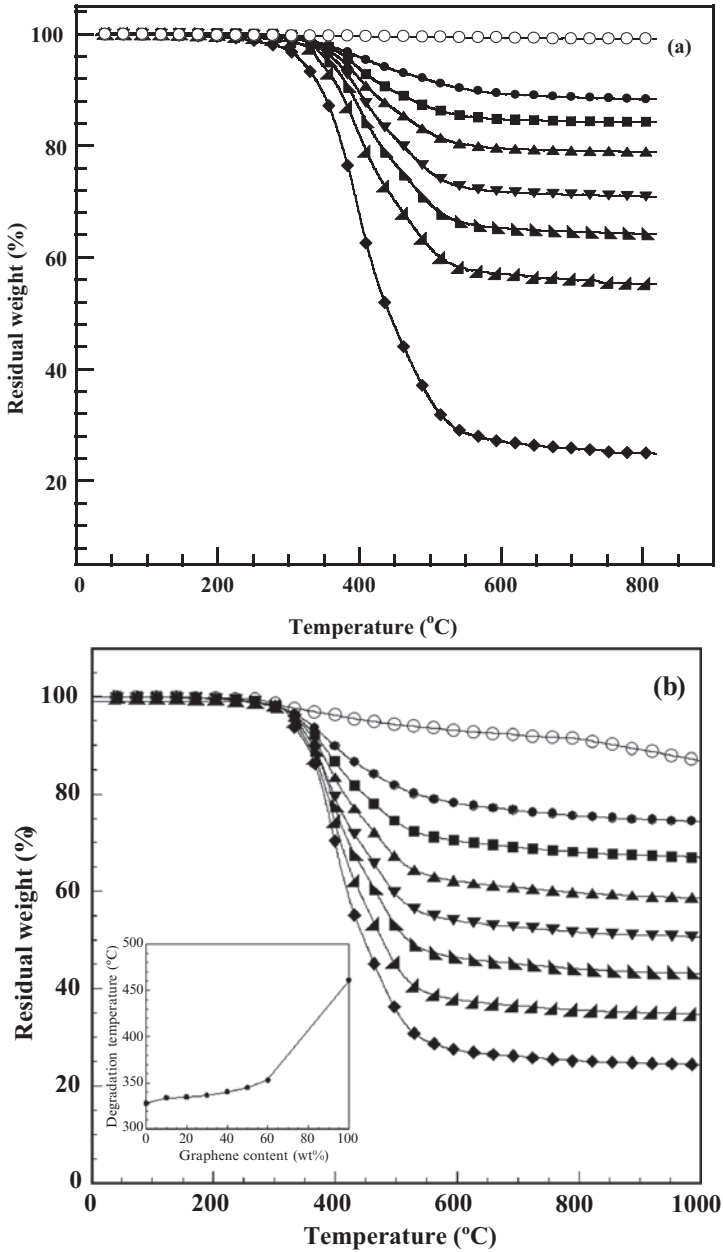


**Fig. 18** TGA thermograms of (a) graphite-filled PBA composites: (○) pure graphite (◆) neat PBA (▲) 40 wt%, (▴) 50 wt%, (▼) 60 wt%, (▲) 70 wt%, (■) 75 wt%, (●) 80 wt%. (b) graphene-filled PBA composites: (○) pure graphene (◆) neat PBA (▲) 10 wt%, (▴) 20 wt%, (▼) 30 wt%, (▲) 40 wt%, (■) 50 wt%, (●) 60 wt% (Reproduced with permission from Refs. [7, 8])

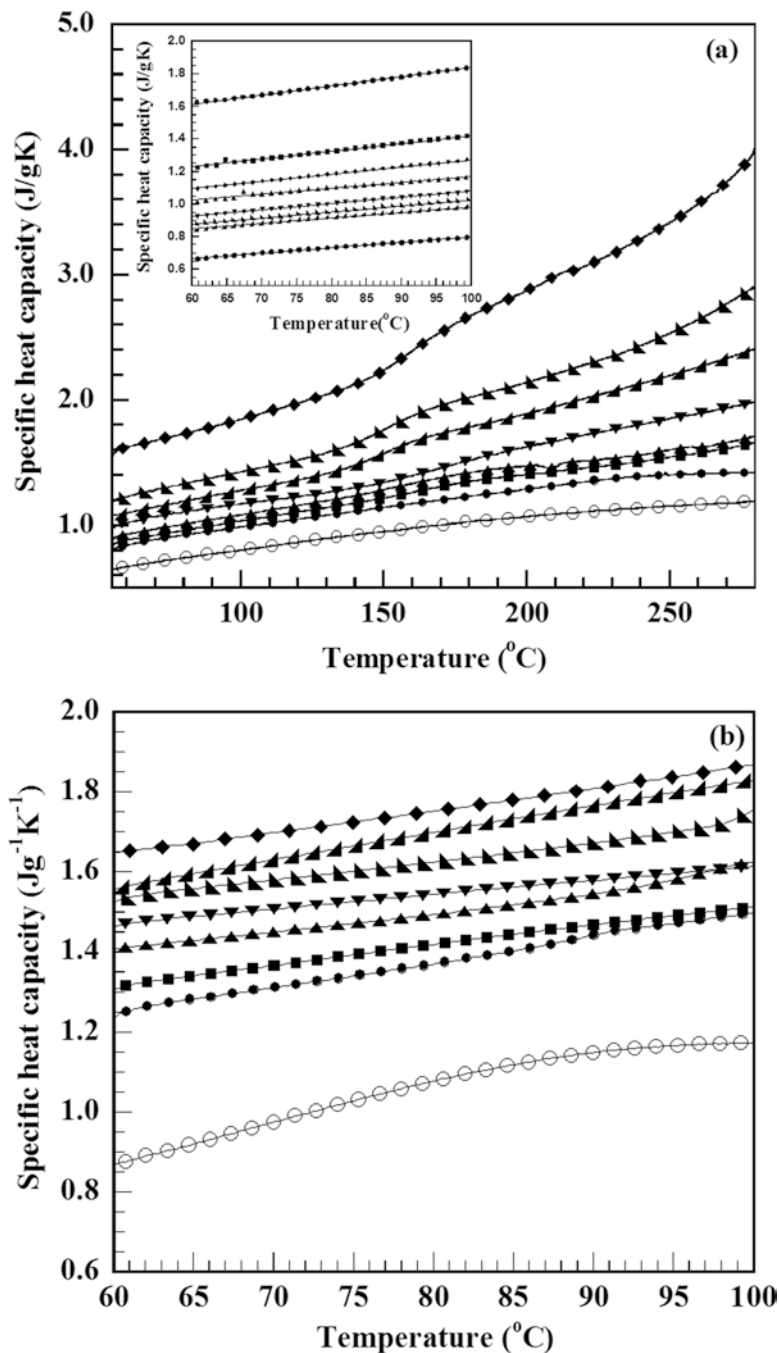


Fig. 19 Specific heat capacity of (a) graphite-filled PBA composites: (o) pure graphite (◆) neat PBA (▲) 40 wt%, (▲) 50 wt%, (▼) 60 wt%, (▲) 70 wt%, (■) 75 wt%, (●) 80 wt%. (b) Graphene-filled PBA composites: (o) pure graphene (◆) neat PBA (▲) 10 wt%, (▲) 20 wt%, (▼) 30 wt%, (▲) 40 wt%, (■) 50 wt%, (●) 60 wt% (Reproduced with permission from Refs. [7, 8])

on the  $C_p$  of the composites can be determined from the slope of the plots. From the experimental results, the fairly low and stable slopes were observed in the composite systems up to about 140 °C. This was due to the high thermal stability and  $T_g$  of PBA matrix used. However, within this temperature range, the inflection of the slope of the plot at the temperature about 150 °C was also noticed which is likely due to the  $T_g$  of these composite materials. The relationship between  $C_p$  of graphene-filled PBA composite and temperature showed the linear trend in temperature up to 100 °C as same as that of graphite-filled PBA composite as illustrated in Fig. 19b. The increase in  $C_p$  of the composite with temperature was attributed to the greater degree of molecular vibrations at elevated temperature [83].

The effect of filler content on  $C_p$  of the PBA composite was also investigated as seen in Fig. 20. From Fig. 20, the  $C_p$  of both graphite-filled PBA composites and graphene-filled PBA composite decreased systematically with an addition of filler, as can be expected from the lower  $C_p$  of the graphite and graphene.

Due to the structure-insensitive characteristic of  $C_p$  of composite, the effect of filler loading on the composite heat capacity can be predicted by the rule of mixture as expressed in Eq. ((3)).

For a two-phase system,

$$C_{pc} = C_{pf}W_f + C_{pp}(1 - W_f) \quad (3)$$

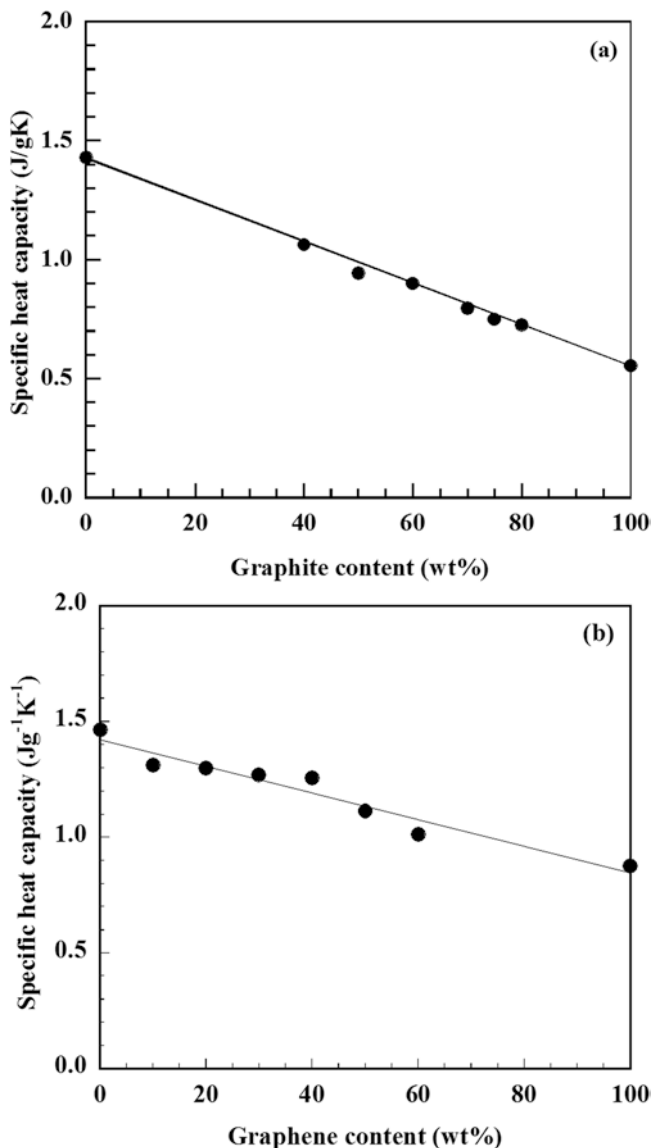
$C_{pc}$ ,  $C_{pf}$ , and  $C_{pp}$  are the specific heat capacities of the composite, filler, and polymer, respectively;  $W_f$  is the mass fraction of the filler.

Fig. 20a shows the plot of the  $C_p$  of composite as a function of graphite loading ranging from 40 to 80 wt% of filler at 25 °C. The  $C_p$  value of pure graphite and neat PBA was 1.756 and 0.753 JK<sup>-1</sup> g<sup>-1</sup>, respectively. The plot reveals a linear relationship between  $C_p$  and filler loading as suggested by Eq. ((3)). The  $C_p$  values of different filler contents from the experimental results are thus in good agreement with those predicted by the rule of mixture with an error within ±1.0 %. Heat capacity and density are important parameters used to convert thermal diffusivity, a very useful transport property of material.

Figure 20b exhibits the plot of the  $C_p$  of graphene-filled PBA composites extrapolated at 25 °C as function of graphene loading ranging from 0 to 60 wt% which exhibited a linear relationship with filler loadings as same as graphite loading in PBA composite. The  $C_p$  of composites is an essential parameter for the determination of thermal conductivity. Thermal conductivity values of the graphite-filled PBA and graphene-filled PBA composites were determined via the measurement of the composites' thermal diffusivity.

## 6.7 Thermal Diffusivity of Graphite/PBA and Graphene/PBA Composites

Thermal diffusivity of graphite-filled PBA and graphene-filled PBA composites as a function of filler content at room temperature was shown in Fig. 21. As seen in Fig. 21, thermal diffusivity of graphite-filled PBA composite was enhanced with an

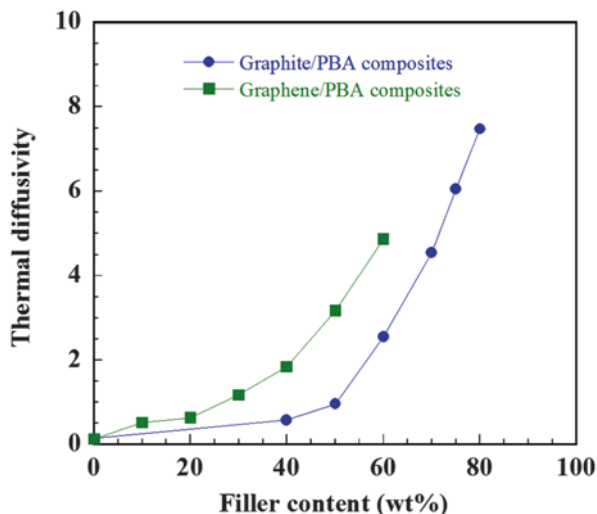


**Fig. 20** Specific heat capacity extrapolated at 25 °C of (a) of graphite-filled PBA (b) Graphene-filled PBA as a function of filler contents (Reproduced with permission from Refs. [7, 8])

addition of highly thermally conductive graphite particularly, at high contents of the graphite. At lower graphite loading up to 50 wt% of graphite, thermal diffusivity of the composites slightly increased with filler loading; however, at graphite loading higher than 50 wt%, the diffusivity values of the composite sharply increased. This behavior was also observed and reported in the highly filled systems of boron nitride and PBA [84], graphite and polystyrene [85], or glass and ethylene vinyl acetate [86].

For the system of graphene-filled PBA, the increase in thermal diffusivity of the composites also increased with graphene filler. Moreover, the behavior could be

**Fig. 21** Thermal diffusivity at 25 °C of (●) graphite-filled PBA composites and (■) graphene-filled PBA composites (Reproduced with permission from Refs. [7, 8])



divided into two regions in accordance with graphene filler content. At filler content up to 20 wt%, a slight increase in thermal diffusivity of the composites was noticed. At the second region at the greater graphene loadings up to 60 wt%, the thermal diffusivity of the composites sharply increased with the amount of the graphene. The behavior of both graphite-filled PBA and graphene-filled PBA was attributed to the formation of tremendous amount of conductive paths in the filled systems with the loading approaching their maximum packing, i.e., highly filled composites.

Furthermore, the thermal diffusivities of graphite-filled PBA and graphene-filled PBA as a function of temperature are shown in Fig. 22a, b. From the figure, it was observed that thermal diffusivity values of both composite systems tended to decrease with increasing temperature as a result of more pronounced phonon-phonon scattering phenomena in the sample [87].

## 6.8 Thermal Conductivity of Graphite/PBA and Graphene/PBA Composites

In theory, thermal diffusivity can be converted into thermal conductivity by the relationship expressed in Eq. 4. Figure 23 shows the measured thermal conductivity of the graphite-filled PBA composites with varying graphite loading. From the figure, thermal conductivity of the composite increased as the graphite content increased. When graphite concentration reached 80 wt%, thermal conductivity of the composite increased to as high as 10.2 W/mK which accounted to be 44 times higher than that of pure PBA with the value of 0.23 W/mK. The graphite-filled PBA composites at 80 wt% of graphite content are a promising bipolar plate for the fuel cell application as it shows relatively high thermal conductivity. The value is substantially greater than the DOE requirement:

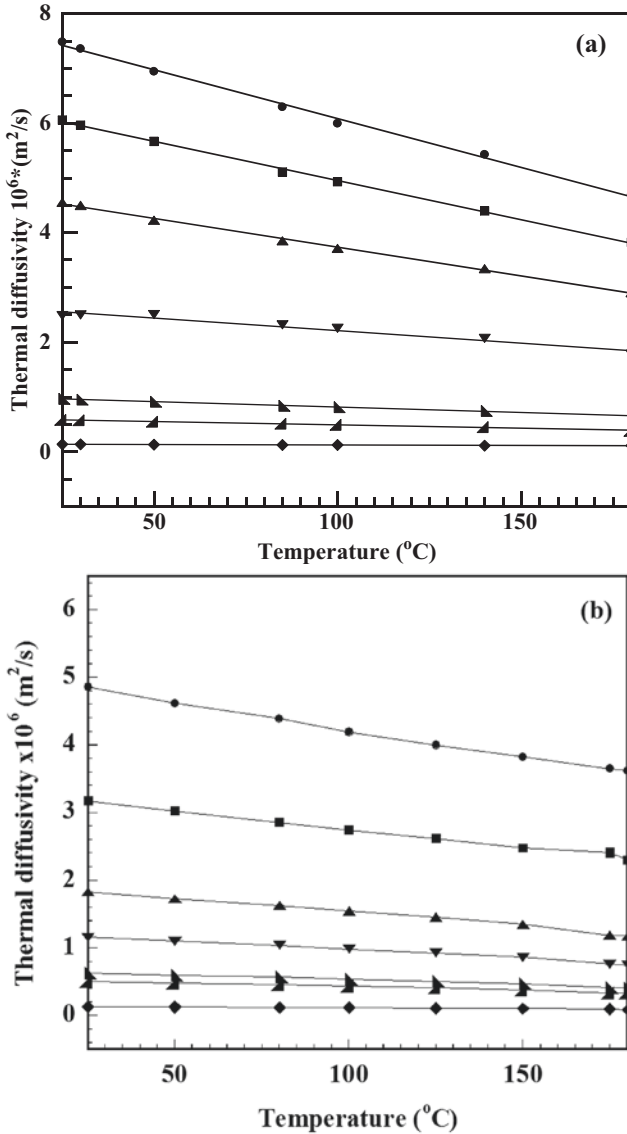


Fig. 22 Thermal diffusivity of (a) graphite-filled PBA composites: (◆) neat PBA (▲) 40 wt%, (▴) 50 wt%, (▼) 60 wt%, (▲) 70 wt%, (■) 75 wt%, (●) 80 wt%. (b) Graphene-filled PBA composites: (◆) neat PBA (▲) 10 wt%, (▴) 20 wt%, (▼) 30 wt%, (▲) 40 wt%, (■) 50 wt%, (●) 60 wt% (Reproduced with permission from Refs. [7, 8])

$$k = \alpha \times \rho \times C_p \tag{4}$$

where  $k$  is the thermal conductivity,  $\alpha$  is the thermal diffusivity,  $C_p$  is the specific heat capacity at constant pressure, and  $\rho$  is the measured density.

**Fig. 23** Thermal conductivity of (●) graphite-filled PBA composites and (■) graphene-filled PBA composites (Reproduced with permission from Refs. [7, 8])

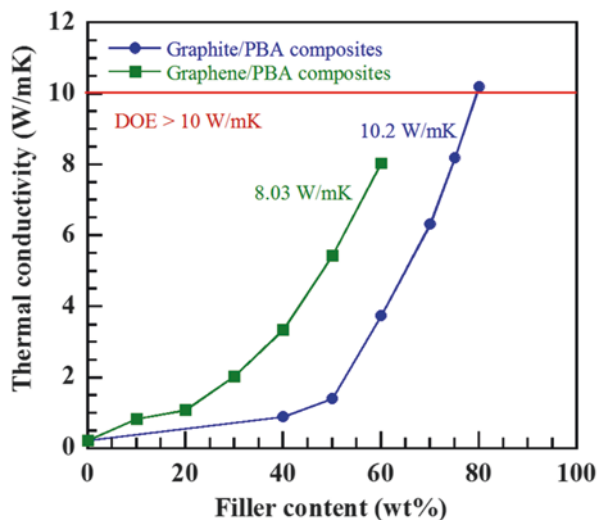
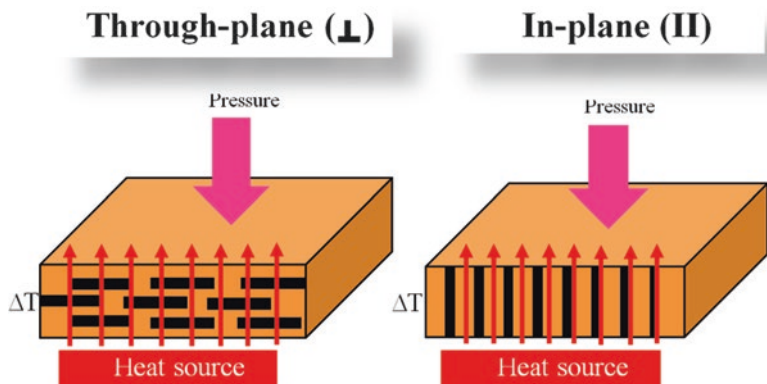


Figure 23 also shows a plot of the thermal conductivity of graphene-filled PBA composites as a function of graphene weight fractions. In the same manner as graphite-filled PBA composite, the thermal conductivity values of the composites were found to systematically increase with increasing graphene content. The maximum thermal conductivity of highly filled graphene-PBA composites was determined to be 8.03 W/mK at 60 wt% of the graphene which is accounted to be about 35 times higher than that of PBA matrix. The relatively high thermal conductivity value obtained in the PBA composite is attributed to the maximizing formation of conductive networks of particles with small heat resistance in this highly filled system. Since efficient heat propagation in graphite and graphene filler is mainly due to diffusion of phonons, a uniform dispersion and network of a highly thermally conductive graphene in the PBA matrix significantly contribute to the steady increase in thermal conductivity in the composites [88].

The thermal conductivity of highly filled graphene-PBA composites was found to be greater than the values obtained from graphite-filled PBA composite compared at the same filler content. This is possibly due to the much smaller particle size as well as a relatively high aspect ratio of the graphene platelets used compared to the graphite particles, i.e., nanometer range vs micrometer range. These characteristics of the graphene particles should render a much greater ability to form conductive network of the filler particles than the graphite particles [89, 90]. Furthermore, highly filled graphene-PBA composites also showed higher thermal conductivity value than some reported high filler loading composites. For example, the thermal conductivity value was reported to be 5.5 W/mK or about 27.5 times enhancement in epoxy/graphene at the maximum graphene content of 50 vol% [91] and 6.6 W/mK in epoxy/graphite nanoplatelets at the maximum filler content of 40 vol% [92].

However, the thermal conductivity values of these graphite and graphene fill PBA composite are through-plane values which were significantly lower than in-



**Fig. 24** Through-plane and in-plane thermal conductivity of polybenzoxazine composite

plane values, resulting from an anisotropic nature of the filler. Figure 24 represents the arrangement of filler in composite in through-plane and in-plane directions which provided the difference in thermal conductivity value of the obtained composite. The bipolar plate must be thermally conductive to conduct the generated heat (reaction byproduct) from an active part of the fuel cell to a cooling channel, to control the stack temperature and to achieve a homogeneous temperature distribution in each cell and over the whole active area; therefore, thermal conductivity is a critical bipolar plate characteristic. As per the recent benchmark given by Department of Energy, USA, the recommended value of thermal conductivity for bipolar plate is to be greater than 10 W/mK [2].

## 6.9 Mechanical Properties of Graphite/PBA and Graphene/PBA Composites

Bipolar plates require good mechanical properties in order to withstand high clamping forces of the stacking, vibrations during vehicular applications, etc. [49, 93]. Flexural modulus and flexural strength of graphite-filled PBA and graphene-filled PBA composites were illustrated as a function of filler content in Figs. 25 and 26, respectively.

As seen in Fig. 25, the modulus values of both graphite composite and graphene composite were found to be substantially enhanced by filler loading up to their maximum loading. The flexural modulus of the neat PBA was determined to be 5.2 GPa, whereas at 40 wt% to 80 wt% of graphite, the modulus of the graphite-filled PBA composites increased from 10.0 to 17.5 GPa. For graphene-filled PBA composite, the flexural modulus of the composite with 0–60 wt% of graphene was determined to be in a range of 5.2–17.5 GPa, and the highest value of 17.5 GPa was obtained at 60 wt% of graphene loading. Additionally, the value obtained from both



**Fig. 25** Flexural modulus of (●) graphite-filled PBA composites and (■) graphene-filled PBA composites (Reproduced with permission from Refs. [7, 8])

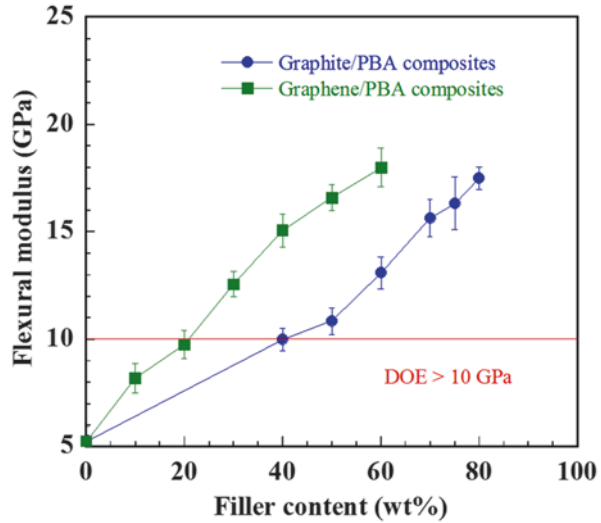
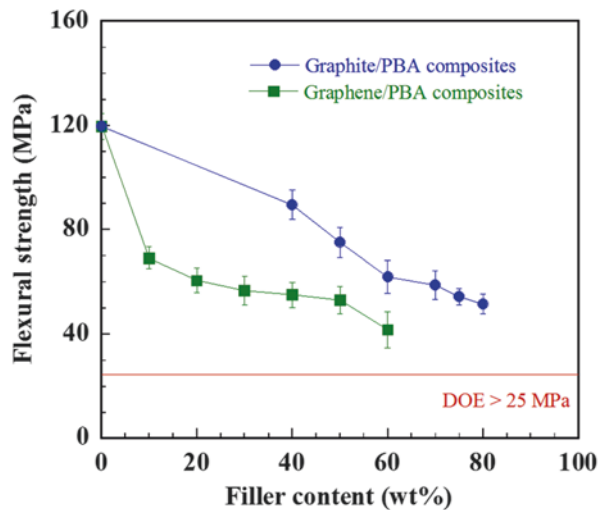


**Fig. 26** Flexural strength of (●) graphite-filled PBA composites and (■) graphene-filled PBA composites (Reproduced with permission from Refs. [7, 8])



graphite and graphene-filled PBA composites was also higher than that of a highly filled system of polyphenylene sulfide and graphene nanoplatelets as reported by X. Jiang et al. [88] for PEM fuel cell, i.e., 15 GPa at graphene content of 60 wt%. The enhancement in flexural modulus was believed to be due to a uniform dispersion and strong interfacial bonding between the filler and the matrix [94]. It is, therefore, evident that an addition of much greater rigidity of particulate graphite and graphene into the PBA matrix attributed to significant enhancement in the stiffness of the obtained PBA composites [7]. Interestingly, the flexural modulus of the composite at higher 50 wt% of graphite and at higher 30 wt% of graphene contents exceeded the DOE requirement of 10 GPa for a bipolar plate application [2].

However, as shown in Fig. 26, the flexural strength of graphite-filled PBA and graphene-filled PBA composite bipolar plates was lower than that of PBA matrix and was found to decrease with increasing filler content. It is postulated that the aggregation and agglomeration may present in the graphite and graphene, thus causing some defects in the composites resulting in lowering of the strength values. Moreover, the lower flexural strength values might be related to the effect of discontinuous longer interparticle distance on stress transferring in the composite [11]. However, the reduced flexural strength of graphene composite was lower than that of graphite composite as observed from the slope of the curve. It is implied that the highly filled graphene particles can form continuous network in the composites thus leading to better continuous stress transferring.

These observed phenomena are often observed in graphite-filled systems, e.g., graphite-epoxy [95], graphite-phenolic resin [95], graphite-phenol formaldehyde resin, and graphite-novolac epoxy [96]. However, all the strength data of the PBA composites were still much higher than the target value of strength set by DOE, i.e., 25 MPa. At maximum graphite loading of 80 wt% in PBA, its flexural strength is 51.5 MPa which is still much higher than that of graphite-filled epoxy (35 MPa) [95], graphite-filled phenolic resin (34 MPa) [95], graphite-filled epoxy novolac (45 MPa) [96], etc.

For graphene composite systems, the strength reduction of composite with an increase in graphene is also observed in highly filled graphene nanoplatelets/polyphenylene sulfide [88]. For low graphene-filled composite system (2 wt%), the strength of the composites was found to show a sharp decrease with increasing graphene content such as system of graphite nanoplatelets/epoxy nanocomposites [97]. This suggested the advantage of making a highly filled system on the enhancement of the composite strength compared to that obtained in the low range of filler content. In addition, at 60 wt% graphene loading, the flexural strength of graphene highly filled composite remains as high as 41.7 MPa, which was significantly greater than the flexural strength value of the DOE targets for bipolar plate material (>25 MPa) [2].

### **6.10 Water Absorption of Graphite/PBA and Graphene/PBA Composites**

The mechanism of water diffusion of the composites was studied from the amount of water absorption by the specimens. The water absorption was calculated based on the change in weight of wet and dry specimens. Water absorption for graphite-filled PBA composites at different graphite contents is exhibited in Fig. 27a. The water absorption trend of all specimens exhibited a similar behavior. The graphite-filled PBA composite absorbed water more rapidly during first stages (0–24 h). The water absorption values of all graphite/PBA-a composites at different filler contents ranging from 40 to 80 wt% had been recorded up to 168 h of the immersion, i.e., beyond their saturation points. These PBA composites showed room temperature water

uptake having values much less than 0.3% which is the value desired in the industrial standard of typical composites for bipolar plate [2].

From the curves, the water uptake of graphite-filled PBA composite up to 168 h was only 0.2% at the filler content of 40 wt% and lower at higher filler contents, which was very low. These values were significantly lower than the water absorption values of graphite filled with epoxy (50 wt% graphite at 24 h) [45].

Water absorption behavior of the neat PBA and its composites filled with graphene (0–60 wt% of graphene) is shown in Fig. 27b. From Fig. 27b, the absorption curves are rapidly increased at the early stage of water uptake (i.e., 0–24 h) as same as graphite-filled PBA composite. The water uptake value of the graphene-filled PBA was calculated to be less than 0.1% at maximum content of graphene at 60 wt%. The water uptakes of the composites were found to steadily increase with time but at a lower rate comparing with the first 24 h. From the curves, the water uptake of the composites up to 60 days of immersion remained less than 0.8% at the filler content of 0–60 wt%.

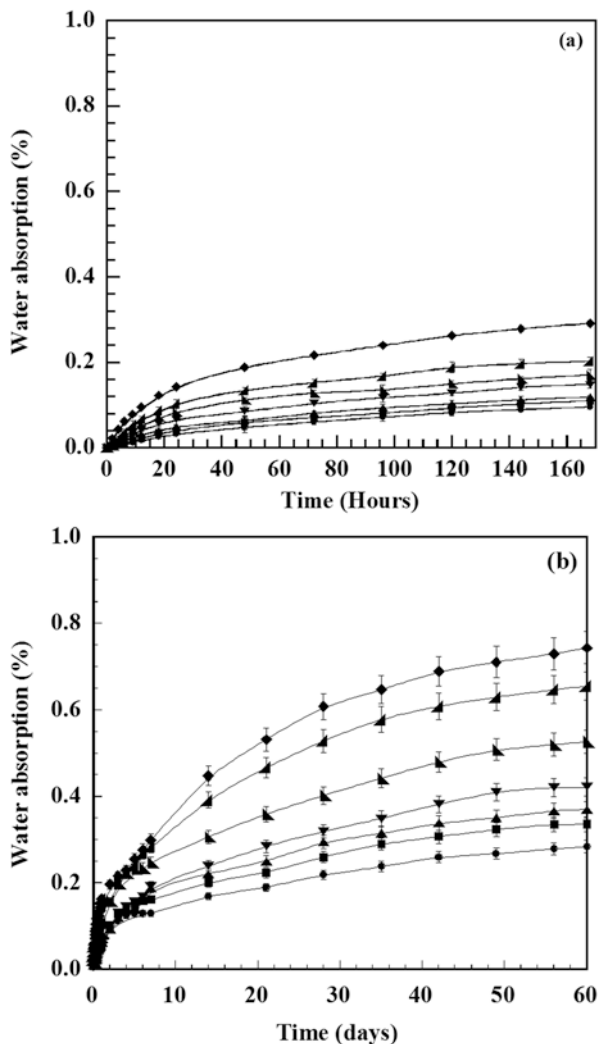
Moreover, the water absorption of both graphite-filled PBA and graphene-filled PBA composites was also observed to systematically decrease with increasing filler content. The phenomenon was attributed to the presence of the more hydrophobic nature of the graphite and graphene filler in the polymer composites which inhibited the water permeation in the polymer matrix [82, 98]. Moreover, the reduction of water absorption resulted from the relatively good filler dispersion and interfacial adhesion between the filler and the matrix that minimized the formation of air gaps between the filler and the matrix. This low water uptake is highly desirable characteristic in bipolar plate application.

### **6.11 Electrical Conductivity of Graphite/PBA and Graphene/PBA Composites**

Bipolar plates collect and transport electrons generated by an electrochemical reaction in fuel cell stacks. Therefore, the materials for bipolar plates should provide high electrical conductivity to minimize voltage loss. In polymer composite, the property is largely influenced by the filler loading and filler type [95]. The composite filled with graphite and graphene has anisotropic electrical conductivity depending on the distribution direction of the fillers.

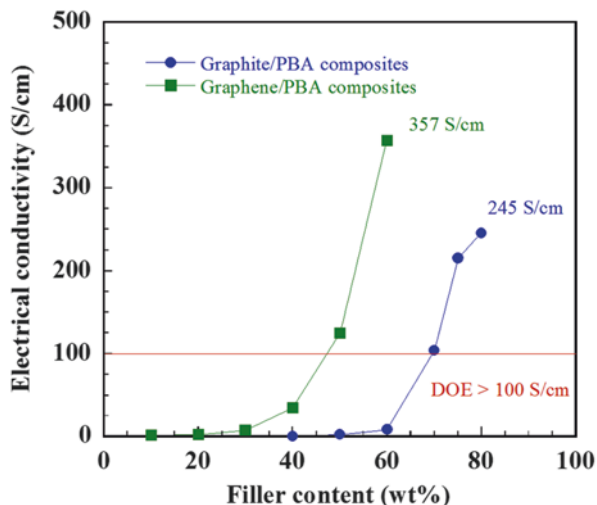
Figure 28 showed electrical conductivity of the highly filled systems of graphite and PBA composites at different weight fraction of graphite. It is evident that the conductivity of the composite increased nonlinearly with an increase in graphite content up to its maximum packing. At 40–60 wt% of the graphite, the electrical conduction values increased only slightly with the filler loading. Beyond 60 wt% of the graphite filler, the conductivity values tended to increase sharply up to about 245 S/cm. As a similar trend in graphite composite, electrical conductivity of graphene-filled PBA also increased nonlinearly with graphene fraction and reached maximum value at its maximum loading. The phenomenon is due to the gradual formation of the percolating network of the graphite and graphene particles within

**Fig. 27** Water absorption of (a) graphite-filled PBA composites: (◆) neat PBA (▲) 40 wt%, (▴) 50 wt%, (▼) 60 wt%, (▲) 70 wt%, (■) 75 wt%, (●) 80 wt%. (b) Graphene-filled PBA composites: (◆) neat PBA (▲) 10 wt%, (▴) 20 wt%, (▼) 30 wt%, (▲) 40 wt%, (■) 50 wt%, (●) 60 wt% (Reproduced with permission from Refs. [7, 8])



the plate with an increase in the filler content [99]. At 50 and 60 wt% of graphene in PBA composite, the electrical conductivity values were measured to be 125 and 357 S/cm, respectively. The observed substantial enhancement in the electrical conductivity values was attributed to the good interfacial bonding between both graphite and graphene filler in PBA matrix. Furthermore, the electrical conductivity value of graphene-filled PBA composite was significantly greater than graphite composite which is due to the formation of the continuous graphene particle network having tremendous amount of the conductivity paths particularly at very high graphene loading. In comparison with graphite-filled PBA, the electrical conductivity of graphene-filled PBA was found to be significantly higher than those obtained using graphite filler comparing at the same percentage of the filler loading. Furthermore, electrical conductivity values of the graphene-filled PBA composites at 50 wt%

**Fig. 28** Electrical conductivity of (●) graphite-filled PBA composites and (■) graphene-filled PBA composites (Reproduced with permission from Refs. [7, 8])



(125 S/cm) and 60 wt% (357 S/cm) meet the value recommended by the US DOE of 100 S/cm for bipolar plate application, whereas at least 70 wt% of graphite contents in graphite-filled PBA having the value of 104 S/cm was required to achieve the DOE requirement.

The overall properties of graphite-filled PBA and graphene-filled PBA composites are summarized and presented in Table 11.

## 7 Conclusions

Bipolar plates based on highly filled systems of graphite-filled PBA composite and graphene-filled PBA composite have been developed. For graphite-filled PBA, the maximum graphite loading in the PBA composite was observed to be as high as 80 wt% which is significantly higher than that of graphene-filled PBA, i.e., 65 wt%. From DSC thermograms, graphene acted as a catalyst for oxazine ring-opening reaction of PBA by carboxyl group on graphene surface, while no catalytic reaction of graphite on benzoxazine polymerization was observed. Mechanical properties, i.e., flexural modulus and flexural strength of both types of composites at their maximum contents, were much greater than those requirements of DOE targets for bipolar plate materials.

Thermal conductivity value of the PBA composite with combination of both graphite and graphene at 7.5 wt% of graphene loading and 75.5 wt% of graphite was found to be as high as 14.5 W/mK. The  $T_g$  and  $T_d$  at 5% weight loss of the composites were found to increase with increasing filler contents. Electrical conductivity of the highly filled PBA composites at their maximum loading was 255 S/cm for graphite composite and 357 S/cm for graphene composite. The  $T_g$  and  $T_d$  at 5% weight loss of the composites were found to increase with increasing filler

**Table 11** Summary properties of graphite-filled PBA and graphene-filled PBA composite

Properties	Graphite-filled PBA composite										Graphene-filled PBA composite									
	0 wt%	40 wt%	50 wt%	60 wt%	70 wt%	75 wt%	80 wt%	0 wt%	10 wt%	20 wt%	30 wt%	40 wt%	50 wt%	60 wt%						
Curing temperature (°C)	233	233	233	233	233	233	233	233	218	212	211	209	202	196						
Storage modulus (GPa)	5.9	10.7	12.7	15.9	17.8	19.2	23.0	5.9	7.9	10.5	12.3	16.6	21.6	25.1						
$T_g$ (°C)	176	185	189	191	192	194	195	174	176	178	181	182	186	188						
$T_{d,5}$ (°C)	320	344	358	368	378	389	418	327	333	335	337	341	345	353						
Flexural modulus (GPa)	5.2	10.0	10.9	13.1	15.6	16.3	17.5	5.2	8.2	9.6	12.6	15.1	16.6	17.5						
Flexural strength (MPa)	119.7	89.4	75.1	61.9	58.8	54.3	51.5	119.7	69.1	60.5	56.7	55.1	53.1	41.7						
Thermal conductivity (W/mK)	0.23	0.89	1.39	3.74	6.31	8.18	10.18	0.23	0.83	1.08	2.03	3.36	5.43	8.03						
Electrical conductivity (S/cm)	–	0.39	2.55	8.40	104	214.95	245.22	–	1.52	2.50	7.42	9.26	125	357						
Water absorption at 24 h (%)	0.143	0.104	0.084	0.067	0.050	0.040	0.032	0.152	0.132	0.108	0.071	0.068	0.067	0.060						

Reproduced with permission from Refs. [7, 8]

contents. Electrical conductivity of the highly filled PBA composites at their maximum loading was 255 S/cm for graphite composite and 357 S/cm for graphene composite. Furthermore, the graphite-filled PBA composite provides thermal conductivity value up to 10.2 W/mK. From those obtained properties of graphite-filled PBA and graphene-filled PBA including flexural modulus, flexural strength, water absorption, electrical conductivity, and thermal conductivity, it is suggested that these materials are suitable to be promising candidates for bipolar plates in PEMFC applications.

## 8 Current Research

Although composite material based on graphite-filled PBA and graphene-filled PBA composite provided sufficient properties as DOE requirement, the development on composite material to enhance the essential properties is an ongoing research. As graphite-filled PBA composite at maximum loading of at 80 wt% provided thermal conductivity value up to 10.2 W/mK, an incorporation of graphene in graphite-filled PBA as a bipolar plate has been further developed by Phuangngamphan M. [9]. The effect of graphene content in the range of 0–7.5 wt% in graphite-filled PBA composite was systematically investigated. Interestingly, the PBA composite with 75.5 wt% of graphite and 7.5 wt% of graphene provided the maximum thermal conductivity value to be as high as 14.5 W/mK, whereas other essential properties of the obtained composite, i.e., mechanical, thermal, and electrical properties, also met DOE requirement.

**Acknowledgments** This work has been supported by the Ratchadapisek Sompoch Endowment Fund (2016), Chulalongkorn University (CU-59-041-EN) and the Royal Golden Jubilee (RGJ) Ph.D. Program (Grant No.PHD/0030/2554) under the Thailand Research Fund (TRF).

## References

1. M. Kumagai, S.T. Myung, S. Kuwata, R. Asaishi, H. Yashiro, Corrosion behavior of austenitic stainless steels as a function of pH for use as bipolar plates in polymer electrolyte membrane fuel cells. *Electrochim. Acta* **53**, 4205–4212 (2008)
2. DOE, U.S. Fuel Cells (2014), Available from: <http://www1.eere.energy.gov/>, cited 21 Aug 2016
3. S. Joseph, J.C. McClure, R. Chianelli, P. Pich, P.J. Sebastian, Conducting polymer-coated stainless steel bipolar plates for proton exchange membrane fuel cells (PEMFC). *Int. J. Hydrogen Energ.* **30**, 1339–1344 (2005)
4. V.V. Nikam, R.G. Reddy, Corrugated bipolar sheets as fuel distributors in PEMFC. *Int. J. Hydrogen Energ.* **31**, 1863–1873 (2006)
5. K. Feng, Y. Shen, H. Sun, D. Liu, Q. An, X. Cai, P.K. Chu, Conductive amorphous carbon-coated 316L stainless steel as bipolar plates in polymer electrolyte membrane fuel cells. *Int. J. Hydrogen Energ.* **34**, 6771–6777 (2009)

6. S. Rimdusit, C. Jubsilp, S. Tipipakorn, *Alloys and Composites of Polybenzoxazines* (Springer, Singapore, 2013)
7. I. Dueramae, A. Pengdum, S. Rimdusit, Highly filled graphite polybenzoxazine composites for an application as bipolar plates in fuel cells. *J. Appl. Polym. Sci.* **130**, 3909–3918 (2013)
8. R. Plengudomkit, M. Okhawilai, S. Rimdusit, Highly filled graphene-benzoxazine composites as bipolar plates in fuel cell applications. *Polym. Compos.* **37**, 715–727 (2014)
9. M. Phuengngamphan, *Development of Highly Thermally Conductive Graphite/Graphene Filled Polybenzoxazine for Bipolar Plates in Fuel Cells*, in *Chemical Engineering*. (Chulalongkorn University, 2016)
10. I. Dueramae, C. Jubsilp, T. Takeichi, S. Rimdusit, High thermal and mechanical properties enhancement obtained in highly filled polybenzoxazine nanocomposites with fumed silica. *Compos. Part B-Eng* **56**, 197–206 (2014)
11. J. Kajohnchaiyagual, C. Jubsilp, I. Dueramae, S. Rimdusit, Thermal and mechanical properties enhancement obtained in highly filled alumina polybenzoxazine composites. *Polym. Compos.* **35**, 2269–2279 (2014)
12. M.H. Mehrir, C. Wang, Fuel cells. in *Electric Renewable Energy Systems* (Elsevier, 2014), pp. 92–113. Available from: <http://www.ingenieurparadies.de/en/ipar/18281/>, cited 21 Aug 2016
13. S.J. Peighambardoust, S. Rowshanzmir, M. Amjadi, Review of the proton exchange membranes for fuel cell applications. *Int. J. Hydrogen Energ.* **35**, 9349–9384 (2010)
14. Technical plan, Fuel cells, 2012
15. The Fuel Cell Industry Review (2015), E4tech Strategic thinking in sustainable energy, available at [www.fuelcellindustryreview.com](http://www.fuelcellindustryreview.com), cited 21 Aug 2016
16. G. Weaver, *World Fuel Cells-An Industry Profile with Market Prospects to 2010* (Elsevier, New York, 2010)
17. M.A. Hickner, *Transport and Structure in Fuel Cell Proton Exchange Membranes in Chemical Engineering* (Virginia Polytechnic Institute and State University, Virginia, 2003)
18. V. Mehta, J.S. Cooper, Review and analysis of PEM fuel cell design and manufacturing. *J. Power Sources* **114**, 32–53 (2003)
19. S. Gottefeld, T. Zawodzinski, Polymer electrolyte fuel cells. *Adv. Electrochem. Sci. Eng.* **5**, 195–301 (1997)
20. S.S. Dibrab, K. Sopian, M.A. Alghou, M.Y. Sulaiman, Review of the membrane and bipolar plates materials for conventional and unitized regenerative fuel cells. *Renew. Sust. Energ. Rev.* **13**, 1663–1668 (2009)
21. G. Hoogers, *Fuel Cell Technology Handbook* (CRC press LLC, Taylor&Francis Group, Boca Raton, 2002)
22. T. Cheng, in *Bipolar Plates and Plate Materials in Proton Exchange Membrane Fuel Cells (Materials Properties and Performance)*, ed. by D.P. Wilkinson, et al. (CRC Press Taylor & Francis Group, Boca Raton, 2010), pp. 305–313
23. J.S. Cooper, Design analysis of PEMFC bipolar plates considering stack manufacturing and environment impact. *J. Power Sources* **129**, 152–169 (2004)
24. A. Hermann, T. Chaudhuri, P. Spagnol, Bipolar plates for PEM fuel cells: a review. *Int. J. Hydrogen Energ* **30**, 1279–1302 (2005)
25. C. Ryan, *Green Machine Competition-Fuel Cell Pressurized Air Bipolar Plate (Cathode Side)*. (2014). Available from: <http://www.chiefdelphi.com/>
26. C.-H. Lin, S.-Y. Tsai, An investigation of coated aluminium bipolar plates for PEMFC. *Appl. Energy* **100**, 87–92 (2012)
27. A. Enin, S.A. Salam, E. Omar, New electroplated aluminum bipolar plate for PEM fuel cell. *J. Power Sources* **177**, 131–136 (2008)
28. D.P. Davies, P.L. Adcock, M. Turpin, S.J. Rowen, Stainless steel as a bipolar plate material for solid polymer fuel cells. *J. Power Sources* **86**, 237–242 (2000)
29. A. Heinzl, F. Mahlendorf, C. Jansen, Fuel cells, proton exchange membrane fuel cells, bipolar plates A2, in *Encyclopedia of Electrochemical Power Sources*, ed. by J. Garche (Elsevier, Amsterdam, 2009), pp. 810–816
30. [www.electrographite.co.za](http://www.electrographite.co.za), cited 21 Aug 2016



31. M. Xiao, Y. Lub, S.J. Wang, Y.F. Zhao, Y.Z. Meng, Poly(arylene disulfide)/graphite nanosheets composites as bipolar plates for polymer electrolyte membrane fuel cells. *J. Power Sources* **160**, 165–174 (2006)
32. C. Du, P. Ming, M. Hou, J. Fu, Q. Shen, D. Liang, Y. Fu, X. Luo, Z. Shao, B. Yi, Preparation and properties of thin epoxy/compressed expanded graphite composite bipolar plates for proton exchange membrane fuel cells. *J. Power Sources* **195**, 794–800 (2010)
33. S.I. Heo, K.S. Oh, J.C. Yun, S.H. Jung, Y.C. Yang, K.S. Han, Development of preform moulding technique using expanded graphite for proton exchange membrane fuel cell bipolar plates. *J. Power Sources* **171**, 396–403 (2007)
34. T. Cheng, *Bipolar plates and plate materials in proton exchange membrane fuel cells (materials properties and performance)* (CRC Press Taylor&Francis Group, Boca Raton, 2010b), pp. 305–313
35. Fuel cells (2014), Available from: <http://www.ingenieurparadies.de>, cited 21 Aug 2016
36. <http://www.ferroceramic.com>, cited 21 Aug 2016
37. C.C. Ku, R. Liepins, *Electrical Properties of Polymers: Chemical Principles* (Hanser Publishing, New York, 1987)
38. S. Allard, *Graphite, Mineral Commodity Profile No.3, Natural Resources Lands*, (Minerals and Petroleum Division)
39. H. Kim, A.A. Abala, C.W. Macosko, Graphene/polymer nanocomposites. *Macromolecules* **43**, 6515 (2010)
40. Integraphene. Nanoplatelets bulk powder. (2013), Available from: <http://integraphene.com>, cited 21 Aug 2016
41. E. Planes, L. Flandin, N. Alberola, Polymer composites bipolar plates for PEMFCs. *Energy Procedia* **20**, 311–323 (2012)
42. B.K. Kakati, D. Deka, Differences in physico-mechanical behaviors of resol(e) and novolac type phenolic resin based composite bipolar plate for proton exchange membrane (PEM) fuel cell. *Electrochim. Acta* **52**, 7330–7336 (2007)
43. B.K. Kakati, D. Sathiyamoorthy, A. Verma, Electrochemical and mechanical behavior of carbon composite bipolar plate for fuel cell. *Int. J. Hydrogen Energy* **35**, 4185–4194 (2010)
44. D. Li, Y. Wang, L. Xu, J. Lu, Q. Wu, Surface modification of a natural graphite/phenol formaldehyde composite plate with expanded graphite. *J. Power Sources* **183**, 571–575 (2008)
45. L. Du, S.C. Jana, Highly conductive epoxy/graphite composites for bipolar plates in proton exchange membrane fuel cells. *J. Power Sources* **172**, 734–741 (2007)
46. L. Du, S.C. Jana, Hygrothermal effects on properties of highly conductive epoxy/graphite composites for applications as bipolar plates. *J. Power Sources* **182**, 223–229 (2008)
47. B. Dursun, F. Yaren, B. Unveroglu, S. Yazici, F. Dundar, Expanded graphite-epoxy-flexible silica composite bipolar plates for PEM fuel cells. *Fuel Cells* **14**, 862–867 (2014)
48. C. Hui, L. Hong-bo, Y. Li, L. Jian-xin, Y. Ki, Study on the preparation and properties of novolac epoxy/graphite composite bipolar plate for PEMFC. *J. Hydrogen Energy* **35**, 3105–3109 (2010)
49. I.U. Hwang, H.Y. Yu, S.S. Kim, D.G. Lee, J.D. Suh, S.H. Lee, B.K. Ahn, S.H. Kim, T.W. Lim, Bipolar plate made of carbon fiber epoxy composite for polymer electrolyte membrane fuel cells. *J. Power Sources* **184**, 90–94 (2008)
50. J.W. Lim, M. Kim, D.G. Lee, Conductive particles embedded carbon composite bipolar plates for proton exchange membrane fuel cells. *Compos. Struct.* **108**, 757–766 (2014)
51. S.H. Liao, M.C. Hsiao, C.Y. Yen, C.C. Ma, S.J. Lee, A. Su, M.C. Tsai, M.Y. Yen, P.L. Liu, Novel functionalized carbon nanotubes as cross-links reinforced vinyl ester/nanocomposite bipolar plates for polymer electrolyte membrane fuel cells. *J. Power Sources* **195**, 7808–7817 (2010)
52. C.Y. Yen, S.H. Liao, Y.F. Lin, C.H. Hung, Y.Y. Lin, C.C. Ma, Preparation and properties of high performance nanocomposite bipolar plate for fuel cell. *J. Power Sources* **162**, 309–315 (2006)
53. P. Katangur, P.K. Patra, S.B. Warner, Nanostructured ultraviolet resistant polymer coatings. *Polym. Degrad. Stab.* **91**(10), 2437–2442 (2006)

54. S. Chunhui, P. Mu, Y. Runzhang, The effect of particle size gradation of conductive fillers on the conductivity and the flexural strength of composite bipolar plate. *J. Hydrogen Energy* **33**, 1035–1039 (2008)
55. T. Arai, Y. Tominaga, S. Asai, M. Sumita, A study on correlation between physical properties and interfacial characteristics in highly loaded graphite-polymer composites. *J. Polym. Sci. Polym. Phys.* **43**, 2568–2577 (2005)
56. M. Wu, L.L. Shaw, On the improved properties of injection-molded, carbon nanotube-filled PET/PVDF blends. *J. Power Sources* **136**, 37–44 (2004)
57. F. Mighri, M.A. Huneault, M.F. Champagne, Electrically conductive thermoplastic blends for injection and compression molding of bipolar plates in the fuel cell application. *Polym. Eng. Sci.* **44**, 1755–1765 (2004)
58. R. Dweiri, J. Sahari, Electrical properties of carbon-based polypropylene composites for bipolar plates in polymer electrolyte membrane fuel cell (PEMFC). *J. Power Sources* **171**, 424–432 (2007)
59. E. Bozkurt, E. Kaya, M. Tanoğlu, Mechanical and thermal behavior of non-crimp glass fiber reinforced layered clay/epoxy nanocomposites. *Compos. Sci. Technol.* **67**, 3394–3403 (2007)
60. S.H. Liao, C.Y. Yen, C.C. Weng, Y.F. Lin, C.C. Ma, C.H. Yang, M.C. Tsai, M.Y. Yen, M.C. Hsiao, S.J. Lee, X.F. Xie, Y.H. Hsiao, Preparation and properties of carbon nanotube/polypropylene nanocomposite bipolar plates for polymer electrolyte membrane fuel cells. *J. Power Sources* **185**, 1225–1232 (2008)
61. B.D. Cunningham, J. Huang, D.G. Baird, Development of bipolar plates for fuel cells from graphite filled wet-lay material and a thermoplastic laminate skin layer. *J. Power Sources* **165**, 764–773 (2007)
62. S.C. Chen, R.D. Chien, P.H. Lee, J.S. Huang, Effects of molding conditions on the electromagnetic interference performance of conductive ABS parts. *J. Appl. Polym. Sci.* **98**, 1072–1080 (2005)
63. E.A. Cho, U.S. Jeon, H.Y. Ha, S.A. Hong, I.H. Oh, Characteristics of composite bipolar plates for polymer electrolyte membrane fuel cells. *J. Power Sources* **125**, 178–182 (2004)
64. B.D. Cunningham, D.G. Baird, Development of bipolar plates for fuel cells from graphite filled wet-lay material and a compatible thermoplastic laminate skin layer. *J. Power Sources* **168**, 418–425 (2007)
65. T. Yang, P. Shi, Study on the mesocarbon microbeads/polyphenylene sulfide composite bipolar plates applied for proton exchange membrane fuel cells. *J. Power Sources* **175**, 390–396 (2008)
66. The fuel cell industry review (2015), available at [www.fuelcellindustryreview.com/](http://www.fuelcellindustryreview.com/), cited 21 Aug 2016
67. S.R. Dhakate, R.B. Mathur, B.K. Kakati, T.L. Dhami, Properties of graphite-composite bipolar plate prepared by compression molding technique for PEM fuel cell. *Int. J. Hydrogen Energy* **32**, 4537–4543 (2007)
68. C. Du, P. Ming, M. Hou, J. Fu, Y. Fu, X. Luo, Q. Shen, Z. Shao, B. Yi, The preparation technique optimization of epoxy/compressed expanded graphite composite bipolar plates for proton exchange membrane fuel cells. *J. Power Sources* **195**, 5312–5319 (2010)
69. S.R. Dhakate, S. Shara, N. Chauhan, R.K. Seth, R.B. Mathur, CNTs nanostructuring effect on the properties of graphite composite bipolar plate. *Int. J. Hydrogen Energy* **35**, 4195–4200 (2010)
70. A. Adloo, M. Sadeghi, M. Masoomi, H.N. Pazhoot, High performance polymeric bipolar plate based on polypropylene/graphite/graphene/nano-carbon black composites for PEM fuel cells. *Renew. Energy* **99**, 867–874 (2016)
71. H. Ishida, Process for preparation of benzoxazine compounds in solventless systems (1996) U.S. patent 5,543,516
72. C. Nair, Advances in addition-cure phenolic resins. *Prog. Polym. Sci.* **29**, 401–498 (2004)
73. S. Rimdusit, H. Ishida, Development of new class of electronic packaging materials based on ternary systems of benzoxazine, epoxy, and phenolics resins. *Polymer* **41**, 7941–7952 (2000)

74. C. Jubsilp, T. Takeichi, S. Rimdusit, Polymerization kinetics, in *Handbook of Benzoxazine Resins*, (Elsevier, Amsterdam, 2011), pp. 157–174
75. H.C. Kuan, C.C.M. Ma, S.M. Chen, Preparation, electrical, mechanical and thermal properties of composite bipolar plate for a fuel cell. *J. Power Sources* **134**, 7–17 (2004)
76. XGScience, Technical Data Sheet of XGnP Grade H Product Characteristics. Available at <http://xgsciences.com/>, cited 21 Aug 2016
77. P. Kasemsiri, S. Hiziroglu, S. Rimdusit, Effect of cashew nut shell liquid on gelation, cure kinetics, and thermomechanical properties of benzoxazine resin. *Thermochim. Acta* **520**, 84–92 (2011)
78. B.S. Rao, A. Palanisamy, Monofunctional benzoxazine from cardanol for bio-composite applications. *React. Funct. Polym.* **71**, 148–154 (2011)
79. S.K. Yadav, J.W. Cho, Functionalized graphene nanoplatelets for enhanced mechanical and thermal properties of polyurethane nanocomposites. *Appl. Surf. Sci.* **266**, 360–367 (2013)
80. G. Gedler, M. Antunes, V. Realinho, J.I. Velasco, Thermal stability of polycarbonate-graphene nanocomposites foams. *Polym. Degrad. Stab.* **97**, 1297–1304 (2012)
81. X. Wang, H. Yang, L. Song, W. Xing, H. Lu, Morphology, mechanical and thermal properties of graphene-reinforced poly(butylene succinate) nanocomposites. *Compos. Sci. Technol.* **72**, 1–6 (2011)
82. S. Sheshmani, A. Ashori, M.A. Fashapoyeh, Wood plastic composite using graphene nanoplatelets. *Int. J. Biol. Macromol.* **58**, 1–6 (2013)
83. H. Ishida, S. Rimdusit, Heat capacity measurement of boron nitride-filled polybenzoxazine. *J. Therm. Anal. Calorim.* **58**, 497–507 (1999)
84. H. Ishida, S. Rimdusit, Very high thermal conductivity obtained by boron nitride-filled polybenzoxazine. *Thermochim. Acta* **320**, 177–186 (1998)
85. T. Haoming, Y. Lin, Thermal conductive PS/graphite composites. *Polym. Adv. Technol.* **20**, 21–27 (2009)
86. B. Agoudjil, L. Ibos, J.C. Majeste, Y. Candau, Y.P. Mamunya, Correlation between transport properties of ethylene vinyl acetate/glass, silver-coated glass spheres composites. *Compos. Part A* **20**, 21–27 (2009)
87. Y. Xu, G. Ray, B.A. Magid, Thermal behavior of single-walled carbon nanotube polymer-matrix composites. *Compos. Part A* **37**, 114–121 (2006)
88. X. Jiang, L.T. Drzal, Exploring the potential of exfoliated graphene nanoplatelets as the conductive filler in polymeric nanocomposites for bipolar plates. *J. Power Sources* **218**, 297–306 (2012)
89. A. Yu, P. Ramesh, M.E. Itkis, E. Bekyarova, R.C. Haddon, Graphite nanoplatelet-epoxy thermal interface material. *J. Phys. Chem. C* **111**, 7565–7569 (2007)
90. C. Min, D. Yu, J. Cao, G. Wang, L. Feng, A graphite nanoplatelet/epoxy composite with high dielectric constant and high thermal conductivity. *Carbon* **55**, 116–125 (2013)
91. X. Huang, C. Zhi, P. Jiang, Toward effective synergetic effects from graphene nanoplatelets and carbon nanotubes on thermal conductivity of ultrahigh volume fraction nanocarbon epoxy composites. *J. Phys. Chem. C* **116**, 23812–23820 (2012)
92. A. Yu, P.R.X. Sun, E. Bekyrova, M.E. Itkis, R.C. Haddon, Enhance thermal conductivity in a hybrid graphite nanoplatelets-carbon nanotube filler for fuel cell applications. *J. Power Sources* **173**, 394–403 (2007)
93. P.H. Maheshwari, R.B. Mathur, T.L. Dhama, Fabrication of high strength and a low weight composite bipolar plate for fuel cell applications. *J. Power Sources* **173**, 394–403 (2007)
94. B. Li, W.H. Zhong, Review on polymer/graphite nanoplatelets nanocomposites. *J. Mater. Sci.* **46**, 5595–5614 (2011)
95. J.K. Kim, N.H. Kim, T. Kuilla, T.J. Kim, K.Y. Rhee, J.H. Lee, Synergy effects of hybrid carbon system on properties of composite bipolar plates for fuel cells. *J. Power Sources* **195**, 5474–5480 (2010)
96. C. Hui, L. Hong-bo, Y. Li, H. Yue-de, Effects of resin type on properties of graphite/polymer composite bipolar plate for proton exchange membrane fuel cell. *J. Mater. Res.* **26**, 2974–2979 (2011)

97. J. Li, M.L. Sham, J.K. Kim, G. Marom, Morphology and properties of UV/ozone treated graphite nanoplatelets/epoxy nanocomposites. *Compos. Sci. Technol.* **67**, 296–305 (2007)
98. J. Wang, X. Wang, C. Xu, M. Zhang, X. Shang, Preparation of graphene/poly (vinyl alcohol) nanocomposites with enhanced mechanical properties and water resistance. *Polym. Int.* **60**, 816–822 (2011)
99. W. Chen, Y. Liu, Q. Xin, Evaluation of a compression molded composite bipolar plate for direct methanol fuel cell. *Int. J. Hydrogen Energ.* **35**, 3783–3788 (2010)

# Electrical Properties of Amorphous Carbon Nitride Thin Films for Pressure Sensor Applications

Masami Aono and Naoyuki Tamura

## 1 Amorphous Carbon Nitride

Primary interest in bulk carbon nitride was initiated in 1989 [1, 2]. Liu and Cohen predicted a theoretical material  $\beta$ - $C_3N_4$  based on  $Si_3N_4$ . The bulk modulus of  $\beta$ - $C_3N_4$  was estimated to be equal to that of the diamond via theoretical calculations. Subsequently, several research groups attempted to synthesize this hypothetical material.

$\beta$ - $C_3N_4$  comprises carbon with a  $sp^3$  bonding state and nitrogen with a plane configuration, as shown in Fig. 1a. It is well known that the most stable state of carbon is a graphite structure that comprises only the  $sp^2$  bonding configuration since its  $sp^3$  bonding configuration is metastable. Similarly, ab initio calculations of the gas-phase  $C_3N_4$  molecules indicate that a linear chain containing  $sp^2$ -hybridized nitrogen is more stable than its planar form and that the pyramidal central nitrogen arrangement is even less stable. Thus,  $\beta$ - $C_3N_4$ , whose size is sufficiently large to allow the evaluation of its physical properties, was never obtained.

Apart from  $\beta$ - $C_3N_4$ , various  $C_3N_4$  structures have been proposed and studied, such as  $\alpha$ - $C_3N_4$  (based on  $\alpha$ - $Si_3N_4$ ) [3], cubic  $C_3N_4$  [4], a  $C_3N_4$  defective zinc blende structure with carbon vacancies [5], and two graphite-like forms [4, 6]. Graphite-like  $C_3N_4$  comprises a  $sp^2$  carbon and  $sp^2$  trigonal planar nitrogen. The lattice constants and bulk moduli for some of the  $C_3N_4$  possible phases are listed in Table 1. Energetically the graphite-like  $C_3N_4$  is the most stable geometry. Among them, graphitic- $C_3N_4$  (g- $C_3N_4$ ) is one of the materials through which acquisition is possible [6]. This is easily obtained from melamine and related organic materials via thermal decomposition methods. These raw materials share the common features of CNH networks. Under thermal conditions, H is isolated from CNH triangle

---

M. Aono (✉) • N. Tamura

Department of Materials Science and Engineering, National Defense Academy,  
1-10-20 Hashirimizu, Yokosuka, Kanagawa 239-8686, Japan  
e-mail: [aono@nda.ac.jp](mailto:aono@nda.ac.jp)

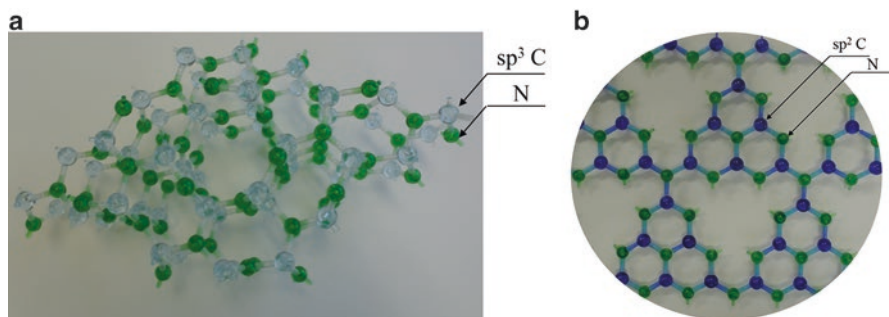


**Fig. 1** Structure of  $\beta$ - $C_3N_4$  (a) and  $g$ - $C_3N_4$  (b)

**Table 1** Equilibrium structural parameters, lattice constants, bulk moduli, and shear moduli for some of the  $C_3N_4$  possible phases

	Lattice constant ( $\text{\AA}$ )		Bulk modulus (GPa)
	a	c	
$\beta$ - $C_3N_4$ [4]	6.41	2.40	437[4] (451 [3])
$\alpha$ - $C_3N_4$ [3]	6.47	4.71	425
Cubic- $C_3N_4$ [3]	5.40		496
Defect zinc blend $C_3N_4$ [4]	3.43		425 (448 [3])
Graphite-like rhombohedral- $C_3N_4$ [4]	4.11		51
Graphite-like (graphitic) $C_3N_4$ [6]	2.52–2.72 <sup>a</sup> ( $C_6N_8$ )		
diamond	3.57		443 <sup>a</sup>

<sup>a</sup>Experimental data

structures. Then, a C-N network is formed in a two-dimensional (2D) sheet, as shown in Fig. 1b. Nowadays,  $g$ - $C_3N_4$  is a well-known photocatalytic material [7].

On the other hand, almost all carbon nitride films prepared via traditional vapor deposition methods using plasma are amorphous phases consisted from several bonding structures. Typical bonding structures included three or four of C-C bonding states, nine of C-N bonding states, and two of N-N bonding states, shown in Fig. 2. Amorphous carbon nitride is based on the C-C bonding structures. Carbon forms four  $\sigma$  bonds with carbon as in diamond. The  $sp^1$  configuration is little in C-C bonding structures. The  $sp^2$  configuration of carbon is based on aromatic rings and chain structures. The single bond of C-N includes three competing structures. Nitrogen forms three  $\sigma$  bonds with the remaining two electrons in a lone pair. Nitrogen at a fourfold coordinated substitutional site  $N_4^+$  uses four electrons in  $s$  bonds with the remaining unpaired electron available for doping. A variant of this site is the  $N_4^+-C_3^-$  pair. The remaining configurations correspond to  $\pi$  bonds. Nitrogen can substitute for carbon in aromatic rings. Nitrogen bonded to three neighbors in a sixfold ring and a fivefold ring. The other variants of  $\pi$  bonding are a double bond unit with nitrogen twofold coordinated. The triple bond with an isolated lone pair acts as a termination of the amorphous networks. Because of a variety of bonding structures, amorphous carbon nitride films with similar nitrogen

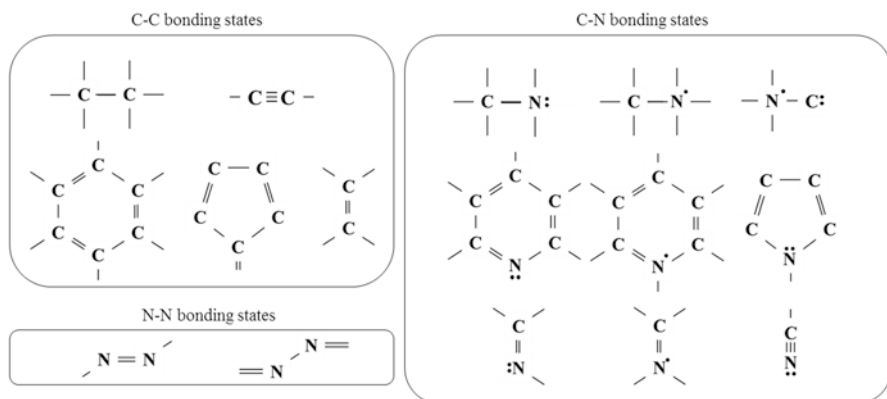


**Fig. 2** Possible bonding configurations of C-C, C-N, and N-N in  $a\text{-CN}_x$  films. Lines represent bonds, dots represent unpaired electrons, and two dots represent lone pairs

concentrations exhibit various properties in different cases. In recent years, several interesting properties have been revealed in the amorphous carbon nitride films, such as low friction coefficient [8, 9], photo response [10, 11], and pressure response [12].

Amorphous carbon nitride films have been prepared using chemical and physical vapor depositions, such as plasma-enhanced chemical vapor deposition (PECVD), sputtering, and laser ablation method. Amorphous carbon nitride films prepared by these methods are categorized into two types of hydrogenated and hydrogen-free carbon nitrides according to raw materials. Each type is different in maximum nitrogen concentration, chemical bonding states, and physical and chemical properties. Thus, amorphous carbon nitrides possess wide characteristics.

For instance, hydrogenated amorphous carbon nitride,  $a\text{-CN}_x\text{:H}$  (this is also described  $a\text{-C:N}$ ,  $\text{DLC:N}$ , and  $\text{ta-C:N}$ . DLC means diamond-like carbon and  $\text{ta-C:N}$  means nitrogen incorporation tetrahedral amorphous carbon), is synthesized from  $\text{CH}_4$ ,  $\text{C}_2\text{H}_6$ , and/or  $\text{NH}_3$  gases [13–15]. Hydrogen in carbon nitride acts to terminate dangling bonds and/or increase the chain structure, such as polymer chains. Thus, the maximum nitrogen concentration is up to 0.3 in almost all  $a\text{-CN}_x\text{:H}$  types. The  $\text{sp}^3$ -rich  $a\text{-CN}_x\text{:H}$  films show high hardness, because of their high  $\text{sp}^3/\text{sp}^2$  bonding ratio [16]. The polymer-like structured  $a\text{-CN}_x\text{:H}$  films show photoluminescence as well as certain polymers [17]. Investigating the electrical properties, the  $a\text{-CN:H}$  films tend to be an insulator.

Furthermore, the hydrogen-free carbon nitride films,  $a\text{-CN}_x$ , are grown from bulk carbon sources and pure nitrogen gas. The  $a\text{-CN}_x$  films have a wider range of nitrogen concentration compared with the  $a\text{-CN}_x\text{:H}$  films. In addition, they provide relatively high thermal stability [18], low friction coefficient [19], and so on. Thus, one of the practical applications of  $a\text{-CN}_x$  is to be used as a solid lubricant. The hydrogen-free carbon nitrides have a wide range of resistivity from semiconductors to insulators [20]. Optical bandgap and electrical resistivity are obviously dependent on the

nitrogen concentration. Moreover, a-CN<sub>x</sub> presents photoconductivity behavior [10]. These properties are possible to assist in designing solar cells with variable band-gap. Recently, we discovered the photoinduced deformation in a-CN<sub>x</sub> prepared by reactive sputtering [11]. This phenomenon includes a change in the form of the films by irradiation of visible light.

We measured the electrical resistive response of the hydrogen-free a-CN<sub>x</sub> prepared by sputtering in this chapter. The resistance of the a-CN<sub>x</sub> changes with the ambient pressure and the gas type. These gas responses are associated with the basic properties of gas sensors and gas pressure sensors.

## 2 Gas Pressure Sensors

Nowadays, gas pressure sensors are utilized in various electrical devices and machines as well as maintenance of vacuum process. For instances, gas pressure sensors have been used to control the compressor of air conditioners and refrigerators, altimeters in watches and mobile phones, and pressure sensors for safety operations in airplanes and satellites. A miniaturization of gas pressure sensors is required. Miniature vacuum sensors offer significant advantages over conventional vacuum gauges such as higher measurement sensitivity, lower power consumption, smaller volume, and lower fabrication costs.

Pirani vacuum gauges have been widely used in vacuum equipment for pressure measurement because they are low cost and easy to operate with high sensitivity for long-term monitoring. Using micromachining technology, various micro-Pirani vacuum gauges have been developed. A single crystal silicon micro-Pirani vacuum gauge is one of the promising devices because it can be easily integrated into hermetically sealed vacuum packages of microelectromechanical systems (MEMS) for in situ pressure measurement [21].

A diaphragm sensor has also several advantages, such as obtaining absolute pressure value, simple structure, and high stability. Typical MEMS-type diaphragm gauge has been made from silicon. For the vacuum measuring realized by MEMS-type friction gauges, the methods using the influence of the gas pressure on the resonant frequency of an oscillating system are applied [22]. There are many variously shaped oscillators: tuning fork-shaped crystal quartz oscillator, optical fiber cantilever, and small resonators.

The piezoelectric sensing mechanism, which translates a mechanical displacement into an electrical signal, has been widely used because of its advantages, such as feasible preparation, low cost, and easy signal collection. The piezo-resistive effect has been widely used in the MEMS sensor field to minimize the structure of the devices. Furthermore, due to the capacitive and resistive sensing mechanisms, the piezoelectric sensors have also potential applications as pressure sensors.

Miniaturization of the gas pressure sensor is one of the important requirements to achieve a smaller-sized device with higher performance. Thus, development of new materials for optimization of nano-sized gas pressure sensors has been



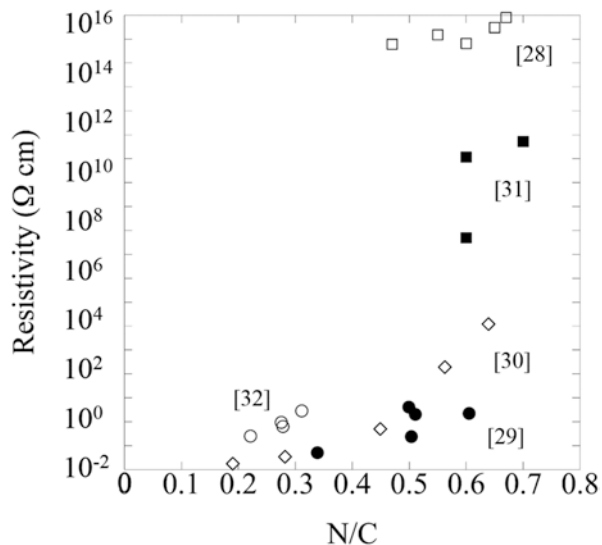
accelerated. Carbon nanotubes (CNTs) and graphene are considered to be candidates for sensor materials due to their high surface-to-volume ratio. In addition, CNT and nanoparticle (NP) hybrid nanostructures can be selectively sensitive toward various species of gas or vapor. Thus, the gas pressure sensor with obvious response in electrical resistance or capacitance has been proposed [23–27].

### 3 Electrical Properties of Hydrogen-Free Amorphous Carbon Nitride Thin Films

Electrical properties of hydrogen-free amorphous carbon nitride ( $a\text{-CN}_x$ ) films are shown in this section. As mentioned, amorphous carbon nitride has a wide range of properties depending on the deposition method. Among them, the  $a\text{-CN}_x$  films prepared by sputtering show semiconducting to insulating behaviors. Figure 3 shows the electrical resistivity of  $a\text{-CN}_x$  films deposited by sputtering methods as a function of the nitrogen concentration. In contrast,  $a\text{-CN:H}$  films deposited by CVD methods have relatively higher resistivity.

As shown in Fig. 3, the nitrogen concentration does not seem to affect electrical resistivity of  $a\text{-CN}_x$  films prepared by sputtering methods [28–32]. When the electrical resistivity is measured for the films with equal amounts of nitrogen concentration, the electrical resistivity of a certain film is a few orders of magnitude greater than the other one. This is due to the fact that the  $sp^2/sp^3$  bonding ratio is different. Basically, resistivity increases with increasing the nitrogen concentration and decreasing the  $sp^2/sp^3$  bonding ratio. The  $sp^2/sp^3$  bonding ratio, as well as the nitrogen concentration, is also controlled by the deposition method and condition. However, they are

**Fig. 3** Various electrical resistivities of  $a\text{-CN}_x$  films prepared using sputtering methods as a function of nitrogen concentration  $N/C$  (Data from Aono et al. [28] (*open square*), Monclus et al. [29] (*solid circle*), Lazar et al. [30] (*open diamond*), Lanter et al. [31] (*solid square*), and Aono et al. [32] (*open circle*))



not completely independent. Dos Santos and Alvarez reported that the  $sp^3$  bonding fraction increases with increasing the nitrogen concentration [33].

For the  $a-CN_x$  films deposited by reactive sputtering, the deposition temperature is one of the key factors affecting the nitrogen concentration and  $sp^2/sp^3$  bonding ratio. At higher temperatures, a decrease in nitrogen concentration and an increase in  $sp^2/sp^3$  ratio are obtained for the deposited film, because the graphitic structures are the most stable states for the carbon network [34]. Hence, the resistivity of the  $a-CN_x$  films decreases with increasing the temperature, as shown in Fig. 4.

Here, we mention the electrical path of the present  $a-CN_x$  films growth by reactive sputtering. The  $a-CN_x$  possesses a columnar structure as shown in Fig. 5. An internal tissue of the columns is amorphous structure. A column interface usually includes large amounts of defects and dangling bonds. Hence, the samples' resistivity increases with decreasing the diameter of the columns. Although the resistivity of the  $a-CN_x$  films increases with increasing the spin density estimated from the electron spin resonance (ESR) signal, which is equal to the defect density, the spin density decreases depending on an increase in the diameter of the column (Fig. 6).

**Fig. 4** Electrical resistivity of  $a-CN_x$  films as a function of deposition temperature

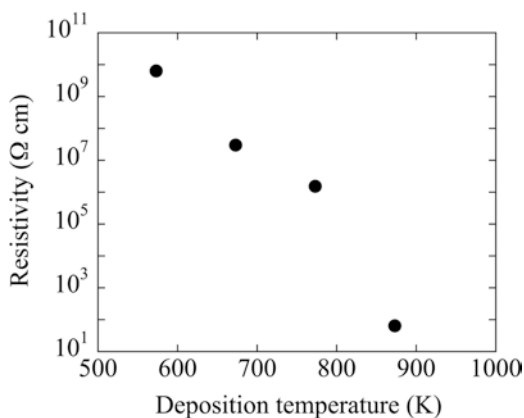


**Fig. 5** A cross-sectional scanning electron microscope (SEM) images of  $a-CN_x$  films

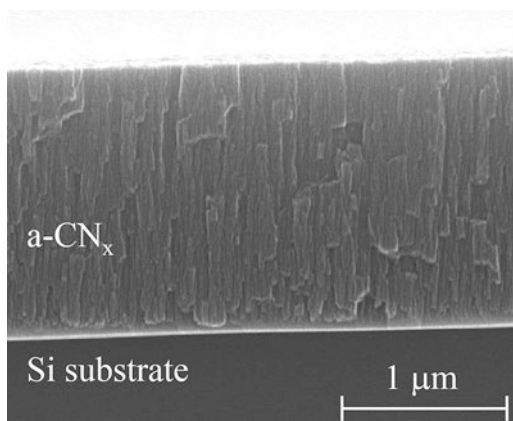


**Fig. 6** Spin density obtained from ESR as a function of the diameter of a-CN<sub>x</sub> columns

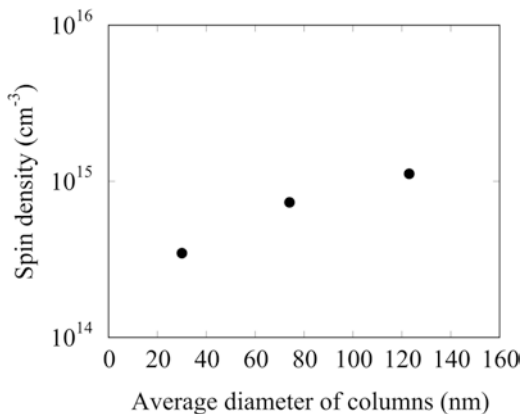
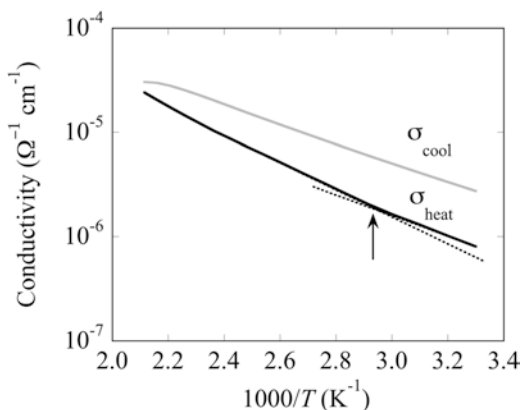


**Fig. 7** Electrical conductivity of a-CN<sub>x</sub> films as a function of the measurement temperature. The conductivity of a-CN<sub>x</sub> obtained from the *I-V* measurement with the heating ( $\sigma_{\text{heat}}$ ) and cooling processes ( $\sigma_{\text{cool}}$ ) in vacuum



This result suggests that the dangling bonds of the columnar a-CN<sub>x</sub> relatively concentrate in the center of the columns rather than the interfaces, i.e., the current path is likely an interface of the columns. In fact, the resistivity of horizontal direction to the column is a few orders of magnitude greater than that in the vertical direction [35]. As far, growth mechanisms of the columnar structured a-CN<sub>x</sub> have been not cleared yet.

The effect of ambient temperature on the electrical conductivity – defined as the inverse of resistivity – of a-CN<sub>x</sub> prepared by sputtering is shown in Fig. 7. A hysteresis loop is shown for the conductivity of a-CN<sub>x</sub> on the *I-V* measurement with the heating ( $\sigma_{\text{heat}}$ ) and cooling processes ( $\sigma_{\text{cool}}$ ) in the vacuum. In addition, an area of the hysteresis loops depends on the initial conductivity [20]. The presented film in Fig. 7 was sputtered at 873 K.

A cause of the hysteresis is that  $\sigma_{\text{cool}}$  is higher compared with  $\sigma_{\text{heat}}$ . The initial conductivity before the heating process and the final conductivity after the cooling process are different at RT. After a few hours, the resistivity almost recovers the initial value. These results suggest that the energy level of electron might not fall to

the initial state after the heating process because amorphous materials have localized states. In addition, it will take a few hours for the electrons to fall from the excitation state to the initial state.

The  $\sigma_{\text{cool}}$  values for all samples yield a linear relationship with the temperature during the cooling process. In contrast, the  $\sigma_{\text{heat}}$  clearly shows an inflection point, indicated by the arrow in Fig. 7. The inflection temperature decreased from 370 to 333 K with increasing the deposition temperature from 573 to 873 K. The change in the slope is also attributed to the change of the energy state of the conductive electrons.

## 4 Influences on the Electrical Resistance of the Ambient Pressure

On the a-CN<sub>x</sub> films prepared by reactive sputtering, the gas pressure response of the electrical resistance value was revealed [36]. At this time, the resistance value was dropped to about 60 MΩ with decreasing the ambient pressure in the chamber from the atmospheric pressure to 2 Pa. The resistance response of about 600 Ω/Pa was obtained from the exposure area of 0.03 mm<sup>2</sup>. As compared with several gas pressure devices, a-CN<sub>x</sub> has a relatively high sensitivity to the gas pressure. Moreover, the sample structure was very simple as presented later in the next paragraph. Then, we investigated the pressure response of resistance in the a-CN<sub>x</sub> films under various gases.

Figure 8 shows the experimental setup for the *I-V* measurement system. The flow gas was chosen as N<sub>2</sub>, O<sub>2</sub>, Ar, and CO<sub>2</sub>, which are the main components of the atmosphere. A sample structure consists of the a-CN<sub>x</sub> film on the glass substrate and gold (Au) electrodes with gap type, as shown in Fig. 9. The electrodes were

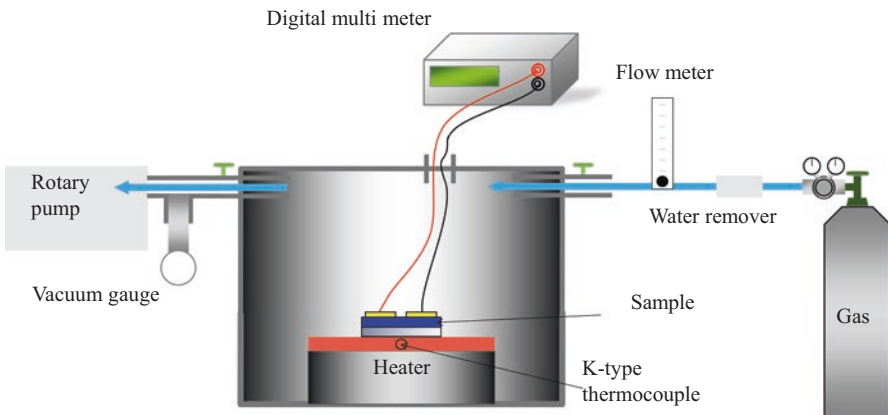
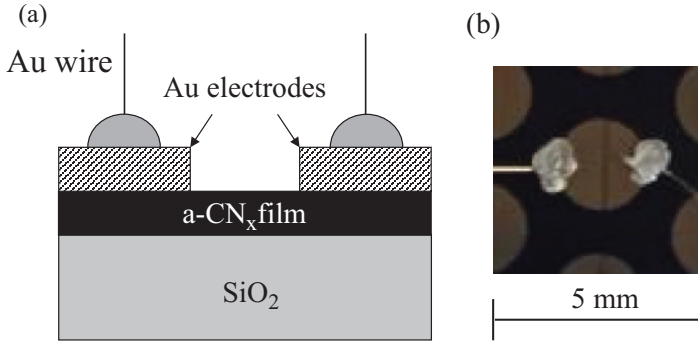


Fig. 8 Schematic illustration of experimental setup for *I-V* measurement



**Fig. 9** A sample structure for  $I$ - $V$  measurement: (a) schematic of the sample, (b) photograph of the sample

formed using the vacuum evaporation method. The width of the gap was  $20\ \mu\text{m}$ . The thickness of the  $\text{a-CN}_x$  film was about  $1\ \mu\text{m}$ . Before the gas exposure, the residual gas in the chamber was evacuated using a rotary pump. The base pressure was about  $2\ \text{Pa}$ . The measurement temperature was kept constant at  $303\ \text{K}$  using a temperature controller unit.

As shown in Fig. 10, the resistance response of  $\text{a-CN}_x$  to ambient pressures is observed in different gas conditions. In all cases, resistance decreases rapidly following the gas injection, and then it increases following the gas evacuation. The resistance response behavior does not depend on the gas type. Compared to the Pirani gauge response (Fig. 10a), the electrical resistance change of  $\text{a-CN}_x$  due to pressure variation is slow. In addition, the response speed for the gas injection is higher than the gas evacuation. Therefore, the resistance response of  $\text{a-CN}_x$  might originate from physical behaviors and not from the chemical reaction between  $\text{a-CN}_x$  and the gas molecules. The resistance change by chemical reactions between the gas molecules and materials is known for some semiconductor metal oxides (MOX), such as  $\text{SnO}_2$  and  $\text{TiO}_2$  [38–40]. Interactions of gas molecules with oxide surfaces can be accompanied by charge exchange, which in turn can affect the MOX electrical resistance. This interaction usually requires a significant activation energy, provided by external heating. On the other hand, the resistivity change by the physical interaction between the gas molecules and materials likely causes deformation of bonding structures, similar to piezoelectricity.

In order to compare the amplitude of each resistance response, the pressure sensitivity factor  $S$  is described by the following equation:

$$S = \left[ (R_0 - R_i) / R_0 \right] \times 100 \quad (1)$$

where  $R_0$  is a resistance under the vacuum state ( $\sim 2\ \text{Pa}$ ), and  $R_i$  is a resistance under the gas states ( $20\ \text{Pa}$ ).

**Fig. 10** (a) Process pressure, (b) resistance response of a-CN<sub>x</sub> films during exposure to N<sub>2</sub>, Ar, O<sub>2</sub>, and CO<sub>2</sub> (This figure reproduced with permission from reference [37])

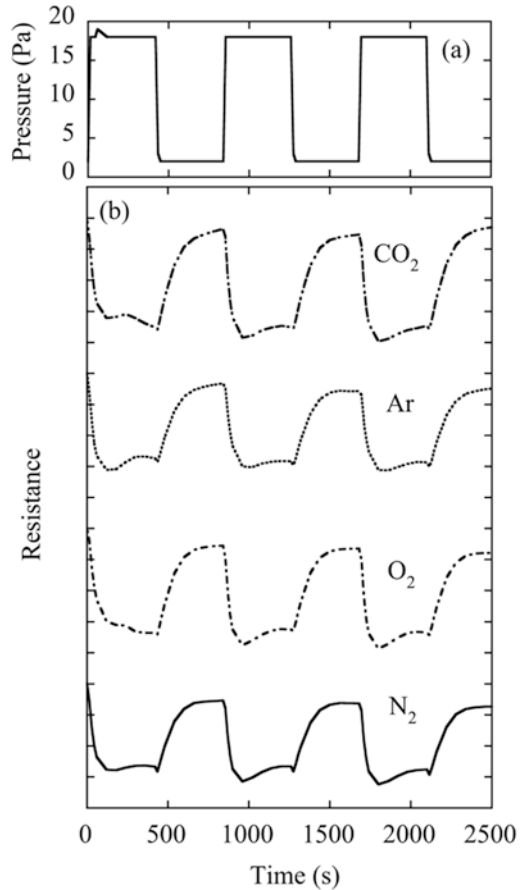
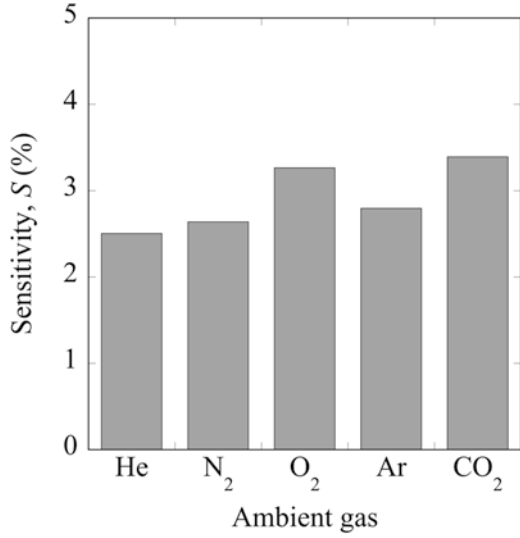


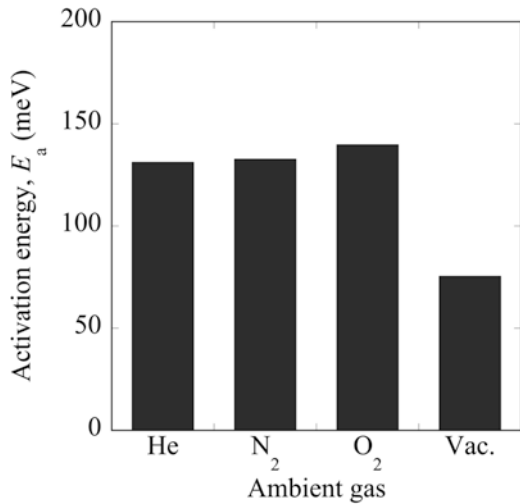
Figure 11 shows the pressure sensitivity factor  $S$  as a function of the gas type. A distinct response in the electrical resistance depending on the gas type was observed. Except for O<sub>2</sub>, the  $S$  value coincides with a hard sphere having the molecule diameter. If no chemical interaction is assumed between the gas molecules and a-CN<sub>x</sub>, a large deformation of the amorphous network might be induced by increasing the size of the gas molecules. Regarding the resistivity response in an O<sub>2</sub> atmosphere, the electronic states of a-CN<sub>x</sub> might be affected by the diffusion of O<sub>2</sub>, which means a change in the electrical state of host materials influenced by guest molecules in fullerene and clathrates [41–43].

A temperature-dependent resistance test was carried out for various gas types. The temperature range was chosen from RT to 337 K, in which the chemical bonding structure of a-CN<sub>x</sub> is not affected. Figure 12 shows the activation energy  $E_a$  under different gas types estimated from Arrhenius plots. As compared with  $E_a$  in the vacuum condition,  $E_a$  increases for gas injection. In this temperature region, the hopping conductivity is predominance in a-CN<sub>x</sub>. Thus, activation energy  $E_a$  gives the following equation [44, 45]:

**Fig. 11** Pressure sensitivity factor of a-CN<sub>x</sub> films as a function of the gas type



**Fig. 12** Activation energy of a-CN<sub>x</sub> films under different gas types



$$E_a = \frac{3}{4\pi R_D^3 N(E_F)} \tag{2}$$

where  $R_D$  is a distance between two different energy levels. When the density of states around Fermi energy  $N(E_F)$  is a constant,  $E_a$  is inversely proportional to  $R_D$ , which means a decrease in  $R_D$  results in an increase in  $E_a$ .

The density of a-CN<sub>x</sub>, which is estimated using the X-ray reflection analysis, is approximately 1.6 g/cm<sup>3</sup>. This value is quite low compared with diamond, 3.51 g/cm<sup>3</sup>, and graphite, 2.26 g/cm<sup>3</sup>. Consequently, the ambient gas molecules likely

diffuse into a-CN<sub>x</sub>. To confirm an expansion in the bonding length of a-CN<sub>x</sub> by diffusion of the gas molecules, X-ray diffraction analysis was carried out. As a result, a small peak characteristic of the amorphous phase shifted slightly toward a lower angle. Simultaneously, the density of a-CN<sub>x</sub> becomes higher depending on the N<sub>2</sub> pressure, as shown in Fig. 13. Measurements confirmed a change in the range of gas pressure with resistance.

The sensitivity of a-CN<sub>x</sub> films increased with increasing the diameter of the columns, as shown in Fig. 14. This result suggests that ambient gas molecules diffuse into the center of columns and temporarily change the bonding structure. The maximum gas sensitivity of about 3 % is obtained from the exposure area of 0.03 mm<sup>2</sup>. As mentioned previously, the dangling bonds of columnar a-CN<sub>x</sub> relatively concentrate in the center of the columns rather than the interfaces. Thus, the diffusing

**Fig. 13** Density of a-CN<sub>x</sub> estimated from XRR as a function of the ambient gas pressure. The ambient gas was N<sub>2</sub>

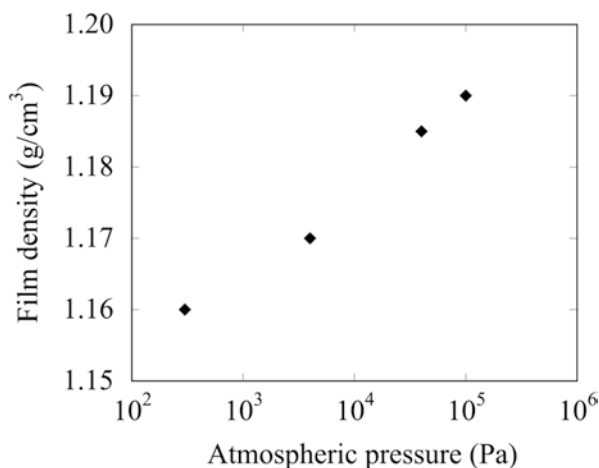


**Fig. 14** Pressure sensitivity factor of a-CN<sub>x</sub> films as a function of the diameter of the columns

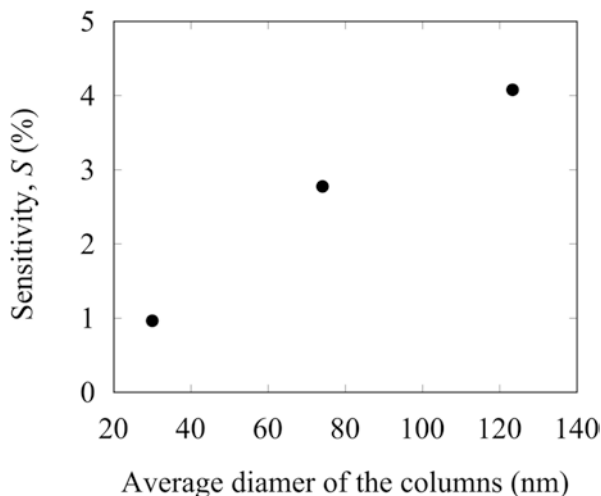
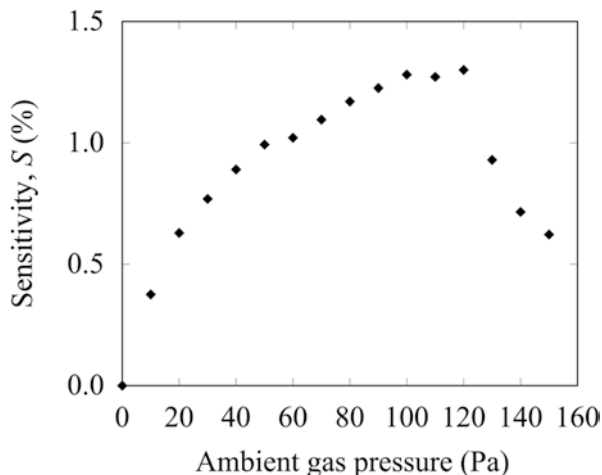




**Fig. 15** Pressure sensitivity factor of a-CN<sub>x</sub> as a function of the ambient gas pressure



molecules can easily penetrate into the center of the columns. However, termination of the dangling bonds has not been confirmed experimentally.

In order to investigate the response range to the gas pressure, the electrical resistance of the a-CN<sub>x</sub> films was measured with a cyclical process of gas injection and evacuation using N<sub>2</sub> gas. Figure 15 shows the pressure sensitivity factor  $S$  under gas injection. With increasing the ambient gas pressure,  $S$  reached a constant value. At higher pressures, the a-CN<sub>x</sub> films became unresponsive to the pressure. The maximum response pressure of a highly sensitive sample was shifted toward a higher pressure. In addition, the sample, which lost the sensitivity, regained it by thermal annealing. From these results, it is inferred that the a-CN<sub>x</sub> has a limit for the number of diffusing gas molecules. Beyond a certain pressure, the deformation of bonding induced by gas diffusion does not return to the initial state under a vacuum.

For higher pressure, the electrical resistance increases following the gas injection, and then it decreases following the gas evacuation. This is an opposite trend to the response at low pressure. An inflection point of the pressure is determined by the diameter of the columns. For the pressure higher than atmospheric pressure, the electrical resistance response of a-CN<sub>x</sub> films is also observed.

## 5 Conclusion

Amorphous carbon nitride films are considered to belong to the carbon material family with fascinating properties. In this chapter, we presented the electrical resistance response of hydrogen-free amorphous carbon nitride (a-CN<sub>x</sub>) depending on the ambient pressure. The a-CN<sub>x</sub> films have a columnar structure consisting of amorphous tissue. The electrical resistance response varies with the change in the bonding structure by diffusion of the gas molecules into the columns. The a-CN<sub>x</sub> sensor device with gap electrodes obtained a relatively high response in various gases. Thus, the a-CN<sub>x</sub> has a high potential value as a material for an economical nano-sized pressure sensor.

## References

1. A.Y. Liu, M.L. Cohen, *Science* **245**, 841 (1989)
2. A.Y. Liu, M.L. Cohen, *Phys. Rev. B* **41**, 10727 (1990)
3. D.M. Teter, R.J. Hemley, *Science* **271**, 53 (1996)
4. A.Y. Liu, R.M. Wentzcovitch, *Phys. Rev. B* **50**, 10362 (1994)
5. J. Martin-Gil, F.J. Martin-Gil, M. Sarikaya, M. Qian, M. José-Yacamán, A. Rubio, *J. Appl. Phys.* **81**, 2555 (1997)
6. A. Thomas, A. Fischer, F. Goettmann, M. Antonietti, J.-O. Müller, R. Schögl, J.M. Carlsson, *J. Mater. Chem.* **18**, 4893 (2008)
7. J. Wen, J. Xie, X. Chen, X. Li, *Appl. Surf. Sci.* **391**, 72 (2016)
8. R. Wäsche, M. Hartelt, U. Springborn, K. Bewilogua, M. Keunecke, *Wear* **269**, 816 (2010)
9. K.H. Lee, R. Ohta, H. Sugimura, Y. Inoue, O. Takai, H. Sugimura, *Thin Solid Films* **475**, 308 (2005)
10. M. Aono, T. Goto, N. Tamura, N. Kitazawa, Y. Watanabe, *Diam. Relat. Mater.* **20**, 1208 (2011)
11. M. Aono, T. Harata, N. Kitazawa, Y. Watanabe, *Diam. Relat. Mater.* **41**, 20 (2014)
12. N. Tamura, M. Aono, H. Abe, N. Kitazawa, Y. Watanabe, *Jpn. J. Appl. Phys.* **54**, 041401 (2015)
13. S. Kundoo, K.K. Chattopadhyay, A.N. Banerjee, S.K. Nandy, *Vacuum* **69**, 495 (2003)
14. M. Othman, R. Ritikos, N.H. Khanis, N.M.A. Rashid, S.M. Ab Gani, S.A. Rahman, *Thin Solid Films* **529**, 439 (2013)
15. D. Dumitriu, P.E. Schmid, R. Sanjinés, A. Karimi, *Diam. Relat. Mater.* **11**, 1905 (2002)
16. D. Bootkul, B. Supsempol, N. Saenphinit, C. Armwit, S. Intarasiri, *Appl. Surf. Sci.* **310**, 284 (2014)
17. G. Fanchini, P. Mandracci, A. Tagliaferro, S.E. Rodil, A. Vomiero, G. Della Mea, *Diam. Relat. Mater.* **14**, 928 (2005)
18. J.J. Li, W.T. Zheng, Z.S. Jin, T.X. Gai, G.R. Gu, H.J. Bian, C.Q. Hu, *Vacuum* **72**, 233 (2004)
19. D.F. Wang, K. Kato, *Wear* **217**, 307 (1998)
20. N. Tamura, M. Aono, T. Harata, H. Kishimura, N. Kitazawa, Y. Watanabe, *Jpn. J. Appl. Phys.* **53**, 02BC03 (2014)
21. W. Jiang, X. Wang, J. Zhang, *Sensors Actuators A* **163**, 159 (2010)
22. A. Górecka-Drzazga, *Vacuum* **83**, 1419 (2009)
23. M.A.S.M. Haniff, S.M. Hafiz, K.A.A. Wahid, Z. Endut, H.W. Lee, D.C.S. Bien, I.A. Azid, M.Z. Abdullah, N.M. Huang, S.A. Rahman, *Sci. Rep.* **5**, 14751 (2015)
24. R.V. Gelamo, F.P. Rouxinol, C. Verissimo, A.R. Vaz, M.A. Bica de Moraes, S.A. Moshkalev, *Chem. Phys. Lett.* **482**, 302 (2009)
25. A.S. Chauhan, A. Nogaret, *Appl. Phys. Lett.* **102**, 233507 (2013)
26. E.S. Snow, F.K. Perkins, E.J. Houser, S.C. Badescu, T.L. Reinecke, *Science* **307**, 1942 (2005)
27. Y.-M. Chen, S.-M. He, C.-H. Huang, C.-C. Huang, W.-P. Shih, C.-L. Chu, J. Kong, J. Li, C.-Y. Su, *Nanoscale* **8**, 3555 (2016)
28. M. Aono, S. Nitta, T. Iwasaki, H. Yokoi, T. Itoh, S. Nonomura, *Mater. Res. Soc. Symp. Proc.* **565**, 291 (1999)
29. M.A. Monclus, D.C. Cameron, A.K.M.S. Chowdhury, *Thin Solid Films* **341**, 94 (1999)
30. G. Lazar, B. Bouchet-Fabre, K. Zellama, M. Clin, D. Ballutaud, C. Godet, *J. Appl. Phys.* **104**, 073534 (2008)
31. W.C. Lanter, D.C. Ingram, C.A. DeJoseph Jr., *Diam. Relat. Mater.* **15**, 259 (2006)
32. M. Aono, T. Takeno, T. Takagi, *Diam. Relat. Mater.* **63**, 120 (2016)
33. M.C. dos Santos, F. Alvarez, *Phys. Rev. B* **58**, 13918 (1998)
34. N. Tamura, M. Aono, H. Kishimura, N. Kitazawa, Y. Watanabe, *Jpn. J. Appl. Phys.* **51**, 121401 (2012)
35. M. Aono, S. Kikuchi, N. Tamura, N. Kitazawa, Y. Watanabe, S. Nitta, *Phys. Status Solid C* **7**, 797 (2010)

36. N. Tamura, M. Aono, H. Kishimura, N. Kitazawa, Y. Watanabe, *Jpn. J. Appl. Phys.* **53**, 11RA09 (2014)
37. M. Aono, ed. By N. Ohtake *Fundamentals and Applications of DLC Films* p. 210 (CMC press, 2016) in Japanese
38. H.-C. Lee, W.-S. Hwang, G.-B. Lee, Y.-M. Lu, *Appl. Surf. Sci.* **252**, 3502 (2006)
39. F. Hossein-Babaei, M. Keshmiri, M. Kakavand, T. Troczynski, *Sensors Actuators B* **110**, 28 (2005)
40. A. Sklorz, S. Janßen, W. Lang, *Sensors Actuators B* **180**, 43 (2013)
41. O.P. Dmytrenko, N.P. Kulish, Y.I. Prylutsky, T.V. Rodionova, T.D. Shatniy, U. Ritter, L. Carta-Abelmann, P. Scharff, T. Braun, *Thin Solid Films* **516**, 7937 (2008)
42. L. Fírllej, A. Zahab, *Phase Transit.* **76**, 247 (2003)
43. B. Liu, X. Jia, H. Sun, B. Sun, Y. Zhang, H. Liu, L. Kong, D. Huo, H. Ma, *J. Solid State Chem.* **233**, 363 (2016)
44. N.F. Mott, *Phil. Mag.* **19**, 835 (1969)
45. M.F. Mott, E.A. Davis, *Electronic processes in non-crystalline materials*, p. 39 (Oxford University Press, 1979)

**Part III**  
**Organic Synthesis and Physical Chemistry**

# Combination of Cross-Coupling and Metal Carbene Transformations for the Development of New Multicomponent Reactions

Lisa Moni, Andrea Basso, and Renata Riva

## 1 Introduction

### 1.1 Metal-Stabilized Carbenes

The most common reactive intermediates in organic chemistry are charged species, such as carbocations or carbanions. However, other two important groups of reactive intermediates exist: (1) radicals, in which the trivalent carbon center has a single nonbonding electron, and (2) carbenes, with two nonbonding electrons on their divalent carbon center. Free carbenes are able to react with organic compounds in several ways, but typically in an unselective and uncontrollable fashion [1]. Highly selective transformations, however, can be achieved by modulating the high reactivity of free carbenes through their association with suitable metal complexes. Generally, the reactivity profile of metal carbenes depends on the electronic character of this carbon center [1, 2], which is governed by:

1. The nature of the metal catalyst. The most effective catalysts for metal carbenoids have been found to be rhodium(II) complexes, although copper(I), palladium(0), and ruthenium complexes can be used as well.
2. The nature of the substituents adjacent to the carbene carbon. Carbenoid intermediates can be classified into three major groups according to the substituents: acceptor, acceptor/acceptor, and donor/acceptor (Fig. 1).

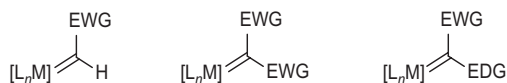
The first two groups are highly reactive species as the electron-withdrawing substituents (EWG, acceptor groups) flank the electrophilic metal carbene center. On the other hand, donor-/acceptor-substituted carbenes are in general more chemoselective because the donor group (EDG) modulates their reactivity.

---

L. Moni (✉) • A. Basso • R. Riva

Department of Chemistry and Industrial Chemistry, University of Genova,  
via Dodecaneso 31, 16146 Genoa, Italy  
e-mail: [lisa.moni@unige.it](mailto:lisa.moni@unige.it)

**Fig. 1** The three classes of metal-stabilized carbenes



## 1.2 Preparation of Metal-Stabilized Carbenes

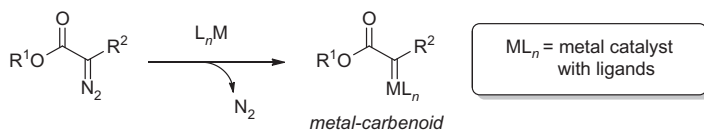
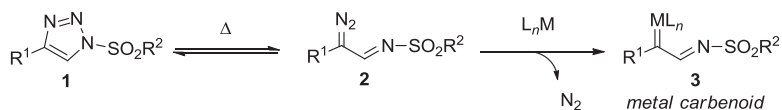
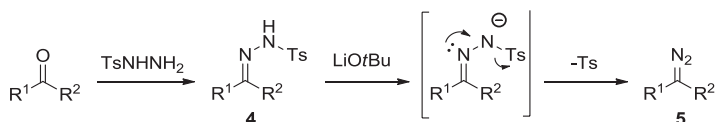
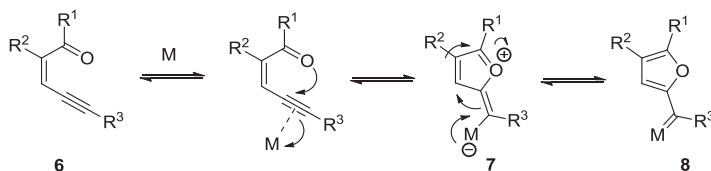
Metal carbenoids can be conveniently formed through decomposition of diazo compounds, such as diazoacetates. Thanks to their ease of formation and reasonable stability, this methodology has been used in a large number of elegant syntheses (Scheme 1) [3].

Alternatively, reactions of metal carbenes derived from *N*-sulfonyl triazoles have generated considerable interest in recent years [4]. The key reaction sequence, illustrated in Scheme 2, is the ring opening of triazoles **1** to generate diazo imines **2** and their subsequent conversion into metal-bound imino carbenes **3**, which can then undergo a wide range of synthetically useful transformations.

Although diazo compounds are largely used, a strong limitation to their use exists, that is, their poor stability when a non-electron-withdrawing substituent is linked on the diazo carbon. In order to circumvent this drawback, organic chemists have devoted many efforts to find a suitable substrate able to generate unstable diazo compounds in situ. In recent years, *N*-tosylhydrazones **4** have been proven to be very useful, because they are able to generate in situ non-stabilized diazo compounds **5**, thanks to the well-known Bamford-Stevens reaction (Scheme 3) [5]. Although harder reaction conditions are required (presence of a strong base and high temperature), diazo compounds bearing non-electron-withdrawing substituents, such as diazoalkanes and aryl-substituted diazomethane derivatives, can be used. Moreover, *N*-tosylhydrazones are readily available from the corresponding ketones or aldehydes.

However, the generation of diazo compounds in situ from *N*-tosylhydrazones or *N*-sulfonyl triazoles does not solve the safety concerns associated with these substrates (toxicity and tendency to explode). In 2002, Uemura and Ohe reported a seminal work on the in situ generation of the metal carbene species through the activation of alkynes with transition metals, as safe and effective alternative to diazo decomposition [6, 7]. Following the mechanism proposed, the enynone **6** is activated by a transition metal, which is then attacked by the carbonyl oxygen through a 5-*exo-dig* cyclization to form zwitterionic intermediate **7** or its resonance structure, metal (2-furyl)carbene complex **8** (Scheme 4).

Based on this background, recently Wang and coworkers published the first palladium-catalyzed cross-coupling reaction involving a metal carbene intermediate generated from a diazo-free compound [8]. This work represents a significant breakthrough in this field, and for this reason, it has opened the way for the discovery of innovative methods and reactions involving metal carbenes [9].

**Scheme 1** Metal-catalyzed decomposition of diazoacetates and metal carbenoid formation**Scheme 2** Formation of metal carbenoids from *N*-sulfonyl triazoles**Scheme 3** Bamford-Stevens reaction**Scheme 4** Formation of metal carbenoids from conjugated ene-yne-ketones

### 1.3 Cross-Coupling Reactions Based on Metal Carbene Migratory Insertion

Once the metal carbene intermediate has been generated through one of the previously described methods, it can undergo different transformations, typically X-H insertions, cyclopropanations, and ylide formations [10, 11]. Besides these traditional reactions, a new type of metal carbene transformation has appeared in the literature in the last 10 years that involves a cross-coupling process in which a diazo compound (or another substrate able to generate a metal carbene) plays the role of the nucleophilic coupling partner. This new reaction is mechanistically different from classical metal-catalyzed cross-coupling reactions, where an electrophilic

partner (usually halides or pseudohalides) and a nucleophilic coupling partner (typically organometallic reagents, except for the Heck-type reaction) are linked, thanks to the transition metal catalysis (see Scheme 5).

The characteristic step of this new cross-coupling reaction is a migratory insertion process, leading to the formation of a new metal specie, which undergoes further transformations completing the catalytic cycle, typically a  $\beta$ -hydride elimination to form a new C = C double bond. The migratory insertion of metal carbenes shows high versatility, both in terms of migratory groups (i.e., aryl, vinyl, benzyl, acyl, allyl, allenyl, and others) and in terms of catalysts (palladium catalysts are the most commonly used, but copper, rhodium, nickel, and cobalt catalysts are also effective for similar couplings) [12].

The first example of catalytic cross-coupling process involving a metal carbene migratory insertion was reported in 2001 by Van Vranken's group, who reported the reaction between trimethylsilyldiazomethane and benzyl halides to obtain styrene derivatives [13]. Although this work had several limitations, such as low efficiency (moderate yields) and limited scope, it has opened up new possibilities in the field of diazo compounds and cross-coupling reactions, and during the last 15 years, the scope of this methodology has been considerably broadened. Five years later, Barluenga and coworkers first employed tosylhydrazones as a source of diazo compounds in this kind of reaction, which greatly expanded its scope [14].

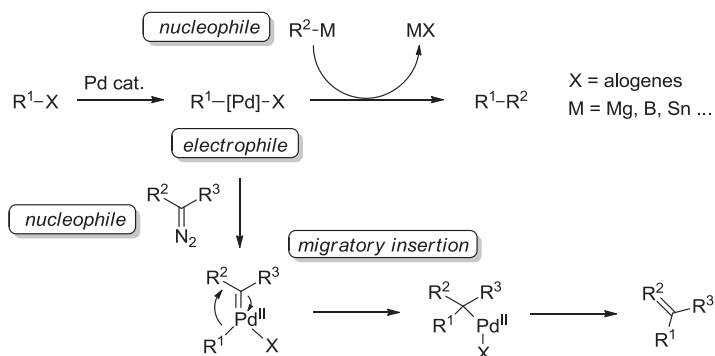
## 2 Multicomponent Reactions Involving Metal Carbene Migratory Insertion

In recent years, metal-stabilized carbenes have been also applied to a series of multicomponent reactions (MCRs) for the synthesis of complex molecules. The presence of a formal divalent carbon, which first acts as an electrophile and then as a nucleophile, explains the success of these compounds in MCRs [15, 16].

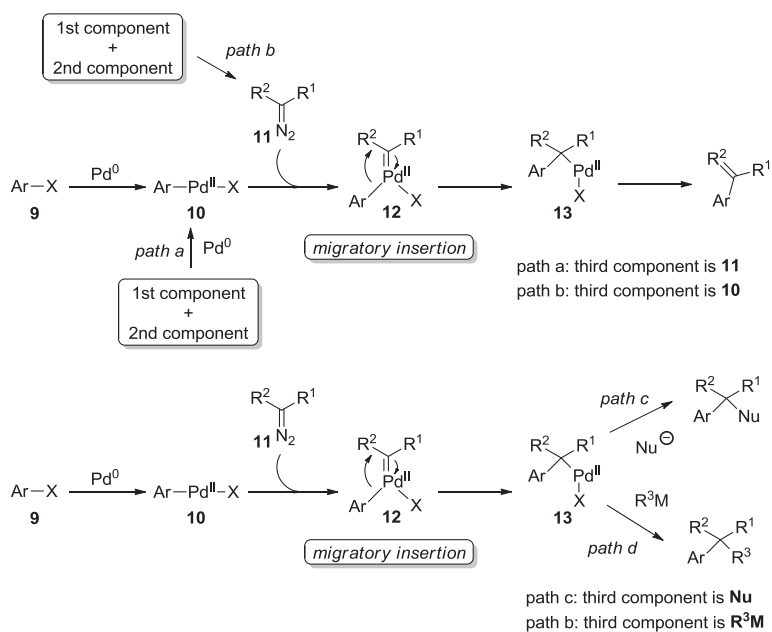
MCRs involving metal carbene migratory insertion can be achieved in different ways (Scheme 6). Usually, a classical oxidative addition of Pd(0) on an aryl halide **9** first occurs in this process. The metal-generated species **10** reacts with diazo compound **11** to form metal carbene **12**. Then, migratory insertion of the carbene ligand to the palladium-carbon bond leads to the formation of the new metal species **13**, which undergoes further transformations, thus completing the catalytic cycle, typically through a  $\beta$ -hydride elimination to form a new C = C double bond.

According to this general pathway, an MCR can be achieved by introducing more than one substrate in generating the first metal species **10** (path a) or the diazo compound **11** (path b). When no  $\beta$ -hydrogens are available, or this pathway is disfavored, the organometal intermediate **13** can be trapped by a nucleophile (path c) or can undergo transmetalation with an organometallic reagent followed by reductive elimination (path d), giving rise to various adducts with at least three points of diversity.





**Scheme 5** Classical palladium-catalyzed cross-coupling reaction versus coupling involving metal carbene migratory insertion



**Scheme 6** Different possibilities to establish an MCR through metal carbene migratory insertion

This chapter will cover advances in the field of MCRs involving metal carbene migratory insertion, focusing especially on palladium-catalyzed cross-coupling reactions. For the sake of clarity, the Pd-catalyzed multicomponent processes described herein are divided into four categories with respect to the different paths showed in Scheme 6. Finally, MCRs catalyzed by other metals will also be discussed, based on significant examples recently appeared in the literature.

## 2.1 Pd-Catalyzed MCRs via Path A

Since 2010, several examples of MCRs involving this type of transformations have been reported. Certainly, the group of Wang has contributed significantly to the development of this kind of chemistry. In 2010, they reported a palladium-catalyzed carbonylation of aryl iodides, diazoacetates, and CO (Scheme 7) [17]. This reaction proceeds with oxidative addition of Pd(0) to aryl iodide **9** and subsequent carbon monoxide insertion to generate intermediate **16**, which reacts with diazo compound **14** producing palladium-carbene **17**. Then, migratory insertion of acyl group into the carbenic carbon atom generates **18**, which undergoes reductive elimination to afford final product **15**. During the optimization process, the authors found that the addition of an external source of hydrogen atom (i.e., triethylsilane), the use of polar solvents and Pd(PPh<sub>3</sub>)<sub>4</sub> as catalyst, increased the yield.

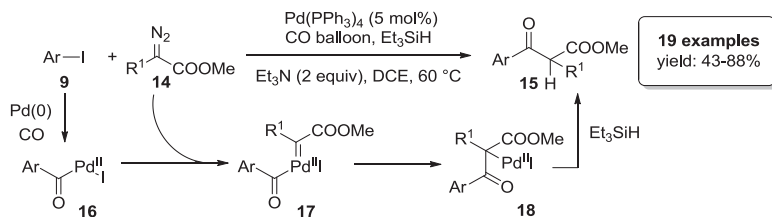
When non-stabilized diazo compounds derived from *N*-tosylhydrazones **4** were used, the concomitant formation of enone **19**, resulting from β-hydride elimination, was observed. Notably, the authors were able to identify the reaction conditions to obtain selectively both ketone **20** and enone **19** (Scheme 8).

Although only two inputs of diversity are introduced because one of the components is not variable, this work represents the first example of acyl group migratory insertion. Moreover, this tandem insertion process showed the convenient possibility to develop new metal-catalyzed cascade reactions.

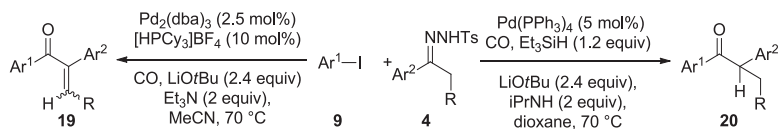
Three years later, Wang's group published also a new three-component reaction of allenes, aryl iodides, and diazo compounds for the synthesis of 1,3 dienes **23** or **24** (Scheme 9) [18].

In this example, aryl iodide **9** and allene **22** interact to generate a Pd-intermediate **25**, which undergoes addition of the diazo compound (**14**, or derived from **21**). As usual, migratory insertion and β-hydride elimination afford the diene product. Remarkably, only *E,E*-1,3-diene is formed (**23** or **24**). The authors suggested that the phenyl-substituted alkenyl moiety is preferred to eclipse with the phenyl group in the transition state of the β-hydride elimination process, thus explaining the high stereoselectivity (Scheme 10). Notably, the new 3CR was conveniently used for the preparation of a small library of ferrocenyl 1,3-butadienes, high value compounds in the field of special polymers used for coating materials in aerospace transportation.

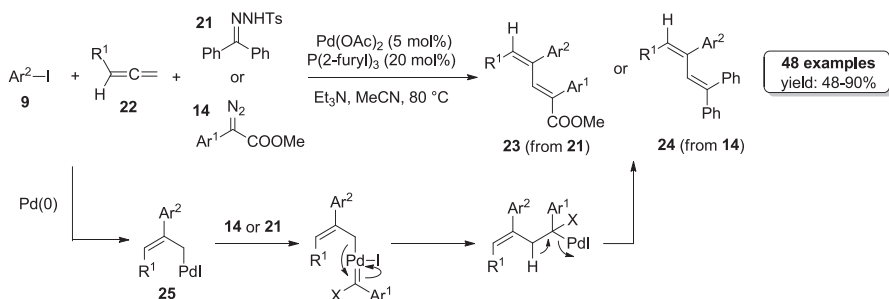
In 2014, Wang and coworkers developed a palladium-catalyzed three-component reaction of *N*-tosylhydrazone **4**, norbornene **26**, and aryl iodide **9** (Scheme 11) [19].



**Scheme 7** Palladium-catalyzed reaction of diazo compounds and aryl halide in the presence of CO

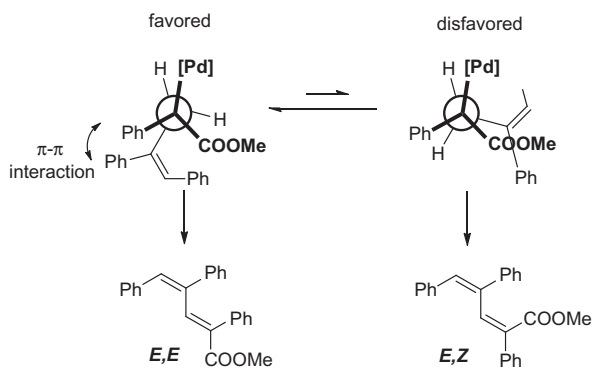


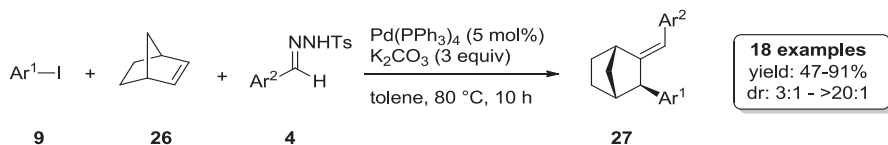
**Scheme 8** Reaction conditions for the selective synthesis of ketone or enone



**Scheme 9** Palladium-catalyzed three-component reaction of diazo compounds, allenes, and aryl halides

**Scheme 10** Possible explanation of stereoselectivity





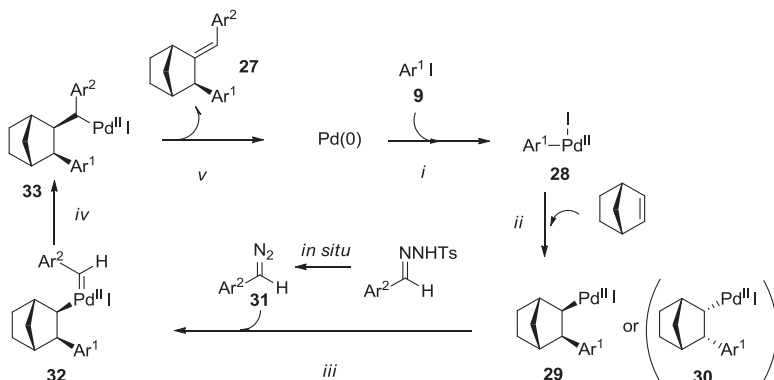
**Scheme 11** Palladium-catalyzed three-component reaction of *N*-tosylhydrazone, norbornene, and aryl halide

In this reaction, the intermolecular insertion of the alkene into an aryl palladium species (Heck-type reaction) is followed by palladium-carbene formation and migratory insertion. Notably, the authors avoided the problem of competitive reactions (such as direct Heck reaction between aryl halide and olefin or the cyclopropanation reaction between carbene precursor and olefin) by choosing norbornene as the olefin component. Indeed, the strained double bond of norbornene is inclined to insert into the Pd-C bond of the aryl palladium species. Since the alkyl palladium adduct generated has no *cis*- $\beta$ -hydride, the cascade reaction could proceed preferentially to afford **27**.

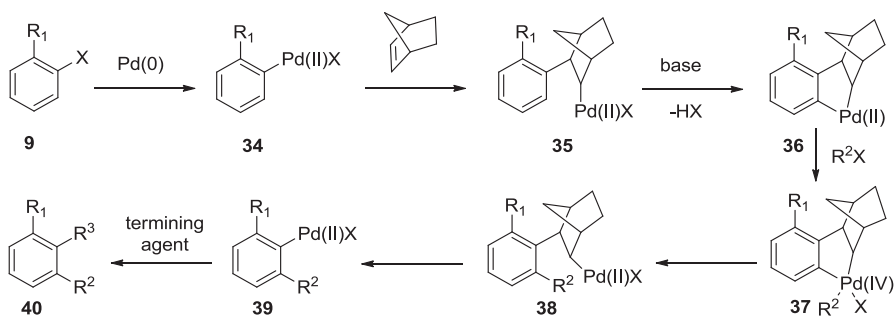
It is noteworthy that only two of the four possible stereoisomers (*E* of double bond and *exo* of aryl group) are formed. On the basis of experimental results, the authors proposed the following mechanism (Scheme 12): (i) oxidative addition of aryl halide **9** to Pd(0); (ii) norbornene insertion into the carbon-palladium bond of **28** with formation of **29** and **30**, where intermediate **29** (with the aryl group in the *exo* position) is favored due to steric hindrance; (iii) reaction of alkyl palladium **29** with in situ generated diazo compound **31**; (iv) migratory insertion of the palladium-carbene **32** to form **33**; and (v)  $\beta$ -hydride elimination with formation of the final product **27** and regeneration of the catalyst.

The Catellani reaction [20, 21] offers a unique approach to activate the *ortho*-C-H bonds of aryl halides and to provide dual functionalizations at both the *ipso*- and *ortho*-positions. In the past years, many Catellani-type reactions have been reported by Lautens and others [22]. As shown in Scheme 13, the reaction starts with oxidative addition of an aryl halide **9** to Pd(0) to give palladium complex **34**, followed by carbopalladation of norbornene (essential for the reaction to occur) to form **35**. Next, C-H activation of the *ortho*-position of the aryl halide and subsequent deprotonation deliver pallada-cycle **36**. This Pd(II) complex reacts with a second alkyl halide, affording Pd(IV) complex **37**. Reductive elimination (with formation of **38**), followed by deinsertion of norbornene through  $\beta$ -carbon elimination, provides Pd(II) species **39**, which can further undergo a terminating event to give final product **40**. Usually, the terminating events are limited to Heck, Suzuki, Cassar-Sonogashira, or hydrogenolysis reactions.

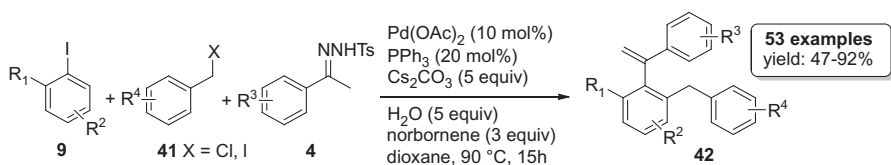
Recently, Liang and coworkers, for the first time, employed diazo compounds in a Catellani-type reaction. At the beginning of 2014, they published two papers on the synthesis of polycyclic substituted vinylarenes through the combination of the Catellani reaction with metal-catalyzed diazo compound insertion [23, 24]. After a careful optimization of the catalyst, base, and solvent, they succeeded to obtain the



**Scheme 12** The proposed mechanism of the three-component reaction between *N*-tosylhydrazone, norbornene, and aryl halide



**Scheme 13** Reaction mechanism of the Catellani reaction



**Scheme 14** Intermolecular benzylolation/carbene migratory insertion reaction

desired products **42** combining *ortho*-substituted iodobenzenes **9**, benzyl chlorides or iodide **41**, and *N*-tosylhydrazones **4** (Scheme 14) [23]. Curiously, they noted that, using water as additive, an improved yield was obtained, although the reason remained unknown [25, 26].

The proposed mechanism follows the classical Catellani reaction up to intermediate **39** (see Scheme 13). At this point, the decomposition of the in situ generated diazo compound **43** affords palladium-carbene **44**, which undergoes migratory

insertion of the aryl group with formation of **45** and  $\beta$ -elimination to give the final product **42** and regenerating the catalyst with the aid of the base (Scheme 15).

The scope of the reaction was expanded in different ways: (1) by preparing dibenzylated products by a double activation of two *ortho*-positions of aryl iodides, (2) by replacing benzyl chlorides with alkyl iodide, (3) by preparing polysubstituted bicyclic molecules using bifunctional substrates, and (4), finally, by performing a one-pot procedure directly starting from carbonyl compounds without the isolation of tosylhydrazones.

The same group also reported a palladium-catalyzed, norbornene-mediated, *ortho*-amination/*N*-tosylhydrazone insertion reaction for the synthesis of *ortho*-aminated vinylarenes **47** by employing *N*-benzoyloxyamine **46** as the third component (Scheme 16) [27].

In 2013, Dong and coworkers developed the first example of the formation of C-N bonds at the *ortho*-position of aryl iodides via Catellani-Lautens-type C-H activation [28]. Inspired by that work, the group of Liang embedded this approach in a multicomponent reaction, where intermediate **36** (seen also in Scheme 13) undergoes further oxidative addition by *N*-benzoyloxyamine **46**, thus generating the cyclic Pd(IV) complex **48** (Scheme 17). A subsequent reductive elimination then affords Pd(II) intermediate **49**, which, after deinsertion of the norbornene, is ready for the palladium-carbene formation. Anyway, the direct electrophilic amination of intermediate **36** cannot be excluded.

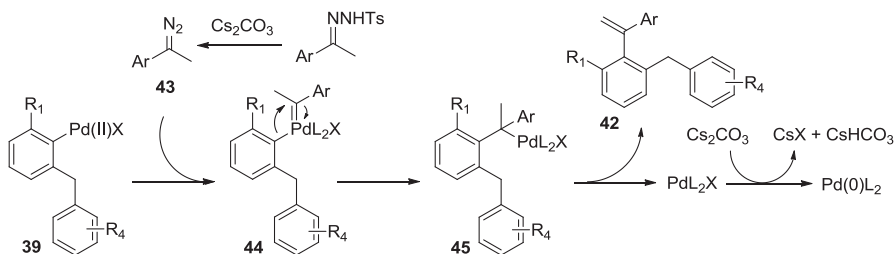
Unlike classical Catellani processes, this reaction proceeded more efficiently in nonpolar solvents, probably because polar media increase the decomposition of *N*-benzoyloxyamine. To further demonstrate the generality of this methodology, a diazocarbonyl compound was also employed as substrate, affording the desired product **50** in acceptable yield (Scheme 18).

## 2.2 Pd-Catalyzed MCRs via Path B

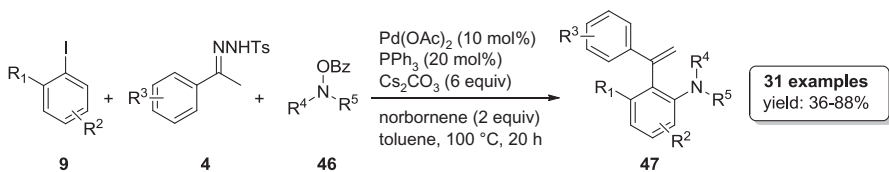
According to this approach, the carbene source, either a diazo compound or a tosylhydrazone, is modified in situ prior to undergo the Pd-catalyzed insertion. Such modifications leave the reactive group untouched, but introduce further elements of diversity that are found in the final products.

This synthetic strategy has been recently introduced by the group of Wang as a modification of an existing methodology, namely, a Pd-catalyzed C-H functionalization of ethyl diazoacetate **51** with aryl or vinyl iodides **9**, developed by the same authors [29] and further exploited by Frantz [30] and Reissig [31] (Scheme 19).

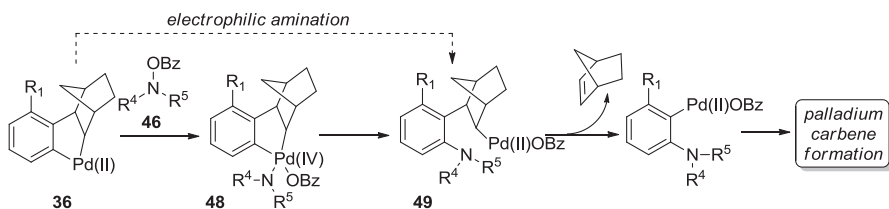
This methodology surprisingly leaves the diazo group untouched and therefore opens up the route to new scenarios, where the product of the reaction can be exploited as a carbene source in a subsequent Pd-catalyzed migratory insertion into an aryl halide (Scheme 20).



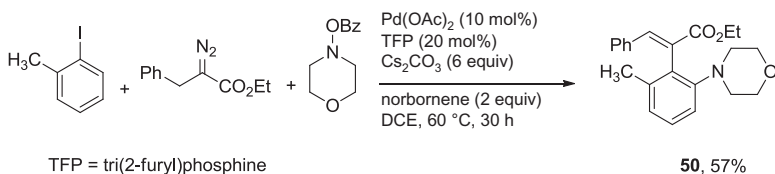
**Scheme 15** Proposed mechanism of *ortho*-C-H activation/carbene migratory/insertion reaction



**Scheme 16** Palladium-catalyzed, norbornene-mediated, *ortho*-amination/*N*-tosylhydrazone insertion reaction

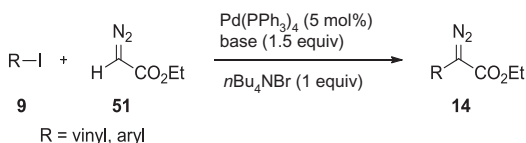


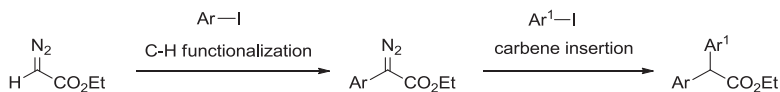
**Scheme 17** Possible mechanism of the *ortho*-amination/*N*-tosylhydrazone insertion reaction



**Scheme 18** Pd-catalyzed *ortho*-amination/diazoacetyl compound insertion reaction

**Scheme 19** C-H functionalization of ethyl diazoacetate





**Scheme 20** Sequential C-H functionalization and cross-coupling reaction of ethyl diazoacetate

After re-optimization of the two-component reaction developed in 2007 (not efficient in terms of yields and scope) and investigation of the optimal conditions for the cross-coupling step, it was found that the same catalyst could be used for the two reactions and that the temperature required by the Pd-catalyzed C-H insertion into ethyl diazoacetate was slightly lower compared to that required by the Pd-catalyzed cross-coupling step.

Also DFT calculations confirmed that the rate-limiting step of the whole process was the hydrogen transfer to the Pd(II) species in the cross-coupling step. Moreover, through the computational studies, it was also possible to find an explanation to the essential role of silver carbonate in both steps of the synthetic pathway.

Thus, a tandem process was possible with the first reaction taking place at room temperature and, the second, upon addition of the second iodoarene, at 65 °C [32]. Interestingly, when the same iodoarene was employed in both steps, two equivalents could be added from the beginning, but yields were lower.

The scope of the reaction was quite broad and was not significantly affected by the electronic properties of the substituents on the aromatic ring of the two iodoarenes. We noticed that *o*-substituted iodoarenes were not tolerated in the first step, probably for steric reasons. Notably, 1-iodonaphthalene was also a suitable substrate for the coupling reaction (Scheme 21).

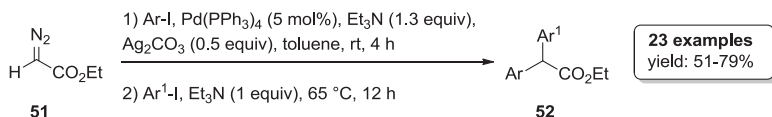
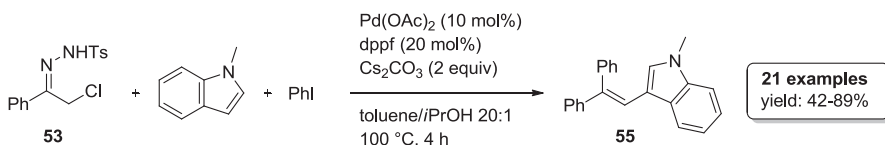
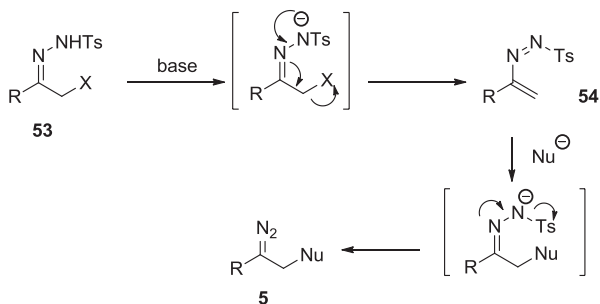
Very recently, it has been demonstrated that also  $\alpha$ -halo-*N*-tosylhydrazones **53** are powerful tools for multiple bond formation. Under basic conditions,  $\alpha$ -halo-*N*-tosylhydrazones are not converted into the corresponding diazo compounds but into azoalkenes **54**, as depicted in Scheme 22. As azoalkenes are susceptible to conjugate addition, reaction with a nucleophile generates the diazo compound **5**, susceptible to other transformations [33].

Wang and coworkers have exploited this transformation in a tandem process where the in situ generated diazo compound is subjected to a Pd-catalyzed cross-coupling reaction with aryl iodides [34].

A thorough optimization of the reaction conditions allowed the authors to react hydrazone **53** with *N*-methylindole and phenyl iodide to give the three-component adduct **55** in a satisfactory 74% yield (Scheme 23). The reaction was performed using Pd(OAc)<sub>2</sub> as catalyst, with 1,1'-ferrocenediyl-bis(diphenylphosphine) (dppf) as a ligand and Cs<sub>2</sub>CO<sub>3</sub> as the base in a toluene/isopropanol solvent mixture at 100 °C.

Upon examining the scope of the reaction, it was found that substituents on the aromatic rings marginally influenced the outcome. On the contrary, only the benzyl group could effectively replace the methyl of the indole component, while *N*-phenylindole did not afford any product, presumably due to electronic effects. In those cases, where the aromatic rings of the hydrazine and the aryl iodide were not



**Scheme 21** Three-component synthesis of diaryl acetates **52****Scheme 22** Generation of diazo compounds from  $\alpha$ -halo-*N*-tosylhydrazones and nucleophiles**Scheme 23** Three-component reaction of  $\alpha$ -halo-*N*-tosylhydrazones, indoles, and aryl iodides

equivalent, nearly 1:1 mixtures of geometric isomers were obtained, apart in a few examples where the *Z* isomer was exclusively isolated.

Interestingly, the generation of diazo compounds from  $\alpha$ -halo-*N*-tosylhydrazones and indoles was also coupled with a metal-free coupling with boronic acids and with a copper-catalyzed 1,2-H shift reaction [33]. However, as these processes fall outside the scope of this chapter, they will not be discussed further.

### 2.3 Pd-Catalyzed MCRs via Path C

According to the general routes depicted in Scheme 6, addition of a diazo compound to a vinylpalladium halide complex generates a vinylpalladium carbene. Migratory insertion of metal carbene to the palladium-carbon bond leads to the formation of an  $\eta^1$ -allylpalladium complex. This isomerizes to the more stable  $\eta^3$ -allylpalladium species that can be then subjected to nucleophilic attack, resulting in a three-component adduct where a new C-C bond and a new C-Nu bond are generated (Scheme 24).

As it appears evident from the mechanism, the use of vinyl iodides as electrophiles is essential to favor the  $\eta^1$ - $\eta^3$  isomerization, while diverse diazo compound and nucleophiles can be employed. Moreover, the nucleophilic attack could occur on either end of the  $\eta^3$ -allylpalladium, thus generating two regioisomeric products; however, the  $R^1$  group deriving from the diazo compound usually directs the attack of the nucleophile, resulting in a regioselective reaction.

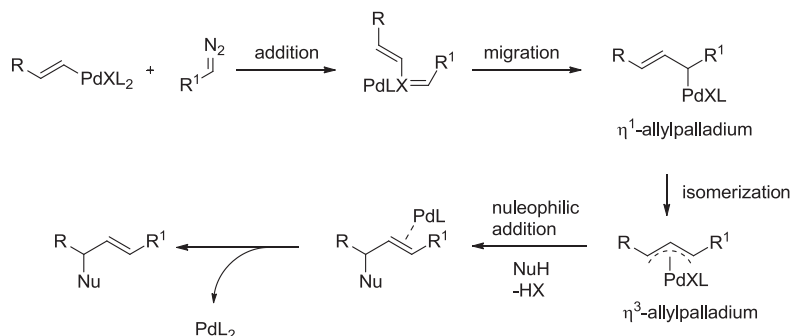
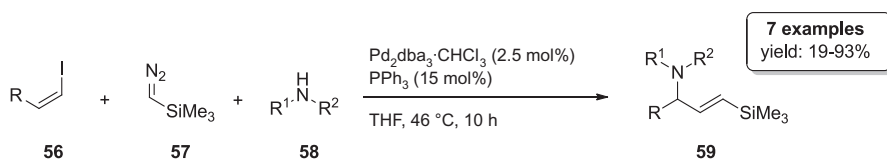
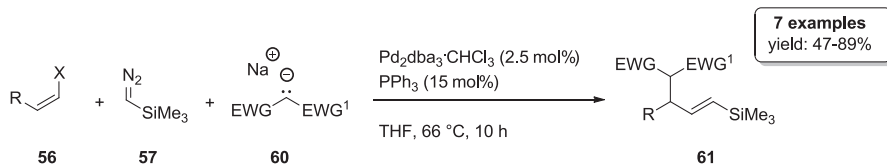
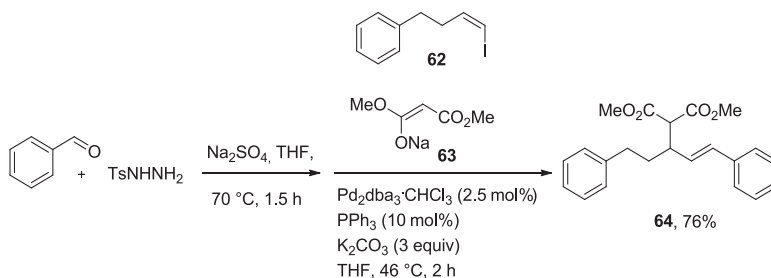
The first example reported in the literature dates back to 2007; Van Vranken reported the synthesis of allylamines **59** from vinyl halides **56**, trimethylsilyldiazomethane **57**, and amines **58**, according to the general reaction reported in Scheme 25 [35]. Various reaction conditions were tested but, unfortunately, general conditions could not be applied, as these were dependent on the nature of the amine. For example, with pyrrolidine, addition of potassium carbonate and phenylboronic acid dramatically improved the yield, probably preventing degradation of the diazo compound. However, these conditions could not be extended to other amines. Piperidine and morpholine gave high yields without additives, although morpholine worked well only if two equivalents were used. In contrast, in case of benzylamine, a higher excess was deleterious. From a general point of view, the use of THF as the solvent at 46 °C and of  $\text{Pd}_2\text{dba}_3\cdot\text{CHCl}_3$  as the catalyst precursor and the addition of the diazo compound by syringe pump over 10 h were the conditions chosen for all the reactions. By using piperidine as the nucleophile, various vinyl halogenides were tested, with iodides performing better than bromides and internal alkenes (with the iodine atom in position 2) affording low yields and mixtures of *E/Z* isomers.

Shortly after this first report, Van Vranken reported also similar reactions with malonates and malonitriles **60** as C-nucleophiles; the reaction conditions were similar to those developed before, although better conversions were obtained raising the temperature up to 66 °C; the nucleophiles were employed as their sodium salts in large excess (12 equivalents) (Scheme 26) [36].

An improvement of this reaction was reported by Liang who, by employing aryl-*N*-tosylhydrazones **4** as carbene source, was able to introduce an additional point of diversity into the final products, infact the substituent on the double bond derived from the diazo compound was no longer limited to the trimethylsilyl group [37]. Reaction conditions were almost identical to those reported by Van Vranken, apart from the presence of potassium carbonate, essential to generate in situ the diazo compound; however, a large excess of malonate was again required to improve the yield. The scope of the reaction was quite broad, in terms of substitution pattern on the aromatic ring of the hydrazine (19 examples with yields ranging from 0 to 84%). Interestingly in one case, the reaction was performed as a four-component condensation, mixing benzaldehyde and tosylhydrazine and then adding vinyl iodide **62** and malonate **63** in a one-pot fashion, without substantial loss in the overall yield of **64** (76% vs. 79% yield) (Scheme 27).

Very recently, Van Vranken extended this methodology also to aliphatic tosylhydrazones that were employed either with malonates or with amines as nucleophiles [38].

The use of diazoacetates as carbene source is somehow more challenging than the use of trimethylsilyldiazomethane or tosylhydrazones, as palladium chloride can

**Scheme 24** General mechanism for MCRs of type C**Scheme 25** Three-component synthesis of allylamines**Scheme 26** Three-component reaction with C-nucleophiles**Scheme 27** Four-component reaction of benzaldehyde, tosylhydrazine, vinyl iodide, and malonate

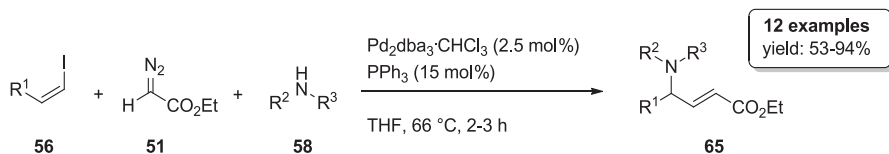
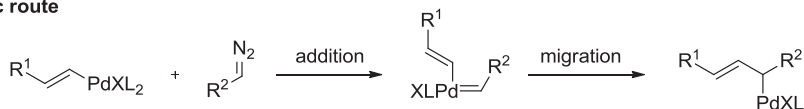
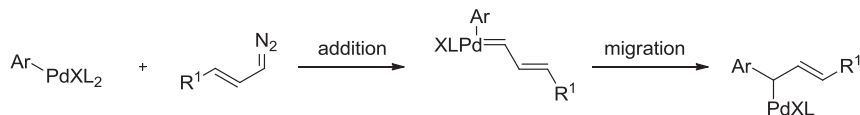
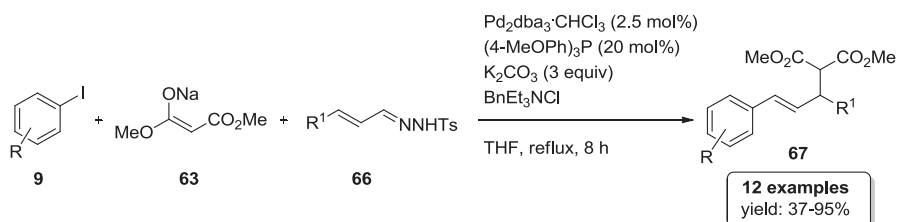
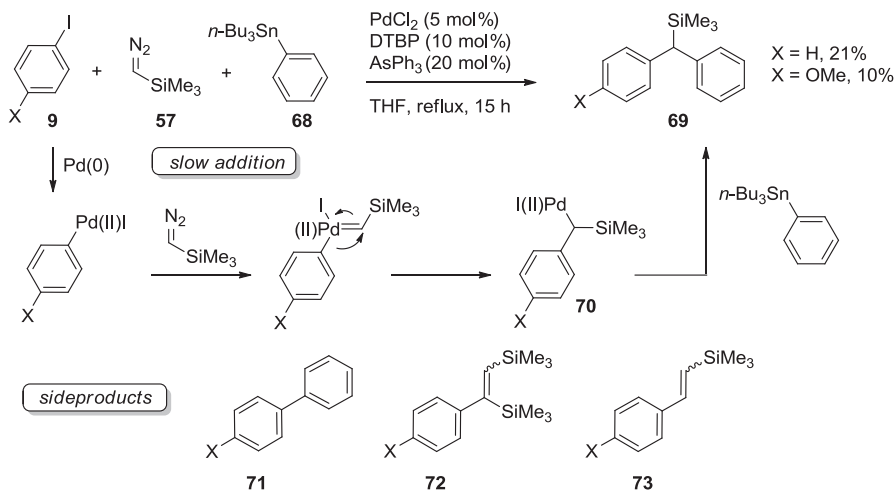
catalyze polymerization of the diazo compound, and the latter can also give a cross-coupling reaction with vinyl iodides. Nevertheless, Van Vranken demonstrated that, under the conditions previously illustrated, ethyl diazoacetate **51** could react with vinyl iodides **56** and amines **58**, given that a large excess of diazoacetate was employed [39]. Fine optimization of the reaction conditions led to the conclusion that the nature and amount of nucleophilic amine were crucial: in general, better yields were obtained when the amount of amine, capable of catalyst deactivation, was limited to three equivalents. However, in those cases where the amine was more basic, an improvement was obtained using only one equivalent and adding two equivalents of triethylamine. The reaction afforded the desired product **65** either with primary or with secondary amines, with terminal and internal vinyl iodides, and with diazoacetates and diazopropionates; in this latter case, *E/Z* mixtures of diastereoisomers were obtained (Scheme 28).

One last example of this methodology employs iodoarenes as electrophiles. As previously discussed, the use of vinyl iodides is essential to the  $\eta^1$ - $\eta^3$  isomerization, the key step to generate a Pd specie capable to undergo the nucleophilic attack. However, if we reconsider the general reaction depicted in Scheme 20, the conjugated double bond able to favor the isomerization of the  $\eta^1$ -allylpalladium intermediate could be placed either on the electrophile or on the diazo compound. This alternative route would still lead to a  $\eta^1$ -allylpalladium specie able to give the required isomerization (Scheme 29).

Indeed, Liang and coworkers, by employing  $\alpha,\beta$ -unsaturated *N*-tosylhydrazones **66**, succeeded in the Pd-catalyzed coupling with iodoarenes **9** and malonate **63** (Scheme 30) [40]. Interestingly, when  $R^1$  was a methyl group, complete regioselectivity was observed, favoring the conjugated product **67**, while, when  $R^1$  was an aromatic ring, mixtures of regioisomers were obtained.

## 2.4 Pd-Catalyzed MCRs via Path D

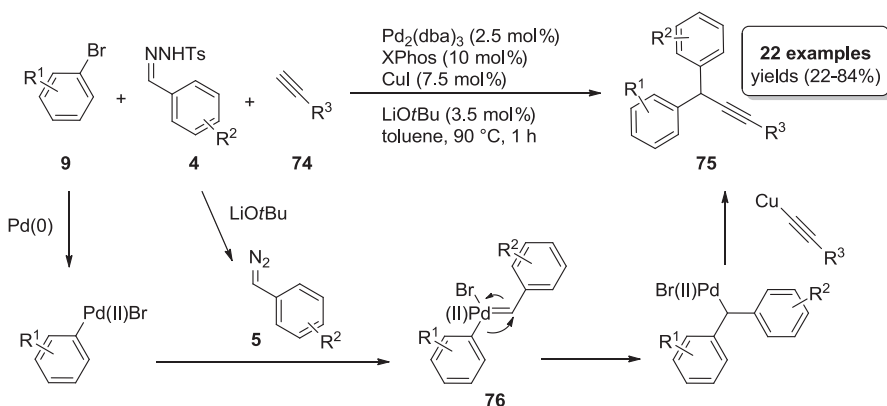
In path D, the metal species originated after the migratory insertion process undergo transmetallation with an organometallic reagent (third component). In his pioneering work published in 2001 regarding the palladium-catalyzed insertion of trimethylsilyldiazomethane [13], Van Vranken reported the three-component reaction between aryl iodides **9**, trimethylsilyldiazomethane **57**, and tributylphenyltin **68** (Scheme 31). The organometallic specie **70**, originated from metal carbene after migratory insertion, undergoes a Stille coupling through transmetallation with tin reagent **68**. Trimethylsilyldiazomethane and tributylphenyltin have to be slowly added in order to obtain the desired product. Unfortunately, the yields and the scope of the reaction are quite poor (just two examples are described), probably due to the formation of side products such as biphenyl compound **71**, in which trimethylsilyldiazomethane is not incorporated, or silylstyrenes **72** and **73**, produced by the reaction of intermediates **70** with **57**, followed by  $\beta$ -hydride or  $\beta$ -silyl elimination. Despite these

**Scheme 28** Three-component reaction of vinyl iodides, amines, and diazoacetates**classic route** $\eta^1$ -allylpalladium**alternative route****Scheme 29** Two possible ways to generate a  $\eta^1$ -palladium species**Scheme 30** Three-component reaction of iodoarenes, malonates, and tosylhydrazones**Scheme 31** Palladium-catalyzed migratory insertion followed by Stille coupling reaction

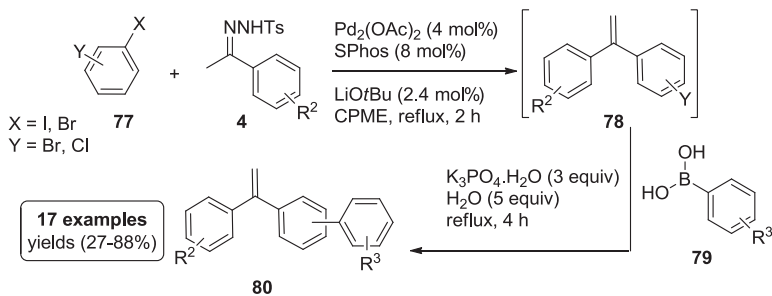
limitations, this reaction demonstrated that the transmetalation and the formation of two separate C-C bonds in a carbonic center were indeed possible.

After this early report, the first study demonstrating the possibility to couple Pd-carbene migratory insertion with a classical cross-coupling reaction via transmetalation appeared in literature only in 2010, thanks to Wang and coworkers [41]. They studied the three-component reaction between *N*-tosylhydrazones **4**, aryl bromides **9**, and terminal alkynes **74** for the preparation of benzhydryl acetylenes **75** (Scheme 32). Obviously, one of the major challenges in this synthetic sequence was the suppression of the possible side products arising from direct Sonogashira coupling or early  $\beta$ -H elimination. In order to avoid direct coupling products, probably formed due to the low concentration of the diazo substrate **5** and subsequent slow formation of Pd-carbene **76**, aryl bromides were used instead of the more reactive aryl iodides. The optimization of reaction conditions revealed that the choice of solvent and ligands was crucial to obtain a satisfactory yield.

Recently, Alami and Hamze reported a new three-component reaction between *N*-tosylhydrazones **4**, dihalogenated arenes **77**, and boronic acids **79** (or esters) producing substituted 1,1-diarylethylenes **80** (Scheme 33) [42]. This work is conceptually



**Scheme 32** Pd-catalyzed three-component reaction of *N*-tosylhydrazones, aryl bromides, and terminal alkynes



**Scheme 33** Pd-catalyzed migratory insertion/Suzuki-Miyaura coupling one-pot reaction

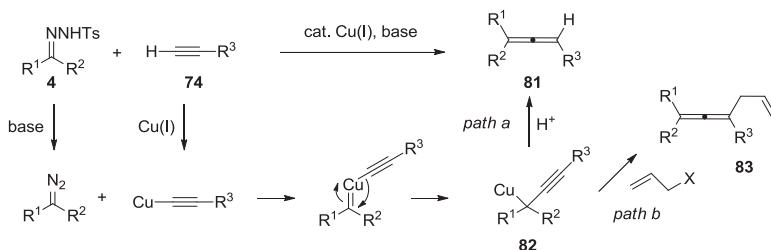
ally different from the others shown before. In fact, the mechanism doesn't involve a cascade process in which the palladium specie, formed after carbene migratory insertion, reacts via transmetalation. Two reactions occur into different sites of the molecule instead: when the carbene migratory insertion reaction is completed with a  $\beta$ -hydride elimination, the Pd catalyst is reused in the Suzuki-Miyaura arylation of **78**, exploiting the second halide functionality of **77**. The authors studied the best conditions able to catalyze the two couplings in a one-pot manner. During the scope of the reaction, they found that the yield rapidly decreased when styryl boronic acids or *ortho*-disubstituted iodo-chloro benzenes were used. The use of more stable pinacol boronic esters allowed the authors to improve the scope of the reaction. Moreover, the authors demonstrated the power and usefulness of this Pd-catalyzed cascade reaction, by synthesizing one of their lead compounds (a molecule with antiproliferative activity against several cancer cell lines), in just two steps in 52% overall yield, which is a remarkable result if compared with the five-step procedure (18% overall yield) previously published.

## 2.5 MCRs Catalyzed by Other Metals

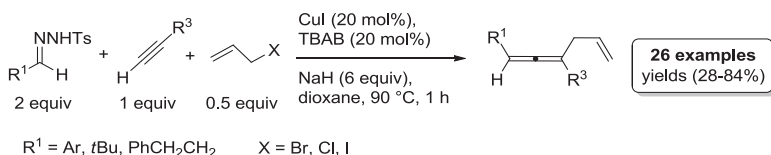
Recent studies have demonstrated that metal-catalyzed carbene-involved cross-coupling reactions are not limited to the use of palladium. In 2011, during the development of a new methodology for the synthesis of substituted allenes, the group of Wang reported the copper-catalyzed reaction between *N*-tosylhydrazones **4** and terminal alkynes **74** [43]. Mechanistically, this work represents an unprecedented copper-carbene migratory insertion process, different from classic copper(I)-catalyzed reactions of diazo compounds, where cyclopropanation [44] or cyclopropenation [45] usually occurs. While the metal intermediate **82** formed after the migratory insertion process undergoes  $\beta$ -hydride elimination in the classical Pd-catalyzed reaction, when Cu(I) is used as catalyst, the last step of the catalytic cycle is generally a protonation to **81** (Scheme 34, *path a*). Based on this idea, 2 years later, they presented the three-component version simply by trapping the nucleophilic organo-copper intermediate by carbon electrophiles, such as allyl halides, preparing tri- and tetrasubstituted allenes **83** (Scheme 34, *path b*) [46].

In a first set of studies, the authors optimized the reaction conditions for the synthesis of trisubstituted allenes: a large amount of base was required in order to suppress the protonation of copper intermediate, and the use of dioxane as solvent, tetra-*n*-butylammonium bromide (TBAB) as additive, and a specific ratio of the substrates produced acceptable yields (Scheme 35).

Moreover, the usefulness and strength of the synthetic procedure were demonstrated by carrying out the reaction on a gram scale, obtaining the corresponding allene in 74% yield. With these results in hand, the authors explored the more challenging synthesis of tetrasubstituted allenes. Starting from ketone-derived *N*-tosylhydrazones and applying modified reaction conditions ( $[\text{Cu}(\text{MeCN})_4]\text{PF}_6$  as catalyst and 1,10-phenanthroline as ligand), the desired tetrasubstituted allene products were obtained, although in moderate yields.



**Scheme 34** Copper-catalyzed alkynyl migration insertion for the synthesis of tri- or tetrasubstituted allenes



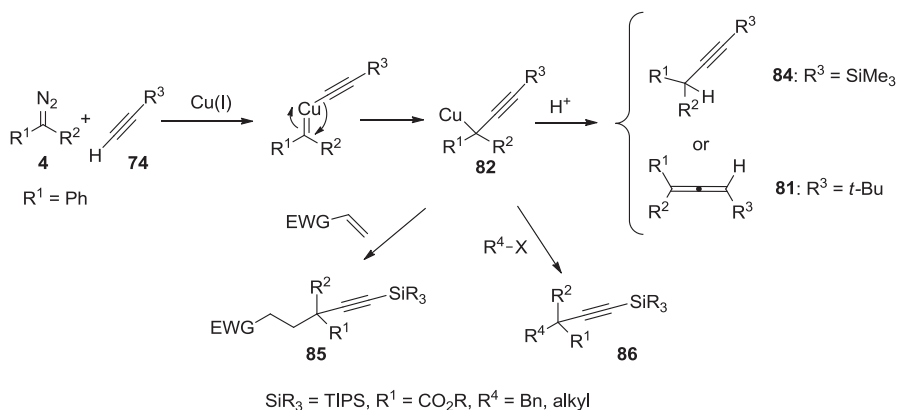
**Scheme 35** Copper-catalyzed three-component coupling of *N*-tosylhydrazones, terminal alkynes, and allyl halides

When the same authors tried to extend the scope of the reaction using trialkylsilylalkynes **74** ( $\text{R}^3 = \text{SiMe}_3$ ), surprisingly the substituted alkynes **84** were obtained instead of the corresponding allenes **81** [47]. In order to explain this outcome, steric effects were excluded, since the coupling with a *tert*-butyl substituted alkyne **74** ( $\text{R}^3 = t\text{Bu}$ ), with analogous steric hindrance, gave the allene **81** as single product. DFT studies allowed to elucidate the mechanism [48], and demonstrated that formation of different Cu complexes in the transition state during the protonation process was crucial for the alkyne/allene selectivity. Recently, taking advantage of this particular reactivity, the same authors realized a three-component reaction, in which the copper intermediate **82** reacted with an electrophile, such as Michael acceptors or alkyl halides, obtaining products **85** and **86** with a remarkable propargylic quaternary carbon (Scheme 36) [49].

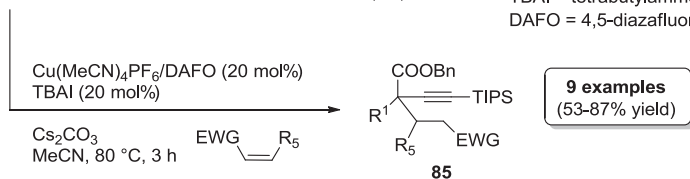
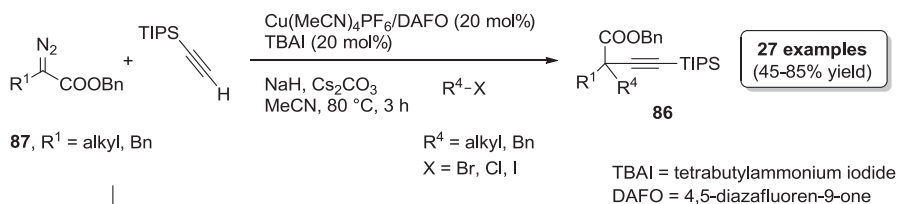
In order to suppress all the possible by-products, the reaction was carefully optimized. The choice of the proper ligand, the use of a phase-transfer catalyst, and a mix of bases were crucial to obtain the product in good yield (a gram-scale experiment was carried out too). When the electrophile was a Michael acceptor, a further optimization was required (the amount of the base was reduced and just  $\text{Cs}_2\text{CO}_3$  was used). Curiously, only diazoesters **87** with alkyl substituents were used in the procedure (Scheme 37).

Simultaneously, Wang's group published the same reaction catalyzed by Rh(I) [50]. They found that in this case, the use of terminal alkynes produced low yields, due to their facile dimerization under Rh(I) catalysis conditions. Based on the knowledge that tertiary alcohols are suitable substrates which can undergo selective cleavage of one of the three C-C bonds to form an organometal intermediate along with a ketone [51], they solved the problem by employing tertiary propargyl alcohols **88** as coupling component (Scheme 38).

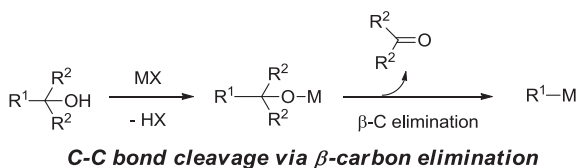




**Scheme 36** Copper-catalyzed three-component reaction for the construction of all-carbon quaternary center



**Scheme 37** Scope of the three-component reaction between diazoesters, terminal alkynes, and alkyl halides or Michael acceptors



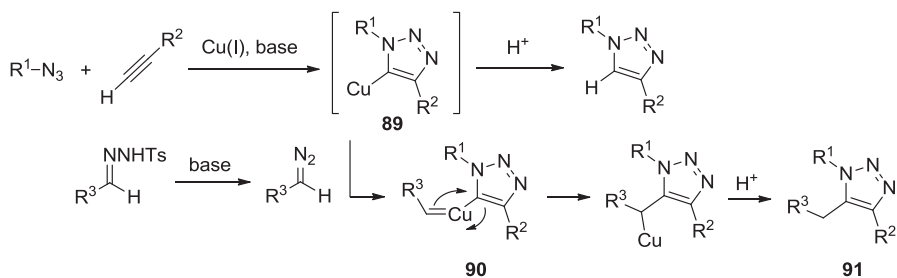
**Scheme 38** Rhodium(I)-catalyzed three-component reaction of *tert*-propargyl alcohol, diazoesters, and alkyl halides

The thermally induced reaction of organic azides with acetylenes is well known as Huisgen 1,3-dipolar cycloaddition [52]. The discovery that catalytic CuI increases the reaction rate and controls the regioselectivity to give the 1,4-disubstituted triazole group, while suppressing the formation of the 1,5-regioisomer, was made independently in 2002 by Sharpless [53] and Meldal [54] and their coworkers. From then, the reaction mechanism has been largely investigated, and, in 2007, the hypothesis that the last step of the reaction could be a protonolysis of the Cu-C bond was demonstrated by the isolation and x-ray characterization of a Cu(I) triazolide intermediate **89** (5-cuprated 1,2,3-triazole) [55]. As a continuation of his work, the Wang's group postulated that a diazo compound generated in situ from the corresponding *N*-tosylhydrazone could react with this copper intermediate, giving insertion adduct **90**, leading to the formation of trisubstituted 1,2,3-triazoles **91** (Scheme 39).

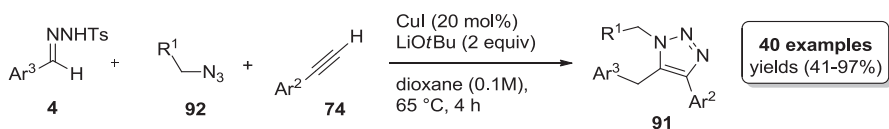
After a short optimization of the reaction conditions, they investigated the scope of both hydrazones **4**, azides **92**, and alkynes **74**, finding that aromatic alkynes or hydrazones bearing electron-donating groups afforded higher yields; alkyl azides and azides bearing heterocycles reacted too in good yield, although the concomitant variation of all the three components gave the desired product **91** in modest yields (Scheme 40).

Rhodium(II) catalysis has been well established in metal carbene chemistry, although the classical carbene transfer mechanism usually occurs [56]. In 2011, Yu and coworkers suggested that organorhodium(I) would couple with a diazo compound in a similar way to Pd(II), being isoelectronic [57]. Based on this idea, they presented the first rhodium-catalyzed three-component cross-coupling reaction between diazoesters **14**, arylboronates **93**, and alkyl halides **94** (Scheme 41).

The reaction conditions have been optimized using phenylboronic acid pinacol ester, benzyl bromide, and 4-chlorophenyldiazoacetate in the presence of *t*BuOK as base, finding that methyl *tert*-butyl ether was the best solvent, [Rh(cod)OH]<sub>2</sub> was essential, while other catalysts, such as [Rh(dppe)Cl]<sub>2</sub> or [Ru(PPh<sub>3</sub>)Cl], were ineffective. Boronic acids, by contrast, did not give the desired products. The scope of the reaction has been well investigated, using also bromo-substituted aryl diazoacetates, not compatible with the Pd(0) catalysis due to their intrinsic reactivity. Mechanistically, the reaction proceeds through the usual migratory insertion process forming an oxa- $\pi$ -allylrhodium complex **96**, which exchanges with *t*BuOK to form a potassium enolate **97**. The second C-C bond formation is achieved by S<sub>N</sub>2 reaction with the alkyl halides. Unfortunately, only very reactive alkyl halides provided the desired product **95**, and a large excess of coupling partners were needed in order to obtain acceptable yields.

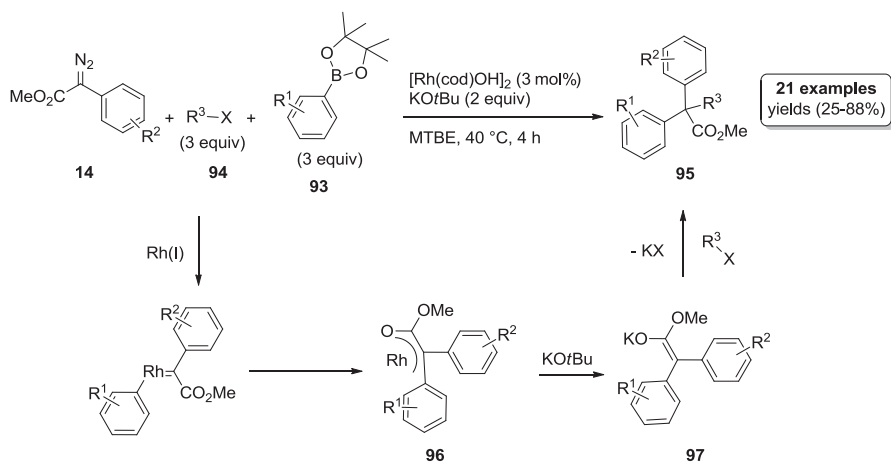


**Scheme 39** Copper(I)-catalyzed azide-alkyne cycloaddition versus three-component reaction with *N*-tosylhydrazones



$R^1 = Ar, alkyl, Py, thiophene$

**Scheme 40** Copper(I)-catalyzed three-component coupling of *N*-tosylhydrazones, alkynes, and azides



**Scheme 41** Rh(I)-catalyzed three-component reaction of arylboronates, diazoesters, and alkyl halides

### 3 Conclusions

This chapter aims to show that the development of multicomponent processes involving metal carbene migratory insertion is a growing research area, which provides efficient routes to generate complexity and diversity in organic synthesis. Thanks to the possibility to couple metal-catalyzed insertion of carbenes with other (metal or not) catalyzed reactions, it is possible to create cascade processes, developing new multicomponent reactions. In this chapter, it has been shown that the diversity can be reached by changing all the possible components. Certainly, palladium remains the most popular transition metal employed, although other metals (copper, rhodium) have shown interesting alternative reactivity. Notably, the recent paper of Wang demonstrated the possibility to generate metal carbene from conjugated eneyne-ketones, avoiding the use of diazo compounds and expanding the potentiality of this chemistry. For all these reasons, cross-coupling reactions based on metal-stabilized carbenes can be considered almost a general process, which can increase the synthetic potential of multicomponent methodologies, allowing the achievement of complexity in a single step.

### References

1. H.M.L. Davies, R.E. Beckwith, *Chem. Rev.* **103**, 2861 (2003)
2. M. Brookhart, W.B. Studabaker, *Chem. Rev.* **87**, 411 (1987)
3. H.M.L. Davies, J.R. Denton, *Chem. Soc. Rev.* **38**, 3061 (2009)
4. H.M.L. Davies, J.S. Alford, *Chem. Soc. Rev.* **43**, 5151 (2014)
5. W.R. Bamford, T.S. Stevens, *J. Chem. Soc.*, 4735 (1952)
6. K. Ohe, T. Yokoi, K. Miki, F. Nishino, S. Uemura, *J. Am. Chem. Soc.* **124**, 526 (2002)
7. K. Miki, F. Nishino, K. Ohe, S. Uemura, *J. Am. Chem. Soc.* **124**, 5260 (2002)
8. Y. Xia, S. Qu, Q. Xiao, Z.-X. Wang, P. Qu, L. Chen, Z. Liu, L. Tian, Z. Huang, Y. Zhang, J. Wang, *J. Am. Chem. Soc.* **135**, 13502 (2013)
9. C.D. Smith, D. France, *J. Chem. Cat. Chem.* **6**, 711 (2014)
10. T. Ye, M.A. McKervey, *Chem. Rev.* **94**, 1091 (1994)
11. A. Padwa, M.D. Weingarten, *Chem. Rev.* **96**, 223 (1996)
12. Q. Xiao, Y. Zhang, J.B. Wang, *Acc. Chem. Res.* **46**, 236 (2013)
13. K.L. Greenman, D.S. Carter, D.L. Van Vranken, *Tetrahedron* **57**, 5219 (2001)
14. J. Barluenga, P. Moriel, C. Valdes, F. Aznar, *Angew. Chem. Int. Ed.* **46**, 5587 (2007)
15. X. Guo, W. Hu, *Acc. Chem. Res.* **46**, 2427 (2013)
16. Y. Xia, Y. Zhang, J.B. Wang, *ACS Catal.* **3**, 2586 (2013)
17. Z. Zhang, Y. Liu, M. Gong, X. Zhao, Y. Zhang, J. Wang, *Angew. Chem. Int. Ed.* **49**, 1139 (2010)
18. Q. Xiao, B. Wang, L. Tian, Y. Yang, J. Ma, Y. Zhang, S. Chen, J. Wang, *Angew. Chem. Int. Ed.* **52**, 9305 (2013)
19. F.D. Hu, Y. Xia, Z.X. Liu, C. Ma, Y. Zhang, J.B. Wang, *Org. Biomol. Chem.* **12**, 3590 (2014)
20. M. Catellani, M.C. Fagnola, *Angew. Chem. Int. Ed.* **33**, 2421 (1994)
21. R. Ferraccioli, *Synthesis* **45**, 581 (2013)
22. A. Martins, B. Mariampillai, M. Lautens, *Top. Curr. Chem.* **292**, 1 (2010)
23. P.X. Zhou, L. Zheng, J.W. Ma, Y.Y. Ye, X.Y. Liu, P.F. Xu, Y.M. Liang, *Chem. Eur. J.* **20**, 6745 (2014)

24. X.X. Wu, P.X. Zhou, L.J. Wang, P.F. Xu, Y.M. Liang, *Chem. Commun.* **50**, 3882 (2014)
25. J. Barluenga, L. Florentino, F. Aznar, C. Valdes, *Org. Lett.* **13**, 510 (2011)
26. J. Barluenga, M. Escribano, F. Aznar, C. Valdes, *Angew. Chem. Int. Ed.* **49**, 6856 (2010)
27. P.X. Zhou, Y.Y. Ye, J.W. Ma, L. Zheng, Q. Tang, Y.F. Qiu, B. Song, Z.H. Qiu, P.F. Xu, Y.M. Liang, *J. Org. Chem.* **79**, 6627 (2014)
28. Z. Dong, G.B. Dong, *J. Am. Chem. Soc.* **135**, 18350 (2013)
29. C. Peng, J. Cheng, J. Wang, *J. Am. Chem. Soc.* **129**, 8708 (2007)
30. D.J. Babinski, H.R. Aguilar, R. Still, D.E. Frantz, *J. Org. Chem.* **76**, 5915 (2011)
31. C. Eidamshaus, P. Hommes, H.-U. Reissig, *Synlett* **23**, 1670 (2012)
32. F. Ye, S. Qu, L. Zhou, C. Peng, C. Wang, J. Cheng, M.L. Hossain, Y. Liu, Y. Zhang, Z.-X. Wang, J. Wang, *J. Am. Chem. Soc.* **137**, 4435 (2015)
33. G. Wu, Y. Deng, H. Luo, J. Zhou, T. Li, Y. Zhang, J. Wang, *Chem. Comm.* **52**, 5266 (2016)
34. G. Wu, Y. Deng, H. Luo, T. Li, Y. Zhang, J. Wang, *J. Asian. Org. Chem.* **5**, 874 (2016)
35. S.K.J. Devine, D.L. Van Vranken, *Org. Lett.* **9**, 2047 (2007)
36. S.K.J. Devine, D.L. Van Vranken, *Org. Lett.* **10**, 1909 (2008)
37. P.-X. Zhou, Y.-Y. Ye, Y.-M. Liang, *Org. Lett.* **15**, 5080 (2013)
38. I.D.U.A. Premachandra, T.A. Nguyen, C. Shen, E.S. Gutman, D.L. Van Vranken, *Org. Lett.* **17**, 5464 (2015)
39. R. Kudirka, S.K.J. Devine, C.S. Adams, D.L. Van Vranken, *Angew. Chem. Int. Ed.* **48**, 3677 (2009)
40. Y.-Y. Ye, P.-X. Zhou, J.-Y. Luo, M.-J. Zhong, Y.-M. Liang, *Chem. Comm.* **49**, 10190 (2013)
41. L. Zhou, F. Ye, Y. Zhang, J. Wang, *J. Am. Chem. Soc.* **132**, 13590 (2010)
42. M. Roche, S.M. Salim, J. Bignon, H. Levaique, J.-D. Brion, M. Alami, A. Hamze, *J. Org. Chem.* **80**, 6715 (2015)
43. Q. Xiao, Y. Xia, H. Li, Y. Zhang, J. Wang, *Angew. Chem. Int. Ed.* **50**, 1114 (2011)
44. R.G. Salomon, J.K. Kochi, *J. Am. Chem. Soc.* **95**, 3300 (1973)
45. M.M. Diaz-Requejo, M.A. Mairena, T.R. Belderrain, M.C. Nicasio, S. Trofimenko, P. Perez, *J. Chem. Comm.*, 1804 (2001)
46. F. Ye, M.L. Hossain, Y. Xu, X. Ma, Q. Xiao, Y. Zhang, J. Wang, *Chem. Asian J.* **8**, 1404 (2013)
47. F. Ye, X. Ma, Q. Xiao, H. Li, Y. Zhang, J. Wang, *J. Am. Chem. Soc.* **134**, 5742 (2012)
48. T. Wang, M. Wang, S. Fang, J.-y. Liu, *Organometallics* **33**, 3941 (2014)
49. C. Wang, F. Ye, C. Wu, Y. Zhang, J. Wang, *J. Org. Chem.* **80**, 8748 (2015)
50. Y. Xia, S. Feng, Z. Liu, Y. Zhang, J. Wang, *Angew. Chem. Int. Ed.* **54**, 7891 (2015)
51. A. Funayama, T. Satoh, M. Miura, *J. Am. Chem. Soc.* **127**, 15354 (2005)
52. R. Huisgen, *Angew. Chem. Int. Ed.* **2**, 565 (1963)
53. V.V. Rostovtsev, L.G. Green, V.V. Fokin, K.B. Sharpless, *Angew. Chem. Int. Ed.* **41**, 2596 (2002)
54. C.W. Tornøe, C. Christensen, M. Meldal, *J. Org. Chem.* **67**, 3057 (2002)
55. C. Nolte, P. Mayer, B.F. Straub, *Angew. Chem. Int. Ed.* **46**, 2101 (2007)
56. M.P. Doyle, *Chem. Rev.* **86**, 919 (1986)
57. Y.-T. Tsoi, Z. Zhou, W.-Y. Yu, *Org. Lett.* **13**, 5370 (2011)

# Synthetic Molecular Springs: Stretched and Contracted Helices with Their Interconversions of Monosubstituted Polyacetylenes Prepared with a Rhodium Complex Catalyst

Yasuteru Mawatari and Masayoshi Tabata

## 1 Helical Substituted Polyacetylenes

### *1.1 Polyacetylene and Substituted Polyacetylenes: A Brief Introduction to Their Basic Properties:*

$\pi$ -Conjugated polymers have been thoroughly investigated as electrically conducting and nonlinear optical materials because they possess unique properties, e.g., conductivity and luminescence [1–5]. The structure of these polymers consists of alternating repeating units of single (C–C) and multiple (C=C or C $\equiv$ C) carbon–carbon bonds or aromatic groups such as benzene, naphthalene, aniline, and thiophene, among others. This characteristic structure is the origin of their unique properties, providing  $\pi$ -electrons in the polymer chain that are free to move between neighboring monomers without affecting the polymer's covalently bonded structure.

---

Y. Mawatari (✉)

Graduate School of Engineering, Muroran Institute of Technology,  
27-1 Mizumoto-cho, Muroran, Hokkaido 050-8585, Japan

Research Center for Environmentally Friendly Materials Engineering  
(MURORAN MATERIA), Muroran Institute of Technology,  
27-1 Mizumoto-cho, Muroran, Hokkaido 050-8585, Japan  
e-mail: [mawatari@mmm.muroran-it.ac.jp](mailto:mawatari@mmm.muroran-it.ac.jp)

M. Tabata

Center of Environmental Science and Disaster Mitigation for Advanced Research, Muroran  
Institute of Technology, 27-1 Mizumoto-cho, Muroran, Hokkaido 050-8585, Japan

Faculty of Science and Technology, Department of Applied Chemistry and Bioscience,  
Chitose Institute of Science and Technology, Bibi 65-758, Chitose,  
Hokkaido 066-8655, Japan  
e-mail: [tabata@mmm.muroran-it.ac.jp](mailto:tabata@mmm.muroran-it.ac.jp)

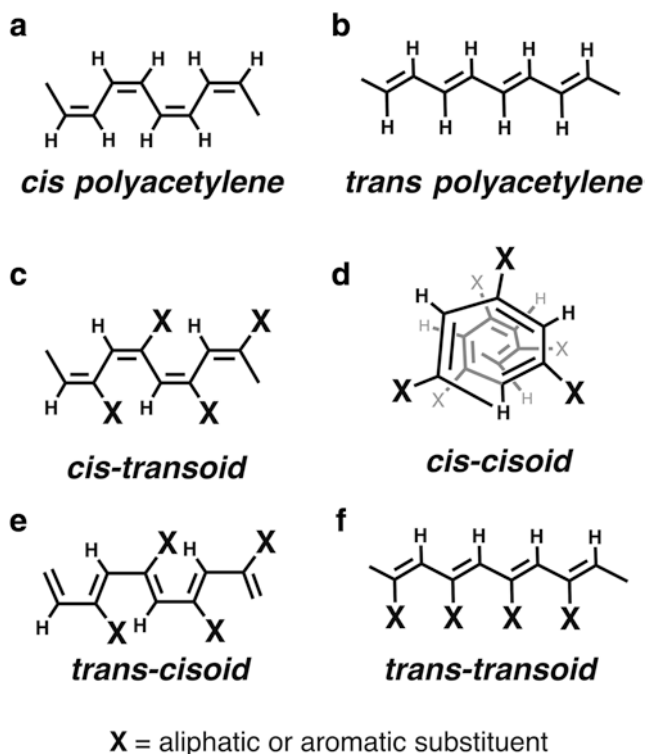


**Fig. 1** Four possible geometrical isomers of monosubstituted polyacetylenes

Polyacetylene (PA) is one of the original and most well-known  $\pi$ -conjugated polymers and bears the simplest repeating units  $(-\text{HC}=\text{CH}-)_n$  (Fig. 1a, b) [6–8]. Unfortunately, PA has two serious problems that hinder its application in devices: instability in the air and poor processability. The ionization energy of PA is low enough to allow oxidation by atmospheric oxygen even at room temperature. Furthermore, PA cannot be processed into a desired shape by melt or solution processing because of its instability and insolubility, although PA films with a hierarchical spiral morphology were synthesized using a chiral liquid crystal as the polymerization medium by Akagi et al. [9].

In contrast, the properties of substituted polyacetylenes (SPAs)  $(-\text{HC}=\text{CX}-)_n$ , (X = aromatic or aliphatic groups) differ from those of PA despite these materials sharing the same polymeric structure [10–16]. For example, poly(phenylacetylene) (PPA) is a typical SPA in which one of the hydrogen atoms in the repeating unit of PA is replaced with a phenyl group (X = phenyl ( $\text{C}_6\text{H}_5$ )) (Fig. 1c–f) [17]. Despite this small difference in the chemical structure, the stability of PPA in air is considerably improved over that of PA; the molecular weight and geometrical structure of a PPA sample were mostly unchanged even after storage for several years in air at room temperature. PPA also has improved processability because it is highly soluble

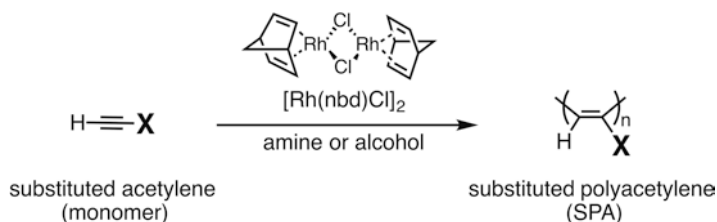


**Fig. 2** Synthesis of stereoregular substituted polyacetylene initiated by a Rh complex catalyst and a cocatalyst

in organic solvents such as chloroform ( $\text{CHCl}_3$ ), dichloromethane, and tetrahydrofuran at room temperature. Most importantly, the chemical and physical properties of PPA can be modified by designing the structures of the corresponding acetylene monomers. SPAs are expected to provide a new advanced material because of the range of interesting properties that have been observed in solid SPAs, including semiconductivity [2, 4], oxygen permeability [18, 19], humidity sensitivity [20, 21], nonlinear optical (NLO) properties [22], enantioselectivity [23, 24], and external stimulus response (e.g., color changeable dosimetric properties [25]).

## 1.2 Synthesis of Highly Stereoregular SPAs Using Rhodium–Diene Catalysts

The stereoregular polymerization of substituted acetylene monomers is most commonly achieved using a bidentate rhodium–diene complex, such as  $[\text{Rh}(\text{nbd})\text{Cl}]_2$  (nbd, norbornadiene), with small lone pair-containing molecules, such as amines or alcohols [26, 27], as a cocatalyst, to produce the corresponding highly stereoregular SPAs (Fig. 2). Other types of catalysts, including Ziegler–Natta ( $\text{Fe}(\text{acac})_3\text{-AlH}(\textit{i}\text{-Bu})_2$ ) [17, 28], nickel chloride complex ( $(n\text{-Bu}_3\text{P})_2\text{NiCl}_2\text{-NaBH}_4$ ) [29],  $\text{RhCl}(\text{PPh}_3)_3$  [30], metathesis catalysts ( $\text{WCl}_6$  or  $\text{MoCl}_5$ ) [10, 11, 31, 32], and zwitterionic mono-Rh complex catalysts [33, 34], among others [12–14], have also been reported for the polymerization of substituted acetylene monomers. However, the Rh–diene polymerization system is advantageous because the Rh complex catalyst is stable in air and is commercially available as the well-known Wilkinson’s catalyst. In addition, an important monomeric propagation species is easily generated by mixing the Rh complex catalyst with an amine or alcohol, which can be used as the cocatalyst or the polymerization solvent [26, 27]. This monomeric Rh species has prompted the development of various monomeric Rh catalysts, which are extremely tolerant of monomers with polar functional groups, i.e., ester [18, 35–40], amino [41], nitro [42–44], hydroxyl [45–49], and nitroxide [45] groups, in contrast to Ziegler–Natta or metathesis catalysts. However, disubstituted polyacetylenes have not yet been prepared using this kind of Rh catalyst, and monomers that contain sulfur atoms frequently deactivate this type of metal catalyst.



Using these Rh complex catalysts, SPAs can be obtained on scales of 10 g or more and in high yield. The advent of these Rh complex catalysts has solved three important problems: (1) whether the so-called four geometrical isomers of SPAs, i.e., the *cis-transoid*, *cis-cisoid*, *trans-transoid*, and *trans-cisoid* isomers, exist (Fig. 1c–f) [17, 27, 50, 51], (2) problems regarding the crystal structure, and (3) evaluation of the properties of the SPA helices, i.e., helical pitch, diameter, and dynamics such as spring motion. In this chapter, we focus on the latter two problems.

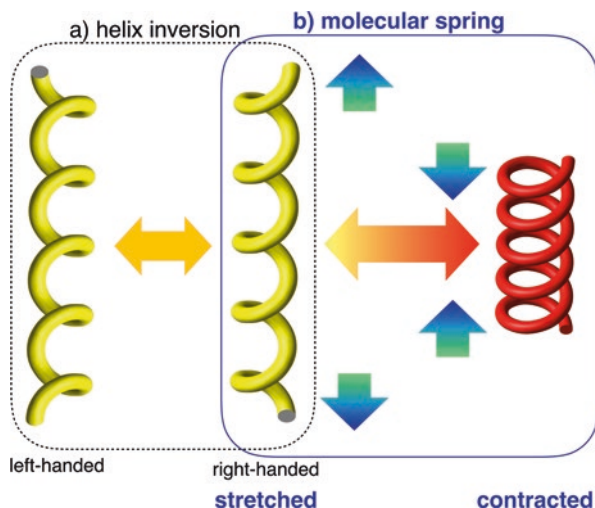
### 1.3 Helical Structure of SPAs: Unique Properties and Our Motivation

We have previously demonstrated the synthesis of  $\pi$ -conjugated, helical, and highly stereoregular SPAs using a Rh-catalyzed polymerization system and found that the resulting SPAs had a *cis-transoidal* structure [50]. The polymer chains of these highly stereoregular SPAs form helical structures to relieve the steric hindrance between the substituent groups of neighboring monomers, although these helices differ greatly from other typical helical polymers, such as deoxyribonucleic acid (DNA) [52]. We also revealed that the helical polymer chains formed columnar aggregates in the crystalline state, i.e., (pseudo)hexagonal or tetragonal packing of the helical polymer chains [18, 35, 38, 53–58].

The important chemical and physical properties of SPAs are strongly related not only to their higher-order structure, i.e., columnar, but also to the helical structure of their main chain in the solid and solution states. However, the relationship between the helical pitch, helical diameter, and crystal structure of SPAs has not yet been investigated in detail in either of these states, except for a report of helix induction, inversion, and memory in PPA derivatives by Yashima et al. [59]. These phenomena have been considered for application as a visible sensor output to indicate the enantiomeric excess of chiral molecules [60] and as a switchable chiral stationary phase for liquid chromatography [24]. These functions are based on the PPA derivatives' ability to undergo dynamic helix inversion between right-handed and left-handed helices (Fig. 3a).

We focused on another method of conversion of the helical structure. We considered the possibility of the helical structure acting as a spring, i.e., interconversion between stretched and contracted shapes (Fig. 3b), in the manner reported for poly(*o*-phenylene) in response to redox reactions by Aida et al. [61]. We investigated whether the helical pitch and packing structures of SPAs helices could be controlled through molecular design and external stimuli. Consequently, we found that the interconversion between a contracted *cis-cisoidal* helix and a stretched *cis-transoidal* helix was readily induced in PPA and its derivatives and was accompanied by a drastic color change after heat treatment or contact with solvents in the solid state [56, 57, 62–64]. Furthermore, we also found that an aliphatic polyacetylene

**Fig. 3** Two different helix interconversions. (a) Helix inversion between left-handed and right-handed helices, (b) molecular spring motion between stretched and contracted helices



ester (APA) also showed both a contracted *cis-cisoidal* helix and a stretched *cis-transoidal* helix in solution. Interestingly, these APA helices showed an accordion-like helix oscillation (HELIOS) that synchronized with the internal rotation of the ester O–C bond in the alkyl side chain [39, 40].

## 2 Stretched and Contracted Substituted Helical Polyacetylenes

### 2.1 Dependence of the Color and Helical Pitch of Solid-State PPA Polymers on the Polymerization Solvent

During our study, we found that the color of PPA and its derivatives in the solid state depended on their preparation conditions and especially the choice of polymerization solvent. This result suggests that a single monomer type can produce polymers with different colors, and the effect can be tuned by changing the polymerization solvent. The *p-n*-hexyloxyphenylacetylene (pHxOPA) monomer has previously been polymerized stereoregularly using the same Rh catalyst system at 25 °C for 30 min. When either ethanol (EtOH) or *n*-hexane was used as the polymerization solvents, the yellow or red poly(*p-n*-hexyloxyphenylacetylene) polymers (PpHxOPA(**Y**)) or (PpHxOPA(**R**)) were obtained, respectively (Fig. 4) [62]. The diffuse reflectance UV-vis spectra (DRUV-vis) of these polymers in the solid phase showed absorption maxima at 445 nm and 575 nm, respectively. Additionally, the spectrum of PpHxOPA(**R**) was composed of two absorption bands, indicating that PpHxOPA(**R**) has at least two components (Fig. 5a). However, these polymers gave almost the same absorption spectra in CHCl<sub>3</sub> solution when measured at room

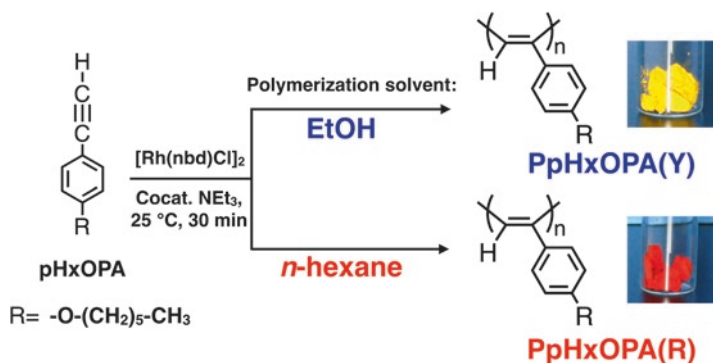


**Fig. 4** Rh-catalyzed polymerization of pHxOPA monomers using ethanol or *n*-hexane as the polymerization solvent

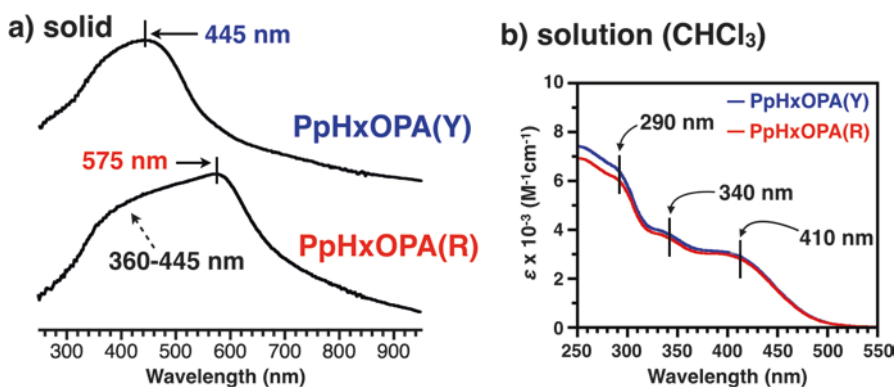
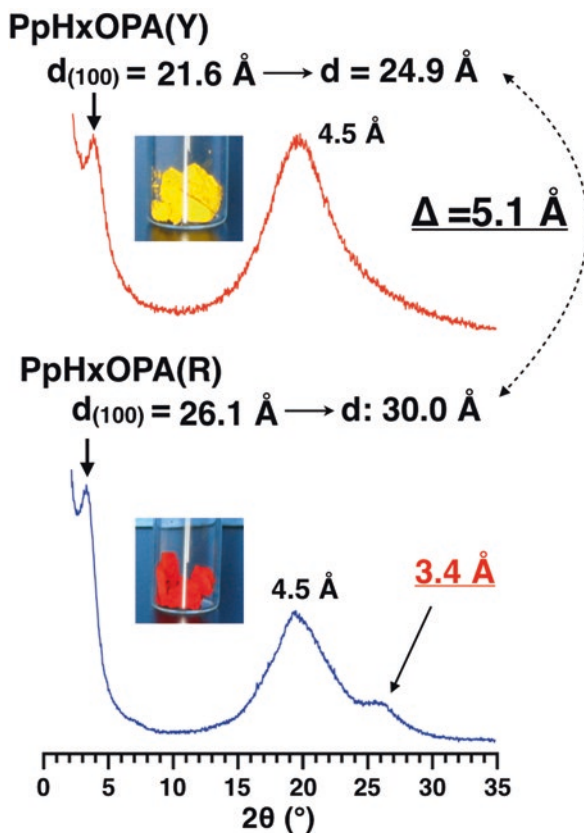


**Fig. 5** UV-vis spectra of yellow and red PpHxOPAs measured (a) in the solid state and (b) in a chloroform solution

temperature (Fig. 5b). Additionally, both the  $^1\text{H}$  and  $^{13}\text{C}$  nuclear magnetic resonance (NMR) spectra of PpHxOPA(Y) were identical to those of PpHxOPA(R). These results indicated that the different polymer colors in the solid state were caused by their morphology and helical structure. The wide-angle X-ray scattering (WAXS) patterns of PpHxOPA(Y) and PpHxOPA(R) exhibited typical hexagonal columnar structures, which were packed with stretched and contracted helices, respectively (Fig. 6). The d-spacing distance in the (100) diffraction peak of PpHxOPA(Y) (21.6 Å), which is related to the helix diameter, was smaller than that of PpHxOPA(R) (26.1 Å), and the peak at 3.4 Å was only observed in the pattern of PpHxOPA(R). Based on the assignment of a hexagonal columnar structure, the diameters of these two helices were calculated to be 24.9 and 30.0 Å, respectively. Model structures of the stretched and contracted helices were calculated using a molecular mechanics (MMFF94) program; these calculations indicated that the helix diameters were 24.7 Å and 29.1 Å, respectively, assuming that the dihedral angles between the C=C bonds in each helical main chain were 150° (*cis-transoid*, Figs. 1c and 7a) and 70° (*cis-cisoid*, Figs. 1d and 7b). Moreover, the layer distance between the phenyl rings

**Fig. 6** WAXS patterns of yellow and red PpHxOPAs measured at room temperature



in the contracted helix model was also calculated to be ca. 3.4 Å, which corresponded to the peak observed in the WAXS pattern of PpHxOPA(R). Thus, these results confirmed that the difference in color observed for these polymers in the solid state was strongly related to the helical pitch, i.e., the presence of stretched and contracted helices. The red shift in the absorption band of the solid PpHxOPA(R) was attributed to the formation of so-called through-space  $\pi$ -conjugated systems between the stacked phenyl rings in the side chain because the distance between the side phenyl rings (3.4 Å) is close to the interlayer distance of graphite, 3.35 Å [65].

## 2.2 Dependences of Functional Groups in PPA Units on Helical Pitch Width Accompanied by Their Color Changes

Fine yellow PPA powders (PPA(Y)) were also obtained using the same Rh catalyst system when EtOH was used as the polymerization solvent (Fig. 8). The color of the PPA could be changed from yellow to red by suspension in acetylacetone (acac) at

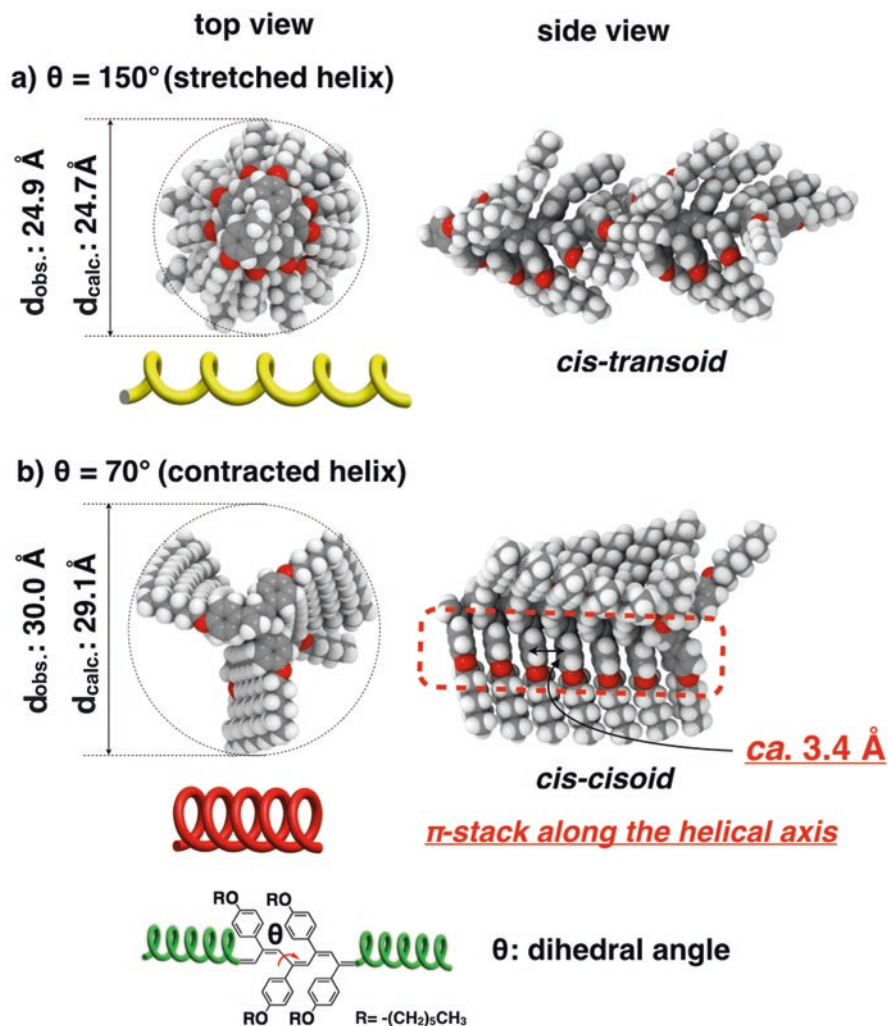


**Fig. 7** Optimized molecular model of PpHxOPAs calculated using molecular mechanics force field (MMFF94). (a) dihedral angle  $\theta$  of  $150^\circ$  (stretched helix), (b)  $\theta$  of  $70^\circ$  (contracted helix)

room temperature (PPA(**R**)), whereas a black polymer was obtained after exposure to  $\text{CHCl}_3$  vapor (PPA(**B**)). Based on analysis of the WAXS patterns, both the PPAs obtained after solvent treatment were interconverted from stretched to contracted helices similar to that of PpHxOPA(**R**). Interestingly, these PPAs could be converted back to the yellow PPA by reprecipitating the  $\text{CHCl}_3$  solution in methanol [56].

Polymerization of *p*-*n*-octylphenylacetylene (pOcPA) using EtOH as a solvent gave an orange polymer at room temperature, whereas a yellow polymer (PpOcPA(**Y**)) was obtained at  $-20^\circ\text{C}$  (Fig. 9) [57]. Despite the WAXS results,

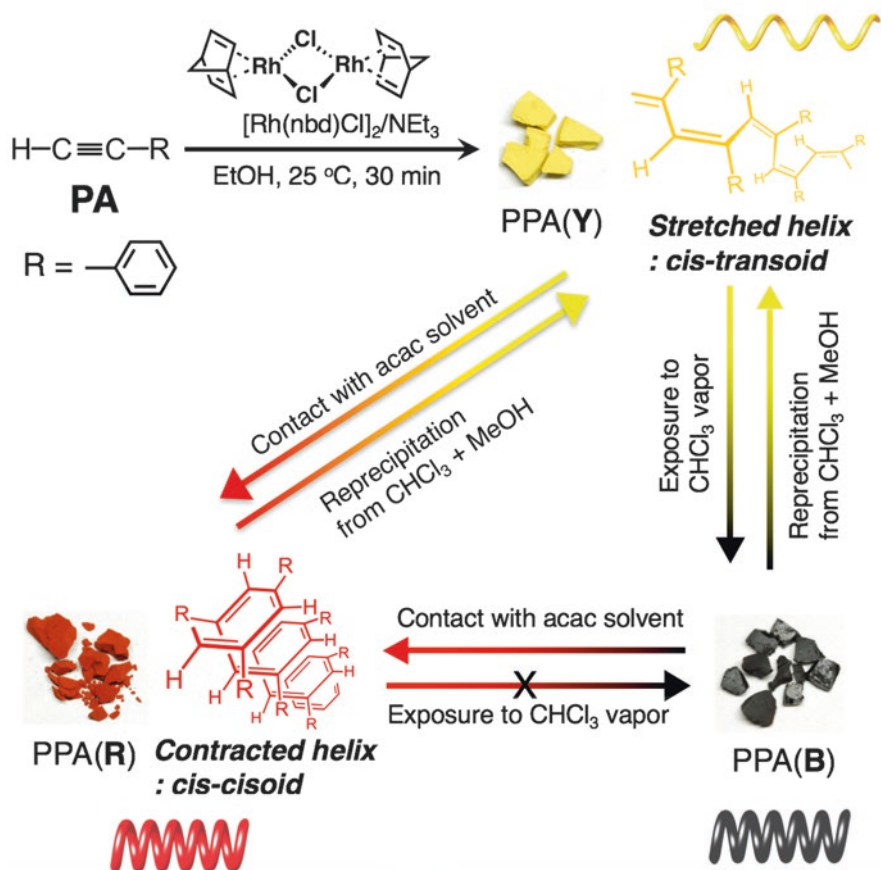


**Fig. 8** Synthesis of PPA(Y) and the drastic color change associated with its helix interconversion

MMFF94 calculations indicated that the structure of the PpOcPA(Y) adopted a contracted helix, unlike the results described previously. The alkyl chains of the alkyl-phenyl side-chain groups had a bent structure, i.e., the alkyl chain deviated from the plane of the phenyl ring. Therefore, the ordered  $\pi$ -stacked structure interferes with the tilted phenyl ring even in the case of the contracted helix. After heat treatment, the hexagonal structure of the pristine PpOcPA(Y) could be converted to two kinds of tetragonal crystals: contracted helices with straight alkyl chains and stretched helices having the original bent alkyl chains. These results lead us to attribute the difference in color, i.e., a red shift of the absorption band, to the formation of an ordered  $\pi$ -stacked structure of phenyl rings in the contracted helices.

In contrast to the above systems, the polymerization of phenylacetylene with *p*-oxyethylene side chains  $(-\text{CH}_2\text{CH}_2\text{O})_m\text{CH}_3$  ( $m = 1$  or  $2$ ) in EtOH produced a violet polymer (**P2V**), even when relatively longer oxyethylene groups ( $m = 2$ ) were

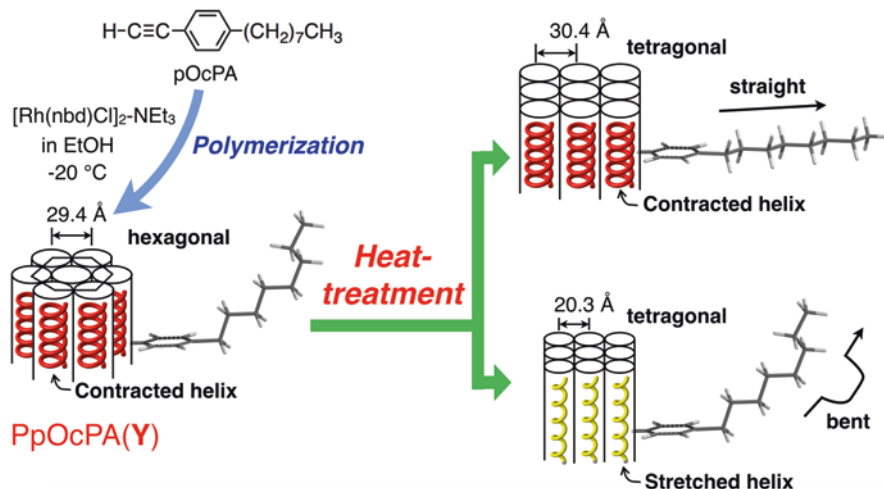


**Fig. 9** Synthesis of PpOcPA(Y) at  $-20\text{ }^{\circ}\text{C}$  and its heat-induced interconversion of crystal structure and helical pitch

introduced to phenyl rings of the monomer (Fig. 10) [64]. The polymer may have converted from a stretched to a contracted helix (*cis-cisoidal*) during the polymerization reaction because EtOH acted as a good solvent for the longer oxyethylene groups, similar to the combination of alkyl chains and *n*-hexane. This result indicates that stretched and contracted helices can be selectively prepared by selecting the appropriate combination of side chains and polymerization solvent. In the case of the shortest oxyethylene group, i.e., methoxyethoxy group (**P1Y**,  $m = 1$ ), the chain was partially bent in the solid phase, as shown by XRD, <sup>13</sup>C cross-polarization magic angle spinning (CPMAS) NMR, and molecular mechanics calculations (Fig. 10). The bent conformation interfered with the formation of the contracted helix because of the steric hindrance between the bent oxyethylene groups.

### 2.3 Substituted Polyacetylene Having Naphthalene as the Side Group

Poly(2-ethynynaphthalene) (P2EN), which has a larger aromatic ring than PPA as the side chain group, was prepared using the same [Rh(norbornadiene)Cl]<sub>2</sub>-NEt<sub>3</sub> catalyst system [63]. A highly ordered, contracted *cis-cisoidal* helix was expected to be formed, and strong  $\pi$ - $\pi$ -interactions due to the larger aromatic rings were also anticipated. When EtOH was used as the polymerization solvent, a bright yellow polymer, P2EN(Y), was obtained in moderate yield (Fig. 11). The use of toluene afforded a red polymer, P2EN(R) in high yield. Both pristine polymers were insoluble in organic solvents. The absorption spectrum of P2EN(Y) showed a  $\lambda_{\text{max}}$  at

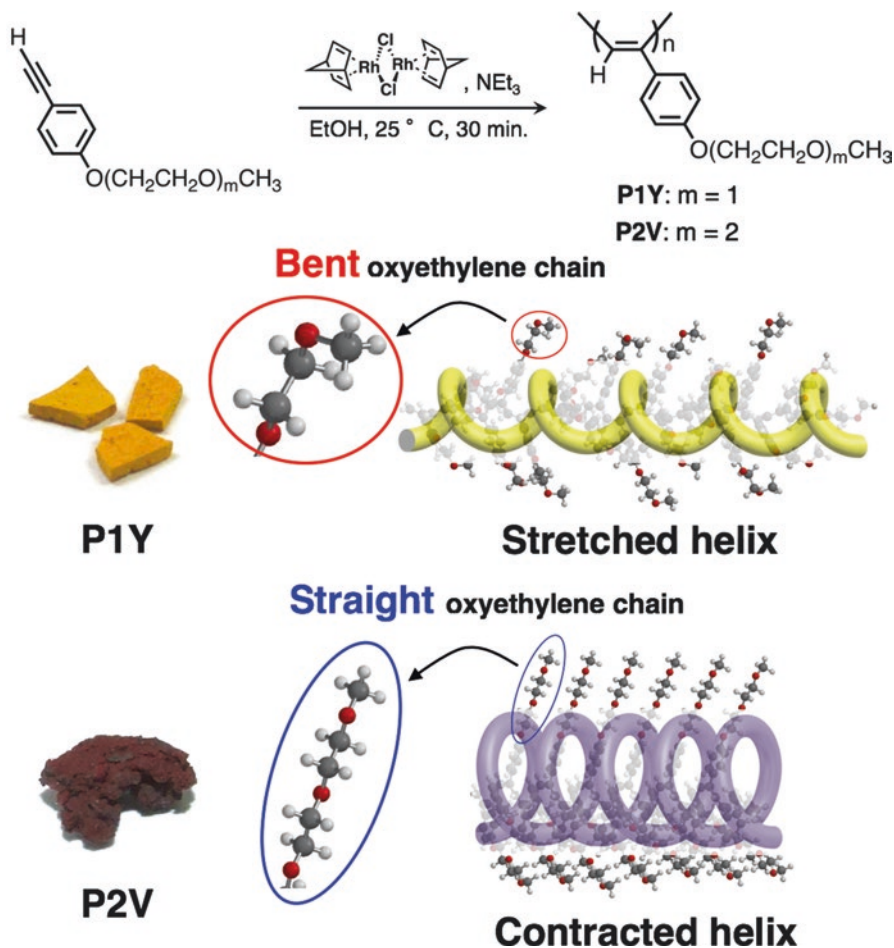
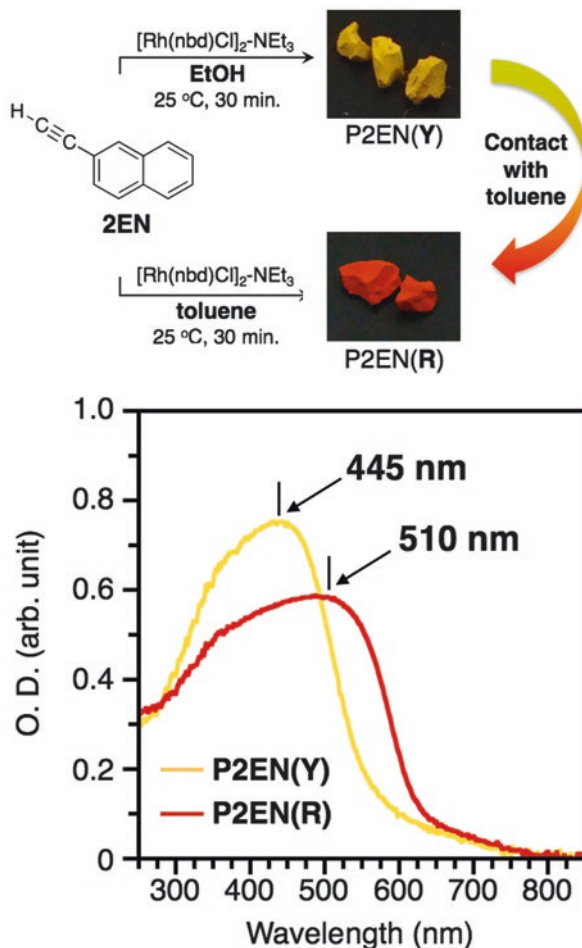


**Fig. 10** Synthesis of PPAs with oxyethylene groups, their colors in the solid state, and the difference in helical structures for different oxyethylene side groups

445 nm, which was almost the same as PPA(Y). P2EN(Y) instantly converted into P2EN(R) with  $\lambda_{\text{max}} = 510$  nm when P2EN(Y) was contacted with toluene, even at room temperature (Fig. 11). Size-exclusion chromatography (SEC) was used to estimate the molecular weights of these polymers. The two P2EN samples were prepared by heat treatment at 200–240 °C for 1 min under an  $\text{N}_2$  atmosphere. All the P2ENs became partially soluble in  $\text{CHCl}_3$  after the heat treatment, although the treatment of the two red polymers required a higher temperature than that of P2EN(Y). As a representative example, the *cis* content and  $M_n$  of P2EN(Y) after heat treatment at 200 °C were approximately 22% and 14,300, respectively, which indicates that a *cis-to-trans* isomerization occurred together with main-chain scission of the pristine P2EN(Y) during heating.



**Fig. 11** Rh-catalyzed polymerization of 2EN using ethanol or *n*-hexane as the polymerization solvent (*upper*). UV-vis spectra of the resulting polymers having different colors in the solid state (*lower*) (Reprinted with permission from Mawatari et al. [63]. Copyright 2014, Elsevier)



The higher-order structure of P2EN(**Y**) was a hexagonal crystal, which was packed with stretched *cis-transoidal* helices, whereas that of P2EN(**R**) was tetragonally packed crystals, which were composed of contracted *cis-cisoidal* helices whose structures were determined by XRD and MMFF94 calculation (Fig. 12). Notably, the WAXS pattern of P2EN(**R**) showed a stronger reflection peak at approximately 3.4 Å than those of *cis-cisoid* PPA and its analogs [56, 62, 64]. The d-spacing was approximately the same as the distance between graphene sheets in graphite, in which  $\pi$ -orbitals of neighboring graphene sheets overlap via  $\pi$ - $\pi$  stacking to increase their  $\pi$ -conjugation [66, 67]. This result suggests that intramolecular  $\pi$ -conjugation, that is, ordered  $\pi$ -stacking, occurred between the neighboring naphthalene rings along the helical axis. Therefore, the degree of through-space  $\pi$ -conjugation in P2EN(**R**) is considerably stronger than that of the contracted helices of PPAs. Thus, we concluded that the stronger  $\pi$ -stacking in P2EN(**R**) caused a

larger red shift compared to that of P2EN(**Y**), as observed in the solid phase DRUV-vis spectra. The WAXS pattern and DRUV-vis spectrum of P2EN(**Y-R**) were almost identical to those of P2EN(**R**). This result indicates that toluene converted the stretched helix of P2EN(**Y**) into the contracted helix, together with rearrangement of the packing structure from hexagonal to tetragonal crystals. Unfortunately, the reason for the switch to tetragonal crystals is still unclear. Interestingly, the *cis-to-trans* isomerization temperatures of P2ENs (>200 °C) were much higher than those of PPAs (~140 °C) [62]. Thus, for the first time, a thermally stable  $\pi$ -conjugated system constructed from the stretched and contracted helices with strong  $\pi$ -stacking exhibited interesting properties as a novel functional material. Therefore, we continued to study other derivatives of P2EN.

### 3 Helical Pitch Control with Temperature in the Solid State and Solution

#### 3.1 Interconversion from Stretched to Contracted Helices in the Solid State

PpHxOPA(**Y**) was transformed into a reddish-black-colored polymer, PpHxOPA(**B**), whose columnar diameter sharply increased and became identical to that of PpHxOPA(**R**) when heated at 80 °C [62]. This result indicated that the conversion of a stretched helix to a contracted helix could be induced by heat treatment. An exothermic peak was clearly observed at ~80 °C in the differential scanning calorimetry (DSC) trace of PpHxOPA(**Y**), whereas no peak at the same temperature was observed for PpHxOPA(**R**) and there was no change in color (Fig. 13). These findings also supported a thermally irreversible interconversion from the thermally unstable stretched helix state of PpHxOPA(**Y**) to the more stable contracted helix state of PpHxOPA(**B**) in the solid phase. Based on the XRD patterns, the distance between every phenyl ring, i.e., the helical pitch of PpHxOPA(**B**), was also 3.4 Å, similar to that of PpHxOPA(**R**). This result was also supported by molecular mechanics (MM) calculations, which showed that the strain energy of the stretched model was higher than that of the contracted model, based on the relationship between the dihedral angles between pairs of double bonds and the strain energy (Fig. 14). These systems can be represented as one of the two types of spring: push or pull springs (Fig. 15). The strain energy of these springs shows the opposite behavior; for example, in the case of a pull spring, the strain energy of the stretched form becomes higher than that of the contracted helix. We can therefore conclude that the helical structure of PpHxOPA corresponds to that of a pull spring. This idea provides a method of interpreting the spectral changes induced by temperature changes, as described below.

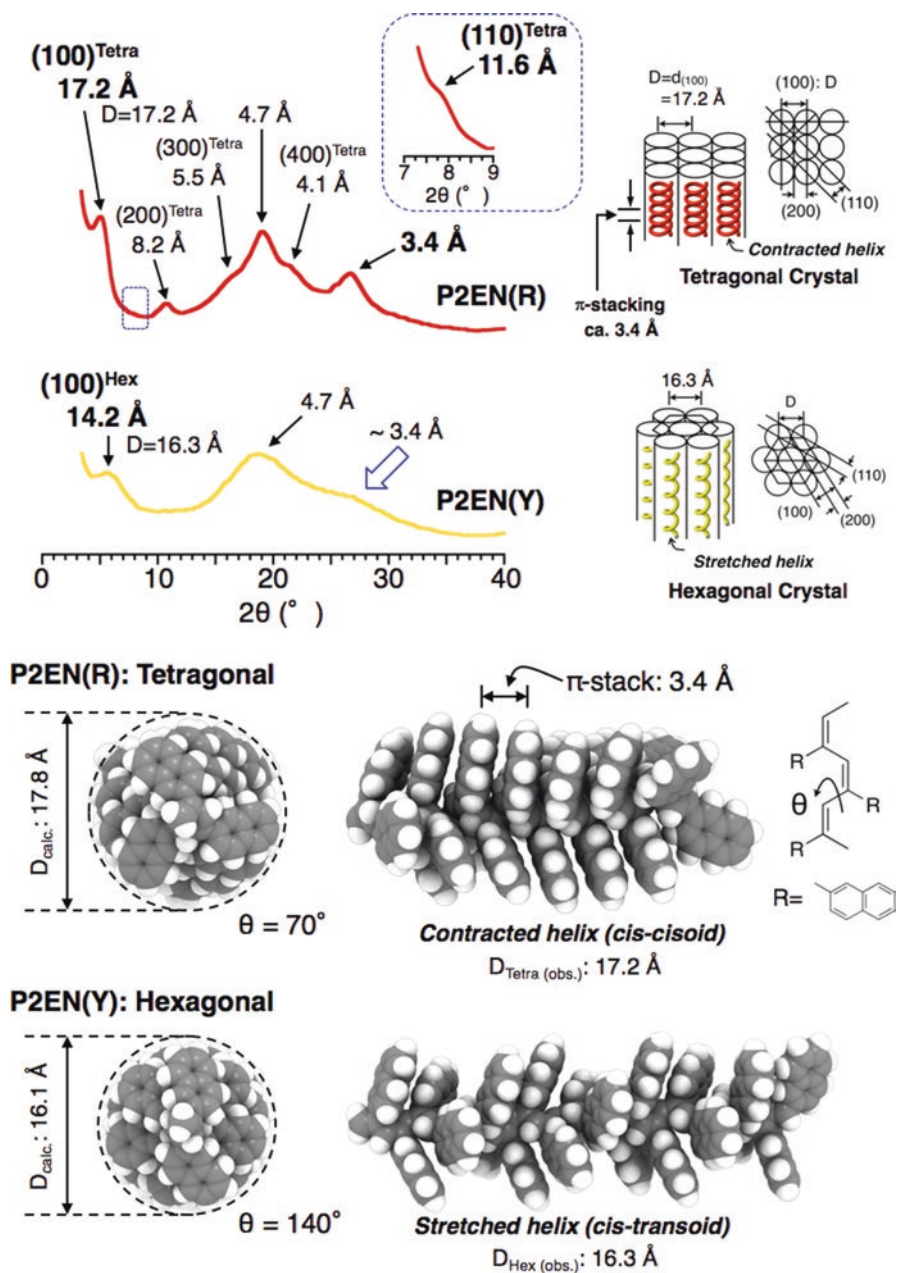


**Fig. 12** XRD patterns of P2EN(Y) and P2EN(R) with columnar structures and helical structures calculated using the MMFF94 program (Reprinted with permission from Mawatari et al. [63]. Copyright 2014, Elsevier)

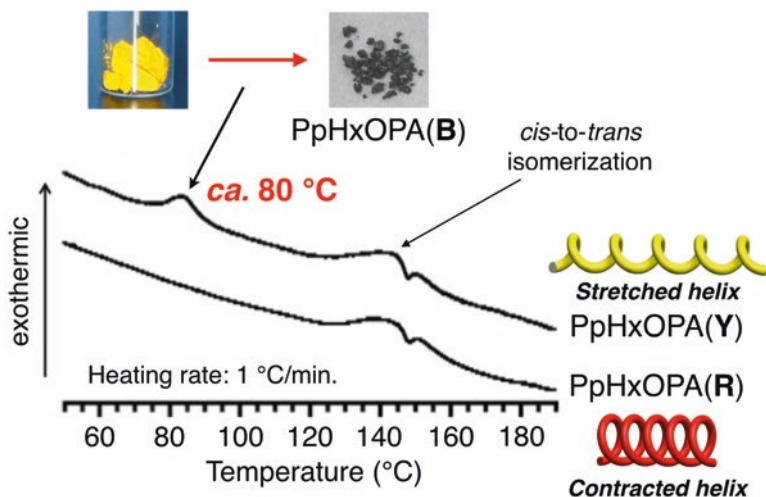
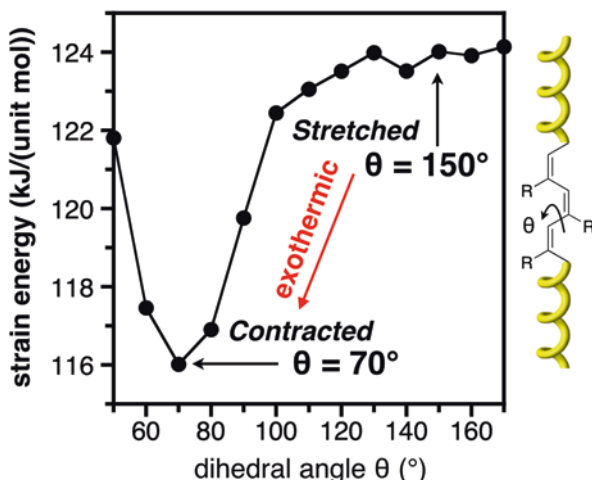


Fig. 13 DSC traces of PpHxOPA(Y) and PpHxOPA(R) under an N<sub>2</sub> atmosphere

Fig. 14 Strain energy dependences of the dihedral angle around the C–C single bond in the C=C–C=C sequence in the main chain



### 3.2 Restricted Rotation of C–O Bonds of Ester Side Chains Clarified by Variable-Temperature NMR Measurements in Solution

An aliphatic acetylene monomer having a chiral alkyl ester group, (*s*)-2-octyl propiolate (s2OcP), was stereoregularly polymerized using the same Rh complex catalyst at 40 °C in methanol solvent to give the corresponding helical polymer, Ps2OcP (Fig. 16) [39]. Triethylamine could not be used as the cocatalyst in this polymerization, unlike the polymerizations used for PA monomers, because of its vigorous

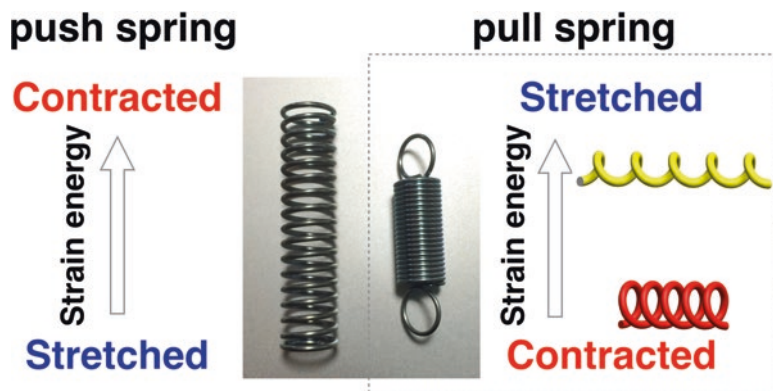


Fig. 15 The difference in strain energy between push and pull springs

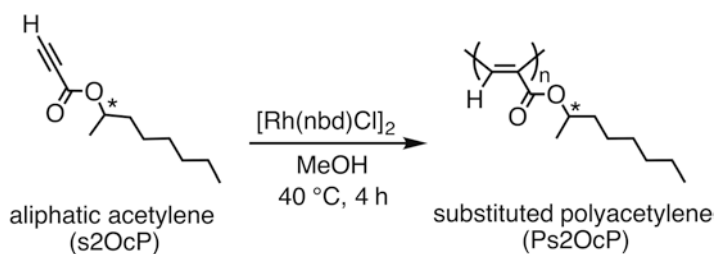
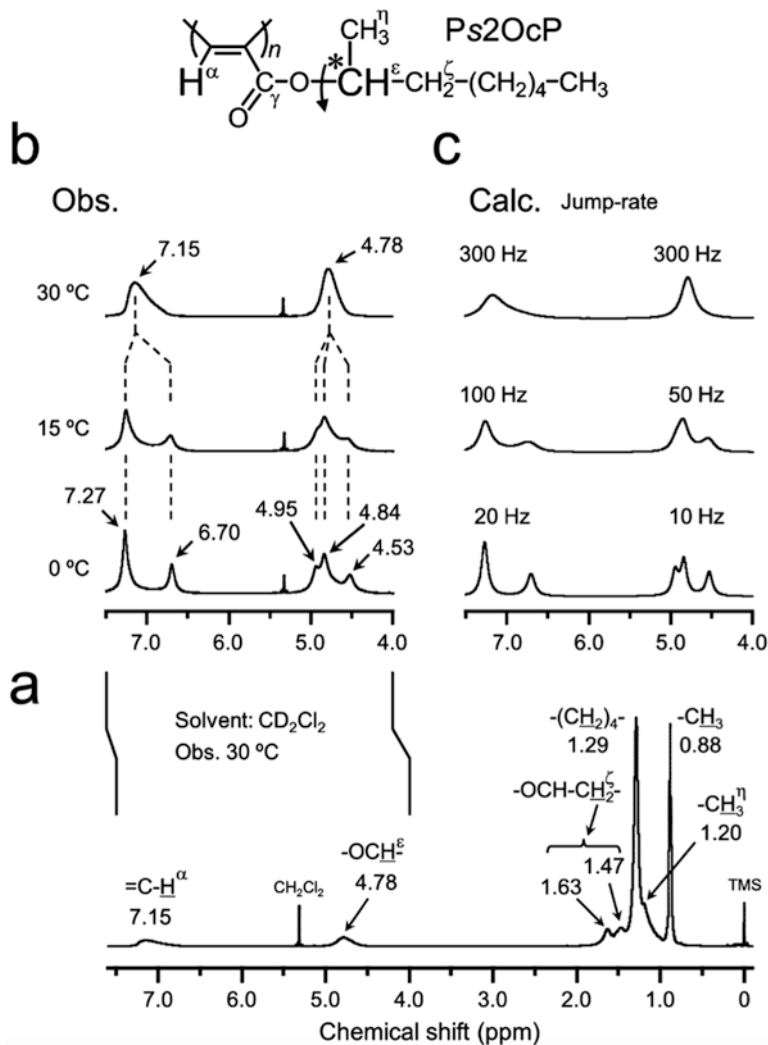


Fig. 16 Synthesis of a polyacetylene ester initiated by a Rh complex catalyst in methanol

exothermic side reaction. The two peaks observed in the  $^1\text{H}$  NMR spectrum of Ps2OcP were assigned to the main-chain proton ( $\text{H}^\alpha$ ) and methyldene proton ( $\text{H}^\beta$ ) on the chiral carbon of the alkyl side chain, respectively (Fig. 17a). These peaks were remarkably broad and asymmetrically shaped in dichloromethane- $d_2$  ( $\text{CD}_2\text{Cl}_2$ ) solution, even at 30  $^\circ\text{C}$ . Surprisingly, each peak could be resolved into two or three peaks using variable-temperature NMR (VT-NMR) measurements (Fig. 17a–c). The observed broad peak corresponding to the  $\text{H}^\alpha$  proton was clearly split into two singlets with relative intensities of approximately 2:1 at 15  $^\circ\text{C}$  (Fig. 17b). In the case of  $\text{H}^\beta$ , an additional split was observed, i.e., three singlets were observed with relative intensities of approximately 1:1:1 at 0  $^\circ\text{C}$  (Fig. 17c). These changes with temperature indicated that a chemical exchange was thermally induced, involving the creation of three different magnetic environments for  $\text{H}^\beta$ , i.e., the restricted rotation around the  $\text{C}^\beta\text{--O}$  bond in the ester group connected to  $\text{H}^\beta$ . In the case of  $\text{H}^\alpha$ , however, the two singlets became narrower without any change in intensity when cooled from 15 to 0  $^\circ\text{C}$ . This observation shows that chemical exchange between three sites is also induced for  $\text{H}^\alpha$ . The peak ratio for these sites of 2:1 indicates that two of these sites were quite similar and resulted in a similar magnetic environment.  $^{13}\text{C}$  VT-NMR also showed a similar chemical exchange for the carbon atoms in the main chain ( $\text{C}^\alpha$  and  $\text{C}^\beta$ ), the carbonyl carbon ( $\text{C}^\gamma$ ) in the ester side group, and even the branched



**Fig. 17** <sup>1</sup>H NMR spectra of Ps2OcP. (a) Observed at 30 °C, (b) expanded temperature-dependent spectra in the range of 7.5–4.0 ppm, and (c) computer-simulated spectra in the range of 7.5–4.0 ppm (Reprinted with permission from Yoshida et al. [39]. Copyright 2013, American Chemical Society)

methyl carbon (C<sup>η</sup>). Consequently, restricted rotation around the ester C<sup>ε</sup>–O bond occurred, with the side chain exploring three possible sites in Ps2OcP (Fig. 18). The restricted rotation arose from the increased double bond order of the C<sup>ε</sup>–O bond, which was a result of the extended conjugation provided by the electron-withdrawing effects of both the C=C bonds and ester groups and the electron-donating effects of the alkyl group. We were fortunate to observe this restricted rotation because the

rotational rate of chemical bonds is rarely slow on the NMR time scale at room temperature. To the best of our knowledge, this is the first observation of restricted rotation around an ester C<sup>e</sup>–O bond in the side chain of a synthetic polymer.

### 3.3 *Accordion-Like Helix Oscillations (HELIOS)*

The NMR peak splitting patterns were simulated to determine the chemical exchange rates of each proton and carbon, assuming a model in which three possible sites are explored (Figs. 17d and 18d). The simulation clearly showed that the exchange rates of H<sup>α</sup> and H<sup>e</sup> were almost the same. Similarly, the same exchange rates were observed for C<sup>α</sup>, C<sup>β</sup>, C<sup>γ</sup>, and C<sup>η</sup>. Moreover, the rate of exchange of protons and carbons was also equivalent. Temperature-dependent UV-vis and CD spectra of Ps2Ocp, together with MMFF calculations, corroborated the presence of contracted and stretched helical polymers in solution, in which the helical pitches and their persistence lengths depend on the temperature. These results indicated that the pitch lengths of the helical rotamer are dynamically exchanging with each other and synchronizing with the restricted rotation of the side chain at the same rate. In other words, the helical structure oscillates like a spring, while a simultaneous rotation around the ester C<sup>e</sup>–O bond occurs, and the two motions are synchronized. Thus, we named this phenomenon “accordion-like helix oscillation (*HELIOS*)” (Fig. 19). Interestingly, the observation of *HELIOS* indicates that both *cis-transoidal* and *cis-cisoidal* structures exist in dichloromethane and are interchanged as the helix stretches and contracts. Thus, *HELIOS* is induced by the dynamic changes in molecular motion that occur to minimize the steric hindrance between neighboring ester groups. Previously, such a <sup>1</sup>H NMR spectral change was explained in terms of the inversion of the helical main chain. However, in the temperature region where such chemical exchanges were clearly observed, no changes in the CD spectra occurred that would support such a helix inversion. We conclude, therefore, that these spectral changes in <sup>1</sup>H and <sup>13</sup>C VT-NMR are attributed to the *HELIOS* mode, which is a new dynamic conversion mode for helical molecules [39, 40].

## 4 Conclusion

In this chapter, we revealed several unique and interesting interconversions between stretched and contracted helices of SPAs, including not only poly(phenylacetylene)s but also aliphatic polyacetylene esters. These acetylene polymers are classified as some of the stiffest helical polymers because they are composed of alternating C–C and C=C conjugated bonds and additional π-conjugation through π-stacking, which is generated in the direction of the helical axis. This unique interconversion between stretched and contracted helices in the solid state, accompanied by the *HELIOS* phenomena, is one of the most important topics in helix chemistry and physics

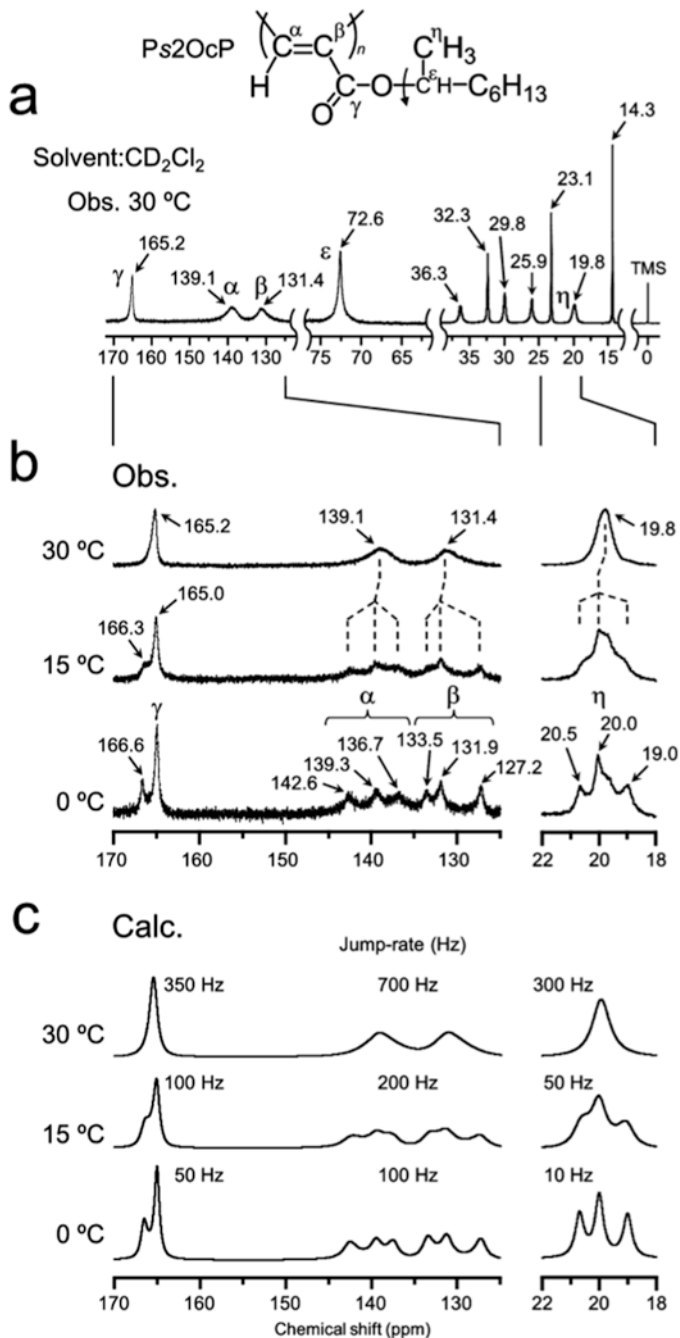


**Fig. 18**  $^{13}\text{C}$  NMR spectra of Ps2OcP. (a) Full spectrum observed at 30 °C, (b) expanded temperature-dependent spectra in the ranges of 170–125 and 22–18 ppm, and (c) computer-simulated spectra in the ranges of 170–125 and 22–18 ppm (Reprinted with permission from Yoshida et al. [39]. Copyright 2013, American Chemical Society)



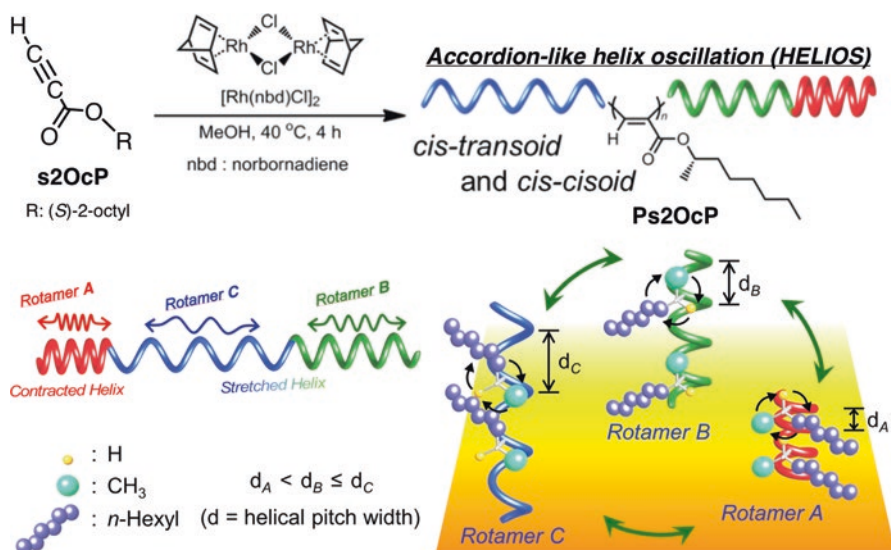


**Fig. 19** Proposed image model of the *accordion-like helix oscillation (HELIOS)* of contracted and stretched helices of Ps2OcP synchronized with the restricted rotation of side chains (Reprinted with permission from Yoshida et al. [39]. Copyright 2013, American Chemical Society)

because of its relevance to various natural and synthetic helical molecules, e.g., polypeptides, DNA, and cellulose.

The observed and calculated helical pitch widths in the contracted helices of SPAs were approximately 3.4–3.6 Å, which is comparable to the interlayer distance of graphite (3.35 Å). In the case of poly(ethyl propiolate), an aliphatic substituted polyacetylene, the electric current of one helical molecule was measured to be approximately  $10^{-8}$  Amperes without doping [68]. The present study is useful for the fabrication of the smallest and most sensitive single-molecule helical nanosensors. This research suggests that a single-molecule nano-device, i.e., the smallest possible electric device, will soon be developed. These results will be published elsewhere.

## References

1. T.A. Skotheim (ed.), *Handbook of Conducting Polymers* (Marcel Dekker, New York, 1986)
2. H.S. Nalwa (ed.), *Handbook of Organic Conductive Molecules and Polymers* (Wiley, New York, 1997)
3. T.A. Skotheim, J.R. Reynolds (eds.), *Handbook of Conducting Polymers, Conjugated Polymers*, 3rd edn. (CRC Press, New York, 2007)
4. D.L. Wise, G.E. Wnek, D.J. Trantolo, T.M. Cooper, J.D. Gresser (eds.), *Electrical and Optical Polymer Systems: Fundamentals, Methods, and Applications* (Marcel Dekker, New York, 1998)

5. K. Müllen, J.R. Reynolds, T. Masuda (eds.), *Conjugated Polymers: A Practical Guide to Synthesis* (RSC Publishing, Cambridge, 2014)
6. H. Shirakawa, *Angew. Chem. Int. Ed.* **40**, 2574 (2001)
7. A. Heeger, *J. Angew. Chem. Int. Ed.* **40**, 2591 (2001)
8. A. MacDiarmid, G. *Angew. Chem. Int. Ed.* **40**, 2581 (2001)
9. K. Akagi, *Chem. Rev.* **109**, 5354 (2009)
10. T. Masuda, F. Sanda, in *Handbook of Metathesis*, vol. 3, ed. by R. H. Grubbs (Wiley-VCH, Weinheim, 2003) pp. 375–406
11. T. Masuda, F. Sanda, M. Shiotsuki, *Comprehensive Organometallic Chemistry III* (Elsevier, Oxford, 2006.) Ch. 11.18
12. M. Shiotsuki, F. Sanda, T. Masuda, *Polym. Chem.* **2**, 1044–1058 (2011)
13. J. Sedláček, J. Vohlřídál, *Collect. Czechoslov. Chem. Commun.* **68**, 1745–1790 (2003)
14. T. Masuda, *J. Polym. Sci. Part A: Polym. Chem.* **45**, 165–180 (2007)
15. J. Liu, J.W.Y. Lam, B.Z. Tang, *Chem. Rev.* **109**, 5799 (2009)
16. T. Aoki, T. Kaneko, M. Teraguchi, *Polymer* **47**, 4867 (2006)
17. C.I. Simionescu, V. Percec, S. Dumitrescu, *J. Polym. Sci. Polym. Chem. Ed.* **15**, 2497–2509 (1977)
18. M. Tabata, Y. Sadahiro, Y. Nozaki, Y. Inaba, K. Yokota, *Macromolecules* **29**, 6673–6675 (1996)
19. T. Masuda, E. Isobe, T. Higashimura, K. Takada, *J. Am. Chem. Soc.* **105**, 7473–7474 (1983)
20. A. Asdente, A. Ottoboni, A. Furlani, M.V. Russo, *Chemtronics* **5**, 75–80 (1991)
21. A. Furlani, G. Iucci, M.V. Russo, A. Bearzotti, A. D'Amico, *Sens Actuators B* **13**, 447–450 (1992)
22. D. Neher, A. Wolf, C. Bubeck, G. Wegner, *Chem. Phys. Lett.* **163**, 116–122 (1989)
23. S. Hadano, M. Teraguchi, T. Kaneko, T. Aoki, *Chem. Lett.* **36**, 220–221 (2007)
24. K. Shimomura, T. Ikai, S. Kanoh, E. Yashima, K. Maeda, *Nat. Chem.* **6**, 429–434 (2014)
25. M. Kozuka, T. Sone, M. Tabata, Y. Sadahiro, T. Enoto, *Radiat. Phys. Chem.* **63**, 59–61 (2002)
26. M. Tabata, W. Yang, K. Yokota, *Polym. J.* **22**, 1105–1107 (1990)
27. M. Tabata, W. Yang, K. Yokota, *J. Polym. Sci. Part A: Polym. Chem.* **32**, 1113–1120 (1994)
28. T.J. Sanford, R.D. Allendoerfer, E.T. Kang, P. Ehrlich, *J. Polym. Sci. Polym. Phys. Ed.* **18**, 2277–2286 (1980)
29. L.B. Luttinger, *J. Org. Chem.* **27**, 1591–1596 (1962)
30. Kern, R. J. *J. Polym. Sci.: Polym. Chem. Ed.* 1969, **7**, 621–631
31. T. Masuda, T. Higashimura, *Adv. Polym. Sci.* **81**, 121–165 (1986)
32. H. Shirakawa, T. Masuda, K. Takeda in *The Chemistry of Triple-Bonded Functional Groups*, ed. by S. Patai, vol. 2 (Wiley, Chichester, 1994) Supplement C2, Ch. 17
33. Y. Kishimoto, M. Itou, T. Miyatake, T. Ikariya, R. Noyori, *Macromolecules* **28**, 6662–6666 (1995)
34. N. Onishi, M. Shiotsuki, F. Sanda, T. Masuda, *Macromolecules* **42**, 4071–4076 (2009)
35. M. Tabata, Y. Inaba, K. Yokota, Nozaki, *J. Macromol. Sci. Pure Appl. Chem.* **A31**, 465–475 (1994)
36. H. Nakako, R. Nomura, M. Tabata, T. Masuda, *Macromolecules* **32**, 2861–2864 (1999)
37. R. Nomura, Y. Fukushima, H. Nakako, T. Masuda, *J. Am. Chem. Soc.* **122**, 8830–8836 (2001)
38. M. Kozuka, T. Sone, Y. Sadahiro, M. Tabata, T. Enoto, *Macromol. Chem. Phys.* **203**, 66–70 (2002)
39. Y. Yoshida, Y. Mawatari, A. Motoshige, R. Motoshige, T. Hiraoki, M. Wagner, K. Müllen, M.J. Tabata, *Am. Chem. Soc.* **135**, 4110–4116 (2013)
40. Y. Yoshida, Y. Mawatari, A. Motoshige, R. Motoshige, T. Hiraoki, M. Tabata, *Polym. Chem.* **4**, 2982–2988 (2013)
41. M. Lindgren, H.-S. Lee, W. Yang, M. Tabata, K. Yokota, *Polymer* **32**, 1531–1534 (1991)
42. M.V. Russo, A. Furlani, R. D'Amato, *J. Polym. Sci. Part A: Polym. Chem.* **36**, 93–102 (1998)
43. R. D'Amato, T. Sone, M. Tabata, Y. Sadahiro, M.V. Russo, A. Furlani, *Macromolecules* **31**, 8660–8665 (1998)

44. T. Sone, R. D'Amato, Y. Mawatari, M. Tabata, A. Furlani, M.V. Russo, J. Polym. Sci. Part A: Polym. Chem. **42**, 2365–2376 (2004)
45. H. Nishide, N. Yoshioka, T. Kaneko, E. Tsuchida, *Macromolecules* **23**, 4487–4488 (1990)
46. N. Yoshioka, H. Nishide, T. Kaneko, H. Yoshiki, E. Tsuchida, *Macromolecules* **25**, 3838–3842 (1992)
47. T. Aoki, T. Kaneko, N. Maruyama, A. Sumi, M. Takahashi, T. Sato, M. Teraguchi, J. Am. Chem. Soc. **125**, 6346–6347 (2003)
48. T. Kaneko, Y. Umeda, T. Yamamoto, M. Teraguchi, T. Aoki, *Macromolecules* **38**, 9420–9426 (2005)
49. Y. Suzuki, M. Shiotsuki, F. Sanda, T. Masuda, *Macromolecules* **40**, 1864–1867 (2007)
50. M. Tabata, T. Sone, Y. Sadahiro, *Macromol. Chem. Phys.* **200**, 265–282 (1999)
51. T. Sone, R. Asako, T. Masuda, M. Tabata, T. Wada, H. Sasabe, *Macromolecules* **34**, 1586–1592 (2001)
52. J.D. Watson, F.H.C. Crick, *Nature* **171**, 737–738 (1953)
53. M. Tabata, S. Kobayashi, Y. Sadahiro, Y. Nozaki, K. Yokota, W. Yang, J. *Macromol. Sci. Pure Appl. Chem.* **A34**, 641–653 (1997)
54. Y. Mawatari, M. Tabata, T. Sone, K. Ito, Y. Sadahiro, *Macromolecules* **34**, 3376–3782 (2001)
55. K. Huang, M. Tabata, Y. Mawatari, A. Miyasaka, E. Sato, Y. Sadahiro, Y. Kashiwaya, K. Ishii, J. Polym. Sci. Part A: Polym. Chem. **43**, 2836–2850 (2005)
56. R. Motoshige, Y. Mawatari, A. Motoshige, Y. Yoshida, T. Sasaki, H. Yoshimizu, T. Suzuki, Y. Tsujita, M. Tabata, J. Polym. Sci. Part A: Polym. Chem. **52**, 752–759 (2014)
57. A. Motoshige, Y. Mawatari, Y. Yoshida, R. Motoshige, M. Tabata, *Polym. Chem.* **5**, 971–978 (2014)
58. T. Sasaki, Y. Yoshida, Y. Mawatari, M. Tabata, *Macromolecules* **48**, 889–897 (2015)
59. E. Yashima, K. Maeda, H. Iida, Y. Furusho, K. Nagai, *Chem. Rev.* **109**, 6102–6211 (2009)
60. K. Maeda, H. Mochizuki, M. Watanabe, T. Yashima, J. Am. Chem. Soc. **128**, 7639 (2006)
61. E. Ohta, H. Sato, S. Ando, A. Kosaka, T. Fukushima, D. Hashizume, M. Yamasaki, K. Hasegawa, A. Muraoka, H. Ushiyama, K. Yamashita, T. Aida, *Nat. Chem.* **3**, 68 (2011)
62. A. Motoshige, Y. Mawatari, Y. Yoshida, C. Seki, H. Matsuyama, M.J. Tabata, *Polym. Sci. Part A: Polym. Chem.* **50**, 3008–3015 (2012)
63. Y. Mawatari, A. Motoshige, Y. Yoshida, R. Motoshige, T. Sasaki, M. Tabata, *Polymer* **55**, 2356–2361 (2014)
64. Y. Mawatari, Y. Yoshida, A. Motoshige, R. Motoshige, T. Sasaki, M. Tabata, *Eur. Polym. J.* **57**, 213–220 (2014)
65. I.L. Spain, in *The Physics of Semimetals and Narrow Band-Gap Semiconductors*, ed. by D.L. Carter, R.T. Bate (Pergamon Press, Oxford, 1971)
66. K.S. Novoselov, A.K. Geim, S.V. Morozov, D. Jiang, Y. Zhang, S.V. Dubonos, I.V. Grigorieva, A.A. Firsov, *Science* **306**, 666–669 (2004)
67. W. Pisula, X. Feng, K. Müllen, *Chem. Mater.* **23**, 554–567 (2011)
68. N. Wang, Y. Zhang, K. Yano, C. Durkan, N. Plank, M.E. Welland, H.E. Unalan, M. Mann, G.A.J. Amaratunga, W.I. Milne, *Nanotechnology* **20**, 105201 (2009)

# The Spin Coupling in the Polyaromatic Hydrocarbons and Carbon-Based Materials

Marilena Ferbinteanu, Cristina Buta, Ana Maria Toader,  
and Fanica Cimpoesu

The work draws a walk along several areas implying the spin-coupling keyword, understood either as very general paradigm of the bonding, particularly with reference to the  $\pi$  delocalized aromatics, or as mechanism for the occurrence of relatively exotic classes of carbon-based magnetic systems.

We offer a self-contained introduction in models dealing with spin coupling at phenomenological level or in first-principle calculations. Prototypic systems were reviewed from different methodological perspectives, following the red line of bonding analysis with the help of exchange coupling ideas and resonance structures. Trying to make a fluent story, simple systems like benzene, naphthalene and anthracene are presented in an original collage. Then, the abstracted ideas are passed to the analysis of larger systems with promising relevance in carbon-based material sciences, touching keywords like molecular electronics, molecular magnetism and spintronics.

Thus, starting from the experimentally proved conducting properties of the linear polyacenes, we devised a conceptual frame for taking such systems as well-suited benchmark for a molecular model of conduction, presented in the heuristic respects of resonance interactions.

A distinct area is devoted to the graphenes with spin induced by topological reasons, taking ideal triangle-shaped systems (triangulenes) as case study. We provide

---

M. Ferbinteanu

Faculty of Chemistry, Inorganic Chemistry Department, University of Bucharest,  
Dumbrava Rosie 23, Bucharest 020462, Romania

C. Buta

Faculty of Chemistry, Inorganic Chemistry Department, University of Bucharest,  
Dumbrava Rosie 23, Bucharest 020462, Romania

Institute of Physical Chemistry, Splaiul Independentei 202, Bucharest 060021, Romania

A.M. Toader • F. Cimpoesu (✉)

Institute of Physical Chemistry, Splaiul Independentei 202, Bucharest 060021, Romania  
e-mail: [cfanica@yahoo.com](mailto:cfanica@yahoo.com)

original structural considerations and a consistent classification. The speculative part regarding the high members of the class is well tempered with the concreteness from the analysis of already synthesized lower members, with focus on phenalenyl core.

## 1 Introduction

The organic chemistry served humankind in diverse ways, from colourants to medicines, offering massive series of molecules with invaluable practical utility. At the same time, the domain is rated with high academic challenges, especially in the matter of innovation and virtuosity in synthetic algorithms, a plethora of named reactions, such as the Suzuki coupling, [1] marking the most important realms and routes. In theoretical respects, the organic chemistry presents important classes of bonding and heuristic concepts, such as the aromaticity and hybridization. In the recent years, the organic chemistry enters firmly, with conceptual and application developments, in the area of material sciences, usually reserved to the inorganic systems, mostly extended lattices, such as oxides or silicon crystals.

The polycyclic aromatic hydrocarbons (PAHs) [2] form a very offering class, able for optical and magnetic properties enabling the functionality of nanoscale devices [3]. Putting in the central role of the causal relationship between desired properties and structural parameters, one may find interesting links between desirable features and bonding regime problems. Thus, the issue of aromaticity, related with the electron delocalization, can be intimately connected with the conduction properties, sharing similar mechanisms.

Organic polymers, or large PAHs (falling in the nanoscale domain), can act as conducting wires or semiconductors [4]. Adding to the problem of charge displacements the details of spin polarization, the traditional electronics, are extended into the so-called spintronics. The domain is yet a desideratum, but many investigations are making firm steps in this sense, finding challenging manifestations among the properties of organic systems [5–7]. Taking the pivotal role of the spin coupling in the bonding theories, one may hope in finding clues for the rational engineering of spintronic materials and machines. Our work is speculatively inscribed in the trend for such goals, debating the spin coupling as a powerful ancillary tool and heuristic beacon.

The modelling by the spin-coupling paradigm incorporates the expression of quantum features determining the special properties entering in the attention of nowadays high technologies. This methodology is not straightforward, in spite of the fact that there are nowadays convenient ways of computing the electronic structure, as is the frame of density functional theory (DFT) [8], supported by the availability of user-friendly codes [9]. We will point methodological hints connecting the popular methods with the lesser-known practice of valence bond methods [10, 11] considering prototypic aromatic systems.

There is a humongous literature playing graph theory around aromatic hydrocarbons and related systems, a good part of it concerning the enumeration of resonance structures (mostly, the Kekulé-type patterns) or of related objects (e.g. conjugated

circuits). Extensive works of pioneers and coryphées (to mention only a few: Balaban, Randić, Hosoya) as well as the intense dedication of the adepts made the domain an interesting art in itself [12–15]. However, the graph theory and related combinatorics developments are somewhat abstract, the cross-pollination with spin-coupling phenomenology building a quantitative dimension to the field, when the question of aromaticity and derived properties comes into focus [16, 17].

## 2 The Spin-Coupling Paradigm

The spin-coupling concept originates from the valence bond (VB) theory, the very first description of the chemical bonding, due to Heitler and London [18], developing Heisenberg's ideas about the so-called exchange and resonance effects, as pure quantum manifestations. Anticipating the following discussion, the keyword “resonance”, standing for the stabilization that resulted in the lower energy state from the interaction of equivalent configurations, seems appropriate to tackle the problem of aromaticity, as the supplement of stability gained from the superposition of the objects represented as Kekulé structures since the pre-quantum era. A phenomenological Hamiltonian based on the exchange coupling parameters  $J_{ij}$  as descriptors of the inter-centre interactions is also due to Heisenberg [19–21]:

$$\hat{H} = \sum_{j < i} (-2\hat{S}_i \cdot \hat{S}_j - 1/2) J_{ij}. \quad (1)$$

Very often, the Heisenberg spin Hamiltonian is used in molecular magnetism [22], to describe the interaction between metal ion centres in coordination compounds or extended lattices (in this case, dropping the  $-1/2$  term in parenthesis, which leads to an overall shift of all energy eigenvalues). The positive  $J$  parameters represent the rather rare cases of ferromagnetism (states stable with parallel arrangement of the spin), while a negative  $J$  describes the antiferromagnetism (the trend for antiparallel coupling). However, as descendant of the VB basic model of the chemical bonding, the Heisenberg effective Hamiltonian is more powerful, the intensive use in magnetochemistry eroding its conceptual virtues. The relatively few uses of spin coupling in the exploration of bonding regime have remarkable examples in organic and carbon chemistry, mentioning, for instance, the description of polyenes [23, 24] and fullerenes [25–27]. The negative  $J$  parameters are carrying the phenomenology of the bond as spin pairing appearance. The true mechanism is, in reality, more complex, but it looks like the antiparallel coupling is the engine. The “phenomenological” epithet goes also in the sense of a resemblance with something which is a suggestive shortcut description.

The tacit assumption behind the spin-coupling Hamiltonian, as in the genuine simplest version of the valence bond, is that the orbital lodge of active electrons (ignoring a certain core part, as is, e.g. the  $\sigma$  skeleton) is the same for all the configurations, which consist only of spin flipping. To reach the full meaning of a valence bond approach, the orbitals have to be conceived as localized on atoms (not the

delocalized molecular orbitals common in most of actual computation techniques). The so-called ionic configurations, matching different orbital occupation schemes, play in principle a significant role, but in modern VB techniques, performing the self-consistent optimization of localized orbitals can restore the desired simplicity of working with unique orbital background, at least in several representative cases, as will be the following discussion dedicated to aromatic hydrocarbons. Having a single orbital pattern means that the one-electron part and the Coulomb interaction is the same in all the configurations, relying then only on the exchange parameters, as the form of Heisenberg Hamiltonian says.

Although very rarely used in the nowadays landscape, otherwise rather abundant in quantum chemical calculations, the valence bond method benefits from very good implementations such as those known under the VB2000 [28, 29] and XMVB [30, 31] acronyms. These are genuine VB developments, working both as independent codes, or embedded, as option, in larger computer packages, such as GAMESS or Gaussian. Other implementations are exploiting the so-called complete active-space self-consistent field (CASSCF) methods, which are appropriate for dealing with multi-configurational wavefunctions and excited state sets. Thus, one may project a CASSCF result in a manner that retrieves a valence bond output [32–35]. A VB method accounting all the possible ionic states, namely, a complete active-space valence bond (CASVB), is, at the end, fully equivalent with a CASSCF procedure set in the same active space. Comprehensive textbooks on valence bond theory are due to Gallup or Shaik and Hiberty [10, 11].

To complete, the introduction to VB must define the nature of spin wavefunction. In the simplest realization, these may consist in all the spin flip configurations of  $n$  electrons solidary with  $n$  orbitals (i.e. confined to non-ionic pattern). These configurations can be classified in accordance with the total spin projection  $S_z$ , needing further linear combinations within their set, to become classified by a non-null  $S$  spin quantum number. This is the usual option for phenomenological applications of the Hamiltonian from the Eq. (1) in simulations of molecular magnetism, when the finding of spin states is realized by the algebra of quantum moments with Clebsch-Gordan coefficients.

Other option is to let initially unsolved the issue of  $S$  proper vectors, applying the spin Hamiltonian to the full spin projection basis, without a preliminary classification, going to the numerical solving of the resulted matrix. However, the full set of local spin projection becomes very large even at moderate numbers of considered electrons, the size growing exponentially as  $2^n$ . In such a situation, the spin symmetry algebra by Clebsch-Gordan coefficients is not convenient as adaptation to the  $S$  quantum numbers. The VB frame uses a very simple procedure for getting spin functions, particularly considering that in most cases of bonding problems must deal with singlet states, with  $S = 0$ . For a couple of electrons placed in the  $i$  and  $j$  orbitals, the singlet state can be formulated simply as the  $(\alpha_i\beta_j - \beta_i\alpha_j)$  combination of the two configurations with  $S_z = 0$ . For a many electron system with even count, a total  $S = 0$  can be obtained by stepwise products of such singlet couples.

If it must be tackled with generally non-null  $S$  number, the state with the highest spin projection  $S=S_z$  is formulated as a product between a sequence of coupled electrons (a subsystem with null spin resultant) and  $2S$  electrons with spin  $\alpha$ :

$$\Phi_{\Omega} = A \Psi_{\text{orb}} \prod_{k=1}^{N_{\beta}} \left( \alpha_{\Omega(2k-1)} \beta_{\Omega(2k)} - \beta_{\Omega(2k-1)} \alpha_{\Omega(2k)} \right) \cdot \prod_{l=N_{\beta}+1}^{N_{\alpha}} \alpha_{\Omega(l)} \quad (2)$$

Here  $N_{\alpha}$  and  $N_{\beta}$  stand for the number of up and down electrons, so that  $S = S_z = (N_{\alpha} - N_{\beta})/2$ , while  $\Omega$  denotes the ordering of centres that renders a given scheme of pairwise coupling in singlet subsystem, continued, if the case, with the product of  $\alpha$ -electrons, until the maximal projection of the selected total spin is reached. In principle, if one must account the whole  $2S + 1$  multiplet, the components should be treated with the algebra of Clebsch-Gordan coefficients, but such an expansion is not among the usual cases of VB treatments. In the above formula, the factor in the front suggests the anti-symmetrized orbital function, the same for all the spin combinations.

The  $\Omega$  elements, called resonance structures, are yielding the wavefunction by corresponding linear combinations. The number of resonance structures needed as basis for a spin state  $S$  (confined only to the block with maximal projection,  $S_z=S$ ) is:

$$\text{count}(S) = \frac{(N_{\alpha} + N_{\beta})!}{N_{\alpha}! N_{\beta}!} - \frac{(N_{\alpha} + N_{\beta})!}{(N_{\alpha} + 1)!(N_{\beta} - 1)!} = \frac{(N_{\alpha} - N_{\beta} + 1)}{(N_{\alpha} + 1)} \cdot \frac{(N_{\alpha} + N_{\beta})!}{N_{\alpha}! N_{\beta}!}. \quad (3)$$

The first and second terms in the middle sequence are the combinatorial counts of states with  $S_z = S$  and  $S_z = S + 1$  projections. Even if being limited to a single  $\Omega$  component, as for instance may be reasonable for the  $\pi$  electrons in localized double bonds of conjugated systems, or for the  $\sigma$  skeleton in non-aromatic molecules, this sort of wavefunction has a multi-configurational nature, since the product of  $(\alpha_{\Omega(2k-1)} \beta_{\Omega(2k)} - \beta_{\Omega(2k-1)} \alpha_{\Omega(2k)})$  components is expanded in  $2^n$  Slater determinants, where  $n$  is the number of coupled pairs.

Let us note that the very often used density functional theory (DFT) calculations are confined to single-configuration wavefunctions, having some intrinsic limitations. In the following, we will try to establish some practicable connections attempting to conciliate the relative difficulties due to non-routine status of VB approach with the temptation to rely on simple frameworks such as the DFT.

### 3 The Benzene by Spin-Coupling Effective Hamiltonian

Let us discuss in the following the case of benzene, as a prototypic example of spin coupling, a favourite subject of the chemical bonding essays. Naturally, there are very many reports on such an important molecule, even if the search filter is confined to valence bond or spin Hamiltonian keywords. One may mention very early studies [36], as well as a continuous line of preoccupations for benzene and other representative conjugated systems in the light of the VB paradigm [37–40]. We are attempting here a personalized review of the problems, redrawing the modelling and



calculations in a compact and consistent manner, reissuing the related conceptual and methodological aspects and suggesting new links and clues.

The difference between the ab initio calculation and the effective Hamiltonian treatment is, of course, the fact that the first one implies a big engine of evaluating many one- and two-electron integrals in the selected atomic basis, resulting in a black box that records the way to the final result, while the phenomenological route contains a transparent set of formulas, workable by hand, or at least by a small piece of code. The first one has predictive power, while the last holds explanatory virtues. A very nice aspect of the phenomenological VB based on resonance structures defined like in Eq. (3), subjected to the Hamiltonian (1), is that it can work with the help of graphical representations. Not only that the resonance structures are getting a picturesque display, as are the celebrated Kekulé and Dewar structures for the case of benzene, but the Hamiltonian itself can be obtained with the help of simple graphic rules, which are making the procedure practically available to everyone interested, not only to theorists.

Figure 1 shows in the upper row, or in the first column, the five known resonance structures. In extension to the usual representation as double bonds, the couplings are annotated by arrows comprising information about ordering in the spin pairs. Thus, the  $i \rightarrow j$  arrow stands for a  $(\alpha_i \beta_j - \beta_i \alpha_j)$  factor, while the reversal of the arrow implies a sign change, i.e.  $j \rightarrow i$  representing  $(\alpha_j \beta_i - \beta_j \alpha_i)$ . Ignoring the normalization and the orbital factor, the resonance structures chosen in Fig. 1 can be ascribed as follows:

$$\Phi_{K_1} = (\alpha_1 \beta_2 - \beta_1 \alpha_2)(\alpha_2 \beta_3 - \beta_2 \alpha_3)(\alpha_5 \beta_6 - \beta_5 \alpha_6), \quad (4.a)$$

$$\Phi_{K_2} = (\alpha_2 \beta_3 - \beta_2 \alpha_3)(\alpha_4 \beta_5 - \beta_4 \alpha_5)(\alpha_6 \beta_1 - \beta_6 \alpha_1), \quad (4.b)$$

$$\Phi_{D_1} = (\alpha_1 \beta_4 - \beta_1 \alpha_4)(\alpha_2 \beta_3 - \beta_2 \alpha_3)(\alpha_6 \beta_5 - \beta_6 \alpha_5), \quad (4.c)$$

$$\Phi_{D_2} = (\alpha_2 \beta_5 - \beta_2 \alpha_5)(\alpha_3 \beta_4 - \beta_3 \alpha_4)(\alpha_1 \beta_6 - \beta_1 \alpha_6), \quad (4.d)$$

$$\Phi_{D_3} = (\alpha_3 \beta_6 - \beta_3 \alpha_6)(\alpha_2 \beta_1 - \beta_2 \alpha_1)(\alpha_4 \beta_5 - \beta_4 \alpha_5), \quad (4.e)$$

where the first two are Kekulé-type and the last three Dewar forms. Altogether with the orbital factor (which would be similar to the product of six  $p_z$  atomic orbitals perpendicular to the ring), we ignored a sign factor. For instance, if convened that reference orbital functions is ordered like 1–6, the overall sign for each resonance structure is the signature of the permutation resulted concatenating the indices comprised in the chosen sequence of pairwise coupling. For example, for the second Kekulé structure in (4.b), the permutation will be  $\{2, 3, 4, 5, 6, 1\}$ , having negative sign. However, this overall factoring is not important, since it corresponds, in Hamiltonian and overlap matrices, to a sign swap on whole rows and columns, which is not affecting the eigenvalues. In turn, the sign conventions regarding the spin part, as comprised in the arrows of graphical representation, are important in the rules of simplified evaluation.

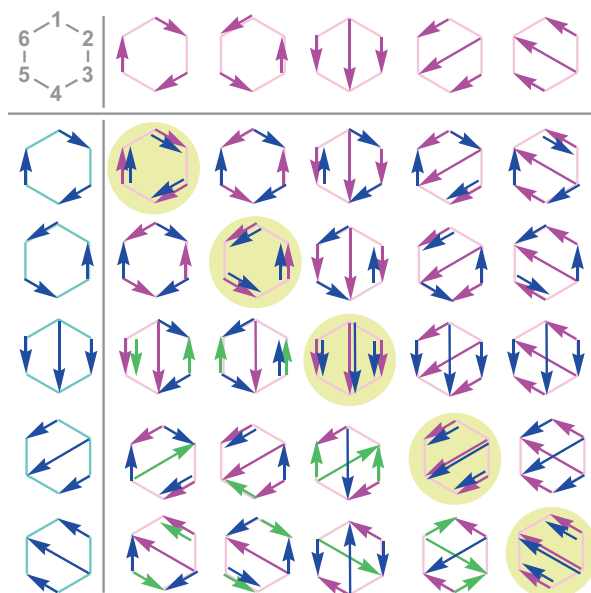


**Fig. 1** The graphic representations rendering the overlap matrix for resonance the structures acting as basis for the five  $S = 0$  states in  $C_6H_6$ . The *upper half* shows the direct superpositions, while the part under diagonal brings each figure to head-to-head or tail-to-tail matching, marking the modified *arrows* in *green ink*

Let us point that the choice of resonance structures, although having a degree of freedom and several alternative conventions available, is not subject of phantasy. For instance, we cannot criticize or rule out Dewar structures, as suggesting unreasonable distant bonding, because their implication was needed to reach the dimension corresponding to a basis for the five  $S = 0$  states, as results from the count with Eq. (3) when  $N_\alpha = 3$  and  $N_\beta = 3$ .

The way of choosing the resonance patterns corresponds to Rumer algorithm [41], which implies the arrangement of the spin carriers on a ring and taking all the couples that correspond to drawing non-crossing lines between the vertices of the polygon. In the case of benzene, it happens that the molecule itself is a ring, but the Rumer procedure uses a circle, irrespective the real geometry (as will see later for naphthalene).

Other algorithms of constructing VB bases are known, as the Young tableaux, imported from permutation group theory, or the Serber and Kotani diagrams [42, 43]. The Rumer-type structures are non-orthogonal. The overlap integrals between two resonance structures, obtained with the aid of the graphical superposition of the Rumer figures are concluded as follows:

$$S_{\Omega,\Omega'} = \langle \Omega | \Omega' \rangle = \delta_E (-1)^{\nu_{\Omega,\Omega'}} 2^{n_{\Omega,\Omega'} - n}, \quad (5)$$

where  $n$  is the total of paired couples (unpaired  $\beta$ -electrons in case of radical structures),  $n_{\Omega,\Omega'}$  is the number of so-called islands and  $\nu_{\Omega,\Omega'}$  is the number of arrow reversal

that brings the figure to a figure containing only tail-to-tail and arrow-to-arrow vertices (named matching form). The  $\delta_E$  symbols the vanishing of the integral if the superposition pattern contains at least one open chain with even number of members (i.e.  $\delta_E = 0$  in this case), while is  $\delta_E = 1$  otherwise. Open chains are encountered only in the case of radical-type resonance structures. The open chains with odd length are contributed as simple unity factors in the overlap integrals. The islands are closed circuits, the trivial one being the superposition of one arrow with itself.

In Fig. 1, one may see easily that in the diagonal superposition patterns, there are a number of such minimal islands equalling the number of electron pairs,  $n_{\Omega\Omega} = n$ , reaching then  $S_{\Omega\Omega} = 1$ , according to Eq. (5). One may also exemplify the superposition of the two Kekulé structures, leading to the unique island comprising all sites, having then the absolute value of the overlap  $1/4$ , if introduce  $n_{\Omega\Omega} = 1$  and  $n = 3$  in the above formula.

With the selected arrow directions, the superposition pattern results already in matching form (arrows all head-to-head or tail-to-tail), the integral being then positive. The superposition of two Dewar structures shows a skewed shape, but a careful examination shows that it leads also to a unique island. In these cases, there is an odd number, needing reversal for perfect matching, the overlap values being then  $-1/4$ . The superposition of a Kekulé and Dewar structure shows two islands, one with four corners and one with two sites, the absolute values of these integrals being  $1/2$ , with the sign varying from case to case.

The Hamiltonian elements can also be worked with graphic tricks. Only the exchange interaction is explicitly accounted, while the kinetic and Coulomb terms are assumed the same for all the configurations. The action of the exchange operator can be formulated as swapping two electrons in the affected wavefunction. Then, the matrix element of the Heisenberg operator (formulated in “bracket” style) can be thought in terms of the overlap integrals between resonance structures (ascribed in the “bra” left side) and patterns resulting from resonances by permuting the corresponding  $i$  and  $j$  sites (in the “ket” right part):

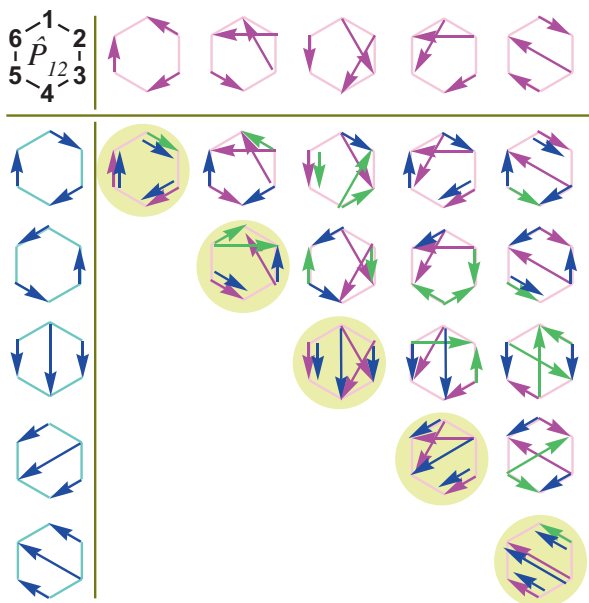
$$H_{\Omega\Omega'} = \langle \Omega | \sum_{j < i} J_{ij} (-2\hat{S}_i \cdot \hat{S}_j - 1/2) | \Omega' \rangle = - \sum_{j < i} J_{ij} \langle \Omega | \hat{P}_{ij} | \Omega' \rangle. \quad (6)$$

In other words, the coefficient of the  $J_{ij}$  parameter in the  $H_{\Omega\Omega'}$  is done as the overlap between the  $\Omega$  resonance structure and the permuted  $\hat{P}_{ij}\Omega'$  one (resulting from  $\Omega'$ ).

There are even simpler rules for getting the Hamiltonian elements, as proportionality with the overlap matrix and factors depending on the mutual position of the  $i$  and  $j$  considered centres with respect to the island partition (the same or different, concerning the possibility to be placed in open chains). But, because is possible to have a non-null Hamiltonian non-diagonal element while the corresponding overlap vanishes, is more general to work in the outlined strategy.

Figure 2 illustrates the action of the operator  $\hat{S}_1 \cdot \hat{S}_2$ , by taking the applied to column entries of the Hamiltonian matrix (with permuted structures depicted on the top row), while the rows are the Kekulé and Dewar resonances. Here also acts the convention of matching form for fitting the arrows heads and tails. For instance, the permutation of

**Fig. 2** The graphic handling needed for the estimation of the factors of the  $J_{12}$  parameter in the spin Hamiltonian matrix evaluating the overlap of resonance structures with those mutated by the permutation of the 1 and 2 sites. The superposition patterns are represented in the matching form showing the switched arrows marked in green



1 and 2 sites in the first Kekulé resonance, which contain the 1→2 arrow, leads to 2→1. Then, to reach the matching form, one must introduce a minus sign, which multiplied with the negative factor from the spin operators makes the first diagonal element to contain a  $+J_{12}$  term.

The superposition between the first Kekulé structure and the mutated second one has a skewed shape which is, topologically, a single island. Considering the figured one-arrow reversal, the overlap results as  $-1/4$ , arriving then at the  $+J_{12}/4$  content of the non-diagonal between the Kekulé structures.

The completion of the Hamiltonian estimation needs the working of permuted  $\hat{P}_{ij}$  structures for all the non-null  $J_{ij}$  parameters of the given topology and summing them up, numerically or symbolically, depending on the approach.

Taking, as is very intuitive, a unique parameter,  $J$ , around the  $C_6H_6$  ring and null for the distant interactions between the sites in mutual *meta* and *para* placement, the Hamiltonian matrix results as follows, aside the corresponding overlap matrix:

$$\mathbf{H} = \begin{pmatrix} \frac{3}{2}J & -\frac{3}{2}J & \frac{3}{2}J & -\frac{3}{2}J & \frac{3}{2}J \\ -\frac{3}{2}J & \frac{3}{2}J & -\frac{3}{2}J & \frac{3}{2}J & -\frac{3}{2}J \\ \frac{3}{2}J & -\frac{3}{2}J & 0 & -\frac{3}{2}J & \frac{3}{2}J \\ -\frac{3}{2}J & \frac{3}{2}J & -\frac{3}{2}J & 0 & -\frac{3}{2}J \\ \frac{3}{2}J & -\frac{3}{2}J & \frac{3}{2}J & -\frac{3}{2}J & 0 \end{pmatrix}, \quad (7.a)$$

$$\mathbf{S} = \begin{pmatrix} 1 & -\frac{1}{4} & \frac{1}{2} & -\frac{1}{2} & \frac{1}{2} \\ -\frac{1}{4} & 1 & -\frac{1}{2} & \frac{1}{2} & -\frac{1}{2} \\ \frac{1}{2} & -\frac{1}{2} & 1 & -\frac{1}{4} & \frac{1}{4} \\ -\frac{1}{2} & \frac{1}{2} & -\frac{1}{4} & 1 & -\frac{1}{4} \\ \frac{1}{2} & -\frac{1}{2} & \frac{1}{4} & -\frac{1}{4} & 1 \end{pmatrix}. \quad (7.b)$$

The  $\mathbf{E}$  energy eigenvalues and the  $\mathbf{C}$  matrix of eigenvectors are resulting from the  $\mathbf{HC}=\mathbf{ESC}$  matrix equation. The energy can be also ascribed as a series of numeric factors,  $E$ , representing the unknowns in the  $\det(\mathbf{HC}-\mathbf{ESC}) = 0$  equation. With the help of Mathematica™ [44, 45] computer algebra code, we determined the following solutions:

$$E = \left\{ -J + \sqrt{13}J, 0, -2J, -2J, -J - \sqrt{13}J \right\} \\ \approx \left\{ 2.6055J, 0, -2J, -2J, -4.6055J \right\}. \quad (8)$$

To express the phenomenology of antiparallel spin pairing, the  $J$  parameter is negative, the above values being then ordered in the increasing energy. The lowest two states can be interpreted as mainly due to Kekulé resonances, while the last three show a Dewar dominant basis. Note the two degenerate  $-2J$  eigenvalues, comprised an orbital doublet,  $E_{2g}$ . The symmetry labels of the states in the given ordering are  $A_{1g}$ ,  $B_{2u}$ ,  $E_{2g}$  and  $A_{1g}$ .

## 4 The Benzene by Ab Initio Valence Bond Calculations

Let us consider in the following the first-principle valence bond calculations, after having introduced previously the simplified spin Hamiltonian approach. Using the VB2000 code [28, 29], the self-consistent result is based on the six equivalent orbitals, the same on each carbon centre, one of them being represented in Fig. 3. Considering the left-side panel, the appearance is of  $p_z$  type, as expected, but the contour representation drawn in the right side suggests a more subtle composition, incorporating neighbour contributions. The relative VB energies for the  $\{A_{1g}, B_{2u}, E_{2g}, A_{1g}\}$  series are  $\{0, 41921, 73234, 118558\} \text{ cm}^{-1}$  with the 6-31G basis and  $\{42588, 74235, 120381\} \text{ cm}^{-1}$  with the 6-311 + G\* set. One may say that the numeric difference between the first case, with a modest basis set, and the richer one is not significant, if the nature of the bonding regime is judged. Therefore, in the following, we will use simple basis sets, for the sake of a simpler discussion.

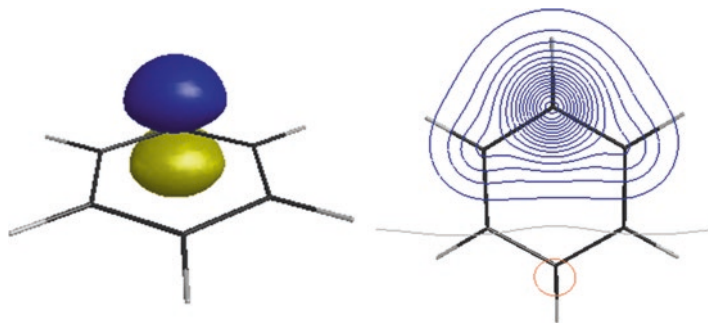


**Fig. 3** Self-consistent orbitals from valence bond calculation of the benzene in the spin-coupled formalism. The 3D isosurface from *left side* is drawn at  $0.1 \text{ e}/\text{\AA}^3$ . The 2D contours from the *right side* are drawn in a plane spaced at  $0.5 \text{ \AA}$  height, parallel to the molecular one

With bases like 6-31G or 6-311G, the atomic orbitals implied in  $\pi$  bonding are pure  $p$ -type, being in line with the intuitive thought. In a polarized basis like 6-311G\*, the  $d$ -type mixing into the carbon-carbon bonds is small, though maybe not insignificant for certain computed quantities, but not really relevant for the bonding itself. Then, one may fit from the simpler calculation the  $J$  exchange parameter that characterizes the bond as  $J = -16,191 \text{ cm}^{-1}$ . This value retrieves the considered series of states at  $\{0, 42187, 74569, 116756\} \text{ cm}^{-1}$ , quite close to the direct calculation.

Relying on the 6-31G calculations, in the ground state, each Kekulé structure has a 40.26% weight, while each Dewar resonance gets 6.93% (estimated by a Mulliken-type formula). In counterpart, in the highest excited state (having the same  $A_{1g}$  symmetry like the ground state) the minority components are the Kekulé resonances, with 9.74% each, while each Dewar has a 26.84% share. By symmetry, the first excited state,  $B_{2u}$ , is entirely made from Kekulé elements (i.e. pure 50% each). The ground and first excited states can be regarded as made from in-phase and out-of-phase (i.e. with plus and minus respective signs) combinations of the Kekulé resonances. However, this is merely a convention, since the sign of a wavefunction can be changed arbitrarily (e.g. choosing a resonance pattern with one pair swapping positions). Also by symmetry reasons, the  $E_{2g}$  doubly degenerate state consists only in Dewar components.

The examination of the weights may suggest as possible approximation the limitation to the two Kekulé resonances. On the other hand, a glance at the matrices from Eq. (7) seems not encouraging in this sense. Thus, a separation of contributions from different basis elements is justified, in the sense of perturbation theory, if their non-diagonal elements are smaller than the difference between the diagonal ones. Here, we find the cross-elements between Kekulé and Dewar resonances having the same absolute value with the diagonal gap between these two types, namely,  $3|J|/2$ . Besides, the non-orthogonality makes the problem more complicated.

Cutting the corresponding  $2 \times 2$  Hamiltonian and overlap matrices, we try however an enforced solution in the space of Kekulé resonances only:

$$\det \left[ \begin{pmatrix} \frac{3}{2}J & -\frac{3}{2}J \\ -\frac{3}{2}J & \frac{3}{2}J \end{pmatrix} - E \cdot \begin{pmatrix} 1 & -\frac{1}{4} \\ -\frac{1}{4} & 1 \end{pmatrix} \right] = 0. \quad (9)$$

One obtains for the ground state and excited levels at,  $12 J/5$  and  $0$ , respectively. The approximated  $2.4 J$  ground state is somehow close to the  $2.6055 J$  exact modeling. Combining the spin-coupling model and the VB calculations, one may estimate the resonance energy. This can be naturally defined as the difference between the energy of the stabilized ground state and the diagonal element of a single Kekulé resonance:

$$E_{\text{res}} = \left( -\frac{5}{2} + \sqrt{13} \right) J \approx 1.1055J. \quad (10)$$

This equation was obtained in an early work [36]. Using the above fitted  $J$  value, the resonance energy results about  $17,900 \text{ cm}^{-1}$  or  $51.2 \text{ kcal/mol}$ , in module. This is larger than the  $36 \text{ kcal/mol}$  amount taken as from the hydrogenation energy of the benzene minus three times those of the cyclohexene. On the other hand, one may criticize the practical estimation as not representing purely the decoupling of resonance, since many other parameters are varying in the process, such as bond lengths and stereochemistry. Based only on the Kekulé resonances, the aromatic stabilization is  $0.9 J$  (i.e. the difference between the estimated  $2.4 J$  ground state and the  $1.5 J$  diagonal element).

## 5 The Benzene by Natural Bond Orbitals and Natural Resonance Theory

In the following, we will test the possibility to reach VB-alike parameters and discussion based on entirely different methodology, reshaping the results of simpler calculations, such as by DFT. To meet such goals, the so-called natural resonance theory (NRT) was created [46–48], in the frame of the more general paradigm called natural bond orbital (NBO) [49, 50]. The NBO is a post-computational analysis of the orbitals which resulted from any type of calculation (e.g. DFT), retrieving intuitive objects, such as hybrids, lone pairs and localized bonds of different types (simple, double, triple). The NRT algorithms do a weighted dichotomy of the total density in contributions from orbital patterns resembling Lewis structures (localized orbitals with integer population). Tempted by the relatively easy availability of such analyses, realized with user-friendly NBO codes and keywords, we will realize a comparison with the previously sketched VB analysis. Thus, the post-computation NRT analysis of the benzene, taken with the B3LYP functional, found the 33.3% weight for each Kekulé structure and 3.7% for each Dewar-type contribution.

Interestingly, these numbers are almost the same for calculations with three different basis sets: 6-31G, 6-311G and 6-311G\*. The weights seem underestimated in comparison with the above VB result, but this occurs because the NRT code recognizes also many small participations resembling the ionic structures in VB terminology. In principle, this can be regarded as a measure of realism of the method, since, in the previous VB treatment, we intentionally avoided to account such structures, accepting however their potential implication.

The NBO has also another option, apparently serving to emulate a VB regime, estimating the energy of a given resonance structure. Thus, one may impose the analysis of a desired resonance structure. The total density can be retrieved on its scaffold on the expense of fractional occupation of the imposed localized orbitals. The occupied orbitals can get populations sensibly smaller than the double occupancy, while many virtual orbitals can carry residual density. The procedure can however enforce strict double occupation of populated local orbitals and null density in the virtual-type NBOs, the energy of such object, computed at imposed frozen density, being tentatively conceivable as those of a VB-alike resonance structure. The  $\pi$ -type NBO simulating the Kekulé and Dewar benzene structures is shown in Fig. 4. However, the energies of these structures are not in line with the VB interpretation. Thus, the Kekulé structure is higher than the DFT ground state, by 343 kcal/mol, 356 kcal/mol or 365 kcal/mol with B3LYP functional and the 6-31G, 6-311G and 6-311G\* respective basis sets. Compared with the previous discussion, the values are large overestimations of the resonance energy. Extracting the exchange parameter by division with the 1.1055 factor, one finds, e.g. with 6-31G, the  $J = -108,467 \text{ cm}^{-1}$  value. This is several times larger than the value fitted from the VB calculation. An overestimated gap is found between the NBO surrogates of the Kekulé and Dewar-alike structures. Result with B3LYP/6-31G is  $57,925 \text{ cm}^{-1}$ . In model, this gap is  $1.5|J|$ , yielding then another estimation of the exchange:  $38,617 \text{ cm}^{-1}$ .

The NBO frozen density schemes do not allow to simulate the VB resonance. In VB, the spin-coupling resonance does not imply density displacements, as the formulation of structures by travelling double bonds may suggest, since only the spin flips are involved. Then, since NBO theory works with density management, it provokes larger rearrangements than expected. If in VB a self-consistency is taken on single resonance structures, one may end with different density patterns for different choices, but not as largely mutually different as in the NBO frozen resonance structure choices. Possibly, if NBO would be restricted to operate only on a limited set of active orbitals, the resonance structure emulation would be closer to the VB approach. In the actual implementation, it uses the full pool of orbitals, having a complex balance of density flows (including the  $\sigma$  skeleton, in the case of aromatics).

Insisting to have an estimation of the  $J$  exchange parameter from a non-VB calculation, we move now to the idea of using the different spin states in Hartree-Fock (HF) or density functional theory. The boldest approach is to use the extreme spin states, i.e. in our case the singlet ground state and the spin septet resulted enforcing six unpaired parallel electrons in the six  $\pi$  orbitals of benzene. For the benzene, the



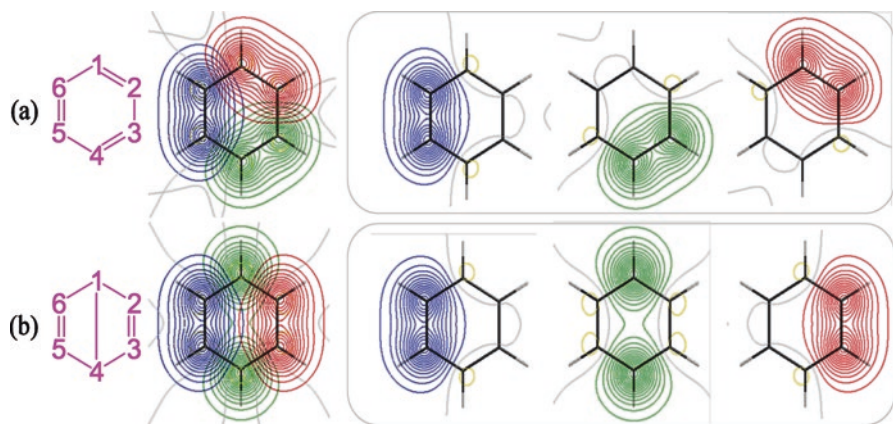


**Fig. 4** Simulated Kekulé and Dewar resonance structures by localized natural bond orbitals (NBOs). The NBOs are shown individually and in superposition (with different colours, to mark their identity). The contours are drawn at 0.5 Å above the molecular plane

energy of spin septet is  $-6J$ . In general, the highest spin energy is the negative from the sum of all the exchange coupling parameters. Then, taking the difference with the above equated ground state, the absolute value of the  $J$  is obtained dividing with  $(5 + 13^{1/2}) \approx 8.6055$  the gap between high septet and the singlet ground state.

The calculation of the ground state is a routine deal, HF or DFT. The calculation of the high-spin state does not pose, in principle, any difficulty, but must take care that the procedure holds the desired  $\pi$  orbitals as lode for the unpaired electrons. It may be possible to have a swap with orbitals from non-bonding  $\sigma$  part. In this case, the calculation must be repeated with a permuted orbital ordering as guess.

With the 6-31G basis set and HF method, one obtains a  $J = -13,862 \text{ cm}^{-1}$  parameter, underestimated in comparison with the VB resulted value. The high-spin state is basically the same in HF and VB. But the HF lacks electron correlation in ground state. As was pointed previously, the HF is a single determinant method, while the VB is multi-configurational, having a better description of the electrons in molecule.

Since DFT includes the electron correlation, in empirical manner, while remaining at the convenient single determinant level, one may hope that a proper functional recovers the effective non-VB estimation of the VB-type parameters. Thus, the simplest functional setting, called local density approximation (LDA) [51, 52], gives  $J = -18,257 \text{ cm}^{-1}$ . This value is slightly overestimated.

Checking the BP86 functional [53, 54], belonging to the generalized gradient approximation (GGA), thought as superior to LDA level, one obtains  $J = -17,402 \text{ cm}^{-1}$ . Finally, with the widely used B3LYP functional, belonging to the hybrid class, combining HF and Becke exchange [53] with Lee-Yang-Parr (LYP) [55] correlation, we got  $J = -17,027 \text{ cm}^{-1}$ , quite close to the VB estimation. Then, it seems that we reached the hope that a DFT simple self-consistent procedure can retrieve the correlation contained in a VB wavefunction. Then, it is possible to

construct a VB language just using the simplified frame of spin Hamiltonian, having the parameters provided by DFT calculations.

Here one must point that the another methodology known from the extraction of exchange coupling parameters from DFT calculations, the so-called broken symmetry (BS) approach [56–59], cannot work in systems with very strong coupling. The method is supposed to converge unrestricted configurations with  $\alpha$ - and  $\beta$ -spin polarization on localized orbitals of the coupled centres. This works for systems from molecular magnetism, with  $J$  parameters in the range of reciprocal centimetres (at most tens or hundreds of  $\text{cm}^{-1}$ ).

For stronger coupling, the iterations are leading the system towards doubly occupied orbitals instead of the aimed  $\alpha$ - $\beta$ -separation. Thus, the BS-DFT cannot be directly attempted on hydrocarbons.

## 6 The Polyaromatic Hydrocarbons. The Naphthalene Case

In the following, we will analyse the naphthalene molecule, the next iconic figure in the issues related with the aromaticity of hydrocarbons. The molecule received the deserved attention along the whole timeline, since the early quantum chemistry, till the modern era of valence bond method [36, 60, 61]. Here, reconstructing the detective story on the bonding regime, the aspect to be debated is its apparent limited aromaticity, given the geometry with non-equivalent bonds. There are four types of carbon-carbon contacts (labelled  $a$ - $d$  in the left side of Fig. 5) and three types of atoms (1, 2 and 3, correspondingly). The figure shows also the well-known three Kekulé-type resonance structures, drawn with arrows, to define the sign of the wavefunction.

The optimized bond lengths are  $l_a = 1.4243 \text{ \AA}$ ,  $l_b = 1.3805 \text{ \AA}$ ,  $l_c = 1.4200 \text{ \AA}$  and  $l_d = 1.4381 \text{ \AA}$  with the B3LYP/6-31G basis set. These results are not strongly dependent on the technical details, being, for instance,  $l_a = 1.4241 \text{ \AA}$ ,  $l_b = 1.3778 \text{ \AA}$ ,  $l_c = 1.4182 \text{ \AA}$  and  $l_d = 1.4365 \text{ \AA}$  with the 6-311G, while  $l_a = 1.4191 \text{ \AA}$ ,  $l_b = 1.3735 \text{ \AA}$ ,  $l_c = 1.4144 \text{ \AA}$  and  $l_d = 1.4314 \text{ \AA}$  with the 6-311G\* bases. As we insisted previously, the basic features of a molecule are reasonably described even with moderate basis sets and standard functional choices. Richer basis sets may be needed in quantitative description of certain quantities, such as atomization energies, but the bonding scheme is sufficiently and clearly described in moderate settings.

For an experimental comparison, we took an averaging over the considered bond types from different reports [62–64], getting  $l_a = 1.4216 \text{ \AA}$ ,  $l_b = 1.3738 \text{ \AA}$ ,  $l_c = 1.4158 \text{ \AA}$  and  $l_d = 1.4167 \text{ \AA}$ . One may see a good experimental-theoretical relationship, except a certain overestimation of the  $l_d$  bond length in the computed geometries.

For a system with ten electrons in ten orbitals, the count with Eq. (3) establishes 42 singlet states, the spin-coupled valence bond demanding then this number of resonance structures. Using the Rumer graphic algorithm [41], the necessary number of resonance structures can be collected arranging the spin carriers on a circle (irrespective the true geometry of the considered molecule) and drawing lines in all

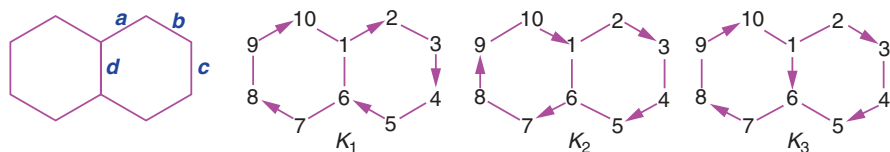


**Fig. 5** Bond and exchange type contacts (*left side*) and Kekulé-type resonance structures of naphthalene

the combinations avoiding their crossing. This method is illustrated in Fig. 6, disregarding the actual geometry of naphthalene. We also dropped the use of arrows, putting just lines instead. Combining the site labelling from Figs. 5 and 6, one may see that the first three resonances from the Rumer algorithm (reading from top to down and left to right) are, in fact, the Kekulé-type resonances which can be drawn taking the realistic skeleton of the molecule.

The Hamiltonian ascribed with four types of coupling parameters ( $J_a$ ,  $J_b$ ,  $J_c$  and  $J_d$ ) matching the different bond types that is given in Eq. (11.a), in the basis of resonance structures labelled  $K_1$ ,  $K_2$  and  $K_3$  in Fig. 5 is:

$$\mathbf{H} = \begin{pmatrix} J_a + J_b + \frac{1}{2}J_c - \frac{1}{2}J_d & \frac{1}{4}J_a + \frac{1}{4}J_b + \frac{1}{8}J_c + \frac{1}{16}J_d & \frac{1}{4}J_a + J_b + \frac{1}{8}J_c + \frac{1}{4}J_d \\ \frac{1}{4}J_a + \frac{1}{4}J_b + \frac{1}{8}J_c + \frac{1}{16}J_d & J_a + J_b + \frac{1}{2}J_c - \frac{1}{2}J_d & \frac{1}{4}J_a + J_b + \frac{1}{8}J_c + \frac{1}{4}J_d \\ \frac{1}{4}J_a + J_b + \frac{1}{8}J_c + \frac{1}{4}J_d & \frac{1}{4}J_a + J_b + \frac{1}{8}J_c + \frac{1}{4}J_d & -2J_a + 4J_b - J_c + J_d \end{pmatrix} \quad (11.a)$$

the related overlap being:

$$\mathbf{S} = \begin{pmatrix} 1 & \frac{1}{16} & \frac{1}{4} \\ \frac{1}{16} & 1 & \frac{1}{4} \\ \frac{1}{4} & \frac{1}{4} & 1 \end{pmatrix}. \quad (11.b)$$

The corresponding overlap matrix is found in Eq. (11.b). The structure  $K_3$  obeys the  $D_{2h}$  symmetry of the molecule. This is expected to mix with a symmetric combination of the  $K_1$  and  $K_2$ , in the formation of the ground state. With the chosen sign of the resonance structures, the symmetric combination is  $K_1 + K_2$ , ignoring the normalization factor. As complement, there is a  $K_1 - K_2$  out-of-phase combination determining an excited state. The phase of combination is subject to the conventional choice of the arrows in the resonance structures. For instance, if one or all three arrows would be reverted in  $K_2$ , its sign will switch, making the  $K_1 - K_2$  combination the total symmetric function and  $K_1 + K_2$  the excited state.

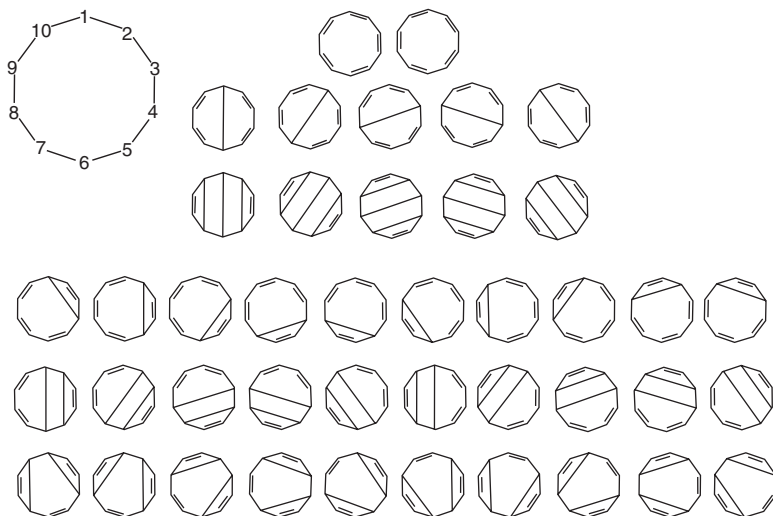


**Fig. 6** The full count of the 42 resonance structures in the spin-coupled VB-type treatment of a system with 10 electrons in 10 localized orbitals obtained the Rumer algorithm. The first three resonances from the *top* of the figure (the two from the *highest row* and the *left-side* one from the second line) are topologically equivalent with the three Kekulé resonance structure of the naphthalene

The difference between diagonal energies of  $K_1$  or  $K_2$  vs.  $K_3$  is due to the difference between the  $J_a$ - $J_d$  individual parameters. If enforcing all the coupling parameters equal to a unique  $J$ , then all the diagonal elements are turning equal to  $2J$ . Since the term resonance originates from the idea of interaction between levels with equal energy, and aromatic stabilization is related with the energy gain from such an effect, one may say that the naphthalene is qualified, in principle, for the aromaticity effect. The question is what determines, at end, the bond alternation and how this alters the aromatic qualities. In the first instance, we will confine to the model case of equal bond lengths and coupling parameters.

With the help of model Hamiltonian from Eq. (11), one may answer to the inquiry about the weights in the case of absolute equivalence of all the bonds, taking  $J_a=J_b=J_c=J_d=J$ . The weight results are different, with 29.5% for  $K_1$  and  $K_2$ , while 41% for the  $K_3$ . Judging the sum of  $K_1$  with  $K_2$  vs. the  $K_3$  weight, one sees that the first object dominates with an approximate 1.5:1 ratio. This distribution is dictated by the non-diagonal elements in the **H** and **S** matrices. Thus, the equal diagonal elements do not lead themselves to equal weights of all the Kekulé-type resonances, as an extrapolation of the benzene case. We used here the Mulliken definition, taking as weight  $w_i$  of a given resonance structure labelled  $i$  in the ground state (gs) the following summation:  $w_i = \sum_j C_{gs,i} C_{gs,j} S_{ij}$ , involving the  $C$  coefficients of the ground state eigenvector and the elements of the overlap matrix **S**. Keeping the simplification of unique  $J$ , but using the full set of 42 resonances, one obtains 8.94% for each of  $K_1$  or  $K_2$  and 14.68% for the  $K_3$ . This reduction is due to the participation

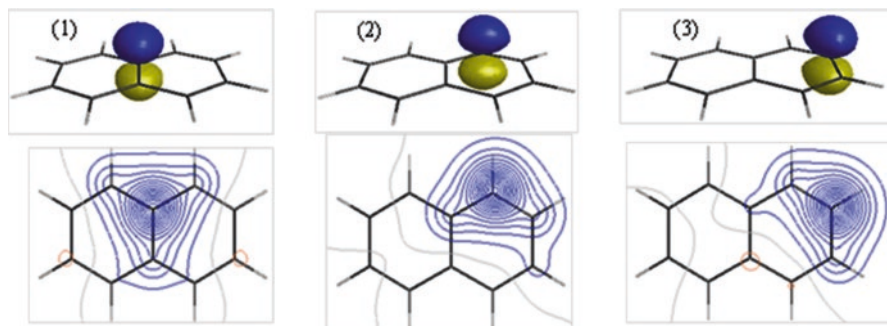


**Fig. 7** Self-consistent orbitals from valence bond calculation on naphthalene. The 3D isosurface is drawn at  $0.1 \text{ e}/\text{\AA}^3$ . The 2D contours are drawn at  $0.5 \text{ \AA}$  above the molecular plane

of the other resonances, with contributions ranging between 0.1% and 5.6%. The ratio between the sum of the first two Kekulé structures and the third one is reduced to about 1.2:1, having, in other words, a relative increase of the  $K_3$  content. With the real geometry, at different  $J_a$  to  $J_d$  parameters, only the  $K_1$  and  $K_2$  are equivalent as energy and fall in mutual resonance relationship.

A deeper insight is gained with the help of valence bond calculations. The valence bond treatment with 6-31G basis set on the naphthalene produced the self-consistent  $p$ -type orbitals, shown in Fig. 7 for the symmetry unique sites. As one may see in the contour diagrams, there are slight differences between these functions, although qualitatively all have a  $p_z$  appearance. The VB calculation can reveal the non-trivial issue of the weights of the resonance structures, considered previously in idealized modelling. Thus, one finds the 22.37% contribution for each of the  $K_1$  and  $K_2$  structures, while 55.25% for the  $K_3$  symmetric resonance (considering the Mulliken convention). The weights are different for the two resonance types, but one may speculate an approximate comparability between the contribution of  $K_3$ , at one side, idealized to 50%, and those of the symmetric combination  $K_1 + K_2$ , on the other side, so that each of these pieces gets almost 25%. This can be interpreted as stepwise resonance: first between the  $K_1$  and  $K_2$ , which are topologically equivalent, and then between their combination and  $K_3$ . Searching the VB configuration interaction matrix, i.e. the first-principle analogue of  $\mathbf{H}$ , one finds that the diagonal element of  $K_3$  is lower than  $K_1$  or  $K_2$ , a factor that favours its larger weight in the ground state. Indeed, the trend to the  $K_1 + K_2 : K_3 \approx 1:1$  ratio from the previous  $\approx 1.5:1$  can be understood in this sense.

Enhancing the VB calculation to all the 42 possible resonance structures, the  $K_1$  and  $K_2$  are retaining 12.36%, while  $K_3$  gets 39.18%. The other resonances are contributing with small weights, ranging from 0.1% to about 4.3%. Thus, one may see that the three Kekulé resonances are holding the main share even in the extended scheme, in line with the belief and hope of chemical intuition. In the extended basis, the  $K_3$  contribution is higher comparatively to  $K_1$  and  $K_2$ , sensibly larger than their sum.

Besides, we enforced a VB calculation for a naphthalene with equal bond lengths, namely, with all C-C fixed at 1.4088 Å, the average value around the carbon perimeter. This yielded 30.6% weights for  $K_1$  and  $K_2$  vs. 38.8 % for  $K_3$  in a non-iterative process, having all the localized orbitals equivalent (pure  $p_z$  AOs). Such result resembles the above discussed  $K_1+K_2: K_3 \approx 1.5:1$  approximate situation in the model with equal  $J$  parameters for all the bonds. Completing the VB self-consistency in the idealized naphthalene with equal carbon-carbon bond lengths, i.e. allowing the resolution of slightly different orbitals on the symmetry distinct atoms, one reaches 25.1% for  $K_1$  and  $K_2$  while 49.8 % for  $K_3$  after the iterations allowed the resolution of slightly different orbitals on the symmetry distinct atoms. Interestingly, this solution is very close to the  $K_1+K_2: K_3 = 1:1$  remarked previously as approximate situation for the VB calculation on the real geometry of naphthalene. One may speculate that this ratio, decided by self-consistency forces, i.e. by a trend towards a minimum of energy, represents another sort of aromatic manifestation, tending to put on equal footing the contributions of the  $K_1+K_2$  normalized combination and  $K_3$ , in spite of the fact that these are not equivalent objects.

Trying to bring at confluence the calculations and the Heisenberg spin Hamiltonian treatments, we will attempt to fit the  $J_a, J_b, J_c$  and  $J_d$  coupling parameters. We cannot compare directly the model and ab initio Hamiltonian matrices, because the first one is done tacitly in the approximation of non-overlapping  $p$ -type orbitals, while the real situation implies non-negligible overlap integrals. However, one may compare the modelled relative energy gaps between the three states expected from combination of the three Kekulé resonances and the computed values. Thus, the VB/6-31G calculation gave the two excited states at 44,154  $\text{cm}^{-1}$  and 57,432  $\text{cm}^{-1}$ , relative to the ground state. One may see that we have two quantities available, while four  $J$  parameters. Then, one must introduce an approximation balancing the data entries with the number of parameters. We can rely on two parameters proposing an exponential form, function of the  $r$  bond length:  $J(r) = A \cdot \exp(-\alpha \cdot r)$ . With  $A = -131,981$  Hartree and  $\alpha = 10.185 \text{ \AA}^{-1}$ , the above energies are fitted perfectly. To avoid the large  $A$  coefficient and its confusing meaning (i.e. the  $J$  at null bond length), one may equivalently rearrange to  $J(r) = J_0 \cdot \exp(-\alpha \cdot (r-r_0))$ , where  $r_0$  is, conventionally, the averaged bond length,  $r_0 = 1.4088 \text{ \AA}$ , having then  $J_0 = -16,994 \text{ cm}^{-1}$ . The coupling value at this reference is well compared with the previously computed  $J$  parameter for benzene. With this function, taking the bond lengths mentioned at beginning, one obtains the following set of exchange parameters:  $J_a = -14,519 \text{ cm}^{-1}$ ,  $J_b = -22,682 \text{ cm}^{-1}$ ,  $J_c = -15,169 \text{ cm}^{-1}$  and  $J_d = -12,615 \text{ cm}^{-1}$ .

Trying to understand the bond alternation from the outlined spin Hamiltonian model, we present the perturbation analysis, taking as zero-order reference, the situation of the system with equal  $J$  parameters. Then, as second-order perturbation, the ground state energy is:

$$E_{\text{gs}} = E_{\text{gs}}^0 - \frac{96(2J_a - 2J_b + J_c - J_d)^2}{\sqrt{31}|46J_a + 16J_b + 23J_c + 8J_d|} \quad (12.a)$$

The zero-order ground state energy is expressed only in terms of unique  $J$ , since it becomes too long as function of the  $J_a$  to  $J_d$  set:

$$E_{\text{gs}}^0 = \frac{1}{10} (17 + 3\sqrt{31}) J. \quad (12.b)$$

The nominator in the fraction from Eq. (12.a) becomes null when all the exchange parameters are identical or at least when  $J_a = J_b$  and  $J_c = J_d$ . Since the second-order correction is negative, one may see that it gives energy stabilization if the equality of the exchange coupling parameters is disrupted. In other words, since the nominator is proportional to the square of a non-diagonal matrix element and the denominator is the gap between the involved diagonal elements, the trend to alternating bond lengths brings more configuration interaction into the system. Then, the same mechanism that is conceived to determine the aromaticity of benzene, namely, the configuration interaction between Kekulé resonances is also inducing the bond alternation trend in naphthalene.

From another perspective of the simplified modelling, relying on the unique  $J$  case, the resonance energy can be obtained subtracting from (12.b) the  $2J$  amount representing the diagonal elements of all the Kekulé structures. Then, one obtains the  $E_{\text{res}} \approx 1.3703J$ . In absolute measure, this is higher than those modelled for benzene in Eq. (10). However, divided per number of active electrons, namely, six for benzene and ten for naphthalene, the first one appears more aromatic, as expected, with  $0.184J$  against  $0.137J$ .

Now, we shall compare the VB results with their emulation in the NBO and NRT post-computational analyses of the DFT calculations. The NRT treatment of a B3LYP/6-31G calculations rendered 26.42% for the  $K_1$  and  $K_2$  structures, while 20.32 for the  $K_3$  resonance. This is in contrast with the VB and spin Hamiltonian modelling result, suggesting a caveat on the limits of the NRT, as replacement for the VB weighting. The reasons can be guessed in the fact that NRT operates with density contributions, nominally different for each type of resonance, while the proper VB does not imply a density flux following the spin flipping. We will keep this comparative assessment in the attention of the following examples. One may add also the analysis of NBO energies simulated for frozen resonance structures. As found also for the benzene case, the energy of an isolated NBO resonance structure is much higher than expected. Thus, the  $K_1$  and  $K_2$  structures are by about 656 kcal/mol higher than the ground state energy. In turn, the VB calculation finds a reasonable amount of 53 kcal/mol. The  $K_3$  is lower in absolute energy, in both NBO and VB calculations (taken as diagonal element of the corresponding matrix, in the last one). The NBO overestimates the gap to 636 kcal/mol, while the VB renders about 15 kcal/mol. The relative energy between the single structures (taken as  $K_3$  minus  $K_1$ ) is 20 kcal/mol in the NBO numeric experiment and 38 kcal/mol from the VB data. Interestingly, here the NBO keeps a certain qualitative comparability with the VB frame.

Taking the departure between ground state and lowest diagonal element, the VB estimation of the aromatic stabilization is 15 kcal/mol, smaller than those of benzene. Considering the situation of alternating bond lengths as established fact, the aromaticity of naphthalene can be judged as a second-order effect, from a different perspective than the above discussion around Eqs. (12). Thus, the resonance notion can be nominally used only in the case of equivalent objects, namely, the  $K_1$  and  $K_2$  couple. However, the  $K_1$  and  $K_2$  elements have higher energy than the  $K_3$  structure. Therefore, one may say that the resonance is involved in ground state in a second-order manner. On the other hand, as observed previously for the real geometry, and also the enforced equalization of bonds, the  $K_1+K_2$  cumulated weights tend to be comparable, about 50%, with those of the  $K_3$ , as if these two objects are effectively equivalent. This situation is achieved through the overlap effects of localized  $p_z$ -like self-consistent VB orbitals.

## 7 The Polyaromatic Hydrocarbons: The Anthracene Example

For a continuation of the analysis, let us take the anthracene case, reconstructing in the previously contoured methodology the bonding aspects partly known from earlier works [65]. Fig. 8 shows the bond types and the Kekulé resonances. The five carbon-carbon bond types, labelled from  $a$  to  $e$ , were collected by averaging on measurements picked up from several X-ray crystal data [66–69], obtaining  $l_a = 1.3975 \text{ \AA}$ ,  $l_b = 1.4318 \text{ \AA}$ ,  $l_c = 1.3588 \text{ \AA}$ ,  $l_d = 1.4163 \text{ \AA}$  and  $l_e = 1.4315 \text{ \AA}$ . The series is well matched by the geometry computed in the B3LYP/6-31G setting:  $l_a = 1.4036 \text{ \AA}$ ,  $l_b = 1.4329 \text{ \AA}$ ,  $l_c = 1.3739 \text{ \AA}$ ,  $l_d = 1.4288 \text{ \AA}$  and  $l_e = 1.4491 \text{ \AA}$ . As discussed previously, other basis sets, as well as different functionals, are yielding similar results.

In order to keep the same format with the above discussions, in spite of the fact that the problems are becoming progressively more complex, let us consider the  $4 \times 4$  spin Hamiltonian having as entries the resonance structures defined in Fig. 8. The generic table is:

$$\mathbf{H} = \begin{pmatrix} H_{1,1} & H_{1,2} & H_{1,3} & H_{1,4} \\ H_{2,1} & H_{2,2} & H_{2,3} & H_{2,4} \\ H_{3,1} & H_{3,2} & H_{3,3} & H_{3,4} \\ H_{4,1} & H_{4,2} & H_{4,3} & H_{4,4} \end{pmatrix} \quad (13.a)$$

having the following elements:

$$H_{1,1} = H_{4,4} = J_a + J_b + J_c + \frac{1}{2}J_d - J_e \quad (13.a1)$$



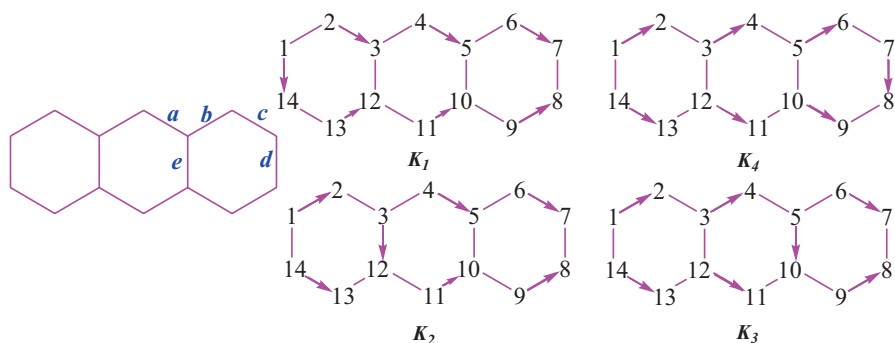


**Fig. 8** Bond and exchange type contacts (*left side*) and Kekulé-type resonance structures of anthracene

$$H_{2,2} = H_{3,3} = J_a - 2J_b + 4J_c - J_d + \frac{1}{2}J_e \quad (13.a2)$$

$$H_{1,2} = H_{2,1} = H_{3,4} = H_{4,3} = \frac{1}{4}J_a + \frac{1}{4}J_b + J_c + \frac{1}{8}J_d + \frac{1}{8}J_e \quad (13.a3)$$

$$H_{1,3} = H_{3,1} = H_{2,4} = H_{4,2} = \frac{1}{4}J_a + \frac{1}{16}J_b + \frac{1}{4}J_c + \frac{1}{32}J_d + \frac{1}{8}J_e \quad (13.a4)$$

$$H_{1,4} = H_{4,1} = \frac{1}{16}J_a + \frac{1}{16}J_b + \frac{1}{16}J_c + \frac{1}{32}J_d + \frac{1}{32}J_e \quad (13.a5)$$

$$H_{2,3} = H_{3,2} = J_a - \frac{1}{2}J_b + J_c - \frac{1}{4}J_d + \frac{1}{2}J_e \quad (13.a6)$$

Correspondingly, the overlap matrix is:

$$\mathbf{S} = \begin{pmatrix} 1 & \frac{1}{4} & \frac{1}{16} & \frac{1}{64} \\ \frac{1}{4} & 1 & \frac{1}{4} & \frac{1}{16} \\ \frac{1}{16} & \frac{1}{4} & 1 & \frac{1}{4} \\ \frac{1}{64} & \frac{1}{16} & \frac{1}{4} & 1 \end{pmatrix} \quad (13.b)$$

In this case, there are two pairs falling in equivalence classes,  $K_1$  and  $K_4$  aside the  $K_3$  and  $K_1$ . These couples are carrying therefore the resonance effects, the ground state corresponding to their summation with the same sign and different weights.

Although the main interest is on the ground state, taking also the excited states of the VB calculation, one may apply a fit of the coupling constants, particularized on each bond type, in a manner similar to the previous treatment of the naphthalene. Thus, the excited VB states computed with a 6-31G basis are at  $37065\text{ cm}^{-1}$ ,  $56,585\text{ cm}^{-1}$  and  $61,442\text{ cm}^{-1}$ . The  $E$  energy solutions of the  $\det(\mathbf{HC-ESC}) = 0$  equation fitted reasonably this set, retrieving  $34,338\text{ cm}^{-1}$ ,  $57,575\text{ cm}^{-1}$  and  $61,835\text{ cm}^{-1}$ . In this view, we assumed a  $J(r) = J_0 \cdot \exp(-\alpha \cdot (r - r_0))$  dependence of the exchange coupling on the  $r$  bond length,  $r_0$  being the averaged bond length of this system,  $r_0 = 1.4123\text{ \AA}$ . The optimal parameters are  $J_0 = -14,707\text{ cm}^{-1}$  and  $\alpha = 6.056\text{ \AA}^{-1}$ , producing the following values for each carbon-carbon bond type:  $J_a = -15,504\text{ cm}^{-1}$ ,  $J_b = -12,986\text{ cm}^{-1}$ ,  $J_c = -18,559\text{ cm}^{-1}$ ,  $J_d = -13,312\text{ cm}^{-1}$  and  $J_e = -17,239\text{ cm}^{-1}$ . The range of parameters and values is similar to those of the previously discussed case of benzene and naphthalene, although the actual parameters reflect the very specific situation of the new case, apparently with weaker  $\pi$  bonding, given the larger  $r_0$  and smaller  $J_0$  values. In rough sense, the  $r_0$  and  $J_0$  can be taken as transferable between different systems or possibly scalable with the number of carbon atoms of the specimen in a given series (e.g. polyacenes, to comprise the naphthalene and anthracene together).

For a touch of concreteness, Fig. 9 represents the orbitals of the self-consistent VB approach, noticing the slight variation of the profiles according to the different carbon atoms. Qualitatively, as in previous cases, their appearance is of  $p_z$ -type atomic functions perpendicular to the molecular plane. The first-principle VB calculation revealed the 14.89 % weight for  $K_1$  and  $K_4$  equivalent resonances, while 35.11% for  $K_2$  and  $K_3$ . The higher content in the middle basis element is related with the lower placement of their diagonal Hamiltonian matrix element, in comparison with the other ones. Thus,  $K_1$  and  $K_4$  resonance structures are with 69.4 kcal/mol above the ground state, while  $K_2$  and  $K_3$  are placed at  $27.7\text{ cm}^{-1}$ . The last value can be judged as the net aromatic stabilization. One observes that it is higher than the magnitude taken in similar way for naphthalene, 15 kcal/mol. This can be interpreted by the fact that anthracene is more predisposed to resonance effects, because one may form two equivalent couples  $K_1$  and  $K_4$  aside the  $K_2$  and  $K_3$ , while the naphthalene contained only the  $K_1$  and  $K_2$  resonant pair.

The predominance of the  $K_2 + K_3$  pair in the weights of the ground state is retrieved also if the simplified case of unique  $J$  coupling parameter is assumed for all the bonded pairs, when all the diagonal elements of the matrix from (13.a) are becoming equal to  $5J/2$ . The resulted weights are 18.75% for  $K_1$  and  $K_4$  while 31.25% for  $K_2$  and  $K_3$ . This can be interpreted as a higher aromatic character of the rings at the middle of the molecule, resulting from topological factors enciphered in the Hamiltonian and overlap matrices of the simplified spin-coupling modelling.

Confined to the simple hypothesis of homogenous bond coupling, the expression of the ground state energy of anthracene looks very simple:  $83J/20$ . The aromatic stabilization is then obtained subtracting from this quantity the  $5J/2$  representing the diagonal elements (the same for all the four Kekulé resonances), being  $33J/20 = 1.65J$ . As absolute value, it is larger than those modelled for naphthalene, which was larger than those of benzene. However, divided by the number of  $\pi$  elec-

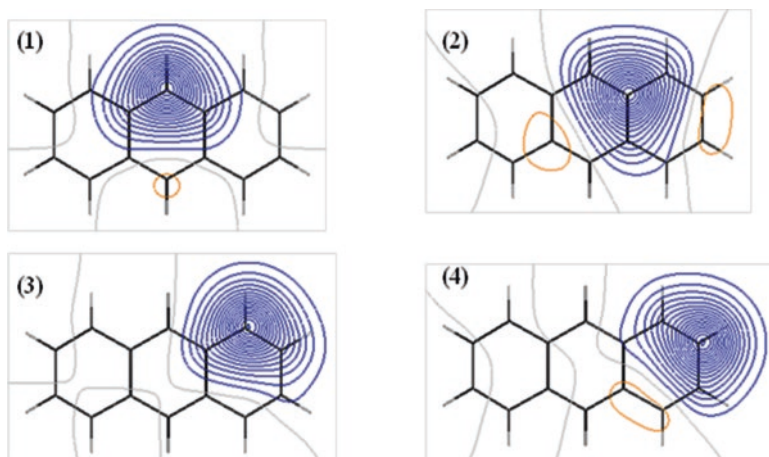


**Fig. 9** Self-consistent orbitals on symmetry unique site types (1–4) from valence bond calculation on anthracene. The 2D contours are drawn at 0.5 Å above the molecular plane

trons, namely, 14 for anthracene, the ordering of resonance energy per electron is reversed in the sketched series, being 0.1178  $J$  for anthracene (while 0.137  $J$  for naphthalene and 0.184  $J$  for benzene).

To complete the assessments started in the previous sections, we are going to compare the VB results against the simulations in the frame of NBO theory. Thus, the resonance weights taken by the NRT algorithm (as post-computational analysis to a B3LYP/6-31G calculations) show the reversed ordering, in comparison with the VB and spin Hamiltonian modelling, getting 27.56% for the  $K_1$  and  $K_4$  elements, while  $K_1$  and  $K_4$  while 31.25% for  $K_2$  and  $K_3$ . The strategy to impose frozen density objects as simulacrum for resonance structures produces very large energies, over 900 kcal/mol above the ground state. Although the gap between the two types of NBO resonances is in an acceptable range, namely, 41.7 kcal/mol, this information is of little use in the given circumstances.

Putting together all the caveats progressively drawn in the previous sections from the VB vs. NBO comparisons, one may conclude that, unfortunately, the natural bond orbital frame and, particularly, the natural resonance theory are not safe replacements for the valence bond calculations. The interest for such a possible conjecture is indebted by the fact that the VB calculations are limited to a relatively small number of electrons.

The used code VB2000 [28, 29] depends on certain map files which are encoding the spin-coupling algebra, limited to 14 electrons in the present release. Thus, the anthracene is at the limit of approachable molecules. Then, it remains to suggest that for larger systems one may yet use the phenomenological spin Hamiltonian, confined to a practicable basis of Kekulé resonances. As illustrated in the previous examples, even with the simplest assumption of unique  $J$  parameter (disregarding the specific bond alternation), the resonance weights are well accounted, with a

semi-quantitative extent. For the simplified case of unique exchange parameter, the pattern of wavefunctions and weights is independent on its value, while the energy spectrum is simply scalable with the  $|J|$  amount.

## 8 The Polyacenes: Molecular Models for Electronic Conduction

Starting from the idea that the electronic delocalization is the engine for the conducting properties, we will speculate a molecular approach of this effect, using spin-coupling modelling and polyacenes as appropriate cases. One can make a parallel with the situation of molecular magnetism [22], which has grown translating in the language of structural chemistry concepts basically known in terms of solid state theories [21]. The actual models of conduction are yet tributary to concepts merely familiar to physicists, such as the ballistic phenomenology [70]. Now, we attempt to turn the explanation in a manner transparent to the chemical intuition, proposing the resonance structures from valence bond formalism as designated drivers of spin and charge, the linear polyacenes being particularly suited for this point.

The polyacenes are polycyclic conjugated hydrocarbons with  $C_{4n+2}H_{2n+4}$  general formula, the simplest pattern being the linear condensation of benzene rings. In idealized mode, the linear polyacenes are planar, spanning the  $D_{2h}$  point group. The series starts with naphthalene ( $n = 2$ ) and anthracene ( $n = 3$ ), ending with heptacene ( $n = 7$ ), the highest known congener [71]. Although small, the class shows various optical and electric properties [72, 73] with potential interest for material sciences and nanotechnologies. Thus, the polyacenes are able to trigger laser radiation [74], and their films are semiconductors spanning field transistor effects [75–77]. The interesting manifestations are accentuated with the increased dimension, being correlated with the progressive reduction of the gap between occupied and virtual orbitals, and also parallel with the trend towards the crossing of singlet and triplet states [75–77]. The lower gap from ground state to triplet determines the reactivity of the high analogues and, presumably, the ending of the series when a quasi-degenerate situation is reached [78, 79].

The clue for considering polyacenes as playground for the conduction models is sketched in Fig. 10. Namely, one may observe that taking Kekulé-type resonance structures, drawing for convenience the paired couples as double bonds (instead of the previously used arrows), only one pairing has a “vertical” placement. The “vertical” labelling comes putting the molecule with the long axis horizontally. A polyacene with  $n$  benzene rings, having a  $C_{4n+2}$  carbon content, can be regarded as made of two  $C_{2n+1}$  polyene chains, going in zigzag along the horizontal axis, connected by  $n + 1$  vertical carbon-carbon bonds.

When drawing the resonance, from the total of  $2n + 1$  double bonds,  $n$  are placed in one polyene moiety, other  $n$  being symmetrically in the other fragment, while one double bond goes vertically. One may place this “vertical” couple in any of the  $n + 1$

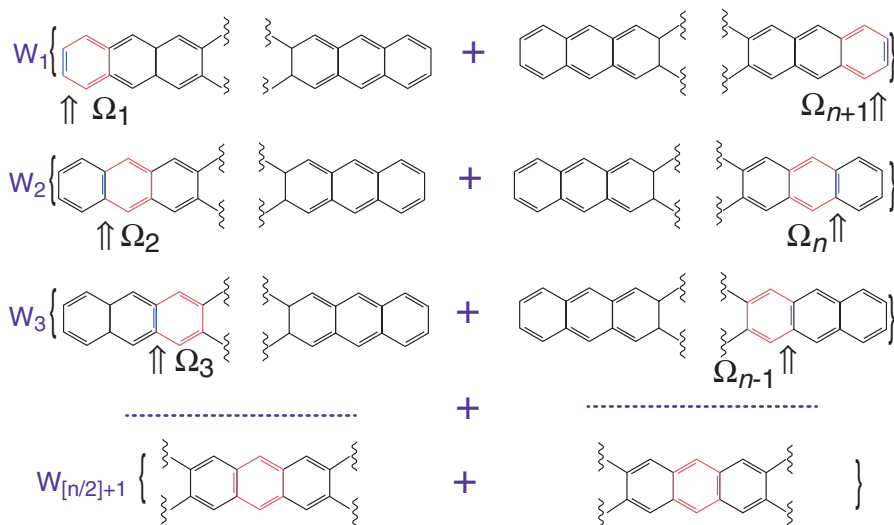


**Fig. 10** The scheme of resonance structures of polyacenes, formulated as a *vertical* double bond travelling from one side of the molecule to the other. The structures are arranged in equivalent couples, related with the mirroring through the middle of the molecule

vertical carbon-carbon linkages. Then, a  $n$ -polyacene has  $n + 1$  Kekulé resonances. This situation is easily seen in the previous examples: naphthalene has three resonance structures, while the anthracene got four. Running the “vertical” double bond for one side of the molecule to the other can be formally regarded as the travelling of an electron couple along the molecular wire represented by the linear skeleton. Thus, confining ourselves to the qualitative level, we propose the linear polyacenes as ideal case studies for a molecular model of conduction, raising as challenge the advanced technical developments.

The resonances, labelled  $\Omega_i$ , can be enumerated according to the  $i$ -th position of the vertical double bond determining entirely their pattern. Without detailing the derivation, we can present general formulas for the overlap and matrix elements in the basis of Kekulé structures of linear polyacenes:

$$H_{i,j} = \langle \Omega_i | H | \Omega_j \rangle = \left( \frac{1}{4} \right)^{|i-j|} \frac{1}{2} (n + 2 + 9|i-j|) \cdot J \quad (14.a)$$

$$S_{i,j} = \langle \Omega_i | \Omega_j \rangle = \left( \frac{1}{4} \right)^{|i-j|} \quad (14.b)$$

With these, we can easily investigate the full spectrum of VB-alike states in large polyacenes, under the simple assumption of Kekulé basis sufficiency. Besides, we will consider also the triplet states. For this goal, we cannot derive simple model

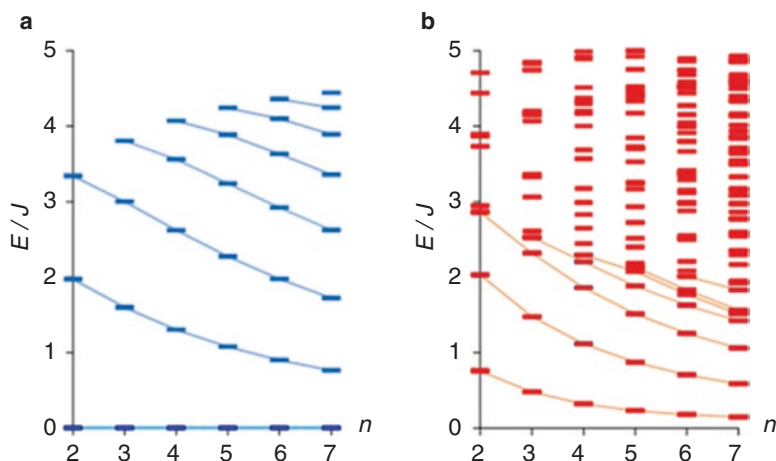


**Fig. 11** The spectra of spin-coupled states for the series of linear polyacenes with  $n$  running from  $n = 2-7$ . The left side (a) shows the singlet states in the basis of  $n + 1$  Kekulé resonance structures. The right panel (b) gives the triplet states in the basis of  $(n + 1)(2n + 1)$  resonances derived from Kekulé references by the successive decoupling of their spin pairing

expressions, remaining to be evaluated by putting in algorithm the general rules mentioned in the beginning. We will also introduce an assumption on the basis of the triplet resonances. Namely, we propose the successive decoupling into pairs of  $\alpha$ -electrons of the couples from a singlet Kekulé reference. Thus, from a Kekulé structure having  $N$  couples, one may draw  $N$  triplets, running the unpaired sites over the former bonding linkages. Then, for a  $n$ -polyacene, having  $2n + 1$  electron pairs and  $n + 1$  singlet resonances, we get a triplet basis with  $(n + 1)(2n + 1)$  dimension. With this model settled, we draw the series of spectra from Fig. 11.

The left panel shows the singlet states, observing the progressive decrease of the gap between ground and first excited state. This parallels the trend expected from molecular orbital diagrams, although the spin Hamiltonian has not an explicit connection with these methods.

A very interesting aspect is noticed in the right-side panel, showing the triplet states relative to the singlet ground level. One finds a rapid reduction of the singlet-triplet gap, which becomes very small nearby the  $n = 7$  congener. This can be nicely correlated with the above-mentioned fact, that heptacene is the last member of the series available experimentally.

The very low triplet levels after this critical point are making the molecule prone to the reactive degradation. Thinking on the oxidation processes, it is well known that these are kinetically hindered for organic compounds (while thermodynamically allowed) by the fact that singlet-triplet processes are spin forbidden. Indeed, the organic systems are usually singlets (closed-shell or completely spin-paired structures), while the oxygen molecule has a triplet ground state. When the molecules show low triplet states, these can get in interaction, making the interaction with oxygen strong, opening the gate for the further degradation steps.

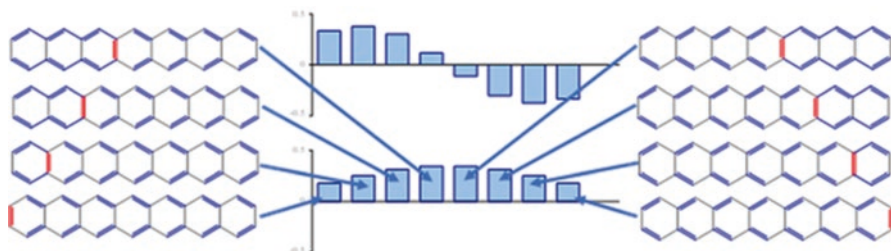


**Fig. 12** The histograms of the coefficients from the eigenvectors of the first two spin-coupled states (ground state and the first excited level) for the heptacene example ( $n = 7$ ). The resonance structures forming the basis are represented on the margins, pointing the links to their corresponding coefficient in the ground state

More things can be observed examining Fig. 12, illustrating the eigenvectors of the ground state and first excited levels in the basis of the Kekulé resonances. One observes that the coefficients are growing from margins to the middle. Note that here is represented the nominal row of the  $C$  eigenvalue matrix. These are parallel, but not identical, with the resonance weights. For full clarity, let us specify the corresponding row of Mulliken weights, as percentages: 2.92, 6.41, 10.55, 14.06, 16.07, 16.07, 14.05, 10.55, 6.41 and 2.92. This row corresponds to the sequence of resonances where the “vertical” double bond “travels” from the left margin to the right side of the molecule. Thus, one notes that the resonances having the double bonds nearby the middle of the molecule are getting higher participation. This can be understood well in heuristic manner. The resonance takes place between symmetry equivalent objects, namely, structures related by mirror or rotation elements. However, the energy gains are not equal for all such couples. One may intuitively guess that the structures having distant “vertical” linkages, such as the  $\Omega_1$ – $\Omega_8$  couple, are less effective for the resonant stabilization. In turn, in the given example, the  $\Omega_4$ – $\Omega_5$  couple yields the most definite aromatic stabilization. Actually, swapping the  $\Omega_4$ – $\Omega_5$  figures, one observes that the central benzene ring plays its Kekulé structures. If one observes the  $\Omega_1$ – $\Omega_2$  pair, one may say that these are representing the Kekulé elements on the first benzene ring. However, this couple is not really a resonance, because the  $\Omega_1$  and  $\Omega_2$  are not symmetry equivalent and, in general, are not showing the same energy expectation value. Then, since the most stabilizing contributions are coming from resonance structures running Kekulé conjugation on the rings from the middle of the molecule, one may understand that these are gaining main weights in the ground state. In other words, the aromaticity of linear polyacenes can be considered as concentrated at the middle of the molecules.

We mentioned previously that the sign of resonance wavefunctions, and therefore the afferent eigenvector coefficients, can be switched somewhat arbitrarily. However, it is a fact that the ground state of polyacenes is totally symmetric, while the first excited state is antisymmetric (with respect to inversion, rotation or reflection through the median plane). Then, if all the coefficients of the ground state are

arranged to be in phase, as in the lower histogram from Fig. 12, then the first excited state gets the aspect with out-of-phase halves (opposed to the sign for coefficients of symmetry-related resonance structures, as seen in the upper histogram).

The first excited state has the same symmetry like a vector directed on the long molecular axis. Given the opposite parity of ground and excited state (even vs. odd), their coupling can be achieved by perturbations with polar nature, such as a properly oriented electric field. Their mutual mixing is stronger when the ground-excited gap is reduced. One may rationalize in this way the conduction properties of large polyacenes [80]. Though qualitative, these correlations are supporting the outlined idea, of considering the conduction along polyacene as the travel of the representative “vertical” bond from one margin to the other, when driven by electric field polar perturbation.

In more detail, the perturbation should imply the mixing of ionic resonance structures, since, as pointed previously, in spin-coupling formalism, the charge rearrangements are not nominally supposed. However, the parameterization of perturbation as a supplementary coupling element between odd-even couples of states can tacitly incorporate a charge displacement following the “travelling” double bond. Besides, a complete modelling should include triplet states.

Confined to singlets and a mobile double bond as density carrier, one may actually speak about superconductivity, because this object is a boson. But, a couple of quasi-degenerate singlet and triplet spin states represents in fact a pair of free, decoupled, electrons. However, we will not enter here the technicalities of this suggested way of modelling that offers a molecular perspective to the conduction mechanisms, particularized to conveniently chosen polyaromatic hydrocarbons.

Since the bases of resonance structures for the triplet states are too large to be coped at intuitive level, we performed other numeric experiments to analyse their nature. Namely, we have drawn the spin density maps by unrestricted DFT calculations set for triplet multiplicity, to have a picturesque account of these states. One may expect that the DFT can reach the same qualitative picture as a VB treatment of the lowest triplet, in a manner similar to the fact that the two methods can describe, on different ways, the same singlet ground states. Looking at the trends from (a) to (d) frames of Fig. 13, one may note that the spin density is concentrated in the centre of the molecule. This parallels the above interpretation that the aromaticity is higher in the median area. Then, the spin can be taken in corresponding numeric experiments as a marker for aromaticity, spreading preferentially on the most aromatic moieties of a conjugated molecule. From this reasoning, we add a thought experiment suggesting the conduction properties of large polyacenes. Suppose that we can have an infinite slab of linearly fused benzene rings. The aromaticity, i.e. the propensity for delocalization, tends to be placed in the middle of the molecule. But, for an infinite system, the middle can be anywhere. Therefore, the wavepacket of spin-coupled states (or the spin wave of unpaired electrons) gets a free mobility. This is an extrapolation.



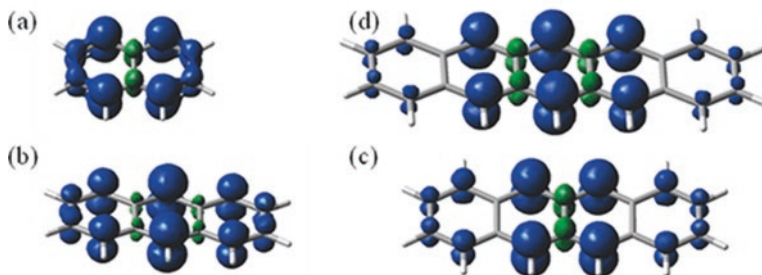


**Fig. 13** Spin density from unrestricted B3LYP/6-31G calculations on triplet states of (a) naphthalene, (b) anthracene, (c) tetracene and (d) pentacene

At large molecules, the mobile spin and electron density is nominally placed at the symmetry centre, but it can be easily displaced around this position. Under a sufficiently firm electric field perturbation, the charge can be transported from one edge to another, the mechanism being the mixing of states with opposed parity of the resonance eigenvectors.

## 9 Triangular Graphenes with Spin

We draw this section in the continuation of earlier preoccupation of triangular-shaped graphene-type molecules where unpaired spins can appear in the ground state, by topological reasons [81, 82]. It was early recognized that in hydrocarbons with appropriate topology, unpaired electrons can be lodged in sets of quasi-degenerate orbitals (or even degenerate, in the limits of Hückel schemes) [83–85]. This opens the challenging idea of the organic molecular magnetism and carbon-based magnetic materials [86].

Shaping graphene flakes in appropriate patterns, one may meet the situation of topologically unpaired spins [87–89]. We will consider the very idealized version of this class, taking equilateral triangles made from benzenoid cells. A short introduction of the topological spin in triangulenes is suggested in the synopsis from Fig. 14. The considered systems are idealized as regular triangles with  $D_{3h}$  symmetry. The margin of the carbon skeleton is a zigzag. A  $n$ -triangulene, having  $n$  benzene rings at one edge, has  $n^2 + 4n + 1$  carbon atoms, carrying a net amount of  $n-1$  unpaired  $\alpha$ -electrons, i.e. a  $n$  spin multiplicity at ground state. The marginal valences are closed with  $3n + 3$  hydrogen atoms.

The example from Fig. 14 corresponds to  $n = 6$ , the molecular skeleton being shown as inset in the upper-right quarter. The left side suggests the excess of  $\alpha$ -electrons resulting from the reasons of spin polarization topology. Thus, the simplest idea about the chemical bonding as spin pairing is arranging the alternation of  $\alpha$ - and  $\beta$ -electrons on neighbour sites. Then, counting the blue balls standing for

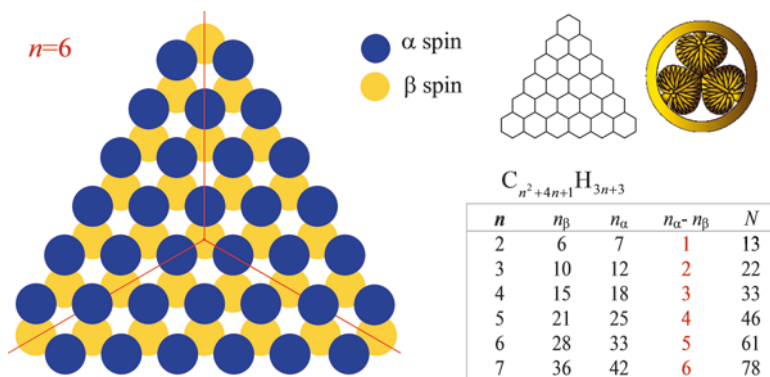


**Fig. 14** The synopsis of topologically determined spin in equilateral triangulenes with  $C_{n^2+4n+1}H_{3n+3}$  formula, where  $n$  is the number of hexagon units at one edge

$\alpha$ -spins and the yellow ones as  $\beta$ -electrons, one obtains the respective 33 vs. 28 result, having a net spin  $S = 5/2$  from the excess of five spin-up particles. The counts for the  $n = 2-7$  series are exemplified in the table from right-down corner of the discussed synopsis. The combinatorial analysis of the general cases yields the following counts of the up and down total electronic populations:

$$n_\alpha = \frac{1}{2}n \cdot (n+5), \quad (15.a)$$

$$n_\beta = \frac{1}{2}(n+1) \cdot (n+2), \quad (15.b)$$

the corresponding spin multiplicity of a regular  $n$ -triangulene being:

$$2S+1 = 2(n_\alpha - n_\beta) / 2 + 1 = n. \quad (16)$$

Remaining in the area of generalities, we observe that there are three classes of triangular PAHs, according to the topology of the resonance structure with the highest imaginable symmetry. The corresponding “periodic” table is shown in Fig. 15. Thus, we identify three types of structures.

The first class starts with the simplest element, at  $n = 2$ , being characterized by the fact that the symmetry centre is occupied by a carbon atom. The following congeners obeying this typology are at  $n$  equal to 5 and 8, drawing the  $n = 2 + 3l$  regularity, with the integer indices  $l = 0, 1, 2$ , etc. If attempting to draw the resonance structure with the highest formal symmetry, the  $\alpha$ -electrons are placed as follows: one at the central carbon atom and the remaining ones on three equivalent lines going from centre to vertices.

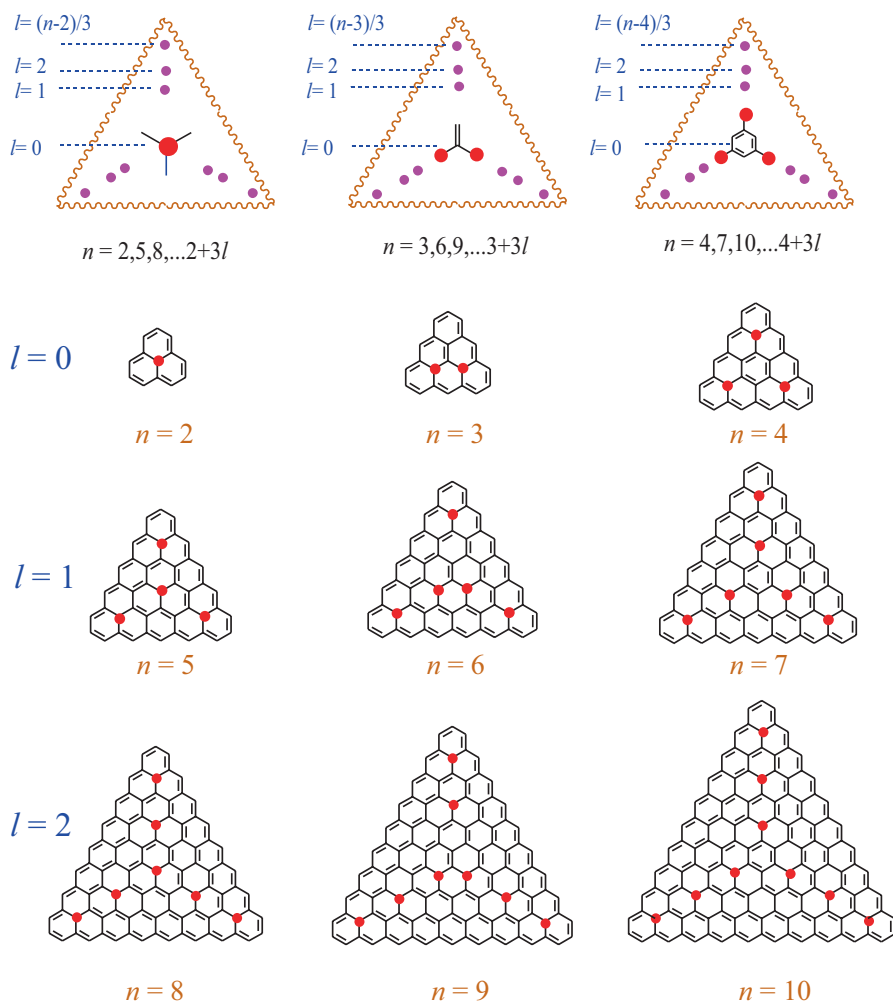


**Fig. 15** The three topological classes of triangulenes, starting with the  $n = 2, 3$  and  $4$  counts (hexagons on the edge). The growth inside each class is controlled by the  $l$  index corresponding to the progressive addition of perimeter shells

The following class starts with  $n = 3$ , spanning the  $n = 3 + 3l$  cases. These molecules have also a carbon atom at the symmetry centre, but if attempting to draw a symmetric resonance structure, one observes that this cannot obey the full  $D_{3h}$  symmetry, getting at most a  $C_{2v}$  pattern. The central region of this type of resonance can be described as a  $C=C(C)_2$  core having the broken symmetry of a double bond aside a biradical moiety. This does not mean that the ground state cannot be symmetric, by a corresponding superposition of three asymmetric resonances drawn as rotated figures. In fact, as will be seen later, the symmetric resonances get a small

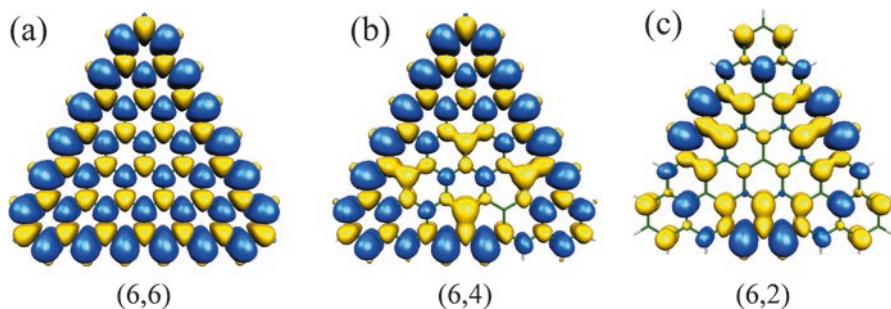


**Fig. 16** The spin density maps from unrestricted DFT calculations on different multiplicities of the  $n = 6$  triangulene. The  $\alpha$ -spin density is shown in *blue*, while the  $\beta$  one is drawn in *yellow*. The indices in parentheses denote the  $(n, \text{multiplicity})$  values

weight in the final wavefunction, obtained at end, by the superposition of many spin-coupling diagrams, whose individual formal symmetry may be low.

The last class runs over the  $n = 4, 7, \dots 4 + 3l$  total counts of edge rings. It is characterized by having a hexagonal ring at the molecular centre (the symmetry point being placed in its central void). The high symmetry resonance structure obeys the  $D_{3h}$  symmetry, the dots symbolizing the unpaired spins being placed on the lines radiating from the 1, 3 and 5 peripheral positions of the central hexagonal ring.

To the best of our knowledge, this classification of triangulenes was not presented before.

The spin polarization on large triangular graphenes is illustrated in Fig. 16 for the  $n = 6$  case. One may see that the alternation of  $\alpha$ - and  $\beta$ -spin densities from Fig. 16a panel matches well the qualitative scheme drawn by intuition in Fig. 14. The ground state of the 6-triangulene is a spin sextet. The (b) and (c) panels are illustrating other possible spin multiplicities, with lower value, namely, quartet and doublet. The quartet state is breaking the trigonal symmetry of the molecule, the spin map getting a  $C_{2v}$  appearance, with the axis passing through the upper vertex and the central carbon atom. The spin doublet state gets again the trigonal symmetry, showing the segregation of spin-up densities on the edges, while the spin-down counterpart is polarized in the central area. In fact, also in the case of high-spin state, the effective accumulation of the spin also occurs on edges. The spin map density is not directly illustrating this fact, but the analysis drawn in Fig. 17 offers details.

To simplify the insight in the spin distribution over the molecular area, it is convenient to turn the calculations to the restricted open shell mode. This switches off the spin polarization, showing only the resultant  $\alpha$ -spin density on the atoms that were carrying this polarization in the unrestricted calculation. The spin map looks qualitatively as retaining only the blue areas from Fig. 16a, while the yellow zones are quenched to null spin density.

Taking the Mulliken spin populations on the atoms, one finds that the marginal ones are getting the major share, as shown in the panel (a) of Fig. 17. The overall scaling of the circles designating the spin population is arbitrary, but their relative

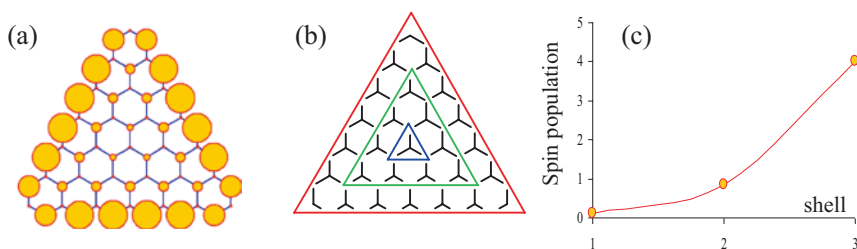


**Fig. 17** Population analysis of the 6-triangulene, based on restricted open shell DFT calculation. The panel (a) shows the Mulliken spin populations on atoms, by circles drawn at relative scale. The panel (b) defines the partition of the molecule in three shells. The panel (c) draws the total spin population cumulated on the defined shells, numbered 1, 2 and 3, from inside to the periphery, respectively

radii keep the quantitative ratios. For a more detailed analysis shown in the panel (c), the panel (b) operates the dichotomy of the molecule in three fragments. The first shell comprises the central C(C)<sub>3</sub> fragment. The second shell, with 21 atoms, has the periphery of the  $n = 3$  subsystem, plus three carbon atoms connected to its vertices. The third shell is the periphery of the actual  $n = 6$  triangulene. Summing the Mulliken spin populations on the atoms from these shells, one sees that the inner one is almost spinless, the second one carries about one electron, while the last gets approximately four (from the total of five) unpaired spins.

The energies of the spin quartet and spin doublet states of the 6-triangulene (see Fig. 16) are placed with 6235 cm<sup>-1</sup> and 9574 cm<sup>-1</sup>, respectively, over the ground spin sextet (from an unrestricted B3LYP/6-31G calculation). The relatively small gaps suggest a possible tuning of the spin state with optical controls in near-infrared or visible domains.

The large graphenes are yet a matter of imagination, brought to a certain concreteness with the help of first-principle simulations. However, along with the optimism generally expressed in introductory parts of works related with the new materials chemistry, the hopes may be not so empty and illusory. There are e-beam lithography techniques that can tailor 2D nanoscale aromatic fragments with triangular patterns, starting from graphite [90, 91].

At the same time, important steps were already made in the synthesis and experimental characterization of the first members of the series. Thus, the nucleus of the  $n = 2$  structure, called phenalenyl, is present in several derivatives well characterized, with X-ray structural data available, and confirmed to have magnetic properties by electron spin resonance (ESR) and magnetic susceptibility measurements [92, 93]. The species closest to the trigonal ideal pattern is the tri-*t*-butyl-phenalenyl [94]. This molecule shows interesting long-range spin-spin interactions in the crystals containing stacked molecules [95, 96]. Other substituted derivatives are 1,9-dithiophenalenyl [97] and tri-*t*-butyl-6-oxophenalenoxyl [98].

A very interesting system is the spiro-bis(3,7-dimethoxy-1,9-dioxophenalenyl) boron, thoroughly investigated in structural and spectroscopy respects. In this system, the phenalenyl nucleus substituted with two oxygen atoms formally act as chelates towards a central boron atom, as ligands placed in different molecular halves, with their planes mutually perpendicular. In alternative description, the  $O_2BO_2$  central fragment has a spiro-pattern. Ignoring the electronic features, the molecule may appear symmetric, but in deeper insight, one may conclude that, formally, one may take one phenalenyl moiety positive (on the expense of a negative charge taken at the boron fragment) while the other remains radical.

The system can be then characterized as mixed valence, having the possibility of full delocalization of the radical character, or its localization on a single ligand. The intermolecular stacking interactions established between the fragments with radical character seem to stabilize the localized form, but the very intriguing properties, such as the manifested thermochromism (the change of the colour with the temperature), suggest the possibility to tune the localized vs. delocalized character [99, 100]. The system, colourless at 100 K, when localized in separated valence states (one radical and one cation fragment), turns to green at 300 K, when the thermal disordering can overcome the barrier of localized radical, the fluxional geometry driving the dynamics of the radical between the opposed sides of the molecule. The bistable behaviour [101–103] hardens the hopes in a spintronics possible with such derivatives.

Moreover, derivatives of the  $n = 3$  congener, named triangulene (from which the name of the whole series was generalized), were synthesized and proven to carry spin [104, 105]. The variety of the species with this root is not very large, but is yet a firm promise of the carbon-based spin chemistry.

Given the already diversified chemistry and physics developed at experimental level for the  $n = 2$  smallest triangulene core, let us bring it to the magnifying glass of the spin-coupling analysis.

Pedantically, the aromatic molecules with topological spin can be characterized as non-Kekulé systems, because the skeleton cannot be drawn completely with alternating simple and double bonds. However, in a more permissive terminology, we will consider as Kekulé-type the resonances that imply spin coupling along the connected sites only, namely, excluding the Dewar-like lines between distant centres. Defined in this way, the Kekulé basis of the phenalenyl has 20 resonance structures, shown in Fig. 18.

The rather large number of resonances suggests already, as qualitative guess, the significant aromaticity of this system. There are 13  $\pi$  electrons, comparable then with anthracene (with 14 electrons), for which only four Kekulé structures were available.

A non-trivial achievement is the VB calculation done in this set of resonance structures, using the VB2000 code [28, 29] and the 6-31G atomic basis set. Due to the mutual placement of the spin-coupled linkages (figured as double bonds), aside from the position of the radical, the resonance structures are falling in four different classes, grouped correspondingly in Fig. 18.

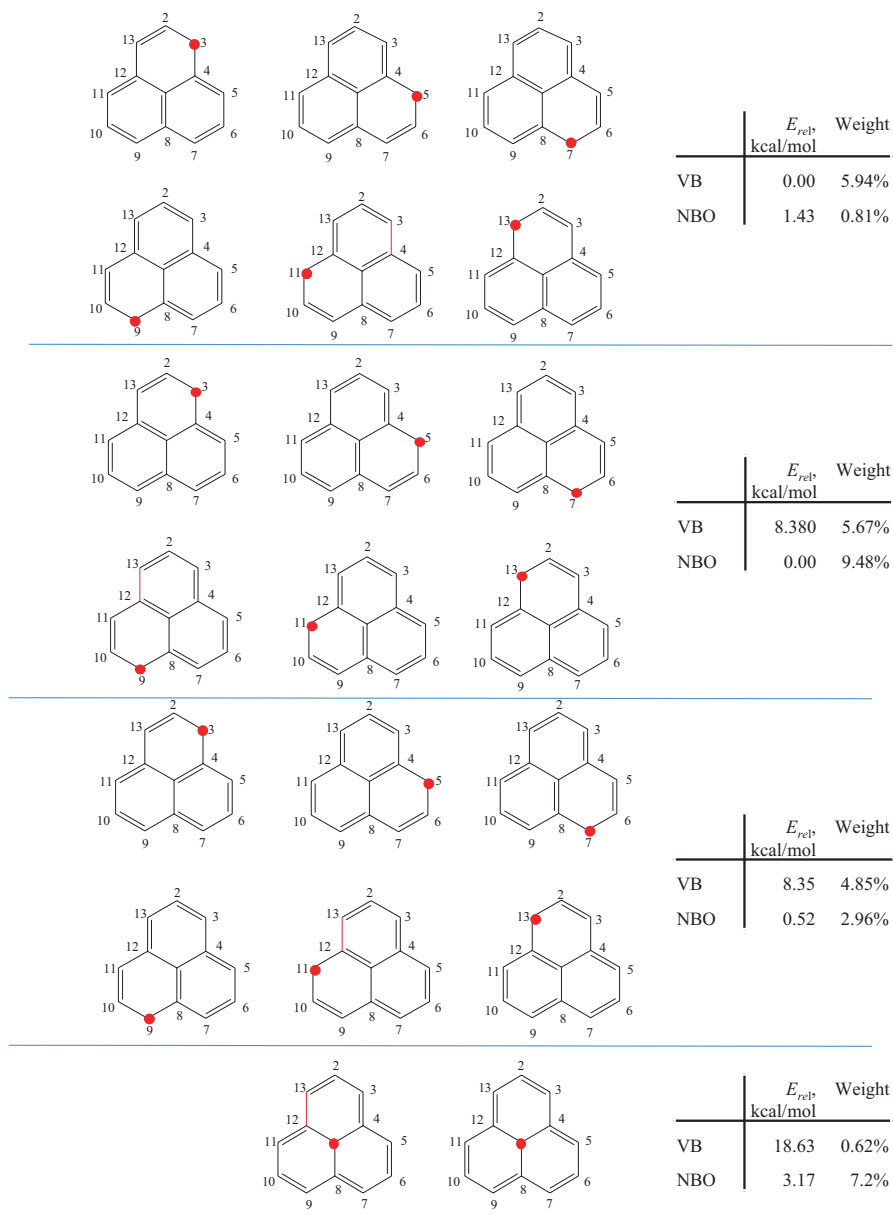


**Fig. 18** Resonance structures of the  $n = 2$  triangulene (the phenalenyl radical), grouped on classes of equivalence (separated by *horizontal lines*). For each class, the results of valence bond (VB) calculations and natural bond orbitals (NBO) post-computation analyses of DFT results are shown comparatively

Taking the energy of resonance structures as their diagonal elements from the Hamiltonian matrix extracted from the calculation, and making them relative to the smallest value, one notes that the two resonances having the unpaired electron in the centre have the largest energy, 18.6 kcal/mol. This gap determines the small VB weight of these resonances, almost negligible, with 0.62%.

Other two classes are quite similar to each other, with 8.35 kcal/mol and 8.38 kcal/mol (accidentally degenerate) relative to the group taken as zero reference. The three classes, with six members each, are showing similar weights in the VB result, around 5% for every element. This suggests again a strong aromaticity of the system. Besides, the ground state energy (converged as superposition of the mentioned resonances) is with 57 kcal/mol lower than the energy of the structure convened as relative zero of the scale. This quantity is assimilated with a rather firm aromatic stabilization.

The parallel analysis in the frame of natural bond orbitals [49, 50] and natural resonance theory [46–48] is comparatively annotated aside the VB briefing in the sections of Fig. 18. As in the previous instances, the results are not well correlated with the VB results. For example, the two symmetric resonance structures with low VB weights are getting a rather high percentage, 7.2% in the NRT version.

The confusion is also increased by the fact that in the case of the systems with spin, the code takes only the unrestricted orbitals. In this conjuncture, one obtains disjoint sets of NRT weights for the  $\alpha$ - and  $\beta$ -subsystems. These two schemes are, indeed, not well correlated into an intuitively acceptable picture. For instance, the NRT decomposition of the  $\beta$ -subsystem (which has a hole in the place of unpaired electron) yielded about 26% contribution for each of the two structures rated with low participation in the VB results. It is unfortunate that the NRT cannot function as approximation of the VB, since, as mentioned, the VB approach becomes prohibitive for larger systems.

We also have as usable tool the spin Hamiltonian approach. Taken in the simplest way, with unique  $J$  parameter, this modelling yielded weights slightly higher or lower than 5% for all the 18 resonances mentioned to be around 5% in the VB calculations. For the two components with central radical, the simplified spin Hamiltonian gave 2.6%. The higher contribution, compared with VB result, is due to the simplified frame, since now all the diagonal elements are equal to  $1.5 J$ . In the model, the ground state is placed at  $4.363 J$ . If equating the energy of stabilization with respect of previous VB value, one estimates the averaged  $J \approx 7000 \text{ cm}^{-1}$  coupling parameter. This quantity is sensibly lower than the previous values for aromatic hydrocarbons. Taken under the reserve of crudeness of the model, it may be yet informative for the fact that the effective coupling is, indeed, lower in this system, interpreting the situation as the weakening of the overall bonding by the “travelling” non-bonded radical.

At the end, we touch a bit the problem of long-range spin coupling, first taking the experimental structure of the supramolecular assemblies of 2,5,8-tri-*t*-butylphenalenyl [94]. Thus, we apply broken symmetry (BS) [56–59] DFT calculations



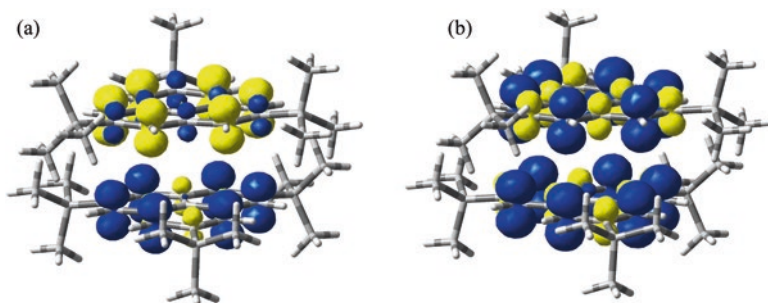


**Fig. 19** The spin density maps for experimental structure of dimeric 2, 5, 8-tri-*t*-butyl-phenalenyl. *Left side (a)*: the broken symmetry (BS) configuration having monomers with distinct  $\alpha$ - and  $\beta$ -spin polarization (shown in *blue* and *yellow*, respectively). *Right side (b)*: the high-spin (HS) configuration with overall  $\alpha$ -density. The monomers are mutually rotated by 180 degrees in their own mean planes

on a dimeric couple. The calculations are illustrated in Fig. 19. The distance between mean molecular planes is about 3.2 Å, the interaction being in the expected weak bonding range, where the BS method works. The approach consists in one unrestricted calculation for the system in high-spin state (HS, with parallel spins on the two monomers) and one calculation enforcing spin  $\alpha$  at one fragment while spin  $\beta$  on the other, a pattern called broken symmetry (BS) configuration. The BS is not a real singlet state, but a numeric experiment enabling information about the spin-coupling strength. In more detail, as we discussed in the VB respects, a dimer in singlet form should be described by a two-configurational wavefunction:  $(\alpha_1\beta_2 - \beta_1\alpha_2)$ . The BS simulates only a single configuration, say the  $\alpha_1\beta_2$  one. However, this is enough to extract useful data.

From the energy difference between the HS and BS results (divided by the corresponding difference of expectation values of the spin square operator, provided also by the output), one estimates the exchange coupling parameter  $J$ . This time, the  $J$  refers to the long-range interactions of the  $\pi$ -type orbitals from each subsystem, which in the intersystem mode are acting actually as distant and weak  $\sigma$ -like overlapping. We estimated a  $J = -1960 \text{ cm}^{-1}$  value. Note that this describes the overall interaction of the stacked molecular planes. While the average molecular planes are parallel, the molecules have opposed orientation, so that the vertex of one triangle is projected approximately on the middle of the edge of the other one. Thus, if each monomer is schematized as a triangle, their stacking is done as an antiprism.

We provoked also the numeric experiment considering the parallel alignment of two monomers with the same orientation. Or, in other words, the assembly is idealized as a trigonal prism. The spin maps of the HS and BS configurations are drawn in Fig. 20. In this case, the carbon atoms from different units are aligned on the same vertical axis. The  $p_z$ -type components of each carbon atom are getting axially overlapped with the mirror partners, in weak  $\sigma$ -like supramolecular bonding. Then, formally, one may divide the estimated inter-dimer exchange coupling by the number of atom pairs, to get the averaged parameter per carbon-carbon stacked

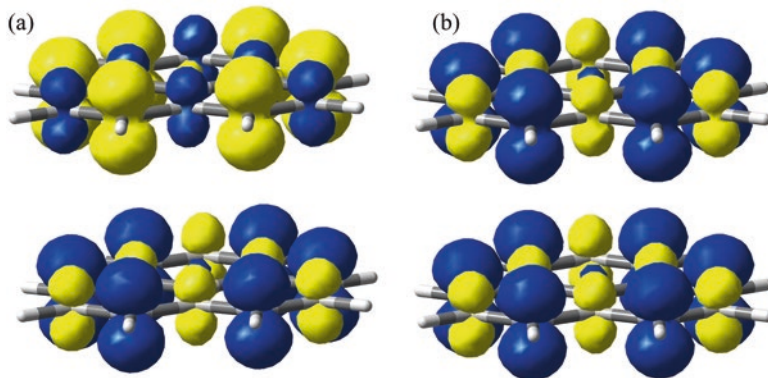


**Fig. 20** The spin density maps for hypothetical phenalenyl dimer when the molecules are imposed parallel (with equivalent atoms on the same verticals). *Left side (a)*: the broken symmetry (BS) configuration. *Right side (b)*: the high-spin (HS) configuration with overall  $\alpha$ -density. The distance between molecular planes is 3.5 Å

coupling. When inter-planar distance is tuned at 3.0 Å, 3.5 Å and 4.0 Å, the inter-dimer exchange coupling, taken as overall value, varies as follows:  $-3440\text{ cm}^{-1}$ ,  $-1262\text{ cm}^{-1}$  and  $-367\text{ cm}^{-1}$ , respectively. Divided per atom pairs, one estimates the following dependence:  $-265\text{ cm}^{-1}$ ,  $-97\text{ cm}^{-1}$  and  $-28\text{ cm}^{-1}$ . This numeric experiment provides valuable information for prospects of further modelling of stacking effects by spin-coupling formalisms, even extrapolating to cases without spin.

## 10 Conclusion

Combining the reviewing mode with constructions from our own research, we have drawn lines connecting the conceptual chemistry of selected aromatic systems with potential applications, in the desiderata of materials engineering. Although the application purposes are yet inherently remote, the revealing of causal structure-property correlations represents useful leverages. Thus, the aromaticity, as electronic delocalization, has basically the same causal roots as the electronic conduction in large organic molecules and carbon-based materials.

The spin-coupling paradigm is a generous general frame that can comprise into effective phenomenology the chemical bonding itself, as well as the description of magnetic properties in systems carrying spins. We explored the model Hamiltonian and ab initio computational sides of the spin-coupling idea, bringing at confluence valence bond (VB) calculations and simplified parametric schemes. Popular methods of computation and modelling, such as the density functional theory (DFT), show certain intrinsic limitations in the account of subtle electronic structure effects, such as the resonance, or in wavefunctions of magnetic systems. On the other hand, VB calculations are not easy to conduct and reach rapidly the bottleneck of molecular size, being confined to a limited number of active electrons.

We pointed some hints for extracting relevant parameters, responding to a VB phenomenology, from simpler levels of computational techniques, which can be transported in effective models that are completing the account, beyond the hindrances of brute force computations. For instance, specifically, well-designed numeric experiments with spin states accountable in the DFT frame can be equated with formulas from effective spin Hamiltonian modelling, in order to extract  $J$  exchange coupling parameters. At the same time, we pointed certain caveats in the capabilities of post-computational analysis methods, such as natural resonance theory (NRT), initially claimed to retrieve VB-alike meaning from DFT calculations.

After outlining the methodological concerns and innovations, we worked two classes of polyaromatic molecules with relevance for special properties in newly aimed technologies. The polyacenes were taken as models for the electron conduction, using the key of resonance structures as objects accomplishing the electron spin and density transport. The triangular polyacenes were taken as playground for the analysis of carbon 2D systems with spin determined from topological reasons. With advanced computational and modelling tools, we went beyond the usual considerations on these systems, drawing a consistent systematization. Both imagined and real structures were considered, in a well-tempered orchestration.

**Acknowledgement** This work is supported by the Roumanian Research Council, UEFISCDI, grant PCE 14/2013. MF is indebted to Professor Tamio Endo for warm cooperation and fruitful discussions. FC is thankful to Professor Yoshiyuki Kawazoe and Michael Philpott for previous cooperation in the debated field.

## References

1. A. Suzuki, Synthetic studies via the cross-coupling reaction of organoboron derivatives with organic halides. *Pure Appl. Chem.* **63**(3), 419–422 (1991)
2. E. Clar, *Polycyclic Hydrocarbons* (Academic Press, London, 1964)
3. Y. Geerts, G. Klärner, K. Müllen, in *Electronic Materials: The Oligomer Approach*, ed. by K. Müllen, G. Wagner (Wiley-VCH, Weinheim, 1998), p. 48
4. C. Joachim, M.A. Ratner, Molecular electronics: Some views on transport junctions and beyond. *Proc. Natl. Acad. Sci.* **102**, 8801–8808 (2005)
5. V.A. Dediu, L.E. Hueso, I. Bergenti, C. Taliani, Spin routes in organic semiconductors. *Nat. Mater.* **8**, 707–716 (2009)
6. S. Sanvito, Organic electronics: Memoirs of a spin. *Nat. Nanotechnol.* **2**, 204–206 (2007)
7. S. Pramanik, C.G. Stefanita, S. Patibandla, S. Bandyopadhyay, K. Garre, N. Harth, M. Cahay, Observation of extremely long spin relaxation times in an organic nanowire spin valve. *Nat. Nanotechnol.* **2**, 216–219 (2007)
8. W. Koch, M.C. Holthausen, *A Chemist's Guide to Density Functional Theory* (VCH, Berlin, 2001)
9. M.J. Frisch, G.W. Trucks, H.B. Schlegel, G.E. Scuseria, M.A. Robb, J.R. Cheeseman, G. Scalmani, V. Barone, B. Mennucci, G.A. Petersson, H. Nakatsuji, M. Caricato, X. Li, H.P. Hratchian, A.F. Izmaylov, J. Bloino, G. Zheng, J.L. Sonnenberg, M. Hada, M. Ehara, K. Toyota, R. Fukuda, J. Hasegawa, M. Ishida, T. Nakajima, Y. Honda, O. Kitao, H. Nakai,

- T. Vreven, J.A. Montgomery Jr., J.E. Peralta, F. Ogliaro, M. Bearpark, J.J. Heyd, E. Brothers, K.N. Kudin, V.N. Staroverov, R. Kobayashi, J. Normand, K. Raghavachari, A. Rendell, J.C. Burant, S.S. Iyengar, J. Tomasi, M. Cossi, N. Rega, J.M. Millam, M. Klene, J.E. Knox, J.B. Cross, V. Bakken, C. Adamo, J. Jaramillo, R. Gomperts, R.E. Stratmann, O. Yazyev, A.J. Austin, R. Cammi, C. Pomelli, J.W. Ochterski, R.L. Martin, K. Morokuma, V.G. Zakrzewski, G.A. Voth, P. Salvador, J.J. Dannenberg, S. Dapprich, A.D. Daniels, Ö. Farkas, J.B. Foresman, J.V. Ortiz, J. Cioslowski, D.J. Fox, *Gaussian 09, Revision E 01* (Gaussian, Wallingford, 2009)
10. G.A. Gallup, *Valence Bond Methods* (Cambridge University Press, Cambridge, 2002)
  11. S. Shaik, P.C. Hiberty, *A Chemist's Guide to Valence Bond Theory* (Wiley, Hoboken, 2007)
  12. A. T. Balaban (ed.), *Chemical Applications of Graph Theory* (Academic, London, 1976)
  13. A.T. Balaban, Challenging problems involving Benzenoid polycyclic and related systems. *Pure Appl. Chem.* **54**, 1075 (1982)
  14. H. Hosoya, Clar's aromatic sextet and sextet polynomial. *Top. Curr. Chem.* **153**, 255 (1990)
  15. M. Randić, Aromaticity of polycyclic conjugated hydrocarbons. *Chem. Rev.* **103**, 3449–3605 (2003)
  16. W.C. Herndon, M.L. Ellzey Jr., Resonance theory. V. Resonance energies of benzenoid and nonbenzenoid  $\pi$  systems. *J. Am. Chem. Soc.* **96**, 6631 (1974)
  17. W.C. Herndon, Resonance energies of  $\pi$  hydrocarbon radicals. Radical reactivities of polycyclic aromatic hydrocarbons. *J. Organomet. Chem.* **46**, 2119–2125 (1981)
  18. W. Heitler, F. London, Interaction between neutral atoms and homopolar binding. *Z. Phys.* **44**, 455–472 (1927)
  19. W.Z. Heisenberg, Zurtheorie des ferromagnetismus. *W. Zeit. Phys.* **49**, 619–636 (1928)
  20. J.H. van Vleck, A. Sherman, The quantum theory of valence. *Rev. Mod. Phys.* **7**, 167–228 (1935)
  21. P.W. Anderson, New approach to the theory of superexchange interactions. *Phys. Rev.* **115**, 2–13 (1959)
  22. O. Kahn, *Molecular Magnetism* (VCH Publisher, New York, 1993)
  23. M. Said, D. Maynau, J.P. Malrieu, Excited-state properties of linear polyenes studied through a nonempirical Heisenberg Hamiltonian. *J. Am. Chem. Soc.* **106**(3), 580–587 (1984)
  24. M.A. Garciabach, P. Blaise, J.P. Malrieu, Dimerization of polyacetylene treated as a spin-Peierls distortion of the Heisenberg Hamiltonian. *Phys. Rev. B Condens. Matter* **46**(24), 15645–15651 (1992)
  25. J. Cioslowski, Graph theoretical approach to the topological spin hamiltonian applied to conjugated molecules. *Chem. Phys. Lett.* **134**(6), 507–511 (1987)
  26. N. Flocke, T.G. Schmalz, D.J. Klein, Variational resonance valence bond study on the ground state of C60 using the Heisenberg model. *J. Chem. Phys.* **109**(3), 873–880 (1998)
  27. D.J. Klein, H. Zhu, R. Valenti, M.A. Garciabach, Many-body valence-bond theory. *Int. J. Quantum Chem.* **65**(5), 421–438 (1997)
  28. J. Li, B. Duke, R. McWeeny, VB2000 Version 2.0. SciNet Technologies, San Diego, (2007)
  29. J. Li, R. McWeeny, VB2000: Pushing valence bond theory to new limits. *Int. J. Quantum Chem.* **89**, 208–216 (2002)
  30. L. Song, Z. Chen, F. Ying, J. Song, X. Chen, P. Su, Y. Mo, Q. Zhang, W. Wu, XMVB 2.0: An ab initio Non-Orthogonal Valence Bond Program. Xiamen University, Xiamen 361005, China (2012)
  31. L. Song, Y. Mo, Q. Zhang, W. Wu, XMVB: a program for ab initio nonorthogonal valence bond computations. *J. Comput. Chem.* **26**, 514–521 (2005)
  32. K. Hirao, H. Nakano, K. Nakayama, M. Dupuis, A complete active space valence bond (CASVB) method. *J. Chem. Phys.* **105**(20), 9227–9239 (1996)
  33. T. Thorsteinsson, D.L. Cooper, Modern valence bond descriptions of molecular excited states: an application of CASVB. *Int. J. Quantum Chem.* **70**(4–5), 637–650 (1998)
  34. M. Raimondi, D.L. Cooper, Ab initio modern valence bond theory. P.R. Surján, R.J. Bartlett, F. Bogár, D.L. Cooper, B. Kirtman, W. Klopper, W. Kutzelnigg, N.H. March, P.G. Mezey,

- H. Müller, J. Noga, J. Paldus, J. Pipek, M. Raimondi, I. Røeggen, J.Q. Sun, P.R. Surján, C. Valdemoro, S. Vogtner, *Topics in Current Chemistry: Localization and Delocalization*, vol. 203 (1999), pp. 105–120
35. H. Nakano, K. Sorakubo, K. Nakayama, K. Hirao, in *Valence Bond Theory*, ed. by D. L. Cooper (Elsevier Science, Amsterdam, 2002), pp. 55–77
36. L. Pauling, G.W. Wheland, The nature of the chemical bond. V. The quantum-mechanical calculation of the resonance energy of benzene and naphthalene and the hydrocarbon free radicals. *J. Chem. Phys.* **1**, 362 (1933)
37. D.L. Cooper, J. Gerratt, M. Raimondi, The electronic structure of the benzene molecule. *Nature. London* **323**, 699 (1986)
38. E.C. da Silva, J. Gerratt, D.L. Cooper, M. Raimondi, Study of the electronic states of the benzene molecule using spin-coupled valence bond theory. *J. Chem. Phys.* **101**, 3866 (1994)
39. R. McWeeny, Classical structures in modern valence bond theory. *Theor. Chim. Acta* **73**, 115 (1988)
40. P.C. Hiberty, D. Danovich, A. Shurki, A. Shaik, Why does benzene possess a  $D_{6h}$  symmetry? A Quasiclassical state approach for probing p-bonding and delocalization energies. *J. Am. Chem. Soc.* **117**, 7760 (1995)
41. G. Rumer, Zum Theorie der Spinvalenz. In: *Nachrichten der Akademie der Wissenschaften in Göttingen, Mathematisch-Physikalische Klasse*, Göttingen, (1932), pp. 337–341
42. R. Serber, Extension of the Dirac vector model to include several configurations. *Phys. Rev.* **45**, 461–467 (1934)
43. M. Kotani, A. Amemiya, E. Ishiguro, T. Kimura, *Table of Molecular Integrals* (Maruzen Co. Ltd., Tokyo, 1955)
44. W. Research, *Inc Mathematica* (Champaign, Illinois, 2014)
45. S. Wolfram, *The Mathematica book* (5. ed.), Wolfram-Media, (2003), pp. I–XXIV, 1–1464
46. E.D. Glendening, F. Weinhold, Natural resonance theory: I. General formalism. *J. Comput. Chem.* **19**(6), 593–609 (1998)
47. E.D. Glendening, F. Weinhold, Natural resonance theory: II. Natural bond order and valency. *J. Comput. Chem.* **19**, 610–627 (1998)
48. E.D. Glendening, J.K. Badenhop, F. Weinhold, Natural resonance theory: III. Chemical applications. *J. Comput. Chem.* **19**, 628–646 (1998)
49. A.E. Reed, L.A. Curtiss, F. Weinhold, Intermolecular interactions from a natural bond orbital, donor-acceptor viewpoint. *Chem. Rev.* **88**, 899–926 (1988)
50. E.D. Glendening, A.E. Reed, J.E. Carpenter, F. Weinhold, The NBO3.0 program, University of Wisconsin, Copyright 1996–2001
51. J.C.A. Slater, Simplification of the Hartree-Fock method. *Phys. Rev.* **81**, 385–390 (1951)
52. S.J. Vosko, L. Wilk, M. Nusair, Accurate spin-dependent electron liquid correlation energies for local spin density calculations: a critical analysis. *Can. J. Phys.* **58**, 1200–1211 (1980)
53. A.D. Becke, Density-functional exchange-energy approximation with correct asymptotic behavior. *Phys. Rev. A* **38**, 3098–3100 (1988)
54. J.P. Perdew, Density-functional approximation for the correlation energy of the inhomogeneous electron gas. *Phys. Rev. B* **33**, 8822–8824 (1986)
55. C. Lee, W. Yang, R.G. Parr, Development of the Colle-Salvetti correlation-energy formula into a functional of the electron density. *Phys. Rev. B* **37**, 785–789 (1988)
56. L. Noodleman, Valence bond description of antiferromagnetic coupling in transition metal dimers. *J. Chem. Phys.* **74**, 5737–5743 (1981)
57. L. Noodleman, E.R. Davidson, Ligand spin polarization and antiferromagnetic coupling in transition metal dimers. *Chem. Phys.* **109**, 131–143 (1986)
58. E. Ruiz, J. Cano, S. Alvarez, P. Alemany, Broken symmetry approach to calculation of exchange coupling constants for homobinuclear and heterobinuclear transition metal complexes. *J. Comput. Chem.* **20**, 1391–1400 (1999)
59. A. Bencini, F. Totti, C.A. Daul, K. Doclo, P. Fantucci, V. Barone, Density functional calculations of magnetic exchange interactions in polynuclear transition metal complexes. *Inorg. Chem.* **36**(22), 5022–5030 (1997)

60. M. Sironi, D.L. Copper, J. Gerratt, M. Raimondi, The modern valence bond description of naphthalene. *J. Chem. Soc. Chem. Commun.* **675** (1989)
61. S. Shaik, S. Zilberg, Y. Haas, A Kekule-crossing model for the “anomalous” behavior of the b<sub>2u</sub> mode of aromatic hydrocarbons in the lowest excited 1B<sub>2u</sub> state. *Acc. Chem. Res.* **29**, 211 (1996)
62. D.L. Packett, C.M. Jensen, R.L. Cowan, C.E. Strouse, W.C. Trogler, Syntheses, structures, and mechanisms of formation of trans-Chlorohydrobis-(trimethylphosphine)platinum(II) and trans-Dihydrobis(trimethylphosphine)platinum(II). Energetics of Cis-Trans Isomerization. *Inorg. Chem.* **24**, 3578 (1985)
63. J. Lefebvre, G. Odou, M. Muller, A. Mierzejewski, T. Luty, Characterization of an Orientational disorder in two charge-transfer complexes: anthracene-Tetracyanobenzene (A-TCNB) and naphthalene-Tetracyanobenzene (N-TCNB). *Acta Crystallogr. Sect. B: Struct. Sci.* **45**, 323 (1989)
64. M. Le Bars-Combe, J. Lajzerowicz-Bonneteau, Complexe naphthalène-dianhydride d'acide pyromellitique. I. Transition ordre-désordre et structure basse température de la forme orange. *Acta Crystallogr. Sect. B: Struct. Crystallogr. Cryst. Chem.* **37**, 1707 (1981)
65. S. Zilberg, Y. Haas, S. Shaik, Electronic Spectrum of anthracene: an ab-initio molecular orbital calculations combined with a valence bond interpretation. *J. Phys. Chem.* **99**, 16558 (1995)
66. R. Mason, The crystallography of anthracene at 95°K and 290°K. *Acta Crystallogr.* **17**, 547 (1964)
67. C.P. Brock, J.D. Dunitz, Temperature dependence of thermal motion in crystalline anthracene. *Acta Crystallogr. Sect. B: Struct. Sci.* **46**, 795 (1990)
68. J.G. Malecki, CSD Communication (Private Communication) (2013)
69. M. Lusi, I.J. Vitorica-Yrezabal, M.J. Zaworotko, Expanding the scope of molecular mixed crystals enabled by three component solid solutions. *Cryst. Growth Des.* **15**, 4098–4103 (2015)
70. X. Du, I. Skachko, A. Barker, E.Y. Andrei, Approaching ballistic transport in suspended graphene. *Nat. Nanotechnol.* **3**(8), 491–495 (2008)
71. M.M. Payne, S.R. Parkin, J.E. Anthony, Functionalized higher acenes: hexacene and heptacene. *J. Am. Chem. Soc.* **127**, 8028–8029 (2005)
72. M. Bendikov, F. Wudl, D.F. Perepichka, Tetrathiafulvalenes, oligoacenes and their buckminsterfullerene derivatives: the brick and mortar of organic electronics. *Chem. Rev.* **104**, 4891–4945 (2004)
73. J.E. Anthony, Functionalized acenes and heteroacenes for organic electronics. *Chem. Rev.* **106**, 5028–5048 (2006)
74. J.H. Schön, C. Kloc, A. Dodabalapur, B. Batlogg, An organic solid state injection laser. *Science* **289**, 599–601 (2000)
75. F.A. Hegmann, R.R. Tykwinski, K.P.H. Lui, J.E. Bullock, J.E. Anthony, Picosecond transient photoconductivity in Functionalized Pentacene molecular crystals probed by terahertz pulse spectroscopy. *Phys. Rev. Lett.* **89**, 227403 (2002)
76. C. Raghu, Y.A. Pati, S. Ramasesha, Structural and electronic instabilities in polyacenes: density-matrix renormalization group study of a long-range interacting model. *Phys. Rev. B* **65**, 155204 (2002)
77. S. Kivelson, O.L. Chapman, Polyacene and a new class of quasi-one-dimensional conductors. *Phys. Rev. B* **28**, 7236–7243 (1983)
78. J. Aihara, Why are some polycyclic aromatic hydrocarbons extremely reactive? *Phys. Chem. Chem. Phys.* **1**, 3193–3197 (1999)
79. A.R. Reddy, M. Bendikov, Diels–Alder reaction of acenes with singlet and triplet oxygen – theoretical study of two-state reactivity. *Chem. Commun.*, 1179–1181 (2006)
80. J.A. Pople, S.H. Walmsley, Bond alternation defects in long polyene molecules. *Mol. Phys.* **5**, 15–20 (1962)
81. M.R. Philpott, F. Cimpoesu, Y. Kawazoe, Bonding and magnetism in high symmetry Nano-sized graphene molecules: Linear Acenes C<sub>4m+2</sub>H<sub>2m+4</sub> (m = 2, ..., 25); zigzag Hexangulenes

- $C_{6m+2}H_{6m}$  ( $m = 2, \dots, 10$ ); crenelated Hexangulenes  $C_{6(3m+2-3m+1)}H_{6(2m-1)}$  ( $m = 2, \dots, 6$ ); zigzag Triangulenes. *Mater. Trans.* **49**(11), 2448–2456 (2008)
82. M.R. Philpott, F. Cimpoesu, Y. Kawazoe, Geometry, bonding and magnetism in planar triangulene-graphenes with D3h symmetry. *Chem. Phys.* **354**, 1–15 (2008)
  83. J. Higuchi, Zero-field Splittings in molecular multiplets: spin-spin interaction of methylene derivatives. *J. Chem. Phys.* **38**, 1237–1245 (1963)
  84. H.C. Longuet-Higgings, Some studies in molecular orbital theory I. Resonance structures and molecular orbitals in unsaturated hydrocarbons. *J. Chem. Phys.* **18**, 265–274 (1950)
  85. E.H. Lieb, Two theorems on the Hubbard model. *Phys. Rev. Lett.* **62**, 1201–1204 (1989)
  86. H. Iwamura, High-spin organic molecules and spin alignment in organic molecular assemblies. *Adv. Phys. Org. Chem.* **26**, 179–253 (1990)
  87. S.E. Stein, R.L. Brown,  $\pi$ -electron properties of large condensed polyaromatic hydrocarbon. *J. Am. Chem. Soc.* **109**, 3721–3729 (1987)
  88. J. Fernandez-Rossier, J.J. Palacios, Magnetism in graphene Nanoislands. *Phys. Rev. Lett.* **99**, 177204–177204 (2007)
  89. E. Clar, D.G. Stewart, Aromatic hydrocarbons LXV. Triangulene derivatives. *J. Am. Chem. Soc.* **75**(11), 2667–2672 (1953)
  90. A.K. Geim, A.H. MacDonald, Graphene: Exploring carbon flatland. *Phys. Today* **60**, 35–41 (2007)
  91. K.S. Novoselov, D. Jiang, F. Schedlin, V.V. Khotkevich, S.V. Morozov, A.K. Giem, Two dimensional atomic crystals. *Proc. Nat. Acad. Sci. (U.S.)* **102**, 10451–10453 (2005)
  92. R.G. Hicks, What's new in stable radical chemistry? *Org. Biomol. Chem.* **5**, 1321–1338 (2007)
  93. Y. Morita, S. Suzuki, K. Sato, T. Takui, Synthetic organic spin chemistry for structurally well-defined open-shell graphene fragments. *Nat. Chem.* **3**, 197 (2011)
  94. K. Goto, T. Kubo, K. Yamamoto, K. Nakasuji, K. Sato, D. Shiomi, T. Takui, M. Kubota, T. Kobayashi, K. Yakusi, J. Ouyang, A stable neutral hydrocarbon radical: synthesis, crystal structure and physical properties of 2,5,8-tri-tert-butyl-phenalenyl. *J. Am. Chem. Soc.* **121**, 1619–1620 (1999)
  95. D. Small, V. Zaitsev, Y. Jung, S.V. Rosokha, M. Head-Gordon, J.K. Kochi, Intermolecular  $\pi$ -to- $\pi$  bonding between stacked aromatic dyads. Experimental and theoretical binding energies and near-IR optical transitions for phenalenyl radical/radical versus radical/cation dimerizations. *J. Am. Chem. Soc.* **126**, 13850–13858 (2004)
  96. S. Suzuki, Y. Morita, K. Fukui, K. Sato, D. Shiomi, T. Takui, K. Nakasuji, Aromaticity on the pancake-bonded dimer of neutral phenalenyl radical as studied by MS and NMR spectroscopies and NICS analysis. *J. Am. Chem. Soc.* **128**, 2530–2531 (2006)
  97. L. Beer, S.K. Mandal, R.W. Reed, R.T. Oakley, F.S. Tham, B. Donnadieu, R.C. Haddon, The first electronically stabilized phenalenyl radical: effect of substituents on solution chemistry and solid-state structure. *Cryst. Growth Des.* **7**, 802–809 (2007)
  98. Y. Morita, T. Ohba, N. Haneda, S. Maki, J. Kawai, K. Hatanaka, K. Sato, D. Shiomi, T. Takui, K. Nakasuji, New persistent radicals: synthesis and electronic spin structure of 2,5-di-tert-butyl-6-oxophenalenoxyl derivatives. *J. Am. Chem. Soc.* **122**, 4825–4826 (2000)
  99. Y. Morita, S. Suzuki, K. Fukui, Thermochromism in an organic crystal based on the coexistence of  $\delta$ - and  $\delta$ -dimers. *Nat. Mater.* **7**, 48–51 (2008)
  100. S. Nishida, Y. Morita, K. Fukui, K. Sato, D. Shiomi, T. Takui, K. Nakasuji, Spin transfer and solvato-/thermochromism induced by intramolecular electron transfer in a purely organic open-shell system. *Angew. Chem. Int. Ed.* **44**, 7277–7280 (2005)
  101. M.E. Itkis, X. Chi, A.W. Cordes, R.C. Haddon, Magneto-optoelectronic bistability in a phenalenyl-based neutral radical. *Science* **296**, 1443–1445 (2002)
  102. S.K. Pal, M.E. Itkis, F.S. Tham, R.W. Reed, R.T. Oakley, R.C. Haddon, Resonating valence-bond ground state in a phenalenyl-based neutral radical conductor. *Science* **309**, 281–284 (2005)
  103. A. Shimizu, M. Uruichi, K. Yakushi, H. Matsuzaki, H. Okamoto, M. Nakano, Y. Hirao, K. Matsumoto, H. Kurata, T. Kubo, Resonance balance shift in stacks of delocalized singlet biradicals. *Angew. Chem. Int. Ed.* **48**, 5482–5486 (2009)

104. J. Inoue, K. Fukui, T. Kubo, S. Nakazawa, K. Sato, D. Shiomi, Y. Morita, K. Yamamoto, T. Takui, K. Nakasuji, The first detection of a Clar's hydrocarbon, 2,6,8-tri-tertbutyltriangulene: a ground-state triplet of non-Kekulébenzenoid hydrocarbon. *J. Am. Chem. Soc.* **123**, 12702–12703 (2001)
105. G. Allinson, R.J. Bushby, M.V. Jesudason, J.L. Paillaud, N. Taylor, The synthesis of singlet ground state derivatives of non-Kekulé polynuclear aromatics. *J. Chem. Soc. Perkin Trans.* **2**, 147–156 (1997)



# Electrocatalytic Hydrogen Production Properties of Polyaniline Doped with Metal-Organic Frameworks

Kabelo E. Ramohlola, Milua Masikini, Siyabonga B. Mdluli, Gobeng R. Monama, Mpitloane J. Hato, Kerileng M. Molapo, Emmanuel I. Iwuoha, and Kwena D. Modibane

## 1 Introduction

Hydrogen fuel cell technology is one of the most promising energy sources for sustainable energy applications because of its numerous advantages, such as recycling, pollution-free and fuel efficient [9, 32, 36, 41]. However, the major limitation of utilizing hydrogen as energy carrier is the need for the hydrogen to be produced in high purity. Electrochemical reduction of water is considered as an alternative route, due to its simplicity and economical way to produce hydrogen in high purity and large quantity [9]. An efficient electrocatalyst for hydrogen evolution reaction is usually required to reduce the overpotential in HER process and achieve large exchange current density [6, 20]. Recently, platinum (Pt)-based electrocatalysts are considered to be the most efficient HER catalysts due to their superior electrochemical property and robust stability [28]. However, the drawback about Pt is that it is not cost-effective to be used on a large scale for hydrogen production technologies [28].

Conducting polymers (CPs) are promising to be used as suitable electrocatalysts due to their impressive structural and physical properties and also having the ability

---

K.E. Ramohlola • G.R. Monama • M.J. Hato (✉)  
Department of Chemistry, School of Physical and Mineral Sciences, University of Limpopo (Turffloop), Polokwane, Sovenga 0727, South Africa  
e-mail: [imaydance@gmail.com](mailto:imaydance@gmail.com); [release.monama@ul.ac.za](mailto:release.monama@ul.ac.za); [Mpitloane.Hato@ul.ac.za](mailto:Mpitloane.Hato@ul.ac.za)

M. Masikini • S.B. Mdluli • K.M. Molapo • E.I. Iwuoha  
SensorLab, Chemistry Department, University of the Western Cape, Cape Town, South Africa  
e-mail: [2914873@myuwc.ac.za](mailto:2914873@myuwc.ac.za); [3680647@myuwc.ac.za](mailto:3680647@myuwc.ac.za); [g.molapo947@gmail.com](mailto:g.molapo947@gmail.com); [eiwuoha@uwc.ac.za](mailto:eiwuoha@uwc.ac.za)

K.D. Modibane (✉)  
Department of Chemistry, School of Physical and Mineral Sciences, University of Limpopo (Turffloop), Polokwane, Sovenga 0727, South Africa  
e-mail: [kwena.modibane@ul.ac.za](mailto:kwena.modibane@ul.ac.za)

to catalyse electrode reactions. This family contains all the currently generally researched conductive polymers: polypyrrole, polyaniline and polythiophene. Among all CPs, polyaniline (PANI) is a promising candidate for HER because of its good photo- and chemical-physical properties, cheap, processibility and conductivity [3, 19]). PANI is synthesized from chemical or electrochemical polymerization of aniline monomer and exists in three oxidative states/bases, i.e. leucoemeraldine (colourless/white), emeraldine (blue/green) and pernigraniline (blue/violet) [21]. The shortcoming of utilizing polyaniline for hydrogen production is that under harsh environmental conditions, the material becomes fragile leading to structural decomposition [34]. Numerous methods have been investigated to overcome these drawbacks; these include incorporation of different materials to the polymer backbone [25]. Other methods that include the incorporation of porous materials such as zeolites, carbon nanotubes and metal-organic frameworks can be advantageous as they will bring great stability as well as some more functional sites on the PANI backbone. This leads to change in mechanical, thermal and electrical properties as compared to freely polymeric material [13].

Among the previously mentioned porous materials, metal-organic frameworks (MOFs) are highly crystalline and consist of tunable metal sites coordinated to organic compounds known as organic linker which can assemble different dimensions (2-D, 3-D) [24]. These porous materials have shown great applications in catalysis, magnetism, sensors as well as drug delivery due to their exceptional properties such as high surface area and adjustable pore size of the material [24]. To the best of our knowledge, there are no reports on the formation and observation of HER from polyaniline doped with metal-organic frameworks (PANI/MOFs). Thus we report the synthesis, characterization and application of the PANI/MOF nanocomposite for the hydrogen production. The PANI/MOF composite has great potential as a tool for analytical applications. The MOF can be easily coupled to the backbone of PANI, and it is found that this MOF is not only robust and thermal stable but also showed good electrocatalyst in both acidic and basic media. The results demonstrated that the pure characteristics of the PANI/MOF composite and the presence of MOF strongly affect the electrocatalyst compared to neat PANI and bare electrode.

## 2 Experimental Section

### 2.1 Materials

Aniline monomer, copper nitrate trihydrate ( $\text{Cu}(\text{NO}_3)_2 \cdot 3\text{H}_2\text{O}$ ), trimesic acid ( $\text{H}_3\text{BTC}$ ) and tetrabutylammonium perchlorate (TBAP) were purchased from Sigma-Aldrich, South Africa. Ammonium persulphate (APS) and iron chloride ( $\text{FeCl}_3$ ) were purchased from Riedel-de Haen and Educhem, respectively. Absolute ethanol was purchased at Merck, South Africa, and hydrochloric acid (HCl), dimethyl sulphoxide (DMSO) and sulphuric acid ( $\text{H}_2\text{SO}_4$ ) were procured from Rochelle Chemicals.

Aniline was distilled before use, and the rest of the reagents were used without further purification.  $\text{H}_2\text{SO}_4$  standard solutions were made in DMSO solution with 0.1 M TBAP as a supporting electrolyte system unless otherwise stated. All measurements were carried out at  $22 \pm 2$  °C.

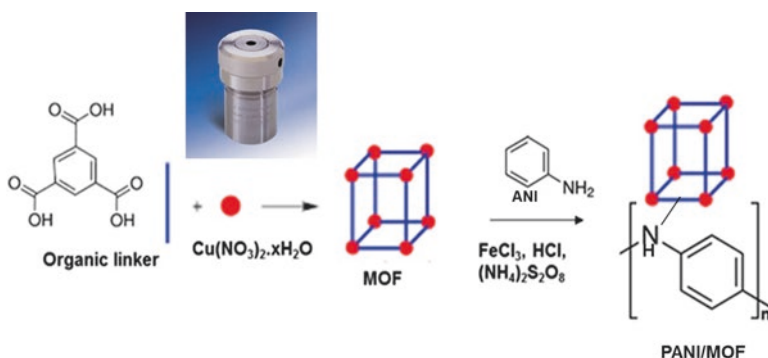
## 2.2 Methods

### 2.2.1 Preparations of PANI, MOF and PANI/MOF Composite

Polyaniline (PANI) was prepared by oxidation polymerization of aniline monomer according to a previously reported method [8]. The synthesis of Cu-trimesic MOF (HKUST-1) was based on a previously reported hydrothermal procedure [12]. The synthesis of polyaniline doped with metal-organic framework composite referred as PANI/MOF is shown in Scheme 1. Approximately, 1 ml of the distilled aniline monomer and 3.6 wt.% MOF were dissolved in a solution of 10 ml HCl/100 ml distilled water in a 250 ml round-bottom flask. The solution was stirred for 30 min at 50 °C whereafter 2.40 g of ammonium persulphate (APS),  $(\text{NH}_4)_2\text{S}_2\text{O}_8$  and 1.88 g of  $\text{FeCl}_3$  were added, respectively, in the solution. The resulted mixture was stirred for another 3 h at 50 °C, and the content of the reaction was placed in the oven at the same temperature for overnight to evaporate the solvents, and remaining content was washed with ethanol and re-dried.

### 2.2.2 Characterization Techniques

Absorbance spectra were recorded on a Varian Cary 300 UV-vis-NIR spectrophotometer using 1 cm optical path length quartz cuvette. The crystal structure of the PANI/MOF nanocomposite was analysed by using Philips PW 1830 model



**Scheme 1** Synthesis of polyaniline-based MOF composite (PANI/MOF) through oxidation polymerization of aniline monomer in the presence of MOF material

XRD. The Raman spectra were recorded using Horiba Jobin-Yvon Labram HR 2000 confocal Raman microscope. Raman spectra were recorded using a laser excitation wavelength of 514 nm. The sample powders were placed on a clean SiO<sub>2</sub>/Si substrate and then used for Raman measurement.

Morphological characterizations were performed using Auriga field emission scanning electron microscope (FESEM) coupled with EDS detector for elemental analysis, and transmission electron micrographs were collected using an FEI Tecnai G2 20 field emission gun (FEG) TEM, operated in bright field mode at an accelerating voltage of 200 kV. Energy-dispersive X-ray spectra were collected using an EDAX liquid nitrogen-cooled lithium-doped silicon detector. The crystal structure of the PABA/MOF nanocomposite was analysed by using SAED and Philips PW 1830 model XRD. The FTIR spectra were acquired on a Cary 600 series FTIR spectrometer (Agilent Technologies). The samples for FTIR measurement were prepared by grinding the dried sample powder mixed with potassium bromide (KBr) to a fine powder and then compressing under high pressure into thin pellets. The elemental analysis of Cu metal in MOF and composite was determined using Varian SpectrAA 110 atomic absorption spectrometer (AAS).

TGA was performed on a Perkin-Elmer TGA 4000 instrument connected to a PolyScience digital temperature controller under N<sub>2</sub> gas purged at a flow rate of 20 ml per minute. The calibration of the instrument was performed using indium (m.p. 156.6 °C) and aluminium (m.p. 660 °C). Small samples (1–4 mg) were weighed in a porcelain crucible, and the temperature range was adjusted between 30 and 500 °C at a constant heating rate of 10 °C/min. The data was collected and analysed using Pyris software<sup>®</sup>. This technique was primarily used to determine the solvent stoichiometry of the compounds from the percentage weight loss. The TGA analysis was performed at the University of the Western Cape, School of Pharmacy.

Electrochemical measurements were performed using EPSILON electrochemical workstation. The data was collected using a conventional three-electrode set-up with gold electrode (3 mm diameter) as a working electrode, platinum wire as a counter electrode and Ag/AgCl wire as a reference electrode. Repetitive scanning of the solutions of the complexes MOF, PANI and PANI/MOF (~10 mg) was from -2.0 to 1.25 V at scan rate of 0.02–0.10 V s<sup>-1</sup>. Electrochemical experiments were performed in 25 ml of 0.1 M DMSO/TBAP electrolytic system. Prior to scans, the working electrode was cleaned by successive polishing using 1, 0.3 and 0.05 μm alumina micro-polish and polishing pads purchased from Buehler, IL, USA, followed by rinsing with deionized water and sonication in ethanol and water to remove all traces of alumina polish. After sonication, the electrodes were rinsed with ethanol and deionized water and dried under a nitrogen stream. Experimental measurements for HER studies have been carried out in different concentration of H<sub>2</sub>SO<sub>4</sub> as hydrogen source in DMSO/TBAP system.

### 3 Results and Discussion

#### 3.1 Spectroscopic Characterization

The FTIR spectrum of synthesized PANI/MOF composite with reference from pure PANI and MOF spectra is shown in Fig. 1a. It can be seen in the figure that the PANI/MOF composite shows the same characteristic peaks similar to the undoped PANI. These characteristic peaks are 806, 1177, 1338, 1505 and 1605  $\text{cm}^{-1}$ , which correspond to C-H out-of-phase bonding of benzenoid ring, C-H in-phase bonding of benzenoid ring, C-N stretching of benzenoid and quinoid rings as well as C=C of aromatic ring, respectively. The broad peak between 2500 and 3500  $\text{cm}^{-1}$  is due to NH bond [1, 39]. In the case of the composite, there is no trace of new peak after doping with MOF. However, there is an increase in the absorption intensities upon doping PANI with MOF. This behaviour shows an evidence of the interaction between PANI and MOF. Figure 1b presents Raman spectra of PANI, MOF and PANI/MOF composite. The spectrum of the composite shows an intense band at  $\sim 1350 \text{ cm}^{-1}$  which corresponds to N-O vibrations. This result confirms an interaction between PANI and MOF materials through electrostatic as shown in Scheme 1. This observation supports the FTIR results as discussed above.

Optical properties of the neat PANI and PANI/MOF composite in DMSO were investigated by employing UV-vis spectroscopy, and the results are shown in (c) and (d) of Fig. 1. It can be seen in Fig. 1c that the neat PANI shows two characteristic peaks at 353 and 550 nm. The band observed at 353 nm corresponds to the  $\pi-\pi^*$  transitions of the benzenoid rings, while the broad peak at around 550 nm corresponds to the  $\pi-\pi^*$  transitions of the quinone-imine groups [15]. Nevertheless, for PANI/MOF composite, there is a slight shift in the two absorption peaks upon composite formation to 357 and 552 nm. The shift in the peaks is attributed to the increase in the  $\pi$  conjugation in the PANI backbone [37]. The peak at 357 nm corresponds to the  $\pi-\pi^*$  transitions of the benzenoid rings and quinone-imine groups, while the second broader peak at around 552 nm is associated to the absorption peak of conducting PANI, which is partially oxidized [15, 37]. Figure 1d shows the concentration-dependent studies of the PANI/MOF composite. The Beer-Lambert assumption was obeyed with an increase in the concentration of the composite, whereby the conduction band on the material did not change, but we observed the increase in the absorbance of the materials. The inset in Fig. 1d shows the plot of absorbance versus concentration which was used to determine the molar extinction coefficient of PANI and PANI/MOF composite. From this figure, it can be seen that the molar extinction coefficient was found to be  $4 \times 10^{-3}$  and  $4.2 \times 10^{-3} \text{ cm}^{-1} \cdot \text{ppm}^{-1}$  and wavelengths of 353 and 357 nm for PANI and PANI/MOF composite, respectively.

The energy gap was calculated by a linear extrapolation of the Tauc plot of variation  $(\alpha h\nu)^2$  versus  $E_g$  to the energy axis as shown in Fig. 2 [2]. The energy band gap of the neat PANI and PANI/MOF composite was found to be 1.50 and 1.35 eV,

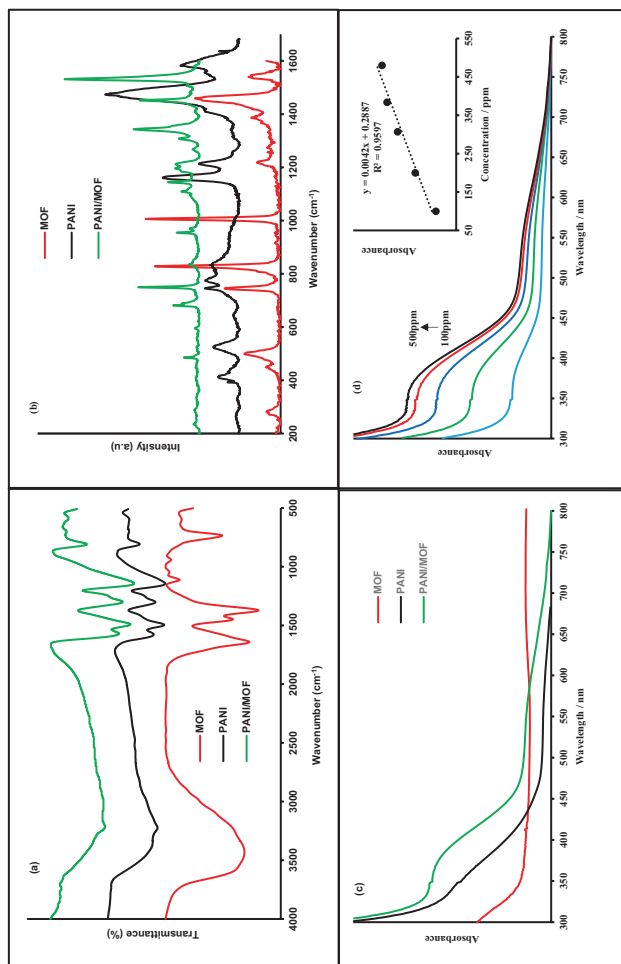


**Fig. 1** (a) FTIR; (b) Raman; (c) UV-vis spectra of MOF, PANI and PANI/MOF in DMSO; and (d) concentration-dependent studies of PANI/MOF in order to determine molar extinction coefficient

**Fig. 2** Tauc plot of PANI and PANI/MOF for energy band gap determinations

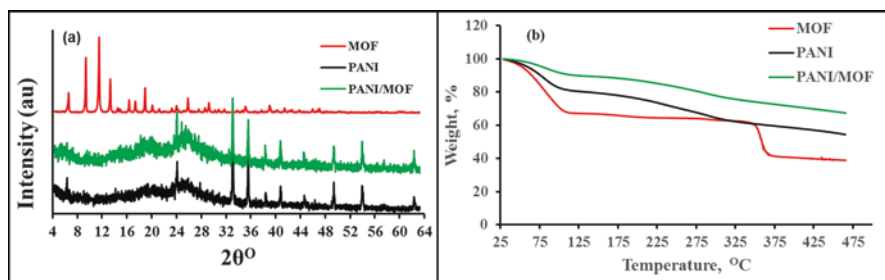
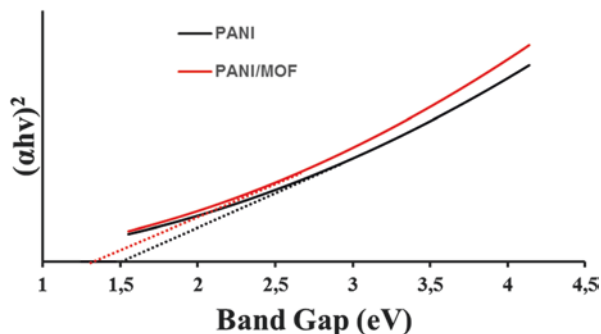


**Fig. 3** (a) XRD and (b) TGA analysis of MOF, PANI and PANI/MOF composite

respectively. The reduction in the optical band gap was due to the increase in electron density of the composite as compared to the neat PANI. This result shows that these materials can be suitable for electrocatalytic applications [33].

The XRD patterns for MOF, PANI and PANI/MOF composite are shown in Fig. 3a. The MOF pattern shows that the MOF phases are highly crystalline, which is an indication of microporous material characteristics [39]. The XRD patterns of PANI show a broad peak at  $2\theta$  angle of  $25^\circ$  which indicate the successful synthesis of PANI in amorphous state, and it is also in accordance to the previous reported data on the XRD result of polyaniline [1, 5]. In situ addition of MOF during polymerization process resulted in decrease in the PANI peaks.

The TGA of MOF, PANI and PANI/MOF under heating rate of  $10^\circ\text{C}/\text{min}$  is shown in Fig. 3b. The thermal analysis of MOF is consistent with prominent weight loss steps similar to the one reported before [10, 17, 38]. The first weight loss from room temperature (RT) to  $120^\circ\text{C}$  is due to loss of water and ethanol physisorbed in the framework of MOF. A sudden weight loss at  $350^\circ\text{C}$  is attributed to total degradation of organic linker BTC, and the remained product was CuO [17, 30]. The TGA results of PANI and PANI/MOF reveal that the trend of PANI/MOF composite degradation is similar to that of pure PANI but with enhanced thermal stabilities. The initial mass loss in terms of weight percentage from RT to  $100^\circ\text{C}$  is mainly due to release of moisture present in the structure of polyaniline [5, 35]. PANI contains up to 20 wt.% of water, whereas PANI/MOF contains up to 10 wt.%. The second

mass loss up to 300 °C is due to the release of anion dopant. Decrease in the weight loss of water and other dopant is due to strong interaction between PANI and MOF which tells that the presence of porous materials can improve the thermal stabilities of PANI [22, 23]. Following the successful confirmation of interaction between PANI and MOF, the amount of Cu atom present in the materials was determined using FAAS. It was found to be 23.99 and 0.05 wt.% for MOF and PANI/MOF composite, respectively.

### 3.2 Morphological Characterization

The morphology of PANI, MOF and PANI/MOF composite was investigated, and the SEM image coupled with EDS is shown in Fig. 4. Morphology of PANI shown in Fig. 4a shows long nanorods/fibre structures that are interconnecting or

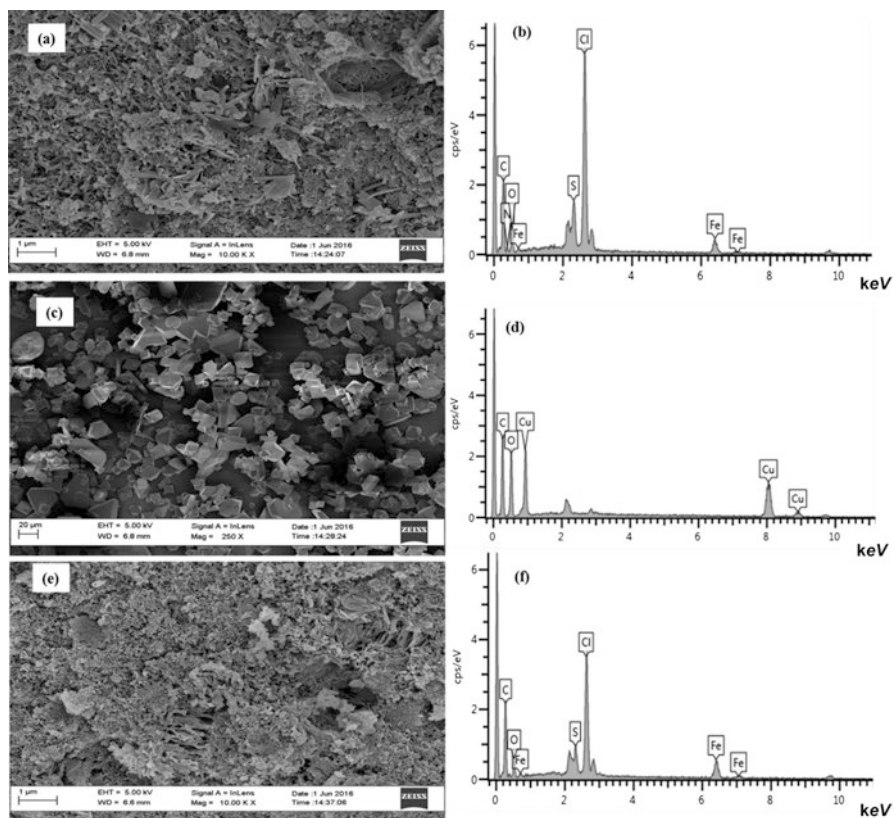


**Fig. 4** SEM image of (a) PANI, (c) MOF, (e) PANI/MOF composite and EDS spectrum of (b) PANI, (d) MOF, (f) PANI/MOF composite



agglomerated to each other and are in accordance to the SEM images of PANI [35]. EDS results of PANI (Fig. 4b) show the presence of iron (Fe), sodium (Na), sulphur (S) and chlorine (Cl) in the polymer backbone. These elements are due to oxidants and acidic medium used during synthesis. Typical morphologies of MOF (Fig. 4c) show that the MOF powder is formed by irregular crystals with octahedral shapes confirming a low control on the crystal growth parameters, and its corresponding EDS (Fig. 4d) reveals the presence of Cu atom [17, 30]. SEM images of PANI/MOF composite (Fig. 4e) were similar to the one of undoped PANI but with small nanorods as compared to long rods of PANI. Octahedral or crystal structures of MOF are not observed, and this tells that MOF is trapped inside polymer backbone or wrapped by PANI. The elemental composition of PANI/MOF composite from EDS (Fig. 4f) showed an increase in the percentage compositions of C and O, and there was no Cu of MOF detected on the surface of polymer which is in agreement with the SEM results indicating wrapping of MOF by PANI.

TEM images in Fig. 5a, c show internal morphologies of PANI, MOF and PANI/MOF composite, respectively. The insets are selected area electron diffraction (SAED) and show ring patterns indicating the orderliness or the arrangement of the molecule at certain definite position in the lattice. TEM images of PANI and MOF show nanofibers and microporous structures as observed in the SEM analysis.

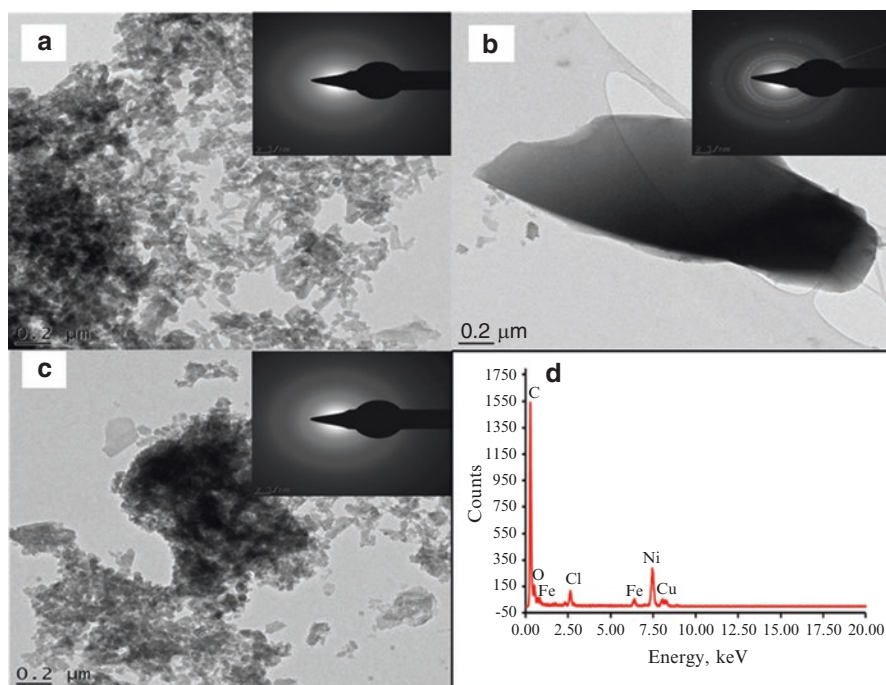


**Fig. 5** TEM images (a) PANI, (b) MOF, (c) PANI/MOF composite and (d) EDX spectrum of PANI/MOF composite. Inset: SAED image

SAED shown that the orderliness of molecules in PANI is not ordered, as indicative of typical amorphous structure [5, 35]. In the SAED of MOF, there are clear ring patterns as an evident that MOF is crystalline [39]. TEM images of PANI/MOF composite (Fig. 5c) show that introduction of MOF material during chemical polymerization of aniline to form PANI-MOF composite has an effect on the internal morphologies of PANI. From Fig. 5c, it can be observed that once the composite is formed, the fibre rod structures of PANI are distracted making shorter rods. The inset image in Fig. 5c is SAED for structural identification, and it showed that the composite maintains its amorphous structure of PANI. However, it has spot where the d-spacing of the composite can be determined as indicative of modification of structural properties of the polymer with MOF and supported by the XRD (Fig. 3a). The PANI wrapping around MOF as an observation in TEM is in agreement with SEM above showing the presence of MOF covered by polymer. The elemental analysis on TEM image using EDX (Fig. 5d) showed an increase in carbon and oxygen content in the composite as compared to PANI. The copper content of MOF was detected; however it overlapped with the foreign species of the grid.

### 3.3 Electrochemical Characterizations

Electrochemistry of functional species is one of the most prominent parameters for potential usage of materials as electrocatalysts for hydrogen production. In order to decide the possible usage of a material, its electrochemical responses should be generally determined in solution. In this work, electrochemical characterizations of PANI, MOF and PANI/MOF composite were investigated using voltammetric analysis. Figure 6a shows typical current-potential curves of the gold electrode in 0.1 M DMSO/TBAP solution with and without MOF, PANI and PANI/MOF composite. It was noticeable that the faradaic contributions (redox process) onto gold electrode (blank) were observed at around  $-0.58$  V. This is a typical redox process of bare Au electrode [31]. However for MOF, two reduction processes were observed which could be related to the copper deposition involving two successive one-electron

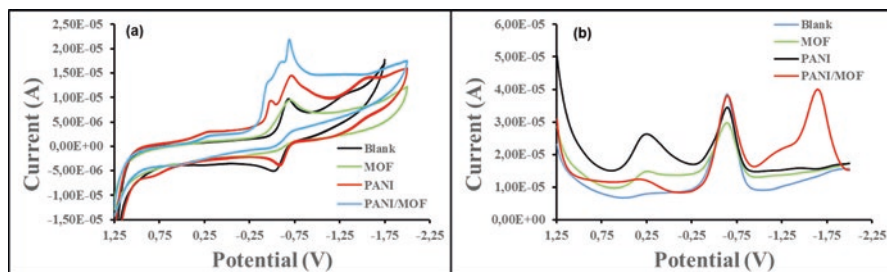


**Fig. 6** (a) CV and (b) SWV results of MOF, PANI and PANI/MOF in 0.1 M DMSO/TBAP electrolyte solution on gold electrode

processes [14]. Nila and Gonzales [27] reported that the electrochemical reduction of  $\text{Cu}^{2+}$  in solutions proceeds in two one-electron reversible waves via a  $\text{Cu}^+$  intermediate, in which the stability of the intermediate was due to the presence of ions in the solution. The shift potential was also observed and reported by Loera-Serna et al. [18] in LiCl solution as indicative that the electrochemical processes of Cu during the direct sweep take place in the MOF. However, in this study, the reduction of  $\text{Cu}^{2+}$  to  $\text{Cu}^+$  occurs to more negative potential which might be due to the electrochemical properties of Au electrode in DMSO/TABP system.

On the other hand, PANI in the potential window of DMSO/TBAP electrolyte system showed a quasi-reversible process. In addition, the voltammogram of PANI indicated a one redox couple as an indicative of the merging of three known oxidation states of PANI [26]. The redox couple observed at cathodic peak potential ( $E_{pc}$ )  $\sim -0.64\text{V}$  are due to polyleucoemeraldine radical cation, transformation of PANI from the reduced leucoemeraldine (LE) state to the partly oxidized emeraldine state (EM) and further oxidized to the pernigraniline (PE). A similar electrochemical characteristic of the synthesized PANI was reported by Genies et al. [11]. The increase in the cathodic current in CV of PANI/MOF composite encourages strong interaction between MOF and PANI and favours the uncoiling of PANI chains. In this uncoiled conformation, the probability of moieties exposed for oxidation is more leading to higher faradaic current [37]. The potential reduction of  $\text{Cu}^{2+}$  to  $\text{Cu}^+$  occurring in composite was *c.a.*  $-0.653\text{V}$ /Au electrode. Meanwhile, the reduction potential at around  $-1.59\text{V}$  in both PANI and composite was an illustration of redox process in PANI ring-based electron-transfer characters. One of the important features observed in the CV of the composite was the merging of new cathodic peak towards negative potential which was clearly visible on the square wave voltammogram (Fig. 6b). The square wave voltammetry (SWV) was utilized as the electrochemical probe of the system due to its higher sensitivity faradaic current [7]. The positive cathodic side was considered as it is the representative of hydrogen evolution prior to evaluating the amount of current.

Scan rate dependent of MOF, PANI and PANI/MOF was achieved in DMSO/TBAP using gold working electrode at different scan rates as given in Fig. 7. The multiscan voltammograms of MOF and PANI are shown in parts (a) and (b) of Fig. 7, respectively. It can be seen from these figures that there is an increase in peak current with increasing scan rate. In Fig. 7c, the PANI/MOF composite shows that as the number of voltammetric cycles increases, peak current also increases. This indicates that the PANI and MOF structure was conductive and diffusion of electrons along the polymer chain was taking place. All redox couples show electrochemical quasi-reversible process with respect to  $\Delta E_p$  (change in peak potential) and  $I_{pa}/I_{pc}$  (ratio of anodic and cathodic peak current) values. Unity of  $I_{pa}/I_{pc}$  ratios at all scan rates and the logarithm of the absolute value of the reductive peak current against the logarithm of the scan rate indicate purely diffusion-controlled characters of the redox processes as shown in Fig. 7d.

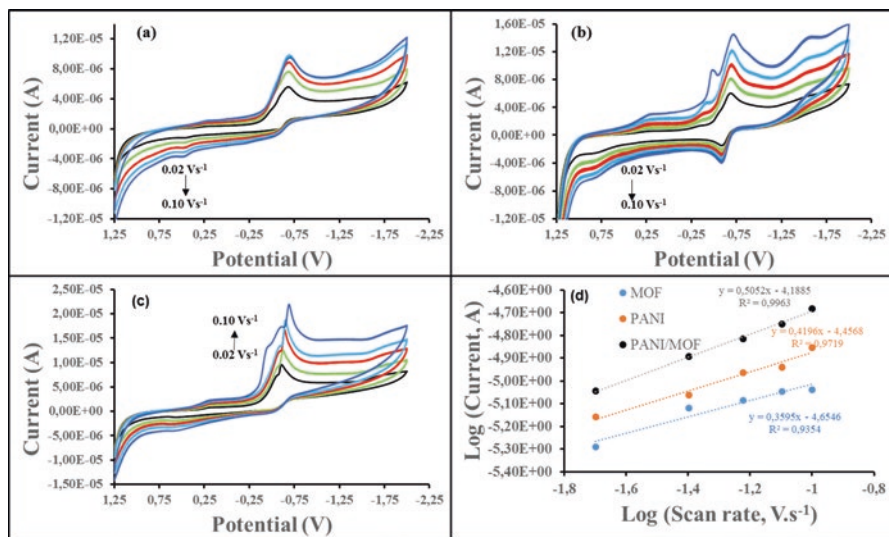
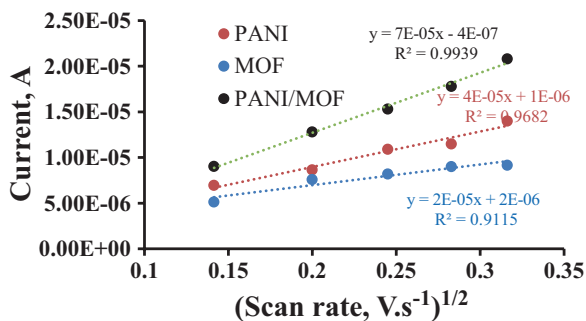


**Fig. 7** Cyclic voltammogram of (a) MOF; (b) PANI; (c) PANI/MOF and (d) peak current as a function of square root of scan rate on gold in 0.1 M DMSO/TBAP electrode system at different scan rate (0.02–0.10 V s<sup>-1</sup>)

**Fig. 8** Peak current as a function of square root of scan rate on gold in 0.1 M DMSO/TBAP electrode system at different scan rate (0.02–0.10 V s<sup>-1</sup>)



The peak current ( $I_p$ ) for diffusion-controlled electron-transfer process is given by Eq. 1 [29]:

$$I_p = nFA[\text{cat}](D)^{1/2} (Fv/RT)^{1/2} \quad (1)$$

where  $n$  is the number of electrons transferred,  $A$  is the area of the working electrode,  $F$  is Faraday's constant and  $[\text{cat}]$  is the concentration of catalyst. Consistent with Eq. 1, Fig. 8 shows that the current increased linearly with increasing  $v^{1/2}$  and the slope that yielded a diffusion coefficient ( $D$ ) was found to be  $3.05 \times 10^{-13}$ ,  $2.40 \times 10^{-13}$  and  $7.34 \times 10^{-13}$  cm<sup>2</sup>.s<sup>-1</sup> for MOF, PANI and PANI/MOF composite, respectively. Significantly, this value of the composite is approximately an order of magnitude faster than the neat PANI.

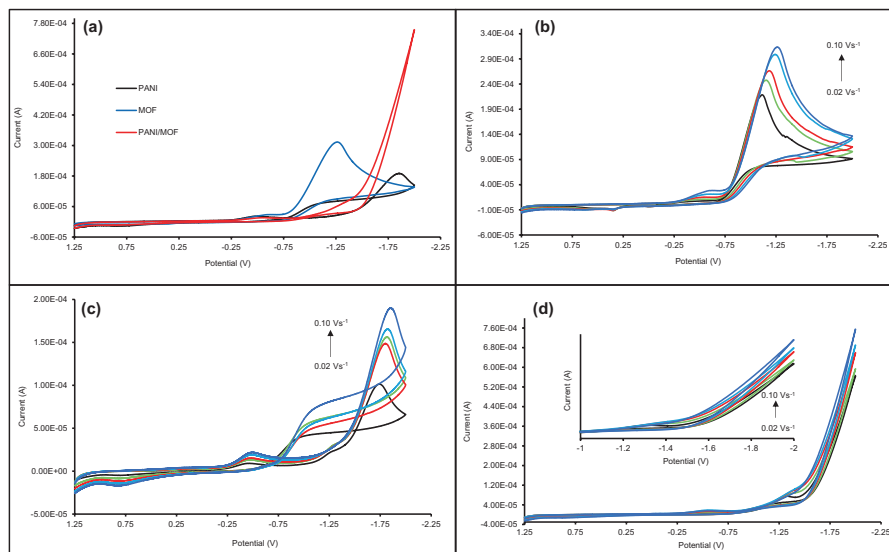


**Fig. 9** (a) CV of MOF, PANI and PANI/MOF at  $0.10 \text{ Vs}^{-1}$ ; CV of MOF (b), PANI (c) and PANI/MOF composite (d) in the presence  $0.15 \text{ M H}_2\text{SO}_4$  at different scan rate on gold electrode in  $0.1 \text{ M DMSO/TBAP}$  electrode system

### 3.4 Electrocatalytic Hydrogen Production

The electrocatalytic activity of the material was evaluated using both voltammetry CV and SWV in  $0.1 \text{ M TBAP/DMSO}$  as electrolytic solution and  $\text{H}_2\text{SO}_4$  as a hydrogen source. The CV and SWV results are represented in parts (a) and (b) of Fig. 9, respectively. Upon addition of  $\text{H}_2\text{SO}_4$ , a wave catalytic near the reduction potential was observed, suggesting that PANI, MOF and PANI/MOF composites are reducing  $\text{H}_2\text{SO}_4$  to  $\text{H}_2$ . The current intensities of the materials can be related to the amount of hydrogen produced; therefore the greater the current reading, large quantity of hydrogen is produced, and thus the distinct material is the best electrocatalyst compared to other materials [16]. There was an intense increase in the current intensity of PANI/MOF composite compared to both bare MOF and PANI. This result indicates that maximum hydrogen can be produced when using PANI/MOF composite as compared to both neat MOF and PANI. Nevertheless, for MOF, the CV results show an appearance of an anodic peak upon addition of hydrogen source. This tells that a small amount of hydrogen produced is trapped or adsorbed on the surface of the MOF material, indicating that MOF can be employed as a hydrogen storage material [40].

Figure 10a, b shows that SWV and Tafel plots, respectively, of MOF, PANI and PANI/MOF composite were recorded to further evaluate electrochemical parameters in the absence and presence of MOF, PANI and PANI/MOF. The SWV shows that upon addition of sulphuric acid, reduction peak appeared within the potential

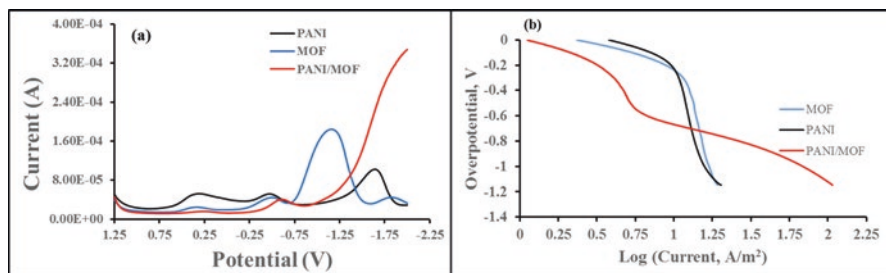


**Fig. 10** (a) SWV and (b) Tafel plots of MOF, PANI and PANI/MOF in the presence 0.15 M  $\text{H}_2\text{SO}_4$  at  $0.10 \text{ V s}^{-1}$  on gold electrode in 0.1 M DMSO/TBAP electrode system

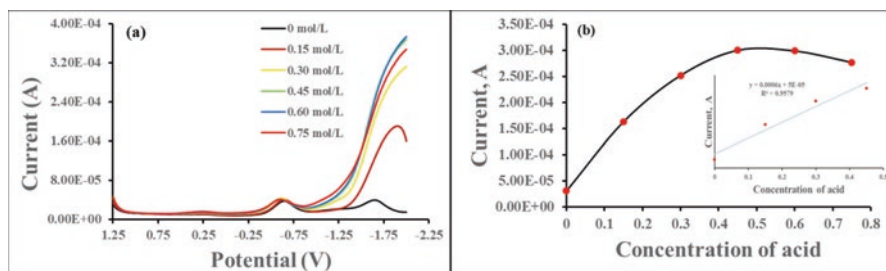


**Fig. 11** (a) SWV of PANI/MOF composite in 0.1 M DMSO/TBAP electrolyte solution and in the presence of 0–0.75 mol/L  $\text{H}_2\text{SO}_4$  and (b) current as a function of addition of  $\text{H}_2\text{SO}_4$  concentration of the composite in 0.1 M DMSO/TBAP electrolyte solution on gold electrode. *Inset*: Linear fitting at low concentration

window of DMSO (Fig. 10a). This reductive wave is followed immediately by a large cathodic current that is assigned to the catalytic reduction of protons to dihydrogen. The Tafel plots (Fig. 10b) present two distinct slopes at low and high overpotential corresponding to the HER controlled by desorption of the hydrogen atoms and charge transfer mechanism as a slow step of the cathodic process, respectively.

Furthermore, concentration dependent of the hydrogen source was investigated using SWV. Figure 11a shows the SWV of PANI/MOF in 0.1 M DMSO/TBAP electrolytic system and the presence of 0–0.75 M  $\text{H}_2\text{SO}_4$  as a hydrogen source using Au electrode. From the figure, it is noticeable that the peak positions are independent of the hydrogen source concentration towards the more negative potential and high values of current. However, at low acid concentration, the peak current of catalytic wave increases linearly with acid concentration as indicative of enhancement of HER. With the help of Fig. 11(a), Fig. 11(b) was plotted using Eq. 2 [29].

$$I_{p_c} = nFA[\text{cat}]\sqrt{Dk[H^+]^2} \quad (2)$$

It is reported that the catalytic current for a reversible electron-transfer process followed by a fast catalytic reaction ( $E_{R}C_{cat}$ ) is given by Eq. 2. However, the plot of  $I_{p_c}$  against acid concentration shows a linear behaviour at low concentration of the acid. Moreover, the average catalytic rate constant can be obtained from the slope of the plot of  $I_{p_c}$  versus acid concentration, and the results are depicted in Fig. 11b inset. This behaviour indicates that the process is second order in acid concentration [4].

## 4 Conclusions

In this work, we demonstrate the preparation of novel polyaniline/metal-organic framework composite through in situ polymerization of aniline monomer in the presence of MOF. Structural and morphological characterizations showed successful incorporation of MOF into the polymer backbone with some wrapping by PANI. Hydrogen studies were evaluated using CV and SWV, in which an intense cathodic peak was observed upon addition of  $H_2SO_4$ . It showed that PANI/MOF composite has a great potential to be used in hydrogen evolution reaction applications as it can easily generate and adsorb hydrogen through straightforward electrochemical process. It has been demonstrated that the PANI/MOF composite is not only robust and stable but also produced considerable  $H_2$  gas. Remarkably, the observed hydrogen generation was dictated by the identity of hydrogen source which opens new avenues for multi-analyte investigation.

**Acknowledgement** KDM and MJH would like to thank financial supports from the National Research Foundation (NRF) of South Africa under the Unique Grant No. 99278 and University of Limpopo (Grants: R202 and R232).

## References

1. A. Abdolahi, E. Hamzah, Z. Ibrahim, S. Hashim, Synthesis of uniform polyaniline nanofibers through interfacial polymerization. *Materials* **5**, 1487–1494 (2012)
2. H.S. Abdulla, A.I. Abbo, Optical and electrical properties of thin films of polyaniline and polypyrrole. *Int. J. Electrochem. Sci.* **7**, 10666–10678 (2012)
3. N.F. Attia, K.E. Geckler, Polyaniline as a material for hydrogen storage applications. *Macromol. Rapid Commun.* **34**, 1043–1055 (2013)
4. A.J. Bard, L.R. Faulkner, *Electrochemical Methods: Fundamentals and Applications*, 2nd edn. (Wiley, New York, 2001)
5. P. Boomi, H.G. Prabu, J. Mathiyarasu, Synthesis and characterization of polyaniline/Ag-Pt nanocomposite for improved antibacterial activity. *Colloids Surf. B: Biointerfaces* **103**, 9–14 (2013)
6. X. Cao, Y. Han, C. Gao, Y. Xu, X. Huang, M. Willander, N. Wang, Highly catalytic active PtNiCu nanochains for hydrogen evolution reaction. *Nano Energy* **9**, 301–308 (2014)

7. C. Dai, P. Song, J.D. Wadhawan, A.C. Fisher, N.S. Lawrence, Screen printed alizarin-based carbon electrodes: monitoring pH in unbuffered media. *Electroanalysis* **27**, 917–923 (2015)
8. T. David, J.K. Mathad, T. Padmavathi, A. Vanaja, Part-A: Synthesis of polyaniline and carboxylic acid functionalized SWCNT composites for electromagnetic interference shielding coatings. *Polymer* **55**, 5665–5672 (2014)
9. M.S. Dresselhaus, I.L. Thomas, Overview alternative energy technologies. *Nature* **414**, 332 (2001)
10. Y. Feng, H. Jiang, S. Li, J. Wang, X. Jing, Y. Wang, M. Chen, Metal organic frameworks HKUST-1 for liquid-phase adsorption of uranium. *Colloids Surf. A Physicochem. Eng. Asp.* **431**, 87–92 (2013)
11. E.M. Geniès, M. Lapkowski, J.F. Penneau, Cyclic voltammetry of polyaniline: interpretation of the middle peak. *J. Electroanal. Chem. Interfacial Electrochem.* **249**, 97–107 (1988)
12. F. Ke, L.G. Qiu, Y.P. Yuan, F.M. Peng, X. Jiang, A.J. Xie, Y.H. Shen, J.F. Zhu, J.F., Thiol-functionalization of metal-organic framework by a facile coordination-based postsynthetic strategy and enhanced removal of  $Hg^{2+}$  from water. *J. Hazard. Mater.* **196**, 36–43 (2011)
13. G. Kickelbick, Concepts for the incorporation of inorganic building blocks into organic polymers on a nanoscale. *Prog. Polym. Sci.* **28**, 83–114 (2003)
14. K.J. Kim, Y.J. Li, P.B. Kreider, C.H. Chang, N. Wammenmacher, P.K. Thallapally, H.G. Ahn, High-rate synthesis of Cu-BTC metal-organic frameworks. *Chem. Commun.* **49**, 11518–11520 (2013)
15. M. Kulkarni, B. Kale, S. Apte, S. Naik, U. Mulik, D. Amalnerkar, Synthesis and characterization of polyaniline nanofibres by rapid liquid-liquid interfacial polymerization method. *Chem. Chem. Technol.* **5**, 55–58 (2011)
16. C.F. Leung, Y.Z. Chen, H.Q. Yu, S.M. Yiu, C.C. Ko, T.C. Lau, Electro- and photocatalytic hydrogen generation in acetonitrile and aqueous solutions by a cobalt macrocyclic Schiff-base complex. *Int. Hydrogen Energy* **36**, 11640–11645 (2011)
17. K.S. Lin, A.K. Adhikari, C.K. Ku, C.L. Chiang, H. Kuo, Synthesis and characterization of porous HKUST-2 metal organic frameworks for hydrogen storage. *Int. J. Hydrog. Energy* **37**, 13865–13871 (2012)
18. S. Loera-Serna, M.A. Oliver-Tolentino, M.L. López-Núñez, A. Santana-Cruz, A. Guzmán-Vargas, R. Cabrera-Sierra, H.I. Beltrán, J. Flores, Electrochemical behavior of  $[Cu_3(BTC)_2]$  metal-organic framework: the effect of the method of synthesis. *J. Alloys Compd.* **540**, 113–120 (2012)
19. A. Malinsuskes, Electrocatalysis at conducting polymers. *Synth. Met.* **107**, 75–83 (1999)
20. S. Mandegarzad, J.B. Raoof, S.R. Hosseini, R. Ojani, Cu-Pt bimetallic nanoparticles supported metal organic framework-derived nanoporous carbon as a catalyst for hydrogen evolution reaction. *Electrochim. Acta* **190**, 729–736 (2016)
21. K.M. Molapo, P.M. Ndagili, R.F. Ajayi, G. Mbambisa, S.M. Mailu, N. Njomo, M. Masikini, P. Baker, E.I. Iwuoha, Electronics of conjugated polymers (I): polyaniline. *Int. J. Electrochem. Sci.* **7**, 11859–11875 (2012)
22. A. Mostafaei, F. Nasirpour, Epoxy/polyaniline-ZnO nanorods hybrid nanocomposite coatings: synthesis, characterization and corrosion protection performance of conducting paints. *Prog. Org. Coat.* **77**, 146–159 (2014)
23. A. Mostafaei, A. Zolriasatein, Synthesis and characterization of conducting polyaniline nanocomposites containing ZnO nanorods. *Prog. Nat. Sci.: Mater. Int.* **22**, 273–280 (2012)
24. M.I. Nandasiri, S.R. Jambovane, B.P. McGrail, H.T. Schaefer, S.K. Nune, Adsorption, separation, and catalytic properties of densified metal-organic frameworks. *Coord. Chem. Rev.* **311**, 38–52 (2016)
25. G. Neetika, O. Kumar, S.K. Tomar, Thermal behaviour of chemically synthesized polyanilines/polystyrene sulphonic acid composites. *Int. J. Mater. Chem.* **2**, 79–85 (2012)
26. R.F. Ngece, N. West, P.M. Ndagili, R. Olowu, A. Williams, N. Hendricks, S. Mailu, P. Baker, E. Iwuoha, A silver nanoparticle/poly (8-anilino-1-naphthalene sulphonic acid) bioelectro-



- chemical biosensor system for the analytical determination of ethambutol. *Int. J. Electrochem. Sci.* **6**, 1820–1834 (2011)
27. C. Nila, I. González, Thermodynamics of  $\text{Cu-H}_2\text{SO}_4\text{-Cl}^- \text{-H}_2\text{O}$  and  $\text{Cu-NH}_4\text{Cl-H}_2\text{O}$  based on predominance-existence diagrams and Pourbaix-type diagrams. *Hydrometallurgy* **42**, 63–82 (1996)
  28. R. Ojani, R. Valiollahi, J.B. Raoof, Comparison between graphene supported Pt hollow nanospheres and graphene supported Pt solid nanoparticles for hydrogen evolution reaction. *Energy* **74**, 871 (2014)
  29. E. Portenkirchner, S. Schlager, D. Apaydin, K. Oppelt, M. Himmelsbach, D.A.M. Egbe, H. Neugebauer, G. Knör, T. Yoshida, N.S. Sariciftc, Using the alkynyl-substituted rhenium(I) complex (4,4'-bisphenyl-ethynyl-2,2'-bipyridyl) $\text{Re}(\text{Co})_3\text{Cl}$  as catalyst for  $\text{CO}_2$  reduction—synthesis, characterization, and application. *Electrocatalysis* **6**, 185–197 (2015)
  30. F. Raganati, V. Gagiulo, P. Ammendola, M. Alfe, R. Chirone,  $\text{CO}_2$  capture of HKUST-1 in a sound assisted fluidized bed. *Chem. Eng. J.* **239**, 75–86 (2014)
  31. M.M. Rahman, I.C. Jeon, Studies of electrochemical behavior of swnt-film electrodes. *J. Braz. Chem. Soc.* **18**, 1150–1157 (2007)
  32. F. Safizadeh, E. Ghali, G. Houlachi, Electrocatalysis developments for hydrogen evolution reaction in alkaline solutions – a review. *Int. J. Hydrog. Energy* **40**, 256–274 (2015)
  33. S. Sharma, B.G. Pollet, Support materials for PEMFC and DMFC electrocatalysts—a review. *J. Power Sources* **208**, 96–119 (2012)
  34. E. Song, J.W. Choi, Conducting polyaniline nanowire and its applications in chemiresistive sensing. *Nano* **3**, 498–523 (2013)
  35. M.S. Tamboli, M.V. Kulkarni, R.H. Patil, W.N. Gade, S.C. Navale, B.B. Kale, Nanowires of silver-polyaniline nanocomposite synthesized via in situ polymerization and its novel functionality as an antibacterial agent. *Colloids Surf. B: Biointerfaces* **92**, 35–41 (2012)
  36. J. Tang, X. Zhao, Y. Zuo, P. Ju, Y. Tang, Electrodeposited Pd-Ni-Mo film as a cathode material for hydrogen evolution reaction. *Electrochim. Acta* **174**, 1041–1049 (2015)
  37. S. Tharani, S.C. Vinayagam, Synthesis of novel cerium doped polyaniline multiwalled carbon nanotubes and their optical and electrochemical properties for supercapacitor applications. *Int. J. Adv. Res.* **3**, 810–822 (2015)
  38. F. Wang, H. Guo, Y. Chai, Y. Li, C. Liu, The controlled regulation of morphology and size of HKUST-1 by “coordination modulation method”. *Microporous Mesoporous Mater.* **173**, 181–188 (2013)
  39. X. Wang, X. Lu, L. Wu, J. Chen, 3D metal-organic framework as highly efficient biosensing platform for ultrasensitive and rapid detection of bisphenol A. *Biosens. Bioelectron.* **65**, 295–301 (2015)
  40. B. Xiao, Q. Yuan, Nanoporous metal organic framework materials for hydrogen storage. *Particuology* **7**, 129–140 (2009)
  41. Z. Xie, P. He, L. Du, F. Dong, K. Dai, T. Zhang, Comparison of four nickel-based electrodes for hydrogen evolution reaction. *Electrochim. Acta* **88**, 390–394 (2013)

# Plasma Bonding of Plastic Films and Applications

**Kenichi Uehara, Lakshmi Reddy, Hiroaki Nishikawa,  
Satoru Kaneko, Yoshinobu Nakamura, Kazuhiro Endo,  
Paolo Mele, David Hui, Rieko Sudo, and Tamio Endo**

## 1 Introduction

### 1.1 Utility of PET Films

Biaxially oriented polyester polymer (polyethylene terephthalate: PET) films have strong merits such as high mechanical strength, high electrical insulation, high transparency, high heat tolerance, and low-temperature durability. Its low production cost is a big merit as well. Then they are used for various applications, for

---

K. Uehara

Mie University, 205 Ahban-misutoraru, 656 Hata, Ichishi-cho, Tsu, Mie 515-2515, Japan  
e-mail: [ken.w3m@gmail.com](mailto:ken.w3m@gmail.com)

L. Reddy

Department of Physics, Sri Venkateswara Degree College, Cuddapah 516 003, India  
e-mail: [drsreddy\\_in@yahoo.com](mailto:drsreddy_in@yahoo.com)

H. Nishikawa

Faculty of Biology-Oriented Science and Technology, Kindai University,  
Kinokawa, Wakayama 649-6493, Japan  
e-mail: [nishik32@waka.kindai.ac.jp](mailto:nishik32@waka.kindai.ac.jp)

S. Kaneko

Kanagawa Institute of Industrial Science and Technology, KISTEC, 705-1 Shimo-Imaizumi,  
Ebina, Kanagawa 243-0435, Japan  
e-mail: [satoru@kanagawa-iri.jp](mailto:satoru@kanagawa-iri.jp)

Y. Nakamura

The University of Tokyo, 7 Chome-3-1, Hongo, Bunkyo, Tokyo 113-0033, Japan  
e-mail: [tnakamu@mail.ecc.u-tokyo.ac.jp](mailto:tnakamu@mail.ecc.u-tokyo.ac.jp)

K. Endo

Research Laboratory for Integrated Technological Systems, Kanazawa Institute of  
Technology, 3-1 Yatsukaho, Hakusan, Ishikawa 924-0838, Japan  
e-mail: [kendo@neptune.kanazawa-it.ac.jp](mailto:kendo@neptune.kanazawa-it.ac.jp)

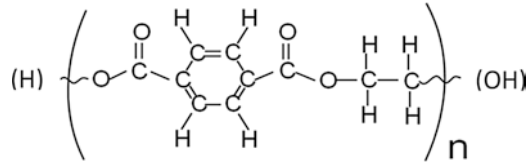


**Fig. 1** Graphic formula of the PET, composed of C-O-H chains and a benzene ring. It is feasible that the left end is terminated by H and the right by OH; these are indicated in two small parentheses. They are not primary constituents of the PET (Original source: ①)

example, magnetic tape bases, liquid crystal display touch panels, food packages [1], and back-sheets in solar cell panels [2, 3].

In most of important utilities, the low-cost PET is mainly used in laminates with various plastic films. A biaxially oriented PET film possesses high performances; it has oriented molecular chains and crystallized structure. A graphic formula of PET molecule is shown in Fig. 1, which is composed of C-O-H chains and a benzene ring. Then the biaxially oriented PET (we call this simply as PET henceforth) cannot be bonded with each other at temperatures lower than the melting point (258 °C). That is, it has no heat-sealing nature. For this reason, the PET films are coated with layers having the heat-sealing nature using glues and organic solvents when they are used for the food packages [1].

## 1.2 Solar Cell Back-Sheets and Issues of Adhesive

A clean energy is urgently necessary in the world. One of essential technologies is solar cell electric generation. It is important to further improve power generation efficiency, weight, and durability for wider applications. A cost performance is also an important factor. Usually laminated PET film is used for the back-sheets of solar cell panel, as shown in Fig. 2. It is composed of a front glass, active cell devices, and

P. Mele

Muroran Institute of Technology, Mizumoto-cho 27-1, Muroran 050-8585, Japan  
e-mail: [pmele@mmm.muroran-it.ac.jp](mailto:pmele@mmm.muroran-it.ac.jp)

D. Hui

Department of Mechanical Engineering, University of New Orleans,  
New Orleans, LA 70148, USA  
e-mail: [dhui@uno.edu](mailto:dhui@uno.edu)

R. Sudo

Sagamihara Surface Treatment Laboratory,  
1880-2 Kamimizo, Chuo-ku Sagamihara, Kanagawa 252-0243, Japan  
e-mail: [r-sudo@sic-sagamihara.jp](mailto:r-sudo@sic-sagamihara.jp)

T. Endo (✉)

Sagamihara Surface Treatment Laboratory, Sagamihara, Kanagawa 252-0243, Japan  
e-mail: [endotamio@yahoo.co.jp](mailto:endotamio@yahoo.co.jp)

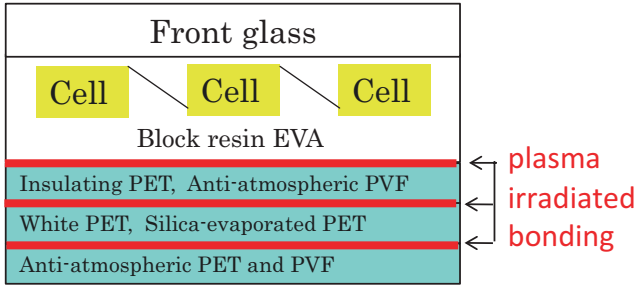


**Fig. 2** Examples of the back-sheet of solar cell panel. It is composed of a front glass, active cell devises, and the back-sheet. The back-sheet is composed of <insulating PET/white PET/anti-atmospheric PET> (complex laminate) or <anti-atmospheric PVF/silica-evaporated PET/anti-atmospheric PVF> (all PET laminate). Our aim is to bond the tri-layer by the plasma technique without using any adhesives

the back-sheet. The cells are embedded in a block resin of ethylene vinyl acetate (EVA). A main function of the back-sheet is to protect the panel from water penetration. Usually a tri-layered back-sheet is composed of <insulating PET/white PET/anti-atmospheric PET>, where the water penetration is protected mainly by the anti-atmospheric PET. This is called as all PET composite back-sheet.

Alternatively DeBergalis [4] proposed a different type of tri-layer back-sheet using fluoropolymer: polyvinyl fluoride (PVF) as PVF/PET/PVF. This is also shown in Fig. 2 by <anti-atmospheric PVF/silica-evaporated PET/anti-atmospheric PVF>. It is expected by this lamination that the water permeation is decreased, the electrical isolation is more increased, and the cost is minimized. Usually these are laminated using adhesives and inevitably organic solvents. If the organic solvents cause environmental and health issues, then we should withdraw the organic solvents during the lamination coating process. Further in the most of cases, the adhesives cause performance deteriorations of devices in a long-term use.

### 1.3 Short Lifetime of Irradiated Surface

To solve such problems caused by the adhesives, we developed a technique of plasma irradiation-induced direct bonding of plastic films without using any adhesives [5]. Normally the plasma irradiation effects on the plastic surfaces have very short lifetime, say several days [6]. A reason for it was reported by Occhiello et al. [7] that plasma-generated functional groups turn back inside at the surface. We, however, report here that the PET films, kept for 6 years in the atmosphere after the plasma irradiation, can still be bonded very tightly in our works. It is quite strange that the activated surface by the plasma can be kept so long, because generally the surface must be easily inactivated due to reactions with the atmosphere (O<sub>2</sub>, N<sub>2</sub>, H<sub>2</sub>O, Na, Cl, S, etc.) even if the generated functional groups do not turn back inside. New concepts should be proposed for such ultralong lifetime of the plasma irradiation effect.

## 1.4 Inorganic Films on PET

The plasma-induced activation of the plastic film surface is also an important technique when we deposit inorganic thin films such as ZnO and TiO<sub>2</sub> on the plastic films in flexible devices. Banerjee et al. [8] have reported that crystalline ZnO thin film is successfully deposited on the PET film at 90 °C utilizing DC-sputtering plasma. Hao et al. [9] reported that electrophoresis chip needs gold deposition on the plastic films, and Audronis et al. [10] reported that Cu deposition is selectively enhanced on the plasma-irradiated surface of PET.

## 1.5 Some Reports on Plasma Effects

It is valuable to mention in this article on some recent reports by several authors regarding the plasma irradiations to the plastic surfaces. Effects of plasma irradiations and their chemical analyses on the plastic surfaces were reported by Cioffi et al. [11] and others [9–14]. Cioffi mentioned that tensile strength of PET fiber-reinforced composites can be improved by the plasma irradiation. Setsuhara et al. [12, 14] mentioned on etching effects of the plasma, and Yang et al. [13] mentioned on increase in surface energy of the irradiated surfaces. Effects on biological responses of adhesion variations on the plasma-irradiated surfaces were reported. Katsikogianni et al. [15] mentioned that bacteria adhesion is reduced by the plasma irradiation due to increase in surface energy, while Vesel et al. [16] mentioned that the adhesion of polysaccharide fucoidan on the plasma-irradiated PET surface can be increased. Pandiyaraj et al. [17, 18] reported that scotch tape adhesive strength can be increased on the plasma-irradiated PET surface which is related to surface roughness, and the surface energy of the irradiated PET is increased due to creation of polar groups. They mentioned a very important phenomenon that crystallinity of the PET is improved by the plasma irradiation. The plasma-induced bonding effects were reported by Dai et al. [19] for between the PET and poly styrene-*co*-maleic anhydride (PSMA) and by Hao et al. [9] for between the PET and PET. Dai et al. mentioned that the plasma-irradiated PET and PSMA can be bonded at low press temperatures of 120–160 °C and this is induced by chemical reactions. However, when they tried to peel off, the laminated sample showed adherent failure implying not so strong adhesion. The plasma-induced chemical reactions for the chemical bonding at such low temperatures were reported also by Scott et al. [20] and Marechal et al. [21] The most closely related research to our work was done by Hao et al. [9] reporting that amorphous PET can be bonded at very low press temperatures of 65–75 °C just after the plasma irradiation. The amorphous PET has softening temperatures of 60–70 °C; then this softening is one of the causes for such the very low bonding temperatures. They also mentioned a quite important point that some condensation reactions are possible to occur between the irradiated interfaces. Friedlich [22] published a book recently summarizing the plasma effects on plastic

surfaces. He suggested that plasma-induced functional groups are -OH, -COOH, -C=O, and O-bridge at the irradiated surface. The present authors [23–31] have reported the related papers concerning the PET-PET and PET-PVF direct bondings by the plasma irradiations. This article introduces these reports using reproduced figures and tables in them (see figure and table captions and acknowledgment in the last part for permissions).

## ***1.6 Scheme of This Work***

We tried to directly bond the PET films without using such coatings and adhesive glues and found that the exposures of oxygen plasma were effective. After the exposure, the PET films can be directly bonded with each other very tightly, i.e., showing a kind of heat-sealing nature. They can be bonded with, for instance, glass plate also at low temperatures as 100 °C.

In this article, we introduce our experimental results on various chemical analyses on the exposed surfaces of PET films, and we discuss mechanisms for the direct tight bonding. Chemical bonding due to condensation reactions and hydrogen bonding concerning the plasma irradiation-induced functional groups such as -COOH and -OH are the most possible origins.

We tried to do some application developments for insulator sheets in motors in electric vehicles (EV).

## **2 Experimental Procedures**

### ***2.1 Samples and Plasma Irradiations***

It has been known so far that unique chemical reactions occur on the surface of polymer resins when they are irradiated by plasma. Complicated collisions due to high-energy particles involved in the plasma induce such reactions. This is a reason why the reactions are unique and they cannot take place in usual soft chemical processes. Thus, we can obtain higher hydrophilic and adhesive properties of the irradiated surface, called as surface modifications by the plasma [32, 33]. However, the effects are usually kept only in short periods, say 1 week at most [34]. We tried to obtain the plasma equipment system which assures persistent effects of the plasma modifications.

In this experiment, we used the PET film samples (Lumirror, Toray) which were produced by two-axes stretch method (biaxially oriented PET). The sample size is 100 mm width and 200 mm length. The film thickness is 100  $\mu\text{m}$  usually with surface roughness of around 0.5 nm and 3.5  $\mu\text{m}$  for Fourier transform infrared (FTIR) measurement. The film with 1  $\mu\text{m}$  thickness was specially used when we prepared

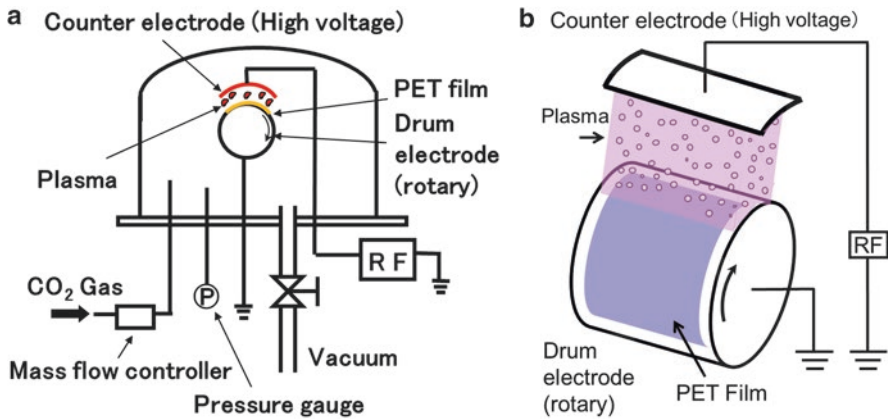


**Fig. 3** (a) The plasma irradiation apparatus in a vacuum chamber. (b) The sample film is attached on the rotating drum electrode. The plasma is generated between the drum and counter electrodes (Original sources: ① and ②)

the bonded sample for the FTIR transmission measurement. The film samples were attached on a grounded drum electrode (150 mm diameter, 150 mm width) in a bell-jar-type vacuum chamber as shown in Fig. 3a [5]. The chamber was evacuated down to a range of 5–10 Pa; then  $O_2$  gas was introduced with 20 cc/min to the chamber oxygen pressures of 15–40 Pa. Oxygen plasma was generated as shown in Fig. 3b between the drum electrode and counter electrode with application of ac voltage at powers of 15 W (500 V, 30 mA)–75 W, and the drum electrode was rotated at 0.5 m/min. The moving sample was irradiated by the plasma for around 10 s at energy of  $E = 200\text{--}1000 \text{ W min/m}^2$ . The irradiated sample was taken out from the chamber to the normal atmosphere after the plasma irradiation.

## 2.2 Bonding Processes and Strength Evaluations

One part of the irradiated films were immediately pressed with their irradiated surfaces faced at various press temperatures  $T_p$ . Some of them were bonded tightly, but others were loosely bonded or not bonded depending on  $T_p$ . We employed two methods of the heat-press as shown in Fig. 4a, b. One is (a) heated roll-press at a pressure of 3 kg/cm with a rolling rate of 0.45 m/min at  $T_p$  from 70 to 160 °C, and the other is (b) heated plate-press (Kitagawa Seiki, VH-1.5) at a pressure of 10 kg/cm<sup>2</sup> at a fixed  $T_p = 140$  °C for 10 min. The plate-press method was employed to get a wide sample for the FTIR transmission measurement. The other part of the irradiated films were kept in the normal atmosphere for 6 years, after that they were heat-pressed by the same way mentioned above.

Bonding strength of the heat-pressed films was measured as peel strength  $S_p$  using T-type 180°-peel test (Touyouseiki Seisaku, E-L) at a pulling rate of 50 mm/

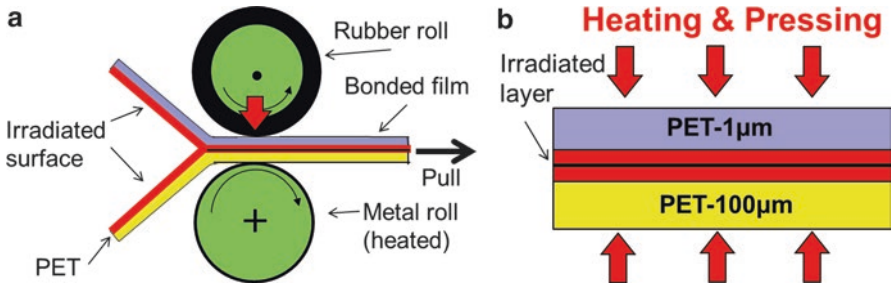
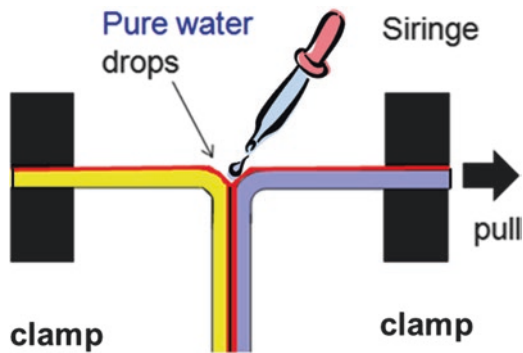


**Fig. 4** The heat-press apparatuses, (a) heated roll-press and (b) heated plate-press. Larger size of the sample film is necessary for the FTIR measurement; then (b) is used (Original source: ①)

**Fig. 5** The 180°(T)-peel test. The dry-peel without water drops and the wet-peel with water drops (Original source: ①)



min as shown in Fig. 5 under JIS-C-2151 standard. It gives the 180°-peel strength  $Sp$ . Two processes were employed, one is called dry-peel test without water drops and the other is called wet-peel test with water drops at the bonded interface as shown in Fig. 5.

### 2.3 Sample Characterizations

The surface morphologies were observed on the irradiated films and non-irradiated films using atomic force microscopy (AFM) (VecoDigital Instrument, Nano Scope III). Surface roughness  $Ra$  (mean value) was evaluated by the AFM images.

The sample surface was chemically analyzed by X-ray photoelectron spectroscopy (XPS) (VG Scientific, ESCALB220iXL). Chemical bonding states and compositions were characterized on the sample surfaces. The samples were measured by gas chemical modification method (GCMM) to get information on functional groups [35]. Trifluoroacetic anhydride (TFAA) was used to detect hydroxyl group (-OH). Poly vinyl alcohol was used as standard sample for the TFAA reaction. Trifluoroethanol with di-tert-butylcarbodiimide and pyridine were used to detect carboxyl group (-COOH). Polyacrylic acid was used as standard sample for



2,2,2-trifluoroethanol reaction. To obtain mean molecular weight, gel permeation chromatography (GPC) measurement was performed on the samples using a type-515 water.

The irradiated and press-bonded samples with the roll-press (a) were characterized by the peel test as mentioned above, and a pure water contact angle  $\theta$  was measured on the corresponding irradiated film surfaces. The samples with the plate-press (b) were characterized by the FTIR. One special sample (irradiated and press bonded) was prepared using the PET films with 100  $\mu\text{m}$  and 1  $\mu\text{m}$  thicknesses for the FTIR transmission measurement. The other part of the irradiated samples was kept in the atmosphere for 5 years; then the angle  $\theta$  was measured on these sample surfaces.

The angle  $\theta$  was measured on the non-irradiated samples in the atmosphere at 25  $^{\circ}\text{C}$  under 55 % humidity and on the irradiated surface of samples just after the irradiation. The irradiated samples were kept in the atmosphere for 5 years, and the angle  $\theta$  was measured. These samples kept in the atmosphere were heated at various elevating temperatures  $T_h$  for 10 min in the atmosphere; then the angle  $\theta$  was measured at room temperature on these heated samples.

Chemical bonding states of the samples were characterized by the FTIR with two methods as shown in Figs. 6a, b. One was attenuation total reflection (ATR) method on the non-irradiated and irradiated samples; the infrared (IR) incident beam was introduced from the irradiated surface for the irradiated sample as shown in (a). The other was transmission method on the non-irradiated (100  $\mu\text{m}$  thickness), irradiated (100  $\mu\text{m}$ ), and bonded samples (total 101  $\mu\text{m}$ ). The IR incident beam was introduced from the irradiated surface for the irradiated sample and from the 1- $\mu\text{m}$  side for the bonded sample with 1- $\mu\text{m}$ /100- $\mu\text{m}$  layer structure as shown in (b).

In order to investigate chemical nature (cross-linking) of the plasma-irradiated surface layer, we conducted solubility test of the irradiated sample. The non-irradiated and irradiated sample films with a size of 40  $\times$  40 mm were cut into small pieces. They were put in o-chlorophenol (OCP) solution heated at 90  $^{\circ}\text{C}$  in a water bath for 30 min. Then remnant in the solution was observed by eyes.

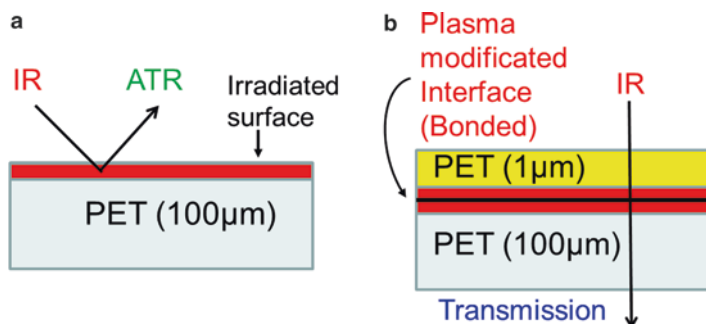


**Fig. 6** Schematic drawings for the FTIR measurements. (a) The ATR type and (b) the transmission type. In case of the irradiated sample, the IR beam is introduced from the irradiated surface in (a) (Original source: ①)

### 2.4 Soaking of Irradiated Films in Liquids

In order to investigate stability of the surface of plasma-irradiated films, the films were soaked in liquids. The one-side plasma-irradiated films were cut into 30 × 150 mm<sup>2</sup> and then soaked in various liquid reagents (100 ml) at room temperature (24 °C) for 24 h in a glass tube (200 mm × 27 mmØ). We employed several types of reagents, namely, pure water, acids, alkalis, organic solvents, and ionic solutions. The concentration of reagents was 0.5 N. After the soaking, the films were rinsed in pure water three times and then dried at room temperature for 24 h in the normal atmosphere. Just after these processes, the water contact angle was measured on their irradiated surfaces; in parallel the films were heat-pressed to check whether they were bonded or not.

## 3 Experimental Results

### 3.1 Press Bonding Temperature Estimated by Peel Test

The result of peel strength  $S_p$  (equivalent to the bonding strength) vs heat-press temperature  $T_p$  by the dry-peel test is shown in Fig. 7 for the laminated film which was roll-pressed immediately after the plasma irradiation. The films are not bonded below  $T_p = 90$  °C, but the films are strongly bonded above 120 °C as shown in a photograph in Fig. 8. When the sample was pulled with peel strength beyond 7 N/cm,

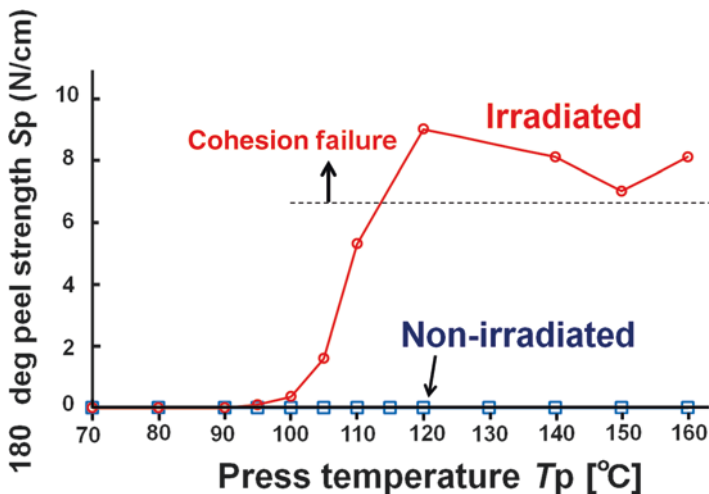
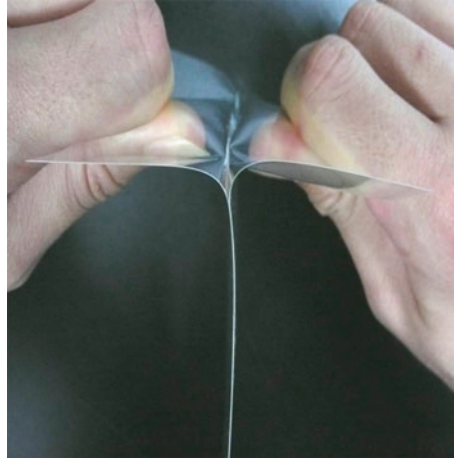


**Fig. 7** The 180°(T)-peel strength (bonding strength)  $S_p$  vs press temperature  $T_p$  for the samples pressed just after the plasma irradiation. The sample shows cohesion failure beyond the pulling strength of 7 N/cm (Original source: ①)

**Fig. 8** A photograph showing hand peeling before the cohesion failure occurs (Original source: ③)



it showed cohesion failure. This cohesion failure indicates that the two films are bonded more tightly than the material chemical bonding strength of the original PET film. The non-irradiated films are not bonded even at the highest  $T_p$  of 160 °C. It indicates that the films cannot be bonded by the heating only. This is a well-known fact, i.e., the PET has no heat-sealing nature below its melting point (258 °C). These two results imply that the plasma-irradiated surface is enormously activated to make bonding reaction under the low pressure at low temperatures below the melting point [13, 15, 17, 18].

### 3.2 *Surface Morphology by AFM*

The AFM surface morphologies are shown in Fig. 9 for (a) the non-irradiated film and (b) the irradiated film. The mean surface roughness  $R_a$  is 0.46 nm and 0.53 nm for the non-irradiated and irradiated films, respectively. This increase by the plasma irradiation is negligibly small, and we have additional results which show that the roughness is rather reduced after the irradiation. Thus, we can rule out an anchor effect for the origins of tight bonding by the plasma irradiation. Looking the surface morphologies carefully, we can recognize that micro-spike-like ragged fluctuation observed on the non-irradiated film disappeared after the irradiation. It implies that weak boundary layer (WBL) adhered on the non-irradiated film surface is removed by the irradiation [36]. This may indicate further that the irradiated surface is chemically activated because active dangling bonds are created due to the WBL removal.

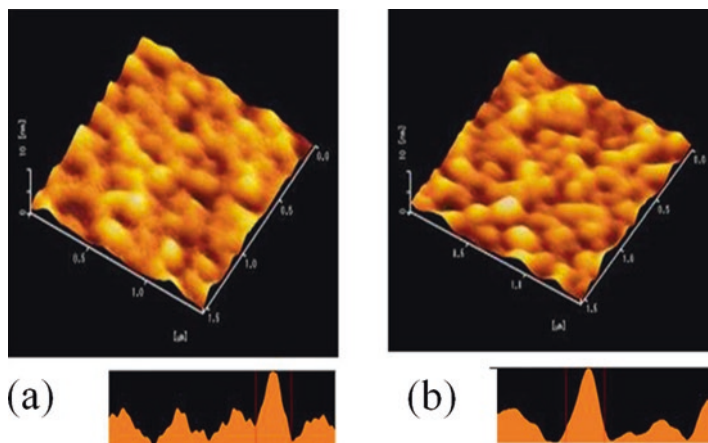


**Fig. 9** The AFM surface images and the sectional profiles for (a) the non-irradiated ( $R_a = 0.46$  nm) and (b) the irradiated ( $R_a = 0.53$  nm) PET films ( $1.5 \times 1.5$   $\mu\text{m}$  area) (Original source: ④)

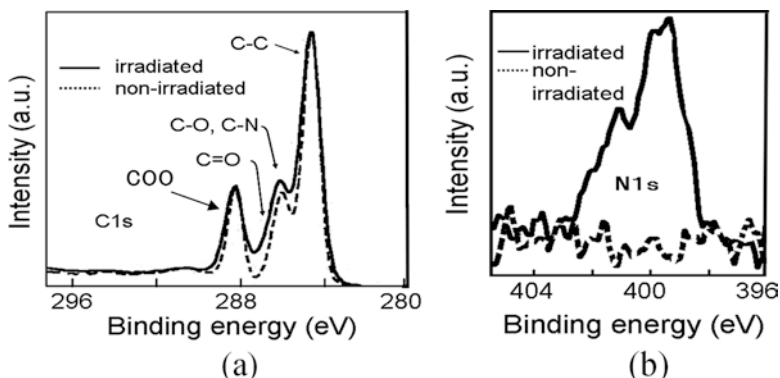


**Fig. 10** The XPS spectra for the non-irradiated and irradiated PET film surfaces. (a) The C1s-related peaks and (b) the N1s-related peak (Original source: ④)

### 3.3 Surface Chemical States by XPS

The results of XPS on C1s-related peaks normalized by C-C bond intensity are shown in Fig. 10a, and N1s-related peak in Fig. 10b, for the non-irradiated and irradiated film surfaces as a function of binding energy. It is known that the intensity corresponding to C=O (carbonyl group) bond indicated in Fig. 10a by an arrow around 287 eV is increased noticeably, and an apparent increase is recognized for C-O and C-N bonds. It should be noted that we cannot actually observe the peak corresponding to the C=O because it is located between the neighboring large peaks. We compare the intensities of C1s-related peaks for typical functional groups; their numerical values are shown in Table 1. Obviously the C=O bond intensity is

**Table 1** The XPS peak intensity ratios of the C1s-related peaks for the various chemical states (Original source: ④)

	$\pi-\pi^*$	COO	C=C	C-O C-N	CHx, C-C C=C
Non-irradiated (%)	5	18	–	22	55
Irradiated (%)	4	17	3	22	54

**Table 2** The surface compositions (atom%) and atomic ratios normalized by C in parentheses obtained by the XPS (Original source: ④)

	C	O	N
Non-irradiated (%)	72.0	28.0	0
	(1.0)	(0.390)	(0)
Irradiated (%)	68.7	30.6	0.4
	(1.0)	(0.445)	(0.005)

increased; then we can conclude at least that the C=O is created by the irradiation. Although actually the C-O is increased, the numerical value for the C-O and C-N in Table 1 is not changed due to subtraction of the C=O peak tail from the C-O and C-N peak (Fig. 10a).

We calculated compositions for the surfaces of films using the XPS results; the numerical values are shown in Table 2. An atomic ratio of oxygen is 0.390 for the non-irradiated film, quite close to the molecular nominal (stoichiometry) value of 0.4. This indicates the result is precise and reliable. After the irradiation, the oxygen composition is much increased to 0.445 from the nominal value. Then we can expect that the oxygen-related functional groups other than the C=O must be created at the surface by the irradiation. Those must be the carboxyl group (COOH) and hydroxyl group (OH). The increase in C-O may be caused by creation of C-OH. In Table 1, the numerical value for COO is relatively decreased, because it is affected by the relative increase in the C=O. Actually COO (properly COOH) should be increased. This is known from a broadening of the 289 eV-peak. This peak comes from the COO bond connecting to the benzene ring in the original molecular structure (see Fig. 1) in the non-irradiated PET. After the irradiation, the higher-energy broadening comes from the additionally created COOH group at the surface; the peak energy of them is little higher than that of the original COO existing inside the molecule.

Figure 10b clearly shows an appearance of N for the irradiated film. It is curious that nitrogen appeared after the irradiation. This is probably because the irradiated surface is chemically active and then it is nitrogenized with air at room temperature after the irradiated sample was taken out from the chamber to the atmosphere. A nitrogen plasma induced by residual air-gas in the chamber is another reason for the N-bonding on the surface.

### 3.4 Functional Groups by GCMM and Molecular Weight by GPC

We show the results of GCMM in Table 3 for amounts of -COOH and -OH. These functional groups (especially COOH) are strikingly increased after the irradiation. Then the above discussions that the COOH and OH are increased (created) can be supported. Table 4 shows the results of GPC, indicating that a mean molecular weight is decreased after the irradiation. This means that original long molecular chains are broken into shorter chains. The shorter chains must be terminated by the functional groups such as the C=O, -COOH, and -OH. One part is bonding to the chains and benzene ring in the regular molecules; the other part is bonding to the additionally created terminals. Then we have two possible states of the COOH and OH bondings to the irradiated PET films.

### 3.5 Bonding After 6 Years and Dry-Peel and Wet-Peel Tests

The irradiated PET films were kept in the normal atmosphere for 6 years and then roll-pressed. The result of  $S_p$  vs  $T_p$  by the dry-peel test is shown in Fig. 11 for the laminated film which was heat-pressed 6 years after the plasma irradiation. The result is almost the same with that shown in Fig. 7 for the sample bonded immediately after the plasma irradiation. The sample showed the cohesion failure beyond the peel strength of 6 N/cm above  $T_p = 110$  °C. It implies that the activated surface by the plasma can be kept in the atmosphere as long as 6 years and it is incredible.

The wet-peel test was done on the samples also bonded 6 years after the irradiation. The result is shown in Fig. 11. The peel strength is considerably weaker for the

**Table 3** The amounts of -COOH and -OH normalized by C obtained by the GCMM. The COOH is increased much compared with the OH after the irradiation. The COOH and OH exist in the non-irradiated film as the terminators of polymer molecule (Original source: ③)

	-OH/ C	-COOH/C
Non-irradiated	0.003	0.001
Irradiated	0.008	0.016

**Table 4** The mean molecular weights obtained by the GPC (Original source: ④)

	Mean molecular weight
Non-irradiated	32100
Irradiated	29700

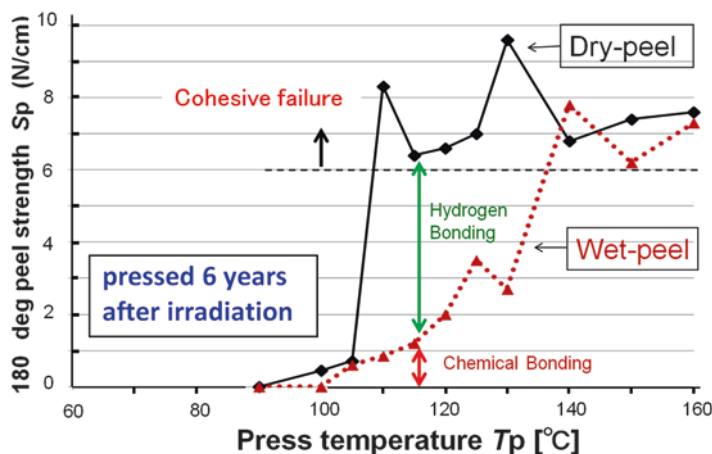


**Fig. 11** The 180°(T)-peel strength (bonding strength)  $S_p$  vs press temperature  $T_p$  for the samples pressed 6 years after the plasma irradiation. The results from normal dry-peel and particular wet-peel tests are shown. The samples show cohesion failure beyond the pulling strength of 6 N/cm (Original source: ①)

wet-peel test than for the dry-peel test in  $T_p$  range of 100–140 °C; however, it is the same for the both for  $T_p > 140$  °C. These two results indicate that there are two types of bonding elements, one element is not stable for (broken by) the water but the other element is very stable for (not broken by) the water.

### 3.6 Bonding Strength and Contact Angle (Surface Activity)

To investigate a reason why the activated surface can be kept so long, we measured the water contact angle  $\theta$  for the irradiated samples kept in the atmosphere. The result is shown in Fig. 12. The angle  $\theta$  before the irradiation shows 60°, and just after the irradiation, it shows 18° at 25 °C. This clearly indicates that the non-irradiated surface (larger  $\theta$ ) is inactive (low surface energy) but the irradiated surface (smaller  $\theta$ ) is excessively active (high surface energy). This irradiated sample was kept in the atmosphere for 5 years and then the angle  $\theta$  was measured, showing 38°. This indicates that the activated surface was gradually inactivated in 5 years, but it was not restored to the original state, that is, “half-activated.” This sample was heated in the atmosphere at various elevating  $T_h$  from 50 to 240 °C for 10 min and then the angle  $\theta$  was measured at room temperature. The angle  $\theta$  increases with increasing  $T_h$  up to 48° at 240 °C. It clearly indicates that the half-activated surface becomes more inactive probably due to thermal annihilation of the plasma-created functional groups. However, it is important that its surface is slightly more active compared with that of the non-irradiated sample ( $\theta = 60^\circ$ ). There observed a step-like increase in angle  $\theta$  in  $120 < T_h < 150$  °C. This might be related to crystallization of non-crystallize part of the original PET.

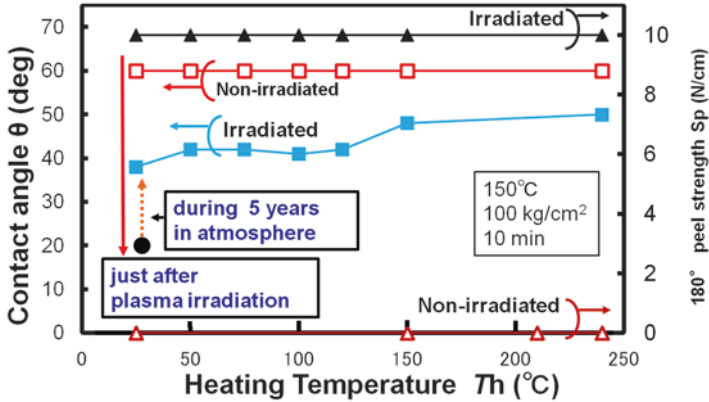


**Fig. 12** The pure water contact angle  $\theta$  vs heating temperature  $T_h$  and the  $180^\circ(T)$ -peel strength  $S_p$  vs  $T_h$  for the non-irradiated and irradiated samples. The contact angle was measured at room temperature after the heating in the atmosphere (Original source: ①)

We tried the heat-press and peel test on these samples heated at the various  $T_h$ . The result of  $S_p$  vs  $T_h$  is shown in Fig. 12. It must be surprise that all the films can be bonded tightly even if the sample is heated at the highest  $T_h$  of 240 °C. This means the surface activation with  $\theta = 48^\circ$  is enough for the bonding. But a possibility cannot be denied that state of activation of the heated sample is different from that of the non-heated sample. However the most useful result is that the films kept in the atmosphere for 5 years after the irradiation can be bonded tightly even the surface activation of this sample ( $\theta = 38^\circ$ ) is restored considerably from that of the sample just after the irradiation ( $\theta = 18^\circ$ ). This result confirms the results of Fig. 11, that is, the surface activation is considerably restored during the long atmosphere exposure but is still sufficient for the tight bonding.

### 3.7 COOH by FTIR (ATR)

In order to clarify origins for the bonding, the water-induced weakening of bonding, and the ultralong lifetime of plasma irradiation effect at the surface, we investigated chemical bonding states of the PET films by the FTIR. The FTIR transmission spectrum for the non-irradiated PET film with 3.5  $\mu\text{m}$  thickness is shown in Fig. 13. Here we assign only two peaks: C=O stretching mode at  $1716\text{ cm}^{-1}$  and OH stretching mode at  $3430\text{ cm}^{-1}$ ; those are analyzed in this work. The C=O bond is involved in the original PET molecule as shown in Fig. 1, but the OH bond is not involved in the primary molecular structure. Then the OH bond absorption must be resulted from the termination members of polymer, the H can be added at the left-, and the OH can be added at the right-hand side of the molecule as shown in smaller parentheses in Fig. 1. This is a reason why the OH absorption is very small compared with high absorption peaks coming from the main polymer molecular bond members.



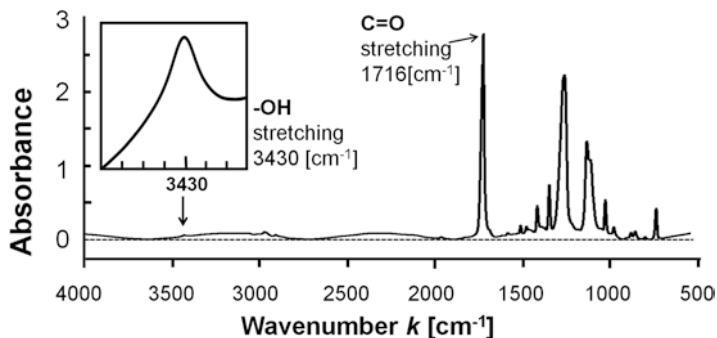
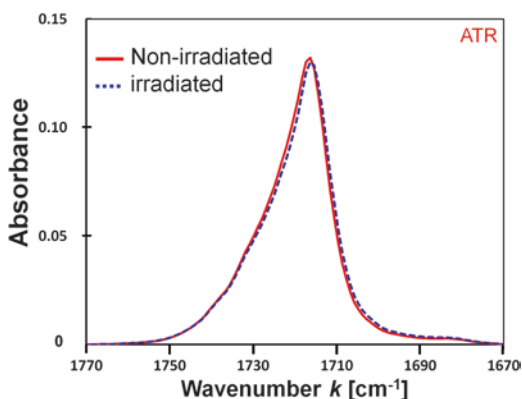


**Fig. 13** The FTIR transmission spectrum for the non-irradiated PET film with 3.5  $\mu\text{m}$  thickness. Many peaks are observed, but we pick up only related two peaks for the C=O and OH bonds (Original source: ①)

**Fig. 14** The FTIR-ATR spectra near 1716  $\text{cm}^{-1}$  for the non-irradiated and irradiated samples. The two peaks are normalized by stable strong peak arising from the benzene ring (not shown). The lower  $k$ -shift is observed for the peak of the irradiated sample (Original source: ①)



The FTIR-ATR is very sensitive to the surface (1–3  $\mu\text{m}$ ) of sample due to reflection mode; then we employed it to investigate the plasma-irradiated surface. The FTIR-ATR spectra around 1716  $\text{cm}^{-1}$  for the non-irradiated and irradiated samples (100  $\mu\text{m}$ ) are shown in Fig. 14. The peak heights are normalized using a constant peak of benzene ring. After the irradiation, the absorption band is shifted to the lower wavenumber  $k$  and then the absorption is increased in the lower  $k$  region. Its difference is very small and then we took the differential spectrum (irradiated-non-irradiated) around 1716  $\text{cm}^{-1}$ . The result is shown in Fig. 15. It shows the minimum at 1719  $\text{cm}^{-1}$  and the maximum at 1711  $\text{cm}^{-1}$ . The minimum corresponds to the C=O bond inside the original PET molecule, indicating this bond is broken by the irradiation and then its absorption is decreased. The maximum must correspond to the C=O bond in the carboxyl COOH group (O=C-O-H) formed at the PET surface by the irradiation. The lower shift of  $k$ , corresponding to lower frequency shift of vibration, may be induced by surface COOH dimer coupling and hydrogen bonding.

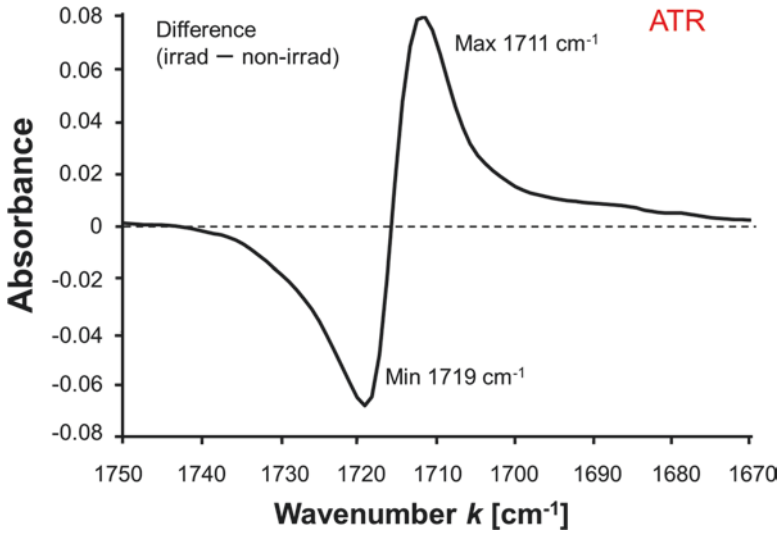


**Fig. 15** The FTIR-ATR differential spectrum (irradiated-non-irradiated) corresponding to Fig. 14 (Original source: ①)

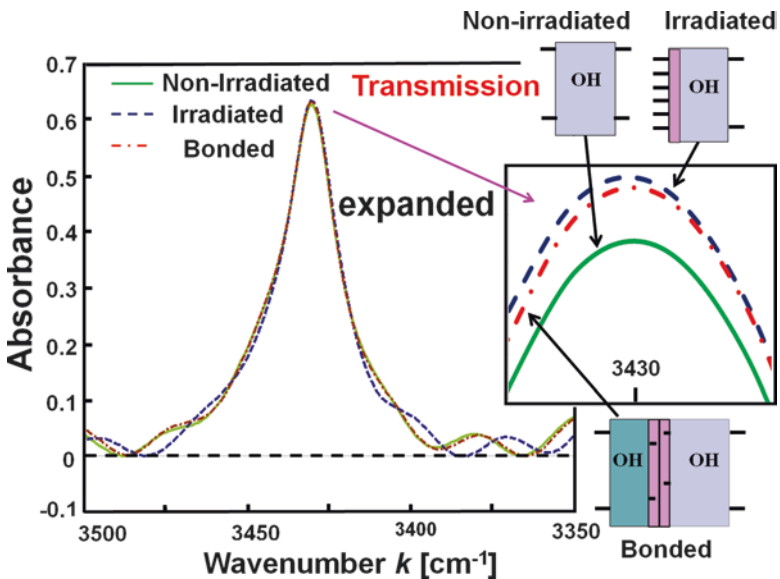


**Fig. 16** The FTIR transmission spectra near  $3430\text{ cm}^{-1}$  for the non-irradiated, irradiated, and bonded samples. The sample pictures are shown in the figure, where *bars* indicate the OH bond. Before the irradiation, the OH bonds already exist in the non-irradiated film as the terminators. After the irradiation, the OH bonds increase on the irradiated surface. After the bonding, the OH bonds decrease at the interface due to the chemical reactions. Inset shows expansion of the peaks attached with the sample pictures (Original source: ①)

### 3.8 OH by FTIR

The expanded FTIR transmission spectra around  $3430\text{ cm}^{-1}$  related to the OH bond are shown in Fig. 16 for the three samples of non-irradiated ( $100\text{ }\mu\text{m}$  thickness), irradiated ( $100\text{ }\mu\text{m}$ ), and bonded PET ( $1\text{ }\mu\text{m}/100\text{ }\mu\text{m}$ ). Further expansion around the peaks is inserted, from which we can recognize that the peak for the irradiated sample is increased from that for the non-irradiated sample and the peak for the bonded sample is slightly decreased from that for the irradiated sample but still much larger than that for the non-irradiated sample. This result indicates as follows. The non-irradiated PET has the OH bond due to termination of PET polymer as mentioned above, and it is schematically drawn by bars in the insert. By the irradiation, the OH group is created at the surface as shown by many bars in the inset; then the absorption is increased. After the heat-press bonding, a part of the created OH remain causing the increased absorption, but the other part of the created OH are consumed probably due to some chemical reactions under the heat-press because the absorption for the bonded sample (having two irradiated surfaces) is not two times larger than that for the irradiated sample (having one irradiated surface).

### 3.9 Cross-Linking Layer by OCP

Here we mention on results of the OCP solution test. The non-irradiated PET film was dissolved completely in the OCP solution. Though, a remnant was observed for the irradiated film. It indicates the plasma-irradiated surface is modified from the pure PET polymer, which is not dissolved. The modified part must be a cross-linking layer formed on the irradiated surface.

## 4 Discussions on the Bonding Mechanism and Long Lifetime of Activated Surface

We discuss the origins of plasma-induced low-temperature bonding of the PET films, the water-induced weakening of bonding, and the ultralong lifetime of plasma-irradiated active surface.

### 4.1 Dehydrated Condensation Reaction (DCR)

It is known from the results of XPS and FTIR that the COOH group and OH group are created at the PET surface by the oxygen plasma irradiation. This is quantitatively confirmed by the GCMM, the rate of creation is much larger for the COOH (16 times) than OH (2.7). It can be understood that the OH is more involved than the COOH in the

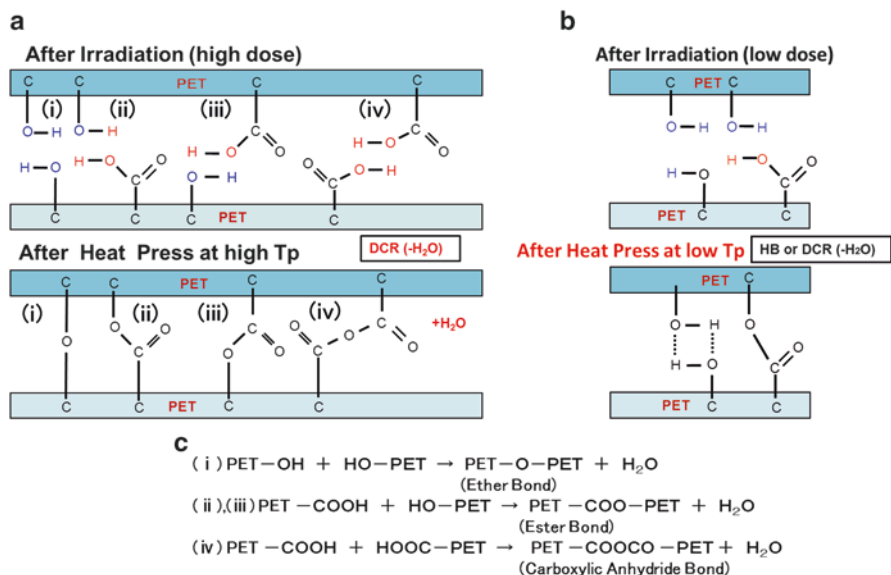


**Fig. 17** The models for the bonding mechanism. (a) High-dose irradiation and high-temperature press. The high densities of COOH and OH groups are created on the surface (*top*), leading to the high densities of bonds (*bottom*). The solid lines indicate the chemical bonds. (b) Low-dose irradiation and low-temperature press. It should be noted that, in this experiment, actually the sample was irradiated with high dose but the low-temperature presses were conducted. The dotted lines indicate the hydrogen bonds. (c) The presumed dehydrated condensation reactions between the two irradiated PET films under the heat-press, corresponding to (a). These reactions produce water H<sub>2</sub>O (Original source: [1])

non-irradiated original PET as the polymer terminator. Figure 17 shows schematic pictures of the two irradiated PET surfaces before the heat-press (top) and after the heat-press (bottom). Figure 17a shows the PET surfaces with high dose of irradiation where high densities of the COOH and OH are formed, while (b) shows the surfaces with low dose where low densities of the COOH and OH are formed. Under the moderate heat-press, these active functional groups might induce a dehydrated condensation reaction (DCR) at the interface as schematically shown in Fig. 17a,b. It does not need excessively high pressure and temperature to get the DCR because (1) the COOH and OH are quite active and (2) the densities of them are quite high. Probably the high densities of surface COOH and OH are more important for the strong bonding.

Dai et al. [19] and Hao et al. [9] also suggested that the chemical reactions can take place at such low temperatures under the press [20, 21]. Hao et al. [9] especially indicated a possibility of the condensation reaction. As a result, after the heat-press, they form strong chemical bonds such as PET-O-PET (ether bond), PET-COO-PET (ester bond), and PET-COOCO-PET (carboxylic anhydride bond) as shown in the bottom of (a). Their DCR formulae are shown in Fig. 17c. This must be the origin for the strongest bonding between the two irradiated PET for T<sub>p</sub>>120 °C in Fig. 7 and for T<sub>p</sub>>140 °C in the dry-peel test in Fig. 11 because substantial thermal energy for the DCR can be supplied in these high-temperature ranges.

While the weaker bondings (smaller peel strength  $S_p$ ) observed in  $90 < T_p < 120$  °C in Fig. 7, and in  $90 < T_p < 110$  °C for the dry-peel test in Fig. 11, are caused by the insufficient DCR due to shortage of thermal energy for the reaction, the films are bonded by small number (low density) of the DCR bondings as simply shown in Fig. 17b. In such the insufficient conditions, the hydrogen bonding is more possible as indicated by dotted bars in the bottom picture. This hydrogen bonding is discussed in more detail later. This figure also shows a possible situation for the low dose. When the irradiation dose is not high enough, the COOH and OH are created, but their densities are low as shown in the top picture. Then the densities of DCR bondings are low as shown in the bottom picture, resulting in the weaker film bonding.

The amorphous PET can be bonded at around 65–75 °C as observed by Hao et al. [9] Our result of bonding temperature of 100 °C is higher, because our biaxially oriented PET sample is crystalline. More exact reason must be clarified hereafter.

## 4.2 Hydrogen Bonding

On the other hand, the weaker bonding in  $100 < T_p < 130$  °C for the wet-peel test in Fig. 11 suggests that there are two bonding elements, one must be the chemical bonding (DCR bonding) and the other must be hydrogen bonding between the created COOH and OH groups, as mentioned above. Not all of the created COOH and OH can take DCR even under the high heat-press because of insubstantial thermal energy and time, resulting in the hydrogen bonding (mixed with the chemical bonding). During the wet-peel test, the water can penetrate into the interface easily as shown in the top of Fig. 18 because the interface is well open to the water (see Fig. 5). Then, the water breaks this direct hydrogen bonding connecting the PET films directly. As the result, the water molecules ( $H_2O$ ) form weaker secondary hydrogen bonding mediated by  $H_2O$  molecules as schematically shown in the bottom of Fig. 18. Then during the wet-peel test, the two PET films are loosely bonded only by the chemical bonding formed by the part of created COOH and OH groups. Thus, we can divide the bonding elements into the chemical bonding and hydrogen bonding for the insufficient temperatures of  $100 < T_p < 130$  °C; these are indicated by two vertical arrows in Fig. 11. In the low  $T_p$  region, the hydrogen bonding is major, but with increasing  $T_p$ , the DCR chemical bonding becomes major gradually; then finally the films are bonded only by the high density of chemical bondings at the highest region of  $T_p > 140$  °C. Thus, the bonding strength estimated by the wet-peel test is the same with that by the dry-peel test in Fig. 11. Incidentally we tried to use poly-phenylene sulfide (PPS) and aramid paper (aramid) and obtained the same results as indicated in the figure by (PPS) and (aramid).

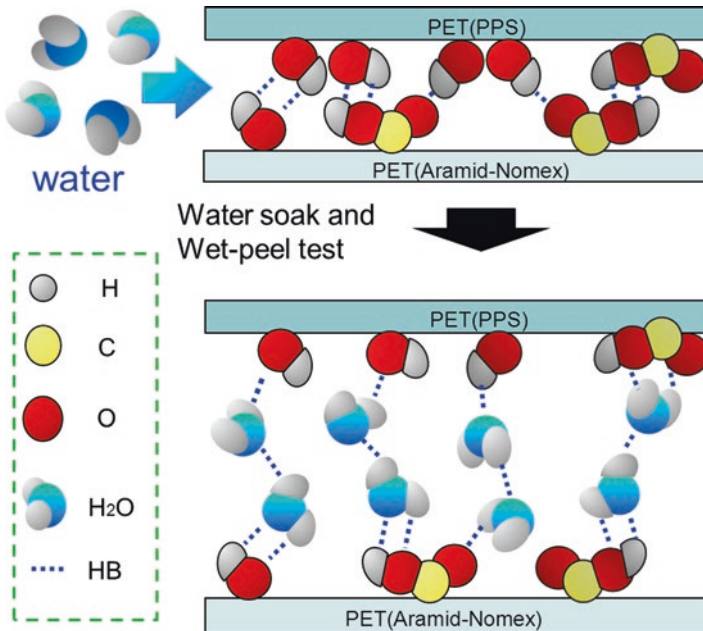


**Fig. 18** The model for the weaker peel strength under the wet-peel test. The water molecules can penetrate into the opened bonding interface (*top*) and break the “direct hydrogen bonds (HB)” connecting the PET-PET directly. This results in the H<sub>2</sub>O-mediated secondary hydrogen bonds (*bottom*). In this experiment, the two PET films were used, but we also tried other films as the PPS and aramid (Original source: ©)

### 4.3 Long Lifetime of Irradiation-Induced Active Surface

The question why the plasma-irradiated surface has so long lifetime for the bonding is very difficult to answer. One of the answers might be the cross-linking reaction at the irradiated surface. As Occhiello et al. [7] suggested, the plasma-created COOH and OH turn back inside from the surface. However, in our case, the plasma-created COOH and OH cannot turn back inside from the surface due to protection by the cross-linking layer [37]; then they remain at the surface so long. Hudis et al. [38] reported that the cross-linking occurs by activated species created by inert gas plasma, called as CASING. The other origin might be water coverage of the irradiated surface. The plasma-created COOH and OH are covered with adsorbed H<sub>2</sub>O in the atmosphere; they are forming the hydrogen bonding with H<sub>2</sub>O. Then the COOH and OH are preserved in the atmosphere. This problem is specialized in our previous paper [30]. In this case, we should consider why the COOH and OH are activated again when the PET films are heat-pressed 6 years after the irradiation. Probably such hydrogen bond with H<sub>2</sub>O is broken easily during the heat-press due to evaporation of the adsorbed water, resulting in restoration of the active COOH and OH.

## 5 Effects of Soaking of Irradiated Films in Liquids

We do not have yet rigid answers to the mechanism for ultralong lifetime of the irradiate active surface in the atmosphere which is effective to the bonding of PET for 6 years after the irradiation. We studied more on the surface of PET irradiated by “our plasma” and obtained curious and quite valuable results.

The plasma-irradiated films were soaked in the various types of liquid reagents of neutral, acid, alkali, and organic solutions; after that they were heat-pressed to make the bonding. All the samples showed  $Sp$  values larger than 10 N/cm, indicating the strong bonding. Then it is clarified that the plasma-bonding effect is not suppressed by the solutions of the pure water, acids, alkalis, and organic solvents. Then the functional groups of COOH and OH created on the irradiated surface do not lose their activity by these solutions or do not react with these solutions. Standing on this fact, it is quite reasonable and no doubtful that the irradiated active surface can be kept so long in the atmosphere. This is very important in terms of practical applications because we do not need to specially care the irradiated films for touching to these solutions before the heat-press process. It means we can keep the irradiated films long in the normal atmosphere with no special attentions. But its reason is not fully clear yet.

On the other hand, we tried to soak the irradiated films in the several ionic solutions and then measured the contact angles  $\theta$  on the irradiated surface. After the soaking, they were heat-pressed, and  $Sp$  of the bonded films were evaluated. These values of  $\theta$  and  $Sp$  are plotted in Fig. 19 against the solutions in order of  $\theta$  magnitude. The non-irradiated film (without soaking) has the largest  $\theta = 72^\circ$  as marked by a blue circle. This indicates the most stable and inactive surface with the smallest surface energy; then the films cannot be bonded (the corresponding  $Sp = 0$ ) by the heat-press. The irradiated film (without soaking) has a considerably small  $\theta = 37^\circ$  as marked by a red circle. This indicates very active surface with larger surface energy; then the films can be bonded (the corresponding  $Sp > 10$  N/cm).

After soaking in  $\text{CaCl}_2$  and  $\text{CuCl}_2$ , the films have further small  $\theta = 36^\circ$  and  $23^\circ$ , respectively, indicating the surface is more activated. The COOH and OH might be increased or new functional groups are created. Its reason is not known yet; anyway the films can be bonded tightly. Then the Ca and Cu ions and Cl and  $\text{SO}_4$  ions have no effect on the bonding. After soaking in the pure water, the  $\theta$  value of the film is recovered to  $46^\circ$ , indicating the surface becomes less active slightly. The COOH and OH might be decreased a little. But the films can be well bonded; this implies that the surface activity becomes less but it is still sufficient for the plasma bonding. This also indicates that we can reduce the plasma energy  $E$  (reduce the densities of created COOH and OH) to get the enough bonding.

The quite interesting result was obtained. The values of  $\theta$  were increased (restored) much to be  $56^\circ$  and  $67^\circ$  after soaking the irradiated films in  $\text{AlCl}_3$  and  $\text{FeCl}_3$  solutions, respectively. This indicates the surfaces of both films become very inactive. Then they cannot be bonded like as the non-irradiated film with  $\theta = 72^\circ$ . This result certainly implies that the COOH and OH should be consumed by some

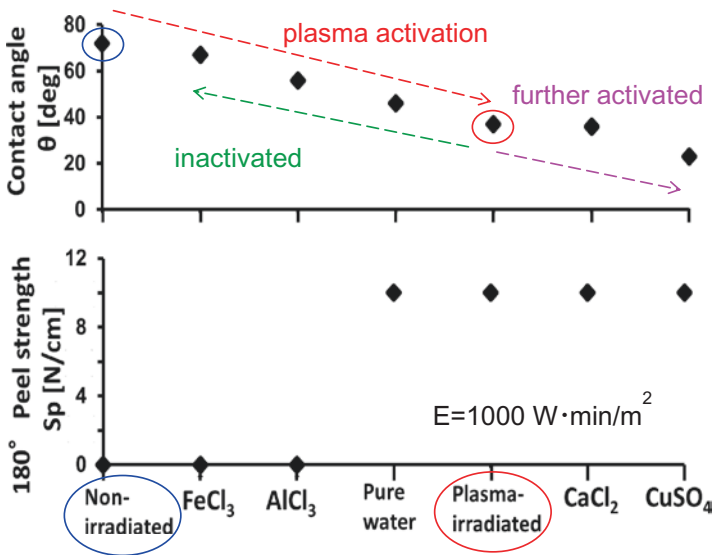


Fig. 19 The contact angle  $\theta$  of the films after the soaking in the liquids and the peel strength  $Sp$  after the heat-press bonding of the soaked films (Original source: ②)

chemical reaction with the Al ions and Fe ions, because it is known from the HCl and  $CaCl_2$  solutions that the Cl ions do not work. However, it is not known yet why the specific Al and Fe ions act, while the Na, Ca, and Cu ions do not act. This may be an important suggestion for the bonding mechanism and long lifetime; the subject must be solved in the near future. We can conclude that the contact angle certainly gives the good measure for the plasma bonding, and the critical value of  $\theta$  which divides bonding and nonbonding is in between  $46^\circ$  and  $56^\circ$ . It of course depends on the heat-press condition. We are now trying to obtain the exact critical value. It can be concluded by this unique experiment that the ability of irradiated surface with COOH and OH for the bonding is stable in the atmosphere and even after the soaking in the usual liquids. Then to keep this bonding ability, we should only mind the specific ions, which are not in the normal atmosphere.

## 6 Examples of Practical Applications

Almost we could clarify the mechanism of plasma bonding and obtain the long lifetime of the bonding ability of the plasma-activated surface. Then we tried application developments of this plasma-bonding technique. Here we present two examples of application-oriented research processes aiming to make use of the laminated plastic films. One is a long-term test of the bonding strengths for the solar cell use. The other is a long-term test of mechanical strengths of the laminated films applied as electrical insulator sheets used in motors of electric vehicle (EV).



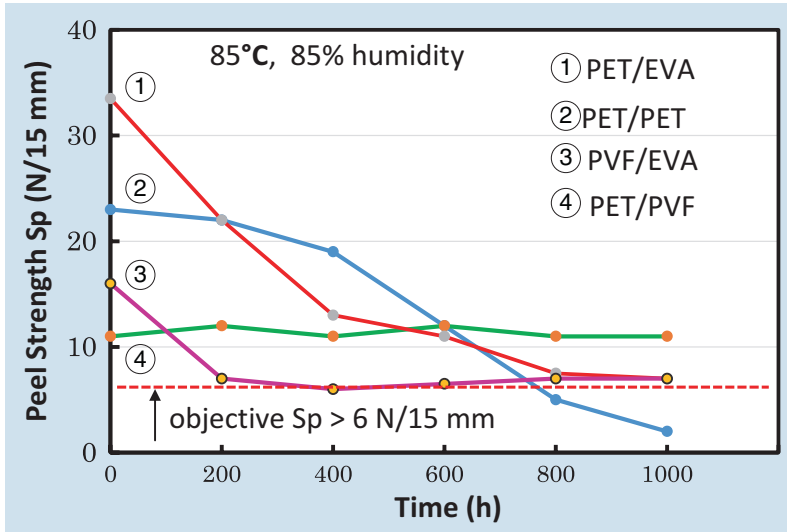


**Fig. 20** The peel strengths  $Sp$  as a function of preserved time  $t$  at 85 °C and 85% humidity for the <PET/PVF>, <PVF/EVA>, <PET/EVA>, and <PET/PET>. The objective value of  $Sp$  is 6 N/15 mm; it is indicated by a dotted line. *PVF* polyvinyl fluoride, *EVA* ethylene vinyl acetate

### 6.1 Solar Cell Back-Sheet

For the application to the back-sheets in solar cells, we laminated the PET films with various plastic films. We preserved the laminated films at 85 °C and 85 % humidity in the atmosphere and then measured their peel strength. Figure 20 shows the long-term test of the peel strengths as a function of preserved time ( $t$ ) for the PET/PVF, PET/EVA, PET/PET, and PVF/EVA. The PET is contacted with the PVF as shown in Fig. 2; then the result for PET/PVF is the most important factor in Fig. 20. The peel strength of PET/PVF shows 11 N/15 mm at the beginning ( $t = 0$ ); this is well stronger than the objective strength of 6 N/15 mm. Then it could clear the necessary bonding strength for the long-term application. As time goes, the strength does not change till 1000 h. This indicates that the PET/PVF laminate can be used as the back-sheet practically. The secondary important factor is the PVF/EVA, because the PVF contacts with the block resin of EVA as shown in Fig. 2. Then we tested it. It shows well-strong bonding at the beginning and a decrease for short time, but it has stronger bonding above the objective strength after long time of 1000 h. Then the PVF/EVA also cleared the necessary condition.

We checked the PET/EVA which is used in the case of the all PET laminate as shown in Fig. 2. It shows stronger bonding above the objective value for long time even it shows rapid decrease, because its initial value is very high. We also checked the PET/PET laminate, showing a large decrease with time. Finally it shows the strength smaller than the objective value above 800 h. Then we should improve the plasma bonding for the PET/PET case.

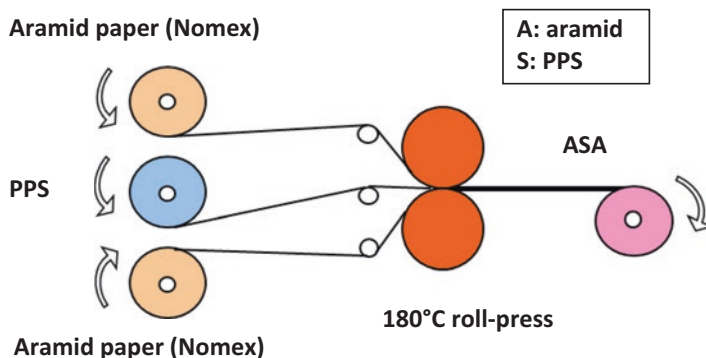


**Fig. 21** The roll-press bonding of the tri-layer <aramid/PPS/aramid> at 180 °C in the roll-to-roll system. *Aramid* aramid paper, *PPS* poly-phenylene sulfide

Thus, we could succeed in the application development of solar cell back-sheet using the <PET/PVF/PET> system. So we can expect this will be practically used in the near future, if people's consciousness will be more oriented to the circumstance issues. It means the people should consider the circumstance issues due to the glues and organic solvents are heavier than the economical merit of low production costs.

## 6.2 Insulator Sheet in EV Motor

Inside the EV motor, temperature and humidity are very high; then the circumstance is very severe for the insulator sheet used in motor oils. The PPS has good electrical insulation, higher mechanical strength, and higher thermal and chemical tolerances. On the other hand, the aramid paper (aramid) especially has high mechanical and thermal tolerances. Then we tried to develop the laminate of <aramid/PPS> by the plasma bonding. We tried to cover both sides of the PPS film with the strong aramid films to protect the PPS. The PPS and aramid films were irradiated by the plasma in roll-to-roll system; then they were bonded by roll-press at 180 °C as shown in Fig. 21. Thus, we could obtain tri-layer of <aramid/PPS/aramid> without using any adhesives.

We tried to test the tri-layer mechanical strength in high-temperature circumstance for long hours. Figure 22 shows for the <aramid/PPS/aramid> a rate for maintenance of strength (initial value is 100 %) as a function of holding time  $t$  at 180 °C in the atmosphere. We also tried for <aramid/PEN/aramid> and <aramid/PET/aramid>, where PEN is polyethylene naphthalate. The <aramid/PET/aramid> is rapidly degraded; it has only 50 % strength of the initial strength at 1000 h. The <aramid/PEN/aramid> can maintain its strength for 1000 h but loses it at 2000 h. Thus, these two cannot be applied to the motor insulator sheet. However, the <aramid/PPS/aramid> can maintain the initial strength over 2000 h. It shows small increase until 500 h. This can be interpreted like that there remained small parts of the non-reacted COOH and OH under the heat-press; they make the additional

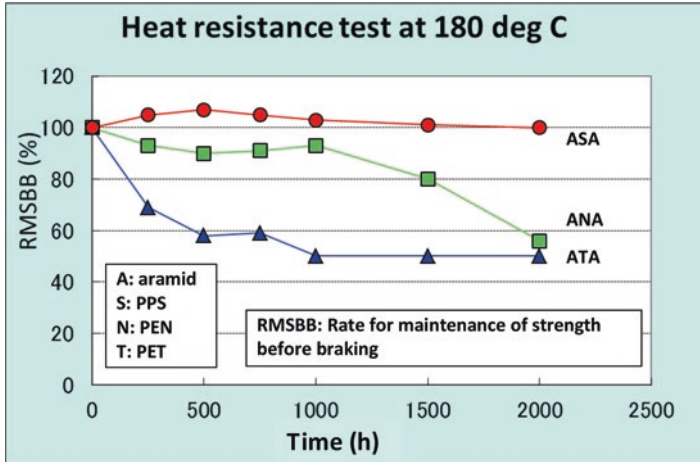


**Fig. 22** The rate for maintenance of the strength before the breaking as a function of preservation time for the tri-layers of ASA (aramid/PPS/aramid), ANA (aramid/PEN/aramid), and ATA (aramid/PET/aramid). *Aramid* aramid paper, *PPS* poly-phenylene sulfide, *PEN* polyethylene naphthalate

bondings by the DCR under 180 °C during this time interval. We tested the <aramid/PPS/aramid> at higher temperatures and higher humidity of 100 %, but it was not degraded for such vicious circumstances. It should be mentioned here that finally the <aramid/PPS/aramid> was actually employed as the motor insulator sheet in the EV. The PET does not have superior heat-resistance nature, and it absorbs water at higher temperatures; then it is not adequate for the EV motor use.

## 7 Summary

The direct laminations of the engineering plastic films without using adhesives are very useful for their practical applications, because each elemental film can cover weak properties of other elements. We worked on the fundamental research to clarify the mechanism of plasma irradiation-induced tight bonding of the plastic PET films.

The functional groups of COOH and OH are detected on the plasma-irradiated PET surface by the XPS, FTIR, and GCMM. The COOH numbers are larger than the OH.

The oxygen plasma-irradiated PET films can be bonded tightly by the heat-press at temperatures higher than 100 °C just after the irradiation. The films, kept in the atmosphere for 6 years after the irradiation, can be strongly bonded. The results of water contact angle show that the film surface is extremely active just after the irradiation, and it becomes less active in the atmosphere with time going but is still active considerably even after 5 years. This is the reason why the films can be bonded after 6 years.

The difference of peel strength between the dry- and wet-peel tests suggests that there are two forms of bonding, the hydrogen bonding and chemical bonding. The hydrogen bonding is major in the lower press temperatures of 100–130 °C because

the chemical bonding by DCR is less possible due to the shortage of thermal energy; then the film bonding strength is weak. The chemical bonding is major at the highest press temperatures of 140–160 °C due to the enough thermal energy for the DCR, resulting in the strong film bonding.

The FTIR results indicate that the plasma-created COOH and OH groups at the surface are responsible for the both bondings. After the heat-press bonding, the OH numbers in the bonded sample are decreased compared with those on the irradiated surface before the bonding. This indicates that the OH is consumed during the heat-press bonding. Thus, the dehydrated condensation reaction is suggested for the chemical bonding. We can propose by the wet-peel test that the water can penetrate into the bonded interface and break the hydrogen bonding, resulting in the weaker peel strength.

The irradiation effects at the surface on the bonding can be preserved in the normal atmosphere for 6 years. It is proposed that the cross-linking layer and water adsorption with hydrogen bonding at the irradiated surface are the origins for ultralong lifetime of the plasma-induced active surface.

We could obtain quite valuable knowledges by the soaking test. The irradiated PET films after soaking in the most of liquids do not lose the bonding ability, but only the films soaked in the solutions of AlCl<sub>3</sub> and FeCl<sub>3</sub> lose it. (1) Thus, we can keep the irradiated films without special cares in the atmosphere. (2) The reality of ultralong lifetime of the plasma effect in the atmosphere can be supported by the soaking test. These are very important in terms of practical production processes.

This article mainly describes the fundamental research of our works on the plasma bonding of the plastic PET films. We have developed some application researches as well on various plastic films, such as polyvinyl fluoride (PVF), aramid paper (aramid), poly-phenylene sulfide (PPS), and polyimide (PI), and obtained the excellent achievements. For example, the <PVF/PET/PVF> tri-layer can be used for the solar cell back-sheet, and the <aramid/PPS/aramid> can be used for the insulator sheet in the EV motors. It was not mentioned here, but the <aramid/PI/aramid> is actually used for insulator sheets in the motors of high speed trains. We would like to report such reviews of other application-oriented researches in other occasions.

**Acknowledgment** In this article, the most of figures and tables are reproduced from ① Jpn. J. Appl. Phys. (JJAP) 51 (2012) 11PG14 [28], ② JJAP 53 (2014) 05FB21 [29], ③ JJAP 53 (2014) 05FB23 [30], and ④ Procedia Eng. 171 (2017) 88 [31]. These are noted in each figure and table caption. We obtained reproduction permissions from the Japan Society of Applied Physics for JJAP and from Elsevier for Procedia Eng. <Reproduction under the terms of the Creative Commons Attribution-Non Commercial-No Derivatives License (CC BY NC ND)>. We would appreciate these society and company for giving us their permissions.

## References

1. S. Adachi, *Convertech* **354**, 40 (2002)
2. E. Sugimoto, *Electron. Parts Mater.* **47**, 103 (2008)
3. K. Ino, E. Sugimoto, *Convertech* **355**, 40 (2002)
4. M. DeBergalis, *J. Fluor. Chem.* **125**, 1255 (2004)
5. M. Yokura, T. Hayashi, T. Yoshii, Y. Maeda, T. Endo, *Trans. Mat. Res. Soc. Japan* **35**(1), 191 (2010)

6. N. Inagaki, K. Narushima, S. Ijima, Y. Ikeda, S. K. Lim, Y. W. Park, K. Miyazaki: *J. Adhesion Sci. Technol.* **17** (2003) 1457.
7. E. Occhiello, G. Morra, F. Garbassi, P. Humphrey, *J. Appl. Polym. Sci.* **42**, 551 (1991)
8. A.N. Banerjee, C.K. Ghosh, K.K. Chattopadhyay, H. Minoura, A.K. Sarkar, A. Akiba, A. Kamiya, T. Endo, *Thin Solid Films* **496**, 112 (2005)
9. Z. Hao, H. Chen, X. Zhu, J. Li, C. Liu, *J. Chromatogr. A* **1209**, 246 (2008)
10. M. Audronis, S.J. Hinder, P. Mack, V. Bellido-Gonzalez, D. Bussey, A. Matthews, M.A. Baker, *Thin Solid Films* **520**, 1564 (2011)
11. M.O.H. Cioffi, H.J.C. Voorwald, R.P. Mota, *M. Charact.* **50**, 209 (2003)
12. Y. Setsuhara, K. Cho, K. Takenaka, A. Ebe, M. Shiratani, M. Sekine, M. Hori, E. Ikenaga, H. Kondo, O. Nakatsuka, S. Zaima, *Thin Solid Films* **518**, 1006 (2009)
13. L. Yang, J. Chen, Y. Guo, Z. Zhang, *Appl. Surface Sci.* **255**, 4446 (2009)
14. Y. Setsuhara, K. Cho, K. Takenaka, M. Shiratani, M. Sekine, M. Hori, *Surf. Coatings Tech.* **205**, S484 (2011)
15. M. Katsikogianni, E. Amanatides, D. Mataras, Y.F. Missirlis, *Colloids Surf. B: Biointerfaces* **65**, 257 (2008)
16. A. Vesel, M. Mozetic, S. Strnad, *Vacuum* **85**, 1083 (2011)
17. K.N. Pandiyaraj, V. Selvarajan, R.R. Deshmukh, M. Bousmina, *Surf. Coatings Tech.* **202**, 4218 (2008)
18. K.N. Pandiyaraj, V. Selvarajan, R.R. Deshmukh, C. Gao, *Vacuum* **83**, 332 (2009)
19. C.-A. Dai, Y.-H. Lee, A.-C. Chiu, T.-A. Tsui, K.-J. Lin, K.-L. Chen, M.-W. Liu, *Polymer* **47**, 8583 (2006)
20. C. Scott, C. Macosko, *J. Polym. Sci. B Polym. Phys.* **32**, 205 (1994)
21. P. Marechal, G. Coppens, R. Legra, J.-M. Dekoninck, *J. Polym. Sci. Part A, Polym. Chem.* **33**, 757 (1995)
22. J. Friedrich, *The Plasma Chemistry of Polymer Surface: Advanced Techniques for Surface Design* (Wiley-VCH, Weinheim, 2012)
23. T. Hayashi, M. Kato, M. Yokura, K. Uehara, X. Guo, Y. Nakamura, T. Endo, *World J. Eng.* **7**(Suppl.2), 520 (2010)
24. M. Yokura, T. Hayashi, H. Katsumata, G. Xiang, T. Yoshii, M. Matsui, T. Endo, *World J. Eng.* **7**(Suppl.2), 519 (2010)
25. M. Yokura, K. Uehara, G. Xiang, A. Okamoto, Y. Nakamura, L. Reddy, T. Endo, *World J. Eng.* **8**(Suppl.3), 1275 (2011)
26. M. Yokura, K. Hanada, K. Uehara, M. Nagashima, H. Nishikawa, Y. Nakamura, H. Kezuka, K. Endo, T. Endo: *Proc. Int. Conf. Composites/Nano Engineering (Beijing) (2012) CDROM*
27. M. Yokura, K. Uehara, G. Xiang, K. Hanada, Y. Nakamura, L.S. Reddy, K. Endo, T. Endo, *Mater. Res. Soc. Symp. Proc.* **1454**, 201 (2012)
28. M. Yokura, K. Hanada, K. Uehara, Y. Nakamura, L.S. Reddy, H. Nishikawa, M. Nagashima, T. Endo, *Jpn. J. Appl. Phys.* **51**, 11PG14 (2012)
29. M. Yokura, K. Uehara, K. Hanada, Y. Nakamura, H. Nishikawa, T. Tsuchiya, S.L. Reddy, R. Philip, Y. Izumi, S. Tomita, T. Endo, *Jpn. J. Appl. Phys.* **53**, 05FB21 (2014)
30. K. Hanada, M. Yokura, M. Nagashima, Y. Nakamura, H. Nishikawa, Y. Strzhemechny, Z. Orel, S.L. Reddy, Y. Izumi, S. Tomita, T. Endo, *Jpn. J. Appl. Phys.* **53**, 05FB23 (2014)
31. T. Endo, L. Reddy, H. Nishikawa, S. Kaneko, Y. Nakamura, K. Endo, *Procedia Eng.* **171**, 88 (2017)
32. S. Teii, *J. Inst. Electr. Eng. Japan* **107**, 1096 (1987)
33. H. Kobayashi, S. Hirose, *Electron. Parts Mater.* **20**, 151 (1981)
34. H. Iriyama, *Convertech* **356**, 46 (2002)
35. Y. Nakayama, T. Takahagi, F. Soeda, K. Hatada, S. Nagaoka, J. Suzuki, A. Ishitani, *J. Polym. Sci. Polym. Chem.* **26**, 559 (1988)
36. M. Mito: *The Mechanism of Organic/Inorganic Interface*, K. Fukushima (Sci. Technol., Tokyo, 2006) 3–9.
37. Y. Iriyama, J. Yasuda: *Appl. Polym. Sci., Appl. Polym. Symp.* **42** (1998) 97.
38. M. Hudis: *Techniques and Applications of Polymer Chemistry*, J. R. Hollahan, A. T. Bell (Wiley, New York, 1974) 113.

**Part IV**  
**Characterization Tools**

# Atomic Force Microscopy for Characterizing Nanocomposites

Yu Liu, Chao Bao, Heng-yong Nie, David Hui, Jun Mei, and Woon-ming Lau

## 1 Introduction

A typical AFM system consists of three key components as shown in Fig. 1, including piezoelectric scanner as an accurate actuator, a proportional integral (PI) controller, and a cantilever with designed sensing mechanism [14, 15]. In the history of AFM, optic fiber, piezo, tuning fork, etc., have been all considered to provide ultra-sensitive force measurements [16–18]. The most widely used one is the optical-level-based sensing module, which includes a microfabricated flexible cantilever beam with an ultra-sharp tip, a laser diode emitting a laser beam

---

Y. Liu (✉)

Jiangsu Key Laboratory of Advanced Food Manufacturing Equipment and Technology,  
Jiangnan University, 1800 Lihu Avenue, Wuxi, Jiangsu 214122, China  
e-mail: [yu.liu@vip.163.com](mailto:yu.liu@vip.163.com)

C. Bao • J. Mei

Chengdu Green Energy and Green Manufacturing Technology R&D Center,  
596 Yinhe Road, Chengdu, Sichuan 610041, China  
e-mail: [bsssbc@163.com](mailto:bsssbc@163.com); [meijun12@126.com](mailto:meijun12@126.com)

H.-y. Nie

Surface Science Western, Western University,  
999 Collip Circle, LL31 (Lower), London, ON N6G 0J3, Canada  
e-mail: [hnie@uwo.ca](mailto:hnie@uwo.ca)

D. Hui

Department of Mechanical Engineering, University of New Orleans,  
2000 Lakeshore Drive, New Orleans, LA 70148, USA  
e-mail: [dhui@uno.edu](mailto:dhui@uno.edu)

W.-m. Lau

School of Mathematics and Physics, University of Science & Technology Beijing,  
No.30 Xueyuan Road, Beijing 100083, China  
e-mail: [leolau@ustb.edu.cn](mailto:leolau@ustb.edu.cn)

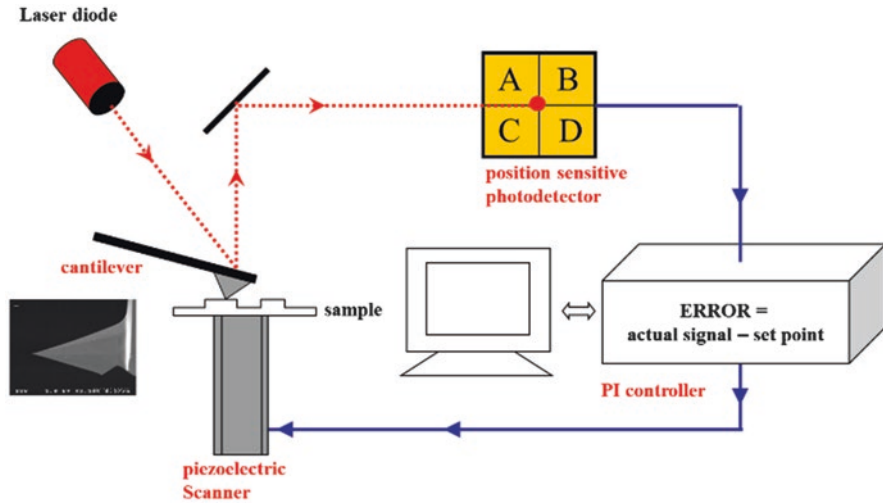


**Fig. 1** Schematics of atomic force microscopy

(collimated) as focused on the cantilever backside, and a quadrant photodetector (PD) to receive reflected laser beam from the cantilever backside [19, 20]. The differential electrical signal from the PD corresponds to the displacement of the laser spot across the face plane of the PD based on optoelectronics. Such an optical-lever sensing system can effectively detect the deflection of the cantilever under a pN force loaded on the tip [21]. The cantilever is commonly made from Si and  $\text{Si}_3\text{N}_4$  materials [22], in which  $\text{Si}_3\text{N}_4$  cantilever was harder and more chemical stable. The backside of the cantilever might be coated with a thin gold or aluminum layer to enhance the light beam reflectivity for obtaining higher measurement sensitivity.

The deflection of the cantilever is regulated by the interacting force between the tip and the sample. The interacting force is nonlinear in nature [23]. When the tip is away from the surface, the dominant forces include attractive Van der Waals and capillary forces, which depend on the materials' properties of the sample. When the tip is in contact with the sample, repulsive forces due to viscoelastic properties of the sample act on the tip. As shown in Fig. 2, the interaction force between the tip and the sample changes with the probe distance from the sample ( $z$  distance). When the tip is far from the surface, there is no deflection for the cantilever. As approaching the sample at a certain distance, the tip will be pulled toward the surface, into the attractive regime. The attractive force will increase with decrement of the distance until to the maximum. Then the attractive force will decrease to zero and transits into repulsive regime. The hard contact between the tip and the surface is implemented in the repulsive regime. In air, we typically only use contact mode and tapping mode of AFM for studying nanocomposites.



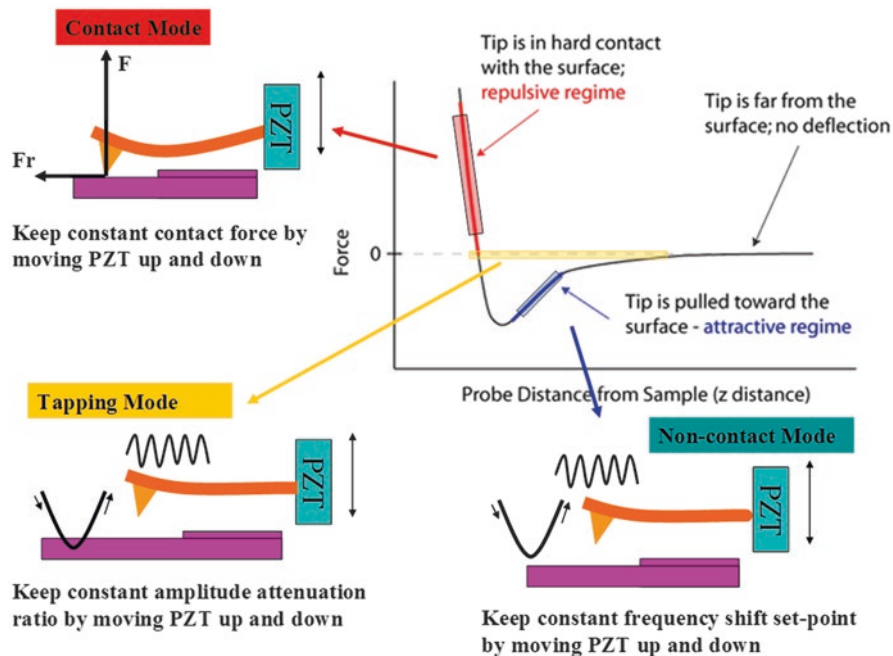
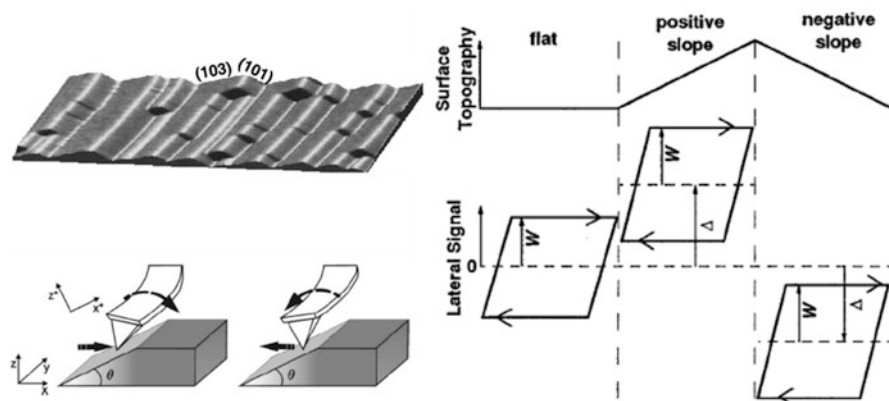


Fig. 2 Schematics of different AFM modes in consideration of tip-sample interaction force

## 2 Contact Mode and Its Relevance

The earlier applications of atomic force microscopy were based on the contact (or static) mode [10, 24]. Of this mode, the AFM tip is in an immediate hard contact with sample surface upon experiencing repulsive force (as in Fig. 2). While scanning a topographic image of a sample, the height position of the Z-translation stage, to control the up-down movement of the AFM tip, is controlled by a feedback loop to maintain a constant contact force between tip and sample. Through an appropriate selection of cantilever spring constant typically ranging from 0.001 N/m up to 3 N/m (herein we mean nominal spring constant), the contact mode AFM can be applied to image diverse hard-soft nanocomposites.

From the contact mode scanning, not only a useful topographical map of the surface is obtainable, but also lateral friction imaging is available through monitoring the lateral signal on the PD. The frictional image was earliest carried out by Mate et al. [24] to observe atomic-scale features on graphite surface and has represented pioneering work of studying tribological properties between micro-/nanoscale contact and macroscale contact. It eventually leads to the advances in nanoscale understanding of frictional phenomena of nanocomposites [25–27]. Exact measurements of friction force are deserved, and two categories of research efforts have been collected, based on direct measurements of friction coefficient or



**Fig. 3** SrTiO<sub>3</sub>-based calibration of friction coefficient (Reprinted with permissions from Refs. [29] and [31])

friction force. For measuring the friction coefficient, successive steps of calibrating the normal signal sensitivity, normal stiffness, lateral signal sensitivity, and lateral stiffness have to be done in advance. Although the normal sensitivity can be directly calibrated in the contact mode, the optical geometry of AFM system is not straightforward for the lateral sensitivity [28]. Therefore, a number of special accessories were designed [29–31]. It also pushes forward several efforts based on well-defined wedge, SrTiO<sub>3</sub> specimen (Fig. 3), or universal platform from Si (100) wafer for directly determining the conversion relationship between friction force coefficient and lateral voltage response.

The friction force AFM technique could also be applied as a chemical force microscopy to provide nanoscale information about the functional groups on a composite surface, which ultimately determines the surface interfaces at the smaller scale [32, 33]. Such as, for nanocomposites with silica particles as fillers, AFM friction images in Fig. 4 show the size-dependent dispersion and averaging friction force. With larger filler size, the average friction forces of the microcomposites were always greater than the nanocomposite. Meanwhile, the region with aggregation of nanofillers such as nanoclusters exhibits higher friction than the regions with uniform distribution of nano-silica in the nanocomposite. If the nanoparticles are well dispersed, strong adhesion appears between filler and polymer matrix to minimize the debonding and delamination, which will decrease the fracture and wear penetration on the nanocomposite surface [34].

The lateral friction is dependent on heterogeneity of surface materials, such as chemical functionalities related with the nanocomposite surfaces. In Fig. 5, WS<sub>2</sub> nanotubes as the fillers in PS/PMMA blends are not observable from the topographic image, but the friction force image clearly shows darker spots with the fillers. The dispersion quality of fillers in heterogeneity with matrix materials, associated with final performances of nanocomposites in many aspects, can be successfully probed by friction mode [35, 36].

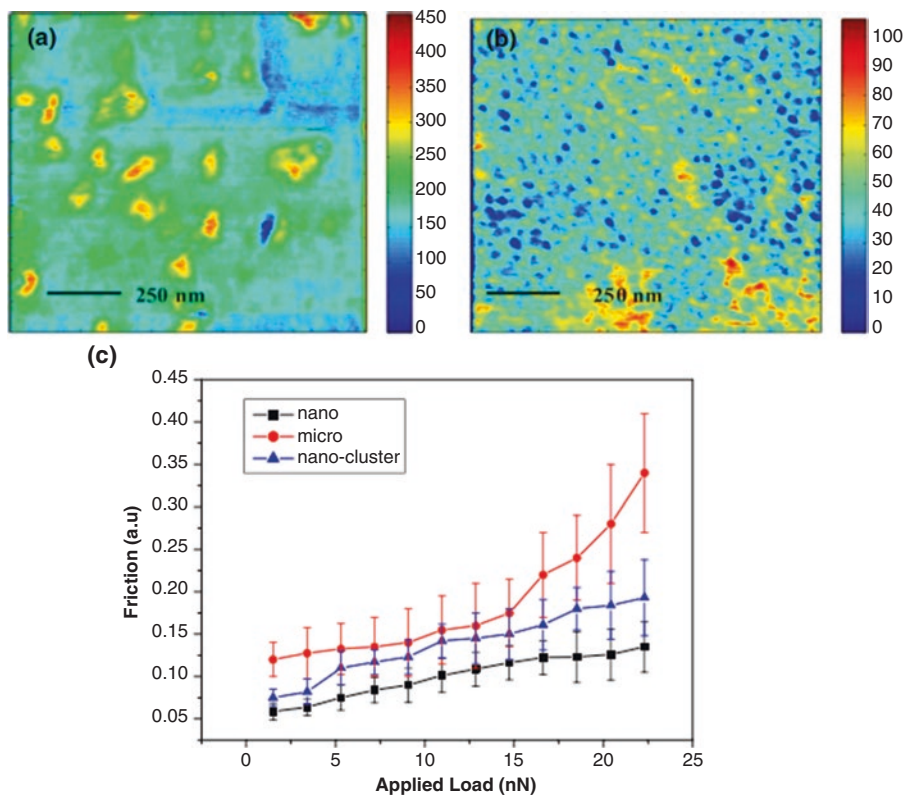


**Fig. 4** AFM friction imaging of microcomposite (a) and nanocomposite (b) and their friction V.S. load measurements (c) (Reprinted with permission from Ref. [34])

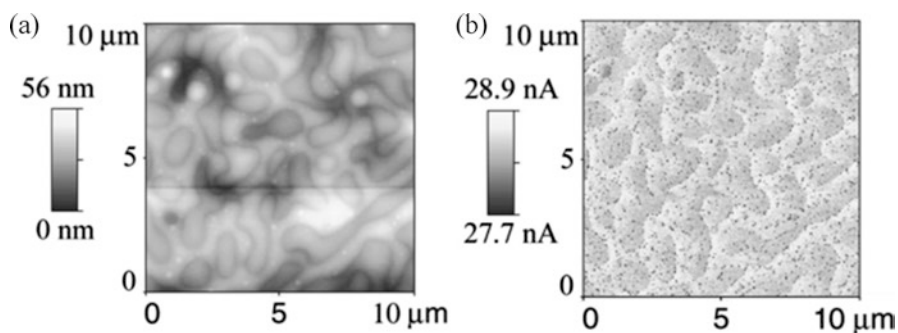


**Fig. 5** AFM topographic (a) and friction images (b) of WS<sub>2</sub> fillers in PS/PMMA blend (Reprinted with permission from Ref. [35])

In practice, for softer materials with Young's modulus at the order of MPa and even less which is common for elastomeric nanocomposites, significant deformation and damage on sample surface often occur in contact mode during imaging in air, because certain loading force must be applied to penetrate contaminants and adsorbed moisture on the material surface [37]. AFM contact mode through setting a preloading on samples may be deployed for scratching composite surfaces. Ebert and Bhushan [38] performed a systematic study on testing transparent superhydrophobic coatings on glass, polycarbonate, and poly(methyl methacrylate) (PMMA) substrates using surface-functionalized SiO<sub>2</sub>, ZnO, and indium tin oxide (ITO) nanoparticles. In Fig. 6, AFM tips induced wear results on the coatings as deposited. All surfaces showed wear resistance for potential commercial use, indicating strong bonding of the silicone resin and sufficient hardness of nanoparticles and resin.

When the piezoelectric tube, which controls the sample position, is driven by a sinusoidal voltage with controlled frequency and amplitude, force modulation mode (Fig. 7) is quickly established to maintain a constant cantilever deflection as in contact mode AFM [37]. The amplitude response of the dynamic cantilever is a function of the driving signal and the surface elasticity. This technique is particularly useful in characterization of hard-soft nanocomposites.

In Fig. 8a [39], the force modulation image displays a clear distinction between the patterned silver electrodes and the surrounding polystyrene with a hydrogen sensor design. Referring to the morphological image, force modulation image shows enhanced contrast based on the variations in local elasticity and reveals interfacial transitions in the local elasticity across the cross section. More attractive results with nanocomposite can be found in Fig. 8b, wherein images of a carbon black deposit in a section of automobile tire rubber [40]. The force modulation image (right) clearly differentiates the stiffer carbon black area in the center from the surrounding rubber. DeVecchio and Bhushan [41] pointed out that force modulation AFM can yield quantitative elasticity on samples with modulus up to several tens of GPa, with low indentation loads as only a few tenths of  $\mu\text{N}$ , eliminating significant plastic deformation on samples. This technique further poses the capability for simultaneously imaging morphological, friction, and elastic compliance.

### 3 Force Curve Mode

AFM has an important function on physical and chemical characterizations of the nanocomposite surfaces. They are implemented by approaching the probe toward the material surface for obtaining force curves as shown in Fig. 9. In this data acquisition process, the loading force will increase with displacement of the Z stage movements with AFM cantilever, after the contact between the probe and the sample. When the force reaches the set point, the probe is quickly retrieved back with continuous force decrease. The force curve has included rich information associated with the surface properties of the nanocomposites [42]. For example, the slope of the approaching curve is typically correlated with elasticity. The indentation depth

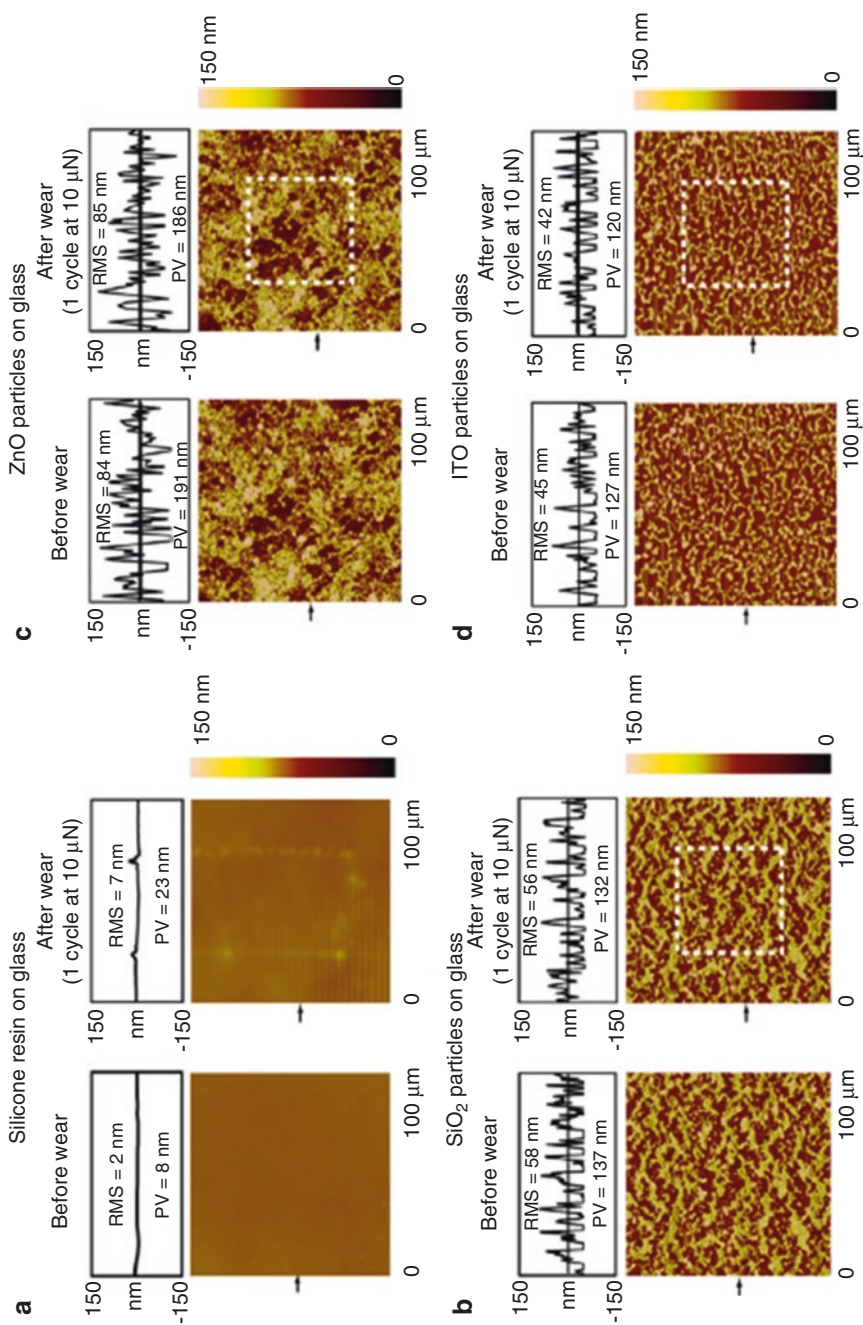


**Fig. 6** AFM images on different hydrophobic coatings with scratching tests. (a) Silicone resin on glass. (b)  $\text{SiO}_2$  particles on glass. (c) ZnO particles on glass. (d) ITO particles on glass (Reprinted with permission from Ref. [38])

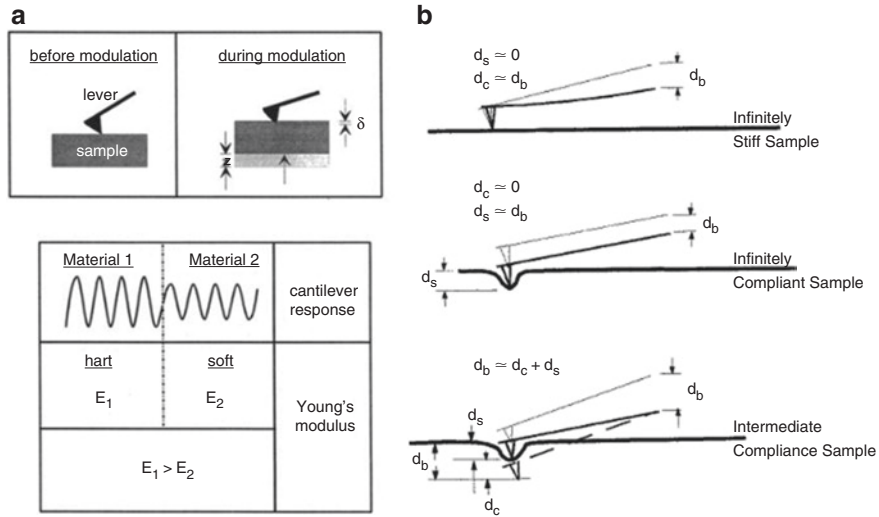


**Fig. 7** Schematics of force modulation microscope (a) and its operating principles (b) (Reprinted with permission from Ref. [39])

of AFM tip into the sample is extracted from Z displacement and the cantilever deflection, and therefore hardness can be got if without considering cantilever compliance during force loading. Within the close plot formed by approach and retract curves (Fig. 9), store and loss energy can be both calculated. The area enclosed between approach and retract curves corresponds to the energy dissipation, which would be interfered by adhesion based hysteresis and viscosity [43]. Directly, the “pull-off” part of retract force curve is right the adhesion force related to the surface chemistry. This observable adhesion information catalyzed AFM as a chemical force microscopy for fishing different functional groups on composite surfaces. Trifonova-Van Haeringen et al. [44] introduced AFM force mode with chemical modified tips for adhesion imaging based on analysis of measured pull-off forces. It helps in differentiating the filler particles from the rubber matrix, with an emphasized merit for distinguishing the types of filler particles.

For calculation of mechanical properties of surfaces, the force curve may be fitted based on different contact mechanic models:

1. Hertz Model

The Hertz model, developed by Hertz in 1982 with assumption of spherical tip as used [45, 46], can be applied to obtain effective elastic modulus  $E^*$ :

$$E^* = \frac{3F}{4R^{1/2}\delta^{2/3}} \tag{1}$$

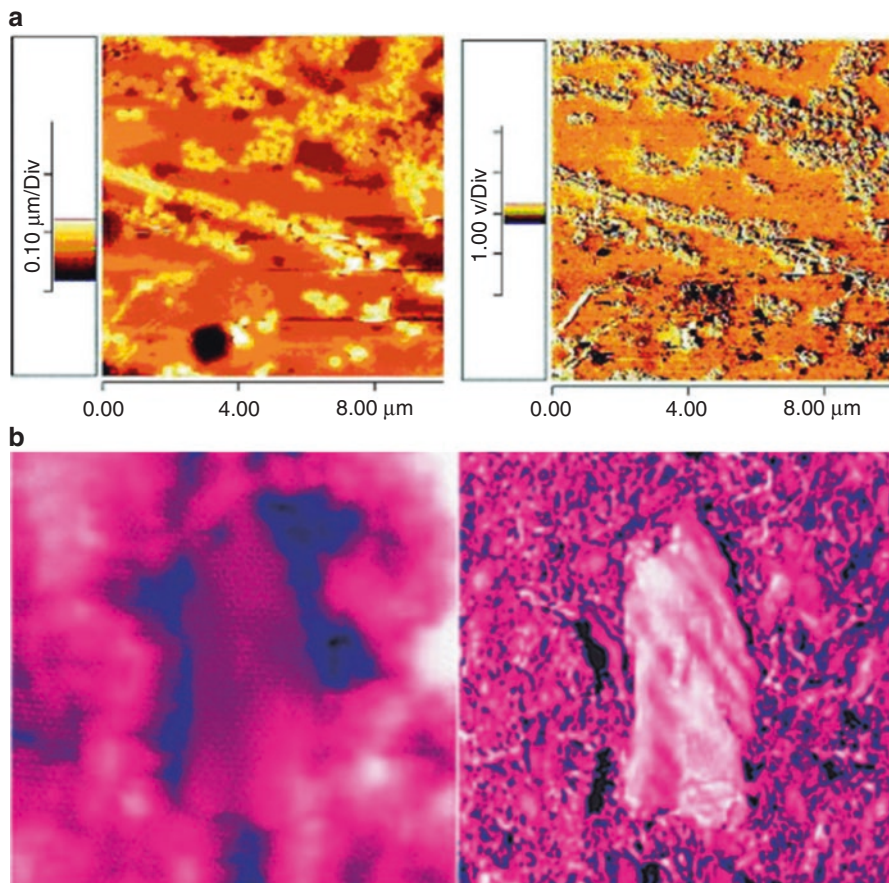
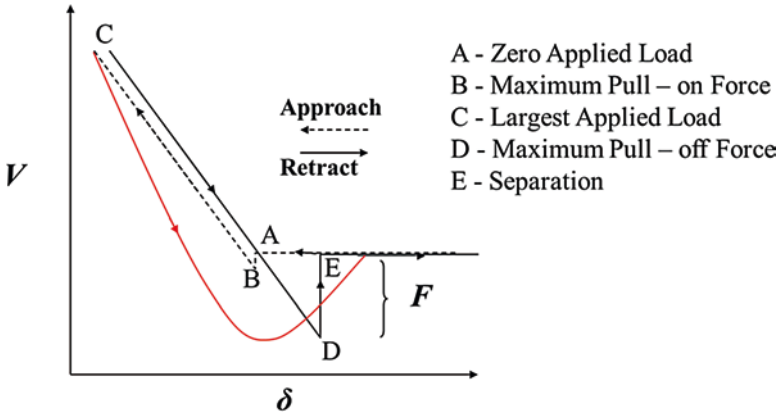


**Fig. 8** Topographic and friction force images of (a) deposited silver electrodes in polystyrene and (b) carbon black filler in tire rubber (Reprinted with permission from Refs. [39] and [40])

where  $R$  is radius of tip end and  $\delta$  is the elastic deformation under the applied load  $F$ . The Hertz model was established with further assumptions of small elastic deformation on an isotropic surface and no adhesive force as pinned out [47]. Based on it, Pakzad et al. [48] applied AFM in combination with analytical contact mechanics for studying the size dependence of transverse elastic moduli of two kinds of cellulose nanocrystals, which are important filler in composite materials. It also showed that wood cellulose nanocrystal had higher transverse elastic moduli rather than the cotton one. As one most fundamental filler, carbon nanotubes were studied by Palaci et al. [49] with considering its radial elasticity as a function of external radius (Fig. 10), based Hertz model. They applied a small indentation to measure the radial stiffness and elastic modulus of multiwalled carbon nanotubes and noticed that the radial Young's modulus strongly decreased with the increased radius.

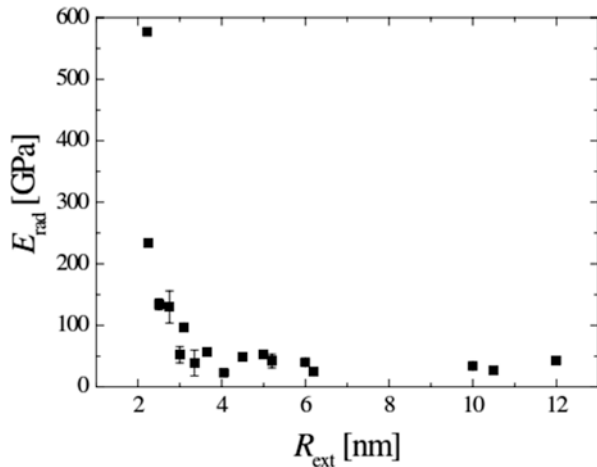


**Information included:**

- 1). Adhesion Force :  $F$
  - 2). Sensitivity of AFM, if on rigid substrate
  - 3). Elasticity of substrate, if on soft substrate
  - 4). Dissipation energy due to adhesion and viscoelasticity
- ...

Fig. 9 Schematics of force curve

Fig. 10 Dependence of Young’s modulus of multiwalled carbon nanotube on external radius, as measured by force curve AFM mode based on Hertz model (Reprinted with permission from Ref. [49])



2. Johnson-Kendall-Roberts (JKR) Model

The JKR model includes the influence of surface energy, which can be used for the adhesive situations [50]. The Hertz model is first modified in JKR to calculate the surface attractive forces:

$$a^3 = \frac{3R}{4E^*} \left( F + 3\gamma\pi R + \sqrt{6\gamma\pi RF + (3\gamma\pi R)^2} \right) \tag{2}$$



where  $\gamma$  refers to surface energy. When the applied force  $F$  equals zero, the equation is

$$a_0^3 = \frac{9\pi R^2 \gamma}{2E^*} \quad (3)$$

The separated force can be obtained at the time when  $a$  equals to zero by the following equation:

$$F = -\frac{3}{2}\gamma\pi R \quad (4)$$

where the separated force can be extracted from the force curves. Finally, we use the above equation to calculate the surface energy  $\gamma$ . Lin et al. [46] measured elastic moduli of polystyrene (PS), polymethylmethacrylate (PMMA), and polydimethylsiloxane (PDMS) films using AFM with a steel microspherical probe tip. It can be found from the force displacement that the pull-off force maximum was varying due to the surface energy diversity. Tests from Hertz and JKR models predicted there is a dramatic difference on the modulus with respect to indentation depth. These results confirm the validity of the proposed method for effectively measuring the elastic properties of polymeric thin films.

### 3. Derjaguin-Muller-Toporov (DMT) Model

JKR model is suitable for short-range forces as occurred within the area of contact. The DMT model is an alternative model for adhesive contact which includes the long-range surface force outside contact area. DMT model shows better for the cases under lower adhesion when a smaller diameter probe punches on a harder material [51, 52]. Herein, long-range force may be described as

$$a^3 = \frac{3R}{4E^*}(F + 2\Delta\gamma\pi R) \quad (5)$$

where  $\Delta\gamma$  refers to the surface energy which can be calculated by the separation force equation:

$$F = -2\Delta\gamma\pi R \quad (6)$$

Because nanocomposite surfaces being examined are heterogenous, it is attractive to collect an array of force curves [53]. Each force curve is measured at a unique X-Y position in the area, and force curves are listed into a three-dimensional array, which represents a map of the distribution of elasticity, adhesion, and dissipation data on the surface. Wang et al. [54] developed a procedure based on combination of JKR contact mechanics and “two-point method” with force curve AFM to obtain topography, elastic modulus, and adhesive energy maps simultaneously for a nature rubber (NR) containing carbon nanotube fillers in Fig. 11. Figure 12 further compares the force-deformation curves and the JKR fitting curves of different region in the elastic modulus map. It is suggested that this combined method can be

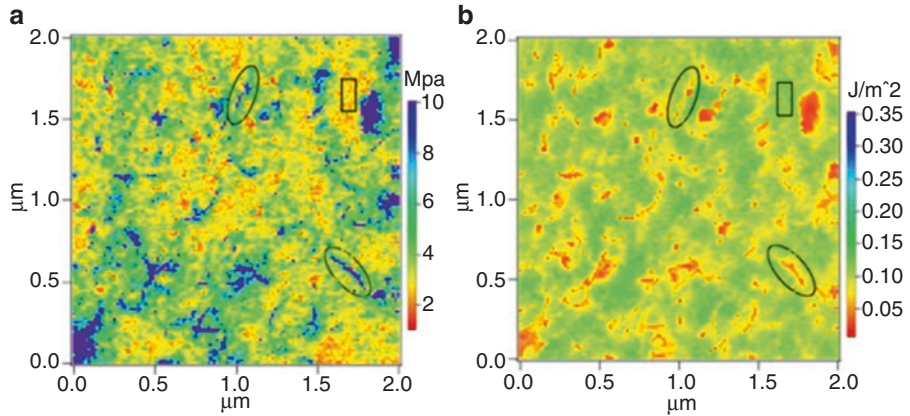


**Fig. 11** AFM force curve imaging of NR5 nanocomposites for distribution of (a) elastic modulus and (b) adhesive energy (Reprinted with permission from Ref. [54])

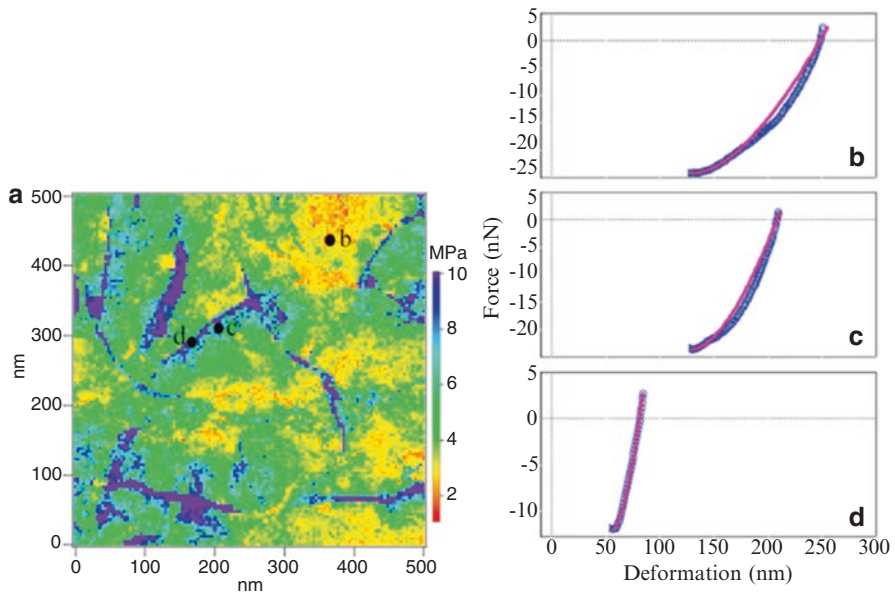


**Fig. 12** (a) The elastic modulus map and (b–d) the force-deformation curves compared with JKR fitting for different regions (Reprinted with permission from Ref. [54])

used to identify carbon nanotubes (CNTs), NR, and intermediate modulus regions effectively in nanocomposites.

Karim et al. [55] use the JKD model to determine the surface modulus of neat epoxy and POSS/epoxy composite with silica and gold particles as fillers. Adhesion measurements were used for determination of surface energy. For neat epoxy, epoxy/POSS composite systems and PS films, the surface modulus value was found

softer than the macroscopic glassy modulus. The variety of elastic modulus under different loads can be eliminated through introducing the influence of adhesive interactions in JKR contact model. Although informative, force volume method is time consuming and alternative means based on dynamic AFM mode have been developed for quicker solutions in the next section.

## 4 Dynamic Force Modes

Dynamic force mode has put its advances in development of AFM for imaging nanocomposites. The aforementioned force modulation, although belonging to dynamic force mode, operates at a frequency of only about several kHz or less. It is far below the fundamental resonance frequency. Meanwhile, force modulation is carried based on constant force contact between tip and sample. In this section, our dynamic force mode is mainly related to tapping mode and its relevance, which are operating at different resonance frequencies. Tapping mode AFM was initiated by Zhong et al. [56] to reduce tip-induced irreversible damage of contact mode on polymer with low modulus. It is probably the one in AFM with highest usage frequency for studying nanocomposites. Tapping AFM allows the ease of imaging soft materials at small forces esp. in air, with suppressing lateral friction force with minimized surface damage [57].

During tapping mode scanning, the AFM oscillates (or tapes) its cantilever with amplitude of up to 100 nm and frequency close to or at its fundamental resonance [58]. The tip is in an intermittent contact with the material surface with a feedback loop to control the translational stage up-down to maintain the damped amplitude of the cantilever at a constant level (set point). Fifty to seventy percent of its freely vibrating amplitude is generally adopted and tuned for obtaining tapping images. However, it has to be paid attention that height anomalies may be associated with tapping mode AFM due to strong tip-sample interaction, which modulates oscillatory movements of the cantilever during scanning [59, 60].

In addition to its topographic imaging, tapping mode has demonstrated its excellence in providing phase contrast in direct relation with heterogeneity of surface compositions [58]. From Fig. 13, carbon black fillers as mixed in the rubber matrix can be distinguished with clear boundary interpretation. It was noticed that phase shift has certain relationship with mechanical property of the surface [61], in that the phase lag between the excitation signal (driving the cantilever vibration) and cantilever response is a parameter about the type of interactions that the tip experiences. For elastic materials, the phase decreases from 90 to 0° as the tip approaches the sample surface. This shift is smaller for softer samples as in Fig. 14. Therefore, stiffer filler areas in Fig. 13 are brighter than softer rubber areas.

Tomayo and Garcia [62] theoretically and experimentally demonstrated the phase shift under condition of adhesion hysteresis and/or viscoelasticity. However, such phase shift is not sensitive to stiffer materials with Young's modulus

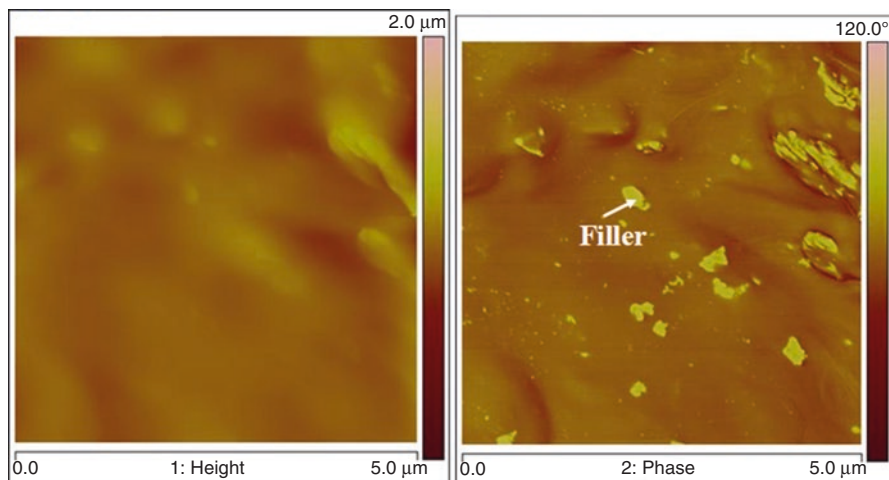


**Fig. 13** Tapping mode AFM images of topography (*left*) and phase (*right*) of carbon black-filled rubber composite

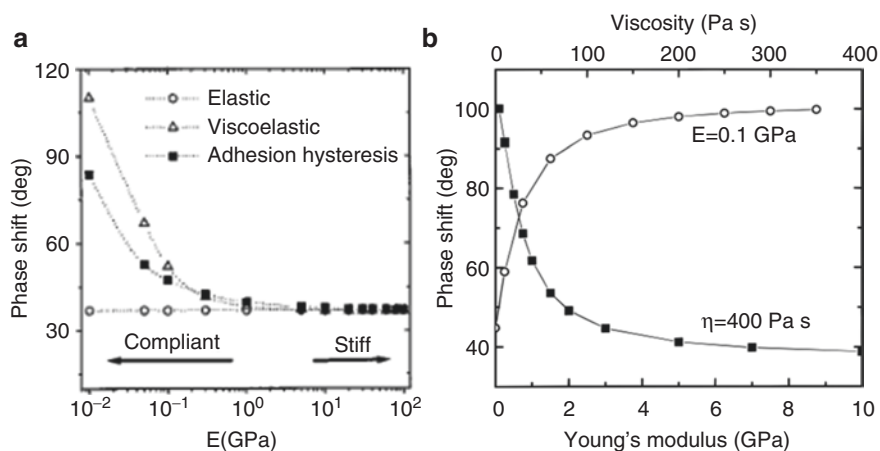


**Fig. 14** Relationship between phase shift and surface elasticity (**a**) /viscosity (**b**) during tapping mode (Reprinted with permission from Ref. [59])

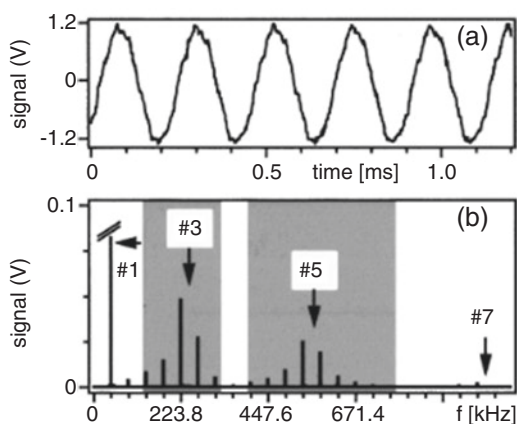
$E > \sim 2\text{GPa}$ , even with energy dissipation involved. Cleveland et al. [63] pointed that the tapping mode AFM phase image should be interpreted in terms of energy dissipation by

$$E = \frac{1}{2} \frac{\pi k C A^2}{Q} \left[ \left( \frac{A_0}{A} \right) \sin \Delta\phi - 1 \right] \quad (7)$$

where  $A_0$  is the driving amplitude,  $A$  is the set-point amplitude, and  $Q$  is the quality factor. Furthermore, the interpretation of phase image is also dependent on the tapping condition [58]. The results in Fig. 14, though describing certain relation between Young's modulus and phase shift, do not provide quantitative mapping between them, in that the phase shift is coupled by complex combination of stiffness with other existent dissipation mechanisms during the intermittent contact between tip and surface, such as adhesion and viscoelasticity. Therefore, for determination of Young's modulus, nanoindentation-based force volume mode and force modulation mode have been used in other sections. However, the force volume mode has low lateral resolution and imaging speed for practical application; and force modulation mode is working in contact mode with certain selection on stiffness of materials. Therefore, there is a necessity to correctly determine different surface properties through establishing a more effective way.

While the oscillating tip approaches to or retracts from the sample surface under tapping amplitude modulation, it experiences a complex and time-varying force field which contains a wealth of information about the materials composition. Such tip-sample interactions generate a disturbance to the vibration of the cantilever while it is tapping at the resonance frequency. Thus, the motion of cantilever becomes a harmonic. Hillenbrand et al. [64] noticed that in AFM tapping mode, other dynamic amplitudes of the vibrating cantilever were stimulated at its higher harmonics (integer times of the fundamental resonance) as in Fig. 15. These harmonic responses exhibit certain relationship with the mechanical property of the surface. Stark et al. [65] studied the origins of the increased an-harmonic responses in higher-order flexural modes due to nonlinear tip-sample interactions. They also resolved the force constants of the tip-sample interactions by analyzing a wide spectrum of flexural motions of the cantilever using Fourier transformation. By simulating the AFM cantilever using finite element method, Song and Bhushan [66] studied the dynamic responses of the cantilever under both of attractive and repulsive force regimes and concluded that the nonlinear force field could excite higher-order modes of the vertical bending.

**Fig. 15** Response of dynamic cantilever at higher flexural modes and harmonics: (a) the monitored cantilever deflection vs time; (b) the amplitude vs frequency (Reprinted with permission from Ref. [64])



Recently, researchers have investigated the possibility of using higher-order flexural modes to explain the origins of the harmonic spectra and therefore being able to extract the information of the tip-sample interactions. At the earlier time, Minne et al. [67] already studied the second flexural mode to monitor the change of ZnO film admittance, which is not possible to probe, while the AFM is operated at the fundamental resonance. Hoummady and Farnault [68] applied the second-order flexural mode to distinguish hydrodynamic damping and attractive interaction. They found that the AFM optical-lever detection sensitivity was enhanced in the second-order flexural mode. Exciting first two flexural modes at the same time was developed as an approach to probe materials' properties [69, 70].

The second-order flexural mode, generally a nonharmonic eigenmode of the cantilever, is less coupled with the first-order mode according to the amplitude of vibration. The first flexural mode was mainly used for scanning sample topography, and composition contrast was obtained simultaneously through locking-in signals at the second flexural modes. As a result, the sensitivity detected at the second-order flexural mode for compositional mapping was promoted by a factor of 10 because of a higher Q-factor. More attractively, this dual frequency dynamic force mode can obtain subsurface information, such as by making use of the nonlinear nanomechanical coupling between the probe and the sample [71] in Fig. 16. An alternative

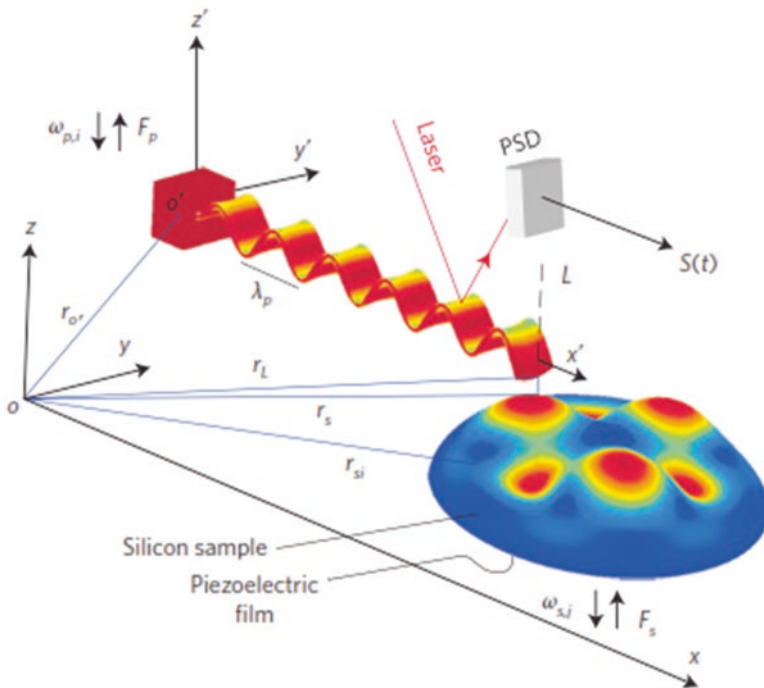


**Fig. 16** Schematics of probing subsurface information through nanomechanical coupling between tip and sample, operating at dual frequency dynamic force mode (Reprinted with permission from Ref. [71])

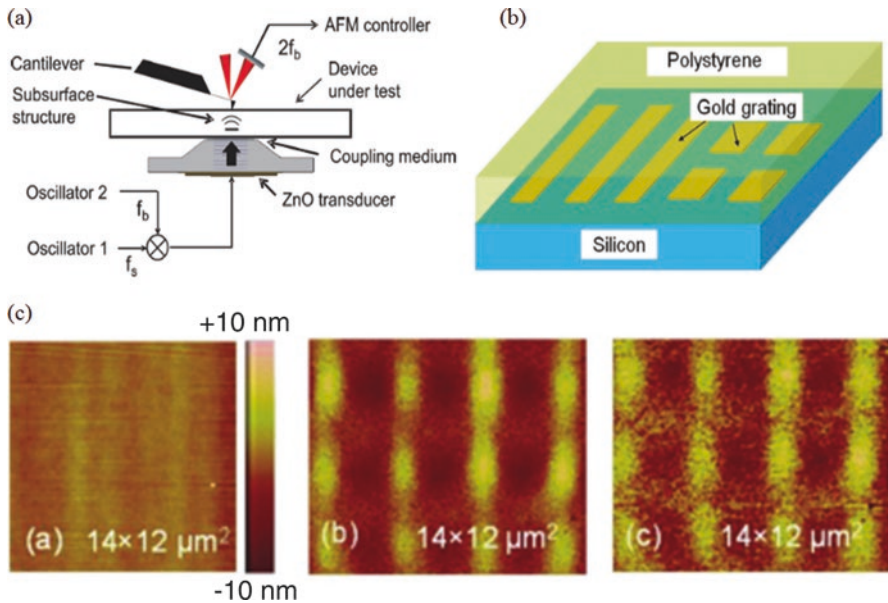


**Fig. 17** Utilization of dual frequency excitation on sample holder for imaging buried gold grating under polystyrene film: (a) experimental setup; (b) gold or aluminum structures were deposited on silicon by sputtering. The structures were covered by 200 nm thick polystyrene which was spin-casted into the gold grating; (c) topographic image of gold-line structures covered with 7  $\mu\text{m}$  PMMA photoresist layer, amplitude image, and phase image of the *gold lines*, buried 7  $\mu\text{m}$  under the photoresist layer (Reprinted with permission from Ref. [72])

implement of dual frequency excitation [72] could be imposed on sample holder instead of on the cantilever in Fig. 17, in which patterned gold grating buried under the surface layer of polystyrene could be imaged through amplitude and phase shift at the second frequency.

Higher flexural mode vibration requires significantly higher driving force for vibrating cantilever at higher-order resonance frequency. As a result, the effective signal-to-noise ratio becomes very lower [73]. Worse case is that higher flexural vibration may cause fatigue problem of the cantilever. Therefore, further attempts have been made by Sahin et al. [74] to enable some specially designed (notched and tip-offset) cantilever in Fig. 18 to more effectively harvest the high-order harmonic signals as the interaction force excites higher-order flexural modes. The notched type of cantilever guarantees the match of first three flexural modes with calculated resonances, and the tip-offset cantilever can intrinsically shift the highest dynamic response at 16th harmonics due to induced torsional resonance at tapping mode [75].

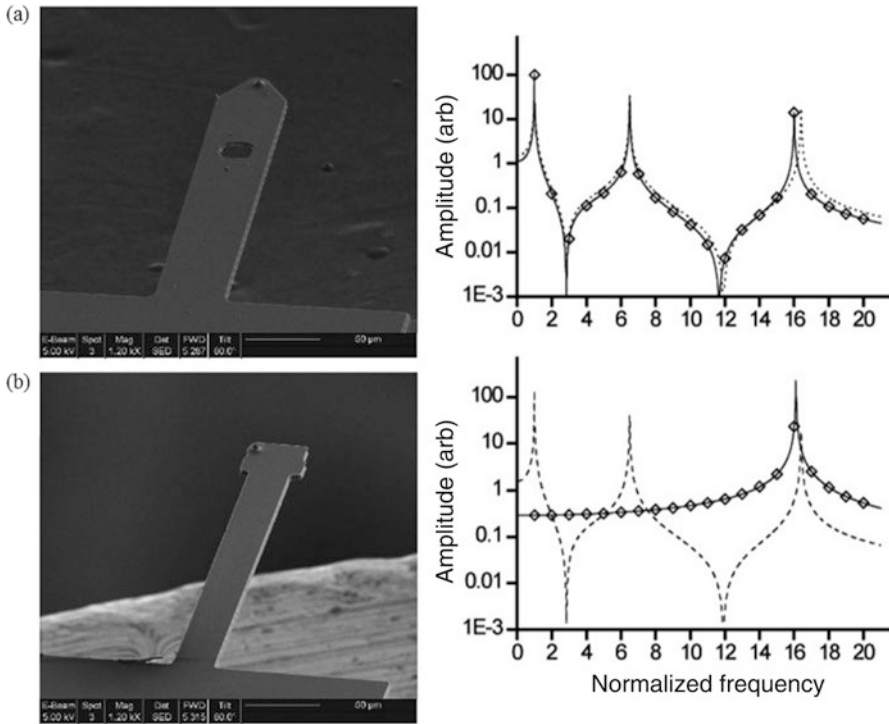


**Fig. 18** (a) Special design of AFM cantilever for harvesting higher harmonic signals to match the third-order resonance frequency to an exact integer multiple of the first resonance frequency. Frequency response curves given to the right compare the response of an unmodified cantilever to a correctly designed cantilever. Diamond markers are placed at harmonic frequencies that come at integer values. (b) A torsional harmonic cantilever designed to use the more efficient torsional vibrations to enhance harmonic signals (Reprinted with permission from Ref. [74])

## 5 Conclusions

With its three decades' development, atomic force microscopy has been widely used for studying composite surfaces. A variety of imaging modes can be found with nanocomposites. Although continuous efforts have been done for comprehensively probing surfaces, appropriate selection or combination of AFM modes is still in need for correctly interpreting material properties. The relevant understandings on AFM imaging data are from multidiscipline, which will keep requesting more researches on resolving force details, spanning from mechanical, thermal, electrostatic, capacitive, and so on. The alliance between AFM and nanocomposite is in trust to finally bring more advances in nanotechnology.



## References

1. R.P. Feynman, There's plenty of room at the bottom: an invitation to enter a new field of physics. First Published in Engineering and Science Magazine, vol. XXIII, no. 5, (1960)
2. R.M. Westervelt, Applied physics: graphene nanoelectronics. *Science* **320**, 324–325 (2008)
3. M.J. Madou, *Fundamentals of Microfabrication and Nanotechnology, Volume III: From MEMS to Bio-MEMS and Bio-NEMS: Manufacturing Techniques and Applications* (CRC Press, Boca Raton, 2011)
4. J. Cumings, A. Zettl, Low-friction nanoscale linear bearing realized from multiwall carbon nanotubes. *Science* **289**, 602–604 (2000)
5. C. Klinke, J.B. Hannon, A. Afzali, P. Avouris, Field-effect transistors assembled from functionalized carbon nanotubes. *Nano Lett.* **6**, 906–910 (2006)
6. M. Lucas, X.H. Zhang, I. Palaci, C. Klinke, E. Tosatti, E. Riedo, Hindered rolling and friction anisotropy in supported carbon nanotubes. *Nat. Mater.* **8**, 876–881 (2009)
7. A.M. Youssef, Polymer nanocomposites as a new trend for packaging applications. *J. Polym. – Plast. Technol. Eng.* **52**, 635–660 (2013)
8. M. Maiti, M. Bhattacharya, A.K. Bhowmick, Elastomeric nanocomposite. *Rubber Chem. Technol.* **81**, 384–469 (2008)
9. V.L. Pushparaj, M.M. Shaijumon, A. Kumar, S. Murugesan, L.J. Ci, R. Vajtai, R.J. Linhardt, O. Nalamasu, P.M. Ajayan, Flexible energy storage devices based on nanocomposite paper. *PNAS* **104**, 13574–13577 (2007)
10. G. Binnig, C.F. Quate, C. Gerber, Atomic force microscope. *Phys. Rev. Lett.* **56**, 930–933 (1986)
11. D.J. Muller, Y.F. Dufrene, Atomic force microscopy as a multifunctional molecular toolbox in nanobiotechnology. *Nat. Nanotechnol.* **3**, 261–269 (2008)
12. B. Brennan, S.J. Spencer, N.A. Belsey, T. Faris, H. Croninb, S.R.P. Silva, T. Sainsbury, I.S. Gilmorea, Z. Stoevab, A.J. Pollard, Structural, chemical and electrical characterisation of conductive graphene-polymer composite films. *Appl. Surf. Sci.* **403**, 403–412 (2017)
13. H. Huang, I. Dobryden, N. Ihrner, M. Johansson, H.Y. Ma, J.S. Pan, P.M. Claesson, Temperature-dependent surface nanomechanical properties of a thermoplastic nanocomposite. *J. Colloid Interf. Sci.* **494**, 204–214 (2017)
14. S. Devasia, E. Eleftheriou, S.O.R. Moheimani, A survey of control issues in nanopositioning. *IEEE Trans. Control Syst. Technol.* **15**, 802–823 (2007)
15. C.M. Su, Industrial perspectives of AFM control. *Asian J. Control* **11**, 104–109 (2009)
16. D. Rugar, H.J. Mamin, R. Erlandsson, J.E. Stern, B.D. Terris, Force microscope using a fiberoptic displacement sensor. *Rev. Sci. Instrum.* **59**, 2337–2340 (1988)
17. S.C. Masmanidis, R.B. Karabalin, I. De Vlaminck, G. Borghs, M.R. Freeman, M.L. Roukes, Multifunctional nanomechanical systems via tunably coupled piezoelectric actuation. *Science* **317**, 780–783 (2007)
18. L.P. Van, V. Kyrylyuk, F. Thoyer, J. Cousty, A stabler non contact atomic force microscopy imaging using a tuning fork for air and liquid environments: the zero phase mode atomic force microscopy. *J. Appl. Phys.* **104**, 074303 (2008)
19. S. Alexander, L. Helleman, O. Marti, J. Schneir, V. Elings, P.K. Hansma, M. Longmire, J. Gurley, An atomic-resolution atomic-force microscope implemented using an optical-lever. *J. Appl. Phys.* **65**, 164–167 (1989)
20. G. Meyer, N.M. Amer, Novel optical approach to atomic force microscopy. *Appl. Phys. Lett.* **53**, 1045–1047 (1988)
21. R. Zhu, S. Howorka, J. Proll, F. Kienberger, J. Priener, J. Hesse, A. Ebner, V.P. Pastushenko, H.J. Gruber, P. Hinterdorfer, Nanomechanical recognition measurements of individual DNA molecules reveal epigenetic methylation patterns. *Nat. Nanotechnol.* **5**, 788–791 (2010)
22. K.B. Gavan, E.W.J.M. van der Drift, W.J. Vensta, M.R. Zuiddam, H.S.J. van der Zant, Effect of undercut on the resonant behavior of silicon nitride cantilevers. *J. Micromech. Microeng.* **19**(2009), 035003.

23. R.W. Stark, W.M. Heckl, Higher harmonics imaging in tapping-mode atomic-force microscopy. *Rev. Sci. Instrum.* **74**, 5111–5114 (2003)
24. C.M. Mate, G.M. McClelland, R. Erlandsson, S. Chiang, Atomic-scale friction of a tungsten tip on a graphite surface. *Phys. Rev. Lett.* **59**, 1942–1945 (1987)
25. I. Szlufarska, M. Chandross, R.W. Carpick, Recent advances in single-asperity nanotribology. *J. Physics D-Appl. Physics.* **41**(2008): p. -
26. S.H. Kim, D.B. Asay, M.T. Dugger, Nanotribology and MEMS. *NanoToday* **2**, 23–29 (2007)
27. Y. Terada, M. Harada, T. Ikehara, T. Nishi, Nanotribology of polymer blends. *J. Appl. Phys.* **87**, 2803–2807 (2000)
28. E. Liu, B. Blanpain, J.P. Celis, Calibration procedures for frictional measurements with a lateral force microscope. *Wear* **192**, 141–150 (1996)
29. R.J. Cannara, M. Eglin, R.W. Carpick, Lateral force calibration in atomic force microscopy: a new lateral force calibration method and general guidelines for optimization. *Rev. Sci. Instrum.* **77**, 053701 (2006)
30. G. Bogdanovic, A. Meurk, M.W. Rutland, Tip friction – torsional spring constant determination. *Colloids Surf B-Biointerfaces* **19**, 397–405 (2000)
31. H. Xie, J. Vitard, S. Haliyo, S. Regnier, Optical lever calibration in atomic force microscope with a mechanical lever. *Rev. Sci. Instrum.* **79**, 096101 (2008)
32. S. Akari, D. Horn, H. Keller, Chemical imaging by scanning force microscopy. *Adv. Mater.* **7**, 549–551 (1995)
33. S. Ibrahim, T. Ito, Surface chemical properties of nanoscale domains on uv-treated polystyrene-poly(methyl methacrylate) diblock copolymer films studied using scanning force microscopy. *Langmuir* **26**, 2119–2123 (2010)
34. D. Devaprakasam, P.V. Hatton, G. Mobus, B.J. Inkson, Nanoscale tribology, energy dissipation and failure mechanisms of nano- and micro-Silica particle-filled polymer composites. *Tribol. Lett.* **34**, 11–19 (2009)
35. W. Zhang, S. Ge, Y. Wang, M.H. Rafailovich, O. Dhez, D.A. Winesett, H. Ade, K.V.P.M. Shafi, A. Ulman, R. Popovitz-Biro, R. Tenne, J. Sokolov, Use of functionalized WS<sub>2</sub> nanotubes to produce new polystyrene/polymethylmethacrylate nanocomposites. *Polymer* **44**, 2109–2115 (2003)
36. A. Mekroud, D. Benachour, S. Bensaad, Influence of organoclay filler on the properties of polystyrene/low-density polyethylene blend. *J. Compos. Interfaces* **22**, 809–822 (2015)
37. P. Maivald, H.T. Butt, G.A.C. Gould, C.B. Prater, B. Drake, J.A. Gurley, V.B. Elings, P.K. Hansma, Using force modulation to image surface elasticities. *Nanotechnology* **2**, 103–106 (1991)
38. D. Ebert, B. Bhushan, Transparent, superhydrophobic, and wear-resistant coatings on glass and polymer substrates using SiO<sub>2</sub>, ZnO, and ITO nanoparticles. *Langmuir* **28**, 11391–11399 (2012)
39. R.M. Overney, E. Meyer, J. Frommer, H.J. Guentherodt, M. Fujihira, H. Takano, Y. Gotoh, Force microscopy study of friction and elastic compliance of phase separated organic thin films. *Langmuir* **10**, 1281–1286 (1994)
40. Force modulation imaging with atomic force microscopy. Veeco Instruments Inc.
41. D. DeVecchio, B. Bhushan, Localized surface elasticity measurements using an atomic force microscope. *Rev. Sci. Instrum.* **68**, 4498–4505 (1997)
42. B. Cappela, G. Dietler, Force-distance curves by atomic force microscopy. *Surf. Sci. Rep.* **34**, 1–104 (1999)
43. J.H. Hoh, J.P. Cleveland, C.B. Prater, J.P. Revel, P.K. Hansma, Quantized adhesion detected with the atomic force microscope. *J. Am. Chem. Soc.* **114**(1992), 4917–4918
44. D. Trifonova-Van Haeringen, H. Schonherr, G.J. Vancso, L. Van Der Does, W.M. Noordermeer, P.J.P. Janssen, Atomic force microscopy of elastomers: morphology, distribution of filler particles and adhesion using chemically modified tips. *Rubber Chem. Technol.* **72**, 862–875 (1999)
45. H. Hertz, Über die Berührung fester elastischer Körper. *J. Für Die Reine Und Angew. Math.* **92**, 156–171 (1882)

46. L.Y. Lin, D.E. Kim, Measurement of the elastic modulus of polymeric films using an AFM with a steel micro-spherical probe tip. *Polym. Test.* **31**, 926–930 (2012)
47. J. Domke, M. Radmacher, Measuring the elastic properties of thin polymer films with the atomic force microscope. *Langmuir* **14**, 3320–3325 (1998)
48. A. Pakzad, J. Simonsen, P.A. Heiden, R.S. Yassar, Size effects on the nanomechanical properties of cellulose I nanocrystals. *J. Mater. Res.* **27**, 528–536 (2012)
49. I. Palaci, S. Fedrigo, H. Brune, C. Klinke, M. Chen, E. Riedo, Radial elasticity of multiwalled carbon nanotubes. *Phys. Rev. Lett.* **94**, 175502 (2005)
50. J. Notbohm, B. Poon, G. Ravichandran, Analysis of nanoindentation of soft materials with an atomic force microscope. *J. Mater. Res.* **27**, 229–237 (2012)
51. A.-Y. Jee, M. Lee, Comparative analysis on the nanoindentation of polymers using atomic force microscopy. *Polym. Test.* **29**, 95–99 (2010)
52. B.V. Derjaguin, V.M. Muller, Y.P. Toporov, Effect of contact deformations on the adhesion of particles. *J. Colloid Interface Sci.* **53**, 314–326 (1975)
53. W.F. Heinz, E. A-Hassen, J.H. Hoh, Application of force volume imaging with atomic force microscopes. Veeco Instruments Inc.
54. D. Wang, S. Fujinami, K. Nakajima, S. Inukai, H. Ueki, A. Magario, T. Noguchi, M. Endo, T. Nishi, Visualization of nanomechanical mapping on polymer nanocomposites by AFM force measurement. *Polymer* **51**, 2455–2459 (2010)
55. T.B. Karim, G.B. McKenna, Evidence of surface softening in polymers and their nanocomposites as determined by spontaneous particle embedment. *Polymer* **52**, 6134–6145 (2011)
56. Q. Zhong, D. Inniss, K. Kjoller, V.B. Elings, Fractured polymer silica fiber surface studied by tapping mode atomic-force microscopy. *Surf. Sci.* **290**, L688–L692 (1993)
57. N.A. Burnham, O.P. Behrend, F. Oulevey, G. Gremaud, P.J. Gallo, D. Gourdon, E. Dupas, A.J. Kulik, H.M. Pollock, G.A.D. Briggs, How does a tip tap? *Nanotechnology* **8**, 67–75 (1997)
58. S.N. Magonov, V. Elings, M.H. Whangbo, Phase imaging and stiffness in tapping-mode atomic force microscopy. *Surf. Sci.* **375**, L385–L391 (1997)
59. S.J.T. Van Noort, K.O. Van der Werf, B.G. De Grooth, N.F. Van Hulst, J. Greve, Height anomalies in tapping mode atomic force microscopy in air caused by adhesion. *Ultramicroscopy* **69**, 117–127 (1997)
60. M. Bai, S. Trogisch, S. Magonov, H. Taub, Explanation and correction of false step heights in amplitude modulation atomic force microscopy measurements on alkane films. *Ultramicroscopy* **108**, 946–952 (2008)
61. J. Tamayo, R. Garcia, Deformation, contact time, and phase contrast in tapping mode scanning force microscopy. *Langmuir* **12**, 4430–4435 (1996)
62. J. Tamayo, R. Garcia, Effects of elastic and inelastic interactions on phase contrast images in tapping-mode scanning force microscopy. *Appl. Phys. Lett.* **71**, 2394–2396 (1997)
63. J.P. Cleveland, B. Anczykowski, A.E. Schmid, V.B. Elings, Energy dissipation in tapping-mode atomic force microscopy. *Appl. Phys. Lett.* **72**, 2613–2615 (1998)
64. R. Hillenbrand, M. Stark, R. Guckenberger, Higher-harmonics generation in tapping-mode atomic-force microscopy: insights into the tip-sample interaction. *Appl. Phys. Lett.* **76**, 3478–3480 (2000)
65. R.W. Stark, T. Drobek, W.M. Heckl, Tapping-mode atomic force microscopy and phase-imaging in higher eigenmodes. *Appl. Phys. Lett.* **74**, 3296–3298 (1999)
66. Y.X. Song, B. Bhushan, Simulation of dynamic modes of atomic force microscopy using a 3D finite element model. *Ultramicroscopy* **106**, 847–873 (2006)
67. S.C. Minne, S.R. Manalis, A. Atalar, C.F. Quate, Contact imaging in the atomic force microscope using a higher order flexural mode combined with a new sensor. *Appl. Phys. Lett.* **68**, 1427–1429 (1996)
68. M. Hoummady, E. Farnault, Enhanced sensitivity to force gradients by using higher flexural modes of the atomic force microscope cantilever. *Appl. Physics a-Mater. Sci. Process.* **66**, S361–S364 (1998)

69. T.R. Rodriguez, R. Garcia, Compositional mapping of surfaces in atomic force microscopy by excitation of the second normal mode of the microcantilever. *Appl. Phys. Lett.* **84**, 449–451 (2004)
70. J.R. Lozano, R. Garcia, Theory of phase spectroscopy in bimodal atomic force microscopy. *Phys. Rev. B* **79**, 014110 (2009)
71. L. Tetard, A. Passian, T. Thundat, New modes for subsurface atomic force microscopy through nanomechanical coupling. *Nat. Nanotechnol.* **5**, 105–109 (2010)
72. S.Q. Hu, C.M. Su, W. Arnold, Imaging of subsurface structures using atomic force acoustic microscopy at GHz frequencies. *J. Appl. Phys.* **109**, 084324 (2011)
73. O. Sahin, G. Yaralioglu, R. Grow, S.F. Zappe, A. Atalar, C. Quate, O. Solgaard, High-resolution imaging of elastic properties using harmonic cantilevers. *Sensors Actuators a-Phys.* **114**, 183–190 (2004)
74. O. Sahin, Accessing time – varying forces on the vibrating tip of the dynamic atomic force microscope to map material composition. *Israel J. Chem.* **48**, 55–63 (2008)
75. S.D. Solares, H. Holscher, Numerical analysis of dynamic force spectroscopy using the torsional harmonic cantilever. *Nanotechnology* **21**, 075702 (2010)

## Editorial Note

Dear Readers,

We are pleased to deliver the Special Book dedicated to Nobel Laureate Prof. Akira Suzuki. The authors of this book are distinguished colleagues and friends, most of them participants and contributors to ICCE 2015 and 2016, honored by Special Lecture delivered by Prof. Suzuki. After almost 2 years, we finalized editing this book and deliver it today.

P.M. and S.K. would like to warmly thank for their precious help during the revision and editing of the book the colleagues:

Dr. Naum Naveh (Shenkar College of Engineering, Israel),  
Prof. Yasuteru Mawatari (Muroran Inst. of Tech., Japan),  
Prof. Sarawut Rimdusit (Chulalongkorn University, Thailand),  
Prof. Shinya Yamanaka (Muroran Inst. of Tech., Japan),  
Prof. Mpitloane Hato (University of Limpopo, South Africa),  
Dr. Marino Lavorgna (Istituto per i Polimeri, Italy),  
Mr. Yan Ma (Kyoto Institute of Technology, Japan),  
Prof. Mario Hofmann (National Cheng Kung University, Taiwan),  
Dr. Alina Pruna (Polytechnic University Of Bucharest, Romania),  
Prof. Edoardo Magnone (Dongguk University, Korea),  
Prof. Andrea Basso (University of Genova, Italy),  
Prof. Yutaka Sawada (Tokyo Polytechnic University, Japan),  
Dr. Hao Lei (Chinese Academy Sciences, China),  
Dr. Takao Ono (Osaka University, Japan),  
Dr. Chihiro Kato (Kanagawa Institute of Industrial Science and Technology, KISTEC, Japan).

We could not deliver the book without their help and contributions.

May 1<sup>st</sup>, 2017

Muroran, Japan

Ebina, Japan

Paolo Mele (Muroran Institute of Technology, Japan)

Satoru Kaneko (Kanagawa Institute of Industrial Science and Technology, KISTEC,  
Japan)

# Index

## A

- Absorbance spectroscopy, 29, 30
- AB-stacked graphene, 44
- Accordion-like helix oscillations (HELIOS), 322, 324
- Acetonitrile, 66, 67, 72
- Acoustic emission (AE)
  - parameters, 123
- Acoustic emission sensors, 120, 121
- Adsorption energy, 14–15
  - amplitude, 142
  - energy and acoustic emission signal, 142
  - signal duration, 142
  - signal end, 142
  - signal start, 142
- AFT
  - strain gauges on, 122
  - tensile strains in, 132, 136
- Ag/graphene composite, 9–12
- Alkaline fuel cell (AFC), 212
- Ambient pressure, 268–273
- Amorphous carbon nitride, 261–264, 273
- Aniline-based benzoxazine, 229
- Anode, 218
- Anthracene, 347–351, 356
- Antiferromagnetism, 329
- Antiprism, 364
- Anti-stokes condition, 33
- Applied nanotech Inc., 120
- Aptamers, DNA, 84, 85
- Aramid CFRPs, 148
- Aramid fiber (AF), 146
- Aromatic stabilization, 349
- Aromaticity, 68, 328, 341, 346, 355, 363
- As-prepared product (AGC-1), 11
- Atomic force microscopy, nanocomposites, 423–431, 433
  - cantilever, 422
  - contact mode
    - elastomeric nanocomposites, 426
    - force modulation, 426, 428
    - friction imaging, microcomposite, 425
    - frictional image, 423
    - hard-soft, 423
    - hydrophobic coatings, scratching tests, 427
    - lateral friction, 424
    - measurements, friction force, 423
    - optical geometry, 424
    - piezoelectric tube, 426
    - SrTiO<sub>3</sub>-based calibration of friction coefficient, 424
    - tip-sample interaction force, 423
    - topographical map, 423
    - transparent superhydrophobic coatings, 426
    - WS<sub>2</sub> fillers, PS/PMMA blend, 425
    - Young's modulus, 426
  - force curve mode, 431
    - approach and retract curves, 428
    - calculation, mechanical properties of surfaces, 428
    - data acquisition process, 426
    - filler particles, 428
    - Hertz model, 428–430
    - JKR model, 430, 431
    - physical and chemical characterizations, 426
    - surface properties, 426

Atomic force microscopy,  
 nanocomposites (*cont.*)  
 hard contact, 422  
 history, 421  
 imaging data, 438  
 interaction force, 422  
 PD, 422  
 piezoelectric scanner, 421  
 schematics, 422  
 van der Waals and capillary forces, 422

Atomic orbitals, 337

Attenuated total reflection (ATR- FTIR), 31

Au-functionalized graphene, 70

Axial fiber (AF), 152, 156, 161, 162

**B**

BA-a-type benzoxazine resin, 230

Band gap, 79

Bending mode, 170, 171

Benzene by Ab initio valence bond  
 calculations, 336–338

Benzene by NBO and NRT, 338–341

Benzene by spin-coupling effective  
 Hamiltonian, 331–336

Benzenoid cells, 356

Benzoxazine  
 DSC thermograms of, 234

Benzoxazine resin, 231

Bidentate rhodium–diene complex, 307

Bilayer graphene-1, 6  
 TEM images of, 7

Biosensing applications of graphene, 80

Bipolar plate, 211, 217, 219–229  
 properties of conductive filler for, 228  
 carbon-polymer composite, 224–229  
 carbon fillers, 224–226  
 polymer matrix, 226–229  
 conductive filler-filled polymer composite,  
 211–212  
 materials for, 211  
 for PEMFCs, 218–223  
 materials, 219–223

Bisphenol A-based benzoxazine monomer,  
 212

Bisphenol A-benzoxazine, 229

Bone fixation, 104

Bovine serum albumin (BSA), 83

Bracket style, 334

Brittle fracture mechanism, 160

Broken symmetry (BS)  
 approach, 341  
 configuration, 364

Buckling mode, 170, 171

**C**

Carbon  
 materials, 74

Carbon atoms, 79

Carbon black, 31

Carbon CFRPs, 148

Carbon fiber (CF), 146

Carbon nanotubes (CNT), 93, 119, 123–140  
 experimental, 121–123  
 materials, 120  
 overview, 119, 120  
 results  
 acoustic emission, failure modes, and  
 failure prediction, 139, 140  
 finite element analysis, 124  
 pressure vessel testing, 125–138  
 pressure vessel winding, 125  
 process optimization, 123–140

Carbon/aramid FRPs (A/C1.6) composites, 157

Carbon/carbon FRPs (C/C1.6) composites, 157

Carbon/epoxy composites, ILSS, 119

Carbon-based bipolar plates, 223

Carbon-based coatings, 221–222

Carbon-based magnetic materials, 356

Carbon-based nanomaterials, 104

Carbon-based spin chemistry, 361

Carbon-carbon bond, 337, 345, 347

Carbon-carbon composites, 223

Carbon-carbon stacked coupling, 364–365

Carbon-polymer composite bipolar plate,  
 224–229  
 carbon fillers, 224–226  
 graphene, 226  
 graphite, 224–226  
 polymer matrix, 226–229

Carbon-polymer composites, 229

Carboxyl-modified CNT, 120

Carboxyl-modified MWCNT, 120

Cathode, 218

CFRPs tubes  
 parameters of designed, 150  
 treatment design at 100 °C, 151

Charge neutrality point, 80

Chelates, 361

Chemical vapor deposition (CVD), 4, 107, 175

Chemical vapor infiltration (CVI), 223

Chemically modified graphene, 67

Chengdu Trustwell Company, 205

Clay-supported graphene materials, 71

Clebsch-Gordan coefficients, 330, 331

CNT-modified vessel, 120, 125, 137, 139

CNT-polymer composite, 93

Cohesion failure, 399, 400, 403, 404

Cold plasma, 61



- Commercial epoxy/CNT, 120  
Complementary DNA, detection of, 85  
Complete active-space self-consistent field (CASSCF) methods, 330  
Complete active-space valence bond (CASVB), 330  
Composite bipolar plates, 223  
Composite matrix, 140  
Composite tubes, 149, 154, 157, 170  
Compression tests, FRPs  
    dynamic tests, 151  
    quasi-static tests, 149–151  
Computer-controlled filament winding machine, 121  
Conducting polymers (CPs), 373  
Conductive graphite, 91  
Confocal illumination methods, 34  
Confocal microscopy, 34  
Confocal Rayleigh mapping, 35  
Congener, 351  
Contrast, 35  
Conventional polymer, 66  
COOH and OH, 411  
Cost-effective stainless steel, 121  
Coulomb interaction, 330  
Covalently bonded organic moieties, 68  
Crashworthiness, 145, 149  
Cross-coupling reactions, metal carbene migratory insertion  
    vs. classical palladium-catalyzed cross-coupling reaction, 283  
    X-H insertions, cyclopropanations, and ylide formations, 281  
Cross-linking reaction, 411  
Crushed specimens, modes of  
    three crushing modes, 170  
Crystallinity, 93  
CTAB, 179  
Cutoff wavelength, 29  
Cyclohexene, 338
- D**  
D-band phonon modes, 33  
Debris wedge, 170  
Debye length, 85  
Debye screening, 85  
Decomposition of organic solvents, 64  
Defect-free graphene, 94  
Defectiveness, graphene  
    infrared spectroscopy, 48–49  
    photoluminescence, 49, 50  
Degradation temperature ( $T_d$ ), 239  
Dehydrated condensation reaction (DCR), 408–410  
Density functional theory (DFT), 13, 14, 328, 331, 339, 365  
Density of states (DOSs)  
    Pd@PdO-NDG, 15, 16  
Dental implants, 106–110  
    surface modification, 104–106  
Dental stem cells (SCs), 110  
Deoxyribonucleic acid (DNA), 308  
Department of energy (DOE), 211  
Derjaguin-Muller-Toporov (DMT) model  
    adhesive contact, 431  
    carbon nanotubes, 432  
    elastic modulus map and force-deformation curves, 432  
    long-range force, 431  
    measures, 431  
    nanocomposite surfaces, 431  
    neat epoxy and POSS/epoxy composite, 432  
    NR5 nanocomposites, 432  
Dewar structure, 333, 334, 339, 340  
Diamond-like carbon, 64, 66  
Dicumyl peroxide (DCP), 179  
Differential scanning calorimetry (DSC), 317  
Dirac point, 41, 80  
Direct methanol fuel cell (DMFC), 212, 213  
Dispersed catalyst layer, 217  
DNA detection, G-FET, 84  
Doping, graphene, 38–41  
    absorbance, 39, 40  
    fast optics, 40, 41  
Double Star Company, 205  
Double-beam UV-Vis spectrometer, 29  
Drops tests, 151  
Drude conductivity, 52  
Dynamic force mode  
    constant force contact, 433  
    design, cantilever, 438  
    elastic materials, 433  
    finite element method, 435  
    frequency, 433  
    harmonic responses, 435  
    higher flexural modes and harmonics, 435  
    higher-order flexural modes, 436  
    interpretation of phase image, 435  
    oscillating tip approaches, 435  
    phase shift and surface elasticity, 434  
    polystyrene film, 437  
    probing subsurface information, 436  
    second-order flexural mode, 436  
    tapping, 433, 434  
    tip-sample interactions, 435  
    topographic imaging, 433  
    Young's modulus, 433, 435  
    ZnO film, 436

Dynamic mechanical analysis method, 235  
Dynamic tests, FRPs, 151

## E

E-beam lithography techniques, 360  
EG, 6  
    high-quality graphene sheets from, 11  
    Raman spectra from graphenes obtained from, 10  
Eigenvalue matrix, 354  
Electrical insulators, 224  
Electrical mobility, graphene, 79  
Electrically conductive filler-polymer composites, 91, 93  
    percolation thresholds of, 92  
Electrocatalytic hydrogen production  
    current intensity, PANI/MOF composite, 385  
    CV and SWV outcomes, 385  
    CV outcomes, 385  
    H<sub>2</sub>SO<sub>4</sub>, 385  
    material, 385  
    SWV and Tafel plots, 385, 386  
    TBAP/DMSO, 385  
Electrochemical galvanic cell device, 212  
Electrochemical reactions in fuel cell, 217  
Electrode, 80, 218  
Electron affinity of nitrogen, 15  
Electron delocalization, 328  
Electron density differences (EDD)  
    for Pd@PdO-NDG, 15  
Electron spin resonance (ESR), 266, 360  
Electron transfer channel, 22  
Electron transfer process, 15  
Electron volt (eV), 61  
Electronic delocalization, 351  
Electronic recorder system, 152  
Electronic structure, graphene  
    infrared spectroscopy, 51, 52  
    photoluminescence, 51  
    Raman spectroscopy, 49–53  
    ultrafast optics, 52–53  
Electrophoretic deposition (EPD), 109  
Energy-tunable Raman scattering, 46, 51  
Entanglement bound rubber tube (EBT)  
    model, 195  
Epitaxial graphene, 30  
Epoxy resin, 139  
Epoxy resin 308A3801, 147  
Ethanol, 66  
    nanocarbon and polymeric materials from, 67

Raman spectrum of nanocarbon synthesized from, 67  
Expandable graphite (EG), 5, 7, 10  
    high quality graphene from, 6

## F

Fab-functionalized G-FET, 85, 86  
Fabricated specimens, 149  
FEA axisymmetric analysis, 124  
Feed graphite particles, 97, 98  
Felicity ratio (FR), 139, 142  
Fermi velocity, 44  
Fermi-level shift, 41  
Few layer graphene, 67, 94, 95  
Fiber-reinforced composites (FRPs), 146–171  
    discussion  
        effect of crushing speed on energy absorption, 159, 160  
        effect of hybrid material on energy absorption, 157–159  
        effect of structure on energy absorption, 154–157  
        effect of temperature treatment, 161–169  
        modes of crushed specimens, 169–171  
    experimental procedure  
        compression tests, 149–151  
        dynamic tests, 151  
        manufacturing and temperature treatment, 149  
        materials and design, 147–149  
        microscopic observation, 151–152  
    results  
        microscopic observation, 154  
        quasi-static and dynamic compression, 152–155  
    tube, 146  
Filament winding method, 147, 149  
Filament winding resin, 121  
Filler-polymer composites, 91, 93  
    percolation thresholds of, 92  
Finite element analysis, 124  
Flaw suspected activity, 123  
Flow flooding chamber (FFC), 119  
Fluorescence quenching microscopy, 43  
Fourier transform IR (FTIR), 31  
Fracture cross sections, 154  
Free-space coupling, 34  
Fuel cell, 213–223  
    features, 213  
    fundamentals of, 212, 213  
    operation of, 214

- overview, 211, 212
  - PEMFC, 213–223
- types of, 212
- use in applications, 215
- Functionalized graphene, 67–70
  - formation of, 62
- FWD
  - strain gauges on, 121
  - tensile strains in, 132, 135
- G**
- Gas diffusion layer (GDL), 217
- Gas phase plasma polymerization, 64
- Gas pressure sensors, 264, 265
- G-band phonon modes, 33
- Generalized gradient approximation (GGA), 340
- G-FET
  - biosensing, 81
  - ion-selective response of, 83
  - normalized drain currents of, 83
  - Optical microscope image of channel in, 89
  - pH sensing by, 82
- Glass fiber (GF), 146
- Glode discharge carbonization, 63
- Grade H graphene nanoplatelets, 235
- Graph theory, 329
- Graphene, 226
  - band gap, 79
  - biosensing applications of, 80
  - depiction of, 28
  - electrical mobility, 79
  - flexible sensors, 87, 88
  - functionalization of, 67
  - molecular structure, 80
  - nitrogen in, 13
  - properties of, 227
  - quenching technology for high-quality, 5–9
  - research on, 79
  - sheets, 80
  - two-dimensional material, 81
- Graphene-1
  - AFM images of, 8
  - room -temperature I-V curves of, 9
- Graphene-2
  - AFM images of, 8
  - room -temperature I-V curves of, 9
- Graphene-based coatings, 110
- Graphene-based composites
  - NDG/Pd@PdO, 12–18
  - overview, 3, 4
  - quenching technology for high-quality graphene, 5–9
  - synthesis and antibacterial application of Ag/graphene composite, 9–12
  - synthesis and antibacterial application of Ag/graphene composite, 9–12
  - Synthesis of (001) Facets TGCS, 18–24
- Graphene-based devices, 67
- Graphene-based nanometal, 70
- Graphene coatings with biological environment, 110–111
- Graphene field-effect transistor (G-FET), 80, 84–87
  - detecting molecules, 80–82
  - functionalization of, 84–87
    - DNA detection using complementary strand, 84
    - HSP detection using antibody fragment, 85–87
    - IgE detection using DNA, 84, 85
  - ion sensing using, 82–84
  - with SAW sensor, 87
- Graphene-filled PBA
  - current research, 254
  - electrical conductivity of, 250–252
  - mechanical properties of, 247–249
  - properties, 253
  - water absorption of, 249, 250
- Graphene-filled PBA composites, 229–252
  - curing behavior of, 233–235
  - dynamic mechanical properties of, 235, 236
  - glass transition temperature of, 236–239
  - highly filled, 231, 232
  - specific heat capacity, 239–242
  - thermal conductivity, 244–247
  - thermal diffusivity, 242–244
  - thermal stability, 239
- Graphene nanomaterials, 104
- Graphene oxide (GO), 4, 106
  - structure from Hummer's method, 4
  - TEM image from Hummer's method, 5
- Graphene/rubber nanocomposites, 177–184
  - electrical properties, 187–190
  - gas barrier properties, 190, 191
  - mechanical properties, 184–187
  - other property, 193–195
  - preparation, 176–184
    - latex mixing method, 177–180
    - mechanical mixing, 181–184
    - solution mixing method, 180, 181
  - thermal properties, 192, 193

- Graphenes, 360
- Graphene sheet structure, 8
- Graphite, 224–226
  - crystal structure of, 225
  - properties of, 225
- Graphite bipolar plate, 222
- Graphite-filled PBA, 229–252
  - curing behavior of, 233–235
  - current research, 254
  - dynamic mechanical properties of, 235, 236
  - electrical conductivity of, 250–252
  - glass transition temperature of, 236–239
  - highly filled, 231, 232
  - mechanical properties of, 247–249
  - specific heat capacity, 239–242
  - thermal conductivity, 244–247
  - thermal diffusivity, 242–244
  - thermal stability, 239
  - water absorption of, 249, 250
- Graphite intercalation compounds (GICs), 95
- Graphite nano-sheets
  - as electrical conductive filler, 93, 94
  - from GICs, 95–99

## H

- Hamiltonian elements, 334
- Hamiltonian matrix, 363
- Hartree-Fock (HF) theory, 339
- Heat-shock protein (HSP), 86
- Heisenberg spin Hamiltonian, 329
- Helical substituted polyacetylenes, 309–322
  - helical structure of SPAs, 308, 309
  - properties, 305–307
  - stereoregular SPAs using hodium diene catalysts, 307–308
  - stretched and contracted substituted, 309–317
    - color and helical pitch of solid-state PPA, 309–311
    - functional groups in PPA units, 311–314
    - naphthalene as side group, 314–317
    - with temperature in solid state from stretched to contracted, 317–319
  - HELIOS, 322
  - restricted rotation of C–O bonds, 319–322
- Heteroatoms, 13, 28
- Heuristic concepts, 328
- HF method, 340
- High-quality graphene, 10

- High-quality multilayer graphenes, 11
  - Raman spectra of, 11
- High-resolution TEM (HRTEM), 17
- Homogenous bond coupling, 349
- Homogenous dispersions, 119
- HOMO-LUMO gap, 35
- HRTEM
  - images of TiO<sub>2</sub>, 20
- Hückel schemes, 356
- Hummer's method, 4, 5
- Hybridization, 328
- Hydrazine hydrate (HHA), 193
- Hydro proof test, 121
- Hydrofluoric acid (HF), 19
- Hydrogen evolution reaction, 373, 387
- Hydrogen-free amorphous carbon nitride thin films, 265–268
- Hydrogen-powered fuel cells, 215
- Hydroxyapatite (HAP), 108

## I

- IgE detection using DNA, G-FET, 84, 85
- ILSS
  - impregnation bath temperature on, 124
- Imaging mode, 421
  - AFMA (*see* Atomic force microscopy, nanocomposites)
- Immunoglobulin E (IgE), 83
- Infinite sp<sup>2</sup> network, 28
- Infrared spectroscopy, 31, 32
  - electronic structure, 51, 52
- Inorganic moieties, 71
- Inorganic nanostructures, 9
- Insulator sheet in EV Motor, 415, 416
- Interconversions of helix, 309
- Interdigital transducers (IDTs), 87
- Interlaminar shear strength (ILSS), 119
- Ionic configurations, 330
- Islands, 333, 334

## J

- Johnson-Kendall-Roberts (JKR) Model, 430, 431

## K

- Kekulé structure, 332, 334, 335, 337–343, 345, 346, 348, 351, 353, 354, 361
- Kekulé-type patterns, 328
- Kelvin (K), 61

**L**

Lab-on-a-graphene, 80  
  wireless operation, 87  
Langmuir adsorption isotherm, 86  
Langmuir, I., 61  
Lasers, 34  
Lee-Yang-Parr (LYP), 340  
Lewis structures, 338  
Liquid phase exfoliation, 94  
Liquid phase micro-plasma, 62  
Load-displacement curves of CFRPs, 153  
Local density approximation (LDA), 340  
Local orbitals, 339

**M**

Matrix-dominated properties, 119  
Maximum stress (MX), 125  
MCFCs, 213  
Membrane electrode assembly (MEA),  
  217, 218  
Mesenchymal stem cells (MSCs), 110  
Metal carbene migratory insertion, 282,  
  285–296  
  cross-coupling reactions, 281–282  
  electrophile, 282  
  MCRs, 283  
  Pd-catalyzed MCRs, path A, 287  
    Catellani reaction, 287  
    diazo compounds, allenes, and aryl  
      halides, 285  
    intermolecular benzylation/carbene,  
      287, 288  
    *N*-tosylhydrazone, norbornene, and aryl  
      halide, 286  
    *ortho*-amination/*N*-tosylhydrazone, 289  
    *ortho*-C-H activation, 289  
    Palladium-catalyzed reaction, diazo  
      compounds and aryl halide, 285  
    stereoselectivity, 285  
    synthesis, ketone or enon, 285  
  Pd-catalyzed MCRs, path B  
    C-H functionalization and cross-  
      coupling reaction, 290  
    C-H functionalization, ethyl  
      diazoacetate, 289  
    generation, diazo compounds, 291  
    three-component synthesis, diaryl  
      acetates, 52, 291  
     $\alpha$ -halo-*N*-tosylhydrazones, indoles, and  
      aryl iodides, 291  
  Pd-catalyzed MCRs, path C  
    allylamines, 293  
    allylamines, 59, 292  
    benzaldehyde, tosylhydrazine, vinyl  
      iodide, and malonate, 293  
    C-nucleophiles, 293  
    iodoarenes, malonates, and  
      tosylhydrazones, 295  
    pyrrolidine, 292  
    vinyl iodides, amines, and  
      diazoacetates, 295  
    vinylpalladium halide complex, 291  
     $\eta^1$ -palladium species, 295  
  Pd-catalyzed MCRs, path D  
    C-C bonds, 296  
    *N*-tosylhydrazones, aryl bromides, and  
      terminal alkynes, 296  
    Stille coupling reaction, 295  
    Suzuki-Miyaura coupling one-pot  
      reaction, 296  
    transmetalation, 294  
    synthesis, 282  
  Metal Pd-catalyzed coupling reaction, 12  
  Metal tube, 146  
  Metal-based bipolar plates, 223  
  Metal-based coatings, 222  
  Metallic bipolar plate, 220–222  
  Metal-organic frameworks (MOFs), 3  
  Metal-stabilized carbenes, 281  
    classes, 280  
    free carbenes, 279  
    highly selective transformations, 279  
    intermediates, organic chemistry, 279  
    preparation  
      Bamford-Stevens reaction, 281  
      conjugated ene-yne-ketones, 281  
      decomposition, diazoacetates and metal  
        carbenoid formation, 281  
      *N*-sulfonyl triazoles, 281  
      reactivity profile, 279  
  Methylene blue (MB), 23  
  Michelson interferometer, 31  
  Microelectromechanical systems (MEMS),  
    264  
  Microelectronic applications, 62  
  Microwave plasma, 62, 64  
  Model system, 27  
  Modes of crushed specimens  
    temperature treatment on crushing modes,  
      170, 171  
    three crushing modes, 170  
    variation of high and low energy  
      absorption composites, 169, 171  
  Moiré pattern of graphene superlattice, 45  
  Molecular mechanics (MM), 317

- Molecular models for electronic conduction, 351–356
- Molten carbonate fuel cell (MCFC), 212
- Molten rubber particles, 178
- Monolayer graphene-1, 6  
TEM images of, 7
- Monolayer graphene-2  
TEM images of, 7
- Monosubstituted polyacetylenes, 306
- Mulliken spin populations, 359, 360
- Mulliken-type formula, 337
- Multicomponent reactions (MCRs), 279, 281–300  
copper(I)-catalyzed three-component coupling, *N*-tosylhydrazones, alkynes, and azides, 301  
copper-catalyzed  
alkynyl migration insertion, 298  
three-component coupling, *N*-tosylhydrazones, terminal alkynes, and allyl halides, 298  
three-component reaction, construction of all-carbon quaternary center, 299  
cross-coupling reactions (*see* Cross-coupling reactions, metal carbene migratory insertion)  
development, 302  
metal (*see* Metal-stabilized carbenes)  
mMetal carbene migratory insertion (*see* Metal carbene migratory insertion)  
Rh(I)-catalyzed three-component reaction, arylboronates, diazoesters, and alkyl halides, 301  
Rhodium(I)-catalyzed three-component reaction, 299  
three-component reaction  
diazoesters, terminal alkynes, and alkyl halides, 299
- Multilayer graphene, 30
- Multilayer graphene sheets, 94
- Multi-walled CNT (MWCNT), 119
- N**
- Nafion  
chemical structure, 217
- Nafion®, 217
- Nanoclay hybrid, 71–73
- Nanocomposites, graphene, 71
- Nanomaterial design, 104
- Nanomaterials, 66
- Nanometal hybrid, 70, 71
- Nanosilica, 120
- Nanostructured carbon, 64–73  
formation in aqueous and nonaqueous solutions, 62–72  
functionalized graphene in submerged liquid plasma processes, 67–70  
nitrogen functionalized graphene and nanoclay hybrid, 71–73  
nitrogen functionalized graphene and nanometal hybrid, 70, 71  
unconventional polymers/oligomers/submerged liquid plasma process, 64–67  
future prospects, 74  
and hybrids synthesized by submerged liquid plasma processes, 74
- Nanotopography, surface chemistry, 111
- Naphthalene  
triplet states of, 356
- Natural bond orbitals (NBO), 338–341, 350
- Natural plasma, 61
- Natural resonance theory (NRT), 338–341, 366
- Neutral gases, 61
- NH<sub>2</sub>-functionalized CNT, 120
- Nickel, 221
- Nitrogen functional group in sp<sup>2</sup> carbon domain of graphene, 67–70
- Nitrogen functionalized graphene, 70–73  
HR-TEM images of, 69  
SAED pattern of, 69
- Nitrogen polymer-stabilized Au nanoparticle (NPs-Au), 70
- Nitrogen-doped graphene, 14, 63, 70
- Nitrogen-doped graphene (NDG)/Pd@PdO, 12–18
- Nitrogen-functionalized graphene, 69  
mechanism for formation of, 68
- Non-diagonal matrix element, 346
- Non-Kekulé systems, 361
- Non-oriented polymers, 66
- Non-porous graphite bipolar plates, 222, 223
- Non-thermal plasma, 61
- NPs-Au-stabilized nitrogen functionalized graphene (NPs-Au-NFG), 70
- NRT algorithm, 350
- Nuclear magnetic resonance (NMR), 310
- Nujol, 31
- O**
- Oligomers, formation of, 64–67
- Optical characterization of graphene, 29–55  
methods

- absorbance spectroscopy, 29, 30
- infrared spectroscopy, 31, 32
- photoluminescence, 35, 36
- Raman spectroscopy, 32–34
- Rayleigh Imaging, 34, 35
- ultrafast optics, 36
- properties
  - defectiveness, 46–50
  - distinction of effects and combination of techniques, 53–55
  - doping, 38–41
  - electronic structure, 49–53
  - strain, 41, 42
  - thermal, 37, 38
  - thickness and stacking, 42–46
- Optical microscopy, 43
- Optothermal technique, 37
- Orbital factor, 332
- Organic chemistry, 328
- Organic compounds, 64
- Organic moieties, 67
- Organic molecular magnetism, 356
- Organic polymer, 68
  - formation of, 66
- Organic polymers, 328
- Organic solvents, 66
- Organic solvents, decomposition of, 64
- Overlap matrices, 337
- Overlap matrix, 333, 335, 342, 348
- Oxygen transmission rate (OTR), 191
  
- P**
- P significant type II activity*, 142
- Packing density of PBA composites, 233
- PAFCs, 212
- PAHs, 328
- Palladium acetate, 14
- PBA, 231–252, 254
  - formation of resin, 230
  - graphite- and graphene-filled, 229–252
    - curing behavior, 233–235
    - current research, 254
    - dynamic mechanical properties of, 235, 236
    - electrical conductivity of, 250–252
    - glass transition temperature of, 236–239
    - highly, 231, 232
    - mechanical properties of, 247–249
    - specific heat capacity, 239–242
    - thermal conductivity, 244–247
    - thermal diffusivity, 242–244
    - thermal stability, 239
    - water absorption of, 249, 250
- PBASE
  - structural formula of, 84
- Pd@PdO clusters, 13–15
  - TDOSs, 15
- Pd@PdO-graphene
  - EDD, 17
- Pd@PdO-NDG
  - DOS of, 15, 16
  - EDD, 17
  - practical application of, 17
  - Suzuki coupling reactions with, 18
  - TEM images of, 17
- Pd@PdO-NDG composite, 14
- PdO clusters, 15
- Peak load, 149
- PEMFC, 213, 216
- Pentacene, triplet states of, 356
- Percolation threshold, 91, 93
- Percolation thresholds, 92
- Periodontal ligament stem cells (PDLSCs), 111
- Phenalenyl, 360
- Phenolic resins, 212
- Phonon annihilation, 33
- Phonons, 32, 36
- Phosphoric acid, 213
- Phosphoric acid fuel cell (PAFC), 212
- Photocatalyst, 23, 24
- Photodegradation of MB, 23
- Photoexcited electrons, 41
- Photoluminescence, 35, 36, 49, 50
- Piezo-electric sensors, 123
- Planar carbon molecules, 28
- Planetary-ball milling, 95
- Plasma, 61
  - classification, 61
  - development in liquid, 64
  - discharges in organic liquids, 62
  - discharges in water, 62
  - radicals generated in, 62
  - submerged liquid plasma, 63
  - temperature generated during, 61
- Plasma bonding of plastic films, 408, 414–416
  - AFM surface morphologies, 400
  - applications
    - insulator sheet, EV Motor, 415, 416
    - solar cell back-sheet, 414, 415
  - back-sheet of solar cell panel, 393
  - COOH and -OH, 395, 403
  - COOH by FTIR, 405–408
  - cross-linking layer, OCP, 408
  - detection, 416

- Plasma bonding of plastic films (*cont.*)
- direct bond, 395
  - FTIR measurements, 398
  - FTIR outcomes, 417
  - FTIR transmission spectrum, non-irradiated PET film, 406
  - FTIR-ATR differential spectrum, 407
  - FTIR-ATR spectra, 406
  - GCMM, 403
  - graphic formula, PET, 392
  - hand peeling, 400
  - heat-press apparatuses, 397
  - inorganic films, PET, 394
  - laminations, 416
  - lifetime of irradiated surface, 393
  - mechanism, 409
  - molecular weight, GPC, 403
  - OH by FTIR, 408
  - oxygen plasma-irradiated PET films, 416
  - peel strength, 416
  - plasma irradiation, 403
  - press bonding temperature, Peel test, 399, 400
  - processes and strength evaluations, 396, 397
  - reports, 394, 395
  - research, 417
  - sample characterizations, 397, 398
  - samples and plasma irradiations, 395, 396
  - soaking, 399
  - soaking test, 417
  - solar cell back-sheets, 392–393
  - Sp vs Tp, 403
  - strength and contact angle, 404, 405
  - surface chemical, XPS, 401, 402
  - ultralong lifetime (*see* Ultralong lifetime of plasma-irradiated active surface)
  - utility, PET Films, 391–392
  - wet-peel test, 403, 411
  - XPS peak intensity ratios, 402
  - XPS spectra, 401
- Plasma-enhanced chemical vapor deposition (PECVD), 263
- p-n*-hexyloxyphenylacetylene (pHxOPA) monomer, 309
- p-n*-octylphenylacetylene (pOcPA), 312
- Polyacenes, 351–356
- Polyacetylene (PA), 306
- Polyacetylene ester, synthesis of, 320
- Polyaniline-based metal-organic framework (PANI/MOF), 375–377, 379–387
- characterization techniques
    - Auriga field emission scanning electron microscope (FESEM), 376
    - crystal structure, 375
    - electrochemical measurements, 376
    - energy-dispersive X-ray spectra, 376
    - FTIR spectra, 376
    - Raman spectra, 376
    - TGA, 376
  - composition, 387
  - CPs, 374
  - electrochemical reduction, 373
  - electrochemistry
    - current-potential curves, gold electrode, 382
    - CV and SWV outcomes, 382
    - cyclic voltammogram, 384
    - diffusion-controlled electron-transfer process, 384
    - DMSO/TABP system, 383
    - DMSO/TBAP, 383
    - materials, 382
    - reduction processes, 382
    - voltammogram, 383
  - HER, 373, 374
  - hydrogen fuel cell technology, 373
  - hydrogen production, 374
  - materials, 374–375
  - morphological characterization
    - composites, 380
    - EDS outcomes, 381
    - nanorods/fibre structures, 380
    - SEM image, 380, 381
    - TEM images, 381
  - outcomes, 374
  - porous materials, 374
  - preparation, 375, 387
  - spectroscopic characterization
    - absorbance vs. concentration, 377
    - composites, 377
    - DMSO, 377
    - energy band gap determinations, 379
    - FTIR spectrum of synthesis, 377
    - outcomes, FTIR, 377
    - Raman spectra, 377
    - TGA outcomes, 379
  - synthesis, 374
- Polyaromatic hydrocarbons, 355
- anthracene, 347–351
  - naphthalene molecule, 341–347
- Polybenzoxazine, 247
- Polybenzoxazine (PBA) resins, 212
- Polycyclic aromatic hydrocarbons (PAHs), 328
- Polycyclic conjugated hydrocarbons, 351
- Polyethylene naphthalate (PEN), 87
- Polymer composites, 223
- Polymer electrolyte membrane, 217
- Polymer electrolyte membrane fuel cell (PEMFC), 212



Polymerizations, 63  
Polymers, 224  
     $\pi$ -Conjugated, 305  
Polyvinylpyrrolidone (PVP), 4  
Post-crush specimens, 151  
Post-crushed tubes, 152  
Pressure vessel testing, 125–138  
    burst of pressure vessels with CNT,  
        135–138  
    burst tests, 131–134  
    proof tests, 125–131  
Pressure vessel winding, 125  
Pristine graphene  
    Raman spectra of, 33  
Pristine graphite, FTIR transmittance spectra  
    of, 32  
Proof test  
    displacements in, 129, 131  
    setup of, 122  
    strains in, 127–130  
Proton exchange membrane fuel cell  
    (PEMFC), 212–223  
    bipolar plates for, 218, 219  
    materials, 219–223  
    components, 216–218  
        anode and cathode, 218  
        electrode, 218  
        MEA, 217, 218  
    operation of, 215, 216  
Proton exchange membrane fuel cells  
    (PEMFCs), 211  
Prototypic systems, 327  
Ps2Ocp, 321, 323  
P<sub>Significant Type II activity</sub>, 139  
Pyrene compounds, 84  
Pyridinic nitrogen, 70  
Pyrrolic nitrogen, 70

**Q**  
Quasi-static tests, FRPs, 149–151  
Quenching technology, 5–9

**R**  
Radical-type resonance structures, 334  
Raman spectra  
    from graphenes obtained from EG, 10  
    of high-quality multilayer graphenes, 11  
Raman spectroscopy, 32–34  
Raman-active modes, 32  
Rayleigh imaging, 34, 35  
Receptor molecules, 84, 85  
Reduced graphene oxide (rGO), 106, 177–179,  
    181, 184–186, 193, 202–205

Resin, 91, 93, 212, 226  
Resin viscosity, 120  
Resins, resonance, 329  
Resonance structures, 331  
Resonance structures of polyacenes, 352  
Rh-catalyzed polymerization, 316  
Rh-catalyzed polymerization of pHxOPA  
    monomers, 310  
Rh–diene polymerization system, 307  
Rubber matrix, 176, 178, 181, 183–185,  
    190–192, 198, 204  
Rubber-carbon/epoxy composite interface, 141  
Rumer algorithm, 333, 342, 343

**S**

SAW-driven G-FET device, 88  
Scanning electron microscope (SEM), 266  
Selected-area electron diffraction (SAED), 69  
Self-consistent orbitals, 337, 344, 350  
Sensors, graphene, 87, 88  
Separator plates, 216  
Shanghai synchrotron radiation facility  
    (SSRF), 22  
Signal detection, 123  
Silicon electrodes, 66  
Silicone rubber frame, 80  
Silver nanoparticle (NP), 9, 10  
    HRTEM image of, 12  
Single layer graphene, 44, 67, 94, 95  
Singlet-triplet processes, 353  
Small angle X-ray scattering (SAXS), 202  
Soaking, irradiated films in liquids, 399  
Sodium dodecyl sulfate (SDS), 10  
Soft X-ray absorption spectroscopy  
    (soft-XAS), 22  
Solar cell back-sheet, 392, 393, 414, 415  
Solid oxide fuel cell (SOFC), 212, 213  
Solid state theories, 351  
Solution-polymerized styrene-butadiene  
    rubber (SSBR), 185, 197–199  
sp<sup>2</sup>-bonded carbon atoms, 11  
sp<sup>3</sup> carbon, 67  
Specific energy absorption (*Es*), 146, 149  
Specimens, 121, 149  
    load-displacement curves of, 153  
    post-crush, 151  
    tested in quasi-static tests, 159  
Spin coupling, 327  
Spin density maps  
    for experimental structure of dimeric, 364  
    for hypothetical phenalenyl dimer, 365  
Spin Hamiltonian matrix, 335  
Spin polarization topology, 356  
Spin-coupled valence bond, 341

- Spin-coupling algebra, 350  
 Spin-coupling effective Hamiltonian, 331–336  
 Spin-coupling paradigm, 328–331, 365  
 Spin-coupling resonance, 339  
 Spintronics, 328  
 Spiro-bis(3,7-dimethoxy-1,9-dioxophenalenyl) boron, 361  
 Splaying mode, 170, 171  
 Sputtering, 263–268  
 Stack, fuel cell, 216  
 Stage index, 95  
 Stage structure, 95–99  
 Stainless steel alloys, 221  
 Standard coordinate system, 149  
*Staphylococcus aureus*, 109  
 Static crushing studies, 145–146  
 Stereoregular mono-substituted polyacetylenes (SPAs), 308, 309  
 Stereoregular substituted polyacetylene, 307  
 Stokes condition, 33  
 Strain gauges (SG), 121  
 Strain, graphene, 41, 42  
   infrared spectroscopy, 41, 42  
 Strain-induced crystallization (SIC), 195  
 Streptavidin (SA), 83  
 Structural health monitoring, 142  
 Styrene-butadiene rubber (SBR), 178  
 Submerged liquid plasma, 63, 64  
 Submerged liquid plasma processes, 64–67  
   functionalized graphene in, 67–70  
   future prospects, 74  
   nanostructured carbon and hybrids synthesized by, 74  
   nitrogen functionalized graphene and nanoclay hybrid by, 71–73  
   nitrogen functionalized graphene and nanometal hybrid by, 70, 71  
 Sulfonated polymer, 217  
 Surface-acoustic wave (SAW) sensor, 87  
 Surface-enhanced Raman scattering, 34  
 Suzuki coupling, 328  
 Suzuki coupling reactions, 18  
 Suzuki-Miyaura reaction, 13, 17
- T**  
 T700SC-12k carbon fiber, 147  
 TEM  
   images of Pd@PdO-NDG, 17  
   images of TGCS-1, 20  
   of AGC-1, 12  
 Tetracene, triplet states of, 356  
 Thermal plasma, 61  
 Thermal properties of graphene  
   Raman Spectroscopy, 37, 38  
   Thermal reduced graphene oxide (TRGO), 181, 185, 190–193  
   Thermal properties of graphene, 37–38  
   Thermochromism, 361  
   Thermoplastics, 227  
   Thermosetting resins, 227, 231  
 Thin graphite sheet, 96  
 Thin graphite sheets, 95  
 Time-resolved spectroscopy techniques, 36  
 TiO<sub>2</sub>/graphene composites (TGCS), 18–24  
   XRD patterns of, 21  
 Tissue engineering, 110  
 Total density of states (TDOSs), 15  
 Transmission electron microscope (TEM), 6  
 Triangular graphenes with spin, 356–365  
 Triangulene  
   population analysis of the 6-, 360  
   resonance structure of, 362  
 Triangulenes, 358, 359  
 Trigonal prism, 364  
 Trigonal symmetry, 359  
 Tri-layer graphene-2  
   TEM images of, 7  
 Tri-t-butyl-6-oxophenalenoxyl, 360  
 TritonX, 98  
 Tunable chemistry, 104, 107  
 Two-dimensional nature of graphene, 28
- U**  
 Ultrafast optics, 36  
   electronic structure, 52–53  
 Ultralong lifetime of plasma-irradiated active surface  
   DCR, 409, 410  
   hydrogen bonding, 410, 411  
   soaking effects, 412, 413  
 Ultra-narrow graphene nanoribbons, 51  
 Ultrasonically assisted latex mixing and in situ reduction (ULMR) method, 177  
 Unconventional NPs, HR-TEM image of, 72  
 Unconventional polymers, 67  
   formation of, 64–67  
 Unsaturated organic solvents/compounds, 66  
 UV-Vis spectroscopy, 29
- V**  
 Valence bond (VB) theory, 329  
 Valence bond approach, 329  
 Valence bond method, 328, 330  
 Valinomycin, 82  
 van der Waals force of attraction, 67  
 van der Waals forces, 5  
 van der Waals interaction, 30, 42, 96

van der Waals interaction energy, 95  
Vapor-grown carbon fibers, 93  
VB approach, 331  
VB method, 330  
Virtual, 49  
Virtual orbitals, 339, 351  
Virtual-type NBOs, 339  
Vulcanization mechanism, 200–203

**W**

W needle, 66  
Water transmission rate (WTR) coefficient,  
190–191  
Water-heated impregnation bath, 121  
WDW-100KN universal testing machine, 149  
wide-angle X-ray scattering (WAXS), 310, 311

**X**

XAS  
Ti L-edge, 22, 23  
X-ray diffraction (XRD), 21  
X-ray photoelectron spectroscopy (XPS), 21,  
202, 203  
of C1s, 22  
X-ray-induced Auger spectra (XAES), 202

**Y**

Young tableaux, 333  
Young's modulus, 3

**Z**

Zero-order ground state energy, 346